

**Document Version**

Final published version

**Citation (APA)**

Timmer, W. A. (2026). *On the Aerodynamic Design and Performance of Wind Turbine Blade Airfoils*. [Dissertation (TU Delft), Delft University of Technology]. <https://doi.org/10.4233/uuid:d5dbe35d-7445-49ba-84ae-5b717100b257>

**Important note**

To cite this publication, please use the final published version (if applicable).  
Please check the document version above.

**Copyright**

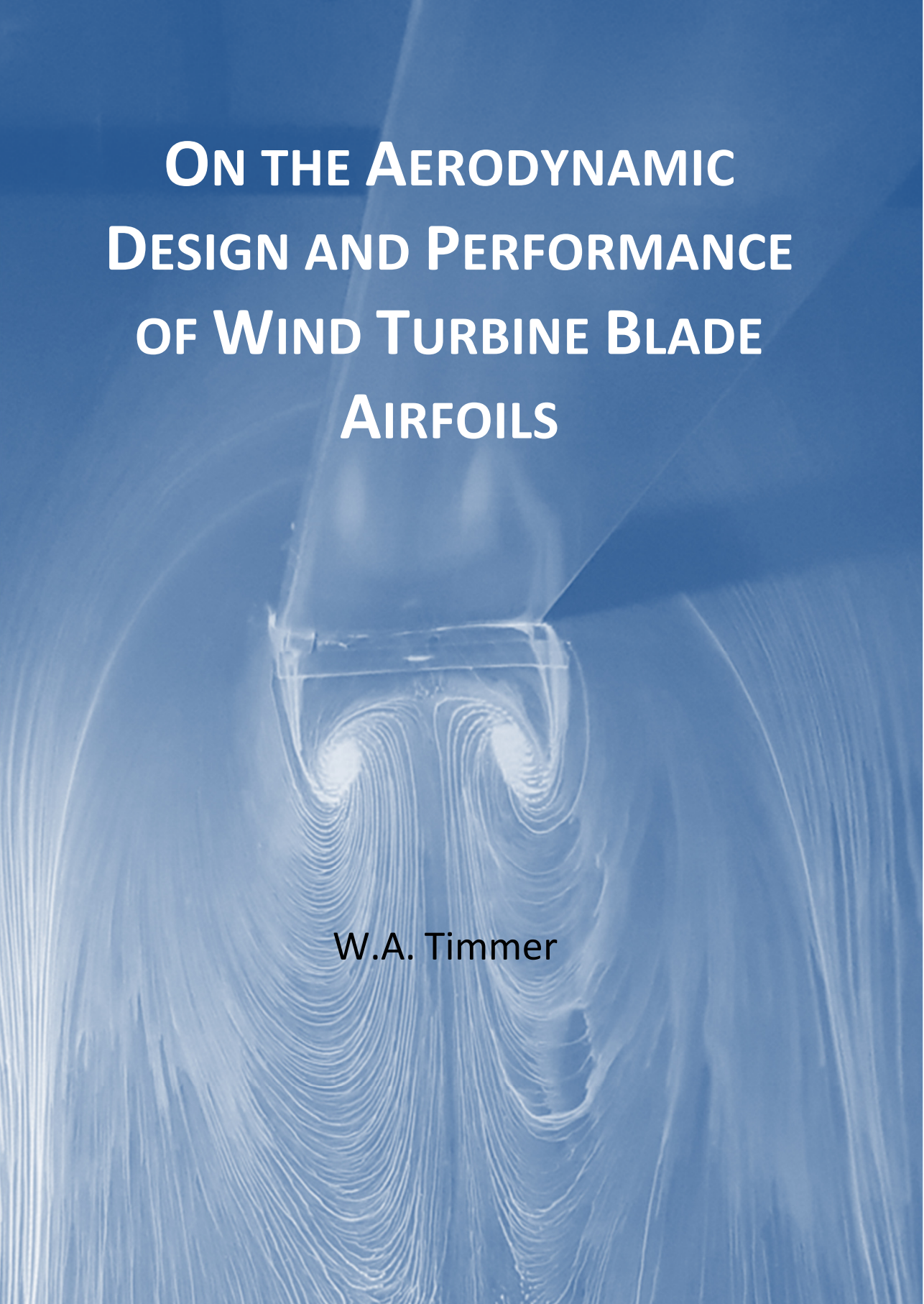
In case the licence states "Dutch Copyright Act (Article 25fa)", this publication was made available Green Open Access via the TU Delft Institutional Repository pursuant to Dutch Copyright Act (Article 25fa, the Taverne amendment). This provision does not affect copyright ownership.  
Unless copyright is transferred by contract or statute, it remains with the copyright holder.

**Sharing and reuse**

Other than for strictly personal use, it is not permitted to download, forward or distribute the text or part of it, without the consent of the author(s) and/or copyright holder(s), unless the work is under an open content license such as Creative Commons.

**Takedown policy**

Please contact us and provide details if you believe this document breaches copyrights.  
We will remove access to the work immediately and investigate your claim.

The background of the cover features a detailed aerodynamic flow visualization around a wind turbine blade airfoil. The flow lines are depicted as a series of fine, white, curved lines that curve around the airfoil, illustrating the complex flow patterns and pressure distribution. The entire scene is set against a solid blue background.

# **ON THE AERODYNAMIC DESIGN AND PERFORMANCE OF WIND TURBINE BLADE AIRFOILS**

W.A. Timmer



# ON THE AERODYNAMIC DESIGN AND PERFORMANCE OF WIND TURBINE BLADE AIRFOILS

Dissertation

for the purpose of obtaining the degree of doctor  
at Delft University of Technology  
by the authority of the Rector Magnificus, Prof.dr.ir. H. Bijl  
chair of the Board for Doctorates  
to be defended publicly on  
7 May 2026 at 15.00 hrs

by

**Wijnand Alex TIMMER**



This dissertation has been approved by the promotor

Composition of the doctoral committee:

Rector magnificus, Prof.dr. F. Scarano	chairperson Delft University of Technology, promotor
---	---

Independent members:

Prof.dr.ir. L.L.M Veldhuis	Delft University of Technology
Prof.dr. S.J. Watson	Delft University of Technology
Prof.dr. H.A. Madsen	Technical University of Denmark
Prof.dr.ir. C.P. van Dam	University of California at Davis, USA
Dr.Ir. J.G. Schepers	TNO, The Netherlands

Other members:

Dr.ir. D.A.M. De Tavernier	Delft University of Technology
----------------------------	--------------------------------

*Keywords*      Airfoils, wind turbine blades, deep-stall, zigzag tape roughness  
Strouhal number

*Printed by*      Gildeprint

*Cover*            Fluorescent oil flow picture of the wake behind an airfoil model  
normal to the wind (figure 9.10, this dissertation)

Copyright © 2026 by W.A. Timmer

ISBN 978-94-6496-567-4

An electronic version of this dissertation is available at  
<http://repository.tudelft.nl/>.





# ACKNOWLEDGEMENTS

The contents of this dissertation oversees some forty years of wind turbine technology. Looking back at the many years being a member of TUDelft's scientific community, it is almost undoable to thank everyone I collaborated with and who supported me in the course of time, without extending this already comprehensive document with many additional pages. Instead, I would like to mention a few people that I feel have particularly helped shaping the work presented here, for which I'm very grateful, hoping that those who are not mentioned will forgive me.

To start with, there's my Master thesis supervisor at TUDelft, Loek Boermans, who taught me the ins and outs of a proper wind tunnel test, encouraged me to always strive for quality and urged me not to forget the first principle of performing meaningful measurements: meticulously log every unexpected thing you encounter, every model configuration tested and every change you make to the setup during the test in great detail. This golden advice helped me many times to explain differences in wind tunnel test results later on. It also enabled me to easily re-process data from 1992 measurements for this dissertation.

Many thanks go to Gijs van Kuik and Gerard van Bussel, who consecutively headed the Wind Energy section many years. Being pioneers in wind energy themselves, their perseverance guided our research group through quite turbulent times, when it was not at all clear to everyone in the university that wind energy could be a valuable contribution to the world's energy mix. They furthermore had the vision to let me do my thing, even if from time to time my experimental skills were spent on sports aerodynamics and not on wind turbine aerodynamics, which, I must admit, contributed greatly to my belief I had a wonderful job.

Utilizing a high quality wind tunnel is only one side of the aerodynamic testing medal. The other side is highly skilled technical staff, taking care of the equipment and testing environment. I would like to thank them all, at the High Speed Lab, but particularly at the Low-Speed Lab (where I spent most of my testing time), in the person of Stefan Bernardy. If it comes to instrumentation, equipment, model construction and manufacture and dozens of other things, Stefan is the man to turn to, which contributes tremendously to a successful test.

And then Leo Veldhuis, friend and colleague. I'm very grateful for the many interesting chats, laughs and discussions we had, on and off work. On aerodynamics, of course, but also on life and a myriad of other topics. Together we developed the Nagano Olympic zigzag strips, which put speed skating aerodynamic drag and race suits back on the research agenda. It even brought us a plaque on the Aerospace Faculty Wall of Fame, of

which, to be frank, I'm quite proud, considering who's plaques are on the wall as well. A big thank you goes to Ruud van Rooij. Coming in as a master student, he became a very appreciated colleague and for many years we worked together on the design and testing of airfoils and blades, which research certainly would not have been as successful without him. Being an aimiable person with a sharp eye for detail, he later on became a valuable asset for the department's management as well. We were office-mates for more than thirty years, so in a way we had a long-term relation. I cannot remember we had an unpleasant conversation in our work-place ever.

This chapter would not be complete without thanking Sylvia Willems and Colette Russo. It is not exaggerated to say that as management assistants they are the oil in the departments management machine. Thank you for answering my questions and solving all the practical problems in such a swift and pleasant way, even in times that your work got busier and busier due to the growing number of staff.

I would also like to thank Elena Llorente (Nordex Energy), Jesper Madsen (LM Wind Power), Andreas Benkel (DNW), Henk-Jan Kooijman (EWT), Nicholas Balaesque (DWG) and Guanqun Xu (TU Delft). The permission to use their experimental data in this dissertation is gratefully acknowledged.

Last, but absolutely not least, I'd like to thank my promotor Fulvio Scarano. I very much admire his patience with me. I put it to the test quite a few times. With his timely questions about the progress I made he stimulated me to not to slow down too much. He reviewed my first concept and unfortunately had to do it all over again, as the second concept was at least 30% different, for which I apologize. He, however, did not complain.

A very special thanks goes to my beloved partner Gera. During the preparation of this dissertation she frequently must have wondered what on earth I was doing, why not just handing it in as it already was good enough. She, however, never complained, knowing that I value quality (at least in my definition) more than speed. She's the (green) fuel of my life-jet already for many years and keeps me, together with her children, Jiri, Yalou and Wus, young at heart. I'm blessed that she chooses to share her life with me and I hope we can enjoy concerts, theatre and movies together still for a very long time.

I would like to dedicate this work to my children Eefje, Jonas and Marieke, whom I love so dearly. They have different characters and are special to me, each in their own quality. I admire the way they choose their path in life and they prevent me from becoming anywhere near a grumpy old man. I'm proud to be their dad.

And then there's Sunny, our grandchild. Her name says it all.

Nando Timmer

April 2026

# SUMMARY

Wind energy has become one of the most important sources of sustainable energy and is still expanding. In the last 40 years, the size of wind turbine rotors has increased with a factor of 10, to a diameter of over 220m at present. Theoretical and experimental aerodynamic research has contributed substantially to this achievement. The aerodynamic performance of the rotor blades, in all kinds of weather conditions, is of paramount importance to the income part of turbine economics and consequently for a successful and economically viable turbine. This makes the blade sections, the airfoils, responsible for the core performance of the blade, an important contributor to a successful design.

This dissertation seeks to investigate airfoil performance; as a result of design strategy or as a result of operational requirements and conditions. The first part, consisting of chapters 2 to 5, is dedicated to airfoil performance in the operational range of angles of attack. The second part treats the characteristics in what is called the deep-stall region, with incidences showing leading edge flow separation.

## **Historic overview of airfoils used for wind turbine blades.**

In chapter 2 a historical overview is given of airfoil development in the past 4 decades. The early big-turbine projects in the 70's and 80's relied on aerospace airfoils predominantly from the NACA 4- and 5-digit series, developed in the 30's and 40's. These are turbulent airfoils, principally generating high lift by a growing suction peak at the section leading edge with increasing angle of attack. After the big-turbine projects failed, in the 80's and 90's initially these airfoils were also used for smaller turbines with fixed blade pitch and constant rpm to control peak power, also referred to as the stall concept. However, in an early stage it appeared that these airfoils were very sensitive to contamination of the leading edge, resulting in substantial power degradation. What follows in the next years, is a quest to find the right airfoils for this type of power control, leading to dedicated designs, better suited for the operational conditions. Bigger turbines emerged, with a variable rotational rotor speed and blade pitch control concept, using a mix of special purpose sections and laminar NACA 6-series airfoils in the blades.

As a result of weight and load limitations, present large rotor diameter blades are long and slender, requiring airfoils with a high design lift coefficient and, as a result of atmospheric turbulence considerations, a high maximum lift coefficient. These airfoils have a turbulent character. Hence, 40 years after turbulent airfoil designs fell out of favour, they are used again for wind turbine blades, albeit with a different combination of angles for maximum lift-drag ratio and maximum lift.

At present, airfoils are being designed with multidisciplinary optimization codes, using direct design, as opposed to the early dedicated sections, resulting from inverse design, which basically is finding a shape on the basis of a prescribed pressure distribution.

### **Analysis and design with XFOIL and RFOIL at high Re-numbers.**

Owing to the very fast solution rate, the flow solver in the vast majority of optimization codes is the panel code XFOIL, or its derivative RFOIL. Chapter 3 reports on the accuracy of predictions with RFOIL and XFOIL for moderate and high Reynolds numbers, mainly by using comparisons with either experiments on DU-airfoils in the TU Delft low-turbulence tunnel LTT, or on airfoil DU00-W-212 in the high pressure tunnel, DNW-HDG, in Göttingen, Germany. It appears, that for Re-numbers up to about  $9 \times 10^6$  RFOIL may still be used due to its better prediction of the maximum lift. For higher Re-numbers XFOIL is the better option, albeit with modification of the A and B parameters in the G- $\beta$  locus equation, to ameliorate stall prediction. For the entire Re-number range from  $3 \times 10^6$  to  $15 \times 10^6$  of the DNW-HDG experiments, RFOIL and XFOIL underpredict drag by approximately 14% and predict the maximum lift coefficient with a good amount of accuracy. XFOIL and RFOIL struggle with performance prediction of airfoils with (severe) leading edge roughness and thick trailing edges, such as flatback sections. As in this dissertation experiments in the LTT are often used for comparison, an exposé is given of the layout and flow quality of that wind tunnel. Methods of data reduction and measurement techniques are described.

### **Requirements for wind turbine blade airfoils and the impact of roughness and erosion.**

Chapter 4 describes the requirements for wind turbine blade airfoils and highlights important issues pertinent to airfoil design. Using an example of airfoil design optimization at  $Re=9 \times 10^6$  involving atmospheric turbulence with 4 perturbations on the angle of attack between  $0^\circ$  and  $6^\circ$ , it is pointed out that good average lift-drag performance in turbulent conditions drives the airfoil shape away from point design and in the direction of sections with forward camber, having a turbulent character.

Using a number of wind tunnel results on various airfoils the remainder of the chapter is dedicated to the impact of roughness (due to zigzag tape, grit roughness and sandpaper) and erosion (mimicking several stages) on section and rotor level. It is shown that wrap-around roughness is giving higher losses than zigzag tape. Roughness (grit) height seems more important than density or wrap-around length. Lift-drag ratio reductions due to grit roughness of 40% or more and maximum lift reductions of 25% are common values. Severe erosion can lead to even worse performance.

An almost endless variation of roughness patterns and erosion stages may be encountered in practice. In general, the impact of roughness or erosion is calculated using

BEM calculations with characteristics representing airfoils with rough or eroded leading edges. Losses in annual energy production concentrate on values between 0.5% to 5%. A study with a view to establish the zigzag tape critical roughness height was only partly successful. While measurements on airfoils DU93 and DU97 using tape of 0.185mm and 0.310mm (DU93) and 0.25mm thickness (DU97) at  $x/c=5\%$  all indicate critical roughness Reynolds numbers in the range  $220\pm 5$ , 0.185mm thick tape on DU97 only showed  $R_{k,crit}=179\pm 4$  for incidences between  $4.1^\circ$  and  $8.2^\circ$ . Would the tape thickness have been 0.205mm, only 0.02mm thicker, values of  $219\pm 4$  would have been found for this incidence range, showing the sensitivity of the calculation to the actual tape height. The tests seem to corroborate a flat plate critical Reynolds number of approximately 200.

### **Impact of surface finish, leading edge protection and trailing edge serrations.**

Chapter 5 reports on a study involving a model drawn from an actual blade mould, representing the NACA 63<sub>4</sub>-421 airfoil. The impact of paint, zigzag tape, trailing edge serrations and leading edge protection (LEP) with and without vortex generators in their practical application is investigated.

It is shown that the edges of the protection layer, when not properly smoothed out cause premature transition and in this case lead to a reduction of 44% in average lift-drag ratio, which could only for a small part be cured by 3mm high vortex generators at the upper side 50% chord station. A modified LEP-layer, stretching further aft, with smoothed steps led to a loss of only 6.4 %.

The characteristics of the model with trailing edge serrations pointing in chord direction ( $\beta=0^\circ$ ) were estimated, based on measurements with  $\beta=11^\circ$  and RFOIL calculations on an airfoil with a flap. The resulting lift-drag values were always lower than the original airfoil. It is further stipulated that regarding all the sources of possible flow disturbances and the increasing Re-number of modern blades, it is hardly imaginable that substantial parts of the blade outboard stations will be, or stay, laminar. This opens the possibility to design airfoil using turbulent flow.

### **Deep-stall angle prediction.**

Chapter 6 describes the impact of airfoil shape, roughness and Reynolds number on the value of the deep-stall angle ( $\alpha_{DS}$ ), which is the angle giving full leading edge separation as a result of leading edge laminar separation bubble bursting. It is marked by a sharp stall and a substantial drag increase. It appears that a linear relation exists between  $\alpha_{DS}$  and the  $y/c$  coordinate at  $x/c=0.0125$  at the airfoil suction side. The angle increases with increasing Reynolds number or increasing 2D blockage ratio  $c/h$ , where  $c$  is the airfoil chord and  $h$  is the effective height of the wind tunnel test section.

It is shown that recovery from a hysteresis loop can only occur at an angle, smaller than

the deep-stall angle, for which the base pressure is equal to or higher than the base pressure at an angle just prior to  $\alpha_{DS}$ .

Suppression of the bubble by tripping the laminar boundary layer, eliminates the sharp stall and drag increase.

### **Airfoil Performance at deep-stall angles.**

Chapter 7 investigates the airfoil characteristics in the angle of attack-range between  $-180^\circ$  and  $180^\circ$ . Results of tests involving several DU airfoils are presented at Re-numbers between  $0.5 \times 10^6$  and  $8 \times 10^6$ .

The most salient result is the fact that airfoils in the range of incidences between  $60^\circ$  and  $90^\circ$  (and the equivalent at negative angles) have equal base pressure irrespective of section shape and Re-number. This is caused by the fact that separation always takes place close or at the apex. Differences in drag come from the velocity differences over the upwind front and rear of the airfoil as a result of lower side section shape.

It is further shown that substantial flow distortion occurs over the downwind side of a model with high blockage ( $c/h > 0.25$ ) and low aspect ratio ( $b/h < 3$ ), where  $b$  is the span of the model.

### **Vortex shedding at very high incidences, Strouhal numbers.**

In chapter 8 the Strouhal numbers ( $St$ ) of DU91 at  $Re = 0.5 \times 10^6$  and  $0.7 \times 10^6$  are presented, measured in the LTT. DU00-W-212  $St$ -values at Re-numbers between  $6 \times 10^6$  and  $8 \times 10^6$  come from tests in the DNW-HDG. In a  $C_d$ - $St$  graph, values for negative and positive angles fall on the same curve. Based on the available data it is stipulated that the curve for DU91 may be generally valid, for all sections and Reynolds numbers.

### **Airfoil maximum drag prediction at low and high Reynolds number.**

Chapter 9 describes a method to predict the maximum drag coefficient of airfoils at Reynolds numbers below approximately  $1.7 \times 10^6$  based on measurements in the TU Delft LTT. The method calculates a contribution due to the airfoil leading edge thickness in terms of the lower- or upper-surface  $y/c$ -coordinate at  $x/c = 0.0125$  using airfoil models with varying leading edge thickness and zero trailing edge angle. The contribution of the trailing edge combines the flow angle at the trailing edge with a sensitivity factor related to the afore mentioned  $y/c$  coordinate. Comparison with measured airfoil maximum drag coefficients in the same Reynolds number range found in the public domain gives differences up to 2.1% with an average of -0.2%

For Reynolds numbers in the order of  $3.5 \times 10^6$  to  $8 \times 10^6$  the contribution of the leading edge thickness was redefined based on measurements in the DNW-HDG wind tunnel. Using the existing formulation for the contribution of the trailing edge angle to the

maximum drag coefficient, prediction errors for airfoils DU91-W2-250 and DU00-W-212 amount to values less than 0.5%

### **The airfoil lift-drag ratio in two-dimensional, non-rotating and rotating configurations.**

Finally, chapter 10 treats the impact of aspect ratio on the lift-drag ratio of airfoils in non-rotating and rotating blades.

As a result of the small value of  $C_t/C_n$  of airfoils in deep-stall :

- The lift-drag ratio of an airfoil is largely independent of aspect ratio.
- The lift-drag ratio of an airfoil is independent of Reynolds number.
- The lift-drag ratios of the various sections of a wind turbine blade coincide with their two-dimensional curve, irrespective of rotation.
- The lift-drag ratio varies with leading edge upwind thickness parameter. The higher the upwind  $y/c$  at  $x/c=0.0125$ , the higher the zero-lift angle and lift-drag ratio at  $90^\circ$ .
- The lift-drag ratio varies with trailing edge angle. The higher the trailing edge angle (measured positive counter-clockwise), the higher the zero-lift angle and the lift-drag ratio at  $90^\circ$ .



# SAMENVATTING

Windenergie is een van de belangrijkste bronnen van duurzame energie geworden en groeit nog steeds. In de afgelopen 40 jaar is de omvang van wind turbine rotoren vertienvoudigd, tot de huidige diameters van meer dan 220m. Theoretisch en experimenteel aerodynamisch onderzoek hebben substantieel bijgedragen aan deze groei. De aerodynamische prestaties van rotorbladen, in allerlei weersomstandigheden, zijn belangrijk als het gaat om de inkomstenkant van het financiële plaatje, en daarmee ook voor het economische succes van de turbine. Dit maakt, dat de bladprofielen, die aan de basis staan van de bladprestaties, een belangrijke bijdrage leveren aan het succes van een turbineontwerp.

In deze dissertatie wordt onderzoek gedaan naar deze profielprestaties; prestaties als het gevolg van ontwerpkeuzes, of als resultaat van vereisten met betrekking tot operationele condities. Deel I, dat bestaat uit de hoofdstukken 2 tot en met 5, behandelt de profielprestaties in de range van invalshoeken die voorkomen bij normale operationele condities van de turbine. Deel II belicht de profiel-karakteristieken in meer extreme situaties, waarbij de grenslaag loslaat van de voorrand.

## Historisch overzicht van profielen voor windturbinebladen.

Hoofdstuk 2 geeft een historisch overzicht van de profielontwikkeling in de afgelopen 40 jaar. De eerste grote turbine-projecten in de 70-er en 80-er jaren gebruikten hoofdzakelijk profielen uit de NACA 4- en 5-cijfer series, in de jaren '30 en '40 ontworpen voor de luchtvaart. Dit zijn turbulente profielen, die hun hoge lift voornamelijk halen uit de stijging van een onderdrukpiek op de neus bij groter wordende invalshoek. Na stopzetting van de grote turbine programma's, werden deze profielen in eerste instantie ook gebruikt voor kleinere turbines met het zogenaamde overtrek of "stall" concept om het maximale turbinevermogen te beperken. Hierbij gaat het om een constante instelhoek van de bladen en een constant toerental van de generator. Echter, al snel werd duidelijk dat deze profielen erg gevoelig zijn voor vervuiling van de profielvoorrand, hetgeen grote vermogensverliezen oplevert. In de volgende jaren werd gezocht naar de optimale profielen voor dergelijke turbines, met betere prestaties onder de voorkomende bedrijfscondities.

Grotere turbines zagen het licht, gebruikmakend van variabele toeren en bladhoekverstelling als vermogensregeling, met een mix van speciale wind turbine profielen en laminaire profielen uit de NACA 6-serie.

Als gevolg van gewicht en belastingsspecificaties, hebben de huidige grote turbines bladen die lang en smal zijn, waardoor profielen nodig zijn die een hoge ontwerp-

liftcoëfficiënt hebben en, met het oog op atmosferische turbulentie, ook een hoge maximale liftcoëfficiënt bezitten.

Tegenwoordig worden profielen ontworpen met multi-disciplinaire optimalisatieprogramma's, die gebruik maken van het variëren van de profielcontour. Dit in tegenstelling tot vroegere ontwerpcodes, waarbij een profielcontour berekend wordt op basis van een voorgeschreven drukverdeling.

### Analyse en ontwerp met RFOIL en XFOIL bij hoge Re-getallen.

Als gevolg van de grote rekensnelheid die panelencodes zoals XFOIL en het daarvan afgeleide RFOIL mogelijk maken, worden zij verreweg het meest gebruikt voor prestatieberekeningen in optimalisatieprogrammatuur. In hoofdstuk 3 wordt ingegaan op de nauwkeurigheid van XFOIL en RFOIL voorspellingen, voornamelijk aan de hand van vergelijkingen met windtunnelmetingen aan DU-profielen in de LTT, of door middel van vergelijkingen met metingen aan profiel DU00-W-212 in de hoge-druk tunnel DNW-HDG in Göttingen, Duitsland. Het blijkt, dat RFOIL tot  $Re=9 \times 10^6$  nog gebruikt kan worden door zijn betere voorspelling van de maximale liftcoëfficiënt. Voor hogere Reynoldsgetallen is XFOIL de beter optie, maar dan wel met andere waarden van A en B in de  $G-\beta$  locus vergelijking voor de turbulente grenslaag, om de voorspelling van overtrek te verbeteren. In de gehele Re-getallen range tussen  $3 \times 10^6$  to  $15 \times 10^6$  voorspellen XFOIL en RFOIL de  $C_d$  te laag en wordt de maximale liftcoëfficiënt redelijk goed berekend. De codes hebben wel moeite met het berekenen van de prestaties van profielen met (hoge) ruwheid op de neus en van profielen met een grote stompe achterrand. Omdat in deze dissertatie vaak gebruikgemaakt wordt van vergelijking met metingen in de LTT, is aandacht besteed aan de layout en stromingskwaliteit van deze tunnel en worden de gebruikte methoden en technieken om de (ruwe) data te behandelen belicht.

### Benodigde prestaties van windturbineprofielen en het effect van ruwheid en erosie.

Hoofdstuk 4 behandelt de eisen voor bladprofielen van windturbines en belicht belangrijke zaken betreffende profielontwerp. Gebruikmakend van een voorbeeld van profieloptimalisatie bij  $Re=9 \times 10^6$ , waarbij turbulentie met verschillende maximale invalshoekvariaties wordt meegenomen, wordt duidelijk gemaakt dat voor een goede gemiddelde lift-weerstandsverhouding (glijgetal), profielontwerp gaat in de richting van turbulente profielen, met grotere welving meer nabij de neus. De rest van het hoofdstuk is gewijd aan het effect van ruwheid (door middel van zigzag tape, variërende hoogte en patronen van grit-ruwheid of schuurpapier) en erosie (in stadia) op profiel en rotorniveau. Aangetoond wordt, dat grit-ruwheid aangebracht op beide zijden van de profielneus grotere verliezen geeft dan zigzag tape. De ruwheidshoogte lijkt belangrijker dan de

korrel-dichtheid, of de lengte vanaf de profielneus van het ruwe oppervlak. Glijgetal verliezen door grit-ruwheid van meer dan 40% en dalingen van de maximale lift met 25% zijn niet ongebruikelijk. Hevige erosie kan nog slechtere prestaties tot gevolg hebben. Een bijna oneindige variëteit aan ruheidspatronen en erosie-stadia kan in de praktijk voorkomen. In het algemeen worden berekeningen met bladelement-impuls methoden (BEM) gebruikt om het effect van ruwheid en erosie op de jaaropbrengst van turbines te bepalen, op basis van profielprestaties representatief voor profielen met een ruwe of geërodeerde profielneus. Verliezen aan jaaropbrengst liggen meestal in de orde van 0,5% tot 5%.

Een poging om het kritieke Reynoldsgetal voor zigzag tape te bepalen, is maar ten dele gelukt. Terwijl metingen aan profielen DU93-W-210 en DU97-W-300 metapediktes van 0,185mm en 0,310mm (DU93) en 0,250mm (DU97) op  $x/c=5%$  allen waardes laten zien in de range  $220\pm 5$ , geeft de test met 0,185mm op DU97 slechts  $179\pm 2$  voor invalshoeken tussen  $4,1^0$  en  $8,2^0$ . Bij eenapedikte van 0,205mm, slechts 0,02mm hoger, zouden waardes van  $219\pm 4$  resulteren, hetgeen de gevoeligheid van de berekeningen voor de juisteapedikte aangeeft. De metingen bevestigen een waarde van ongeveer 200 voor een vlakke plaat.

### **Het effect van oppervlak-afwerking, anti-erosie coating en getande achterranden op de profielprestaties.**

Hoofdstuk 5 beschrijft een studie, waarbij gebruik gemaakt is van een LTT-model gevormd in de mal van een windturbineblad, compleet met de geringe variatie in koorde en wrong. Het effect van een verfcoating, zigzag tape, achterrand vertanding en anti-erosiecoating met en zonder vortex generatoren is onderzocht. Duidelijk wordt, dat de randen van de anti-erosielaag voortijdige omslag teweegbrengen als ze niet netjes glad worden gemaakt, hetgeen in dit geval een verlies in glijgetal van 44% oplevert. Dit kan alleen maar zeer gedeeltelijk verminderd worden door 3mm hoge wervelgeneratoren geplaatst op  $x/c=50%$ . Een gemodificeerde anti-erosielaag, die veel verder stroomafwaarts ophoudt, met gladgemaakte randen, levert slechts een verlies op van 6,4%. De prestaties van het model met een getande klep in koorde-richting werden geschat, op basis van metingen aan de klep onder een hoek van  $11^0$  en RFOIL berekeningen. Het glijgetal was in de hele range van invalshoeken lager dan het model zonder klep.

### **Voorspelling van de hoek waarbij de stroming loslaat van de voorrand.**

In hoofdstuk 6 wordt het effect beschreven van de profielvorm, ruwheid en het Reynoldsgetal op de invalshoek waarbij stromingsloslating van de voorrand optreedt (deep-stall) als gevolg van het barsten van een loslaatblaas op de neus. Deze situatie wordt gekenmerkt door een scherpe daling van de lift en een scherpe stijging van de

weerstand. Gevonden werd, dat de hoek lineair afhangt van de dikte-coördinaat  $y/c$  van de profielbovenzijde bij  $x/c=0.0125$ . De hoek wordt groter bij toenemend Reynoldsgetal en toenemende blokkering. Herstel van de originele situatie bij afnemende invalshoek vanuit de overtrokken situatie is pas mogelijk als de gemiddelde druk van de bovenzijde minstens gelijk is aan de waarde die hij had vlak voor voorrandloslating. Het onderdrukken van de blaas op de neus door de grenslaag al eerder turbulent te maken, elimineert de scherpe overgangen in lift en weerstand.

### **Profielprestaties bij deep-stall hoeken.**

In hoofdstuk 7 worden de resultaten van metingen besproken aan diverse DU-profielen in de range van invalshoeken tussen  $-180^{\circ}$  en  $180^{\circ}$  en Reynoldsgetalen tussen  $0.5 \times 10^6$  en  $8.1 \times 10^6$ .

Het meest saillante resultaat is het feit, dat profielen in het bereik van invalshoeken tussen  $60^{\circ}$  en  $90^{\circ}$  (en de equivalente waardes bij negatieve hoeken) dezelfde gemiddelde druk aan de overtrokken zijde hebben, onafhankelijk van profielvorm en Reynoldsgetal. Dit vindt zijn oorzaak in het feit dat loslating altijd plaatsvindt vlak bij of net op de voorrand. Verschillen in weerstand ontstaan derhalve door verschillen in de profielvorm van de drukzijde. Verder is gevonden dat een combinatie van hoge blokkering ( $c/h > 0.25$ ) en lage slankheid ( $b/h < 3$ ) tot grote stromingsdeformatie aan de onderdrukzijde van het profiel leidt. Daarbij is  $b$  de spanwijdte van het model.

### **Wervelafschudding bij deep-stall hoeken, het Strouhalgetal.**

Hoofdstuk 8 beschrijft de variatie van het Strouhalgetal ( $St$ ) met de invalshoek voor DU91-W2-250 gemeten in de LTT voor  $Re=0.5 \times 10^6$  en  $0.7 \times 10^6$ .  $St$ -waarden voor profiel DU00-W-212 zijn gemeten in de DNW-HDG windtunnel bij Reynoldsgetalen tussen  $6 \times 10^6$  en  $8.1 \times 10^6$ . In een  $C_d$ - $St$  grafiek vallen de waardes voor negatieve en positieve invalshoeken op dezelfde kromme. Op basis van de beschikbare data wordt voorzichtig geconcludeerd, dat de lijn voor DU91 wel eens algemeen geldig zou kunnen zijn voor alle profielen en Reynoldsgetalen.

### **Voorspelling van de maximale weerstandscoefficient bij lage en hoge Reynoldsgetalen.**

In hoofdstuk 9 wordt een methode ontwikkeld om de maximale  $C_d$  van profielen bij Reynoldsgetalen tot ongeveer  $1.7 \times 10^6$  te bepalen op basis van metingen in de LTT. De methode berekent de bijdrage van de dikte van de voorrand in termen van  $y/c$  bij  $x/c=0.0125$  aan de drukzijde bij een hoek van nul graden van de achterrاند. De bijdrage van de achterrاند combineert de afstroomhoek aan de drukzijde met een gevoeligheidsfactor gelieerd aan de reeds genoemde  $y/c$ -waarde. Vergelijking met

bestaande metingen geeft afwijkingen tot 2.1%, met een gemiddelde van -0.2%. Voor Re-getallen van  $3.5 \times 10^6$  tot  $8 \times 10^6$  werd de bijdrage van de achterrand gehandhaafd, maar werd met behulp van metingen in de DNW-HDG windtunnel aan DU00-W-212 en DU91-W2-250 de bijdrage van de voorrand opnieuw bepaald, zodat de afwijkingen voor deze profielen nu vallen binnen de 0.5%

### Het glijgetal van een profiel in een stilstaand en roterend blad.

In hoofdstuk 10 wordt het glijgetal onderzocht, en het effect daarop van de slankheid van een model en als profiel in een stilstaand of roterend turbineblad.

Door de zeer kleine waarde van de verhouding  $C_t/C_n$  in deep-stall volgt:

- Het glijgetal is in hoge mate onafhankelijk van de modelslankheid.
- Het glijgetal is onafhankelijk van het Reynoldsgetal.
- De glijgetallen van de diverse profielen in een turbineblad vallen samen met hun twee-dimensionale kromme, onafhankelijk van rotatie.
- Het glijgetal varieert met de dikte van de profielneus aan de drukzijde. Hoe hoger deze  $y/c$  bij  $x/c=0.0125$ , hoe hoger de nullift-hoek en het glijgetal bij  $90^\circ$ .
- Het glijgetal varieert met de achterrandhoek. Hoe hoger deze hoek (positief tegen de klok in), hoe hoger de nullift-hoek en het glijgetal bij  $90^\circ$ .



# CONTENTS

<i>ACKNOWLEDGEMENTS</i> .....	1
<i>SUMMARY</i> .....	3
<i>SAMENVATTING</i> .....	9
<i>CONTENTS</i> .....	15
<i>LIST OF SYMBOLS</i> .....	21
<b>1 INTRODUCTION</b> .....	27
1.1 Oil and Wind .....	27
1.2 Wind energy as a vital part of the global energy mix .....	27
1.3 Wind turbine blades and airfoil design .....	28
1.4 Airfoil performance at deep-stall angles .....	31
1.5 Thesis outline .....	31
1.6 References .....	32

## **PART I: AIRFOILS AND BLADE AERODYNAMIC DESIGN**

<b>2 EARLY WIND TURBINE BLADE AIRFOILS</b> .....	39
2.1 The first years .....	39
2.2 The stall control concept .....	46
2.3 The next generation wind turbine dedicated airfoils .....	49
2.3.1 SERI/NREL airfoils .....	49
2.3.2 FFA airfoils .....	51
2.3.3 DU airfoils .....	52
2.3.4 NTUA airfoils .....	54
2.3.5 Risø airfoils .....	54
2.4 Other, and more recent developments in Europe .....	56
2.5 Airfoil developments in China .....	57
2.6 Flatback airfoils .....	58
2.6.1 Truncation .....	59
2.6.2 Creating a blunt trailing edge .....	60
2.6.3 Vortex shedding .....	60
2.7 Conclusions .....	61
2.8 References .....	62

<b>3 DESIGN AND ANALYSIS TOOLS</b> .....	71
3.1 Two-dimensional airfoil characteristics prediction using XFOIL and RFOIL .....	71
3.1.1 XFOIL .....	71
3.1.2 RFOIL .....	71
3.1.3 Application of multiplication factors .....	76
3.1.4 RFOIL predictions for an airfoil with roughness .....	79
3.1.5 RFOIL predictions for airfoils with a very thick trailing edge .....	81
3.1.6 RFOIL pred. of airfoil performance at high Reynolds numbers .....	82
3.1.7 Other sources for experimental high Reynolds number data .....	84
3.1.8 Comparison with CFD codes at high Reynolds numbers .....	85
3.1.9 RFOIL pred. with turbulent flow at high Reynolds numbers .....	86
3.2 Wind tunnel measurements .....	88
3.2.1 Introduction .....	88
3.2.2 The low-speed low-turbulence wind tunnel LTT .....	89
3.2.2.1 Wind tunnel layout .....	89
3.2.2.2 Test section flow quality .....	91
3.2.2.3 The test section free-stream dynamic pressure .....	94
3.2.2.4 Repeatability .....	95
3.2.2.5 Models .....	95
3.2.3 Methods .....	96
3.2.3.1 Pressure coefficients .....	96
3.2.3.2 Force coefficients .....	96
3.2.3.3 Wake rake measurements .....	98
3.2.3.4 Calibration of the wake rake .....	99
3.2.3.5 The impact of wake rake downstream position .....	100
3.2.3.6 Traverse measurements .....	102
3.3 Conclusions .....	103
3.4 References .....	104
<b>4 ON THE AERODYNAMIC DESIGN OF AIRFOILS</b> .....	109
4.1 Definitions and properties of a rotor blade element .....	109
4.1.1 BEM theory .....	112
4.2 Airfoil characteristics and the power curve .....	113
4.2.1 Blade and airfoil chord size .....	115
4.3 The design angle and $C_{l,max}$ .....	116
4.3.1 Angle of attack fluctuations .....	116
4.3.2 Airfoil shape impacted by fluctuating inflow .....	118
4.4 The impact of leading edge flow distortion .....	120
4.4.1 The impact of leading edge roughness .....	122
4.4.2 The critical roughness height of zigzag tape .....	130
4.4.2.1 Verification of $R_{k,crit1}$ .....	134
4.4.2.2 The critical Re-number for transition right behind the tape .....	135

4.4.3	Scaling roughness	139
4.4.4	Insect impact distribution	140
4.4.5	Using sandpaper in wind tunnel testing	142
4.4.6	Sandpaper tests in IRPWIND project	143
4.4.6.1	Wind tunnel test	144
4.4.6.2	Field experiments	145
4.4.7	Sandpaper testing in general	146
4.5	The impact of leading edge erosion	147
4.5.1	AEP losses due to leading edge erosion	147
4.5.2	Impact of erosion on section performance	148
4.5.3	Erosion and wind tunnel testing	149
4.5.4	Erosion mitigation concepts	149
4.5.4.1	Leading edge protection	150
4.5.4.2	Erosion safe mode control	151
4.6	Conclusions	151
4.7	References	154

## **5 BLADE SECTION AERODYNAMIC EFFICIENCY IN PRACTICE** . . . . . 160

5.1	Test case	160
5.1.1	NACA 63 <sub>4</sub> -421 Aerodynamic performance	161
5.1.1.1	RFOIL predictions	161
5.1.1.2	Comparison of predictions with experimental Characteristics	162
5.1.2	Test setup	163
5.1.2.1	Data correction	163
5.2	Results	164
5.2.1	Paint	164
5.2.2	Leading edge protection (LEP)	166
5.2.3	Comparison with fixed transition	167
5.3	Blade section efficiency in turbulent conditions	167
5.4	Modified leading edge protection	169
5.5	Trailing edge serrations	171
5.5.1	The EWT-serrations	172
5.5.2	Approximation of the $\beta=0^\circ$ characteristics	174
5.5.3	Blade segment efficiency	175
5.5.4	Higher loads	176
5.5.5	Estimation of the lift increase due to serrations	177
5.6	Conclusions	179

5.7 References .....	180
----------------------	-----

## **PART II: DYNAMIC EFFECTS AND PERFORMANCE IN SEPARATED FLOW**

<i>BACKGROUND</i> .....	185
<i>AIRFOIL CHARACTERISTICS IN DEEP-STALL</i> .....	187
<i>CHAPTERS IN PART II</i> .....	189
<i>REFERENCES</i> .....	189

### **6 LEADING EDGE SEPARATION AT DEEP STALL** .....

6.1 Introduction .....	191
6.2 Research question .....	191
6.3 The impact of leading edge shape .....	192
6.3.1 The leading edge laminar separation bubble .....	193
6.3.2 Stratford’s separation criterion .....	195
6.3.3 Crabtree’s bubble bursting criterion .....	197
6.3.4 Extrapolation of measurements to find bubble bursting .....	198
6.3.5 Inviscid calculations .....	199
6.4 Measured deep-stall angles .....	200
6.5 The impact of the Reynolds number on the deep-stall angle .....	202
6.6 The effect of the TE flow angle on the onset of deep-stall .....	203
6.7 The recovery angle; hysteresis in relation to the LE-thickness .....	208
6.8 The impact of blockage on the deep-stall and recovery angles .....	212
6.9 Blockage-free deep-stall and recovery angles for DU 91-W2-250 .....	214
6.10 The impact of blockage on the hysteresis loop .....	216
6.11 Conclusions .....	216
6.12 References .....	217

### **7 PERFORMANCE CHARACTERISTICS AT HIGH INCIDENCES** .....

7.1 Introduction .....	221
7.2 The importance of establishing the right test section dyn pressure .....	222
7.3 Flat plate deep-stall characteristics .....	224
7.4 Deep-stall performance of 3 DU-airfoils .....	228
7.4.1 Measurements on DU96-W-180 and DU97-W-300 .....	228
7.4.2 Measurements on DU91-W2-250 .....	231
7.4.2.1 Model chord of 0.25m .....	231
7.4.2.2 Model chord of 0.15m .....	234

7.5 The impact of the Reynolds number .....	235
7.5.1 DU00-W-212 .....	235
7.5.1.1 Reynolds numbers between $0.5 \times 10^6$ and $1.7 \times 10^6$ .....	235
7.5.1.2 Reynolds numbers between $6 \times 10^6$ and $8.1 \times 10^6$ .....	239
7.5.2 DU91-W2-250 .....	240
7.6 The impact of shape, reynolds number and incidence on the base pressure .....	242
7.7 The impact of model aspect ratio on the deep-stall characteristics .....	245
7.8 The impact roughness .....	249
7.9 Conclusions .....	253
7.10 References .....	254
<b>8 UNSTEADY FORCES AND VORTEX SHEDDING FREQUENCY IN DEEP-STALL ...</b>	<b>259</b>
8.1 The Strouhal number .....	259
8.2 Unsteady flow field of DU91-W2-250 .....	262
8.2.1 Measurements on a 25cm chord model. ....	262
8.2.2 Measurements on a 15cm chord model. ....	263
8.3 The Strouhal number of other airfoils .....	265
8.4 The Strouhal number at a high Reynolds number .....	266
8.5 The variation of the Strouhal number with the drag coefficient. ....	268
8.6 The projection of the airfoil perpendicular to the flow .....	270
8.7 Standard deviation of fluctuations of $C_l$ and $C_d$ .....	271
8.8 Conclusions .....	271
8.9 References .....	272
<b>9 THE AIRFOIL MAXIMUM DRAG COEFFICIENT .....</b>	<b>275</b>
9.1 Introduction .....	275
9.2 The impact of the leading edge thickness .....	276
9.2.1 Test setup and handling .....	277
9.2.2 Blockage corrections .....	278
9.2.3 Results .....	278
9.3 The effect of the trailing edge angle .....	279
9.4 The impact of the Reynolds number .....	281
9.5 Near-surface flow Topology .....	282
9.6 Prediction of airfoil maximum drag coefficient. ....	285
9.6.1 Results from literature .....	285
9.6.2 Re-calculating available data .....	286
9.7 Comparison of predictions with measurements .....	288

9.8 Prediction of the maximum drag coefficient at higher Re-number . . . . .	290
9.8.1 Reynolds number traverse measurements for DU91-W2-250 . . . . .	290
9.8.2 A new formulation for $C_{d,max}$ at high Reynolds numbers . . . . .	292
9.8.2.1 Application of the high Re-number equation in conditions with roughness . . . . .	294
9.9 Conclusions . . . . .	294
9.10 References . . . . .	294
<b>10 THE LIFT-DRAG RATIO OF AIRFOILS IN DEEP-STALL . . . . .</b>	<b>297</b>
10.1 Introduction . . . . .	297
10.2 The impact of aspect ratio . . . . .	297
10.2.1 Airfoils NACA 4415 and NACA 4418 . . . . .	297
10.2.2 The flat plate . . . . .	299
10.2.3 The variation of pressure distribution with aspect ratio . . . . .	299
10.3 The ratio of forces on a wind turbine blade . . . . .	300
10.3.1 The non-rotating blade . . . . .	301
10.3.2 The rotating blade . . . . .	303
10.4 The variation of the lift-drag ratio with airfoil shape . . . . .	306
10.4.1 Variation with airfoil leading edge thickness . . . . .	306
10.4.2 Variation with airfoil trailing edge angle . . . . .	306
10.4.3 Sensitivity to variation in Reynolds number . . . . .	307
10.5 Conclusions . . . . .	308
10.6 References . . . . .	309
 <b>APPENDICES</b>	
Appendix A     Wind tunnel wall corrections for two-dimensional . . . . .	315
testing up to large angles of attack	
Appendix B     The impact of a flap deflection on the maximum. . . . .	337
drag coefficient of airfoil DU95-W-180	
 <b>LIST OF PUBLICATIONS . . . . .</b>	<b>343</b>
 <b>CURRICULIM VITAE . . . . .</b>	<b>349</b>

# LIST OF SYMBOLS

A	Aspect ratio	
A	Constant in Clauser's G- $\beta$ relation	
$a$	Induction factor in axial direction	
$a'$	Induction factor in tangential direction	
B	Number of rotor blades	
B	Constant in Clauser's G- $\beta$ relation	
$c$	Airfoil chord	[m]
C	Test section area	[m <sup>2</sup> ]
$C_d$	Drag coefficient	
$C_{dM}$	Drag coefficient, corrected with Maskell method	
$C_{dp}$	Pressure drag coefficient, derived from the pressure distribution	
$C_{ds}$	Drag coefficient due to separated flow, Maskell method	
$C_{dw}$	Drag coefficient derived from wake rake pressures	
$C_f$	Friction coefficient	
$C_l$	Lift coefficient	
$C_m$	Moment coefficient around airfoil quarter-chord point	
$C_n$	Normal force coefficient	
$C_p$	Pressure coefficient	
$C_{pb}$	Base pressure coefficient	
$C_t$	Tangential force coefficient	
D	Drag force	[N]
f	Frequency	[Hz]
G	Shape parameter in Clauser's G- $\beta$ locus	
h	Tunnel height	[m]
H	Boundary layer shape parameter	
k	Parameter used in Maskell method, $1-C_{pb}$	
L	Lift force	[N]
M	Mach number	
N	Power in the e <sup>N</sup> -method to predict transition	
p	Static pressure	[N/m <sup>2</sup> ]
q	Dynamic pressure	[N/m <sup>2</sup> ]
r	Radius, distance from axis of rotation	[m]
R	Resultant force	[N]
R	Rotor radius	[m]

Re	Reynolds number	
S	Projected model area	[m <sup>2</sup> ]
St	Strouhal number	
Tu	Turbulence intensity	
U	Velocity, Wind speed	[m/s]
V	Velocity, Wind speed	[m/s]
$x$	Airfoil coordinate along the chord	[m]
$y$	Airfoil coordinate perpendicular to the chord	[m]

### Greek Symbols

$\alpha$	Angle of attack	[°]
$\beta$	Prandtl-Glauert compressibility factor, $\sqrt{1-M^2}$	
$\beta$	Pressure gradient in XFOIL turbulent BL computation	
$\delta^*$	Boundary layer displacement thickness	[mm]
$\theta$	Combined twist-pitch angle of blade segment	[°]
$\theta$	Blockage factor in Maskell's method	
$\varphi$	Angle of inflow	[°]
$\mathcal{E}_b$	Total blockage factor, $\mathcal{E}_s + \mathcal{E}_w$	
$\mathcal{E}_M$	Blockage factor in Maskell's method	
$\mathcal{E}_s$	Solid blockage factor	
$\mathcal{E}_w$	Wake blockage factor	
$\rho$	Density	[kg/m <sup>3</sup> ]
$\mu$	Viscosity	[kg/ms]
$\tau$	Tunnel blockage parameter, $\frac{1}{4}(c/h)$	
$\tau$	Shear stress	[N/m <sup>2</sup> ]
$\xi_r$	Aerodynamic efficiency of a rotor blade element	
$\zeta$	Trailing edge angle	[°]
$\lambda$	Blade spanwise velocity ratio	
$\lambda$	Weight factor between clean and rough surface (eq. 4.16)	
$\Lambda$	Airfoil body shape factor	
$\Lambda$	Rotor tip speed ratio	
$\Omega$	Rotational frequency	[rad/s]
$\Delta p_c$	Pressure difference in LTT contraction	[N/m <sup>2</sup> ]

### Subscripts

b	Refers to buoyancy
rel	Relative

$o, \infty$	Free stream, Undisturbed
l	Lower surface
u	Upper surface
max	Maximum
min	Minimum
M	Refers to Maskell's method
s	Refers to static pressure
t	Refers to total pressure
w	Refers to the wake rake or to the wall

### Superscripts

'	Uncorrected
---	-------------

### List of Acronyms

AEP	Annual energy production
AVATAR	<u>A</u> dvanced <u>a</u> erodynamic <u>t</u> ools for <u>l</u> arge <u>r</u> otors. EU-funded research project
BEM	Blade element momentum method
BL	Boundary layer
DES	Detached Eddy Simulation. A method in Computational Fluid Dynamics (CFD)
DNW	German-Dutch Wind Tunnels
DTU	Danish Technical University
DWG	Deutsche WindGuard Engineering, Germany
ECN	Netherlands Energy Research Centre, Petten (now TNO)
ESM	Erosion safe mode. Turbine control mode during rain
EWT	Emergya Wind Technologies B.V.
HAT	Horizontal axis wind turbine
HDG	High Pressure Tunnel in Göttingen, Germany. Operated by DNW until 2020
IEA	International Energy Agency
LE	Leading edge
LEP	Leading edge protection
LES	Leading edge separation
LES	Large eddy simulation. A method in Computational Fluid Dynamics (CFD)
l.s.	Lower surface
LTT	Low-turbulence wind tunnel of TU Delft
NACA	National Advisory Committee for Aeronautics, USA
NASA	National Aeronautics and Space Administration, USA

NREL	National Renewable Energy Laboratory, USA. At present National Laboratory of the Rockies
OPEC	Organisation of Petroleum Exporting Countries
PLCT	Poul La Cour Tunnel, wind tunnel at DTU, Denmark
RANS	Reynolds-averaged Navier-Stokes. A method in Computational Fluid Dynamics (CFD)
TE	Trailing edge
TUD	Delft University of Technology
UAE	Unsteady Aerodynamics Experiment, NREL research project
U.S., USA	United States of America
u.s.	Upper surface
VAWT	Vertical axis wind turbine
VG	Vortex generator





# 1

## INTRODUCTION

### *1.1 OIL AND WIND*

The price and availability of oil has evidently played a prominent role in wind energy research. The first time considerable resources were allocated to research and development in wind energy was after the 1973 oil crisis, when the OPEC not only dramatically raised their oil price, but also drastically limited oil export to Western countries. In a year's time the price of oil almost quadrupled (Historiek, 2024). The report by the Club of Rome, "The limits to growth" (Meadows et al., 1972) published a year before, aimed at making (western) countries aware of threats posed by the use of fossil fuels to their life style. Although the conclusions of the report resonated among many in the western hemisphere, full awareness only came, when the oil crisis revealed the dangers of a weakening energy supply chain. Financial uncertainty and economic decline forced decision makers to act (Rapid Transition Alliance, 2019).

Since the 1973 oil crisis and its mirror in 1978-1979 (after the Iranian revolution), the focus on energy from wind systems has received fluctuating attention, strongly related (and with some time lag) to international relations between oil producing countries and customers.

Although the application of alternative energy sources has tremendously improved the situation, much more recent, wars at the borders of the European Union and in the Middle-east, again involving important oil producing countries, mark how vulnerable Europe's energy supply still is when based on fossil fuels.

### *1.2 WIND ENERGY AS PART OF THE GLOBAL ENERGY MIX*

The ninetenseventies oil crises spurred governments to encourage improvements in energy efficiency and consumption, alongside with an acceleration of investments in application and research of alternative energy sources, such as wind, solar and geothermal.

Last, but certainly not least, a sense of urgency to move away from coal, oil and gas and find alternative and sustainable energy sources already emerged in the past decades, due

to climate monitoring reports verifying the negative impact of energy production based on fossil fuels (UKRI).

Due to national and international favourable policies and funding schemes (e.g EU Energy programmes) wind energy application and research developed from the pioneering stage in the 1970's, with just a few installations, into a mature business with large companies, numerous wind farms on and off shore, and well founded activities in research institutes and academia at present. The advances in wind turbine technology and efficiency is also reflected in the continuously increasing size of turbines, presented in fig. 1.1. Wind energy now meets an average of nearly 20% of the European Union electricity demand (29% in the Netherlands, WindEurope 2025).

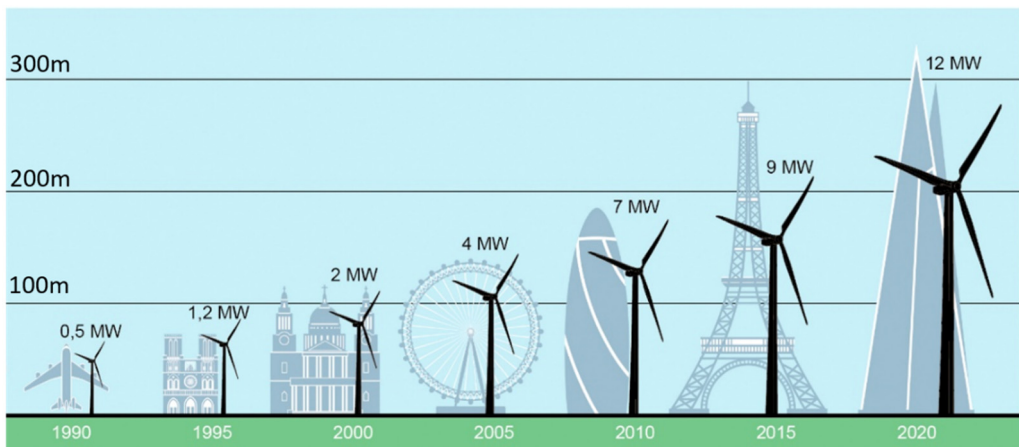


Figure 1.1: Development of turbine size during three decades. Picture adapted from Johansen (2021). Original picture BloombergNEF, used with permission.

A wind turbine is a complex system owing to the unsteady environment from which it extracts the energy. At present wind turbines are the largest fatigue machines on earth. Aerodynamic efficiency, structural integrity, aero-elastic behaviour and noise are all important design drivers. But the most important, to compete with fossil fuel, is the cost of a kWh. Wind energy: It must be good (e.g. predictable and durable) and cheap. Prices have indeed decreased continuously from over 50 €cent/kWh in 1980, to the current levelised cost of energy ranging from  $9.7 \pm 2.4$  €Cent/kWh for off-shore turbines and  $6.1 \pm 2.2$  €Cent/kWh for onshore turbines (Kost, 2021).

### 1.3 WIND TURBINE BLADES AND AIRFOIL DESIGN

Wind turbine blades are the most important connection of the turbine with the environment/wind. They generate the loads and the rotation energy that can be transformed into electricity.

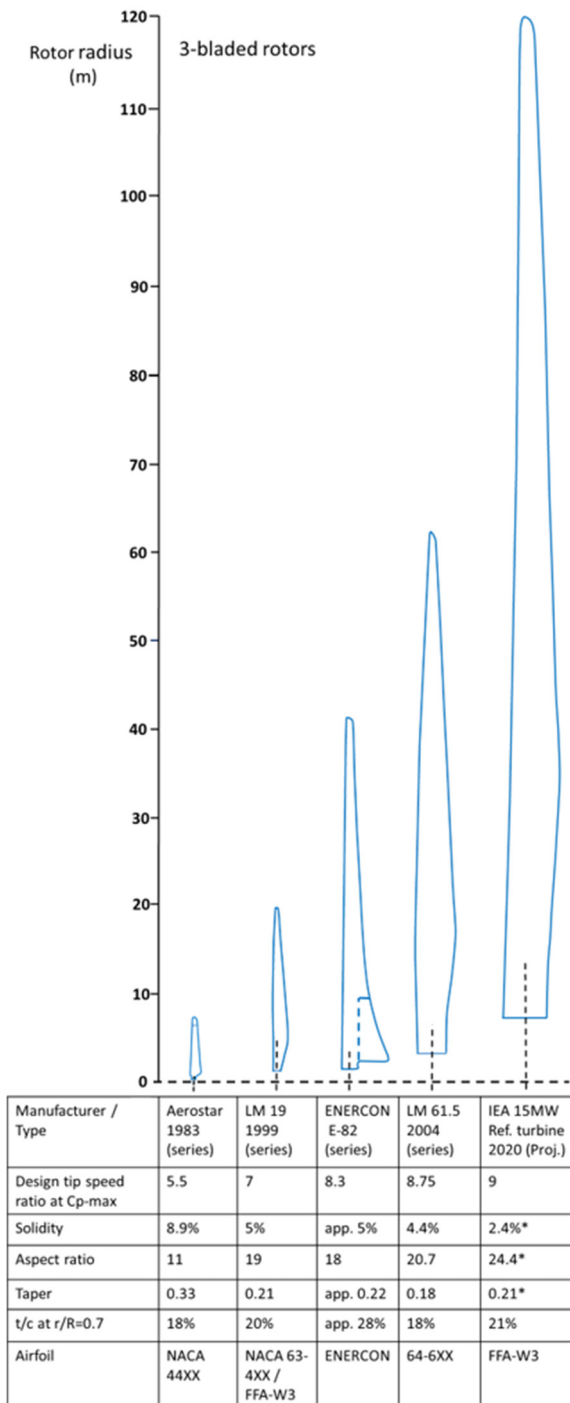


Figure 1.2: Development in wind turbine blade size and shape of three-bladed rotors since the 1980's. Partly adapted from Hau (2013).

Thus, the various blade sections play a pivotal role in the turbine system. The flow over the airfoils is the primary source for the torque and the loads. If the airfoils fail, the price of wind energy goes up. Research on wind turbine blade airfoils has developed from finding the most appropriate existing general aviation airfoils for small turbines in the late 1970's and 1980's to design using advanced multi-point and multi-disciplinary optimization computer codes for the multi-MW machines we see today.

Following machine size in fig 1.1, fig 1.2 nicely shows an example of blade size and shape development since the 1980's. The 15 MW reference rotor blade shape is exemplary for recent bigger turbines with higher maximum power and rotor diameters over 250m (e.g. the 2023 Goldwind GWH252-16MW turbine with a blade length of 123m, first erected in China).

Airfoil design at TU Delft specifically for wind turbines started with the 1989 wind tunnel experiment on a NACA 63<sub>421</sub>-425 airfoil, planned for the blade of a 30m diameter 350kW stall machine. The very high sensitivity to disturbances in the boundary layer flow over the airfoil and the associated severe drag rise, was the reason to design and test a new 25% thick airfoil to replace it: DU91-W2-250. More DU airfoils followed, most of which were developed in conjunction with industry, and their performance in various configurations (e.g with a tripped boundary layer or with vortex generators) was experimentally verified in the TUDelft low-turbulence wind tunnel. Despite the continual increase in turbine size, nowadays there still is a field of application for these airfoils, as some companies still produce sub-MW scale machines.

Due to the possibilities provided by present multidisciplinary design optimization (MDO) codes, beside the pioneering institutes like FFA, NREL, Risø and TU Delft and big turbine manufacturers with their in-house design teams, quite a number of research institutes have made advancements in airfoil design (e.g. Grasso et al. 2012, Hansen 2017 and Li et al. 2016).

Experimental performance verification is a key aspect of airfoil development. Designers need feedback on the effectiveness and reliability of their design tools, which makes numerical code validation by experiments of paramount importance. Although the capabilities of computational fluid dynamics (CFD) have tremendously grown in the last decade, for determination of the full impact of soiling, erosion and add-ons like vortex generators, stall strips and trailing edge serrations with sufficient accuracy, a wind tunnel remains an essential tool. For this reason e.g. in Germany the Deutsche WindGuard 1.25x2.75m<sup>2</sup> (2008) and in Denmark the LM 1.35x2.7m<sup>2</sup> (2006) and the 2x3m Risø/DTU "Poul la Cour" (2018) wind turbine blade airfoil dedicated wind tunnels were constructed. The latter, apart from erected for aerodynamic tests at Reynolds numbers up to 7x10<sup>6</sup>,

was particularly laid out for acoustics measurements as well. Dedicated acoustic experiments were also the goal for the reconstruction of the 0.6m diameter Delft University anechoic wind tunnel facility (2018) and the 1.83x1.83m Virginia Tech Stability Tunnel in the USA (2005).

## **1.4 AIRFOIL PERFORMANCE AT DEEP-STALL ANGLES**

Since the 1980's, common turbine power regulation shifted from the passive fixed-pitch stall-control system of turbines up to about 1MW installed power, to the active system of variable-speed pitch-controlled machines we find today. Turbines using stall-control require airfoils with a certain optimal behaviour at angles far beyond stall, where the section even at times may enter deep-stall. This is a heavily unsteady flow condition where the flow separates both from the leading edge and the trailing edge, forming an alternating row of vortices, the complex aerodynamic phenomenon called a Von Kármán Vortex Street.

Performance optimisation and noise attenuation of new airfoils for variable-speed pitch-controlled machines focusses mainly on the incidences between negative and positive stall, since this is their most important working range. However, during starts, stops, idling and hoisting of the blades, aerodynamic regimes at angles considerably higher, comparable to stall turbines and even higher, also become relevant. At the time of the early stall regulated turbines, performance data at these very high angles of attack were scarce. The characteristics needed for calculation of the turbine stall performance were generally based on the method of Viterna and Janetzke (1982), who used tests on flat plates and airfoil NACA 0012. Since the 1980's more test results of airfoils in deep-stall became available, e.g. Massini et al. (1988), Bloy and Roberts (1995) and Jacobs (2015). However the choice of airfoils was mostly ad hoc and the coherence between data sets of different airfoils from various wind tunnels was lacking, including information on the impact of blockage, Reynolds number and model aspect ratio. Airfoil performance at very high incidences still remained relatively uncharted territory.

This knowledge gap is the motivation for the second part of the research presented in this work, in which aerodynamic analysis of airfoil performance encompasses the full range of angles of attack from  $0^{\circ}$ - $360^{\circ}$ .

## **1.5 THESIS OUTLINE**

The thesis consists of two parts.

**Part I** starts with a retrospective overview of airfoils used for wind turbine blades and associated design efforts in the past four decades. This survey is motivated by the following underlying question: where and how have airfoils for wind turbine blades evolved during the past 40 years?

The following chapter presents the airfoil analysis and design tools most widely used in past and current wind turbine airfoils research: XFOIL and its derivative RFOIL. Their suitability is investigated for future airfoil design of large wind turbine blades. The discussion also introduces the TUDelft low-speed low-turbulence wind tunnel LTT as invaluable tool for aerodynamic analysis and design verification. The tunnel has been extensively used to develop the DU-airfoils and to measure the impact of roughness and aerodynamic devices such as vortex generators, stall strips and Gurney flaps.

The following chapter presents general design considerations and a more specific discussion on what is considered the critical issue in blade design: the impact of leading-edge roughness and erosion on rotor performance. Chapter 5 takes this discussion one step further. Using measurements in the LTT on a segment of a real wind turbine blade, the impact on airfoil performance and efficiency of paint and leading edge protection as applied by a blade manufacturer in practice is highlighted. Furthermore, the chapter describes the impact of trailing edge serrations and an equation is derived to predict the aerodynamic performance variation with serrations angle.

**Part II** comprises the study of airfoil characteristics in the deep-stall range of incidences, typified by flow separation at the section leading edge. The first chapter in this part presents the analysis of deep-stall phenomena and the associated incidence angle  $\alpha_{DS}$  of a variety of airfoils. A study was conducted, establishing the relation between  $\alpha_{DS}$  and the shape of the airfoil (viz. blade) leading edge. In the following chapter the previous discussion is contextualised: four designs of the DU-airfoils family are examined at high angles of attack to characterise their behaviour in deep-stall. In addition, the impact of roughness and the base pressure dependency of airfoil shape, angle of attack and Reynolds number is investigated.

Airfoils at very large incidences feature large flow separation, leading to a strong unsteady behaviour. Such regime is dominated by the vortex shedding phenomenon, which is examined in the next chapter. Chapter 9 shows the impact of the leading edge shape on the maximum drag coefficient,  $C_{d,max}$ , of airfoils and a method is proposed that allows predicting it for relatively low and high Reynolds numbers, also taking into account the trailing edge angle. The last chapter of part II investigates section efficiency in terms of the lift-drag ratio and the impact on efficiency of wind tunnel model or blade aspect ratio. The latter is examined both in a rotating motion and at standstill.

## 1.6 REFERENCES

- Bloy, A.W. and Roberts, D.G. (1993) *Aerodynamic characteristics of the NACA 63<sub>2</sub>-215 aerofoil for use in wind turbines*, Wind Engineering Vol. 17, No.2, 1993.
- Grasso, F. (2012) *Design of a Family of Advanced Airfoils for Low Wind Class Turbines*,

EWEA, Torque 2012, October 2012, Oldenburg, Germany.

Hansen, T.H. (2018) *Airfoil optimization for wind turbine application*. Wind Energy 21:502–514. <https://doi.org/10.1002/we.2174>

Hau, E. (2013) *Wind Turbines*. Springer Verlag, Germany. DOI 10.1007/978-3-642-27151-9

Historiek <https://historiek.net/oliecrisis-van-1973-gevolgen-autoloze-zondag/>  
Retrieved March 2024

Jacobs, M. (2015) *High Reynolds Number Airfoil Test in DNW-HDG*. Report DNW-GUK-2014 C-04. Göttingen, July 2015

Johansen, K. (2021) *Blowing in the wind: A brief history of wind energy and wind power technologies in Denmark*. Energy Policy, Volume 152, 2021 112139, ISSN 0301-4215, <https://doi.org/10.1016/j.enpol.2021.112139>.

Kost, C. (2021) *Levelised cost of electricity* Renewable Energy Technologies. Fraunhofer Institute for Solar Energy Systems ISE, Germany, June 2021

Li, X., Yang, K., Bai, J., Xu, J. (2016) *A new optimization approach to improve the overall performance of thick wind turbine airfoils*. Energy 116 (2016) 202-213, Elsevier Ltd.

Massini, G., Rossi, E. and D'Angelo, S. (1988) *Wind tunnel measurements of aerodynamic coefficients of asymmetrical airfoil sections for wind turbine blades extended to high angles of attack*. EC DG-XII Contract number: EN3W - 0018 - I, Conclusive Report. ENEA, Roma, 1988

Meadows, D. H., Meadows, D. L., Randers, J., Behrens III, W.W. (1972). *The Limits to Growth; A Report for the Club of Rome's Project on the Predicament of Mankind*. New York: Universe Books. [ISBN 0876631650](https://www.isbn-international.org/product/0876631650).

Rapid Transition Alliance (2019) <https://rapidtransition.org/stories/from-oil-crisis-to-energy-revolution-how-nations-once-before-planned-to-kick-the-oil-habit/> Retrieved March 2024.

UKRI- UK Research and Innovation. *A brief history of climate change discoveries*. <https://www.discover.ukri.org/a-brief-history-of-climate-change-discoveries/index.html>,

Retrieved April 2026

Viterna, L. A. and Janetzke, D.C. (1982) *Theoretical and Experimental Power From Large Horizontal-Axis Wind Turbines*. NASA Lewis Research Center, September 1982, Doe/NASA/20320-41, NASA TM 82944

Windeurope *Wind energy in Europe, 2025 statistics and the outlook for 2026-2030*. Windeurope.org, Retrieved April 2026





# PART I

## Airfoils and blade aerodynamic design



# 2

## EARLY HORIZONTAL AXIS WIND TURBINE AIRFOILS

It could be argued where to start when discussing the development of profiles for rotating machinery designed to use the wind as source of energy. Though maybe interesting from a historical point of view, since wind turbines date back to the Persians of about 500 AD, that would be quite a long period to review. As this dissertation aims at the design and testing of airfoils for *modern horizontal axis* machines a suitable starting point would be the first oil crises in 1973, when increasing energy consumption and an oil embargo against western countries boosted the interest for alternative energy sources and important funding was allocated to technology development in the field of wind energy in a broad sense, including research on blades and rotors. Some of the material in the following sections was first presented in Timmer (1993).

### 2.1 THE FIRST YEARS

Starting in 1974 in the USA, the Cleveland, Ohio, based NASA Glenn Research Center headed the US Wind Energy program with a view to develop large commercially feasible machines. As of 1975 this led to the design and operation of a series of 2-bladed, pitch or partial pitch regulated, wind turbines (see fig. 2.1) with power in the range of 100kW for the 1<sup>st</sup> Mod-0 to the 4MW WTS-4 produced by Hamilton Standard, which was the world's first 4MW machine.

Erected in 1987, the last one from this series, the 3.2MW Mod-5B with a rotor diameter of 97.5 meters designed by Boeing, was taken out of service in 1996 and dismantled in 1998.

With the exception of the WTS-4 and the Mod-5A, which was never built, the blades of these machines incorporated airfoils from the NACA 44xx and 230xx series. This may not come as a surprise, since in the beginning of the seventies no other low-speed airfoil series with experimentally verified performance data for a suited relative thickness range were available than those developed by NACA for general aviation in the course of the previous 40 years (Abbott et al., 1945). Airfoils NACA 0012 and 23012 e.g. already had an

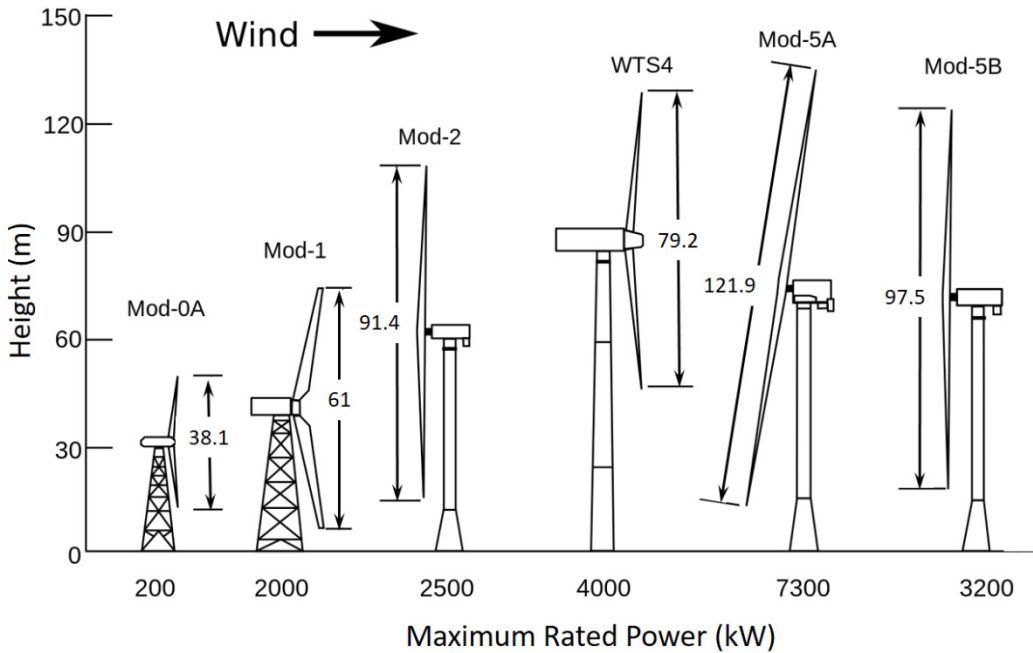


Fig. 2.1: Comparison of turbines designed in the framework of the 1974 US wind energy program. Rotor diameter in meters. Slightly altered original picture from US DOE and NASA (1995)

application in rotors as they were being used in helicopter blades for their low moment coefficients.

The relatively flat lower surface of the NACA 44xx series was very convenient, since the first wind turbine rotors had metal blades, which material –in view of ease of manufacturing- did not allow for much curvature in the blade profile. Airfoil shapes are available with maximum thickness-to-chord ratios in the range of 12% to 24% (see fig. 2.2). The required thick root profiles were achieved by linearly scaling the coordinates of airfoils with smaller thickness.

When metal blades were abandoned in favor of glass fiber-composite or wood-composite blades also airfoils from the laminar NACA 6-digit series 63<sub>x</sub>-xxx and 64<sub>x</sub>-xxx were applied. The NACA airfoils are well documented, since the NACA wind tunnel test campaigns in the 1930's and 40's resulted in airfoil performance data for Reynolds numbers of 3, 6 and 9 million (some even as low as  $0.7 \times 10^6$ ), which could conveniently be used in blade-element momentum calculations to determine the power and loads curves of the new machines. These measurements were predominantly performed in the Langley 0.91 x 2.28m<sup>2</sup> Low-turbulence Pressure Tunnel (LTPT) in the USA and also showed the effect of wrap-around roughness on the airfoil performance. Still at present, airfoils from the NACA 6-digit series

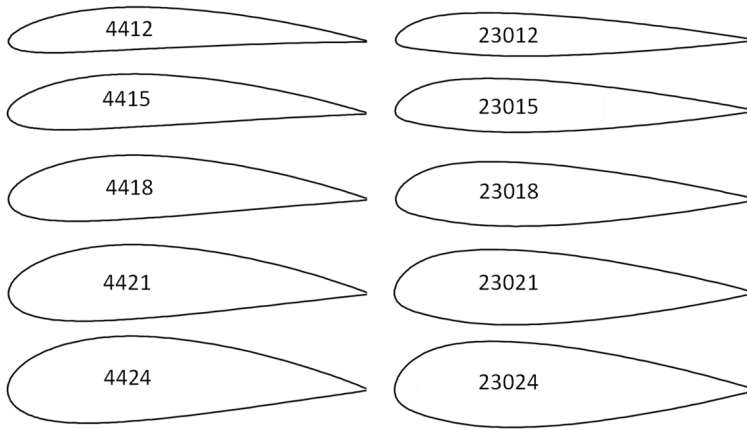


Figure 2.2: Airfoil shapes of the NACA44xx and NACA 230xx series of airfoils, Abbott et al. (1945)

are being used in wind turbine blade designs, which marks the importance of the NACA airfoil development, not only for the aviation industry but also for wind turbine blade designers.

The development of NASA general aviation airfoils in the beginning and mid-seventies resulted in the NASA LS(1)-04xx series and modified, more turbulent, versions, McGhee et al. (1979), which were also occasionally used in blade designs (fig. 2.3), as was the 16% thick natural laminar flow airfoil NLF(1)-0416 designed in the early 1980's, Somers (1981). The latter was mainly applied in relatively small turbines whose blades had little variation in the airfoil thickness, e.g. the 10m diameter two-bladed test turbine of the Delft University Institute for Wind Energy, operated during the 1990's.

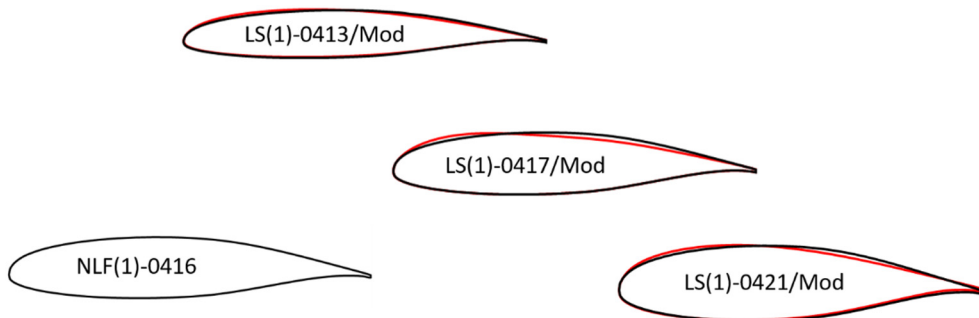


Figure 2.3: The NLF(1)-0416 and the LS(1)-04xx series of general aviation airfoils. Red shapes are modified (-Mod) versions.

Also in Europe, large experimental machines were erected, in the framework of national or European Commission funded programs (e.g. the WEGA I and II programs). Maximum installed power of the early prototypes ranged from relatively modest values of 630kW (Nibe I and 2, 1979 Denmark) and 1MW (NEW ECS 45, 1985 the Netherlands, using the LS(1) series of airfoils) with rotor diameters of 40m and 45m respectively, via the 1.5MW 60m rotor diameter Gamma-60 turbine (Italy 1987) and the 61m rotor diameter 2MW Tjaereborg turbine in Denmark (1989), to 3MW designs such as GROWIAN (1982) and Aeolus II (1990) in Germany, WTS-3 in Sweden (1982) and LS-I in the UK (1988) with rotor diameters of 100m, 80m, 78m and 60m respectively. Throughout the 1970's and 80's, also in Europe the use of the NACA airfoils was widespread, with exception of the 3MW 100m diameter German GROWIAN rotor, which contained the FX 77-W-xxx series of airfoils, designed by F.X. Wortmann at the Institute for Aerodynamics and Gas Dynamics of Stuttgart University (Wortmann, 1978), see fig. 2.4 . These FX-airfoils all have high design lift coefficients ranging from 1.4 to 1.7, and consequently also high maximum lift

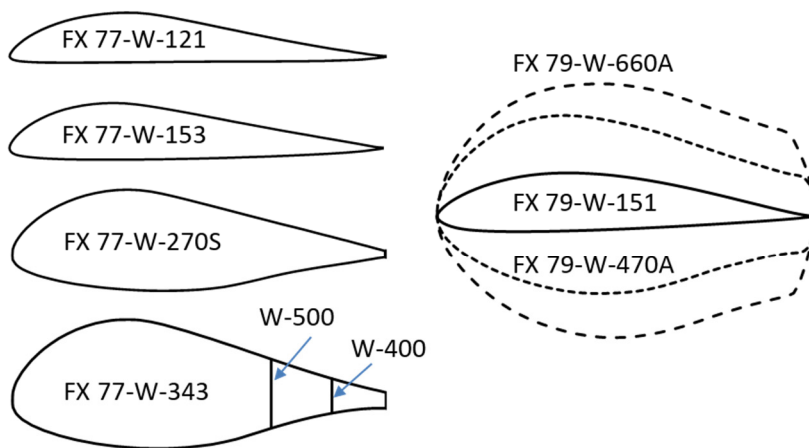


Figure 2.4: The FX 77- and FX 79-W-xxx airfoils designed by F.X. Wortmann (1978)

coefficients, ranging from 1.7 to 2.0.

The design concept of the FX 77 airfoils series focused on high lift resulting from high suction peaks at the front, which unfortunately also makes the thicker airfoils from the series very sensitive to off-design conditions, as is corroborated by fig. 2.5. It presents the performance of the 27% thick airfoil of the series with and without trip wires at the 3% chord position on the upper and lower surface. On the left, the lift coefficient in relation to the drag coefficient is depicted. At the right, the lift curves are shown. Due to tripwires at  $x/c=3%$  on the section upper and lower surface, the airfoil loses 52 % of its maximum lift and 72% of its efficiency (lift-drag ratio). Because of a variety of operational issues, including structural problems, the turbine was taken out of service in 1987, after only 420 hours of operation since commissioning in October 1983. In fig. 2.4, note the truncation

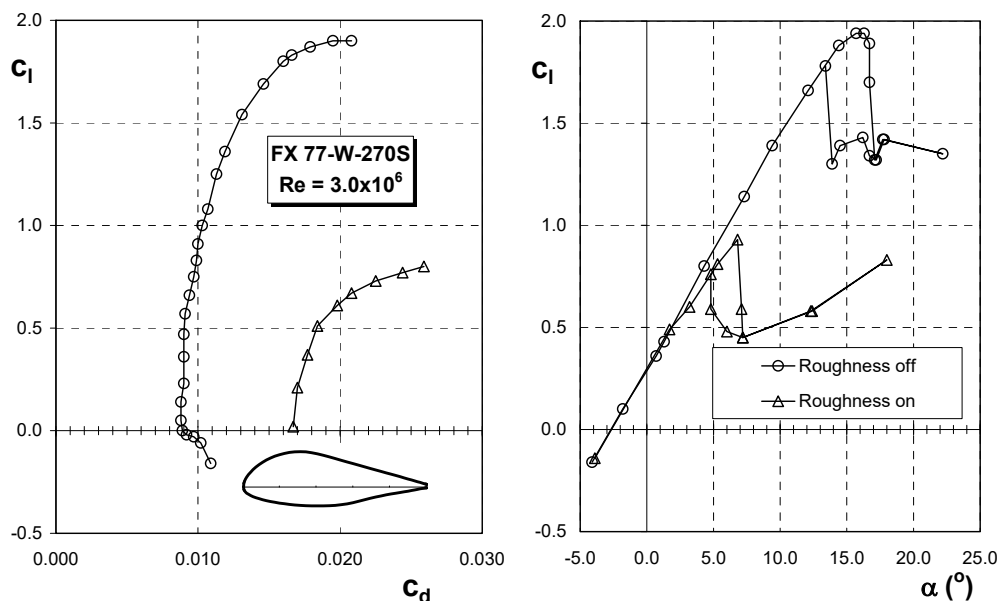


Figure 2.5: The clean and rough performance of airfoil FX 77-W-270S. Roughness consisted of trip wires at 3% chord on upper and lower surface (Althaus,1998).

of FX77-W-343 to obtain two blunt trailing edge airfoils with maximum thickness-to-chord ratios of 40% and 50% for the blade root region. Apart from a 15.1% thick airfoil, the 3 member FX-79 series also contains two blunt TE-edge airfoils, with 47% and even 66% thickness.

Though the turbine obviously was not very successful, with shapes significantly different from aerospace airfoils, one could say this was the first special purpose airfoil series dedicated to wind turbine application.

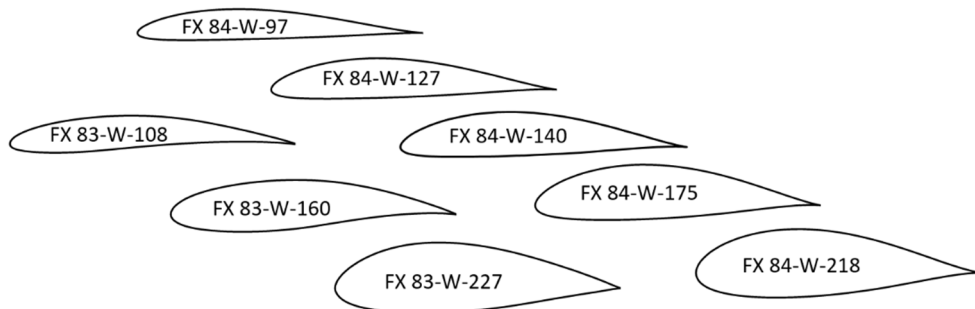


Figure 2.6: The FX 83-W-xxx and FX 84-W-xxx series of airfoils designed by F.X. Wortmann, Althaus (1984)

For much smaller turbines, with blade section Reynolds numbers in the range of  $0.5 \times 10^6$  to  $1.5 \times 10^6$ , Wortmann also designed the FX-84-W-xxx series of airfoils (fig 2.6), (Althaus,

1984) with thicknesses of 9.7% to 21.8%, characterized by a flat moderate maximum lift curve, comparable to the NACA 63<sub>3</sub>-618 airfoil. These airfoils showed improved performance over an earlier series of three airfoils (FX 83-W-xxx) for about the same Reynolds number range.

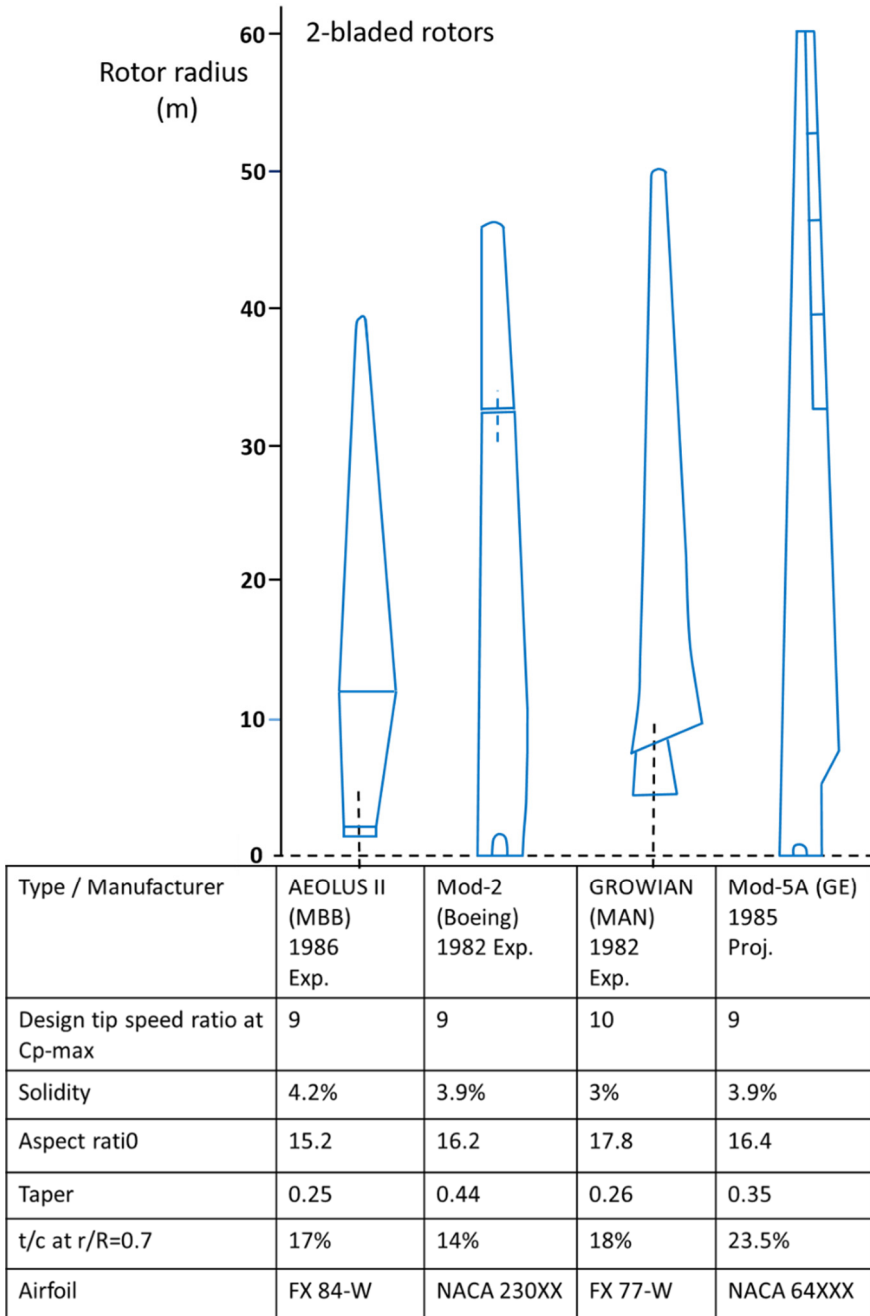
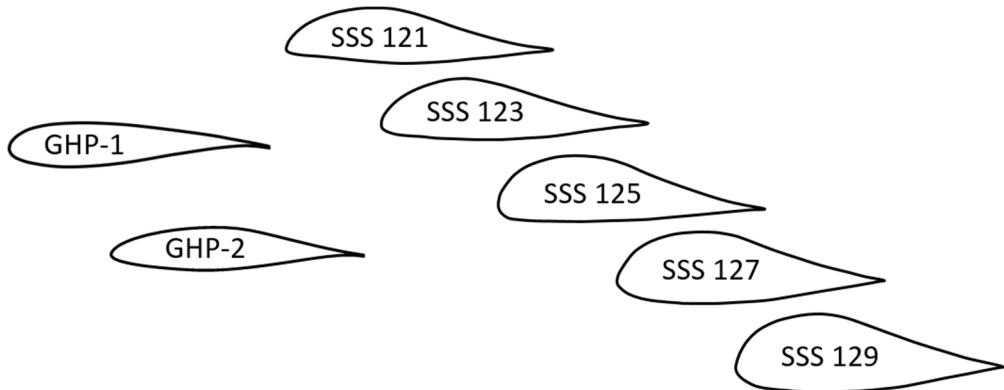


Figure 2.7: Blades for two-bladed rotors and their characteristics, Adapted from Hau (2013).

Althaus (Althaus, 1998) presented a series of 5 airfoils in the thickness range of 14.5% (AH93-W-145) to 30% (AH93-W-300), with moderately high maximum lift coefficients of approximately 1.4, benign stall and design-lift coefficients of 1.1 to 1.2. The AH and FX airfoils, like most of their sailplane counterparts, were tested in the Institute for Aerodynamics and Gasdynamics low-turbulence wind tunnel of Stuttgart University, Germany. The FX airfoils were predominantly used by German blade manufacturers. An application containing the AH airfoils is unknown.

Figure 2.7, adapted from Hau (2008), illustrates the variety of airfoils for different 2-bladed rotor designs in the 1980's. Note the ailerons in the blade of the Mod5A project, systems that at present are being considered in future blade designs, albeit now as potential morphing elements.

At the end of the 1980's a number of new airfoils specifically targeted for wind turbine application saw the light in the United Kingdom. A design effort by Garrad & Hassan and RAE Farnborough resulted in the GHP-1 and GHP-2 airfoils, both 17% thick and designed for a Reynolds number of  $4 \times 10^6$  (Garrad, 1990), fig 2.8. The GHP-1 was developed for the blade root and based on LS(1)-0417Mod, aiming at a very high maximum lift coefficient of 2.4. The airfoil was unfortunately not wind tunnel tested.



*Figure 2.8: The GHP (Garad, 1990) and SSS airfoils (Satchwell and Turnock, 1989) from the UK in 1989 and 1990*

GHP-2 was targeted for the mid-section of a blade and had the laminar NACA 63-series as a basis. It was tested by Imperial College (Khoo and Graham, 1990), at relatively low Reynolds numbers ( $1.8 \times 10^6$  and below). The performance with free and fixed transition appeared to be not better than the LS(1)-0417 it had to compete with and the airfoil was not used in actual blade designs.

An attempt was made by the Southampton University Ship Science Department to design a series of structurally efficient airfoils with maximum thickness ratios ranging from 21 % to 29% (SSS-airfoils, Satchwell and Turnock, 1989), fig 2.8. The characteristic airfoil upper

surface shape points in the direction of a Stratford pressure distribution, which was first introduced by Liebeck (1976). A Stratford -type pressure distribution tends to result in abrupt stall characteristics and poor off-design aerodynamic performance characteristics especially for airfoils with higher thickness-to-chord ratios. The airfoils were tested in the 3.4x2.4m<sup>2</sup> Southampton University wind tunnel and the tests confirmed the disappointing behavior under conditions with roughness on the leading edge, as already at low angles of attack it was difficult to maintain a two-dimensional situation as a result of the tunnel wall-model interference.

## 2.2 THE STALL-CONTROL CONCEPT

The early big turbine programs in the US and in Europe demonstrated that large machines were a bridge too far in the development of reliable and cost-effective wind power. Already during the execution of these big turbine programs, in the 1980's smaller turbines, with power ratings of 50 to 500kW were built, using robust upwind, three-bladed fiberglass rotor blades combined with fixed blade pitch and fixed rotational speed or "stall-control" as a means of limiting the maximum power. This type became also known as the "Danish concept", since Danish turbine manufacturers exported this kind of turbines after ample experience on their home-market. In the stall concept, the blade angles increase with increasing wind speed. When stall is reached, the diminishing lift and increasing drag due to separation in the post-stall region of incidences maximize the power output.

During the Californian Wind Rush from 1983 to 1986, when US federal energy credits and Californian State tax credits boosted the foundation of big wind farms like Tehachapi (north of Los Angeles) and Altamont Pass (east of San Francisco), large numbers of 55kW

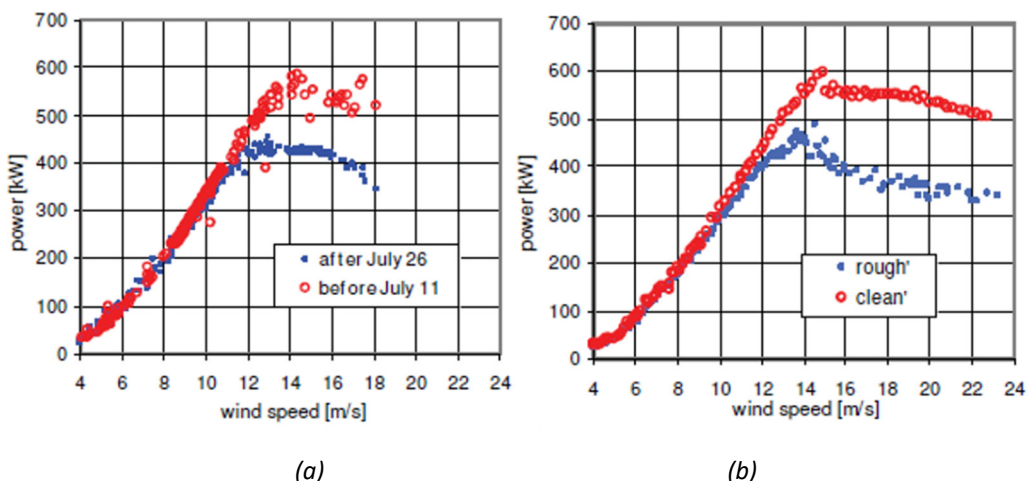


Figure 2.9: The 1999 measured impact of leading edge bug accumulation (a) and zigzag tape (b) on the power curve of a NEG Micon 700/44 stall turbine. (Corten and Veldkamp, 2001).

turbines were exported to the US by companies like Vestas, Bonus and Nordtank. These stall-controlled turbines, however, appeared to suffer from a severe performance degradation due to insect debris contaminating the blade leading edges. Operators of Californian wind farms reported turbine output reductions up to 30% at high wind speeds already after 3 months of turbine operation. Fig 2.9 presents measurements by Oak Creek Energy in 1999, on one of its NEG Micon 700/44 stall turbines showing the significant impact of blade soiling (2.9a). Bug accumulation at low wind speeds between July 11<sup>th</sup> and 16<sup>th</sup> led to a maximum power decrease of about 25% at higher wind speeds, while powers over 630 kW had been measured for a thoroughly cleaned turbine. The application of 1.15mm thick zigzag tape at  $x/c=0\%$  between 0.55R and the tip on all three blades gave a similar picture (fig. 2.9b).

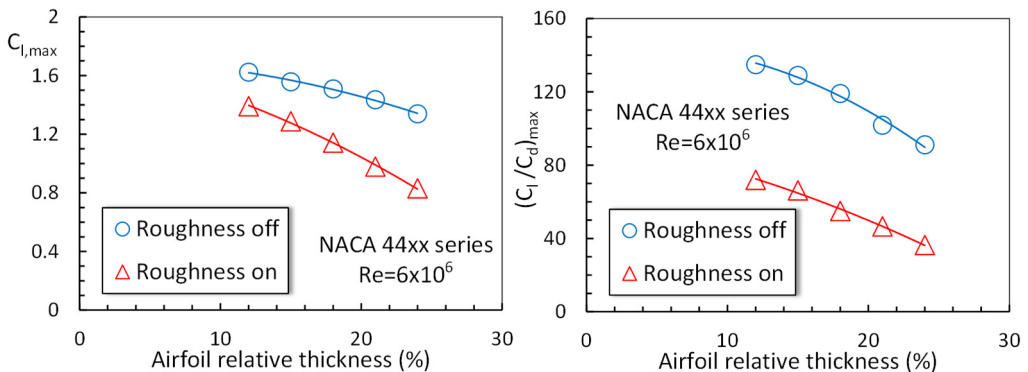


Figure 2.10: The effect of wrap-around roughness on the 2-dimensional measured performance of the NACA 44xx airfoil series. Data from Abbott et al. (1945).

The majority of the smaller turbines in the Californian wind farms were equipped with AeroStar blades manufactured by Alternegy in plants both in Denmark and the US. These blades incorporated the NACA 44xx series of airfoils. Figure 2.10 depicts the measured effect of standard NACA wrap-around roughness on the two-dimensional performance of this airfoil series.

This type of roughness consisted of 0.28 mm carborundum grains spread sparsely over the airfoil leading edge from 8% chord on the upper surface to 8% on the lower surface covering 5% to 10% of the area. Model chords typically were 0.61m long. Figure 2.10 demonstrates the significant impact on performance of this type of roughness. The NACA 4421 airfoil e.g. loses over 30% of its maximum lift, while the maximum lift-to-drag ratio is reduced with more than 50%. This performance degradation, both in efficiency and maximum lift, shown here for a Reynolds number of  $6 \times 10^6$ , is noticeable over the entire range of Reynolds numbers occurring on the blades of stall machines, with the tendency to even worsening at lower Reynolds numbers. Results for the NACA 230xx

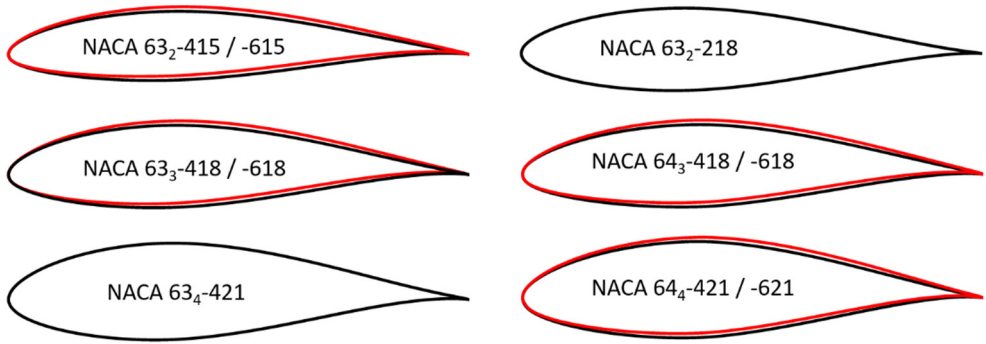


Figure 2.11: The most applied airfoils from the NACA 6-series. Red contours denote highest camber (6xx) of 15%, 18% and 21% thick sections.

series show comparable behavior. Although the wrap-around roughness not specifically mimics the soiling encountered on wind turbine blades, the measurements do show a high sensitivity to premature transition due to roughness elements distributed across the leading edge.

The application of laminar airfoils from the NACA-63 and -64 series (like was envisaged for the Mod-5A turbine), see fig. 2.11, alleviated the problem to some extent. These series show about the same lift reduction due to roughness up to  $C_{l,max}$ , but the loss in stall performance is much smaller, as is shown in fig. 2.12 (left) for a 21% thick airfoil. This particularly helps to maintain stall turbine maximum power. In addition, the clean and rough laminar airfoil lift-drag ratio at the relevant incidences (fig. 2.12 right) is much better.

AeroStar blades were sold to more than 25 countries worldwide. The company went bankrupt after the Californian tax credits expired.

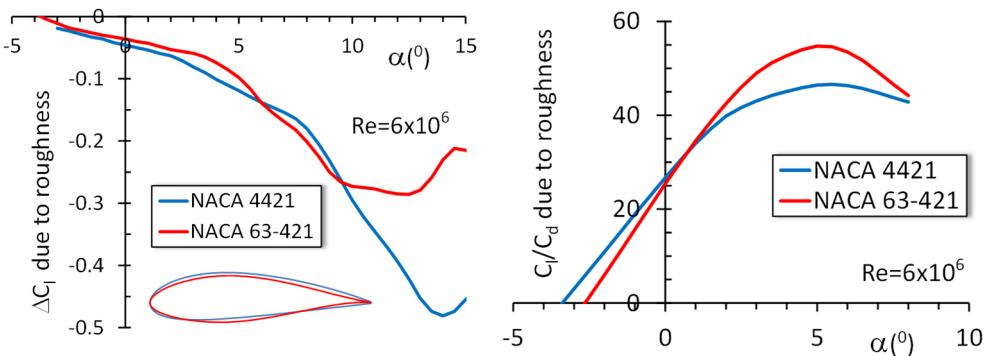


Figure 2.12: Comparison of roughness performance between NACA 4421 and NACA 63<sub>4</sub>-421 at  $Re=6 \times 10^6$ .

## 2.3 THE NEXT GENERATION WIND TURBINE DEDICATED AIRFOILS

### 2.3.1 SERI/ NREL airfoils

With the large power losses due to blade contamination as a background, the development of new wind turbine dedicated airfoils, of which some are still used today, started with the airfoil family presented by Somers and Tangler in the mid-eighties (Tangler, 1986).

The design effort was performed under the auspices of the Solar Energy Research Institute (later National Renewable Energy Laboratory and now National Laboratory of the Rockies) and funded by the U.S. Department of Energy. The airfoils were designed by Somers (Airfoils Inc.) with the Eppler airfoil analysis and design code, which is based on inverse design with conformal transformation. From the first designs, three airfoils (S805, S809 and S814) were tested in the Delft University Low Turbulence wind tunnel to validate the code. The S809 (fig. 2.13) is the most widely known, as it was used in the blades of the NREL 10m diameter stall controlled research turbine, which underwent comprehensive testing both during field tests and in the 24.4x36.6m<sup>2</sup> NASA-Ames wind tunnel in the USA. Test results were disseminated in several task reports of the International Energy Association (IEA) research program.

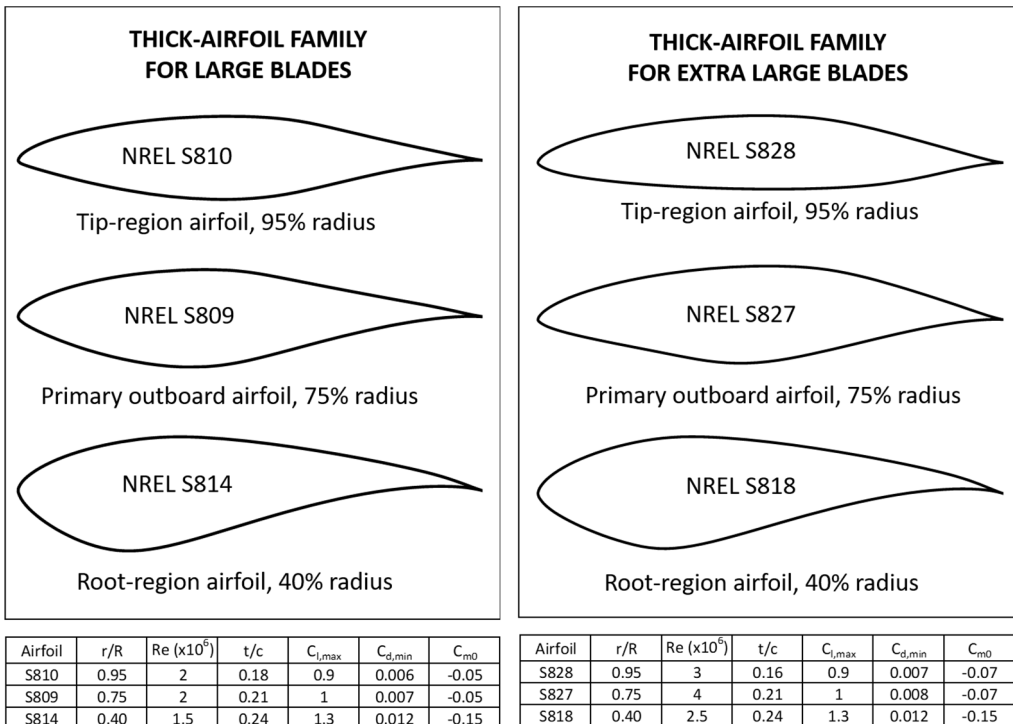


Figure 2.13: Airfoil shape and design parameters of two of the nine families in table 2.1. Note that extra-large blades were targeted for turbine diameters up to 50m.

Table 2.1: An overview of the early NREL airfoil families (Somers, 2005)

Wind Turbine		Thickness Category	Airfoil		
Diameter	Type		Primary	Tip	Root
3-10 m	Variable speed Variable pitch	Thick	–	S822	S823
10-20 m	Variable speed Variable pitch	Thin	S801	S802 S803	S804
	Stall Control	Thin	S805 S805A	S606 S806A	S807 S808
		Thick	S819	S820	S821
20-30 m	Stall Control	Thick	S809	S810	S811
			S812	S813	S814/ S815
20-40 m	Variable speed Variable pitch	–	S825	S826	S814/ S815
30-50 m	Stall Control	Thick	S816	S817	S818
40-50 m	Stall Control	Thick	S827	S828	S818

The 21% thick S809 is typified with a restrained upper surface thickness to reduce the adverse pressure gradients at higher angles of attack prior to  $C_{l,max}$ . From this point on this became typical for most new airfoil designs with moderate to high thickness. The lower adverse pressure gradients lead to postponed flow separation compared to equally thick conventional aerospace airfoils. Especially in soiled conditions excessive drag can thus be avoided. Limited roughness sensitivity was accomplished by shaping the pressure distribution such that natural transition from a laminar to a turbulent boundary layer occurs near the airfoil leading edge prior to reaching the maximum lift coefficient, a way to reduce losses around stall in soiled conditions. Benign post stall behavior was another design requirement to alleviate fatigue loads at the higher wind speeds.

The S809 airfoil has a relatively low maximum lift coefficient, which helps to reduce peak-power overshoot of relatively small stall turbines and keeps adverse pressure gradients low.

After the early verification of the design concept, in the following decade some 9 airfoil families were designed, comprising over 30 different airfoils (see table 2.1). Fig. 2.13 shows the section shapes of two families, one for turbines rated less than 500 kW and the second for turbines rated greater than 500 kW (Tangler and Somers, 1995).

Aerostar blades were generally set at an unfavourable pitch angle for operation at low wind speeds to limit peak rotor power at high wind speeds, while rotors still suffered from machine shutdowns due to generator excessive temperatures. The first rotors with SERI blades were extensively field tested on Micon, Bonus and Nordtank 65 kW stall machines (e.g. Tangler et al., 1990). With comparable loads, the relatively low maximum lift outboard airfoils, with a lower roughness sensitivity, enabled the increase of the rotor diameter from 16m to 17m, enlarging the swept rotor disc area by 14%. Combined with refined blade layout (a non-linear twist of  $20^{\circ}$ , against an Aerostar linear twist of  $8.4^{\circ}$ ) annual energy improvements were reported to be 10% to 20% for clean blades and around 30% for contaminated blades (Tangler et al., 1992).

### 2.3.2 FFA airfoils

In Europe, at FFA (Flygtekniska Försökanstalten -the Aeronautical Research Institute, at present FOI) in Sweden, Björck designed the FFA-W1-xxx series of airfoils in which xxx stands for 10 times the airfoil maximum thickness-to-chord ratio in %. It was initially intended for a 45m diameter variable speed yaw controlled rotor with a tip speed ratio of 8. The sections feature fairly high design lift coefficients in the order of 1.2 (at  $Re=3 \times 10^6$ ) and have maximum relative thicknesses ranging from 12.8% to 27.1% (Björck 1989). The design-Reynolds number was targeted at values beyond  $3 \times 10^6$ .

A second series, FFA-W3-xxx (Björck 1990, fig. 2.14), was given slightly more camber and consequently has higher design-lift coefficients (order 1.3). The high design lift coefficient

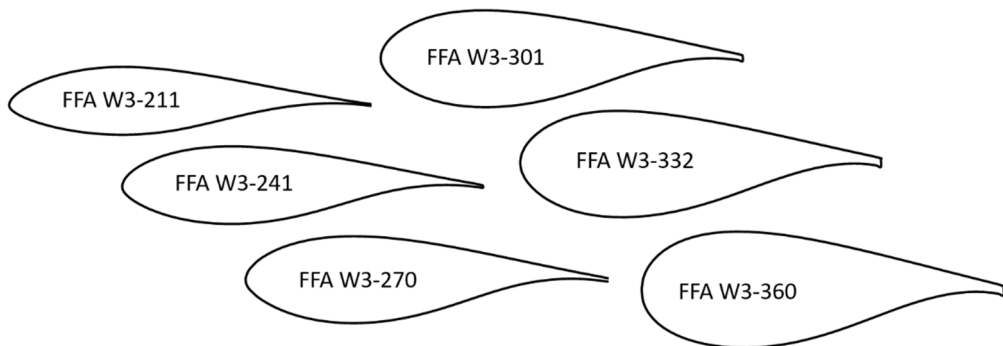


Figure 2.14: The FFA-W3 airfoil series designed by Björck in 1990 for variable speed machines.

makes the airfoils attractive for comparative studies regarding long and slender blades. The series contains airfoil thicknesses between 21.1% and 36% and was intended to work with thinner airfoils from the NACA 63-6xx series. FFA-W3 airfoils were e.g. applied in the Vestas V66 blades (2003) and thick members of the family also appeared in the LM19 blade in 1999. The series later also formed the basis for the DTU 10MW reference turbine developed in the European project INNWIND.EU, presented in 2013, with FFA-W3-241 at

the outboard 60% to 100% radius. Also the rotor of the IEA 15-MW off shore reference wind turbine (fig. 1.2), developed in the IEA-Wind Task 37 project (Gaertner et al. 2020), contains members of this family.

Two airfoils were designed with design lift coefficients around 1 and moderate maximum lift coefficients: FFA-W2-152 and FFA-W2-210.

### 2.3.3 DU airfoils

In the same period Timmer and van Rooij started to develop airfoils at the Delft University of Technology, the Netherlands (Timmer and van Rooij, 2003). Most of the DU airfoils were designed in cooperation with turbine or independent blade manufacturers. The general designation of the DU airfoils is DUyy-W-xxx, in which DU stands for Delft University, followed by the last two digits of the year in which the airfoil was designed. The W denotes the wind energy application, to distinguish the airfoil from the ones designed for sailplanes and general aviation. The last 3 digits give 10 times the airfoil maximum thickness in percent of the chord. In the case of DU91 there is an additional number following the W to denote that there has been more than one design with a thickness of 25% that year. The DU-airfoils (fig. 2.15) were not per se designed as a family (which is also evident from their names, showing the different years of design), although the airfoil characteristics of earlier designs were taken into account with new designs of thicker or thinner shape. The primary design driver for the Delft airfoils was to keep the sensitivity of the airfoils to contamination and contour imperfections of the nose as low

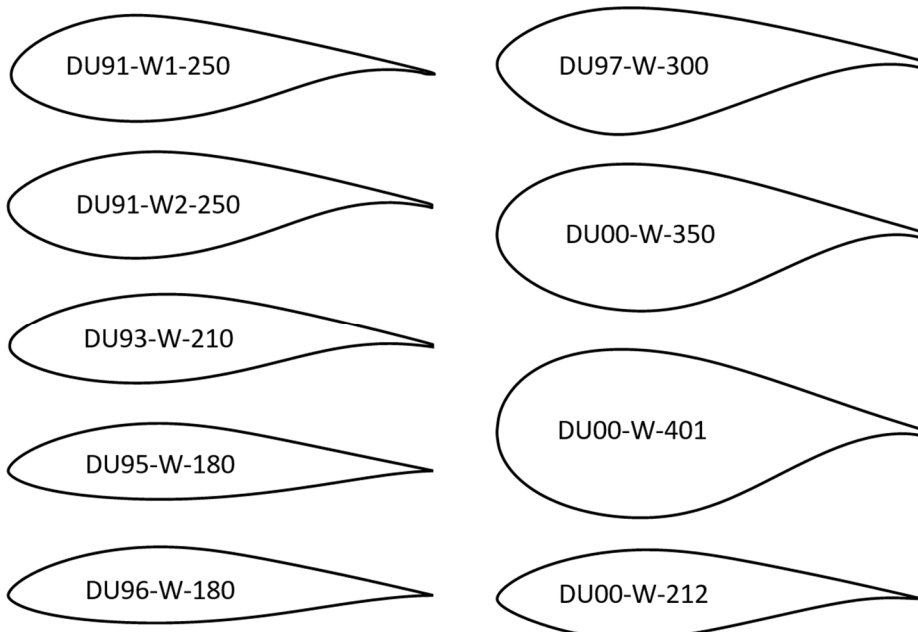


Figure 2.15: The shape of the early DU-airfoils

as possible. To accomplish this, transition was designed to occur close to the airfoil leading edge at incidences approaching stall.

Airfoil DU91-W2-250 was targeted for the blade mid-span of a 350 kW, 30m diameter, stall turbine. The Dutch manufacturer of this turbine aimed at adopting the NACA 63-series for the blades, but uncertainty existed regarding the performance of the thick members of this NACA family. Wind tunnel tests confirmed the undesirable performance of the NACA 63<sub>(421)</sub>-425 airfoil in the rough condition (fig. 2.16) and the improvement with

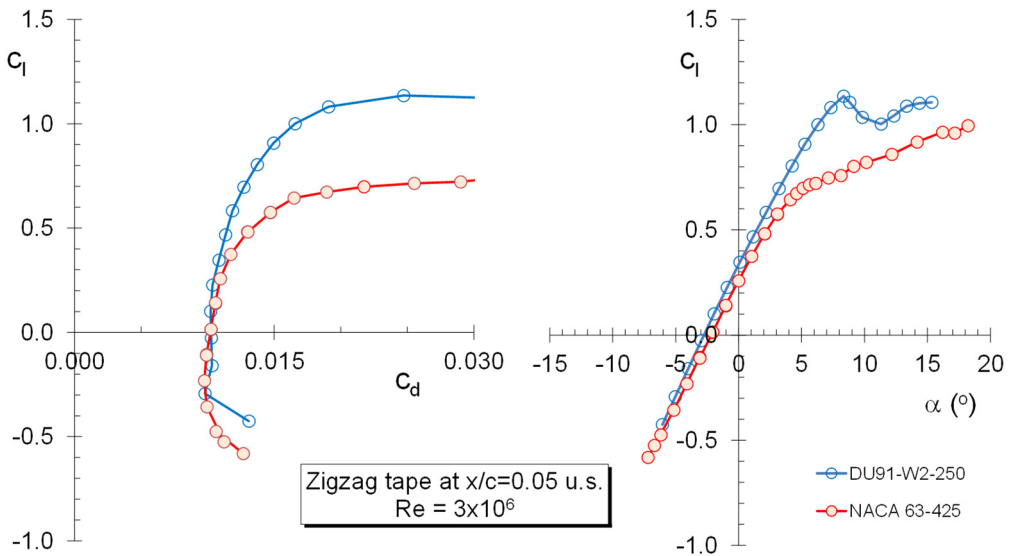


Figure 2.16: The performance of airfoils DU91 and NACA 63<sub>(421)</sub>-425 with 0.30 mm thick zigzag tape at the 5% upper surface chord station.

the new profile.

For commercial reasons many blade manufacturers offered their blades for application both on stall and variable speed controlled turbines.

For the early DU-airfoils this resulted in some compromising regarding the different demands for stall and post stall behaviour, since airfoils for variable speed rotors have a much more limited range of operational angles of attack.

Most of the early designs were tested in the Delft University low-speed low-turbulence tunnel LTT for Reynolds numbers between  $0.7 \times 10^6$  and  $3.5 \times 10^6$ . DU 93-W-210 was intended to perform in a blade having the NACA 63<sub>3</sub>-618 as a tip airfoil. DU 96-W-180 served as an alternative for other existing airfoils with low maximum lift coefficients (e.g. NACA 63-218), showing relatively high lift-to-drag ratio's. The shape was derived from DU95-W-180, which was measured with a 20% chord flap. A flap deflection of  $2^\circ$  gave the targeted maximum lift coefficient of 1.25 at  $Re=3 \times 10^6$ . Later designs were made to either replace DU93 when used with DU96 and DU91 to increase shape compatibility (DU00-W-212) or as assignment to generate customer specific sections, such as DU98-W-210, DU00-

W-300 and DU10-W-240.

Thick airfoils were generated to be used with vortex generators (e.g. DU00-W-350 and DU00-W-401). Modifications of the 21%, 25% and 30% airfoils (mainly to reduce the TE-thickness) were used in the Dutch 6MW DOWEC-project (Kooijman et al., 2003) and the 5MW NREL reference turbine (Jonkman et al., 2009). Examples of DU-airfoil performance using add-ons like vortex generators, trailing edge wedges, Gurney flaps and trip wires can be found in Timmer and van Rooij (2003).

### 2.3.4 NTUA sections

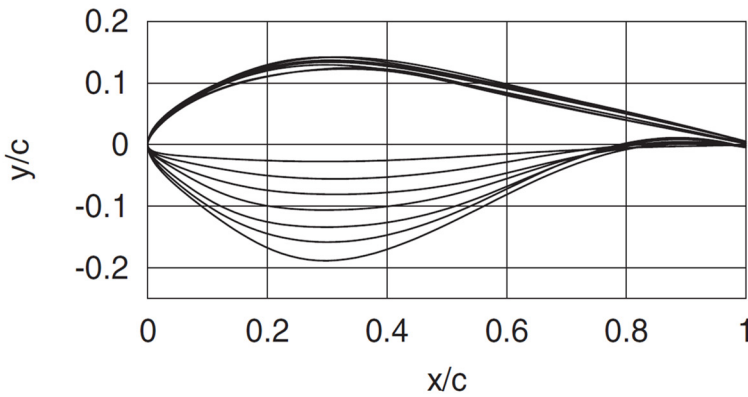
A design effort was undertaken by the National Technical University of Athens in cooperation with Risø, Denmark and the University of Southampton (SU), UK in view of producing a number of airfoils for a reference stall-regulated horizontal axis turbine (Chaviaropoulos, 1993). The Reynolds numbers ranged from  $1.8 \times 10^6$  at the root to  $2.35 \times 10^6$  at the tip. In this research Risø provided the required optimized lift and drag coefficients for a 20m diameter Danwind turbine and SU performed measurement on one of the airfoils. The design methodology consisted of an inverse viscous (for the suction side) and an inverse inviscid part. The design philosophy, unfortunately, involved point design aimed at low drag, which leads to airfoils with extended runs of laminar flow. Off-design performance may therefore be disappointing. The wind tunnel measurements on a clean airfoil confirmed the intended relatively docile stall characteristic. A root, mid and tip section were designed with maximum lift coefficients of 1.80, 1.40 and 1.10 respectively.

### 2.3.5 Risø airfoils

At the Wind Energy Department of Risø National Laboratory in Denmark a design effort started in 1996 with the development of their optimization tool AirfoilOpt (Fuglsang and Bak, 2004). They were the first to utilize numerical optimization in the design of airfoils for wind turbines with direct design. Airfoil shapes are described by a 5<sup>th</sup> or higher order B-splines and the panel code XFOIL was used to calculate the performance in the optimization process.

Design objectives were geometric compatibility, low roughness sensitivity, high cross section bending stiffness and high  $C_{l,max}$ . A number of airfoil series have been presented: Risø-A1-xx (1998), Risø-P-xx (2001), Risø-B1-xx (2001) and Risø-C2-xx (Bak, 2008), in which xx stands for the section maximum thickness in % of the chord.

Wind tunnel and field tests (Fuglsang et al., 2002), proved that the A-series (fig. 2.17) was very promising, especially, as a result of greater blade stiffness and strength, in terms of fatigue reduction for the same power. The roughness sensitivity of the airfoils, however, was found to be higher than expected. The design lift coefficients of the series is approximately 1.15, and thicknesses range from 15% to 33% in steps of 3%. The P-series



	$x/c$ at max $t/c$	$y/c$ at T.E.	$Re \times 10^6$	$\alpha_0$	Max $c_l$	Design $\alpha$	Design $c_l$	Max. $c_l/c_d$
Risø-A1-15	0.325	0.0025	3.0	-4.0	1.50	6.0	1.13	168
Risø-A1-18	0.336	0.0025	3.0	-3.6 (-3.8)	1.53 (1.43)	6.0 (7.5)	1.15 (1.22)	167 (107)
Risø-A1-21	0.298	0.005	3.0	-3.3 (-3.3)	1.45 (1.38)	7.0 (6.3)	1.15 (1.10)	161 (96)
Risø-A1-24	0.302	0.01	2.75	-3.4 (-3.3)	1.48 (1.36)	7.0 (6.5)	1.19 (1.15)	157 (91)
Risø-A1-27	0.303	0.01	2.75	-3.2	1.44	7.0	1.15	N/A
Risø-A1-30	0.300	0.01	2.50	-2.7	1.35	7.0	1.05	N/A
Risø-A1-33	0.304	0.01	2.50	-1.6	1.20	7.0	0.93	N/A

Figure 2.17: Theoretical properties of the Risø-A1 family of airfoils (1999) intended for machines with a rated power of over 600 kW and fixed rotor speed with either passive or active stall control. Picture and table from Fuglsang and Bak (2004). Numbers between brackets are values from Velux wind tunnel measurements at  $Re=1.6 \times 10^6$

(fig. 2.18) was intended for pitch controlled machines with a rated power greater than 1 MW and either fixed or variable speed control.

Design parameters were similar to A1-series, however with the maximum thickness at a slightly higher chord location ( $x/c \approx 0.33$ ). For bigger variable speed turbines with pitch control the B1-series (fig.2.18) offers sections with thicknesses from 15% to 36% with a design Reynolds number of  $6 \times 10^6$ . Airfoils for the outer 50% of the blade have design lift coefficients ranging from 1.15 to 1.21 and maximum lift coefficients in the order of 1.8 to 1.9. The chord location for maximum thickness varies between  $x/c=0.27$  and  $0.28$ .

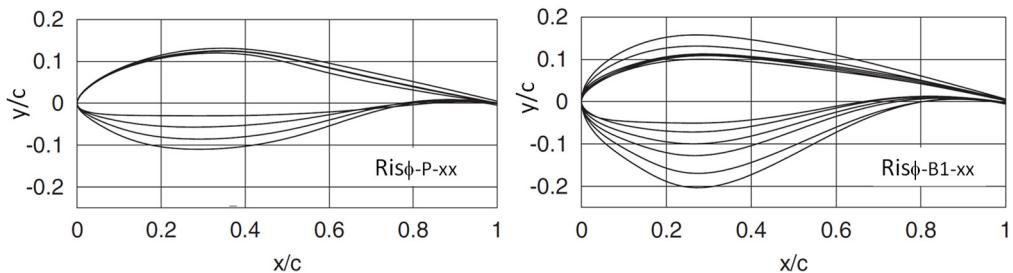


Figure 2.18 The Risø-P and Risø-B1 family of airfoils developed in 2001, intended for variable speed pitch controlled machines with a rated power greater than 1MW. Design Reynolds number of P and B1- series is  $3 \times 10^6$  and  $Re=6 \times 10^6$  respectively (Fuglsang and Bak, 2004).

Noise was an additional objective for the C2 series (fig. 2.19) and it was designed in conjunction with complete blade shape optimization, also taking structural properties into account. To generate high maximum lift they have higher camber at the trailing edge and a more forward located maximum thickness compared to earlier designs in view of better performance at high lift in the soiled condition.

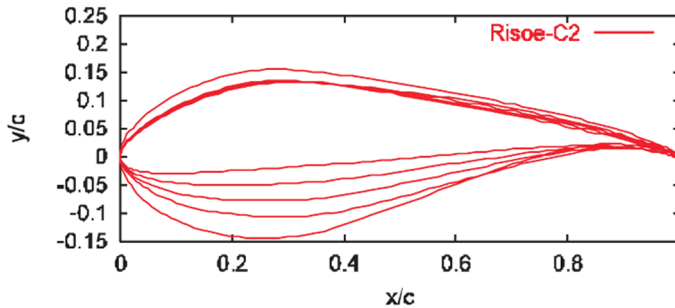


Figure 2.19 The Risø-C2 family of airfoils, intended for variable speed pitch controlled machines with a rated power in the order of 3MW and slender blades.  $Re=6 \times 10^6$ . Picture from Bak et al. (2008). For proprietary reasons a sharper picture of the shapes is not available.

The first airfoil designs were verified in the  $3.4 \times 3.4 \text{ m}^2$  Velux open jet wind tunnel, with a maximum Reynolds number of  $1.6 \times 10^6$ . Later designs were measured in the wind tunnel of LM Glasfiber in Denmark, the LTT of TU Delft or in the Laminar Wind Tunnel of Stuttgart University. No more recent Risø airfoil series can be found in the public domain.

## 2.4 OTHER, AND MORE RECENT, DEVELOPMENTS IN EUROPE

Wind turbine rotors continue to grow in size. In the USA e.g., average rotor diameters of land-based machines have grown almost linearly from around 80m in 2008 to about 140m in 2023 (US DOE, 2024). The steady increase in rotor diameter combined with the advances made in direct design coupled to optimization techniques, encouraged also other researchers to enter the field of airfoil design, resulting in a large number of design studies, predominantly aiming at multi-MW, pitch-regulated, variable-speed machines. The majority of these projects focused on the requirements for increased rotor size with long, slender blades: low noise (e.g. Lutz, 2004), improved thicker airfoils at blade outboard stations (e.g. Zahle et al., 2014; Boorsma et al., 2015; Munoz et al., 2016; Caboni et al., 2018), high design lift coefficients (Grasso, 2012 and 2014) and high Reynolds numbers (Mendez et al., 2014; Canal and Alfaro, 2015 and Ananda et al., 2018), combined with improved performance in conditions with a soiled blade leading edge. Within the INNWIND.EU program (2012-2017) Chavariopoulos and Sieros performed a study with a view to generate airfoils for a low-induction rotor as an alternative to the programs 10MW reference rotor (Chavariopoulos and Sieros, 2014). Hansen (2018) investigated the suitability for airfoil optimization using the Covariance Matrix Adaption Evolution Strategy

(CMA-ES) algorithm. Three airfoils for a MW-scale turbine were designed, with 18%, 21% and 25% maximum thickness-to-chord ratios, using similar performance constraints as equally thick DU-airfoils.

## 2.5 AIRFOIL DEVELOPMENTS IN CHINA

Regarding installed wind energy capacity, China has now become the world leader (IRENA, 2021). The fast penetration of wind energy into the Chinese energy mix also boosted Chinese national research into all fields of technology pertinent to wind turbine efficiency and many research groups became active on the subject of airfoil design. One of the earlier design studies was conducted by the Institute of Thermophysics Engineering of the China Academy of Sciences (CAS), targeted to generate airfoils exhibiting good aerodynamic performance in conditions with a soiled leading edge, while having good structural properties in the Reynolds number range from  $2 \times 10^6$  to  $5 \times 10^6$  for turbines of the 1 to 2 MW scale (Li et al. 2013). Later studies concentrated on better performance of airfoils of 30% thickness and beyond (Li et al., 2014 and 2017) and improved airfoil characteristics for low wind speed regions and turbulent inflow conditions with low noise characteristics (Li et al., 2019). Several of these CAS-W airfoils were tested in the  $0.8 \times 1.6 \text{ m}^2$  NF-3 wind tunnel at Northwestern Polytechnical University (NPU) or in the  $1.5 \times 3 \text{ m}^2$  wind tunnel of North China Electric Power University (NCEPU).

Improved performance over existing airfoils in the Reynolds number range up to  $3 \times 10^6$  also was the aim of a cooperation between the Chongqing University with the Nuclear Power Institute of China (CQUL-xxx airfoils, Pang, 2018) and the School of Mechanical Engineering of the Hubei University of Technology (WQ-B300 airfoil, Wang et al., 2019). A cooperation of the Chongqing University with the Technical University of Denmark resulted in the CQU-DTU-LN1xx series with 4 airfoils having thicknesses between 15% and 24% (CQU-DTU-LN124) (Cheng et al., 2014), fig. 2.20. Compared to existing airfoil series in this category, the thicker sections lack a pronounced aft-loading region (cusp) towards

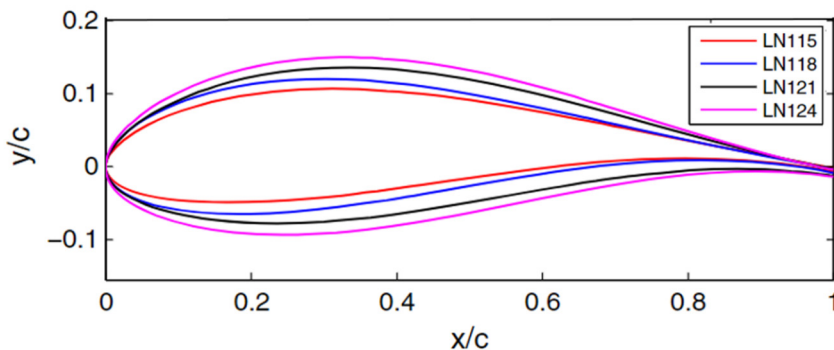


Figure 2.20: The CQU-DTU-LN1 low noise airfoils series (Cheng et al. 2014)

the lower side trailing edge.

Apart from good aerodynamic performance in clean and rough conditions and geometric compatibility, the optimization was specifically targeted to high design- lift coefficients and lift-drag ratios and low trailing edge noise in the Reynolds number range of  $2 \times 10^6$  to  $6 \times 10^6$ . Design-lift coefficients range from about 1.2 to 1.63 for the thickest airfoil. The 18% thick airfoil was tested in the  $1.83 \times 1.83 \text{ m}^2$  Hybrid Anechoic Test Section of the Virginia Tech Stability wind tunnel, USA, to measure the aerodynamic and the acoustic properties of the 0.6m chord model. The measured maximum lift coefficients at  $Re=2 \times 10^6$  for the clean and tripped conditions (1.77 and 1.5 respectively) appeared to be substantially lower than the XFOIL predicted values of 2.04 and 1.83. Compared to the NACA 64<sub>3</sub>-618 airfoil, frequently used for the outer part of wind turbine blades, the new airfoil has a lower noise emission. The agreement between the noise predictions using the BPM method (Brooks et al., 1989) and the measurements appeared to be good.

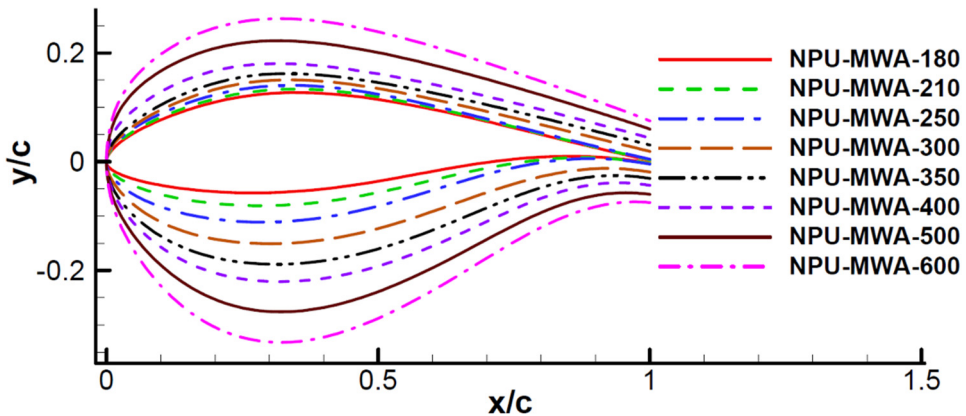


Figure 2.21: The NPU series of airfoils for large blades (Xu et al, 2019)

The Institute of Aerodynamic and Multidisciplinary Design Optimization of the Northwestern Polytechnical University (NPU) in Xi'an, China, concentrated on generating advanced airfoils for multi-Megawatt turbines. Improvements on an earlier series from 2013 were reported by Han et al. (2016). The airfoils are designated NPU-MWA-xxx, fig. 2.21. A great number of airfoils were tested in their NF-3 wind tunnel in the range of  $Re=3 \times 10^6$  to  $5 \times 10^6$ , confirming the predicted high design-lift coefficients of 1.2 or larger in the clean configuration.

The sections were used to redesign the blade for the 5MW NREL reference turbine (Xu et al., 2019), which resulted in a lighter blade with a better power coefficient owing to the use of the high lift and flatback airfoils of the series.

## 2.6 FLATBACK AIRFOILS

From an aerodynamic perspective high lift is required in the root part of a blade, while

from a structural standpoint high strength and stiffness are required, which leads to thick airfoils. A thickness of 40% chord or more is no exception at blade inboard stations. Conventional thick sections, unfortunately, are inherently sensitive to flow distortion and have notoriously disappointing performance under soiled conditions. To mitigate the undesired rough performance, airfoil series for large wind turbine blades, e.g. those presented in fig. 2.21, contain “flatback” airfoils, thick airfoils with a blunt trailing edge. These blunt sections have improved aerodynamic performance and larger cross-sectional area and moment of inertia than conventional root airfoils. They enable smaller root chords, saving blade weight.

### 2.6.1 Truncation

Blunt trailing edges were already used by Wortmann for the Growian turbine by truncation of the aft portion of airfoil FX 77-W-343, see fig. 2.4, giving a new airfoil, e.g. FX-W-400 with a 10.4% thick trailing edge. By truncation the stiffness properties of the section improve. However, as depicted in fig. 2.22, truncation also impacts the aerodynamic characteristics, as the section overall thickness increases, and, moreover, it introduces increased pressure drag, which combined effects adversely affect total drag (in this case with a factor of about 2). While the zero-lift angle changes, truncation does not seem to significantly impact the lift coefficient, after scaling the chord to 100%. This result confirms some earlier findings of Smith and Schaefer (1950) who performed measurements on a NACA 0012 airfoil with truncations giving a 4% thick trailing edge thickness. Law and Gregoreg (1987) experimentally confirmed that a NACA 64<sub>4</sub>-621 airfoil, truncated to a 30% thick airfoil with a 16% thick blunt trailing edge outweighs the performance of a conventional 30% thick airfoil such as NACA 0030 used for streamlining

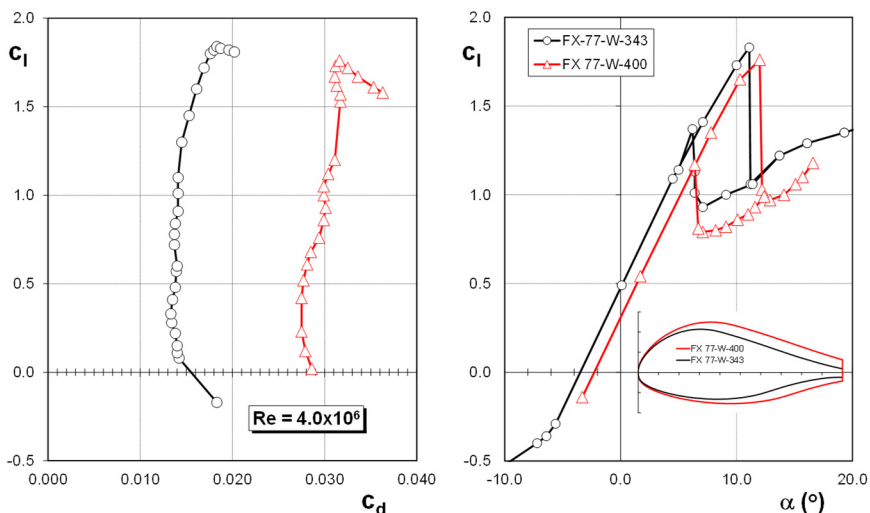


Figure 2.22: The experimental aerodynamic characteristics of airfoil FX 77-W-343 and its truncated counterpart FX 77-W-400. Data from Althaus (1972).

cables.

### 2.6.2 Creating a blunt trailing edge

Standish and van Dam (2003) introduced the flatback airfoil and performed a numerical study in which they separated the adverse increased thickness effect and a possible lift reduction by truncation, from the potentially beneficial impact a blunt trailing edge may have on the lift and on the roughness sensitivity of the section.

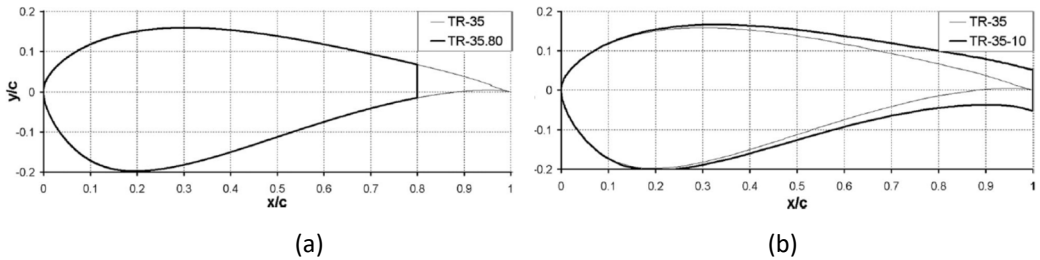


Figure 2.23: Two ways of creating a 10% thick trailing edge; by truncation (a) or by adding additional thickness to the camber line (b), Standish and van Dam (2003).

The 35% thick TR-35 airfoil was truncated to create a 10% thick trailing edge (fig.2.23a) giving a section with a relative maximum thickness of 44%. The increased thickness and its potential increase in aft adverse pressure gradient, the loss in camber, and hence in lift, and the increased pressure drag due to the truncation outweigh the improved roughness sensitivity due to the negative pressure at the back.

The same 10% trailing edge thickness resulted from symmetrically adding thickness to both sides of the camber line of the original airfoil, varying from 0 at the thickest point, to 10% at the TE (fig 2.23b), without a noticeable effect on the maximum thickness of the section. The latter modification results in less severe adverse pressure gradients at the two sides of the airfoil compared to the original section. The simulations show a significant improvement in maximum lift and roughness sensitivity owing to postponement of turbulent separation. Especially in the inboard portion of a blade, where due to the low rotational speed inflow angles are large, the lift is more important than the drag of a section. Despite the much higher base drag of the flat back airfoil, the higher lift contributes more to the torque of the rotor.

### 2.6.3 Vortex shedding

While a flatback airfoil potentially improves the airfoil lift generation and roughness insensitivity and provides better structural stiffness due to a larger cross-sectional area compared to conventional airfoils for a given thickness, it also creates periodic vortex shedding from the upper and lower surface trailing edges, which creates noise and variation in the aerodynamic characteristics. The latter may, when not properly dealt

with, affect the aero-elastic behaviour of the rotor blade.

To mitigate the unsteadiness in the wake behind the thick TE, a split flap of the length of the base thickness, placed at the middle of the TE, proved to be a simple and relatively efficient way to increase the base pressure, thereby lowering overall drag. It also impacts the frequency of vortex shedding from the trailing edge. Strictly speaking, this also enlarges the local chord of the blade and it increases upper surface adverse pressure gradients.

As panel codes like XFOIL cannot resolve the unsteady wake and its impact on the aerodynamic characteristics, Navier-Stokes solvers need to be used to simulate the unsteady flow field behind the bluff trailing edge and to predict the aero-acoustic behaviour.

Since 2003, a fair amount of studies have been devoted to shape optimization of flatback airfoils, e.g. Chen et al. (2012), Grasso (2013), and Madsen (2015), to numerical simulation of the flow over bluff airfoils, e.g. Papadakis et al. (2014) and Manolesos and Papadakis (2020, 2021) and to base drag reduction and general flow improvement by devices such as a swallow tail (Grasso and Ceyhan, 2015), vortex generators, trailing edge flaps, Gurney flaps and splitter plates to influence the vortex shedding behind the airfoil, e.g. Cene et al. (2021, 2022), see fig. 2.24

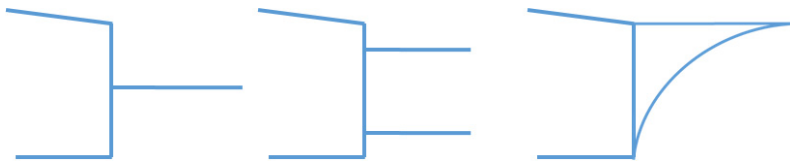


*Figure 2.24: Three solutions to mitigate the unsteadiness in the wake due to vortex shedding, with splitter plates (the two on the left) and with a swallow tail (right).*

## 2.7 CONCLUSIONS

Big blades in the early multi-MW-projects with pitch or partial pitch controlled machines incorporated airfoils predominantly of the turbulent type, such as the NACA 4 and 5-digit series and the FX airfoils designed by Wortmann. They are characterized by a leading edge suction pressure peak increasing with incidence due to forward camber to generate lift, leading to relatively high maximum lift coefficients. During the early big turbine programs it was concluded that wind turbine technology was not yet mature enough to come to commercially viable turbines. A reset to much smaller machines with a different power control strategy followed. The development of stall turbines gave a switch towards more laminar type of airfoils, such as the NACA 63 and 64 airfoil series, and to specially designed dedicated airfoils in the Reynolds number range of  $1 \times 10^6$  to  $6 \times 10^6$ , such as Sxxx, FFA, Risø

and DU airfoils.

Over the past 40 years, the rotor diameter of commercial turbines increased with a factor of 10, to over 220m at present. This constant upscaling of wind turbines has led to different requirements for the blade sections.

Three important issues have changed requirements over the years:

- Control strategies for commercial turbines developed from predominantly fixed rotational speed (rpm) and fixed pitch (stall control) to variable rpm and pitch control, which made the required post-stall behaviour of the airfoils less important.
- With turbine size also the Reynolds numbers based on chord increased with a factor of about 10, to approximately  $15 \times 10^6$ . Due to less noise restrictions, the tip-speed of offshore turbines is higher than of land-based machines, which also contributed to higher Reynolds numbers.
- As blade weight should be kept low, the relative chord length  $c/R$  over the blade span decreased. With bigger rotor diameters we see increasingly slender blades. A slender blade necessitates higher design-lift coefficients to keep the contribution to the power of the various span wise blade segments at a sufficiently high level (see chapter 4). As airfoils consequently now need higher design-lift coefficients and also should be insensitive to leading edge contamination (for which transition should be on the leading edge approaching stall), present airfoils are typified by more pronounced forward and trailing edge camber to reach high lift coefficients. These airfoils typically have sharper stall.

Airfoil shape development shifted from inverse design (finding a shape for a specified pressure distribution) to direct design using multi-disciplinary numerical optimization procedures. By varying the section shape, the latter searches an optimum on the bases of a specified matrix, satisfying aerodynamic, structural and noise targets and constraints. This enables the designer to generate many more airfoil sections potentially suitable to fulfil the requirements.

For the root of the blade at present flatback airfoils are applied. By using a bluff trailing edge of 10% to 20% chord on the thick blade root sections, stiffness and roughness characteristics are ameliorated, despite increased drag due to a more negative base pressure. Splitter plates can be attached to partly suppress the associated vortex shedding.

## 2.8 REFERENCES

Abbott, I.H., von Doenhoff, A.E. and Stivers, S., jr. (1945) *Summary of airfoil data*. NACA Report no. 824

Althaus, D. (1972) *Stuttgarter Profilkatalog I*. Institute for Aerodynamics and Gasdynamics, Stuttgart University, Germany.

Althaus, D. (1984) *Polarmessungen an den Profilen FX 84-W-xxx*. Institute for Aerodynamics and Gasdynamics, Stuttgart University, Germany.

Althaus, D. (1998) *Niedriggeschwindigkeitsprofile*. Friedrich Vieweg & Sohn, Germany, April 1998.

Ananda, G.K., Bansa, I.S. and Selig, M.S. (2018) *Aerodynamic Design of the 13.2 MW SUMR-13i Wind Turbine Rotor*. AIAA SciTech Forum, 2018 Wind Energy Symposium, January 2018, Kissimmee, Florida, USA DOI:10.2514/6.2018-0994

Bak, C., Andersen, P.B., Madsen, H.A., Gaunaa, M., Fuglsang, P. and Bove, S. (2008) *Design and Verification of Airfoils Resistant to Surface Contamination and Turbulence Intensity*. AIAA 2008-7050

Bak, C., Gaudern, N., Zahle, F. and Vronsky, T. (2014) *Airfoil design: Finding the balance between design lift and structural stiffness*. Journal of Physics: Conference Series, Volume 524, *The Science of Making Torque from Wind 2014 (TORQUE 2014)* 18–20 June 2014, Copenhagen, Denmark.

Bak, C. (2021), *Airfoil design* in: Handbook of Wind Energy Aerodynamics. B. Stoevesandt et al. (eds.), Springer Nature Switzerland AG 2021, [https://doi.org/10.1007/978-3-030-05455-7\\_3-1](https://doi.org/10.1007/978-3-030-05455-7_3-1)

Björck, A. (1989) *Airfoil Design for Variable RPM Horizontal Axis Wind Turbines*. Conference proceedings, EWEC'89, European Wind Energy Conference and Exhibition. Glasgow, Scotland, July 1989.

Björck, A. (1990) *Coordinates and calculations for the FFA-W1-xxx, FFA-W2-xxx and FFA-W3-xxx series of airfoils for horizontal axis wind turbines*. Report FFA TN 1990-15, Stockholm, Sweden.

Boorsma, K., Munoz, A., Mendez, B., Gomez, S., Irisarri, A., Munduate, X., Sieros, M.G., Chaviaropoulos, P., Voutsina, S., Prospathopoulos, J., Manolesos, M., Shen, W.Z., Zhu, W.J., Madsen, H.A. (2015). *New airfoils for high rotational speed wind turbines*, Innwind.eu, Deliverable 2.12.

Braslow, A.L. and Knox, E.C. (1958) *Simplified method for the determination of critical height of distributed roughness particles for boundary-layer transition at Mach numbers from 0 to 5*. NACA Technical Note 4363.

Brooks, T.F., Pope, D.S. and Marcolini, M.A. (1989). *Airfoil self-noise and prediction*. NASA Reference Publication 1218, NASA, USA

Canal, M. and Alfaro, D. M. (2015) *New airfoil family design for large wind turbine blades*. 33rd Wind Energy Symposium, Florida, USA, 2015

Cene, A., Grasso, F., Manolesos M. (2021). *Thick airfoils, Vortex Generators, Gurney Flaps and Flatback Solutions: How to get better performance out of the blade inner region?* Wind Energy Science Conference - EAWC, May 2021, Hannover, Germany

Cene, A., Grasso, F., Manolesos M. (2022). *Aerodynamic and Aeroacoustic Measurements of the Flow Past a Very Thick Flatback Airfoil with Passive Flow Control Devices*, 2022 AIAA SciTech Forum, 10.2514/6.2022-0279.

Chaviaropoulos, P.K., Bouras, B., Leoutsakos, G. and Papailiou, K. D. (1993) Design of Optimized Profiles for Stall Regulated HAWTs: Part 1: Design Concepts and Method Formulation. Wind Engineering Vol. 17, No. 6, pp. 275-287

Chaviaropoulos, P.K. and Sieros, S. (2014) *Design of Low Induction Rotors for use in large offshore wind farms*, Proc. Scientific Track, EWEA 2014, Barcelona.

Chen, X. and Agarwal, R. (2012) *Optimization of Flatback Airfoils for Wind-Turbine Blades Using a Genetic Algorithm*. Journal of Aircraft Vol. 49, No. 2, March–April 2012.

Chen, J., Wang, Q. and Sun, Z., eds. (2018) *Wind turbine airfoils and blades*. Science Press Ltd, and Walter de Gruyter GmbH, Beijing/Berlin/Boston.

Cheng, J., Zhu, W.J., Fischer, A., Garcia, N.R., Madsen, J., Chen, J. and Shen, W.Z. (2014) *Design and validation of the high performance and low noise CQU-DTU-LN1 airfoils*. Wind Energy 17(12):1817–1833

Corten, G.P. and Veldkamp, H.F. (2001) *Insects cause double stall*. Proceedings EWEC 2001, Copenhagen, Denmark.

Fuglsang, P., Sangill, O., and Hansen, P. *Design of a 21m blade with Riso-A1 airfoils for active stall controlled wind turbines*. Denmark. Forskningscenter Risoe. Risoe-R No. 1374(EN).

Fuglsang, P. and Bak, C. (2004) *Development of the Risø wind turbine airfoils*. Wind Energy 2004; 7,145–162 (DOI: 10.1002/we.117)

Gaertner, E, et al. (2020) *Definition of the IEA Wind 15-Megawatt Offshore Reference Wind turbine*. IEA Wind TCP Task 37. Technical Report.

Garrad, A.D. (1990) *New aerofoils and some thoughts on wind turbine aerodynamics*, in: Proceedings BWEA\_DoEn workshop, Recent developments in the aerodynamics of wind turbines. University of Nottingham UK.

Grasso, F. (2012) *Design of a Family of Advanced Airfoils for Low Wind Class Turbines*, EWEA, Torque 2012, October 2012, Oldenburg, Germany.

Grasso, F. (2013) *Development of Thick Airfoils for Wind Turbines*. Journal of Aircraft Vol. 50, No. 3, May-June 2013.

Grasso, F. (2014), *ECN Airfoils for large offshore wind turbines; Design and wind tunnel testing*. EWEA 2014, Barcelona, Spain.

Grasso, F. and Ceyhan, Ö. (2015) *Non-conventional flat back airfoils for very large offshore wind turbines*. AIAA SciTech Forum January 2015 Kissimmee, Florida, USA.

Han, Z.H., Zhang, K.S., Liu, J. and Song, W.P. (2013) *Surrogate-based aerodynamic shape optimization with application to wind turbine airfoils*. AIAA-2013-1108.

Han, Z., Song, W., Gao, Y., and Chen, J. (2016) *Design and verification of airfoil families for large-size wind turbine blades* J. Applied Mathematics and Mechanics (English Edition), 2016, 37(S1): S67-S84.

Hansen, T.H. (2018) *Airfoil optimization for wind turbine application*. Wind Energy 21:502–514. <https://doi.org/10.1002/we.2174>

Hau, E. (2013) *Wind Turbines*. Springer Verlag, Germany. DOI 10.1007/978-3-642-27151-9

Hill, D.C and Garrad, A.D. (1989) *Design of aerofoils for wind turbine use*. Conference proceedings European Wind Energy Conference , Glasgow UK.

IRENA (2021). *Renewable Energy Capacity Statistics 2021*. International Renewable Energy Agency (IRENA), [www.irena.org](http://www.irena.org)

Jonkman, J., Butterfield,S., Musial, W. and Scott, G. (2009) *Definition of a 5-MW Reference Wind Turbine for Offshore System Development*. Technical Report NREL/TP-500-38060, February 2009

Khoo, H. and Graham, J.M.R. (1990) *Stall control of wind turbine blades*. Department of Aeronautics, Imperial College, London ETSU WN5095.

Kim, C. W., Cho, T. H. (2011) *Wind tunnel test of the 2D airfoil for the MW size wind turbine*, Journal of Wind Energy, Vol. 2 Num. 2, 2011, pp. 38-42

Kooijman, H.J.T., Lindenburg, C., Winkelaar, D. and Hooft, E.L. van der (2003) *DOWEC 6 MW PRE-DESIGN: Aero-elastic modelling of the DOWEC 6 MW pre-design in PHATAS*. DOWEC-F1W2-HJK-01-046/9 September 2003, public version.

Law, S.P.,Gregorek G.M., (1987) *Wind Tunnel Evaluation of a Truncated NACA 64-621 Airfoil for Wind Turbine Applications*, DOE/NASA/0330-2 NASA CR-180803

Li X., Yang K, Bai J. and Xu J. (2013) *A method to evaluate the overall performance of the CAS-W1 airfoils for wind turbines*, J. Renewable Sustainable Energy 5(6), 063118.

Li X., Yang K., Zhang L., Bai J. and Xu J. (2014) *Large thickness airfoils with high lift in the operating range of angle of attack*. J Renew Sustain Energy 2014;6(3):033110.

Li X., Yang K., Zhang L. and Bai J. (2017) *Experimental study of Reynolds number effects on performance of thick CAS wind turbine airfoils*, J. Renew. Sustain. Energy 9 (6) (2017) 063309.

Li X., Zhang L., Song J., Bian F. and Yang K. (2019) *Airfoil design for large horizontal axis wind turbines in low wind speed regions*. Renewable Energy 145 (2020) [doi.org/10.1016/j.renene.2019.07.163](https://doi.org/10.1016/j.renene.2019.07.163)

Liebeck, R.H. (1976) *On the design of subsonic airfoils for high lift*. AIAA 9<sup>th</sup> Fluid and Plasma Dynamics Conference, San Diego, California, USA, 1976

Madsen, H.A. (ed.) (2015) *New airfoils for high rotational speed wind turbines*. DTU-Wind, InnWind-EU deliverable 2.12, September 2015, Denmark.

Manolesos, M. and Papadakis, G. (2021) *Investigation of the three-dimensional flow past a flatback wind turbine airfoil at high angles of attack*. Phys. Fluids 33, 085106 (2021); <https://doi.org/10.1063/5.0055822>

McGhee, R.J., Beasley, W.D. and Whitcomb R.T., (1979) *NASA Low- and Medium speed airfoil development*. NASA Technical Memorandum 78709

Mendez, B., Mundiata, X., and San Miguel, U. (2014) *Airfoil family design for large offshore wind turbine blades*. J. Phys.: Conf. Ser. 524 012022, doi:10.1088/1742-6596/524/1/012022

Merino-Martinez, R., Avallone, F., van der Velden, W. and Ragni, D. (2017) *Acoustic measurements of a DU96-W-180 airfoil with flow-misaligned serrations at a high Reynolds number in a closed wind tunnel*. 7<sup>th</sup> international conference on wind turbine noise, Rotterdam May 2017

Papadakis, G., Voutsinas, S., Sieros, G., and Chaviaropoulos, T. (2014) *CFD aerodynamic analysis of non-conventional airfoil sections for very large rotor blades*. Journal of Physics: Conference Series 555 (2014) 012104 doi:10.1088/1742-6596/555/1/012104

Papadakis, G. and Manolesos, M. (2020) *The flow past a flatback airfoil with flow control devices: benchmarking numerical simulations against wind tunnel data*, Wind Energ. Sci., 5, 911–927, <https://doi.org/10.5194/wes-5-911-2020>, 2020.

Ragni, D., Avallone, F., van der Velden, W.C.P. et al. (2019) *Measurements of near-wall pressure fluctuations for trailing-edge serrations and slits*. Exp Fluids 60, 6 (2019). <https://doi.org/10.1007/s00348-018-2654-5>

Rooij, R.P.J.O.M. van (1996) *Modification of the boundary layer calculation in RFOIL for improved airfoil stall prediction*. Report IW-96087R, TU-Delft, The Netherlands

Satchwell C.J. and Turnock S.R. (1989) *Structurally efficient aerofoils for wind turbines*. Conference proceedings European Wind Energy Conference, Glasgow UK.

Smith H.A. and Schaefer R.F. (1950) *Aerodynamic characteristics at Reynolds numbers of*

$3 \times 10^6$  and  $6 \times 10^6$  of three airfoil sections formed by cutting off various amounts from the rear of the NACA 0012 airfoil section. NACA TN 2074

Somers, D.M. (1981) *Design and experimental results for a Natural-Laminar-Flow airfoil for general aviation applications*. NASA-TP-1861

Somers, D.M. (2005) *Design and experimental results for the S827 airfoil*. NREL/SR-500-36345, Jan. 2005.

Standish, K. J., and van Dam, C. P. (2003) *Aerodynamic Analysis of Blunt Trailing Edge Airfoils*, ASME J. Sol. Energy Eng., 125\_4\_, pp. 479–487.

Tangler, J.L. and Somers, D.M. (1986) A low Reynolds number airfoil family for horizontal axis wind turbines. *Conference proceedings "Aerodynamics at low Reynolds numbers"*, London UK.

Tangler, J.L. and Somers, D.M. (1987) *Status of the special- purpose airfoil families*, Conference Proceedings Windpower '87, San Francisco, CA, USA.

Tangler, J.L., Smith, B., Jager, D. and Olsen, T. (1990) *Atmospheric Performance of the Special-Purpose SERI Thin-Airfoil Family: Final Results*. Proc. European Wind Energy Conference, Madrid, Spain, September 1990.

Tangler, J.L., Smith, B. and Jager, D. (1992) *SERI advanced wind turbine blades*. NREL/TP-257-4492, Feb. 1992

Tangler, J.L. and Somers, D.M. (1995) *NREL Airfoil Families for HAWTs*, NREL/TP-442-7109, Jan. 1995

Timmer, W. A., (1992) *New Section Shapes for Wind Turbines: a Literature Study*, Report IW-92056R, Institute for Wind Energy, TU Delft, The Netherlands. In Dutch.

Timmer, W.A. and Bak, C. (2013) *Aerodynamic characteristics of wind turbine blade airfoils*. In: *Advances in wind turbine blade design and materials*. Woodhead Publishing Series in Energy, 2013 pp 109-149 DOI : 10.1533/9780857097286.1.109

Timmer, W.A. and van Rooij, R.P.J.O.M. (2003) "Summary of the Delft University Wind Turbine Dedicated Airfoils". *Journal of Solar Energy Engineering*, Vol. 125, pp 488-496.

U.S. Department of Energy and NASA (1995). [https://en.wikipedia.org/wiki/NASA\\_wind\\_turbines#/media/File:Wind\\_generator\\_comparison.svg](https://en.wikipedia.org/wiki/NASA_wind_turbines#/media/File:Wind_generator_comparison.svg)

Viterna , L. A. and Janetzke. D.C. (1982) *Theoretical and Experimental Power From Large Horizontal-Axis Wind Turbines*. NASA Lewis Research Center, September 1982, Doe/NASA/20320-41, NASA TM 82944

Wang Q., Huang P., Gan D. and Wang J. (2019) *Integrated Design of Aerodynamic Performance and Structural Characteristics for Medium Thickness Wind Turbine Airfoil*. Appl. Sci. 2019, 9, 5243; doi:10.3390/app9235243

WindEurope (2024) <https://windeurope.org/about-wind/wind-energy-today/> Retrieved August 2024

Wortmann F.X. (1978) *Tragflügel für Windturbinen*. Instituts Bericht 78-9. Institute for Aerodynamics and Gasdynamics, Stuttgart University, Germany.

Parchen, R. (1998) Progress report DRAW: *A prediction scheme for trailing-edge noise based on detailed boundary-layer characteristics*. TNO Report HAG-RPT-980023, TNO Institute of Applied Physics, The Netherlands.

Xu J. , Han Z., Yan X. and Song W. (2019) *Design Optimization of a Multi-Megawatt Wind Turbine Blade with the NPU-MWA Airfoil Family*. Energies 2019, 12, 3330; doi:10.3390/en12173330

Zahle F., Bak C., Sørensen N.N., Vronsky T., Gaudern N. (2014) *Design of the LRP airfoil series using 2D CFD*. J. Phys.: Conf. Ser. 524 012020.



# 3

## DESIGN AND ANALYSIS TOOLS

### *3.1 TWO-DIMENSIONAL AIRFOIL CHARACTERISTICS PREDICTION USING XFOIL AND RFOIL*

#### **3.1.1 XFOIL**

At present, the vast majority of the airfoil shape optimization codes is utilizing XFOIL or RFOIL as flow solver. Solutions utilizing CFD codes are still too time consuming to be used for this purpose. Between 1990 and 1996 wind turbine airfoils at TU Delft were also designed with XFOIL (Drela, 1989), starting with one of the earliest versions, XFOILv5.4. XFOIL is a viscid-inviscid interaction code based on a potential flow panel method for the outer flow, coupled to an integral boundary layer formulation for the inner flow shear layer. Natural transition is determined using the well-known  $e^N$ -method (van Ingen, 2008), where  $N$  is the ratio of the critical over the neutral wave amplitudes in the laminar boundary layer. Closure relations for the laminar and turbulent boundary layers provide a framework for solution of the ordinary differential equations. These type of panel codes are known to have difficulties in solving flows with increased turbulence (due to long and thick turbulent boundary layers or surface roughness) and turbulent separation. Generally, drag is underpredicted and lift is overpredicted. Since the first release, XFOIL has undergone quite a number of modifications, mostly aiming e.g. at improved design and plotting capabilities, but also directed towards ameliorated transition location prediction. After the release of version 6.99 in 2013 the code was frozen.

#### **3.1.2 RFOIL**

A relatively early adaptation of XFOIL is RFOIL (van Rooij, 1996), resulting from a project called TIDIS (Three Dimensional effects in Stall), funded by the Netherlands Agency for Energy and the Environment (NOVEM) and carried out by the Netherlands Energy Research Foundation ECN, the National Aerospace Laboratory NLR and TU Delft. RFOIL is primarily based on XFOIL v5.4. The goal of TIDIS was to generate a code to calculate the effect of rotation on airfoil performance using the strong viscous/inviscid interaction scheme of XFOIL. To this end, first the prediction of the airfoil performance around the

maximum lift was enhanced. The numerical stability was improved by using Schlichting velocity profiles for the turbulent boundary layer instead those of Swafford (van Rooij, 1996).

The equations to calculate the turbulent boundary layer are built around the concept of ‘equilibrium’ or self ‘preserving’ flows. In such flows the mainstream velocity distribution is characterized by a constant value of the parameter

$$\beta = \frac{\delta^*}{\tau_w} \frac{dp}{dx} \quad (3.1)$$

where  $\delta^*$  is the boundary layer (BL) displacement thickness,  $\tau_w$  is the wall shear stress and  $dp/dx$  the pressure gradient in stream direction. The parameter, first obtained experimentally by Clauser (1954), represents the ratio of shear forces to pressure forces in a section of the boundary layer. For equilibrium flows Clauser derived the (constant) shape parameter  $G$  of the velocity deficit (with respect to the edge velocity) profile, which for incompressible flow is depending on the BL-shape parameter  $H$  and the friction coefficient. Furthermore a relation was found between  $G$  and  $\beta$

$$G = A \sqrt{1 + B \beta} \quad (3.2)$$

which is called the  $G$ - $\beta$  locus. The constants  $A$  and  $B$  need to be established empirically. Their value controls the impact of the pressure gradient on the shear stress in the BL outer region and the wall shear stress and consequently also on the location of separation. The XFOIL values are  $A=6.7$  and  $B=0.75$ . Based on the maximum lift coefficients and the pressure distributions of a number of airfoils (e.g. NLF(1)-0416) Van Rooij (1996) found the RFOIL values  $A=6.75$  and  $B=0.83$ .

In addition, the shear lag coefficient in Green’s lag equation of the turbulent boundary layer model was adjusted and deviation from the equilibrium flow was coupled to the shape factor of the boundary layer by an engineering approach based on considerations of Melnik and Brooks (1985).

The transition calculation in XFOIL, and consequently also in RFOIL, used a linear approximation of the spatial amplification curves of the Orr-Sommerfeld equations, describing the stability of the Tollmien-Schlichting (T-S) waves in the laminar boundary layer (van Ingen, 2008). A first version of the so called “van Ingen full or non-linear amplification calculation method” (van Ingen, 2008) was implemented in XFOIL by Ferreira (2002) to enable damping of the T-S waves, as would occur when applying suction (having decreasing amplification). That code was named XFOILSUC and the transition scheme was also inserted in RFOIL as an alternative to the already existing one by Drela. Van Ingen later developed a new and improved  $e^N$ -method for XFOILSUC (van Ingen, 2008), which was implemented by Bongers (2006). All RFOIL calculations in this document have the original linear amplification scheme, unless indicated otherwise. In XFOIL

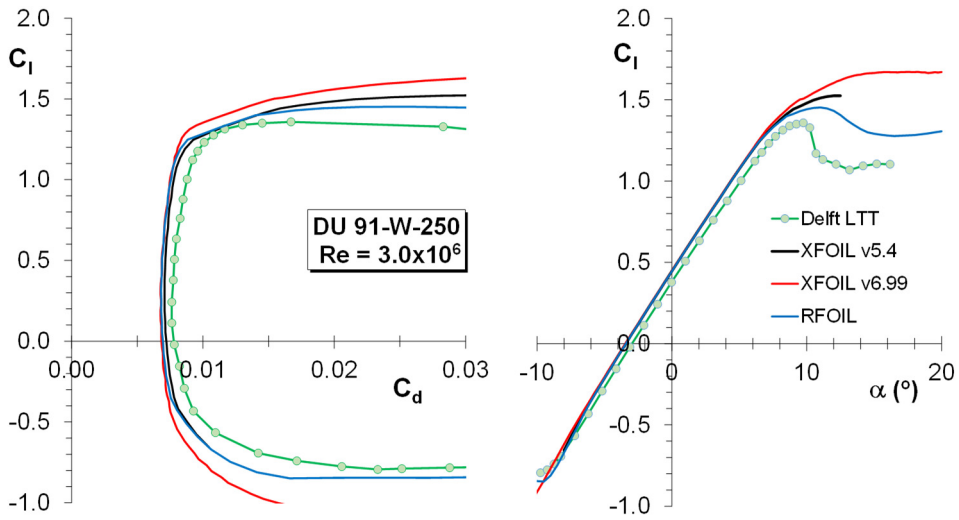


Figure 3.1: The predicted DU91-W2-250 characteristics with two versions of XFOIL and with RFOIL (both with  $M=0$  and  $N=9$ ), compared to the wind tunnel results.

versions after v6.9, the linear amplification approximation was replaced by one using a database of solutions of the Orr-Sommerfeld stability equations.

Figure 3.1 shows a comparison of test results for DU91-W2-250 with simulations using the “old” XFOIL version 5.4, using the last version 6.99 and RFOIL. Version 5.4 had a convergence problem around  $C_{l,max}$ , which was solved in one of the later versions. However, it produced a maximum lift coefficient closer to the wind tunnel value than the last version.

The RFOIL result follows the measured lift curve fairly well. The drag, however, remains underpredicted and the lift gradient is too steep. Note that the Mach number is set to 0 in the calculations. During the measurements it was 0.23.

Though the default value of  $N$  in XFOIL and RFOIL is 9, transition actually is sensitive to disturbances in the free-stream such as noise, vibrations and turbulence. The value of  $N$  therefor depends on an “effective” turbulence intensity ( $Tu$ ). Van Ingen (2008) derived equation (3.3), based on measurements on flat plates and data from Mack (1975), who himself (Mack, 1977) published equation (3.4), with  $Tu$  in %.

$$N = 2.13 - 6.18^{10} \log Tu \quad (3.3)$$

$$N = -8.43 - 2.4 \ln(Tu / 100) \quad (3.4)$$

To reach a Reynolds number of  $3 \times 10^6$  in the Delft LTT with a model chord of 60cm, the test section velocity should be around 80 m/s, at which speed measurements show a longitudinal component of the turbulence in the test section of about 0.04% (see chapter

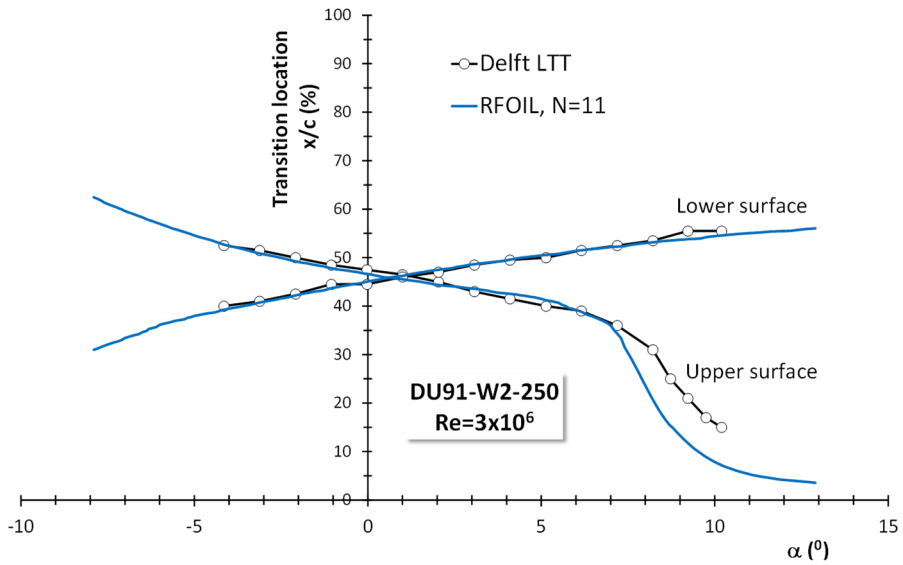


Figure 3.2: The measured and predicted transition locations using  $N=11$  for airfoil DU91-W2-250 at  $Re=3 \times 10^6$ ,  $M=0.23$  in both datasets

3.2).

Assuming the transversal turbulence components are small, according to eq. (3.3) the critical amplification factor  $N$  is in the order of 10.8, while eq. (3.4) gives 10.4. RFOIL calculations using  $N$  in the order of 10.5 to 11 indeed show the best agreement with measurements in the Delft LTT at a Reynolds number of  $3 \times 10^6$ . Figure 3.2 shows the predicted transition location for DU91-W2-250 using  $N=11$  and the transition location measured with a stethoscope in the wind tunnel at  $Re=3 \times 10^6$ .

The figure shows a very good agreement between the measured and predicted transition

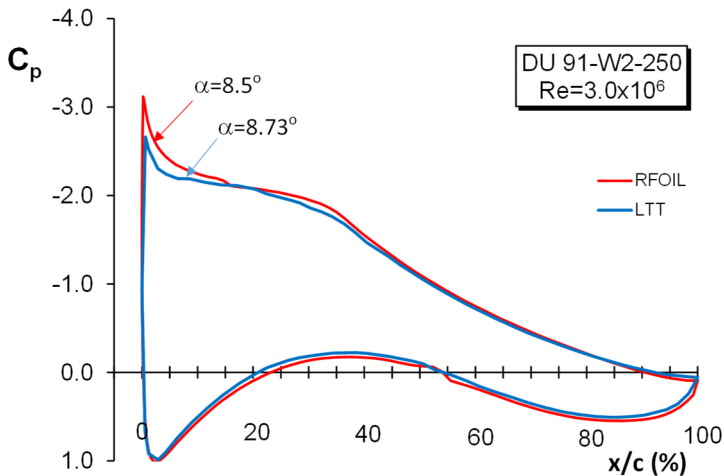


Figure 3.3: The RFOIL calculated and measured pressure distributions for DU91-W2-250 at  $Re=3 \times 10^6$ ,  $M=0.23$  and  $N=11$

locations up to  $7^\circ$  angle of attack. After  $\alpha=7^\circ$ , RFOIL predicts a substantially more forward located transition, which increases the calculated drag. This may, however, not be attributed to failing of the transition prediction method, as is shown in figure 3.3. The figure depicts the pressure distributions at an angle of  $8.7^\circ$ . Taking a small zero-lift angle difference into account, the  $C_p$ -distribution of the RFOIL simulation shows a higher peak at the leading edge, giving a higher adverse pressure gradient compared to the measurements and consequently to a more forward located transition point. The reason for the disparity between the transition locations beyond  $\alpha=7^\circ$  in figure 3.2 must therefore in first instance be found in an aberrant XFOIL/RFOIL edge velocity determination.

This discrepancy in transition location for angles approaching stall has caused the early DU-airfoils to be more roughness sensitive at the design-Reynolds number than intended, as transition at stall in reality is not close to the leading edge (a design goal), but lies much further backwards.

A comparison of XFOIL v6.99 and RFOIL predictions at the proper Mach number with the measurements is shown in figure 3.4. Here, the critical amplification factor  $N$  equals 11 and the parameters  $A$  and  $B$  in the  $G-\beta$  locus determination (see paragraph 3.1.2) in XFOIL v6.99 were set to the RFOIL values. As expected, due to the higher Mach number, the lift gradient differences between predictions and measurements have increased compared to fig. 3.1. The maximum lift predicted by XFOIL v6.99 has levelled off due to the change in the  $A$  and  $B$  parameters, but is still significantly higher than calculated by RFOIL. The drag still is underpredicted, but the shape of the drag curve at the upper and lower

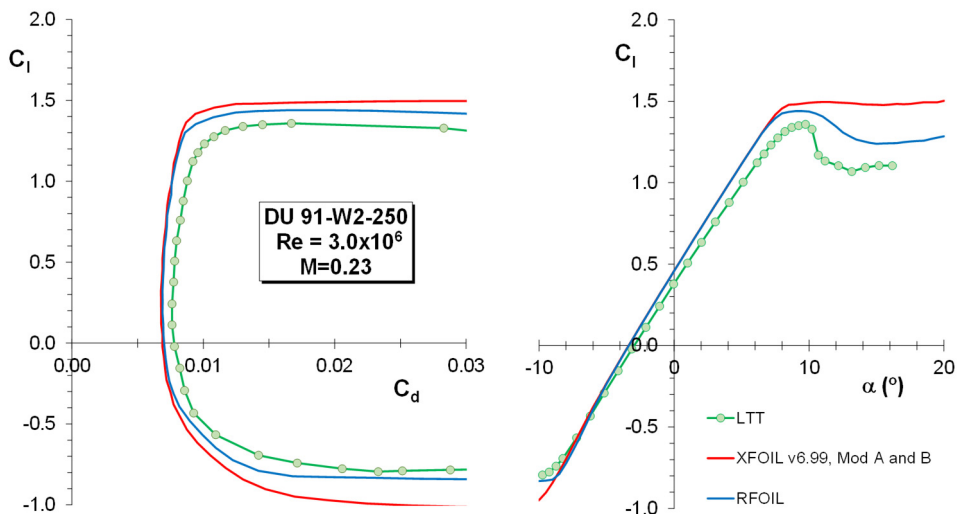


Figure 3.4: The predicted DU91-W2-250 characteristics with RFOIL and XFOIL v6.99, both with  $M=0.23$  and  $N=11$ , compared to the wind tunnel results.  $A$  and  $B$  parameters in the XFOIL v6.99  $G-\beta$  locus computation set to RFOIL values.

boundaries of the drag bucket seem to match those of the measurements.

There is no indication that the wake-based drag measurements used in comparison with the computations are inaccurate. Nor is there any sign of 3D flow on the models in the low-drag range of angles of attack during the experiments. Since RFOIL and XFOIL predict the transition location quite well in the low-drag region and treatment of the laminar boundary layer is assumed to be rather straightforward, the reason for the differences in drag must lie in the contribution of the turbulent boundary layer.

With some success researchers have tackled the drag prediction deficiencies in XFOIL and RFOIL in various ways, aiming at improved prediction of the turbulent boundary layer friction coefficient, e.g. de Oliviera et al. (2018), Hansen (2018) and Olsen et al. (2020), or by a different formulation of the momentum loss equation for the wake (Ramanujam et al, 2016).

Ramanujam and Özdemir (2017) traced the deviation in lift back to a simplification of the downwash behind the airfoil, which is primarily based on the determination of the dividing streamline in the wake coming from an inviscid calculation. This results in an overprediction of lift with increasing angle of attack and airfoil thickness. The researchers succeeded in improving the lift prediction in the low-drag region by including viscous effects in determining the wake geometry, which reduces the downwash and renders more accurate lift-drag ratios. The maximum lift, however, was now underpredicted, especially at Reynolds numbers beyond  $3 \times 10^6$ .

### **3.1.3 Application of multiplication factors**

Despite the improvements mentioned above, sometimes requiring major modifications to the source code, in many studies a more direct approach is chosen to account for the deficiencies in drag and lift, simply by applying corrections or multiplication factors to the predicted coefficients (e.g. Madsen, 2015), mainly depending on the thickness of the airfoil and its trailing edge, or by application to the calculated turbulent friction coefficient (Hansen, 2018). For the class of airfoils considered for application in the outboard part of wind turbine blades this works to a satisfying degree in cases of free transition of the boundary layer. An example is presented in fig 3.5, showing the measured characteristics of DU91-W2-250 and the RFOIL predicted performance, using multiplication factors of 1.11 for the drag and 0.94 for the lift. The latter was chosen to match the maximum measured lift, not the lift gradient. A zero-lift angle difference of  $0.43^\circ$  was applied to the predicted lift curve.

Apparently, when the maximum lift coefficient matches the measurements and the level of the  $C_d$  is brought to the wind tunnel value the shape of the predicted curve is in very good agreement with the measurements. When the prediction matches the maximum lift also the minimum lift is at the level of the measurements.

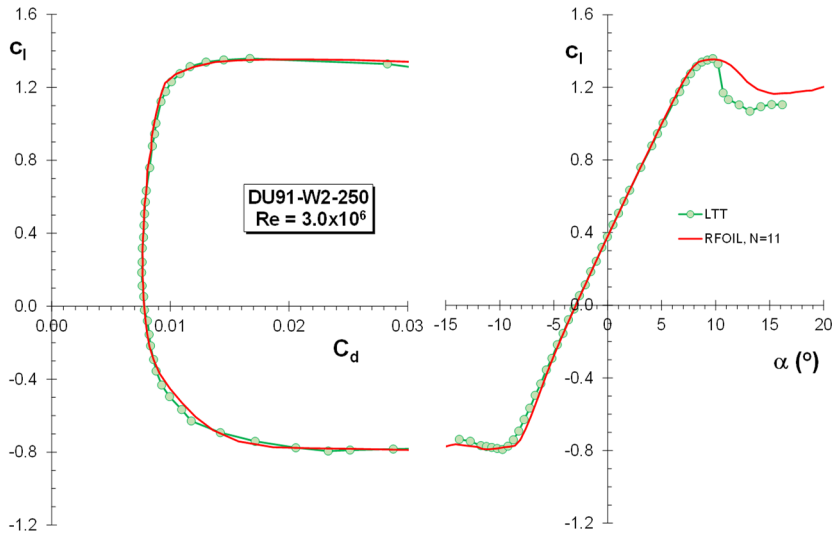


Figure 3.5: Comparison of the predicted DU91-W2-250 characteristics with RFOIL and wind tunnel results. Multiplication factors of 1.11 to the predicted  $C_d$  and 0.94 to the lift coefficient to match the measured maximum lift.

The 25% thick DU91-W2-250 has a trailing edge thickness of 0.65%. A thinner airfoil with nominally zero trailing edge thickness is DU96-W-180. This 18% thick airfoil was derived from measurements on DU95-W-180. The wind tunnel model has a 20% chord flap and produced the target maximum lift coefficient of 1.25 at a flap deflection of  $2^\circ$ . The coordinates were then smoothed and the airfoil was designated DU96-W-180.

Figure 3.6 presents a comparison with RFOIL predictions using the coordinates of DU96-W-180 and measurements for DU95-W-180 with a flap deflection of  $2^\circ$  (DU 95-W-180f2). In the results the wind tunnel angle of attack was shifted  $0.4^\circ$  to match DU96 incidences.

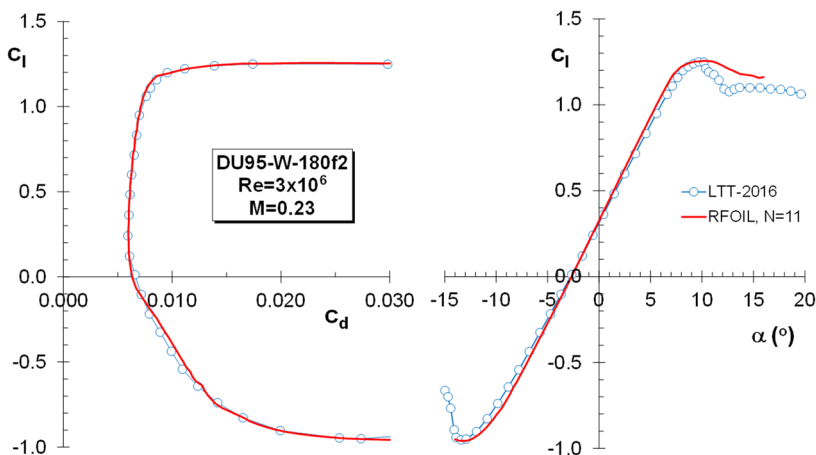


Figure 3.6: The predicted and (in 2016) measured characteristics of airfoil DU95-W-180 with a  $2^\circ$  flap deflection. Measured angle of attack shifted  $0.4^\circ$  (longest chord). DU96-W-180 coordinates fed to RFOIL. RFOIL drag multiplied by 1.14, unchanged lift curve.

In this case the calculated and measured maximum lift coefficients match, and the drag curves agree very well with a multiplication factor of 1.14. The values of 1.14 for  $C_d$  and 1 for  $C_{l,max}$  appear to be typical for laminar

18% thick airfoils with zero trailing edge thickness at  $Re=3 \times 10^6$ .

Comparison of measurements in the NACA Low Turbulence Pressure Tunnel (LTPT; Abbott et al., 1945) and RFOIL predictions for the 18% thick NACA airfoils from the 63 and 64 series using the tunnel related value  $N=10$  and  $M \approx 0$ , all show a  $C_d$  multiplication factor of around 1.14 at  $Re=3 \times 10^6$  (with the exception of 64<sub>3</sub>-618, giving a factor of 1.10), and a matching  $C_{l,max}$ , (factor=1).

Also for NACA 63<sub>4</sub>-421 and 64<sub>4</sub>-421 these factors hold. A comparison for the 21% thick DU93-W-210 gives 1.10 for  $C_d$  and 0.955 for  $C_l$ .

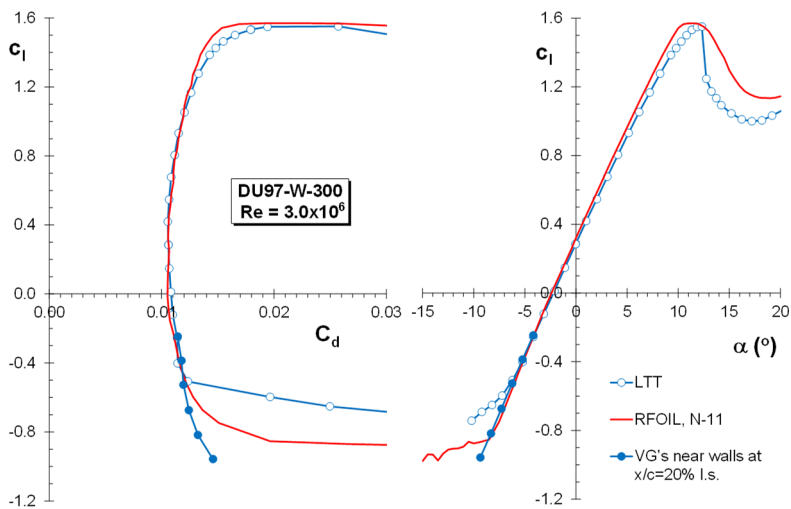


Figure 3.7: The predicted and measured characteristics of airfoil DU97-W-300. RFOIL drag multiplied by 1.14, lift by 0.94. To suppress interference with the wall boundary layers two pairs of vortex generators were placed at the l.s. 20% chord station near the upper and lower wall.

For thicker airfoils, like the 30% thick DU97-W-300 (see fig. 3.7), the match is still good for the drag and fair for the lift with the proper factors. In the measurements, the interference between the test section wall and airfoil boundary layers causes early separation on the lower surface at negative angles, which was attempted to suppress by placing a strip with two pairs of vortex generators (VG's) near the upper and lower walls at  $x/c=0.2$  on the lower surface. The VG's most likely prevented massive separation near the walls even when the flow on the other parts of the model was detached, which is noticeable in the further decreasing lift coefficient and associated lower drag with decreasing angle.

The airfoil has a blunt trailing edge ( $t_{TE}/c=1.74\%$ ), which is just at the edge of the range for which XFOIL was tuned (Drela, 1989). According to Ramanujam and Özdemir (2017), lift

prediction for airfoils with a blunt trailing edge could be improved by reconsidering RFOIL's trailing edge formulation (the distribution of the trailing edge panel source strength) and the Kutta condition.

### 3.1.4 RFOIL predictions for an airfoil with roughness

According to Hansen (2018), the drag differences between the airfoil model measured in the wind tunnel and RFOIL/XFOIL predictions for the greater part result from an undervaluation of the turbulent skin friction coefficient (he raises it with a multiplier of 1.3). Consequently, it can be expected that the disparity will grow with little laminar flow and thicker turbulent boundary layers on the airfoil, which is the case when the BL is tripped near the leading edge. An example is presented in fig. 3.8, where the impact of a 0.195 mm thick zigzag strip on the 5% upper surface chord station of DU97-W-300 is compared to the RFOIL prediction with fixed transition at  $x/c=5\%$ . From about  $2^\circ$  incidence onwards the difference between the measured and calculated drag, with a trip at 5%

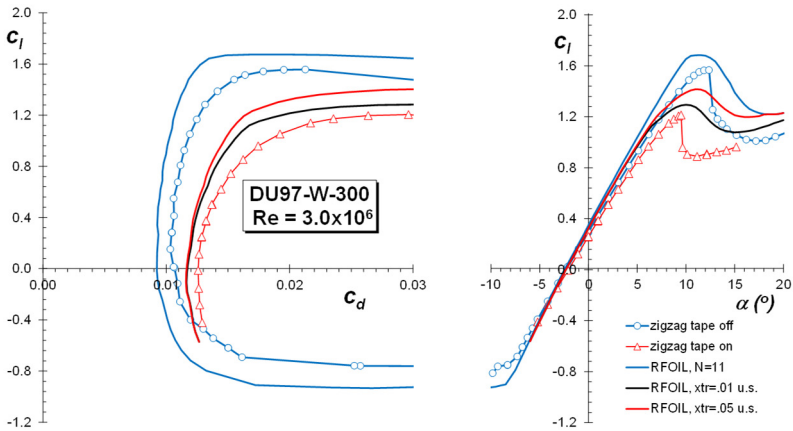


Figure 3.8: RFOIL predictions for DU97 with and without zigzag tape at  $x/c=5\%$  upper surface, no multiplication factors.

chord, grows increasingly more than in the clean case, combined with a significant overshoot in lift.

The comparison is, however, not fair, since the zigzag tape in the experiment caused additional momentum loss, which is not modelled in the computations.

The zigzag tape used is about twice as thick as required to trigger transition (method of Braslow and Knox, see chapter 4.4.2) for the incidence range from  $0^\circ$  to  $8^\circ$ . The only way to minimize this difference in momentum loss at  $x/c=5\%$  is to start the calculation of the turbulent boundary layer further upstream, shown in fig. 3.8 by RFOIL computations with fixed transition at  $x/c=1\%$  u.s. The required multipliers for the lift and drag with an almost entire turbulent upper surface are 1.07 on  $C_d$  and 0.94 on  $C_l$ . The curves are depicted in fig. 3.9. Interestingly, since the flow over the lower surface is unchanged, the difference

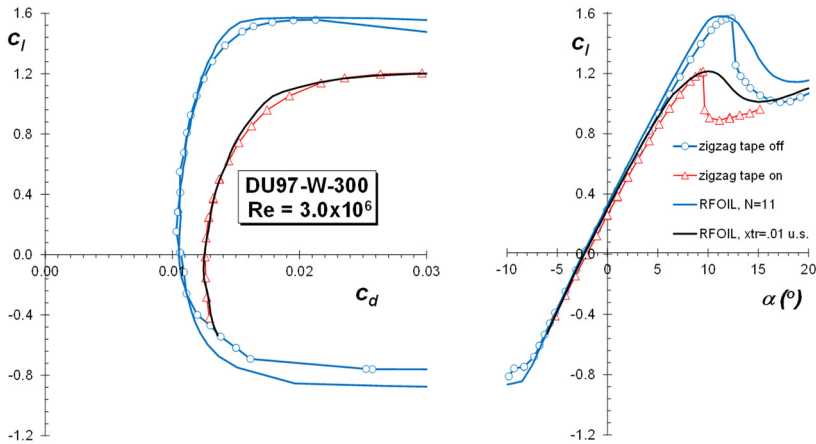


Figure 3.9: Curves of figure 3.8 with multiplication factors on  $C_d$  and  $C_l$  of 1.14 and 0.94 for the clean case and 1.07 and 0.94 respectively in case of zigzag tape at  $x/c=.05$ .  $M=0.21$

in computed drag with the experiment appears to be less in case of an almost fully turbulent upper surface, not only percentage-wise, but also in absolute value. As in the range of incidences between  $0^\circ$  and  $8^\circ$  the first 30% to 40% of the smooth airfoil upper surface boundary layer is laminar, this implies that in the computations 60% to 70% of the clean airfoil turbulent boundary layer contributes more to the difference in drag than a near complete turbulent upper surface. Consequently, it may not only be the undervaluation of the turbulent boundary layer skin friction coefficient causing the drag disparity, but -assuming the laminar part is computed correctly- in addition the starting conditions of the turbulent boundary layer after transition may play a role here. Although interesting from a modelling point of view, addressing this is outside the scope of this chapter and it has not been further investigated.

The multiplication factors for  $C_d$  and  $C_l$  of 1.07 and 0.94 respectively also approximately hold for DU93 with 0.2 mm zigzag tape at 5% chord and for DU95 with  $2^\circ$  flap deflection (DU96) using 0.32mm thick zigzag tape at the same location, when compared to RFOIL calculations with fixed u.s. transition at  $x/c=1\%$ .

At present, airfoil roughness performance is often experimentally verified with zigzag tape placed at  $x/c=5\%$  u.s. (and 10% l.s.). Choosing an upstream fixed transition in RFOIL to create additional momentum loss at  $x/c=5\%$  for comparison with the experiment may work when the trip thickness is not excessive compared to the required thickness. However, the impact of tripping devices on the boundary layer flow depends on airfoil shape, trip-shape, thickness and chord location, Reynolds number and angle of attack. Effective tripping over a wide range of angles of attack with a single, constant thickness trip is difficult and trip strips often appear to be too tall.

The modifications in RFOIL focused on the stall behaviour of the airfoil. All other calculations, such as the computations of the laminar boundary layer parameters, of the transition location, and of the contribution of a non-zero trailing edge thickness are those from the original XFOIL code. The changes in RFOIL were tuned in the Reynolds number range up to about  $Re=4 \times 10^6$ . Outside the range of calibration, RFOIL will increasingly perform inadequate. Two examples are shown in the next paragraphs.

### 3.1.5 RFOIL predictions for airfoils with a very thick trailing edge

In the XFOIL/RFOIL thick trailing edge model the Kutta condition is satisfied using a base (trailing edge) panel with a certain source strength to enable separation at the upper and

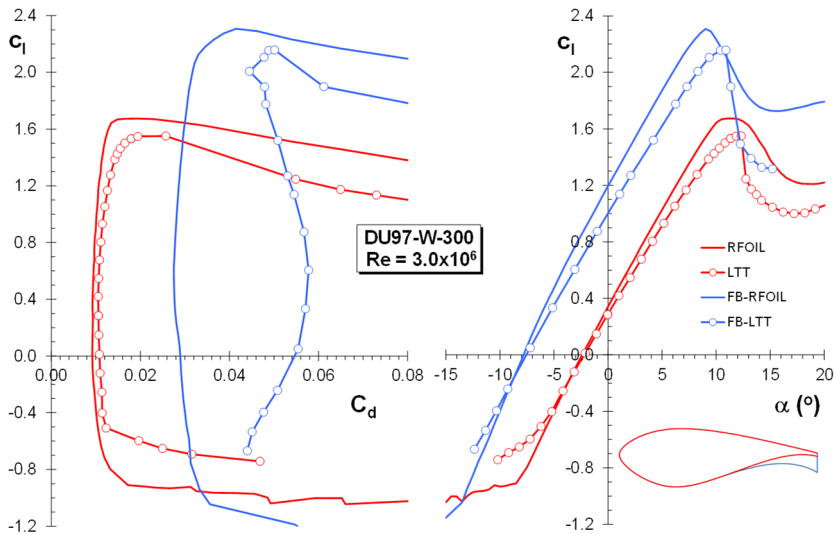


Figure 3.10: RFOIL predictions versus experimental results for DU97-W-300 and the flatback version (FB) of the same airfoil with a 10% thick trailing edge.  $M=0.21$ . No multiplication factors.

lower trailing edges, which has a significant impact on the wake geometry. With increasing bluntness of the trailing edge this model seriously underestimates the base pressure, since the resulting flow pattern does not at all resembles reality. As the thickness of DU97 trailing edge ( $t_{TE}/c=1.74\%$ ) already was at the limit for which XFOIL/RFOIL gives calibrated results (approximately 2%), it will not come as a surprise that simulations for airfoils with much thicker trailing edges will increasingly deviate from measurements. This becomes particularly manifest for airfoils with blunt trailing edges, as is illustrated by figure 3.10. The model of DU97 was turned into a 10% flatback (FB) airfoil by adding a substantial thickness to the last 40% of the lower side (Ceyhan-Yilmaz and Timmer, 2018), as is shown in the insert. While the original airfoil drag was underpredicted by 14%, the flatback version has about twice the calculated drag in the middle of the low-drag bucket. The calculated maximum lift coefficient matches the measurement when a multiplication

factor equal to the base airfoil (0.94) is applied. Fortunately, in the root of a blade, where the flat back airfoils find their application, the inflow angles are high, with airfoils in this region operating at lift coefficients near stall. Here, it's the contribution to the blade tangential force that matters (i.e. a high airfoil lift coefficient), and to a lesser extent the lift-drag ratio.

As long as a panel codes like RFOIL can give converged solutions in the angle of attack range a few degrees prior to stall, it may still be used to discriminate between a suited and a non-suited solution in an optimization process when considering a smooth surface.

### 3.1.6 RFOIL predictions of airfoil performance at high Reynolds numbers

The examples given above are all for a Reynolds number of  $3 \times 10^6$ . Operational Reynolds numbers of a 3MW wind turbine blade are in the order of  $6 \times 10^6$ . Although RFOIL was tuned for Re-numbers up to about  $4 \times 10^6$ , it can still be used for somewhat higher values, as is shown in fig. 3.11. It presents the measured and calculated characteristics of DU00-W-212 at a Reynolds number of  $6 \times 10^6$ . The measurements were carried out in the high

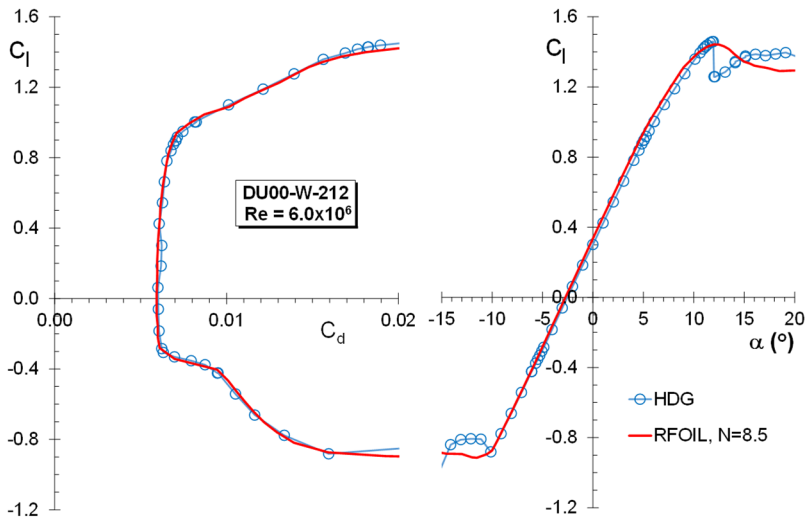


Figure 3.11: The RFOIL predicted performance for DU00-W-212 at  $Re=6 \times 10^6$ ,  $N=8.5$ . Factor on  $C_d$  is 1.14.

pressure tunnel DNW-HDG in Göttingen, Germany in the frame work of the AVATAR project (Ceyhan-Yilmaz, 2017). The HDG was operated by DNW until 2020.

Calculations were performed with the measured model coordinates (DU00-W-212AV), rather than the nominal coordinates. Prior to the model measurements the turbulence intensity in the test section was measured at various combinations of test section velocity and tunnel pressure.

With the proper N-factor (derived from the measured turbulence intensity and eq. 3.3) and multiplication of the drag with 1.14, there is a perfect fit of the drag bucket and even the maximum lift coefficient is only slightly underpredicted. However, higher Reynolds

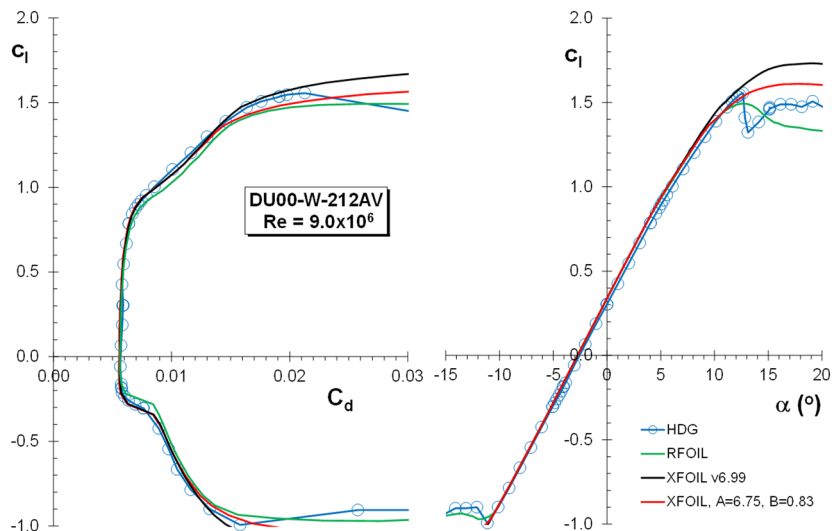


Figure 3.12: The measured and predicted characteristics of airfoil DU00-W-212 for a Reynolds number of  $9 \times 10^6$ .  $N=6$ . Multiplication factor for the drag is 1.12

numbers will give increasingly unsatisfactory results regarding  $C_{l,max}$ . Blades of wind turbines rated at approximately 12MW yield Reynolds numbers in the range of  $12 \times 10^6$  to  $15 \times 10^6$ . Figure 3.12 presents the measured and calculated characteristics of DU00-W-212 using AVATARproject data at  $Re= 9 \times 10^6$ . In accordance with the findings in a study on NACA airfoils presented by Timmer (2009), it is shown that RFOIL starts to underpredict the maximum lift, while XFOIL significantly over predicts it. XFOIL with the G- $\beta$  locus A and B constants equal to the values used in RFOIL, comes close. In view of the turbulence intensity in the test section during the measurements, the N-factor used in the predictions

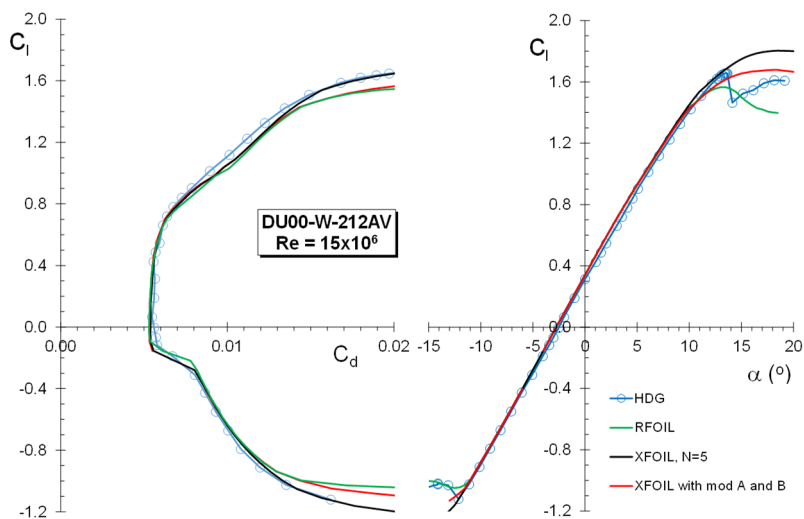


Figure 3.13: The measured and predicted characteristics of airfoil DU00-W-212 for a Reynolds number of  $15 \times 10^6$ .  $N=5$ . Multiplication factor for the drag is 1.14

is 6. The highest Reynolds number tested during the AVATAR-campaign was  $15 \times 10^6$ . The predicted characteristics, with  $N=5$ , are presented in fig. 3.13, showing in fact the same pattern as fig. 3.12.

The lift-drag ratio of the characteristics presented in fig. 3.12 and 3.13 are plotted in fig. 3.14. It can be concluded that XFOIL comes closest to the measurements up to stall in the Re-range roughly above  $Re=6 \times 10^6$ . The factors 1.14 on drag and 1 on the lift seem to give good results for the entire Reynolds number range from  $3 \times 10^6$  to  $15 \times 10^6$  measured in the AVATAR-project. In the post-stall region the measurements may be impacted by three-dimensional stall cells. In addition, panel code predictions in stall are less reliable. The approximate maximum lift can be calculated with XFOIL using the RFOIL A and B parameters.

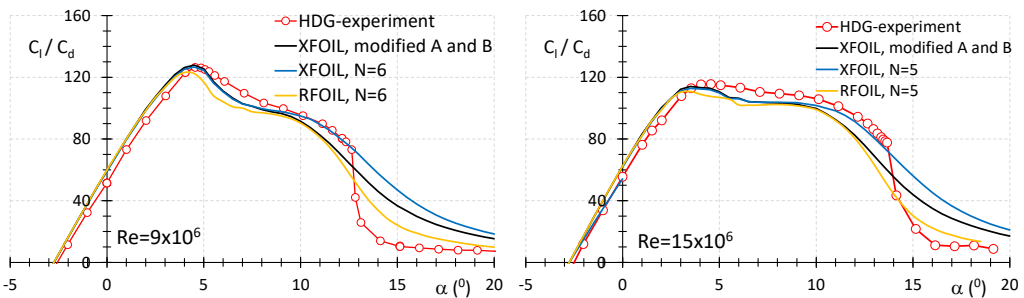


Figure 3.14: The lift-drag ratio of the characteristics shown in fig. 3.12 and 3.13.

It must be noted that with the method of multiplication factors only the measured and predicted characteristics are brought closer together, while the pressure distributions and the boundary layer parameters still differ.

### 3.1.7 Other sources for experimental high Reynolds number data

Reliable experimental data of two-dimensional wind tunnel tests for airfoils with a thickness over 16% at Reynolds numbers higher than  $9 \times 10^6$  and relatively low Mach numbers are scarce. The measurements available in the public domain (see table 3.1) are all conducted in the NASA LTPT. Loftin and Bursnal (1948) measured the characteristics of NACA 63-018 up to a Reynolds number of  $20 \times 10^6$ . Although the airfoil is symmetric, the lift and drag coefficients for positive and negative angles differ, which makes it difficult to judge whether calculations agree with the experiment. However, the multiplication factor of 1.14 on drag seems to give satisfactory results for  $Re=15 \times 10^6$ . In the development of low-speed and medium-speed general aviation airfoil sections, McGhee and Beasley (table 3.1) performed quite a number of wind tunnel measurements with model chords of 0.61m for various model surface roughness and Mach numbers up to  $M=0.28$ . The reports present data uncorrected for wall-interference effects (2% to 3%) and the drag coefficients seem to be on the high side.

Table 3.1: Experimental studies on airfoils at Reynolds number higher than  $9 \times 10^6$

Airfoil	Re ( $\times 10^6$ ), $\geq 6 \times 10^6$	Reference
NACA 63-018	6, 9, 12, 15, 20	Loftin & Bursnal, 1948
LS(1)-0417	6, 9, 12, 16, 20	McGhee & Beasley, 1973
LS(1)-0417Mod	6, 9, 12	McGhee & Beasley, 1981
LS(1)-0421	6, 9	McGhee & Beasley, 1976
LS(1)-0421Mod	6, 9	McGhee & Beasley, 1978
MS(1)-0317	6, 9, 12	McGhee & Beasley, 1980

This may find its origin in the position of the wake rake, which is one chord downstream from the TE on the test section centreline. The row of model pressure orifices is located 5 cm off the mid-span and in high Reynolds number cases may have disturbed the flow downstream and hence have negatively impacted the wake rake total pressure readings.

### 3.1.8 Comparison with CFD codes at high Reynolds numbers

A blind comparison test was performed within the AVATAR project to compare predictions from panel codes and various full-CFD methods at high Reynolds numbers (Schepers et al., 2016). Figures 3.15 and 3.16 present the results of the computations at  $Re=3 \times 10^6$  and  $15 \times 10^6$ . The two panel methods involve XFOIL calculations (ORE uses XFV6.96 and the University of Stuttgart implemented non-linear amplification for transition). The CFD codes mainly use the  $e^N$ -method for transition. ForWind's Open-Foam computations are fully turbulent. In both  $Re$ -cases XFOIL produces very high lift-drag ratios due to the underprediction of the drag coefficient, resulting in an overprediction of the lift-drag ratio of 11% at  $Re=15 \times 10^6$ . DTU's EllipSys3D and the University of Kiel's -TAU code come closest to the measurements.

The codes that struggle with the transition location perform better at the higher Reynolds

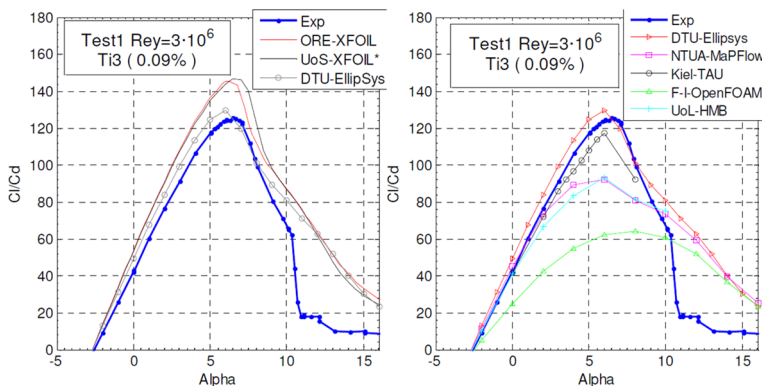


Figure 3.15: Results of the AVATAR-project blind comparison showing differences between experiment and predictions with panel codes (left) and CFD codes (right) for  $Re=3 \times 10^6$ .

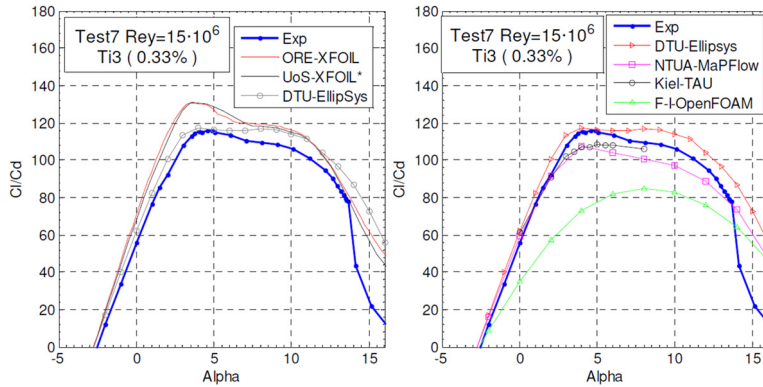


Figure 3.16: Results of the AVATAR-project blind comparison showing differences between experiment and predictions with panel codes (left) and CFD codes (right) for  $Re=15 \times 10^6$ .

number, since upper surface transition at the higher incidences moves towards the leading edge. After ample deliberation between the participants on grid generation and grid independency checks, cell size in the near-wall region, time steps and domain size, the differences in lift-drag ratio between the various codes in full turbulent cases could be brought back to 2%.

In general, the physics of the flow can best be approached by CFD computations (e.g. Sørensen et al., 2016, Rogowski et al., 2018, Sezer-Uzol, 2021). However, the type of code (e.g. RANS, URANS, DES or LES) and the chosen turbulence model are crucial and heavily depend on the expected flow regime (attached flow with varying transition location, turbulent flow or separated flow in various stages). The CPU-time necessary for detailed CFD computations generally is still too long for optimization processes, when a great number of possible solutions need to be evaluated.

### 3.1.9 RFOIL predictions with turbulent flow at high Reynolds numbers

The DU00-W-212 model was also tested in the HDG with transition fixed at the leading edge. In this case a unique roughness type was used, consisting of a row of 1.27mm diameter dots, 2.54mm apart. The characteristics with the thinnest roughness, 0.038mm at  $x/c=5\%$  on the upper side and 0.079mm at 10% on the lower side will be highlighted here (see insert of fig 3.17), as this thickness appeared to be enough to just trigger transition at the higher Re-numbers.

Figure 3.17 presents a comparison of the HDG measurements at  $Re=9 \times 10^6$  and RFOIL calculations with two sets of fixed transition locations:  $x/c=5\%$  on the upper side and  $x/c=10\%$  on the lower side to mimic the locations of the dots in the test, and  $x/c=1\%$  and  $x/c=5\%$  to generate some momentum loss at the locations of the dots as a result of the impact of the dots not only on transition, but also on the local boundary layer parameters. It appears that without any multiplication factors RFOIL comes close to the test results,

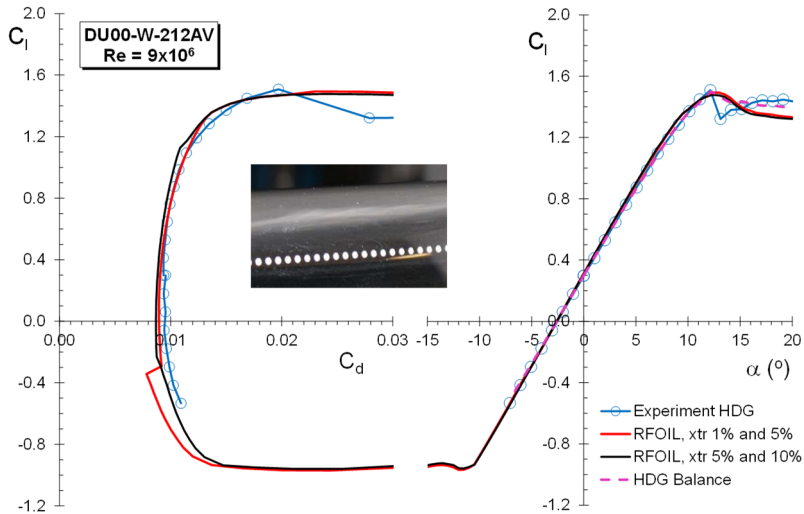


Figure 3.17: Comparison of HDG measurements and RFOIL predictions for fixed transition at the leading edge. Insert: the row of transition dots on the upper surface 5% chord station.

both in shape and level of the drag bucket (with a 3% difference between the two RFOIL drag curves) and regarding the maximum lift. The lift curve measured with a balance shows that for post stall angles due to strong 3-dimensional flow the location of the pressure orifices impacts the determination of the lift coefficients. The calculations with the earlier transition to make up for the impact of the dots fits best between  $0^\circ$  and  $9^\circ$  (with a drag multiplier of approximately 1), however without dramatic differences. It was found that XFOIL v6.99 did not converge after  $\alpha=11.5^\circ$ .

A comparison at  $Re=15 \times 10^6$  gives a similar image, albeit that the maximum lift is underpredicted by 3.5% instead of 1%. The lift-drag ratios of both Re-numbers are depicted in fig. 3.18

The fit between the measurements and the curve with fixed transition at 1% and 5% is good up to stall. However, the maximum lift-drag ratio is overpredicted with 3.5% for  $Re=9 \times 10^6$  and 5% for the higher Re-number.

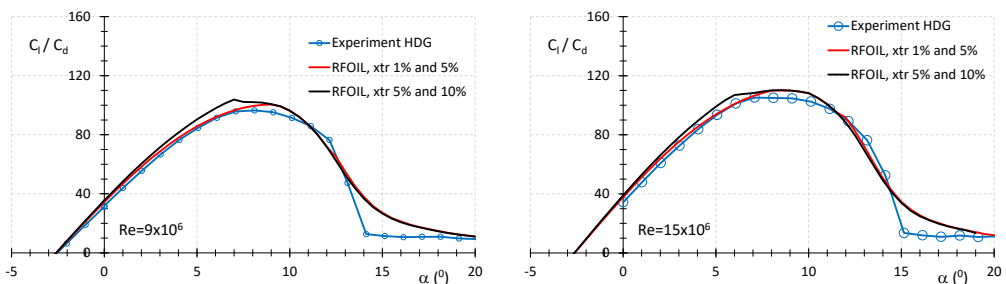


Figure 3.18: Comparison of HDG measurements and RFOIL predictions with fixed transition for  $Re=9 \times 10^6$  and  $Re=15 \times 10^6$ .

## 3.2 WIND TUNNEL MEASUREMENTS

### 3.2.1 Introduction

Wind tunnels are frequently used to analyse the performance of existing airfoils, to verify the characteristics designed into new airfoils or to validate design codes. In this respect the wind tunnel is also a design and analysis tool.

For the verification of airfoil performance in the clean condition in general a high quality flow field is required at the appropriate Reynolds number. The flow in the test section should have little spatial and temporal velocity variation across the test section area, with a turbulence intensity preferably well below 0.1% (Schlichting and Gersten, 2000, after measurements of Schubauer). High turbulence intensity may cause bypass transition, which negatively affects the natural transition location on an airfoil and may lead to drag reduction at low Reynolds numbers (reduction of potentially harmful laminar separation bubbles) and a drag increase at high Reynolds numbers (loss of laminar flow). Testing at a lower Reynolds number may necessitate extrapolation to the required Reynolds number, which generally for a clean airfoil gives satisfying results if the Reynolds number gap is not too large, but in the case of leading edge roughness may seriously over- or underestimate the lift-drag ratio or the maximum lift coefficient at the proper Reynolds number.

As in the first decade of this century testing at Reynolds numbers up to  $4 \times 10^6$  still gave good overlap with Reynolds numbers occurring along the blades of a wind turbine, in Europe atmospheric low-turbulence wind tunnels such as the TUDelft LTT, ONERA's F2 wind tunnel and the Stuttgart University low-turbulence tunnel were frequently used for airfoil testing at the required Reynolds number. However, due to the ever increasing size of wind turbines, also blade Reynolds numbers increased, forming the background of the erection of the Danish LM 1.35x2.70m wind tunnel in 2006 and the DTU 2.0x3.0m Poul la Cour tunnel in 2018, enabling testing at  $6 \times 10^6$  to  $7 \times 10^6$ . In Europe, higher Reynolds numbers, up to  $20 \times 10^6$ , can only be reached in cryogenic tunnels such as the Kryo Kanal Köln (Schaffarczyk 2003) or pressure tunnels like the HDG in Göttingen (Llorente 2014), both in Germany. Testing at high Reynolds numbers involves high costs, as the rental costs of special purpose tunnels are much higher than those of atmospheric tunnels. Also models are more expensive, since high demands are placed on the model surface finish (HDG) or contour deformation sensitivity to low temperatures (cryogenic tunnels). In addition, configuration changes take more time as the test section generally has to be brought back to atmospheric pressure or temperature prior to attaching roughness elements and add-ons. A side effect of testing in special purpose tunnels, which could be regarded as an advantage, is that the impact of the Reynolds number can be studied separately from Mach number effects, as Reynolds number changes in that type of wind

tunnels are predominantly accomplished through kinematic viscosity changes of the tunnel gas. Reynolds number changes by test section velocity changes in atmospheric tunnels also impact the Mach number. The present mismatch between multi-MW machine blade Reynolds numbers and the capability of most atmospheric tunnels doesn't make testing in these tunnels unnecessary and results at lower Reynolds numbers superfluous. Quite the opposite, they serve as a good basis for evaluation of add-ons such as vortex generators, Gurney flaps and serrations and they enable the verification and validation of prediction codes at relatively low costs, provided that the Reynolds gap is not too wide. Measurements of add-ons at  $Re=3 \times 10^6$  may provide good insight in their behaviour up to  $9 \times 10^6$ .

The testing campaigns involving the DU airfoils aimed at generating experimental data, by testing in high quality flow with precision testing equipment and accurate models. As most of the DU-airfoil designs were verified in this tunnel and the resulting characteristics are frequently used in this dissertation for comparison against computations and data from other sources, a complete description of the tunnel layout, the methods, the flow quality, the testing procedure and test setup and the repeatability of the measurements seems appropriate.

### **3.2.2 The low-speed low-turbulence wind tunnel LTT**

#### **3.2.2.1 Wind tunnel layout**

A schematic of the tunnel layout is given in figure 3.15. The tunnel was built in the vertical plane. It has 7 interchangeable 2.6 m. long, 1.25 m high, and 1.80 m wide octagonal test sections (A in fig. 3.15). The circuit is of the closed, single-return type with a total circuit length of 71.8 m, measured along the centre-line. The test section is followed by a 2.33 aspect ratio diffuser with an equivalent cone angle of  $4.51^\circ$ . The channel has a post-fan diffuser with an aspect ratio of 2.55 and an equivalent cone angle of  $5.5^\circ$ . This diffuser ends with a screen just prior to entering the third corner. A wide-angle diffuser with aspect ratio 1.7 and an equivalent cone angle of  $30.5^\circ$ , contains two curved screens, one halfway the diffuser length and one at the exit, upon entering the settling chamber. This plenum chamber contains 6 curved anti-turbulence screens and with a plenum area of  $36.87 \text{ m}^2$  the circuit has a contraction ratio of 17.8 to 1. Figure 3.16 shows the cross-sectional area variation of the circuit with the distance along the centreline. A 580 kW DC motor drives a 2.9 m diameter six-bladed fan, giving a maximum test section velocity of about 120 m/s. Electrically actuated turntables flush with the test-section top and bottom wall provide positioning and attachment for a two-dimensional model.

Apart from the last 2.5 meters of the contraction, the first 2.25 meters of the test section diffuser and the fan section, the entire channel is of concrete. This provides sufficient heat capacity for testing up to about 50 m/s under average outside temperature conditions.

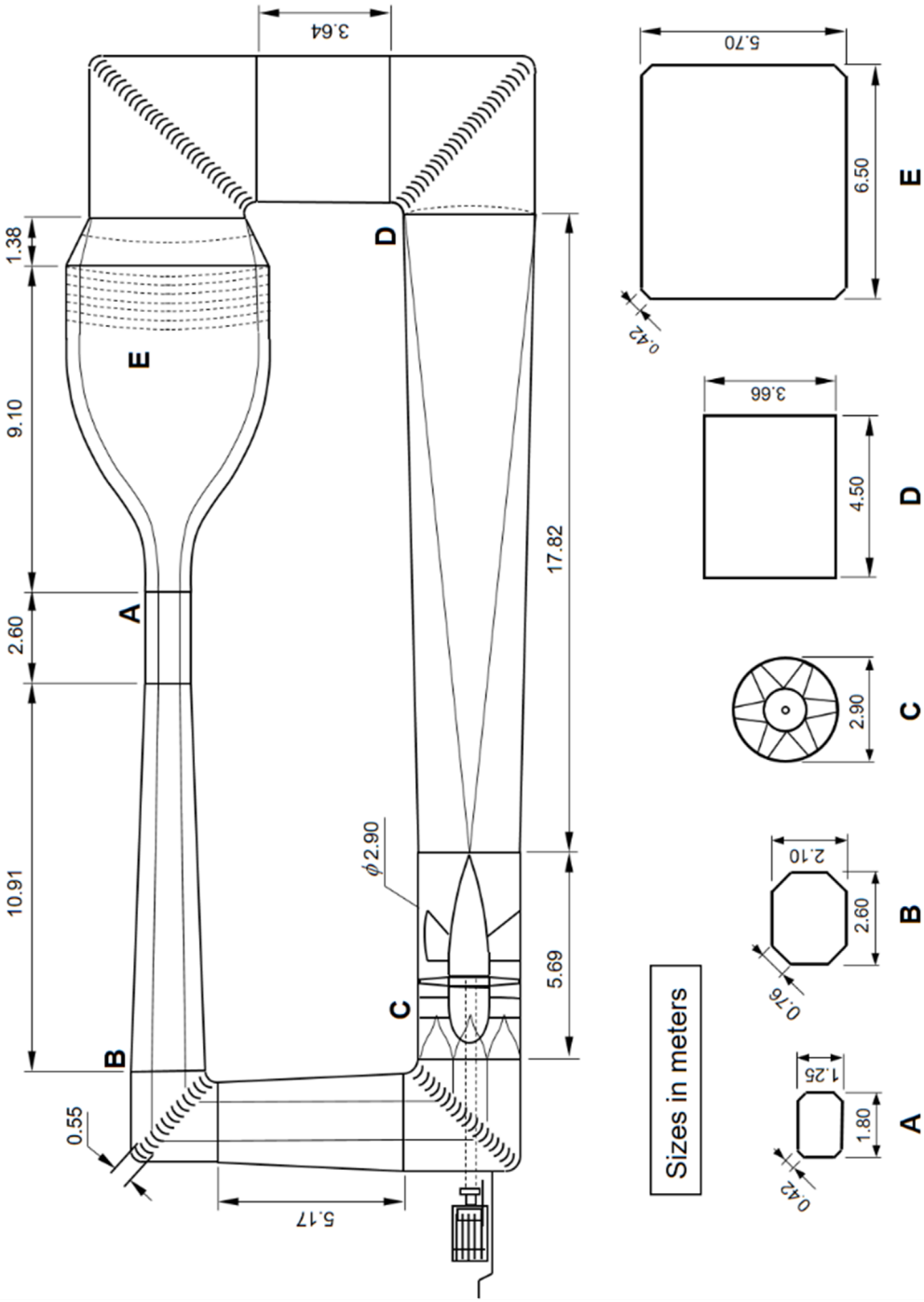


Figure 3.15: A schematic of the LTT circuit layout

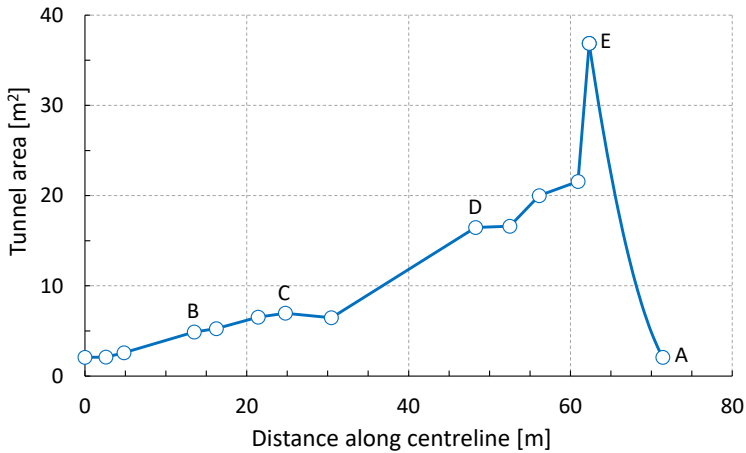


Figure 3.16: The variation of the circuit cross-sectional area with the distance along the centreline of the LTT. See fig. 3.15 for locations A to E

For additional cooling, the 1<sup>st</sup> and 2<sup>rd</sup> corners are equipped with cooling vanes. The other two bends contain curved sheet metal plates. All corner vanes have a chord length of 0.55m. The entire inside of the channel, including all screens, is inspected and thoroughly cleaned on a yearly basis, in order to maintain a high flow quality. Figure 3.17 shows the observation room of the wind tunnel laboratory with the LTT-test section.



Figure 3.17: View on the LTT-test section, with in the middle the contraction. Also visible the overhead balance system. (Photo Henk Jan Siemer)

### 3.2.2.2. Test section flow quality

#### Buoyancy

The test sections used for airfoil measurements have 9 mm diverging side walls to

compensate for the growing boundary layers along the 4 test section walls, which gives a 1.818 m width at the end of the test section. Without this divergence the test section area in flow direction reduces due to the BL displacement thickness, leading to a velocity increase and a negative pressure gradient towards the test section exit, a phenomenon called buoyancy.

The resulting drag increase should be subtracted from the drag measurements before other data reduction actions take place. Already in early measurements (Dobbinga and van Ghesel Grothe, 1955) the chosen widening of the walls appeared to be a slight over compensation; the BL does not grow as expected (or the BL-thickness at the entrance of the test section is smaller than anticipated) and a small positive pressure gradient (slightly varying with Reynolds number) was the result. More recent measurements of the static

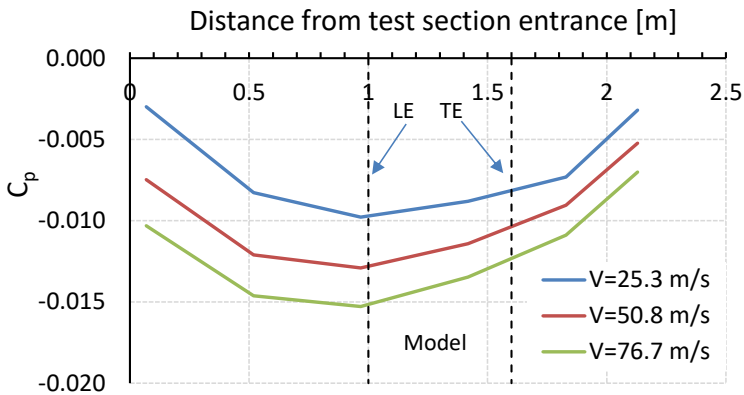


Figure 3.18: The longitudinal pressure gradient in the LTT test section.

Dashed lines give 0.60 m chord model leading and trailing edge locations.

pressure gradient in the empty test section (Bernardy 2015) indeed showed a positive axial pressure gradient at the usual location of two-dimensional models (see fig. 3.18). The indicated test section velocities correspond to Reynolds numbers of  $1 \times 10^6$ ,  $2 \times 10^6$  and  $3 \times 10^6$  using 0.60m chord models.

The additional drag force due to horizontal buoyancy for a constant longitudinal pressure gradient is given by eq. 3.5 (Allen and Vincenti, 1944):

$$D_b = -\frac{6h^2}{\pi} \Lambda \sigma \frac{dp}{dx} \quad (3.5)$$

It contains the height of the test section  $h$ , the body-shape factor  $\Lambda$  and the tunnel blockage factor  $\sigma$  from the work of Allen and Vincenti, defined in Appendix A. In terms of the drag coefficient and the longitudinal pressure coefficient distribution, eq. 3.5 changes into:

$$\Delta C_{d_b} = -\frac{6h^2}{\pi c} \Lambda \sigma \frac{dC_p}{dx} \quad (3.6)$$

For the smaller angles of attack, at which a wake rake is used to measure the drag coefficient, this overcompensation is corrected by a calibration of the wake rake static pressures, which will be treated in section 3.2.3.4. The pressure drag, however, calculated from the pressure distribution, should be treated accordingly, which, since generally the wake rake drag is used up to  $C_{l,max}$ , will only be of interest in the post stall region. For the 25% thick DU91-W2-250 airfoil ( $\Lambda\sigma=0.01306$ ) the correction due to buoyancy is calculated with eq. 3.5 at an angle of attack one degree beyond the maximum lift coefficient.

The drag coefficient correction due to buoyancy amounts to -0.00033 (-0.9%) at  $Re=1 \times 10^6$  and -0.00058 (-1.2%) at  $Re=3 \times 10^6$ . As the correction should be subtracted from the measurement, the actual drag coefficient becomes higher. At incidences beyond  $2^\circ$  from the maximum lift the correction is already well below 1% for all Reynolds numbers.

### Turbulence intensity

The axial temporal velocity fluctuations in one of the test sections generally used for airfoil testing was last measured in 2015. Figure 3.19 shows the results of hot wire measurements of longitudinal free-stream turbulence intensity during almost 60 years of operation. The 2015 data were acquired during 30 seconds with a frequency of 50 kHz using a low pass filter of 20 kHz. Prior to the measurements the hot-wire was calibrated

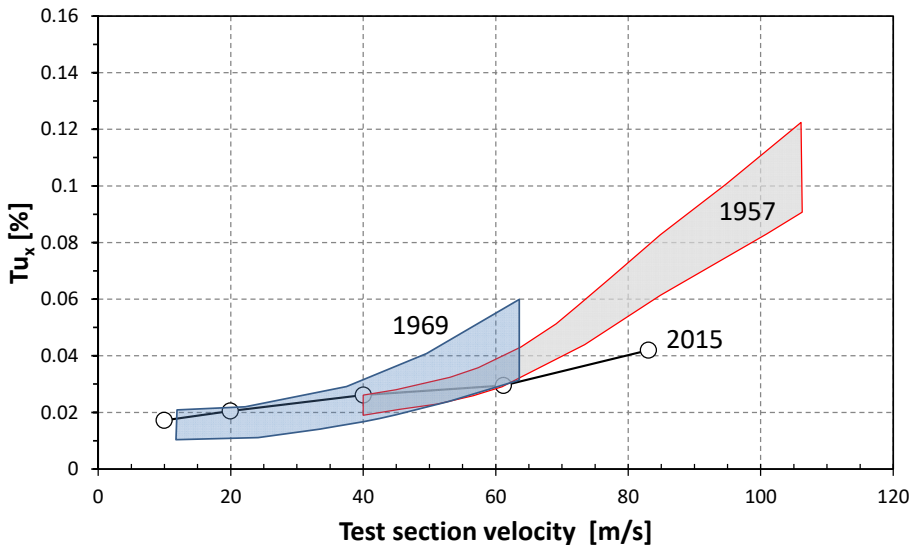


Figure 3.19: The longitudinal turbulence intensity of the LTT test section flow during 60 years of operation. Data from 1957: van Genderen (1957), 1969: Boermans (1994) and 2015: Bernardy (2015).

in situ. The average speed was subtracted from the measurements and the samples were filtered using a third order Butterworth band pass filter (2-5000 Hz), from which the standard deviation was calculated and divided by the average speed to arrive at the longitudinal turbulence intensity.

The 1957 data were reported to have a 30% uncertainty, partly due to frequent wire break, calibrations and support vibrations. Due to the very large spread at higher velocities, the 1969 data have only been shown up to a velocity of 64 m/s.

### Flow Angularity

The flow angularity was measured some time after commissioning of the tunnel (Boeker, 1961) and was found to be approximately 0.02 degrees.

#### *3.2.2.3 The test section free-stream dynamic pressure*

For every test section a dedicated dynamic pressure calibration curve is available, which is regularly updated. This calibration curve links the test section dynamic pressure ( $q_o$ ) in the centre of an empty test section (but with the presence of the wake rake) measured with a Casella pitot-static tube (see fig. 3.20) to the tunnel control pressure ( $\Delta p_b$ ). This control pressure is a dynamic pressure formed by the difference between the plenum total pressure and the static (wall) pressure at a station 1.75m upstream from the entrance to the test section, sufficiently far from a model inside the test section. This static pressure is an average of 4 pressures located around the circumference of the tunnel.

Both  $q_o$  and  $\Delta p_b$  are measured with Mensor precision quartz manometers. The test section velocity is varied by changing the fan rpm, giving different values of  $\Delta p_b$ . Using the latter as input, in any model configuration the undisturbed (free-stream)) test section velocity



*Figure 3.20: the Casella pitot-static tube used for test section dynamic pressure calibration curves.*

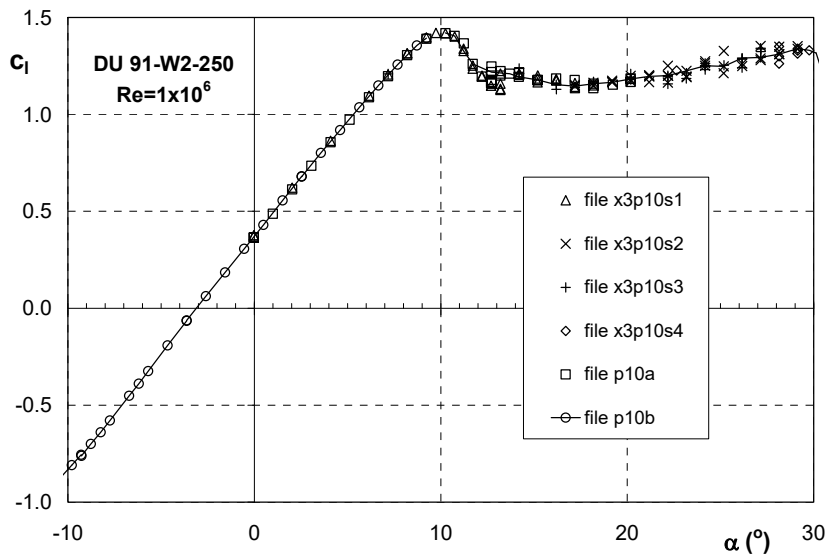


Figure 3.21: Repeatability of measurements at a Reynolds number of  $1 \times 10^6$ , airfoil DU 91-W2-250.

can be determined using the test section dynamic pressure calibration curve and the air density calculated from the tunnel air temperature measured in the plenum chamber and the atmospheric pressure.

Fig. 3.21 presents the measured lift curve of DU 91-W2-250. These measurements were performed with a 200 tubes liquid multi-manometer filled with mono-chloride benzene. As a result of the low dynamics of such a system, the post stall  $C_l$ -bandwidth is about 0.1. The post stall characteristics adopted for DU91 are formed by the points that come closest to a least squares fit. In later years, when using fast pressure scanners, 20 second averages were taken in the post stall region.

#### 3.2.2.4 Repeatability

The comparison in fig. 3.21, which is typical for this type of measurements, shows that a high repeatability can be achieved for pre-stall angles. The files x3p10s1 to s4 were measured 4 months after p10a and p10b, without taking the model out between the two test campaigns.

#### 3.2.2.5 Models

The composite models of the DU-airfoils referred to in this dissertation had a chord of 0.60 m (except DU 97-W-300, which chord was 0.65 m) and completely spanned the height of the test section. Around 90 to 100 pressure orifices with a diameter of 0.4 mm., drilled perpendicular to the model contour, were installed in staggered formation at a small distance above the tunnel centre line. The polyester gel coat surface of the models was sanded and polished. The DU91-W2-250 model was constructed by a sailplane

manufacturer in Bielsko-Bialo, Poland. The other models come from Glasfaser-Flugzeug-Service, Grabenstätten, Germany. The model contour of the airfoils presented here was not measured. However, the deviation from the prescribed shape of similar sail plane wind tunnel models from the German manufacturer has always been below 0.1mm.

### 3.2.3 Methods

#### 3.2.3.1 Pressure coefficients

The measured pressures are reduced to pressure coefficients using:

$$C_p = \frac{p - p_0}{q_0} \quad (3.7)$$

The value of  $q_0$  is determined from the dynamic pressure calibration curve and  $p_0$  was calculated using

$$p_0 = p_{t_0} - q_0 \quad (3.8)$$

The total pressure in equation (3.8) is an average of all the wake rake total pressures outside the wake (see section 3.2.3.3).

#### 3.2.3.2 Force coefficients

The model pressure distributions are integrated to obtain normal force and tangential force coefficients  $C_n$  and  $C_t$  and moment coefficients  $C_m$  around the quarter-chord point according to equations (3.9), (3.10) and (3.11).

$$C_n = \int_{x/c=0}^1 (C_{p_l} - C_{p_u}) d \frac{x}{c} \quad (3.9)$$

$$C_t = \int_{x/c=0}^1 (C_{p_u}) d \frac{y_u}{c} - \int_{x/c=0}^1 (C_{p_l}) d \frac{y_l}{c} \quad (3.10)$$

$$C_m = \int_{x/c=0}^1 (C_{p_l} - C_{p_u}) \left( \frac{x}{c} - 0.25 \right) d \frac{x}{c} + \int_{x/c=0}^1 C_{p_u} \cdot y_u d \frac{y_u}{c} - \int_{x/c=0}^1 C_{p_l} \cdot y_l d \frac{y_l}{c} \quad (3.11)$$

The indices  $u$  and  $l$  refer to upper surface and lower surface quantities respectively.

Lift coefficients are computed using  $C_n$  and the wake rake drag according to equation:

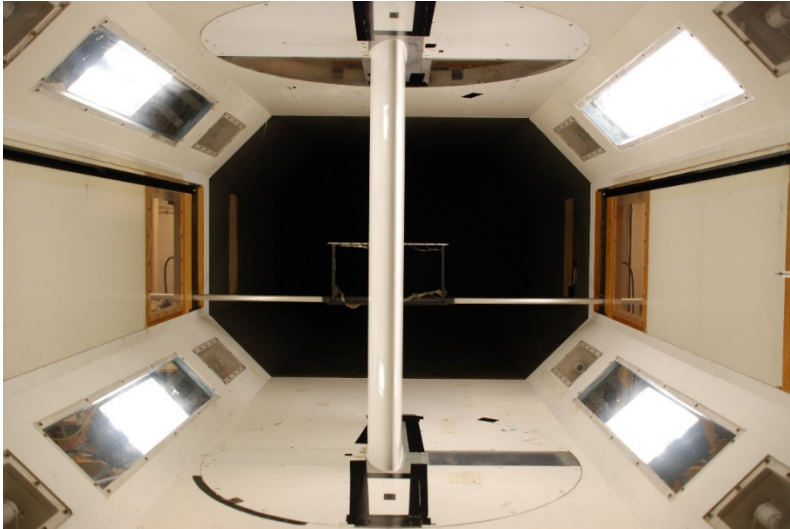
$$C_l = \frac{C_n}{\cos \alpha} - C_d \tan \alpha \quad (3.12)$$

In the post stall region the pressure drag is used, computed from the pressure

distributions using:

$$C_d = C_n \sin \alpha + C_t \cos \alpha \quad (3.13)$$

The post stall lift coefficient was calculated with:



(a)



(b)

*Fig. 3.22: Downstream (a) and upstream view of the model and wake rake inside the test section*

$$C_l = C_n \cos \alpha - C_t \sin \alpha \quad (3.14)$$

### 3.2.3.3 Wake rake measurements

The total and static pressures in the wake are measured with a wake rake. The early measurements on DU 91 and DU 93 had a wake rake containing 12 static pressures with 6 mm spacing. The total pressure rake was 219 mm wide and had 36 tubes, 3 mm apart, of which, towards the ends, a number were not connected to give 6 mm and 12 mm spacing. The static pressure wake rake was located 142 mm above the total pressure wake. A second rake assembly was used in later years with 16 static pressures (24 mm and 48 apart towards the ends) and 67 total pressure tubes, having 3mm spacing in the middle, going to 6, 12 and 24 mm towards the end. Both rakes are 504 mm wide. Fig. 3.22a shows the test setup looking downstream from the test section entrance, with the wake rake in the back and fig. 3.22b shows the model, looking upstream from behind the wake rake assembly and strut.

To calculate the drag coefficient from the wake rake total and static pressures the method of Jones (1936) is adopted. The method, based on momentum conservation considerations, leads to an evaluation of

$$C_d = 2 \int \sqrt{C_{p_t} - C_{p_s}} (1 - \sqrt{C_{p_t}}) d \frac{y}{c} \quad (3.15)$$

across the wake. The pressure coefficients in (3.15) for every one of the 67 total pressure tubes are defined as:

$$C_{p_t} = \frac{p_t - p_0}{q_0} \quad (3.16)$$

and

$$C_{p_s} = \frac{p_w - p_0}{q_0} \quad (3.17)$$

with the subscript w denoting the local wake properties. Outside the wake the total pressure becomes the free-stream total pressure  $p_{t_0}$ , which makes  $C_{p_t} = 1$  and the contribution to  $C_d$  zero.

The free-stream total pressure  $p_{t_0}$  and the boundaries of the wake are determined in two steps. With the total pressure of a pitot-static tube at the entrance of the test section as a starting value of the average total pressure, the  $n$  rake total pressures are evaluated against the following criterion:

$$(p_{t_{average}} - p_{t_n})^2 < b p_{t_{average}} \quad (3.18)$$

where  $p_{t_n}$  is the pressure measured by total pressure tube  $n$ , for  $n=1$  through 67.

Two iterations are performed using  $b=0.01$ . All tubes meeting this criterion contribute to a new average. After the second step we find:

$$p_{t_0} = p_{t_{average}} \quad (3.19)$$

Now the wake boundaries have been determined (the tubes that just do not meet the criterion on either side of the minimum), all total pressures outside the wake are set to  $p_{t,average}$ .

This procedure ensures that any leaking or defect total pressure tubes outside the wake do not contribute to the average free-stream total pressure and that the tubes outside the wake do not impact the calculation of the drag coefficient. In a typical calibration of the wake rake in 2022 the standard deviation of the total pressures of the wake rake was 0.06% at  $Re \approx 1 \times 10^6$  and 0.02% at  $Re \approx 3 \times 10^6$ , for 0.60 m chord models. The difference of the average wake rake total pressure with the total pressure measured with the pitot tube at the entrance of the test section was 0.22% and 0.07% respectively.

#### 3.2.3.4 Calibration of the wake rake.

Despite the fact that the wake rake static and total pressure tubes are relatively far apart, the total assembly of rakes and strut block the flow to some extent, which makes the static pressure measured by the wake rake in an empty test section to deviate from the free-stream static pressure  $p_0$  determined from equation (3.8). In addition, the buoyancy, presented in section 3.2.2.2, results in yet another deviation of the static pressure at the location of the wake rake.

To determine the impact of the model only on the static pressure field at the wake rake location,  $p_0$  in eq. (3.16) and (3.17) should be replaced by the static pressure measured by the wake rake in an empty test section.

Calibrations of the static pressure wake rake tubes in an empty test section are frequently performed for several tunnel control pressures. Rather than storing all the detailed tube pressures for all Reynolds numbers, the average of 8 static pressures in the middle of the rake is established (is  $p_{0,w}$ ), and together with the average of the total pressures ( $=p_{t,0}$ , eq. 3.19) a dynamic pressure calibration curve for the wake rake is formed ( $q_{0,w} = p_{t,0} - p_{0,w}$ ). An example of the measured static pressure coefficients for  $x/c=0.825$  is given in fig. 3.23. For every tunnel control pressure now a free-stream wake rake dynamic pressure is available, giving a dynamic pressure  $q_{0,w}$  and a static pressure  $p_{0,w}$  ( $=p_{t,0} - q_{0,w}$ ), which can be used to calculate the drag coefficients using equations (3.16) and (3.17) when the

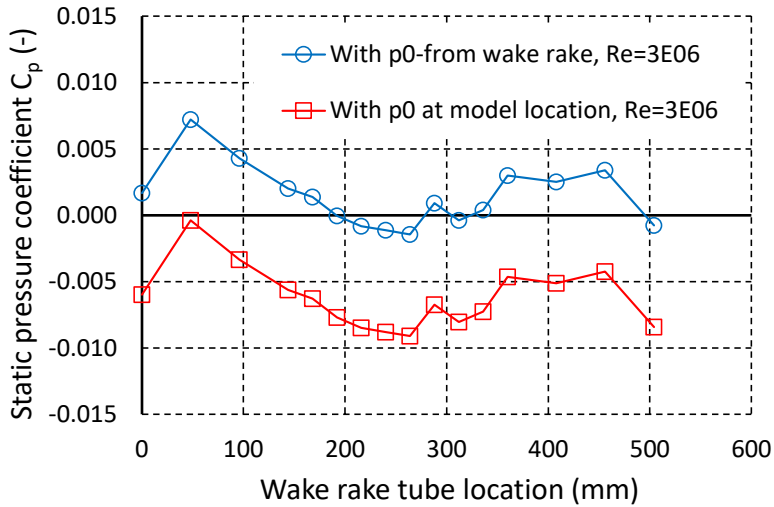


Figure 3.23: The wake rake static pressure coefficients at  $Re=3 \times 10^6$  using free-stream static pressures resulting from the model - and the wake rake dynamic pressure calibration curves.

model is present. The difference with a drag coefficient calculated using the free-stream static pressure at the model location according to eq. (3.8), amounts to app. -0.5% for most models and Reynolds numbers.

### 3.2.3.5 The impact of wake rake downstream position

After 1996, the strut with the wake rake assembly was always placed at the same downstream location at the end of the test section ( $x/c=0.825$ , see fig 3.24). No specific investigation was performed to establish drag-deviations related to streamwise wake rake position. However, from the existing data, the following comparison could be made. Measurements of Timmer (1984) on a 1.0m chord model of sailplane airfoil HQ17/14.38

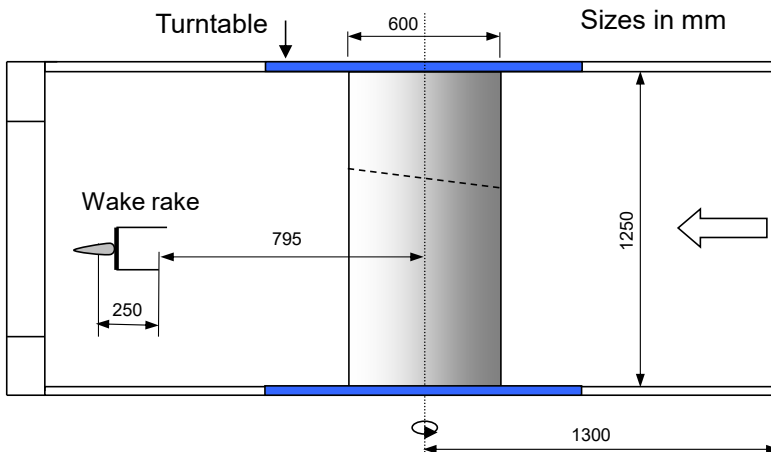


Fig. 3.24: Side view of a typical setup of a 0.60 m chord model.

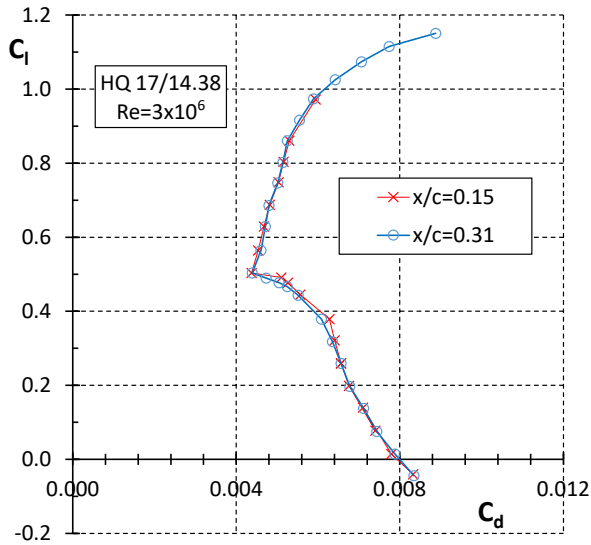


Figure 3.25: Measurements at two distances behind the trailing edge of a 1.0m chord model of airfoil HQ17/14.38 (Timmer, 1984)

were performed at two distances behind the trailing edge, at  $x/c=0.15$  and  $0.31$  respectively. The resulting performance is depicted in fig. 3.25. Apart from 3 outliers below a lift coefficient of  $0.5$ , which primarily might be linked to a small lower surface laminar separation bubble size variation, the drag differences are in the range  $-1\% < \Delta C_d < 1.6\%$ , with an average of  $0.02\%$ .

The drag of the 0.60m chord DU91-W2-250 model, with a  $0.65\%$  thick trailing edge, was

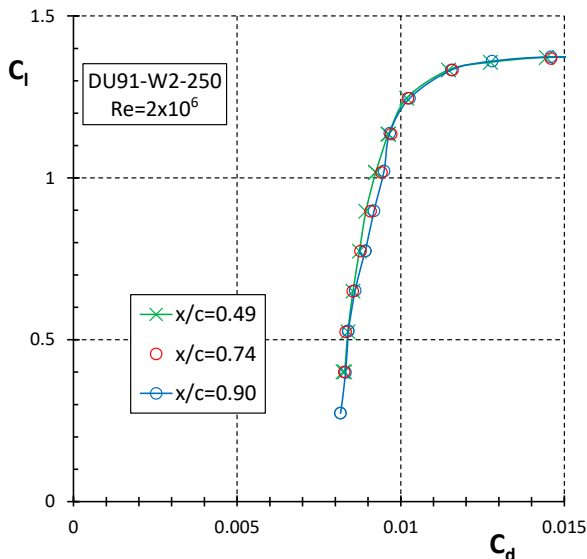


Figure 3.26: Measurements with a wake rake at three distances behind the trailing edge of a 0.60m chord model of airfoil DU91-W2-250.

determined with a previous, smaller, wake rake at three stations behind the trailing edge for a Reynolds number of  $2.0 \times 10^6$  and a span position of 459 mm above the wind tunnel floor. The resulting drag characteristics are shown in fig. 3.26. It indicates there is a very slight tendency of a higher measured drag between  $x/c=0.49$  and 0.90, however the average difference is approximately 1.2%, which is within the drag variation in span-wise direction.

The biggest differences are noted at angles between  $3^\circ$  and  $6^\circ$ , while at  $9.2^\circ$ , which gives  $C_{l,max}$  for this airfoil at  $Re=2 \times 10^6$ , the deviation is small. At the latter, with turbulent separation at about 95% on the suction surface, one would expect the highest difference. The deviations between  $x/c=0.74$  and 0.90 are on average smaller than 0.5%, well within the normal range encountered during consecutive measurements.

Regarding the regular position of the wake rake ( $x/c=0.825$  with 0.60m chord models), it seems there is no impact of the wake rake downstream position on the measured drag, if the static pressure in the wake is taken into account.

### 3.2.3.6 Traverse measurements

Although the models have been constructed with the utmost care, there will be some small drag differences in span wise direction, due to deviations in transition location, a combined effect of very small deviations in shape, variations in laminar separation bubble size, surface smoothness and flow disturbances e.g. from pressure orifices.

The testing of each new model configuration starts with a number of wake rake traverse measurements in spanwise direction at various angles-of-attack and Reynolds numbers to confirm the two-dimensionality and to establish the wake rake position (or a span

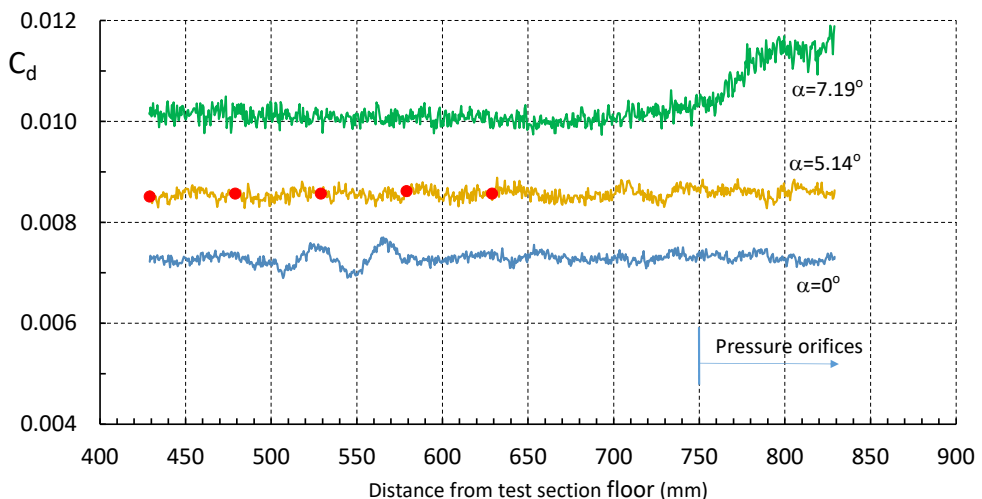


Figure 3.27: The drag variation in span direction of the DU93 model for various angles of attack at  $Re=2 \times 10^6$ . The red solid circles denote 20sec averages at constant span location.

length), giving an average drag value representative for the model. In earlier tests this was done manually, later tests were performed using the automatic traversing mechanism of the tunnel. A typical example of such a measurement is depicted in fig. 3.27, showing the drag variation of the DU93-W-210 model between 430 mm and 830 mm from the test section bottom wall at various angles of attack and a Reynolds number of  $Re=2 \times 10^6$ . The graph shows two distinct areas where the drag deviates from the regular behaviour.

The wavy character of the curve for  $\alpha=0^\circ$  between 500mm and 580mm span is due to a leading edge disturbance at a span of about 550mm producing a turbulent wedge, which was removed before further tests were conducted. The drag for an angle of attack of  $7.2^\circ$  degrees beyond 750 mm span is impacted by the flow disturbance of the pressure orifices that are located between 750mm and 930 mm span. The standard deviation of the drag values in the areas not affected by disturbances for  $\alpha=0^\circ$ ,  $5.14^\circ$  and  $7.19^\circ$  is respectively 1.10%, 1.25% and 1.31%. The 20s averages at constant span shown as the red solid circles in fig. 3.27 deviate within  $\pm 1.3\%$  from the value in the traverse at the same span position and within  $\pm 0.7\%$  from the traverse average.

### 3.3 CONCLUSIONS

As CFD computations still are too time consuming to serve as flow solver in optimization processes in which a large number of solutions need to be evaluated, panel codes, such as XFOIL and RFOIL are a good choice, when the focus is on single element airfoils. Although panel code predictions have their own issues, they can provide solutions for a number of flow states around airfoils with moderate thickness. From the comparisons in this chapter the following conclusions emerge.

#### Clean airfoil performance

In the Re-number range from  $3 \times 10^6$  to  $6 \times 10^6$ , RFOIL generally underpredicts drag and overpredicts lift, but not necessarily overpredicts the maximum lift coefficient. The underprediction of drag in both XFOIL and RFOIL is in the range of 10% to 14%. In many cases the underprediction is found to be 14%, irrespective of Reynolds number and section thickness, provided that:

- The turbulence intensity in the test section during the measurements is accounted for by choosing the right amplification (N-) factor.
- The Mach number during the measurements is accounted for.
- The section has limited trailing edge thickness.

The N-factor in the transition prediction for the TU Delft LTT is found to be 11 at  $Re=3 \times 10^6$ . The factor established for the NASA LTPT is 10.

The overprediction of maximum lift, ranging from 0% to 6%, is generally found for airfoils

with a thickness of 21% and beyond. While predictions for NACA sections with a thickness of 21% mostly have a matching  $C_{l,max}$ , this overprediction for measurements in the LTT already starts at the 21% thick DU93-W-210 section (4.5%).

Above  $Re=6 \times 10^6$ , RFOIL gradually starts to underpredict the maximum lift coefficient (up to 5.8% at  $Re=15 \times 10^6$ ), while XFOIL with RFOIL A and B parameters of the  $G-\beta$  locus provides increasingly closer solutions (only +1.3% at  $Re=15 \times 10^6$ ).

Panel codes like XFOIL and RFOIL do not predict the flow over blunt trailing edges well. The base pressure is heavily overestimated, resulting in massive underprediction of the total section drag.

### **Section characteristics with a tripped boundary layer**

In configurations where in the experiment transition is forced with a relatively small roughness height (e.g. fig. 3.9 and fig. 3.17), the underprediction of drag is lower than in the clean case. For DU97 in fig. 3.9 (and also for DU96 and DU93, as mentioned) this is 7% with an almost completely turbulent upper surface BL against 14% with a clean section upper side with transition between  $x/c=30\%$  and  $40\%$ . For DU00 in fig. 3.17 this underprediction with a tripped BL at the leading edge of both sides is even approximately 0% to 1%.

The underprediction of drag with a fully turbulent BL appears to be far less than in a smooth situation with a mixed laminar-turbulent part. The prediction of the transition location is generally good in the low-drag bucket (fig. 3.2) and calculation of the laminar part is assumed to be reasonably straightforward. This implies that the underprediction of the drag in the clean case may not per se only be found in the growth of the turbulent boundary layer (i.e. the value of the turbulent friction coefficient), but also may be due to the starting conditions of the turbulent BL after transition has been established. Apparently this difference in  $C_d$  can amount to about 7% per side.

### **Measurements in the TUDelft LTT**

A description was given of the layout and flow quality of the TUDelft LTT. Low turbulence intensity and frequent calibrations of the test section flow speed and the wake rake total and static pressures assure high quality airfoil characteristics up to  $Re=3 \times 10^6$  for 0.60m chord models. Drag coefficients generally are the result of traverse measurements in spanwise direction with a wake rake located at the end of the test section. For 0.60m chord models this is at a distance of 82.5% chord behind the model trailing edge.

## **3.4 REFERENCES**

Abott, I.R.A, van Doenhoff, A.E. and Stivers, L.S. (1945) *Summary of airfoil data*. Report No. 824. National Advisory Committee for Aeronautics, Langley Field, Va, USA, 1945.

Allen, H.J., and Vincenti, W.G. (1944) *Wall interference in a two-dimensional wind tunnel, with consideration of the effect of compressibility*. NACA Report no. 782, (1944).

Bernardy S. *Private communication*, October 2015

Boeker, J. (1961) *Fluctuations in the total pressure, the static pressure and the flow direction measured in the test section of the low-turbulence tunnel (in Dutch)*. Memorandum M50, Aeronautical Department, Delft University of Technology, 1961

Boermans L.M.M. *Private communication*, 1994

Bongers, J. (2006) Implementation of a new transition prediction method in XFOIL. Master Thesis TU Delft, July 2006.

Ceyhan-Yilmaz, Ö., Pires, O., Mundiate, X., Sørensen, N., Reichstein, T., Schaffarczyk, A.P., Diakakis, K., Papadakis, G., Daniele, E., Schwarz, M., Lutz, T. and Prieto, R. (2017) *Summary of the Blind Test Campaign to predict the high Reynolds number performance of DU00-W-210 airfoil*. AIAA SciTech Forum, January 2017, Texas, USA

Ceyhan-Yilmaz, Ö. and Timmer, W.A. (2018) *Experimental evaluation of a non-conventional flat back thick airfoil concept for large offshore wind turbines*. AIAA 2018-3827, doi: 10.2514/6.2018-3827

Clauser, F.H. (1954) *Turbulent boundary layers in adverse pressure gradient*. Journal of Aeronautical Science 21 (1954) 91

Dobbinga, E. and van Ghesel Grothe, J.A. (1955) *The low-speed wind tunnel of the department of Aeronautical Engineering of the TUDelft (in Dutch)*. De Ingenieur, no 38, 1955.

De Oliveira, G., Pereira, R., Timmer, W.A., van Rooij, R. (2018) *Improved airfoil polar predictions with data-driven boundary-layer closure relations*. Journal of Physics: Conf. Series 1037 (2018) 022009, doi :10.1088/1742-6596/1037/2/022009

Drela, M. (1989) *XFOIL: An analysis and design system for low Reynolds number airfoils*. Conference on Low Reynolds Number Airfoil Aerodynamics, University of Notre Dame, USA, June 1989.

Drela, M. (1989) *Integral boundary layer formulation for blunt trailing edges*. 7th Applied Aerodynamics Conference, Fluid Dynamics and Co-located Conferences, No. 89-2166-CP, AIAA, 1989.

Ewald, B.F.R. (Ed.) (1998) *Wind tunnel wall corrections*. AGARDograph 336.

Ferreira, C. (2002) *Implementation of Boundary Layer Suction in Xfoil and Application of Suction Powered by Solar Cells at High Performance Sailplanes.*, Delft University of Technology, 2002

Garner, H.C. , Rogers, E.W.E., Acum, W.E.A. and Maskell, E.C. (1966) *Subsonic wind tunnel wall corrections*, AGARDograph 109, (1966).

Genderen, G. van (1957) *Turbulence measurements in the low-speed wind tunnel of the Aeronautical Department of the Technical University Delft*. (in Dutch). Report AA. 147, National Aerospace Laboratory, April 1957.

Grasso, F. and Ceyhan, Ö. (2015) *Non-conventional flat back airfoils for very large offshore wind turbines*. AIAA SciTech Forum January 2015 Kissimmee, Florida, USA

Hansen, T.H. (2018) *Airfoil Optimisation for Wind Turbine Application*. Wind Energy.; 2018; 21:502-514. <https://doi.org/10.1002/we.1274>

Huang, T.T., Purtell, L.P. and Lee, Y.T. (1990) *Turbulent characteristics of trailing edge flows on thick and thin hydrofoils*. Numerical and Physical Aspects of Aerodynamic Flows IV, T. Cebeci ed. Springer-Verlag, Berlin (1990)

Jones, B.M. (1936) *Measurement of profile drag by the pitot-traverse method*. ARC R&M No. 1688. (1936)

Loftin, K.L., Jr. and Bursnall, W.J. (1948) *Effects of Variations in Reynolds Number Between  $3.0 \times 10^6$  and  $25 \times 10^6$  upon the Aerodynamic Characteristics of a number of NACA 6-Series Airfoil Sections*, NACA-TN-1773, 1948.

Llorente, E., Gorostidi, A., Jacobs, M., Timmer, W.A., Munduate, X. and Pires, O. (2014) *Wind Tunnel Tests of Wind Turbine Airfoils at High Reynolds Numbers*. Journal of Physics: Conference Series 524 (2014) 012012 doi:10.1088/1742-6596/524/1/012012

Mack, L.M. (1975) *Aerodynamic Analysis Requiring Advanced Computers*. Paper nr. 4.

Technical Report SP-347, NASA, 1975

Mack, L.M. (1977) Transition and laminar instability. NASA JPL Publication 77-15, May 1977.

McGhee, R.J. and Beasley, W.D. (1973) *Low-speed aerodynamic characteristics of a 17-percent-thick airfoil section designed for general aviation applications*. NASA TN D-7428

McGhee, R.J. and Beasley, W.D. (1976) *Effects of thickness on the aerodynamic characteristics of an initial low-speed family of airfoils for general aviation applications*. NASA TM X-72843

McGhee, R.J. and Beasley, W.D. (1978) *Wind-tunnel results for an improved 21-percent-thick low-speed airfoil section*. NASA Technical Memorandum 78650.

McGhee, R.J. and Beasley, W.D. (1980) *Low-speed aerodynamic characteristics of a 17-percent-thick medium-speed airfoil designed for general aviation applications*. NASA TP 1786

McGhee, R.J. and Beasley, W.D. (1981) *Wind-tunnel results for a modified 17-percent-thick low-speed airfoil section*. NASA -TP-1919

Melnik, R.E. and Brooks, J.W. *The computation of viscous-inviscid interaction on airfoils with separated flow*. Numerical and physical aspects of aerodynamic flows III, Springer Verlag, Berlin 1985

Olsen, A.S., Ramos-García, N., Bak, C. (2020) *Improved roughness model for turbulent flow in 2D viscous-inviscid panel methods*, Wind Energy 23 (3) (2020) 608-616.

Rogowski, K, Hansen, M.O.L., Hansen, R., Piechna, J. and Lichota, P. *Detached eddy simulation model for the DU91-W2-250 airfoil* Journal of Physics: Conf. Series **1037** (2018) 022019 doi :10.1088/1742-6596/1037/2/022019.

Rooij, R.P.J.O.M. van (1996) *Modification of the boundary layer calculation in RFOIL for an improved stall prediction*, Tech. Rep. IW-96087R, Delft University of Technology, 1996.

Schaffarczyk, A.P., Winkler, H., Rebstock, R. (2003) *Selected results of experimental investigations for a thick wind turbine profile at high Reynolds numbers*. Proceedings of the 16th IEA Symposium on the Aerodynamics of Wind Turbines, Boulder, CO, 2003.

Schlichting H. and Gersten K. (2000) *Boundary layer theory*, 8<sup>th</sup> edition ISBN 3-540-66270-7 Springer Verlag Berlin, (2000)

Sezer Uzol, N. Uzol, O. and Orbay-Akcengiz., E. *CFD simulations for airfoil polars*. In: Handbook of wind energy aerodynamics. B. Stoevesant et al. (eds.) Springer Nature Switzerland, doi.org/10.1007/978-3-030-05455-7\_12-1.

Sørensen, N.N. et al. (2016) *CFD code comparison for 2D airfoil flow*. Journal of Physics: Conference Series **753** (2016) 082019. doi:10.1088/1742-6596/753/8/082019

Timmer, W.A. (1984) *The aerodynamic performance of airfoil HQ17/14.38*. (in Dutch), Master thesis Delft University of Technology, 1984

Timmer, W. A. (2009) *An overview of NACA 6-digit airfoil series characteristics with reference to airfoils for large wind turbine blades*. AIAA 2009-268

Townsend, A.A. (1976) *The structure of turbulent shear flow*. Cambridge University Press, 1976

Van Ingen, J.L. (1956) *A suggested semi-empirical method for the calculation of the boundary layer transition region*. Report VTH-74, 1956, Delft University of Technology.

Van Ingen, J.L. (2008) *The  $e^N$  method for transition prediction. Historical review of work at TU Delft*, AIAA 2008-3830, 38th Fluid Dynamics Conference and Exhibit, 23-26 June 2008, Seattle, Washington.

Zhou, M.D. and Squire, L.C. (1985) *The interaction of a wake with a turbulent boundary layer*. Aeronautical Journal, 72-81 (1985).

# 4

## ON THE AERODYNAMIC DESIGN OF AIRFOILS

### 4.1 DEFINITIONS AND PROPERTIES OF A ROTOR BLADE ELEMENT

When jointly considering basic wind turbine aerodynamics and their mechanical loads, airfoil characteristics can be derived, which are, unfortunately, in some cases conflicting. Figure 4.1 presents the cross section of a blade segment with a span wise length  $dr$  at a distance  $r$  from the rotor axis, showing the definition of relevant properties such as the radial and inflow velocity vectors and the forces acting on it.

The velocity  $U$  is the wind speed approaching the rotor,  $\Omega$  is the rotor rotational speed and  $a$  the axial induction factor induced by the wake. The tangential induction factor  $a'$  is due to wake rotation in the far wake of the rotor.

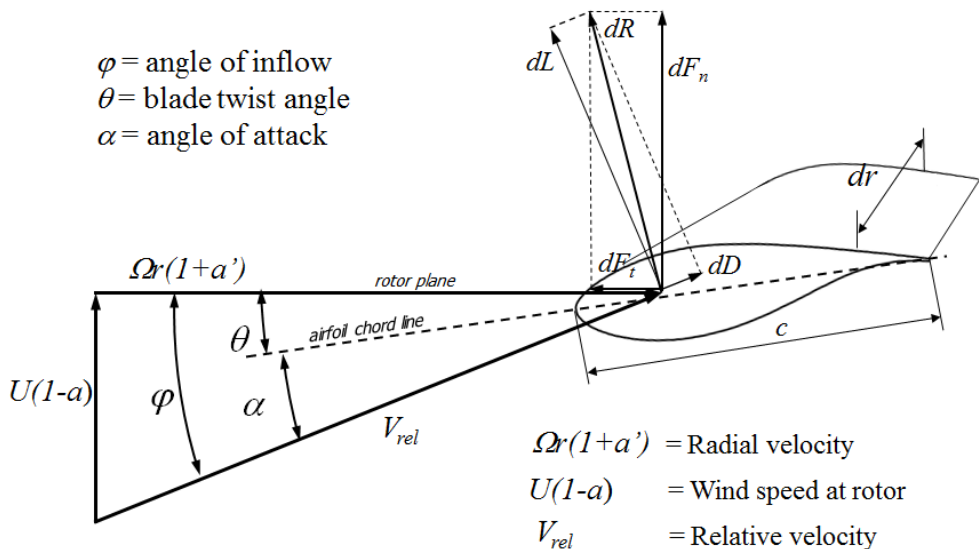


Figure 4.1: Velocities and forces diagram for a wind turbine blade segment

The elemental lift force  $dL$ , defined in the direction perpendicular to the relative velocity vector of the flow approaching the blade segment, can be written as

$$dL = C_l \frac{1}{2} \rho V_{rel}^2 c dr \quad (4.1)$$

The drag force  $dD$  is a component perpendicular to the lift. Both  $dL$  and  $dD$  operate at a distance  $r$  from the centre of rotation.

$$dD = C_d \frac{1}{2} \rho V_{rel}^2 c dr \quad (4.2)$$

The component in the rotor plane of the resultant force  $dR$  of lift and drag can be decomposed into the tangential and normal components,  $dF_t$  and  $dF_n$  respectively. The former is most relevant to the work performed by the wind turbine.

$$dF_t = dL \sin \varphi - dD \cos \varphi \quad (4.3)$$

Or, written differently:

$$dF_t = dL \left( \sin \varphi - \frac{\cos \varphi}{dL / dD} \right) \quad (4.4)$$

Combining equations (4.1) and (4.4), for the tangential force that drives the turbine blade we find:

$$dF_t = \frac{1}{2} \rho V_{rel}^2 C_l c \left( \sin \varphi - \frac{\cos \varphi}{C_l / C_d} \right) dr \quad (4.5)$$

Likewise, the normal force on a blade segment, contributing to the thrust on the rotor, can be expressed as:

$$dF_n = \frac{1}{2} \rho V_{rel}^2 C_l c \left( \cos \varphi + \frac{\sin \varphi}{C_l / C_d} \right) dr \quad (4.6)$$

The rotor aerodynamic torque  $Q$  due to the tangential force  $dF_t$  working on the blade at a distance  $r$  from the rotor axis is given by :

$$Q_{aer} = B \int_0^R dF_t r dr \quad (4.7)$$

in which  $B$  is the number of blades. The aerodynamic power then is expressed by

$$P_{aer} = M_{aer} \Omega \quad (4.8)$$

where  $\Omega$  is the rotor angular velocity in rad/s. The thrust  $T$  on the turbine follows from

$$T = B \int_0^R dF_n dr \quad (4.9)$$

For a given wind speed, equations (4.5) and (4.6) show four design variables. The relative velocity  $V_{rel}$  is depending on the rotational frequency of the rotor  $\Omega$ , generally expressed in the tip-speed ratio  $\lambda = \Omega R / U$ , in which  $R$  is the radius of the rotor. For a given tip-speed ratio, the blade performance is governed by the terms  $C_l c$  and  $C_l / C_d$ . High values of  $C_l c$  maximize the turbine power, but at the same time increase the blade bending moments.

To show the relative importance of the design lift-coefficient (the lift coefficient giving the maximum lift-drag ratio) and the associated airfoil efficiency (maximum  $C_l/C_d$ ) on the rotor torque, let us look at the variation of the tangential force coefficient with lift-drag ratio on a blade segment of unit span for three design lift coefficients. The main rotor parameters are given in table 4.1.

Reworking of eq. 4.5 yields:

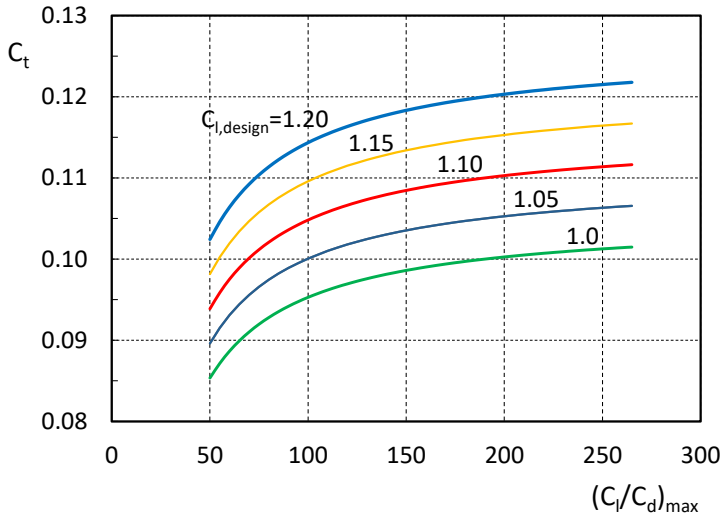


Figure 4.2: The variation of the tangential force coefficient with maximum lift-drag ratio on a blade element at 70% span for several design-lift coefficients

$$C_t = \frac{dF_t}{\frac{1}{2}\rho V_{rel}^2} = C_l c \left( \sin \varphi - \frac{\cos \varphi}{C_l / C_d} \right) dr \quad (4.10)$$

Using the parameters from table 4.1 and an air density  $\rho = 1.225 \text{ kg/m}^3$  we find the relations depicted in figure 4.2, where the design-lift coefficient varies between 1.0 and 1.2.

Table 4.1: Main rotor parameters for the calculation of  $C_t$  (eq. 4.10)

$\Lambda$	9
U	8 m/s
$V_{tip}$	72 m/s
a	1/3
a'	$\approx 0$
r/R	0.70
chord	1 m

The figure shows that changes in the tangential force can best be accomplished by variation in the design-lift coefficient. To realize a 5% increase in the tangential force coefficient at a  $C_l/C_d$  of 100 and a  $C_{l,design}$  of 1.1 (from  $C_t = 0.105$  to 0.110) would require a

change in  $(C_l/C_d)_{\max}$  from 100 to 190, while the same could be accomplished with an increase of  $C_{l,\text{design}}$  to 1.15. In terms of airfoil aerodynamics the first would be a tremendous effort and in practice hard to realize, while the second could relatively easily be accomplished by applying more camber to the airfoil. The latter, however, will go at the cost of a 4.5% higher normal force.

If we define the aerodynamic efficiency of a rotor blade segment as:

$$\xi_r = \frac{dF_t}{dF_n} = \frac{\left( \sin \varphi - \frac{\cos \varphi}{C_l / C_d} \right)}{\left( \cos \varphi + \frac{\sin \varphi}{C_l / C_d} \right)} \quad (4.11)$$

it follows that the only way to actually increase the blade *efficiency* is to maximize the segment lift-drag ratio.

The cosine term in equation (4.10) is a viscous loss term due to the section drag, and is, as shown in eq. (4.5) and (4.6), of direct influence on the torque of the turbine (eq. 4.7) and consequently on the turbine's power (eq. 4.8). As can be deduced from figure 4.1, going from the root of the blade to the tip, the in-plane velocity increases due to the blade rotation, which causes the inflow angle  $\varphi$  to decrease and the cosine of the inflow angle to increase. Consequently, to minimize viscous losses, a high lift-drag ratio becomes increasingly important towards the tip.

An increase in the normal force coefficient  $C_t$ , caused by a higher design-lift coefficient, and subsequently an increase in the bending moments on the blade, can only be counter-balanced by increasing the section's moment of inertia, so by adding more material, by using other (stiffer) materials or by increasing the thickness of the structure. A heavier rotor, however, is generally undesirable as this impacts the tower and the foundation as well (snowball effect). The application of better materials (such as carbon fibers) will work, but may also increase costs (material cost, other ways of handling/production). Thicker airfoils generally have lower lift-drag ratios so the envisaged increase in  $C_t$  cannot be totally realized and comes at the cost of reduced rotor efficiency. This example already shows that careful balancing is needed and airfoil optimization should include some kind of cost function with respect to blade mass.

#### 4.1.1 BEM theory

Equations 4.5 to 4.9, containing the forces on an element  $dr$  of a rotor blade, form the basic relations for the blade element side of the Blade Element Momentum (BEM) method (Glauert, in Durand, 1963), which is used for blade design and has been described in many

text books (e.g. Burton et al. 2001, Manwell et al. 2002). The momentum part is based on momentum conservation of the flow through an energy extracting disc. It gives, per disc annulus with width  $dr$ , the torque  $dQ$  and the axial force  $dT$ , equivalent to the integrand of eq. (4.7) and (4.9) respectively. They are both also depending on the axial and tangential induction factors  $a$  and  $a'$ . By iteration these induction factors can be resolved. In its simplest one-dimensional form for an ideal rotor (no tangential induction), using the power coefficient  $C_p$  and the thrust coefficient  $C_T$  defined as:

$$C_p = \frac{P}{\frac{1}{2}\rho U^3 A} \quad \text{and} \quad C_T = \frac{T}{\frac{1}{2}\rho U^2 A} \quad (4.12)$$

we find:

$$C_p = 4a(1-a)^2 \quad \text{and} \quad C_T = 4a(1-a) \quad (4.13)$$

from which the so-called Betz maximum of  $C_p=16/27$  (Betz, 1926) or 59.26% maximum energy extraction can be derived (for  $dC_p/da=0$ ) and the associated optimum induction for  $a=1/3$ . Corrections were applied by Prandtl (described by Glauert, reported by Durand, 1963) for the finite number of blades (which generally is called tip correction; a bit misleading, as it does not correct for the *blade* being finite).

In the course of time the BEM theory was modified to cover deficiencies in the theory or was further extended with engineering methods to account for e.g.:

- Axial induction factors bigger than 1/3, giving increasingly unrealistic results
- Turbulence in the inflow
- Yaw-misalignment of the rotor
- Dynamic inflow to the rotor
- Rotational effects, predominantly in the root of the blade
- Blade dynamic stall
- Wake interference effects
- Blade and turbine dynamics

## 4.2 AIRFOIL CHARACTERISTICS AND THE POWER CURVE.

In fig. 4.3a the airfoil lift and drag curves with varying angle of attack are sketched, presenting the most important design parameters. Fig. 4.3b shows a sketch of the power curve both for a stall controlled turbine and for a variable speed, variable pitch machine with three distinct area's depending on airfoil design, corresponding to the boxes I+II and III in fig. 4.3a .

With increasing wind speed the power goes up as sketched in fig. 4.3b, area I. The mean angle of attack ideally is at a value giving the maximum efficiency ( $C_l/C_d$ ), as indicated in box I of the lift curve in fig. 4.3a. To accomplish this, the rotor works at constant tip speed ratio, defined as  $\Lambda = \Omega R/U$ .

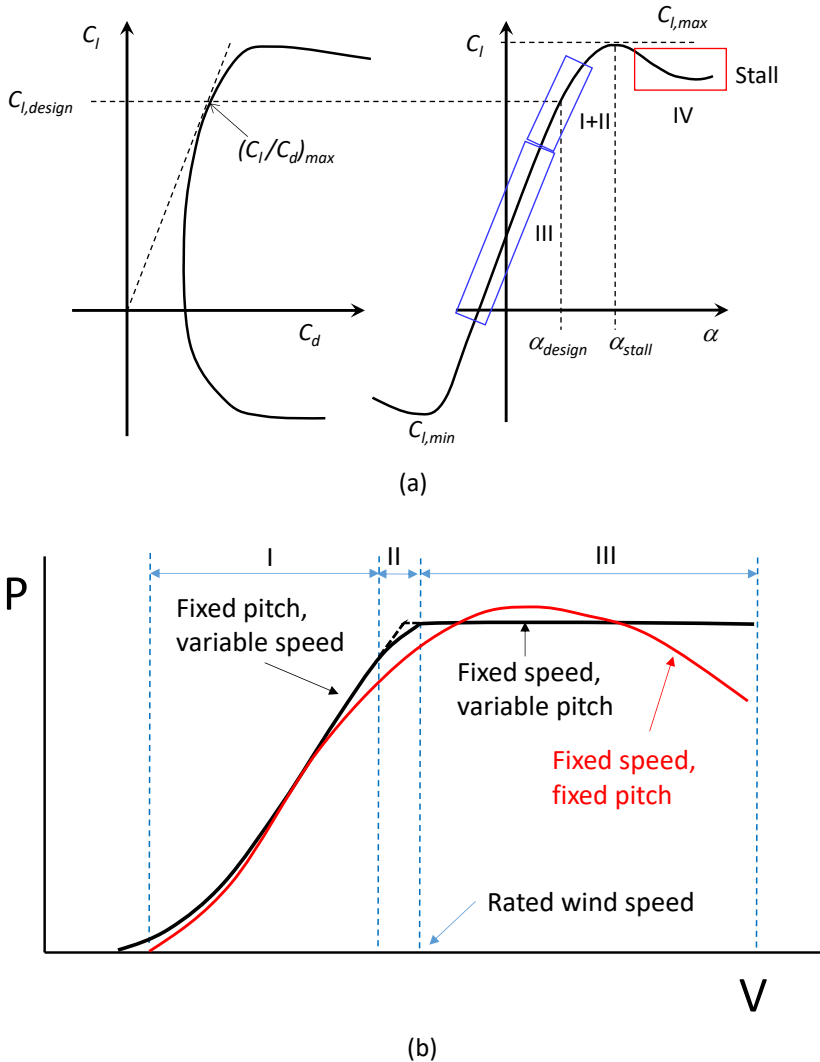


Figure 4.3: Sketches of an airfoil characteristic with the most important design parameters (a) and the associated power curve for a turbine with variable speed and pitch control (b). Also depicted the power curve for a turbine with passive stall control.

As a consequence, the rate of rotation increases linearly with the wind speed. This could go on until the maximum power is reached (dashed line in fig 4.3b). However, in that condition the rotor also experiences the maximum axial force. In order to reduce the loads (thrust) on the turbine entering zone II, the rotor speed is kept

constant and the blade pitch is changed to reduce the angle of attack with increasing wind speed. This is called “peak shaving” (Savenije and Peeringa, 2009).

The disadvantage is, that some power is lost. Turbine manufacturers have their own turbine specific control algorithm, optimized with respect to rotor rotational speed and blade pitch to minimize the power losses in this small wind speed range.

Since a significant part of the turbine power is generated in zones I and II, the airfoils in the blade in that wind speed range should perform at their best in all conditions. It is, therefore, of paramount importance that the airfoil characteristics do not suffer too much from a contaminated or damaged leading edge. Drag increase due to early separation and a significant reduction in airfoil maximum lift would give a notable reduction in the power. To this end the natural transition location on the airfoil suction surface in the upper part of box I and II, shown in the lift curve of fig. 4.3a, should already be at the leading edge.

A third regime (Zone III) is identified in the power curve, where the control system keeps the power at its maximum using a constant rotor circumferential speed and blade-pitch movements to decrease the angle of attack when the wind speed increases. The airfoil working point moves down the lift curve into box III, towards the minimum  $C_l$ , which magnitude should be as small as possible, to minimize the deflection of the rotor at high wind speeds and to reduce the structural loads during emergency stops.

The red curve in fig. 4.3b presents the power curve for a stall controlled turbine, for which the maximum power is limited as a result of increased stalling of the blades. Due to the constant rotational speed of the rotor, the angle of attack of the airfoils in the blade increases with increasing wind speed, covering the entire range of angles of attack into stall (boxes I+II, III and IV in fig. 4.3a). This type of control needs a robust design as the loads are higher compared to constant lambda designs. The power curve matches the one for a constant lambda machine just in one point, where the rotor rotational speed and the wind speed create the conditions for which the airfoils work at their most efficient angle. Airfoils for stall controlled rotors should have benign post stall characteristics to avoid large fluctuating loads when the blade, due to unsteadiness in the wind speed and consequently fluctuating angles of attack, goes into and out of stall. Also for airfoils in blades of constant lambda machines this would be a good quality (additional safety) when, while angles are high, gusts appear and the control system is not fast enough. A relatively flat rotor stall curve is not straightforward to achieve, especially when dealing with airfoils featuring a very large maximum lift coefficient (see fig. 2.5 and 3.6).

#### **4.2.1 Blade and airfoil chord size**

The most common approach to increase the yield of wind turbines is that of upscaling their size (increased rotor area) and height (increased average wind speed). However,

longer blades may result in increased weight and flexibility. The in-plane force fluctuations due to blade weight (gravitational loads) occur twice per revolution and have become a relevant design driver. A possible option is that of adopting blades with small chords. In addition, to restrict the loads in the parked condition or while hoisting a blade during installation, the blade area and consequently the chord of the blades should be kept small accordingly. Following from the term  $C_l c$  in eq. 4.6, with angle of attack changes and resulting lift variations in the linear part of the lift curve, the loads on a blade with a small chord fluctuate less than on one with a larger chord. The constant upscaling of wind turbines and the necessity to keep the weight down indeed leads to long and slender blades.

As equation 4.5 shows, blades with smaller chords require a relatively high design lift coefficient of the airfoils. However, airfoils with such a high design lift coefficient (especially thick ones) tend to have a peaky and hence less desirable stall behavior and may have increased sensitivity to leading edge flow distortion (see fig. 2.5).

To limit blade weight, airfoils with a high relative thickness can be used. However, thick airfoils may have increased pressure drag due to higher upper surface velocities causing boundary layer thickness growth and premature turbulent separation in cases of leading edge roughness. The 18% thick airfoil NACA 64<sub>3</sub>-418 is still widely used in the blade-tip region of turbines up to 1 MW installed power. At  $Re=6 \times 10^6$  the reduction of the lift-drag ratio due to a rough leading edge of this airfoil is 52%. A thicker alternative would be the 21% thick NACA 63<sub>4</sub>-421. However, its lift-drag ratio reduction would be almost 60% (data from Abbott and von Doenhoff, 1945). If it comes to aerodynamic efficiency, especially in the rough condition, thick airfoils cannot compete with thinner airfoils.

In summary, desirable airfoil characteristics are:

- A high lift-to-drag ratio to optimize aerodynamic performance
- For the blade root, a high lift coefficient
- Benign stall characteristics to reduce fatigue loads
- A high relative thickness to reduce blade weight
- Low susceptibility to leading edge contamination
- A high design lift coefficient giving small chords to reduce weight and parking loads
- Low noise

### **4.3. THE DESIGN ANGLE AND $C_{L,MAX}$**

#### **4.3.1 Angle of attack fluctuations**

The blades of a wind turbine need to perform in an unsteady environment. The variations in angle of attack that a certain section of a blade encounters are predominantly due to

the following phenomenon:

#### Wind shear

In the atmospheric boundary layer the wind speed increases with height. This results in a smaller angle of attack when the blade is pointing downwards and a higher angle of attack when it is pointing upwards. The deviations at a certain blade location are depending on the local shape of the atmospheric boundary layer and the diameter of the turbine. The height and shape of the atmospheric boundary layer are also impacted by orography and terrain roughness. Therefore, the above unsteadiness is location specific.

#### Yaw misalignment.

The turbine yaw mechanism turns the nacelle normal to the wind. When the wind is rapidly and frequently changing direction, the turbine orientation may suffer a delay, resulting in a yawed regime of the turbine. Certification bodies such as Germanische Lloyd consider yaw actions to occur in 10% of the turbine's life time. An average of  $\pm 8^\circ$  yaw misalignment needs to be adopted in load calculations. The angle of attack varies between the downwind (retreating blade, smaller angles) and the upwind part (advancing blade, higher angles) of the turbine and as a result of the skewness of the wake.

#### Atmospheric turbulence.

Unsteady variations of wind speed over relatively short time scales (in the order of 1 to 10s) are due to the turbulent state of the atmospheric boundary layer. The turbulence intensity is defined as the ratio of the standard deviation of the fluctuations in wind speed over the mean. Instantaneous fluctuations in the wind speed result in a change of the angle of attack. For very large blades variations of the angle of attack are even experienced along the span. The wind climate is divided in several classes, each with their respective turbulence intensity, requiring a dedicated design for the blade.

#### Blade flapping motions.

This aspect is associated with the aero elastic behavior of the blade. Fluctuations increase towards the tip.

#### Tower shadow.

This name may be a bit misleading, as it might be associated with a turbine blade passing *behind* the tower, through the lower speed region of the tower wake. However, as a result of the presence of the tower, once per revolution the blade will pass a region in front of the tower where the flow speed is also lower, causing higher angles of attack. This effect, however, is generally considered small.

Based on eq. 4.5 and 4.9 (and fig 4.3a) it is clear that any variation in the angle of attack introduces fluctuating loads, in turn causing mechanical fatigue, which adversely affects the turbine life time. For a rotor with variable speed and pitch control one would avoid the blade to go frequently into stall, which requires sufficient margin of the airfoils in the blade to their respective stall angle of attack.

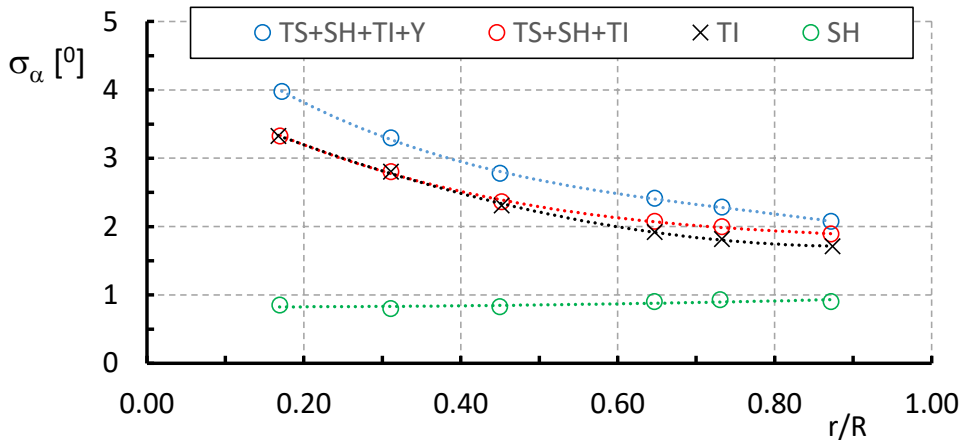


Figure 4.5: The standard deviation in angle of attack for a number of unsteady cases involving TS=tower shadow, SH=wind shear, TI=turbulence intensity and Y=yaw. DTU 10MW turbine  $V=8$  m/s, Class 1A. Data taken from Rezaeihaa et al. (2017)

A number of aero-elastic codes exist (e.g. OpenFast, HAWC2, see websites) to account for these fluctuations. An example of the magnitude of the fluctuations for a big turbine (178.3m rotor diameter) is given in Rezaeihaa et al (2017). Using simulations with DTU software HAWC2 the fluctuations along the blade for the DTU 10MW Reference turbine have been established and illustrated in fig. 4.5.

A total of 90% of the expected variations in incidence is given by  $1.64 \cdot \sigma$ . For a location at 70% of the blade radius this would mean excursions up to  $4^\circ$  from the mean angle. The turbulence intensity is the main cause for angle of attack fluctuations, which have a more pronounced effect towards the root of the blade, where fluctuations up to  $5^\circ$  to  $6^\circ$  can be attained. Such excursions will bring most thick airfoils into stall. The risk is mitigated by the use of vortex generators as reported in many studies (e.g. Timmer and van Rooij 1994, Skrzypiński et al. 2014, Hwangbo et al. 2017).

#### 4.3.2 Airfoil shape impacted by fluctuating inflow

A probabilistic approach for the same turbine was chosen by Pereira et al. (2018), resulting in comparable impact of the unsteady perturbations mentioned above. To show the impact of angle of attack fluctuations on the section shape, an optimization was performed for a 21% thick airfoil at  $Re = 9 \times 10^6$ .

The multi-objective optimization is solved with a genetic algorithm using class and shape function parametrization to describe the airfoil geometry.

Two objective functions, one for free transition (“clean”) and one for fixed transition at  $x/c=0.05$  on the upper side and  $x/c=.10$  on the lower side (“rough”) are described by:

$$\frac{\bar{L}}{D}(\alpha_{des}) = \frac{1}{0.9} \int_{\alpha_{des}-1.64\sigma_{\alpha}}^{\alpha_{des}+1.64\sigma_{\alpha}} \frac{C_l(\alpha)}{C_d(\alpha)} p(\alpha) d\alpha \quad (4.14)$$

Equation 4.14 represents the expected overall lift-drag ratio covering 90% of the angle of attack occurrences, described by the standard deviation  $\sigma_{\alpha}$  in a normal probability distribution given by  $p(\alpha)$ . The design angle of attack  $\alpha_{des} = 7^{\circ}$ . Two cost functions for the optimization process are derived:

$$CF_1 = -\frac{1}{100} \left[ \frac{\bar{L}}{D}(\alpha_{des}) \right]_{clean} \quad \text{and} \quad CF_2 = -\frac{1}{100} \left[ \frac{\bar{L}}{D}(\alpha_{des}) \right]_{rough} \quad (4.15)$$

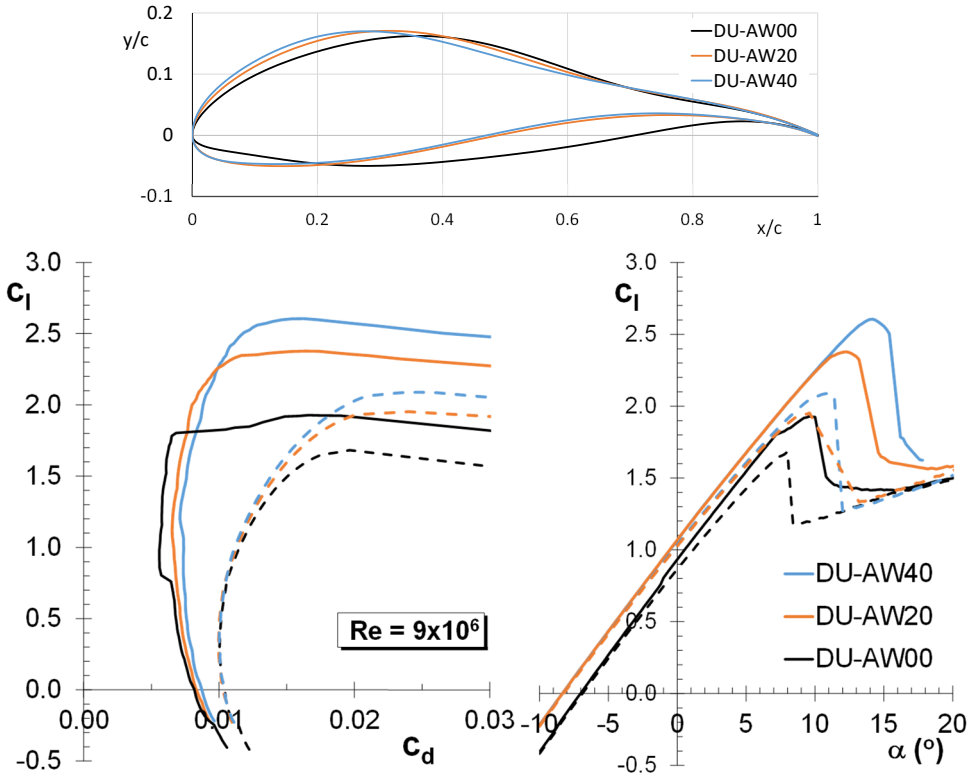


Figure 4.6: The optimization result for a 21% thick airfoil using 3 different standard deviations of the angle of attack. Computations with RFOIL. Equal weight between clean and rough performance ( $\lambda=0.5$ ). Dashed lines are “rough” characteristics. Number behind the section name corresponds to  $10x\sigma$ . Pereira et al. (2018)

By minimizing the cost functions, the optimizer maximizes the overall efficiency. A weight factor  $\lambda$   $[0,1]$  is introduced to account for different levels of compromise between clean and rough performance, both calculated with RFOIL, using  $N=9$ . The final cost function to minimize is:

$$CF = (1 - \lambda)CF_1 + \lambda CF_2 \quad (4.16)$$

The optimization is executed for four standard deviations of the angle of attack,  $0^\circ$ ,  $2^\circ$ ,  $4^\circ$  and  $6^\circ$ . The result of the process, in terms of airfoil shape and performance, using  $\lambda=0.5$ , for  $\sigma=0^\circ$ ,  $2^\circ$  and  $4^\circ$  is shown in fig 4.6.

With no incidence fluctuations at all, it is obvious that the design point can be chosen directly at, or just below, the upper boundary of the drag bucket.

The study also shows that a higher standard deviation drives the maximum thickness of the airfoil in the direction of the leading edge (from  $x/c=0.34$  to  $0.24$ ), towards a more turbulent airfoil.

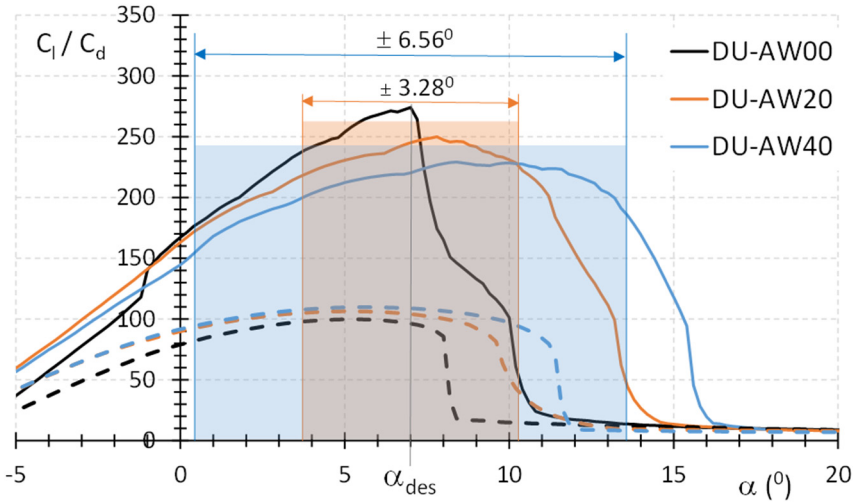


Figure 4.7: The lift-drag ratio of the optimized shapes. 90% occurrence ( $1.64\sigma$ ) boundaries indicated for  $\sigma=2^\circ$  and  $4^\circ$ . Dashed curves denote fixed transition.

The lift-drag ratios presented in fig. 4.7 indicate that, given the upper integration boundary in eq. 4.14, to deliver high L/D performance at angle of attack excursions beyond the design angle of  $7^\circ$ , the airfoils in fact exhibit a higher angle for maximum lift-drag ratio, hence a higher design lift with associated higher maximum lift. The two high lift airfoils both have a very sharp stall, inherent to (turbulent) airfoils with increased forward camber.

It must be noted that no constraint was set to accommodate a load-carrying structure inside the contour. This might appreciably change the (lower side) shape, however leaving the overall conclusion intact.

#### 4.4 THE IMPACT OF LEADING EDGE FLOW DISTORTION

As explained in Chapter 2 the apparent drop in power attributed to leading edge contamination was the primary reason to start the design of new airfoils tailored for wind turbine blades in the eighties. Ever since, the sensitivity of wind turbine airfoils to soiling,

or more in general to flow distortion at the leading edge, has had considerable attention and all airfoils produced by wind turbine manufacturers, independent blade manufacturers and research institutes have aerodynamic characteristics, each for their own Reynolds number range, based on roughness considerations. With improved airfoils and the entrance of variable speed, pitch controlled machines, turbines had no problem in reaching their peak performance (albeit at a higher wind speed). What remains are varying losses in the range of wind speeds between cut-in and rated. Still, according to Boccard (2009), manufacturer estimations of wind farm capacity factors (the ratio of realized over calculated energy production) are overestimated by more than 10%. A significant part of this may be attributed to combined leading edge soiling and erosion. So also with dedicated airfoils the energy capture of a wind turbine decreases with time, since there is no airfoil completely insensitive to roughness.

Although the problem is clear, there has long been (and in fact there still is) very little information in the public domain about actual blade soiling and insect and erosion patterns. The last decade this subject gained increasingly more attention, starting with e.g. Keegen (2013), Ehrmann et al. (2013) and Langel et al. (2014) for a number of reasons. Due to the ever increasing size of turbines any percentage points loss in annual energy production due to blade soiling has great impact on the economics of the machine. Manufacturers offering production guarantees may want to predict the energy capture as accurately as possible. Because of the financial consequences turbines are more frequently monitored as well.

Due to blade mass considerations blade design has moved into the direction of using higher design lift coefficients and lift-drag ratios and to apply thicker airfoils at higher Reynolds numbers towards the tip, all potentially contributing to the risk of introducing greater susceptibility to distortion of the flow at the leading edge. Furthermore, distorted flow over the blade, possibly leading to premature flow separation, may induce vibrations, adversely affecting the turbine lifetime.

In summary, the problem of flow distortion on the leading edges of wind turbine blades is covered by the following questions:

*RQ4-1) How can blade surface soiling and erosion be characterized? In other words, what is the nature, the degree, the pattern and the rate of change of actual surface soiling and degradation?*

*RQ4-2) How can this be incorporated into new designs? In other words, how should this be modelled in codes to be able to predict the airfoil aerodynamic performance and be used in optimization processes.*

RQ4-3) How can real contamination or erosion be transferred to the wind tunnel practice to be able to experimentally verify the aerodynamic characteristics designed into new airfoils in a reproducible manner?

#### 4.4.1 The impact of leading edge roughness

It is obvious that it is not economically feasible to equip a turbine with blades especially tailored to the explicit location of the turbine. However, the turbine's environment does have an impact on machine performance. An example is given in figure 4.8. The blade shown here is from a machine located in the Magallon 26 wind farm near Zaragoza in Spain [Bladecleaning 2005].

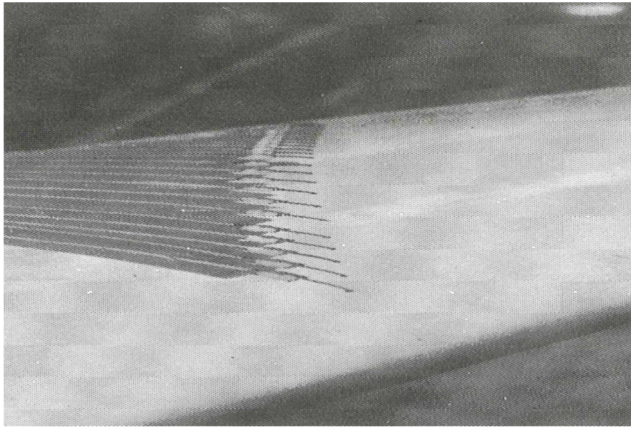
The insect debris come from an insect (*Omplus Lepturoides*) that lives for a period of one week. The insects fly for a few weeks and contaminate the blades. If it doesn't rain, the



Figure 4.8: Insect debris on blades of turbines in the Magallon wind farm, Spain (Bladecleaning, 2005)

soiling remains for many months. Other reports exist from the year 2000 of operators of wind farms with stall regulated turbines near Monte Cierzo, Spain, stating that blades cleaned by a storm got soiled again within 3 days due to the presence of a nearby relatively wet rice plantation, attracting insects. AEP reductions ultimately may amount to 10%, which for the windfarm in figure 4.8 would cause a deficit of several ten thousands of Euro's per year. Needless to state that blades able to withstand the performance reduction by this type of contamination are to be preferred.

A contrast to this example is the result of a study performed by van Groenewoud in the early 80's (van Groenewoud et al. 1983) involving a 2-bladed 25 m diameter horizontal axis turbine on the premises of ECN in Petten, on the west-coast of the Netherlands. The blades featured the NACA 230xx airfoil series. To detect transition the turbine was equipped with small microphones arranged in a staggered formation at the 75% span position (figure 4.9). From signal analysis it could be detected if a microphone was in a turbulent or in a laminar flow. The first configuration tested was the transition location



*Figure 4.9: Microphones to detect the nature of the boundary layer on a blade of the 25m HAT in Petten. Van Groenewoud et al., 1983*

after 2 years of operation. After blade cleaning, the tests were repeated and compared to the first measurements.

Then the local shape of the blade was measured (closely resembling the NACA 23018 airfoil) and predictions of the transition location at the appropriate Reynolds number were compared with the measurements.

Taking into account the resolution of the microphones (3% chord) and the impact of wind shear on the angle of attack it was concluded that after 2 years of operation the blades still were aerodynamically smooth. The combination of the polyurethane anti-erosion coating and the frequently occurring rain presumably made the blade more or less self-cleaning. This cleansing effect by rain was also found by Spruce (2006) and Ehrmann (2014).

In conclusion one could say that depending on the location the contamination may vary considerably.

Since real blade roughness characteristics were -and perhaps still are- unclear due to their large variation, there is an abundant amount of literature about the influence of roughness on wind turbine airfoils. The general method to establish the amount of roughness insensitivity designed into new airfoils is to verify their performance in the wind tunnel. Preferably also with a roughness type representing actual roughness occurring on blades (or having the same impact), which can easily be reproduced and is scalable. Several forms of roughness have been applied in the past, among which grit roughness wrapped around the leading edge (NACA roughness), sandpaper, bump tape, grit roughness strips (NASA roughness), zigzag tape and trip wires are the most popular ones. All of these roughness types have their own effect on performance, for the greater part also depending on the design philosophy of the airfoil.

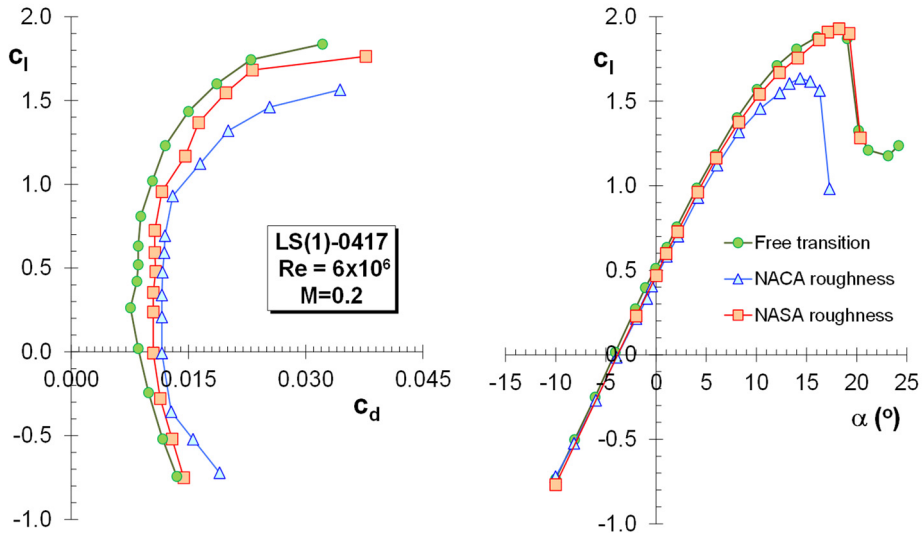


Figure 4.10: The impact of wrap-around (NACA) and strip roughness (NASA) on the performance of airfoil LS(1)-0417 at a Reynolds number of  $6 \times 10^6$ . McGee & Beasley 1973. Data uncorrected for wall-effects (2% to 3%)

As an example of the impact of different size and shape of roughness, figure 4.10 demonstrates the effect of NACA and NASA roughness on airfoil LS(1)-0417. (McGhee and Beasley, 1973). The shape of this airfoil was already depicted in figure 1.3. The NACA standard roughness is of the wrap-around type between the 8% chord stations on upper and lower surface with an average grain size of .011 inch (0.297 mm), covering 5% to 10% of the area.

The newer NASA standard roughness consists of 2.5 mm wide strips with number 80 grain size (0.211 mm, table 2.2) placed at 8% chord on both the suction and the pressure side of the airfoil. Since at this Reynolds number the airfoil has transition in the clean case located at about 2% chord at  $C_{l,max}$ , the NASA roughness has no notable effect on the maximum lift. Clearly, the NACA roughness is more severe and not only triggers transition in an early stage but also adds considerable thickness and momentum loss to the boundary layer, leading to aerodynamic decambering of the airfoil, a reduction of the maximum lift coefficient from 1.93 to 1.63 and a drag increase of more than 35% in the low-drag region.

Different roughness types can give comparable performance reductions as is shown in figure 4.11. It presents data from measurements in the Delft Low-speed low-turbulence tunnel on the 25% thick DU91-W2-250 airfoil. Both the zigzag tape and the tape with bulges (bump tape) were placed with their respective leading edges at the 5% chord station on the airfoil suction side. It appears that the bulges tape with half the thickness of the zigzag tape, which is considered to be an effective means of triggering transition, gives similar disturbance of the boundary layer, most likely due to the alternating

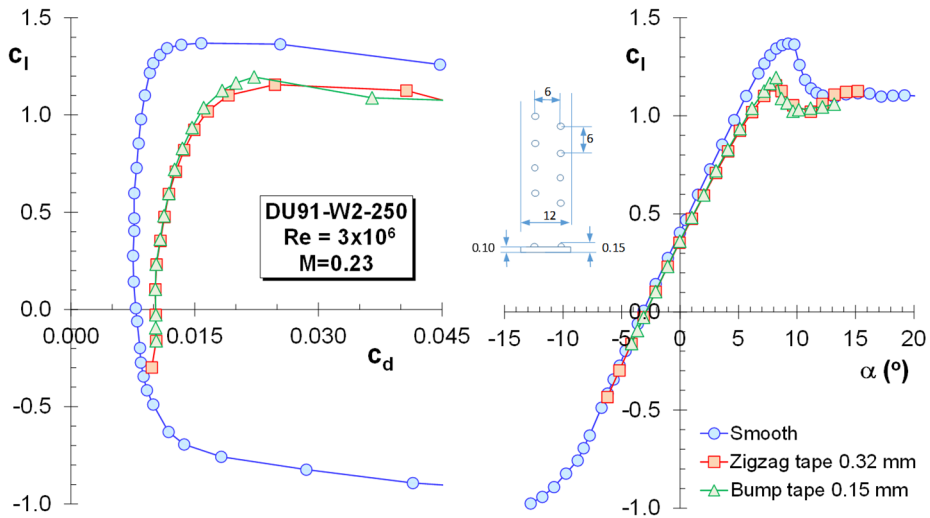


Figure 4.11: The effect of zigzag tape and bump tape on the performance of airfoil DU91-W2-250. The tape leading edges were located at  $x/c=5\%$  on the airfoil suction side. Measurements TU Delft LTT .

placement of the bulges 6 mm apart, just as the zigs and the zags of the other tape. The roughness on wind turbine blades coming from insect debris is of the distributed roughness type, as figure 4.8 clearly demonstrates. Of all the types of roughness applied in wind tunnel testing this comes closest to grit roughness distributed along the airfoil leading edge, resembling the NACA standard wrap-around roughness. This type of roughness is recognized as a severe type of roughness using .011 inch grains (0.297mm) on a 2 feet model (610mm) giving a roughness height-to-chord ratio  $k/c = 4.59 \times 10^{-4}$  with a density of 5% to 10%. A problem with this type of roughness in wind tunnel testing is its reproducibility.

The grains should be glued to the model surface with lacquer, which may not hold all the grit under a high wind speed (and may contaminate the tunnel) and the exact density is hard to realize since there is no standard way of applying the bare grains. To avoid having to apply the roughness on the model in the test section, generally the grains are spread on double sided adhesive tape with the appropriate span and width to cover the envisaged surface.

This method has the disadvantage that the tape, having a thickness of its own, due to the backward facing step at the tape trailing edges by itself already disturbs the flow, which adds to the effect of the grains. An example is presented in fig. 4.12, showing LTT-measurements on DU08-W-180Mod (TE-thickness modified from 0 to 0.23%). The impact of the 0.16 mm thick tape, running from 7.5% on the upper surface to 7.5% on the lower surface is already considerable, with the maximum lift-drag ratio almost halved (49.5%) and a reduction in maximum  $C_l$  of 11%.

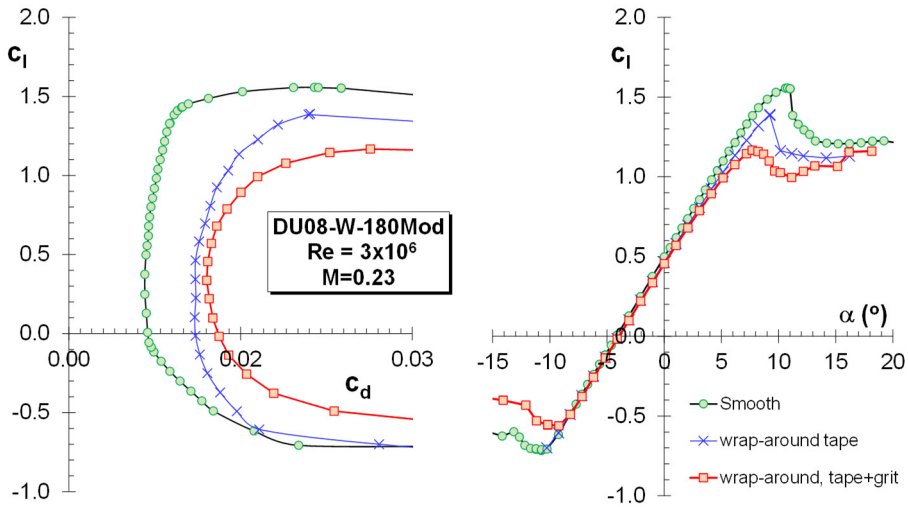


Fig. 4.12: The impact of 0.16mm thick adhesive tape and the tape with no 60 grit roughness on the performance of DU08-W-180Mod at  $Re=3 \times 10^6$ . Tape  $\pm 7.5\%$  wrapped around the LE. Grit density 15% (Courtesy Nordex SE)

In this case the tape result was similar to the combined impact of 0.2mm thick zigzag tape at the upper side 1% chord station combined with 0.25mm thick zigzag tape at  $x/c=10\%$  on the lower side.

The grit size often is generally denoted by a number. This introduces another uncertainty

Table 4.2: Definition of several grit roughness standards in mm.

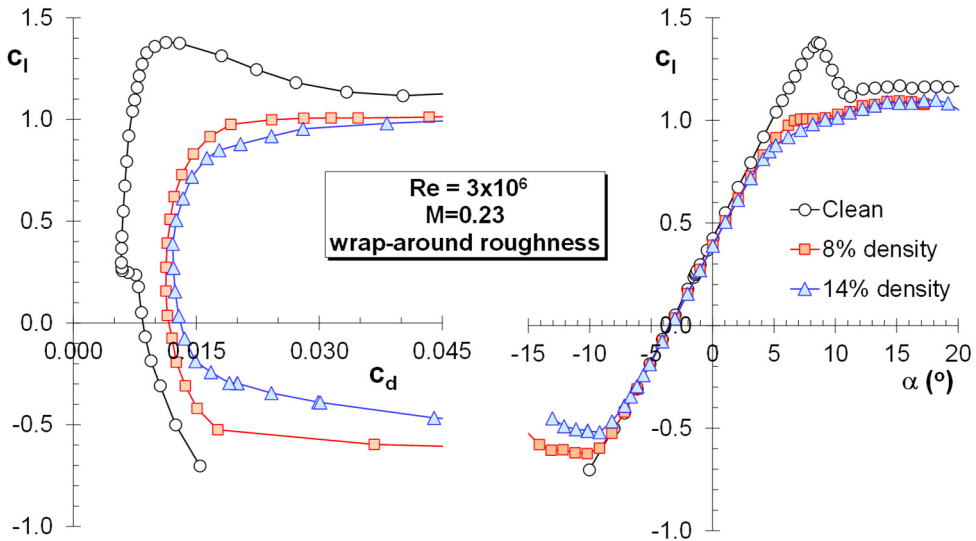
No.	Barlow et al.	CAMI*	FEPA -P**
30	0.711	0.638	0.642
36	0.589	0.535	0.538
40		0.428	0.425
46	0.419		
50		0.351	0.336
54	0.351		
60	0.297	0.268	0.269
80	0.211	0.192	0.201
100	0.150	0.141	0.162
120	0.124	0.116	0.125
150	0.104	0.093	0.100
180	0.089	0.078	0.082
220	0.074	0.066	0.068

\* Coated Abrasive Manufacturers Institute, now part of the Unified Abrasives Manufacturer's Association

\*\* Federation of European Producers of Abrasives (also ISO 6344 standard)

in the use of grit roughness since at present there are several definitions of grit size, as is shown in table 4.2. The first column dates from the NACA period and is given in Barlow, Rae and Pope (1999).

Also, variations in density of the grit spread over the leading edge cause differences in performance, as is demonstrated by figure 4.13.



Figur 4.13: The impact of different densities of wrap-around grit roughness on the performance of an 18% thick airfoil. (Courtesy Nordex SE).

It shows the performance of an 18% thick wind turbine airfoil under the same conditions as in figure 4.12, but with two distinct differences in density of the grit. It is clear that a substantially denser grit has a more detrimental effect on the drag of the airfoil and through de-cambering due to a thick turbulent boundary layer also on the airfoil lift.

Due to the practical implications of using grit roughness in terms of ease of application and reproducibility, over the years other turbulators have been investigated, leading to the widespread use of zigzag tape (figure 4.14).

The tape shape was developed by Boermans (TU Delft, Aerospace Faculty) and Horstmann and Quast (DFVLR Braunschweig, Germany). Just as the grains, the zigzag tape also disturbs the flow in a 3D manner, by generating small vortices to speed-up the amplification process to transition of the Tollmien-Schlichting waves in the laminar boundary-layer.

In contrast to grit roughness the zigzag tape is easy to apply, it comes in a great variety of thicknesses and sizes, it is reproducible and -if sized correctly- has little drag of its own.

For a long time the zigzag tape only had an application in aeronautics and more specifically in sailplane applications, however in 1998 it was introduced in speed skating as well (Timmer and Veldhuis, 2020).

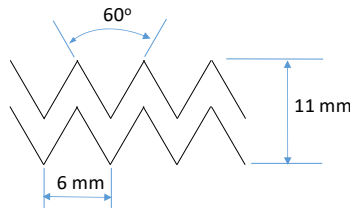


Figure 4.14: Example of zigzag tape layout

The wrap-around grit and the zigzag tape at distinct chord locations have a different effect on the boundary layer. Figure 4.15 presents the effect on a 21% thick airfoil for wind turbine application. The figure shows that the grit roughness has a much greater impact not only on the drag, but also on the lift coefficient. Compared to the zigzag tape, at the design lift coefficient the loss in lift has more than doubled and the maximum lift coefficient is significantly decreased with over 30% from 1.386 to 0.920.

It must be noted that the roughness, with a combined 0.16mm step and a relative grit roughness  $k/c$  of  $4.50 \times 10^{-4}$  along 15% of the chord, is a much heavier disturbance of the flow than the 0.25mm thick zigzag tape with  $k/c=4.17 \times 10^{-4}$ , which already gives transition close behind the tape.

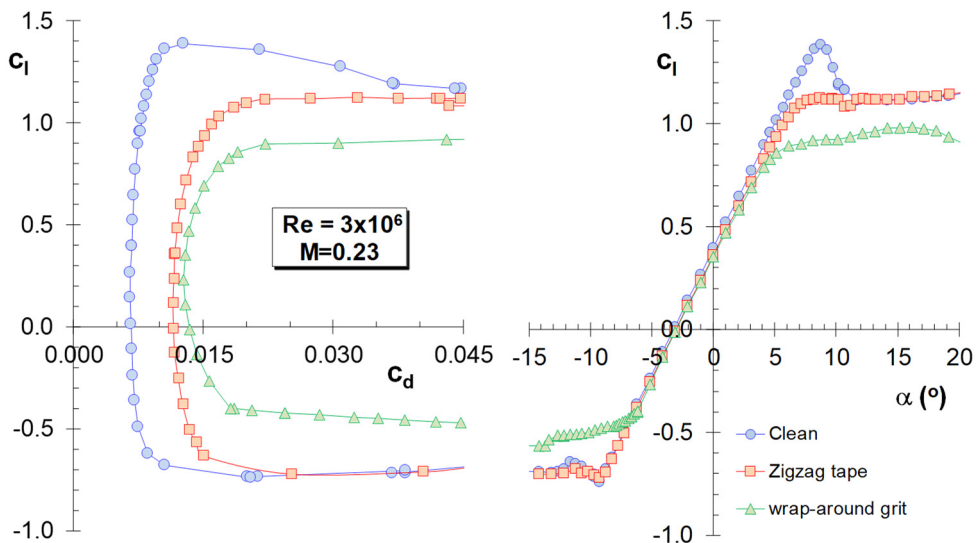


Figure 4.15: The impact on the performance of a 21% thick airfoil of zigzag tape and no. 60 wrap-around grit (8% density, between 7.5% on upper and lower surface) on 0.16 mm thick tape. Zigzag tape 0.2 mm at 5% chord suction side and 0.25 mm on  $x/c=0.10$  pressure side. (Courtesy Nordex SE)

The previous examples all have a fixed Reynolds number of  $3 \times 10^6$ . With variation of the Reynolds number to values of 10 million, reached on modern turbine blades, the wrap-around grit roughness still reduces the performance significantly more, even when in this case the relative thickness of the zigzag tape is higher compared to the grit roughness

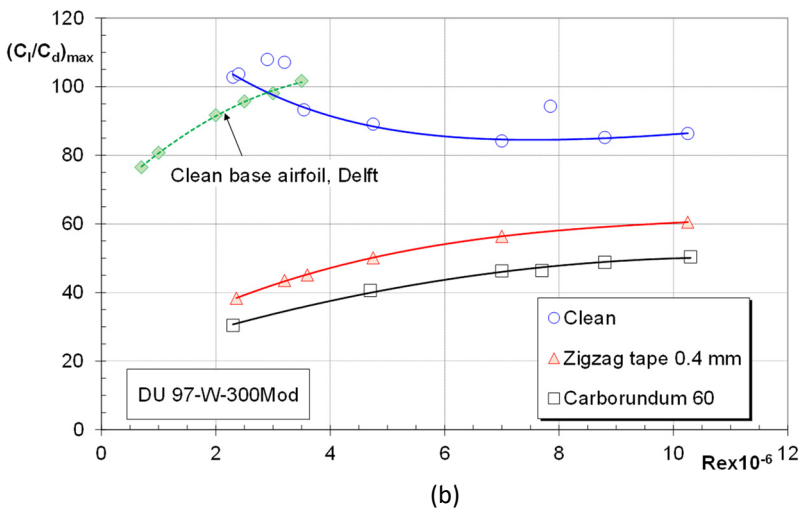
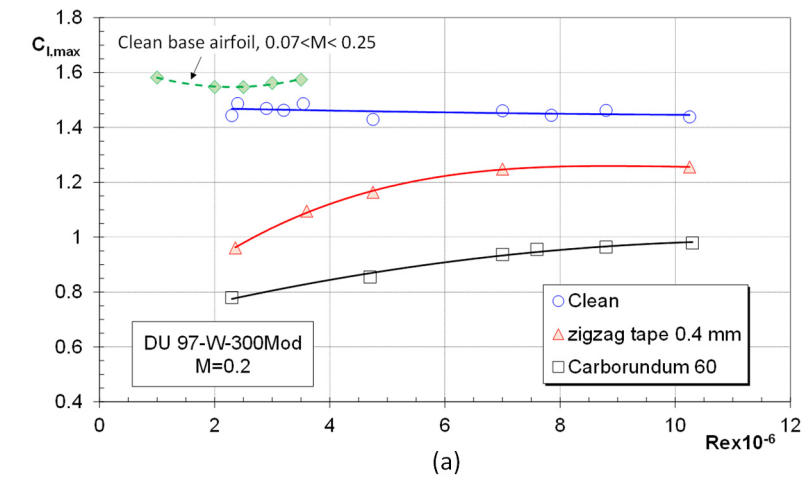


Figure 4.16: The maximum lift coefficient (a) and the maximum lift-drag ratio (b) for a 0.5m chord model of airfoil DU97-W-300Mod. Zigzag tape at 5% upper surface and 10% lower surface. Grit roughness covered first 7% of upper and lower surfaces (Timmer and Schaffarczyk, 2004)

( $k/c= 8 \times 10^{-4}$  against  $5.36 \times 10^{-4}$ ), as is demonstrated in figures 4.16a and b. They show the maximum lift coefficient and the maximum efficiency of airfoil DU97-W-300Mod measured in the DNW-KKK (Kryo Kanal Köln), the cryogenic wind tunnel in Cologne.

The airfoil modification consisted of reducing the trailing edge thickness of the base airfoil from 1.74% to 0.49%. The measurements were performed and reported by Freudenreich et al. (2004) and also analyzed by Timmer and Schaffarczyk (2004).

Due to a presumed temporary malfunction of the dryer installation of the tunnel gas, it was suspected that a mist of ice crystals was formed at the leading edge of the model with increasing Reynolds number (decreasing tunnel gas temperature), which may have unfavorably influenced the transition process. This is reflected in the fact that the

maximum lift coefficient and the maximum lift drag ratio in the clean case do not increase with Re-number. The density of the grit was not specified, but is believed to be higher than 15%. Although a comparable trend with Reynolds number is seen for both roughness types, still the grit roughness has a higher negative impact on the performance than the zigzag tape.

#### 4.4.2 The critical roughness height of zigzag tape

In the light of the foregoing discussion on roughness and roughness particles it is important to establish what height of the particles is critical to promote immediate transition. A first order calculation is given by Braslow and Knox (1958). Their method, which is still widely used, is based on smooth flat plate laminar boundary layer profiles. It calculates the minimum (critical) roughness height of sand grain particles in a narrow band of just a few millimeters submerged in the boundary layer to trigger transition, using local BL parameters. First, a dimensionless roughness particle height is defined:

$$\eta_k = \frac{k}{2x} \sqrt{R_x} \quad (4.9)$$

With the local Reynolds number  $R_x$  at the downstream location of the roughness defined as  $R_x = u_e x / \nu_0$ , where  $u_e$  is the local BL edge velocity, based on the velocity distribution around the airfoil in the smooth surface configuration. It must be noted, that when using the equations for an airfoil,  $x$  should be replaced by  $s$ , the distance of the turbulator trailing edge from the stagnation point along the section contour. However, to maintain the analogy with the flat plate,  $x$  is continued to be used in all following derivations.

Furthermore the roughness Reynolds number is specified as

$$R_k = \frac{u_k k}{\nu_k} \quad (4.10)$$

In which  $k$  is the roughness height and  $u_k$  is the velocity at the top of the roughness particle. The roughness Reynolds number may also be written as:

$$R_k = \frac{k}{x} R_x \frac{u_k}{U} \frac{\nu_0}{\nu_k} \quad (4.11)$$

Eq. 4.11 can be rewritten in the form

$$\frac{R_k}{\sqrt{R_x}} = \frac{k}{x} \sqrt{R_x} \cdot \frac{u_k}{U} \cdot \frac{\nu_0}{\nu_k} \quad (4.12)$$

or, including (4.9):

$$\frac{R_k}{\sqrt{R_x}} = 2\eta_k \frac{u_k}{U} \cdot \frac{\nu_0}{\nu_k} \quad (4.13)$$

To be able to solve equation 4.13, an evaluation is needed of the velocity and temperature

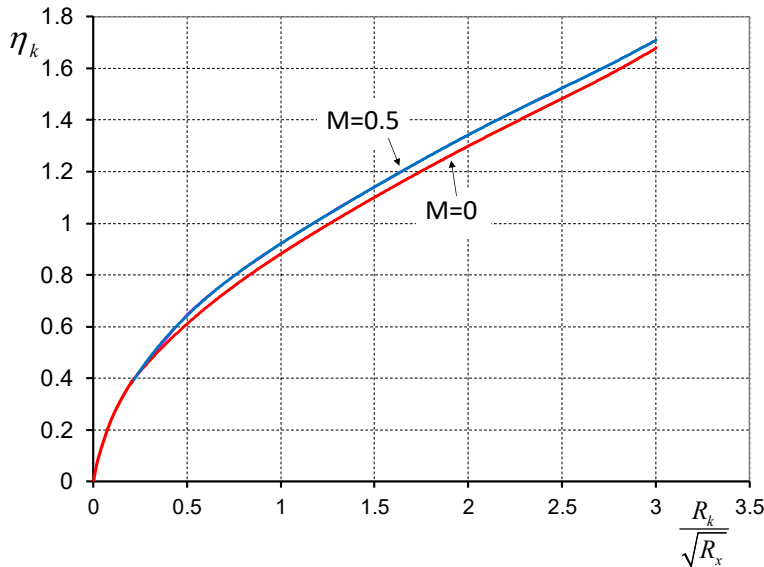


Figure 4.17: The variation of the non-dimensional particle height in the boundary layer with the ratio of the roughness Reynolds number and the square root of the station Reynolds number (Braslow and Knox, 1958).

variation through the boundary layer. For low Mach subsonic flows the ratio of the kinematic viscosities does not deviate from unity, however Braslow and Knox extend their method to Mach numbers up to 5.

Figure 4.17 gives the relation they found between the non-dimensional particle height in the boundary layer with the ratio of the roughness Reynolds number and the square root of the station Reynolds number for the lowest Mach numbers. To complete the calculation a critical roughness Reynolds number should be established at which transition actually is realized.  $R_{k,crit}$  very much depends on the type of roughness. Braslow and Knox mention values between 250 and 600 to be a reasonable value for the sand grain roughness strips.

The latter value has been adopted frequently for distributed roughness as well, and seems to have given reasonable results (Langel et al., 2015) but was suggested by the authors to be more suited for conditions in which compressibility plays a role.  $R_{k,crit}$  in the definition of Braslow and Knox would be the value at which turbulent spots develop at the roughness elements.

To have transition move to the roughness location a slightly higher value should be applied.

The station Reynolds number can be calculated from:

$$R_x = \frac{x}{c} \cdot \frac{u_e}{U} \cdot Re = Re \cdot \frac{x}{c} \sqrt{(1 - C_{p_{x/c}})} \quad (4.14)$$

with  $C_p$  the pressure coefficient at station  $x/c$  in the clean configuration.

Once  $R_{k,crit}$  and  $R_x$  have been established the value of  $\eta_k$  can be determined from figure 4.17. The roughness height now follows from

$$\frac{k}{c} = 2 \frac{x}{c} \frac{\eta_k}{\sqrt{R_x}} \quad (4.15)$$

which is essentially a rewritten version of equation (4.11).

As the roughness element is placed inside the laminar boundary layer, an alternative equation for the critical roughness height can be derived based on the velocity profile and the friction coefficient of a laminar boundary layer over a flat plate (Young and Paterson, 1981).

According to laminar flow theory, a flat plate laminar boundary layer velocity profile for  $y/\delta \leq 0.6$  is linear and the velocity at the top of the roughness element  $u_k$  in eq. (4.10) can be written as

$$u_k = k \left( \frac{\partial u}{\partial y} \right)_0 \quad (4.16)$$

The shear stress is given as

$$\tau_0 = \mu \left( \frac{\partial u}{\partial y} \right)_0 = C_f \frac{1}{2} \rho U^2 \quad (4.17)$$

with

$$C_f = \frac{0.664}{\sqrt{Re_x}} \quad (4.18)$$

Combining equations (4.10) and (4.16), (4.17) and (4.18) we find

$$k = 1.736 \frac{\sqrt{R_{k,crit}}}{R_x^{3/4}} x \quad (4.19)$$

Although, using figure 4.17, the Mach number can be included in the calculations of  $k$ , in the case of wind turbine applications this will not have a significant impact on the result, since Mach numbers typically do not exceed 0.3. For DU 93-W-210 measured at a Reynolds number of  $3 \times 10^6$  the difference in  $k$  for  $x/c=5\%$  and  $R_k=400$  would be about 1.5% at the design angle when using the in-tunnel value  $M=0.23$  instead of  $M=0$ . The two methods, therefore, give similar results.

Both derivations are based on zero-pressure gradient, while obviously going through the various angles of attack in many cases the flow over the leading edge of an airfoil feels a

favorable pressure gradient, helping the boundary layer to speed up. Dependency on pressure gradient would cause  $R_{k,crit}$  to vary with angle of attack. According to Smith and Clutter (1959) this relationship is minimal, while Ehrmann (2014) establishes it to be weak. The reason for the relative insensitivity to pressure gradient may be the fact that, although a favourable gradient makes the BL-profile fuller and stabilizes the flow, the increased velocity enhances disturbances induced by roughness elements.

### Two critical roughness heights

Young and Paterson (1981) distinguish two critical roughness heights. One that destabilizes the boundary layer in such a way that transition starts to move upstream, and one that causes transition to occur immediately behind the roughness element, giving the critical Reynolds number values  $R_{k,crit1}$  and  $R_{k,crit2}$  respectively. Based on results by Smith and Clutter (1959) they come to  $(R_{k,crit1})^{0.5} = 11 \pm 4$  in case of two-dimensional roughness. It is found that  $k_{crit2}$  is approximately twice  $k_{crit1}$ .

Based on measurements in the LM-wind tunnel on a 900mm chord model of DU00-W-212 at  $Re=2 \times 10^6$ ,  $4 \times 10^6$  and  $6 \times 10^6$ , using zigzag tape thicknesses of 0.125mm, 0.205mm and 0.4mm, Janoff (2023) found  $R_{k,crit1} \approx 125$ . This number followed from tests only with the thinnest tape positioned at locations between  $x/c=3\%$  and  $12\%$  at the lowest Re-number. All other combinations (e.g. higher Reynolds numbers or locations closer to the LE) gave instantaneous transition behind the tape, or were too close to the stagnation point, in which the allowable roughness is very high. The tape thickness in the study seems to be the size given by the manufacturer. The actual tape thickness may not have been established. The latter is an important step in the calculations. According to eq. (4.19)  $R_{k,crit}$  varies with the square of the thickness  $k$ . The actual tape thickness may deviate from

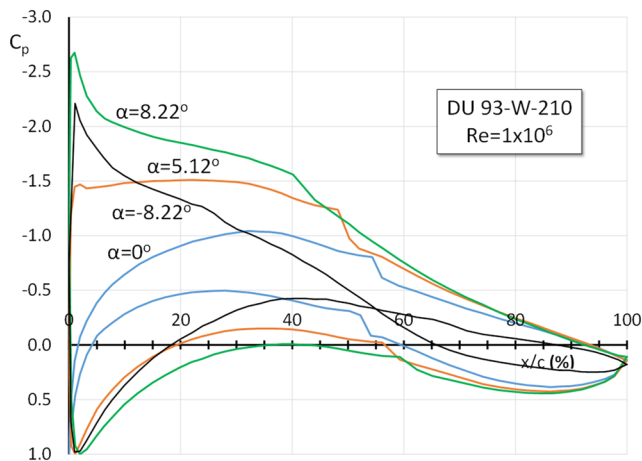


Figure 4.18: Measured pressure distributions of airfoil DU93-W-210 at a Reynolds number of  $1 \times 10^6$ . Surface smooth.

the size indicated by the manufacturer. In the following measurements the nominal tape thicknesses were 0.205mm, 0.25mm and 0.30mm. After checking the sizes with a micrometer they appeared to be 0.185mm, 0.250mm (and 0.255mm) and 0.310 mm.

#### 4.4.2.1 Verification of $R_{k,crit1}$

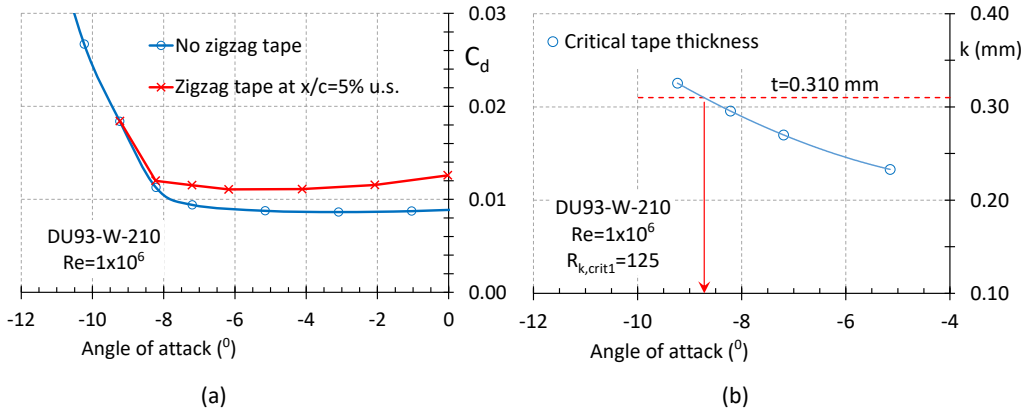


Figure 4.19: The impact of 0.310 mm thick zigzag tape at  $x/c=5\%$  u.s. on the drag coefficient at  $Re=1 \times 10^6$  (a), and the angle for which the tape thickness is critical when  $R_{k,crit1}=125$  (b), calculated using eq. 4.19. The intersection lies at  $\alpha=-8.72^\circ$ . The model chord is 600mm.

The value of  $R_{k,crit1}=125$  found by Janoff can be verified by a test performed on DU93-W-210 with 0.310 mm thick zigzag tape located just behind the suction side pressure orifice at  $x/c=4.94\%$ . Fig. 4.18 presents a number of pressure distributions of the clean airfoil at the test Reynolds number of  $1.0 \times 10^6$ . The impact of the zigzag tape on the drag coefficient at negative angles is shown in fig. 4.19a. The tape starts to work at an angle slightly lower than  $\alpha=-8.22^\circ$ , where already a small drag increase is noticeable and the mechanism of natural transition is bypassed. Combination of eq. (4.19) and  $R_{k,crit1}=125$  gives the variation of the critical tape thickness with incidence depicted in fig. 4.19b. Using a tape thickness of 0.310 mm, the critical angle is  $-8.72^\circ$ , which makes a value of  $R_{k,crit1}$  of approximately 125 plausible. Unfortunately, the angle resolution is only one degree, as a result of which the value could not be established more accurately. According to the numbers given in table 4.3,  $R_{k,crit1}$  could have a value between 119 and 138.

Table 4.3: The  $R_k$  for bypass transition ( $R_{k,crit1}$ ) with zigzag tape thickness  $t=0.310$  mm on DU93.

$\alpha$ (deg.)	$Re/10^6$	$s/c$ (%)	M	$C_p$	k (mm)	$R_{k,crit}$
-9.233	1.001	5.730	0.072	0.7808	0.318	119
-8.216	1.003	6.375	0.072	0.7132	0.295	138
-7.196	1.003	6.852	0.072	0.6294	0.273	162
-6.161	1.003	7.265	0.072	0.5259	0.252	189

#### 4.4.2.2 The critical Re-number for transition right behind the tape

##### Measurements on airfoil DU93-W-210

In the following, the value of  $R_{k,crit}$  is defined as the number for which the boundary layer is turbulent right downstream of the turbulator, hence  $R_{k,crit2}$  using the distinction of Smith and Clutter (1959). Values of  $R_{k,crit}$  for zigzag tape of 175 (mean value, tape with a  $90^\circ$  top angle, Boermans and Waibel, 1987), 200 for a flat plate and the relatively flat lower surface of a sailplane airfoil (Boermans, 2015) and in the range of 330 to 480 (Selle, 1999) have been reported in literature.

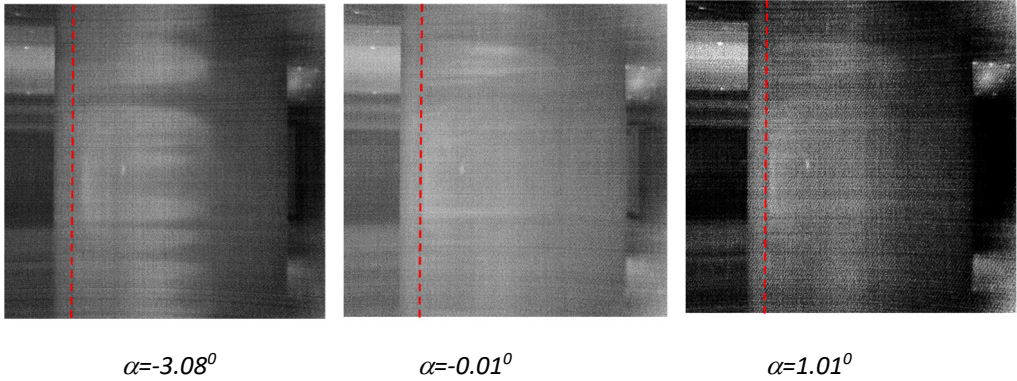


Figure 4.20: The transition location on DU93 with 0.305 mm thick zigzag tape at  $x/c=0.05$  on the suction side for three angles of attack.  $Re=0.66 \times 10^6$ , the flow comes from the left.

##### A tape thickness of 0.310 mm at $x/c=5\%$ on the suction side

Still in the configuration mentioned above, now at a Reynolds numbers of  $0.664 \times 10^6$ , the angle of attack was varied between  $-4^\circ$  and  $2^\circ$  until transition, which was established with an infra-red (IR) camera, reached the tape trailing edge. Fig. 4.20 shows the transition location for three angles of attack. At  $1^\circ$ , transition has almost reached the back of the tape over the entire span. Full transition followed after  $1.01^\circ$ , but before  $\alpha=1.52^\circ$ .

Reworking of eq. (4.19) gives:

$$R_{k,crit} = 0.332 \left( \frac{k}{x} \right)^2 R_x^{3/2} \quad (4.20)$$

To predict a tape thickness of 0.310mm for instantaneous transition behind the tape, using the appropriate flow variables at  $\alpha=1.266^\circ$  (right in the middle between  $1.01^\circ$  and  $1.52^\circ$ ), equation (4.20) gives  $R_{k,crit} = 217$ . Incidence variation at  $Re=0.74 \times 10^6$  gives transition behind the tape at  $-1.04^\circ$ , also leading to  $R_{k,crit}=217$ . The underlying numbers are tabulated in table 4.4. For both configurations the measured clean model  $C_p$ -values at  $Re=0.7 \times 10^6$  have been used. Interpolation between  $Re=0.7 \times 10^6$  and  $1.0 \times 10^6$  to calculate the  $C_p$ -value at  $Re=0.74 \times 10^6$  did not have any impact on the  $R_{k,crit}$  value.

Table 4.4: The required  $R_{k,crit}$  for transition at  $x/c=5\%$  with zigzag tape thickness  $t$  on DU93.

$\alpha$ (deg.)	$Re/10^6$	$s/c$ (%)	M	$C_p$	$t$ (mm)	$R_k$
1.266	0.6643	10.555	0.049	-0.6686	0.310	217
-1.040	0.7415	9.394	0.055	-0.2403	0.310	217
9.233	1.0040	13.238	0.072	-2.2967	0.185	214
5.130	1.0277	37.903	0.074	-1.4798	0.255	201

A tape thickness of 0.185 mm at  $x/c=5\%$  on the suction side

The 0.310 mm thick tape was replaced with a 0.185mm thick zigzag tape and the Reynolds number was increased to  $1.0 \times 10^6$ . The angle of attack was varied between  $0^\circ$  and  $10^\circ$  and a procedure similar to the thick tape was followed. Fig. 4.21 presents IR-images at two angles of attack. It is clear that transition at  $\alpha=8.21^\circ$  has not yet reached the back of the tape, which was accomplished at  $\alpha=9.185^\circ$ . In this situation eq. (4.20) gives  $R_{k,crit} = 214$ . Table 4.4 shows the variables leading to this value.

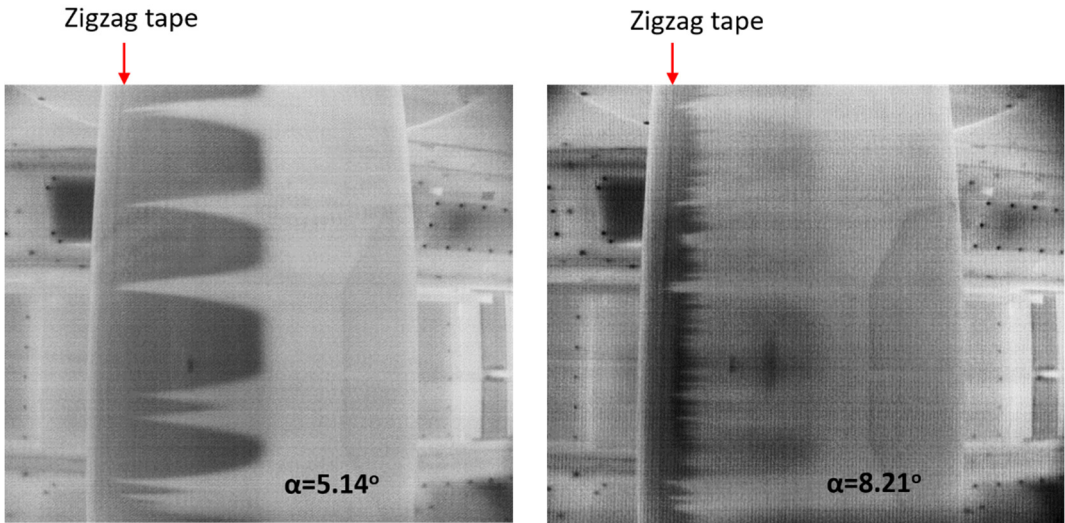


Figure 4.21: Infra-red pictures of the transition location on DU 93 at  $Re=1 \times 10^6$ . Zigzag tape of 0.185 mm thickness at  $x/c=.05$  on the suction side. Flow comes from the left.

Simulating flat plate flow

Fig. 4.18 shows a fairly constant upper surface  $C_p$ -value between  $x/c=0.05$  and  $0.35$  at  $5.12^\circ$  incidence. This configuration comes close to a constant flat plate velocity distribution, as is depicted in fig. 4.22. The average velocity ratio over the 20% chord upstream of the tape is 1.579, with a standard deviation of 0.0033.

A 0.255mm thick tape was placed at the upper surface 30% chord station. At  $\alpha=5.13^\circ$ , the Reynolds number was varied, starting at  $Re=0.807 \times 10^6$  until transition reached the tape-

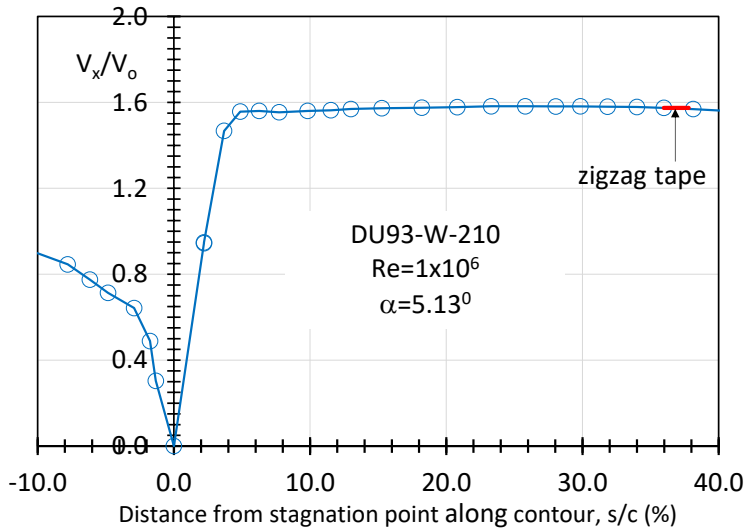


Figure 4.22: The measured relative velocity distribution along the contour of airfoil DU93 at  $\alpha=5.13^\circ$  and  $Re=1 \times 10^6$ .

trailing edge at  $Re=1.0277 \times 10^6$ , giving  $R_{k,crit} = 201$ , which corroborates the value of 200 mentioned by Boermans (2015) for a flat plate. The associated numbers are given in table 4.4.

### Measurements on DU97-W-300

Another test was performed, on airfoil DU97-W-300, with two tape thicknesses 0.250 and 0.185 mm. At constant  $\alpha$  between  $0$  and  $8^\circ$ , the test section wind speed (and consequently

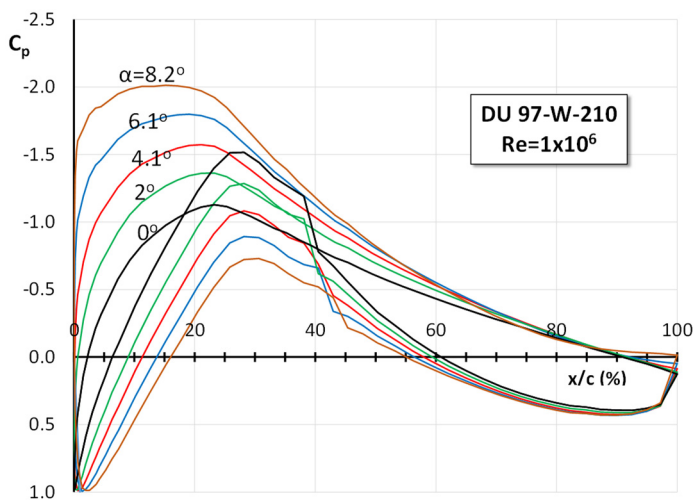


Figure 4.23: Measured pressure distributions of airfoil DU97-W-300 at the Reynolds numbers of table 4.5. Zigzag tape  $t=0.185$  at  $x/c=5\%$

the Reynolds number) was increased until transition reached the tape which had the front tips at  $x/c=5\%$  on the suction side. Fig 4.23 shows the pressure distribution for various angles of attack.

Using the flow parameters at this Reynolds number the required  $R_{k,crit}$  from the method described above was calculated to predict a thickness of 0.250 mm and 0.185 mm. Both exercises are presented in tables 4.5 and 4.6.

Table 4.5: The required  $R_{k,crit}$  for transition at  $x/c=5\%$  of DU97 with zigzag tape  $t=0.25\text{mm}$

$\alpha$ (degr.)	$Re/10^6$	$s/c$ (%)	M	$C_p$	t (mm)	$R_k$
-0.04	1.0746	11.003	0.071	-0.4364	0.250	216
2.02	0.9980	12.106	0.065	-0.8178	0.250	220
4.09	0.9300	13.329	0.060	-1.2341	0.250	220
6.15	0.8867	14.646	0.058	-1.6729	0.250	224

Table 4.6: The required  $R_{k,crit}$  for transition at  $x/c=5\%$  of DU97 with zigzag tape  $t=0.185\text{mm}$

$\alpha$ (degr.)	$Re/10^6$	$s/c$ (%)	M	$C_p$	t (mm)	$R_k$
-0.04	1.2714	11.003	0.086	-0.4403	0.185	153
2.03	1.2226	12.106	0.082	-0.8235	0.185	164
4.09	1.1141	13.329	0.078	-1.6881	0.185	182
6.15	1.1358	14.646	0.076	-1.6893	0.185	179
8.22	1.0660	16.055	0.073	-2.1571	0.185	175

The results appear to be not very consistent. While the values of  $R_{k,crit}$  for the 0.25mm tape are comparable with the results for DU93 with the 0.185 mm tape (in the range  $219 \pm 5$ ), the values for DU97 with the thinnest tape are much lower, between 153 and 182. Both tables show a variation with angle of attack between  $0^\circ$  and  $6^\circ$ , which most certainly has to do with the stabilizing favorable pressure gradient over the first 15% of the chord (see fig. 4.23). The difference, however, is about 19% in the average critical Reynolds number. The Reynolds number range is not so very different, with only a slight increase for the thinner tape. The absolute pressure difference over the front of the leading edge will be a little higher for the thinner tape. Although during the test all the experimental ingredients were logged with the utmost care, it cannot be excluded that the used tape thickness might have differed from 0.185mm. A tape thickness of 0.205mm would already give results for angles between  $4.1^\circ$  and  $8.2^\circ$ , comparable with those found in the other experiments ( $R_{k,crit} = 219 \pm 4$ ). This also shows the sensitivity of the calculation to the applied tape thickness, as a change in thickness of 0.02mm gives a change in  $R_{k,crit}$  of about 19%. Fortunately, vice versa, a slight difference in  $R_{k,crit}$  will not give a significant change in roughness size.

The Reynolds number was increased by an increase of the tunnel fan rotational speed with steps of 5 rpm ( $\Delta Re=2.2 \times 10^4$ ). Complete span transition was established by visual inspection of the camera images. This resolution of 5 rpm introduced some uncertainty in the value for  $R_{k,crit}$ . Tables 4.4 to 4.6 give the lower boundary of the values. Uncertainty is in the order of 5 to 8 in  $R_k$ .

The fairly large differences between tables 4.5 and 4.6 prevent a firm conclusion on a specific value for the critical roughness Reynolds number using the flat plate equations based on *all* measurements. Nevertheless, the value for  $R_{k,crit}$  seems to be approximately 200 for a flat plate. The highest values in this study was 217, found for DU93 at  $Re=1 \times 10^6$  with zigzag tape of 0.185mm thickness at  $x/c=5\%$  and 224 for DU97 with 0.25 mm tape on the same location at  $Re=0.87 \times 10^6$ . For practical purposes, using this method for airfoils, a value of  $220 \pm 5$  would suffice, with the higher value for thicker leading edges.

#### 4.4.3 Scaling roughness.

As the critical Reynolds number for zigzag tape seems to vary to some extent, it may be difficult to establish a scaling factor for the roughness using modelling for a flat plate. However, the results indicate that transition behind the tape is most likely to occur above a certain threshold, which showed to be in the order of 220. Since the method of Braslow and Knox returns a *relative* value,  $k/c$ , it seems to be possible to determine a critical roughness height with varying chord  $c$ .q. scale of the airfoil with a fair amount of accuracy. Finding a suitable scaling may be more difficult for randomly distributed grit roughness of

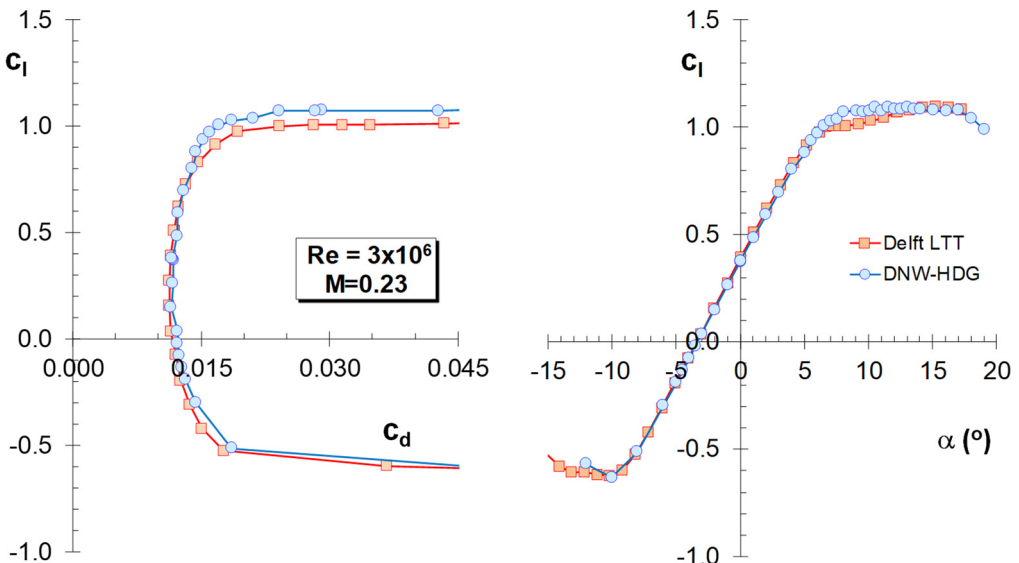


Figure 4.24: Performance comparison of an 18% thick airfoil with wrap-around roughness measured in two facilities. LTT had a chord of 0.6m, HDG was 0.1m. Results from HDG corrected from 0.03 to  $M=0.23$  (Courtesy Nordex SE).

the wrap-around type. An example of the impact of scaling is given in figure 4.24. It compares measurements on an 18% thick airfoil from the 0.6x0.6m<sup>2</sup> DNW-HDG pressure tunnel and the 1.25x1.80m<sup>2</sup> TUDelft LTT. The model chords are 100mm and 600mm respectively.

On the small model .046mm grit roughness was applied with lacquer from 8% on the lower surface to 8% on the upper surface with a density between 5% and 10%.

The relative grit thickness  $k/c$  is  $4.6 \times 10^{-4}$ . The grit on the 0.6m chord model covered the same surface area with a density of approximately 8% using no. 60 carborundum grains with an average grain size of 0.268mm (see CAMI table 4.2) giving  $k/c=4.5 \times 10^{-4}$ , on a thin adhesive tape of 0.16mm thickness.

The lift coefficient from the HDG measurements was corrected for Mach number with the Prandtl-Glauert correction, going from  $M=0.03$  to  $M=0.23$ . The roughness on the bigger model has the highest impact on the performance around the maximum lift coefficient, although there is virtually not much difference in the  $C_{l,max}$ . Although the relative roughness of the grit on the small model is higher than the bare grit relative roughness on the 0.6m chord model, it appears that the combination with the tape on the bigger model gives the greatest disturbance in the upper part of the drag curve.

The combination in the HDG, therefore, has the highest lift-drag ratio. Despite the big scale differences between the HDG model of 10cm and the model in the Delft tunnel of 60cm, there is great similarity between the results.

#### 4.4.4 Insect impact distribution

Apart from the height of the roughness particles, the particle distribution is of importance. The insect problem has been investigated in the past also for sailplane application. One of the studies was performed by Boermans and Selen (1981). They gathered insect collisions during flight on a number of sailplanes of different make, with different airfoils in the wing and with and without flaps, by flying with 0.08mm thick self-adhesive matted polyester film attached to part of the wings.

Figure 4.25 gives a typical overview of the results. The 3 wings with a flap had an asymmetric distribution of the debris and the 4 ones without a flap looked more symmetric. All sailplanes went through a range of Reynolds numbers roughly between  $1 \times 10^6$  and  $3.5 \times 10^6$  (low and high flight speed).

However, the range of angles of attack and stagnation point positions is much more extended for the non-flapped wings. The presence of the flap permits the pilot to stay at low angles of attack and consequently at low drag. Obviously, it is the orientation of the wing towards the incoming flow that makes the pattern. For the non-flapped wings the distribution between the upper and lower surfaces roughly is 55% to 45% between  $x/c=0.10$  on both sides while for the flapped wings the ratio was 80% to 20% between  $x/c=.15$  at the upper surface and  $x/c=.03$  at the lower surface. The researchers note that

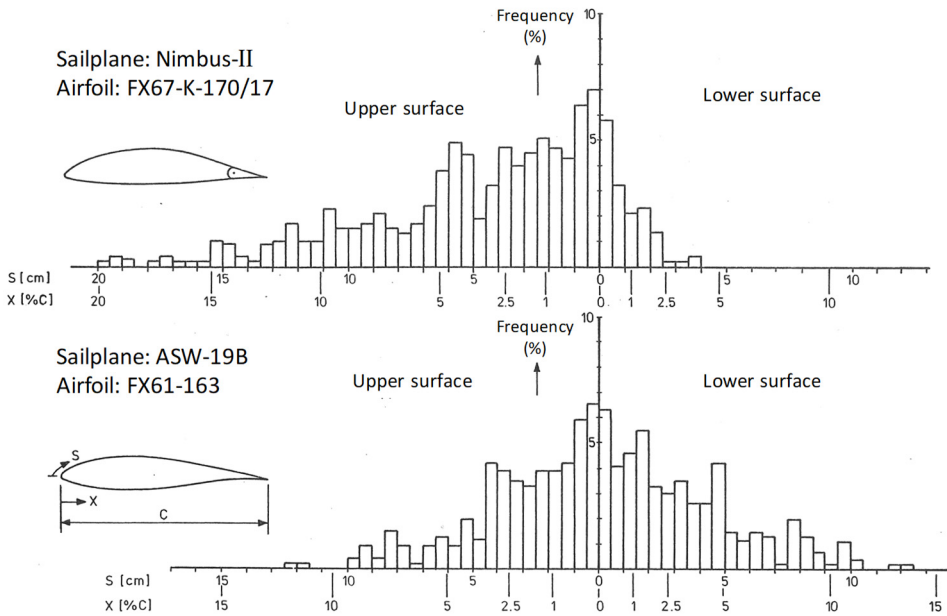


Figure 4.25: Insect impact distributions on a flapped and non-flapped sailplane airfoil [Boermans and Selen, 1981]

the results of the flapped case may partly be influenced by the relatively flat lower surface of the flapped airfoils used. The pattern for the non-flapped cases was comparable with the ones found on the blades of stall regulated turbines in the nineties where the angle of attack varies significantly with wind speed during power production.

On present day large blades of variable speed machines the control systems ideally allows only little variation of the angle of attack around the design angle below the rated wind speed. Since insects only fly at low wind speeds the contamination takes place when the orientation of the outboard part of the blade is at the design angle of attack, which is generally  $6^\circ$  or higher. This would imply that the insect distribution would have about the same pattern as the flapped sailplane wings in figure 4.25, but then mirrored around the apex, with the greater mass impact on the lower surface.

Ehrmann (2014) conducted an extensive investigation on wind turbine blade roughness and, resulting from the absence of sufficient in-service impact information, calculated the impingement pattern on a NACA 63<sub>3</sub>-418 airfoil in a blade of a 80 m diameter variable speed wind turbine with NASA's code LEWICE, a code to estimate ice accumulation on wing /blade leading edges.

With the application of a standard insect drag coefficient, frontal area and mass the particle distribution is calculated on the basis of the inviscid airfoil flow field. The resulting mass distribution, figure 4.26, shows great similarity with the inverse distribution of the flapped wing contamination depicted in figure 4.25, showing a high density around the

apex and on the first 15% of the pressure side.

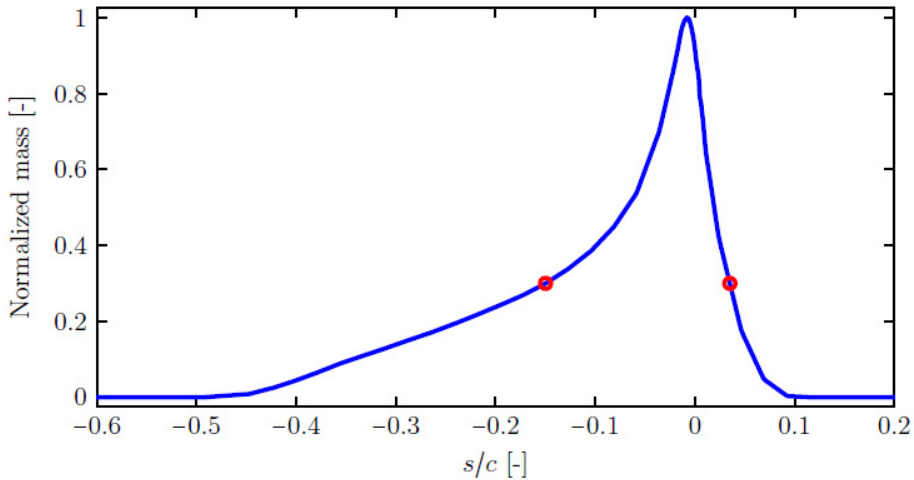


Figure 4.26: LEWICE simulated insect distribution. [Ehrmann 2014]. 30% cut-off between 2 and 13% chord locations

#### 4.4.5 Using sandpaper in wind tunnel testing.

The contamination of wind turbine blades comes in stages, varying between a smooth surface and a complete rough leading edge. Whereas roughness particles sometimes are washed off by a good rain shower leaving the blade relatively clean again, erosion of the leading edge is an irreversible process, which also comes in stages. In all cases of pollution and erosion wind turbine manufacturers need to know the impact on rotor performance. The most convenient way of doing this is by computation, since access to a wind tunnel is not always possible and the number of variables may be multiple. It remains, however, necessary to validate these codes by wind tunnel tests. Among others, researchers both in the US (Maniaci et al, 2016) and in Denmark (Kruse 2018) have been working on modelling for CFD computations using wind tunnel measurements.

A study to investigate the similarity between computations and experiment is presented in Kruse et al. (2018). Experiments were performed in the wind tunnel of the Institute for Aerodynamics and Gas Dynamics, University of Stuttgart on a 0.60m chord model of airfoil NACA 63<sub>3</sub>-418 at  $Re=3 \times 10^6$ . Among other configurations with sandpaper, the lift and drag was measured due to zigzag tape of 0.4 and 0.8mm at the 2% u.s. and 10% l.s. chord stations. The DTU in-house codes ElipSys2D and EllispSys3D were used to compute the performance of the airfoil, not by changing the turbulence model, but by modelling the zigzag tape as protuberances on the airfoil surface. A generally good agreement was found with the experiment within certain limits for the height of the protuberance (up to 1%c), although the 3D version struggled with convergence for angles of attack higher than

9° (the airfoil stalls at about 12°), and the maximum lift was overpredicted. In view of the complexity and CPU time, the 2D code was adopted for further evaluation of 2D simulations of the impact of roughness elements on airfoils. The zigzag tape results could be modelled by taking a somewhat thicker height in the simulations. The sandpaper results, unfortunately, could not be computed with satisfying accuracy since “the increase in drag was significantly overestimated compared to the decrease in lift”.

The same airfoil was used by Maniaci et al. (2016), in a study where the performance was measured of this airfoil and of S814 for a variety of roughness conditions in the 2.1x3.05m<sup>2</sup> low-speed wind tunnel of Texas A&M University, USA at Reynolds numbers between 0.8x10<sup>6</sup> and 4.8x10<sup>6</sup>. The 0.81m chord model had a 15% chord removable leading edge and printed field-measured erosion patterns could be installed. Roughness patterns included simulated insect carcasses and distributed roughness of various heights, densities and area coverage. It appeared that all tests using 0.1mm high grit roughness with densities between 3% and 15%, 0.14 and 0.2mm high grit with densities of 3% were bounded by the clean characteristics and those with 0.5mm thick zigzag tape on  $x/c=2\%$  u.s. and  $x/c=5\%$  l.s. It was found that roughness height was more important than density. The measurements were used to calibrate a turbulence model for their CFD code, one of the challenges being to parameterize the roughness distributions into a suitable equivalent sand grain roughness height. The first results to simulate grit roughness were found to be promising. Erosion modelling proved to be much more challenging. Maniaci et al. (2020) model erosion damage on airfoil S825 using wind tunnel measured losses of airfoil NACA 63<sub>3</sub>-418, not by CFD computations.

There is a large variety of roughness heights and distributions possible and one of the ways to simplify choices and handling in wind tunnel testing seems to be the use of sandpaper. The height and distribution density of the grains is regulated within certain limits, it is obtainable in a large variety of widths and lengths and relatively easy to apply.

#### **4.4.6 Sandpaper tests in IRPWIND project**

In the framework of the IRPWIND project (Integrated Research Program on Wind energy, a European FP-7 Energy program) measurements were performed in the Delft LTT with the objective to link measured losses in the wind tunnel to measured power degradation in the field. (Pires et al., 2018). To this end the aerodynamic characteristics of a NACA 63<sub>3</sub>-418 airfoil with 3 LE roughness heights was measured using sandpaper and two zigzag tape heights (0.25mm and 0.6 mm at 8% u.s. and l.s.). The sandpaper was wrapped around the leading edge with three different chord extensions: 4%, 8% and 15%. Three different grit sizes were used: P40, P80 and P240.



Figure 4.27: The test setup in the Delft LTT (left) and the test turbine blade with the sand paper installed. Right photo by I. Alting (ECN).

4.4.6.1 Wind tunnel test

The majority of the wind tunnel experiments was at  $Re=3 \times 10^6$ . The drag coefficients resulted from a wake rake traverse of at least 10cm of span after a thorough drag inspection along the span for several incidences. This specific airfoil is located between 29.3m and 39.2m radius of a N80 2.5MW wind turbine situated on the test field of TNO in the Netherlands.

A picture of the sand paper on the wind tunnel model and on the turbine blade is presented in fig. 4.27. The tunnel data show a near linear increase of the minimum drag and the loss in lift-drag ratio with roughness chord extension variation at constant grit size

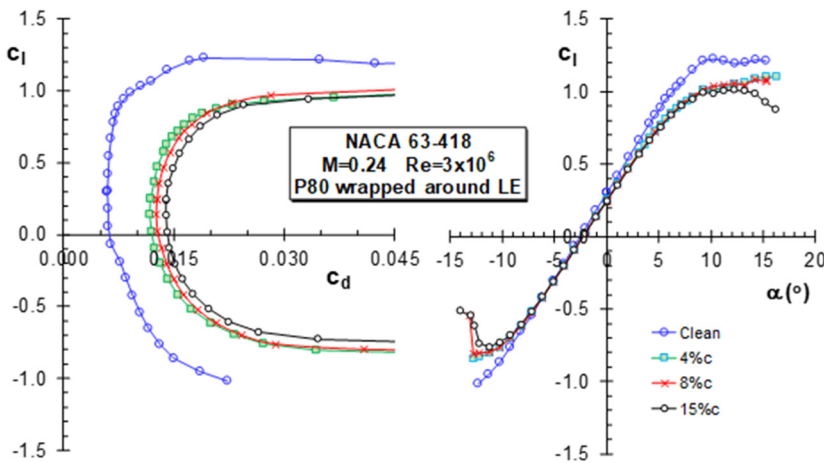


Figure 4.28: The impact of the wrap-around length on the performance for no. 80 sandpaper (0.201mm). Indicated is the chord extension on both sides.

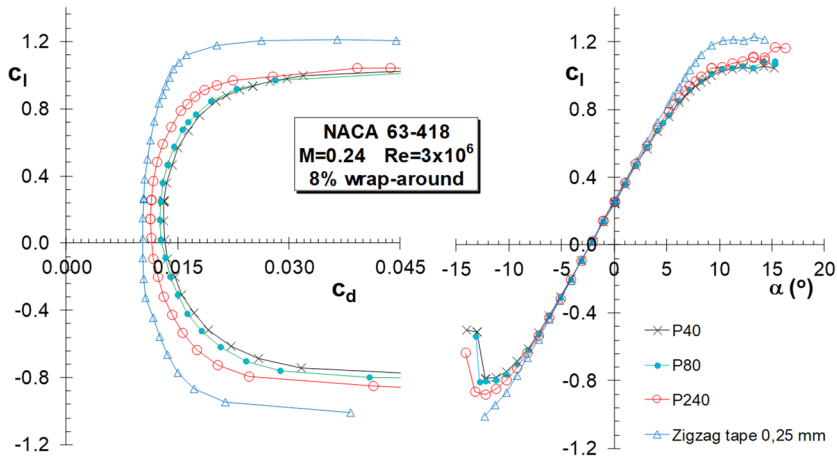


Figure 4.29: The impact of sandpaper grit size on the performance with  $\pm 8\%$  wrap compared to the effect of 0.25mm thick zigzag tape at 8% upper and lower surface.

(see fig. 4.28 for P80).

This was not the case for grain size variation at constant chord extension (fig. 4.29). The bigger grit size has the largest effect on drag, however there is not a large step from P40 to P80 grit. Maximum lift coefficients are comparable. The total thickness of the P40 sandpaper including the adhesive tape is 0.75mm, which is considerable.

Fig. 4.30 shows the significant impact of the sandpaper on the airfoil efficiency. The maximum lift-drag ratio goes down from 118 in the clean case to 51 and 42 for P240 and P40 respectively. Losses in annual energy production (AEP) calculated with these results show reductions of 3.1% for the zigzag tape and 6% and 7.7% for the P240 and P40 sandpaper respectively.

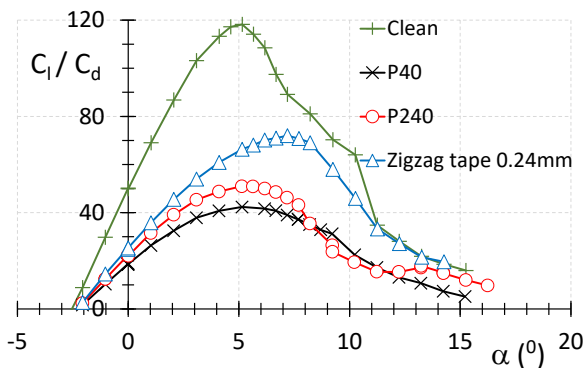


Figure 4.30: The lift-drag ratio of the 8% wrap sandpaper test at  $Re=3 \times 10^6$ . Zigzag tape at  $x/c=8\%$  on u.s. and l.s

#### 4.4.6.2 Field experiments

In view of the higher Reynolds numbers during turbine operation (between  $4 \times 10^6$  and  $6 \times 10^6$ ) and the larger chord (between 1m and 1.5m) field tests with P60 sandpaper

wrapped around 15% of the upper and lower surfaces was regarded to be representative for the wind tunnel tests.

The performance was evaluated against a neighboring turbine for one month. Ten minute bins were taken in the wind speed range of 5 to 12 m/s with steps of 1m/s. The losses against the reference turbine are presented in fig. 4.31. Due to the limited amount of testing time the uncertainty is rather large. However, looking at the BEM simulations using the wind tunnel results in the calculations, the image is clear: due to sandpaper the loss in power is at least 5% in a major part of the power curve.

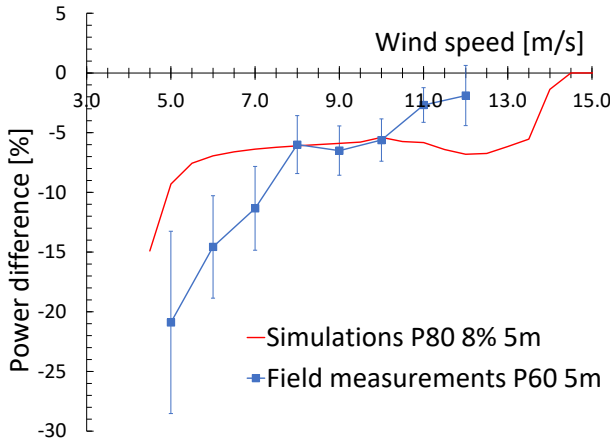


Figure 4.31: Result of the field measurements with P60 sandpaper over 5m span, 15% wrap. Comparison with simulations using P80 with 8% wrap over 5m span.

It must be noted that the roughness of this configuration of the sandpaper is quite severe. The total thickness of the sandpaper (backing plus grit) is approximately 1.5 mm, while the grit height only is 0.27 mm. The double sided adhesive tape used to attach the sandpaper to the blade has a thickness of 0.21 mm, giving the total package a thickness of 1.71 mm. No attempt was made to smoothen the step at the edges, which is similar to the wind tunnel test. The chord of the 5m span covered with the sandpaper varied between approximately 1 and 1.5 m, giving a relative roughness height  $k/c$  between  $1.71 \times 10^{-3}$  and  $1.14 \times 10^{-3}$ .

#### 4.4.7 Sandpaper testing in general

Though the use of sandpaper is convenient in wind tunnel testing, regarding the various grit sizes available and the relative ease of application, it is also a severe roughness due to the relatively dense packing of the grit, the density also varying with grit size. For the sake of robustness, the paper backing generally is much thicker than the grit size, which increases the impact on drag as a result of step at the aft edges. This already explains why it proves so hard to model the sandpaper in NS-flow solvers.

## 4.5 THE IMPACT OF LEADING EDGE EROSION.

### 4.5.1 AEP losses due to leading edge erosion

The potentially biggest threat to wind turbine performance and the associated energy yield is leading edge erosion. The frequent impact of rain drops, hail and other floating abrasive elements on a fast rotating leading edge affects the surface in such a way that at first the coating is damaged and later on, when erosion starts to affect the subsurface



*Figure 4.32 Leading edge erosion in various stages (Rempel 2012)*

fiber structure, structural integrity may be at risk. Figure 4.32 left shows the beginning of erosion with pits and gouges, which may end in serious subsurface damage to the fiberglass laminate seen at the right. Long before the underlying structure of a blade may be damaged, the aerodynamic performance of it has decreased considerably. In addition, due to the changed flow over the leading edge, vibration might be introduced not taken into account in the blade design.

The higher permissible tip speed enabled by the offshore placement of wind turbines has potentially aggravated the problem. Apart from the loss in revenue due to operation with blade erosion, also the down time during expensive repairs significantly adds to the costs. Due to the gradual increase of erosion damage and the various stages encountered, a consistent view on the actual impact of erosion on the annual energy production (AEP) of a wind turbine and the variation in time has long been missing. As shown in paragraph 4.4.6, most of AEP-loss numbers use the same approach: running BEM calculations with airfoil performance characteristics (from CFD computations or wind tunnel tests) representing various stages of roughness or erosion to calculate a power curve. The AEP

is computed using a certain wind climate. Where frequently the studies differ, is the amount of chord coverage and blade span wise variation of the damage towards the tip. An overview of LER issues is given in Herring et al. (2019) and Mishnaevsky (2021). The losses in AEP mentioned, also based on work of Zidane and co-workers (2016), range from 0.5% to a staggering 25% (Sareen et al., 2015) for heavy erosion. At present, with accumulating operational information on erosion of service and repair teams, numbers tend to converge around the range of 0.5% to 5%, and about 0.7% to 1% for the first few years of operation (Duffy et al, 2021).

#### 4.5.2 Impact of erosion on section performance

The variety of predicted AEP losses already highlights the diversity in research in terms of shape, size and density of erosion damage, the chord coverage and the variation along the blade span.

Owing to the various impact factors such as tip-speed and turbine location (rain climate) and the progressive stages of erosion that exist, as is shown in fig. 4.32, the effect on blade performance remains a complex matter.

Many studies (see a.o. the overview by Duffy et al., 2021) have been devoted to the impact of various stages of erosion, ranging from an occasional pit, to delamination, with changing patterns and gouge/cavity depths on the performance of a limited number of airfoils at Reynolds numbers varying from  $1 \times 10^6$  (Sareen 2015) to  $6 \times 10^6$  (Veraart 2017).

An example of the impact variety of schematized roughness /erosion types at a fairly high

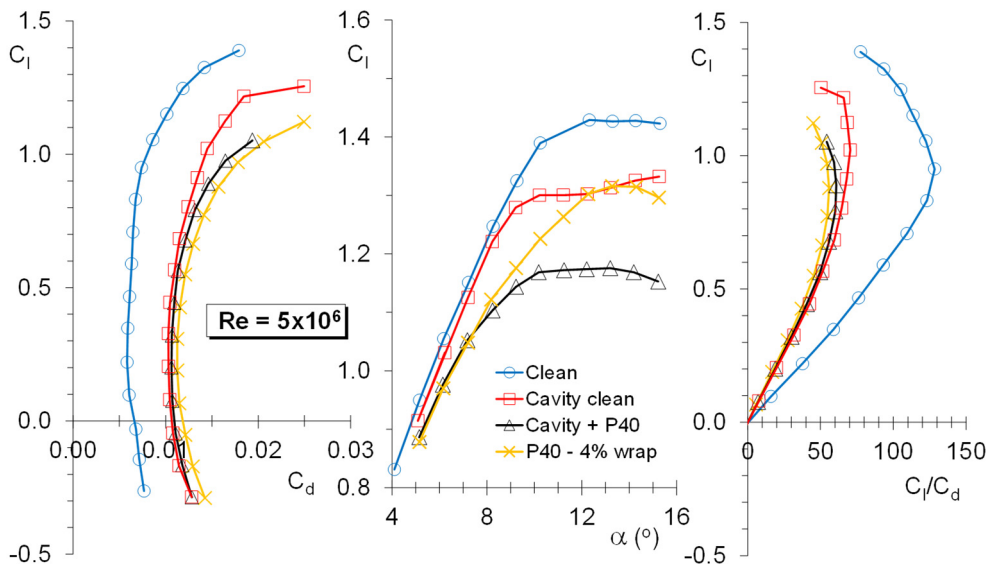


Figure 4.33: The impact of variation of roughness types on the performance of airfoil NACA 63-418 measured in the Poul La Cour wind tunnel (PLCT) of DTU at a Reynolds number of  $5 \times 10^6$ . Taken from Kruse et al. (2021). Cavity has 3% chord extension on u.s. and l.s.

Reynolds number of  $5 \times 10^6$  can be found in a study by Kruse et al. (2021) in the DTU PLCT (fig. 4.33). The 1.0m chord NACA 63<sub>3</sub>-418 model had an exchangeable leading edge, such that a printed part with cavities could be installed. The exchangeable part had a span wise cavity of 3mm deep (0.3% chord) from  $x/c=3\%$  l.s to 3% u.s. with sharp edges.

The graphs show a tremendous loss in maximum lift due to P40 sandpaper with 4% chord extension on l.s and u.s. The maximum lift is reduced with about 8% and the lift-drag ratio goes from 128 to 56, a loss of 56%. The presence of the cavity, more specific the forward facing step on the upper surface does harm the flow, however, to a lesser extent than the sandpaper. They have the same maximum lift coefficient, but the clean cavity has a better maximum lift-drag ratio (70).

Remarkable is the large impact of P40 sandpaper placed inside the cavity. This configuration produces the lowest maximum lift coefficient (1.18) and a maximum lift-drag ratio of 61, a reduction of 42%. It appeared that configurations only using zigzag tape on the upper side could not produce the same amount of losses. The study shows, that not only the presence of protuberances and cavities, but also their location close to the LE and the surface conditions in the cavities are of importance for the final losses.

#### **4.5.3 Erosion and wind tunnel testing**

The variation in surface conditions of the section front end in combination with variation in airfoil shape and operational Reynolds numbers is almost limitless.

Unfortunately, the studied airfoil sections (e.g. DU96-W-180, NACA 63<sub>3</sub>-418, S814 and DU00-W-212) and Reynolds numbers are not representative for the present large off-shore turbines and some of the found losses may be airfoil specific.

The study by Maniaci (2016) showed that the performance with zigzag tape of 0.5mm thickness (on a 813mm chord model, giving  $k/c=.615 \times 10^{-3}$ ) placed at 2% chord on the upper surface and  $x/c=5\%$  on the lower side formed the lower boundary of the characteristics impacted by a great number of roughness and erosion types. In the light of the challenges existing when testing with sandpaper and the varying paper backing thickness and the endless possibilities in erosion type and stage it may be necessary to standardize roughness testing in this regard: zigzag tape of considerable thickness placed at  $x/c=1\%$  or 2% on the suction side and 5% on the pressure side. The latter location maybe shifted downstream slightly regarding the stagnation point variation with increasing angle.

#### **4.5.4 Erosion mitigation concepts**

In view of the high impact of erosion on blade efficiency and AEP, which significantly depend on site rain characteristics, a number of measures can be taken to mitigate the detrimental effect.

#### 4.5.4.1 Leading edge protection

To negate, or at least postpone, the detrimental impact of erosion, blades are equipped with leading edge protection in the form of special impact resistant substances sprayed, painted or rolled on the blade or a special protective tape, like the so-called 3M-helicopter tape, a thermoplastic polyurethane elastomer.

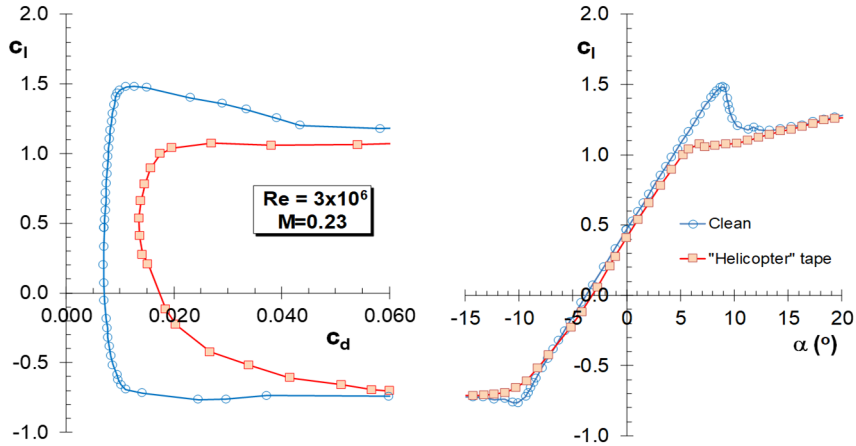


Figure 4.34: The measured impact on performance of 0.36 mm thick 3M helicopter tape wrapped around app. 7% of the leading edge of a 24% thick airfoil.

The problem, however, is that every element added to the leading edge surface may potentially harm the flow development over the blade. A good example is given in figure 4.34. It shows the effect of helicopter tape on a 24% thick 0.75m chord wind turbine airfoil model measured in the TU Delft LTT. The tape is 0.36 mm thick and covers the leading edge, roughly between  $x/c=7\%$  on the upper and lower surfaces. Clearly, due to the aft edges of the tape forming backward facing steps, there is a significant performance reduction, as the maximum lift-drag ratio is reduced with over 60% and the maximum lift coefficient with 25%.

In this case the airfoil was designed for a Reynolds number of about  $6 \times 10^6$ , so the measurements were done in an off-design condition, hence in practice the performance decrease might not be as serious as depicted, since transition in the clean case will be closer to the LE. However, even with half the reduction in performance the figure does show the potential impact on the blade aerodynamics and without proper treatment of the step at the edges of the tape, for some time in the life of the blade “the cure might be worse than the illness”. The adverse effect of the tape can be mitigated by letting it end at a more downstream location.

It is clear that to reach their projected lifetime and to maintain sufficient aerodynamic performance, smart anti-erosion measures, inspection, and timely repair of wind turbine blades are of paramount importance (Maniaci et al., 2020).

#### 4.5.4.2 Erosion safe mode control

Impingement of rain droplets causes blades to erode. In this process droplet speed is a vital component. Beyond a certain speed the droplet causes erosion damage. A number of studies treat the possibility of running the turbine in erosion safe mode (ESM), by reducing the circumferential speed of the turbine during rain events to lower impingement speed (Hasager et al., 2021, Barfknecht et al., 2022). It is found that erosion mainly causes losses in the turbine partial load operation up to rated wind speed, where ESM operation predominantly impacts maximum power. A break-even point can be found, which heavily depends on the site-specific rain characteristics, rain forecasting and wind climate. Hasager et al. calculated an 1.51% average loss in profit of turbines in the Danish and German North Sea stations due to blade erosion, repair costs and downtime during repairs. A gain of 70% could be accomplished by running the turbines in ESM. Barfknecht and von Terzi (2025) found that smaller droplets are significantly slowed down when approaching the blade leading edge, causing important damage-reduction. Smaller drops may be more deformed by the presence of the section leading edge (and therefore have a higher aerodynamic drag and speed reduction), a process in which a larger nose radius of the airfoil may have a positive contribution. Drop-size should therefore not be ignored in erosion-damage modelling.

Successful ESM strategies heavily rely on rain forecasting. Uncertainties in modelling rain damage, in forecasting damaging rain-events and managing wind farm power output during ESM operation are future research subjects.

## 4.6 CONCLUSIONS

### On the design of airfoils for large blades

Due to the constant upscaling of wind turbines, blades have relatively smaller chords and consequently higher design lift coefficients. In combination with roughness insensitivity requirements and angle of attack variations due to inflow unsteadiness in general and turbulence in particular this leads to a more turbulent type of airfoils with a high maximum lift coefficient.

By means of an optimization for a 21% thick airfoil at a Reynolds number of  $9 \times 10^6$  prescribing equal weight between the clean and “rough” characteristics, it is shown that perturbations in the angle of attack due to turbulence drive the design into the direction of airfoils with more forward located camber. The example shows that, in view of blade efficiency in turbulent conditions, the design-angle should be chosen approximately  $4^\circ$  below the stalling angle and slightly below the angle for maximum lift-drag ratio, both values being governed mostly by the turbulence intensity of the incoming flow and the frequency of occurrence and hence the wind climate at the turbine location.

## **Roughness and erosion**

*RQ4-1 How can blade surface soiling and erosion be characterized? In other words, what is the nature, the degree, the pattern and the rate of change of actual surface soiling and degradation?*

Blade leading edge contamination and erosion are the biggest threats to wind turbine performance. A vast number of studies deal with the effect of roughness patterns and erosion stages on airfoil characteristics and the associated impact on turbine efficiency. There is, however no clear indications of the rate of change of soiling, also because this depends on the local weather conditions. Calculations with the code Lewice seem to be able to approximate the pattern of a heavily soiled leading edge.

The general way of establishing the loss in AEP is through BEM calculations using the calculated or experimental section characteristics impacted by roughness or erosion, assuming roughness height and density or erosion stage. Although some studies arrived at AEP-losses due to erosion up to 25%, current estimates concentrate on numbers in the range of 0.5% to 5%.

Though limited in testing time, one of a few studies involving a large turbine creating a direct link between roughness patterns and wind turbine output, is the IRPWIND study concerning sandpaper with a 15% wrap around the leading edge over 5m span of a 3MW wind turbine blade. Recognizing that the sandpaper used was a severe type of roughness (and perhaps more resembles heavy erosion) an approximate average of 5% power loss in a large part of the power curve was established, which was corroborated by BEM calculations using experimental data.

Leading edge protection measures against erosion may trigger early transition due to the backward facing steps at the edges of the protection area. Depending on the location of the edges, the height of the step and the pressure distribution of the airfoil (shape) this can have a significant impact on the airfoil performance.

As an example, fig. 4.31 presents the characteristics of a 24% thick airfoil where the erosion resistant tape edges at the upper and lower surface 7% chord station cause a 60% reduction in lift-drag ratio and a 25% reduction in  $C_{l,max}$ .

*RQ4-2 How can this be incorporated into new designs? In other words, how should this be modelled in codes to be able to predict the airfoil aerodynamic performance and be used in optimization processes.*

To ensure that in the design transition is on the leading edge of the airfoil while

approaching the maximum lift coefficient has been a remedy against excessive losses due to blade soiling.

There is no method to account for erosion in several stages in airfoil design at present. If such a method would emerge, it would most likely be a CFD application, which is generally not suited for optimization processes when a large number of calculations have to be evaluated.

Two ways of modeling in CFD to tackle the problem exist at present: the modeling of the roughness elements / protuberances on the surface and the method of finding a representative surface roughness height to account for the leading edge pattern of soiling and erosion and roughness depth/height.

The first method seems to work with 2D computations to account for zigzag tape on the model (which would be an equivalent for certain types of roughness). Modelling does not give accurate results in case of erosion, despite the 3D nature of the simulations. The second method can work for both types of surface conditions, however the challenge is to find the right equivalent roughness height.

*RQ4-3 How can real contamination or erosion be transferred to the wind tunnel practice to be able to experimentally verify the aerodynamic characteristics designed into new airfoils in a reproducible manner?*

A great number of roughness patterns and erosion stages have been experimentally verified at relatively low Reynolds numbers ( $Re \leq 6 \times 10^6$ ) on a limited number of airfoils not used in current big machines. The studies give a view on the impact roughness and erosion may have on section performance.

However, there is in principle no standard way to test airfoils with erosion (and to a lesser degree with roughness) and there is no standard for roughness or erosion experiments on airfoils for wind turbine application at present, neither is there a consensus on scaling. Zigzag tape, grit roughness and sandpaper are all being used to account for different stages of blade soiling. Sandpaper tests have the disadvantage of being thicker than the roughness particles due to the paper back and the adhesive tape needed to attach it to a model and the density changes with particle size. These tests seem to have been performed only on NACA 63<sub>3</sub>-418.

The almost limitless variety of configurations possible, calls for a more coordinated action to establish a standard way of testing the performance loss of blade sections. In such a case a certain stage of erosion will be linked to the performance of the section with a certain equivalent type of (relative) roughness at both sides of the leading edge. As zigzag tape is easy to apply and comes in a variety of thicknesses, it is well suited for this purpose.

The location could be 1% on the upper side and 5% on the lower side and vice versa for negative angles. A first check should be done to establish the lowest roughness to trigger transition just behind the tape.

The experimental study on the zigzag tape critical Reynolds number using tape at the 5% chord station of DU93 and DU97 had a mixed outcome. Based on flat plate laminar boundary layer theory, the required roughness height Reynolds number for a specific thickness was computed, using IR-images to establish the transition location. The DU93 measurements showed a value of 217 for 0.310mm thick tape, while a thinner tape of 0.185mm thickness gave a value of 214. The DU97 test resulted in values of  $220 \pm 4$  for angles between  $0^\circ$  and  $6.2^\circ$  using 0.250mm thick tape. A tape with 0.185mm thickness showed deviant values between 153 and 182 over the entire range of incidences from  $0^\circ$  to  $8.2^\circ$ , and more in particular  $R_{k,crit} \approx 179 \pm 4$  for angles between  $4^\circ$  and  $8.2^\circ$ .

With only a 0.02mm increase of the tape thickness, the DU97 thin tape experiment for the higher incidences would have resulted in  $R_{k,crit}$  values well in the range of  $220 \pm 4$  resulting from the 0.250mm measurements. The latter indicates that vice versa the required tape thickness for transition behind the tape is not highly sensitive to the value of  $R_{k,crit}$ . It is therefore concluded that  $R_{k,crit} = 220 \pm 5$  for an airfoil is a fair conclusion of the study. The value of  $R_{k,crit} \approx 200$  for flat plate flow frequently mentioned in literature was confirmed using 0.255mm zigzag tape on  $x/c = 0.35\%$  of airfoil DU93 at  $\alpha = 5.12^\circ$  and  $Re = 1.03 \times 10^6$ .

## 4.7 REFERENCES

Abbott, I.H. ,von Doenhoff, A.E. and Stivers, S., jr. (1945) *Summary of airfoil data*. NACA Report no. 824, 1945.

Barfknecht, N. and von Terzi, D. (2025) *Drop-size-dependent effects in leading-edge rain erosion and their impact on erosion-safe mode operation*. Wind Energ. Sci., 10, 315–346, <https://doi.org/10.5194/wes-10-315-2025>, 2025.

Barfknecht, N., Kreuseler, M., De Tavernier, D., von Terzi, D. (2022) *Performance analysis of wind turbines with leading-edge erosion and erosion-safe mode operation*. Journal of Physics: Conference Series **2265** (2022) 032009 doi:10.1088/1742-6596/2265/3/032009

Barlow, J.B. , Rae, W.H. Pope, A. (1999) *Low-Speed Wind Tunnel Testing*. (3rd ed.), John Wiley & Sons Publ. (1999)

Betz, A. (1926) *Wind-Energie und ihre Ausnutzung durch Windmühlen*. Aerodynamische

Versuchsanstalt zu Göttingen, 1926.

Bladecleaning, [www.bladecleaning.com](http://www.bladecleaning.com), accessed July 2022

Boccard, N. (2009) *Capacity factor of wind power realized values vs. estimates*, Journal of Energy Policy, Vol. 37, 2009.

Boermans, L.M.M. (2015) *Turbulators in practice*. Symposium for Sailplane development, Darmstadt, Germany, November 2015

Boermans, L.M.M and Selen, H.J.W. (1982) *Design and tests of airfoils for sailplanes with an application to the ASW-19B*. ICAS-82-5.5.2, 1982

Boermans, L.M.M and Waibel, G. (1987) *Aerodynamic design of the standard class sailplane ASW-24*. Technical Soaring VIII, No.3, 1987

Boorsma, K. (2025) Personal communication, March 2025

Braslow, A.L., Knox, E.C. (1958) *Simplified method for the determination of critical height of distributed roughness particles for boundary-layer transition at Mach numbers from 0 to 5*. NACA Technical Note 4363, 1958

Burton, T., Sharpe, D., Jenkins, N. and Bossanyi, E. (2001) *Wind Energy Handbook*. John Wiley & Sons Ltd. Chichester, England. 2001

Corten G.P., Veldkamp H.F. (2001) *Insects cause double stall*. In: Proceedings of the European wind energy conference, Copenhagen, Denmark 2001.

Duffy, A., Ingram, G. and Hogg, S. (2021) *The significance of bypass transition on the annual energy production of an offshore wind turbine*. Wind Energy Nov 2021 [doi.org/10.1002/we.2697](https://doi.org/10.1002/we.2697)

Ehrmann, R.S., White, E.B., Maniaci, D.C., Chow, R. Langel, C.M., van Dam, C.P. (2013) *Realistic leading-edge roughness effects on airfoil performance*. 31st AIAA Applied Aerodynamics Conference, June 24-27, 2013, San Diego, CA, USA.

Ehrmann, R.S. (2014) *Effect of surface roughness on wind turbine performance*. Dissertation, Texas A&M University, USA. August 2014

Freudenreich, K., Kaiser K., Schaffarczyk, A.P. (2004) Winkler H. and Stahl, B., *Reynolds Number and Roughness Effects on Thick Airfoils for Wind Turbines*. Wind Engineering, Volume 28, no. 5, 2004 pp 529–546

Van Groenewoud, G.J.H., Boermans L.M.M. and van Ingen J.L. (1983) *Investigation into the boundary-layer transition on the rotor blades of the 25m HAT wind turbine* (in Dutch). Report LR-390. Delft University of Technology, May 1983

Han, W., Kim, J. and Kim, B. (2018) Effects of contamination and erosion at the leading edge of blade tip airfoils on the annual energy production of wind turbines. *Renewable Energy* 115 (2018) 817-823

Hasager, C. B., Vejen, F., Skrzypinski, W. R., & Tilg, A-M. (2021). *Rain Erosion Load and Its Effect on Leading-Edge Lifetime and Potential of Erosion-Safe Mode at Wind Turbines in the North Sea and Baltic Sea*. *Energies*, 14(7), [1959]. <https://doi.org/10.3390/en14071959>

Hwangbo, H., Ding, Y., Eisele, O., Weinzierl, G., Lang, U. and Pechlivanoglou, G. (2017) *Quantifying the effect of vortex generator installation on wind power production: An academia-industry case study*. *Renewable Energy* 113(2017) 1589-1597. <http://dx.doi.org/10.1016/j.renene.2017.07.009>

HAWC2 website: <https://www.hawc2.dk/HAWC2-info>

Herring R., Dyer K., Martin F. and Ward G. (2019) *The increasing importance of leading edge erosion and a review of existing protection solutions*. *Renewable and Sustainable Energy Reviews* Volume 115, November 2019, 109382

Janoff, P. *Aerodynamics of airfoils with leading edge roughness*. MSc. Thesis, DTU-Wind-M-0631. Denmark, July 2023.

Jonkman, J., Butterfield, S., Musial, W., Scott, G. (2006) *Definition of a 5 MW Reference Wind Turbine for Offshore Wind System Development*, National Renewable Energy Laboratory, Golden, CO, USA, 2006.

Keegan, M.H., Nash, D.H. and Stack, M.M. (2013) *On erosion issues associated with the leading edge of wind turbine blades*. *J. Phys. D: Appl. Phys.* 46 (2013) 383001 (20pp)

Kim, M-G. and Dalhoff, P. H. (2014) *Yaw Systems for wind turbines- Overview of concepts*,

*current challenges and design methods*. Journal of Physics: Conference Series 524 (2014). 012086 doi:10.1088/1742-6596/524/1/012086

Kruse, E. (2019). *A Method for Quantifying Wind Turbine Leading Edge Roughness and its Influence on Energy Production: LER2AEP*. DTU Wind Energy. DTU Wind Energy PhD thesis 2019

Kruse E., Bak C., Olsen A.S. (2021) *Wind tunnel experiments on a NACA 63<sub>3</sub>-418 airfoil with different types of leading edge roughness*. Wind Energy. 2021;24(11):1263-1274. <https://doi.org/10.1002/we.2630>

Kruse E., Sørensen N.N., Bak C. (2021) *A two-dimensional quantitative parametric investigation of simplified surface imperfections on the aerodynamic characteristics of a NACA 63<sub>3</sub>-418 airfoil*. Wind Energy. 2021;24:310–322. <https://doi.org/10.1002/we.2573>

Langel, C.M., Chow, R., van Dam, C.P., Maniaci, D., Ehrmann, R.S. and White, E.B. (2014) *A computational approach to simulating the effects of realistic surface roughness on boundary layer transition*. AIAA-conference, 23 January 2014. DOI: 10.2514/6.2014-0234.

Langel, C.M., Chow, R., Hurley, O.F., van Dam, C.P., Ehrmann, R.S., White, E.B. and Maniaci, D. (2015) *Analysis of the impact of leading edge surface degradation on wind turbine performance*. AIAA-conference, January 2015

Llorente, E., & Ragni, D. (2020). *Trailing-edge serrations effect on the performance of a wind turbine*. Renewable Energy, 147, 437-446. <https://doi.org/10.1016/j.renene.2019.08.128>

Maniaci D.C., White E.B., Wilcox B., Langel C.M., van Dam C.P. and Paquette J.A. (2016) *Experimental Measurement and CFD Model Development of Thick Wind Turbine Airfoils with Leading Edge Erosion*, Journal of Physics: Conference Series, 753, Issue 2

Maniaci, D.C., Westergaard, C., Hsieh, A. , and Paquette, (2020) J.A. *Uncertainty Quantification of Leading Edge Erosion Impacts on Wind Turbine Performance*. Journal of Physics: Conf. Series 1618 (2020) 052082 doi:10.1088/1742-6596/1618/5/052082

Manwell, J.F., McGowan, J.G. and Rogers, A.L. (2002) *Wind Energy Explained*. John Wiley & Sons Ltd. Chichester, England 2002.

McGhee, R.J. and Beasley, W.D. (1973) *Low-speed aerodynamic characteristics of a 17-*

*percent-thick airfoil section designed for general aviation applications.* NASA TN D-7428. Washington D.C. December 1973.

Mishnaevsky Jr., L. Bay Hasager, C. , Bak, C. Tilg, A. Bech, J.I., Doagou Rad, C. and Faester, S. (2021) *Leading edge erosion of wind turbine blades: Understanding, prevention and protection.* Renewable Energy 169 (2021) 953-969

OpenFast website: <https://www.nrel.gov/wind/nwtc/openfast.html>

Pereira R., de Oliviera, G., Timmer, W.A. and Quaeghebeur, E. (2018) *Probabilistic Design of Airfoils for Horizontal Axis Wind Turbines.* Journal of Physics: Conf. Series 1037 (2018) 022042 doi :10.1088/1742-6596/1037/2/022042.

Pires, O., Munduate, X., Boorsma, K., Ceyhan Yilmaz, O., Madsen, H., and Timmer, W.A. (2018) *Experimental investigation of Surface Roughness effects and Transition on Wind Turbine performance.* Journal of Physics: Conference Series, 1037(5), [052018]. <https://doi.org/10.1088/1742-6596/1037/5/052018> , 2018

Rempel, L. (2012) *Rotor blade leading edge erosion - Real Life Experiences,* Wind Systems Magazine, Oct. 2012

Rezaeihaa, A., Pereira, R. and Kotsonis, M. (2017) *Fluctuations of angle of attack and lift coefficient and the resultant fatigue loads for a large Horizontal Axis Wind turbines.* 2017 Renewable Energy 114(Part B) 904–916

Sareen, A. , Sapre, C.A. and Selig, M.S. (2014) *Effects of leading edge erosion on turbine blade performance.* Wind Energy 17 (10) October 2014 1531-1542

Savenije, F.J., and Peeringa, J. (2009) M. *Aero-elastic simulation of offshore wind turbines in the frequency domain.* Energy Research Center of the Netherlands. The Netherlands. Tech. Report, ECN-E-09-060, 2009

Selle, J. (1999) *Study on the effectiveness of turbulator tape on boundary-layer transition.* Report, University of California at Davis, USA. May 1999

Skrzypiński W., Gaunaa, M. and Bak, C. (2014) *The Effect of Mounting Vortex Generators on the DTU 10MW Reference Wind Turbine Blade.* Journal of Physics: Conference Series 524 (2014) 012034. doi:10.1088/1742-6596/524/1/012034

Smith, A.M.O. and Clutter, D.W. (1959) *The Smallest Height of Roughness Capable of affecting Boundary-Layer Transition*, Journal of Aerospace Sciences, Vol. 26, No. 4, 1959, pp. 229-245.

Spruce, C. (2006) *Power performance of active stall wind turbines with blade contamination*. Proceedings European Wind Energy Conference, Athens, 2006.

Timmer, N. and Veldhuis, L. (2021) *The Impact of Skinsuit Zigzag Tape Turbulators on Speed Skating Performance*. Appl. Sci. 2021, 11, 988.

Timmer, W.A. (2009) *An overview of NACA 6-digit airfoil series characteristics with reference to airfoils for large wind turbine blades*. AIAA 2009-268

Timmer, W.A. and van Rooij, R.P.J.O.M. (1994) *The impact of Gurney flaps and vortex generators on the power curve of a rotor with APX-40 blades (in Dutch)*. Report IW-94076R, Institute for Wind Energy, TUDelft, September 1994.

Timmer, W.A. and Schaffarczyk, A.P. (2004) *The Effect of Roughness at High Reynolds Numbers on the Performance of DU 97-W-300Mod*. Wind Energy 2004, Volume 7 pp 295-307

Veraart, L.M.W. (2017) *Deterioration in aerodynamic performance due to leading edge rain erosion*. Master thesis TU Delft and DTU, July 2017

Young, A.D. and Paterson, J.H. *Aircraft excrescence drag*. AGARD-AG- 264. AGARD Fluid Dynamics Panel, London, July 1981.

Zidane I.F., Saqr, K.M., Swadener, G., Ma, X. and Shehadeh, M.F. (2016) *On the role of surface roughness in the aerodynamic performance and energy conversion of horizontal wind turbine blades: a review*. Int. Journal of Energy Research 40 2054-2077

# 5

## BLADE SECTION AERODYNAMIC EFFICIENCY IN PRACTICE

As described in the foregoing chapter, leading edge protection is applied on modern blades to mitigate the effects of blade surface deterioration. In addition, the outboard part of blades is equipped with trailing edge serrations to reduce trailing edge-boundary layer interaction leading to noise. Consequently, despite careful airfoil optimization, due to these additions the aerodynamic behaviour of airfoils as part of the blade may appreciably depart from the intended characteristics. It is a real challenge for blade manufacturers to prepare a blade with all additional treatment and devices without repercussions on the intended blade aerodynamic efficiency. The matter may best be highlighted by the following case.

### 5.1 TEST CASE

In cooperation with Dutch wind turbine manufacturer EWT, the impact of paint, leading edge protection and serrations on the aerodynamic efficiency of a blade segment was studied. During a number of LTT wind tunnel tests, measurements were performed on two identical models extracted from a segment of an actual 1MW turbine blade mould. The wind tunnel model and its location at about 75% span of the 29.15m long blade are depicted in fig. 5.1. As the chord and twist of the blade vary with span location, the wind tunnel models are not two-dimensional. The model chord varies with +/- 3.8 % compared to the reference, tunnel centre-line, length of 0.86 m. As the model is not rotating, the angle of attack, induced by the blade local twist distribution, varies over the span with  $0.67^\circ$ . Despite these deviations from a pure two-dimensional test, the model is expected to have characteristics close to those for airfoil NACA 63<sub>4</sub>-421.

## 5.1.1 NACA 63<sub>4</sub>-421 aerodynamic performance

### 5.1.1.1 RFOIL predictions

RFOIL calculations were performed for this 21% thick airfoil under the test conditions in the LTT:  $Re=3 \times 10^6$  and  $M=0.15$ . RFOIL tends to underestimate the drag coefficient and overestimate the lift coefficient, the extent of which depends on the Reynolds number, the airfoil shape and thickness, the trailing edge thickness, the free-stream turbulence and the type of surface roughness.

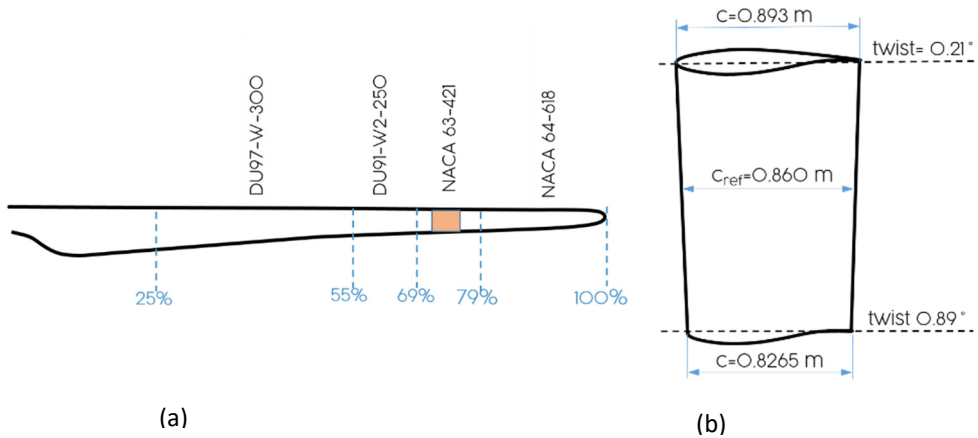


Figure 5.1: EWT-29 turbine blade, and position and sizes of the extracted model. Courtesy EWT.

Often, the calculated characteristics are multiplied with a factor to bring the lift, drag and moment coefficients to the level measured in wind tunnels. (see chapter 3). These factors for the LTT are derived from performance measurements on DU 93-W-210, also a 21% thick laminar airfoil of which the first 40% of the shape closely resembles the NACA airfoil (fig. 5.2), at  $Re=3 \times 10^6$  and  $M=0.22$ .

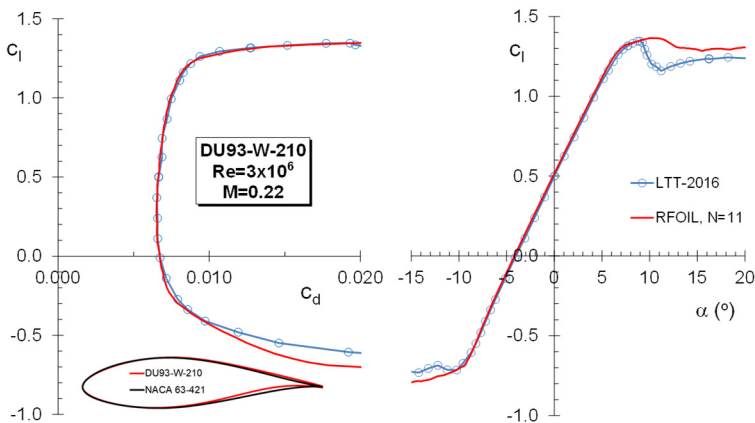


Figure 5.2: Comparison of measurements in the Delft LTT for airfoil DU93-W-210 at  $Re=3 \times 10^6$  and RFOIL calculations, using multiplication factors on  $C_d$  (1.10) and  $C_l$  (0.955).

After scaling the calculated lift coefficient in such a way that the lift gradient and the maximum lift coefficient are best reproduced, the corners of the drag bucket are best matched by RFOIL calculations using  $N=11$ , a common value for tests on thin trailing-edged airfoils in the LTT at this Reynolds number (chapter 3). As shown in fig. 5.2, with multiplication factors of 1.10 for the drag coefficient and 0.955 for the lift coefficient a very good match exists between the calculations and the experimental values of  $C_l$  and  $C_d$

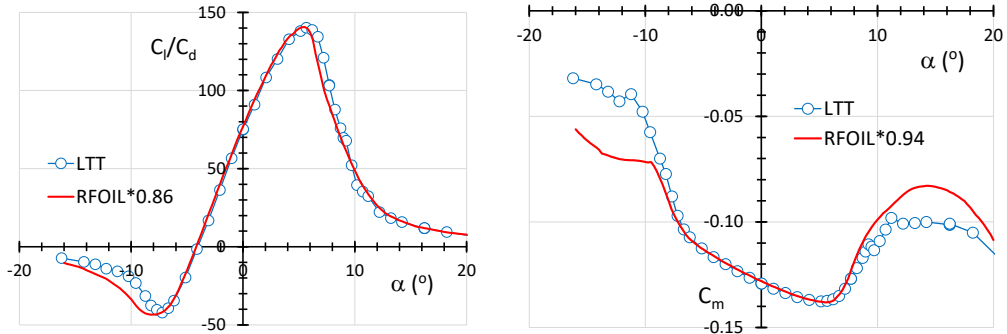


Figure 5.3: Comparison of measurements in the Delft LTT for airfoil DU93-W-210 at  $Re=3 \times 10^6$  and RFOIL calculations, using multiplication factors on  $C_m(0.94)$  and the lift-drag ratio  $C_l/C_d$  (0.86).

for the range of angles of attack between the minimum and maximum lift coefficients. With the multiplication factors presented in fig 5.3, also the moment coefficient  $C_m$  and  $C_l/C_d$  ratio are relatively well matched in this range, although for  $5.8^\circ \leq \alpha \leq 9^\circ$  the calculated  $C_l/C_d$  curve corrected in this way falls off a little sharper than the measurements. Due to difficulties in simulating advancing separated flow, the post stall lift and moment coefficients differ appreciably. It must be noted, however, that generally the measured post stall lift curve just after  $C_{l,max}$  is sharper for measurements using the model surface pressure distribution to determine the lift. This finds its origin in the existence of strongly three-dimensional stall cells, which makes the amount of separation present in the pressure distributions depending on the span position. The loss in lift determined with a balance and with the pressure footprint on the walls is less pronounced as they tend to take the average over the span.

#### 5.1.1.2 Comparison of predictions with experimental characteristics

Fig. 5.4 shows a comparison of the RFOIL calculations using the factors derived above with the two-dimensional characteristics as measured in the NACA LTPT (Abbott et al. 1945) and the University of Stuttgart low-speed wind tunnel (Althaus, 1998). The lift in both cases was derived from the pressure footprint on the walls. The minimum drag coefficients are the same in both experimental datasets, but there is a distinct difference in the maximum lift coefficient (1.33 against 1.24) and the maximum lift-drag ratio (128

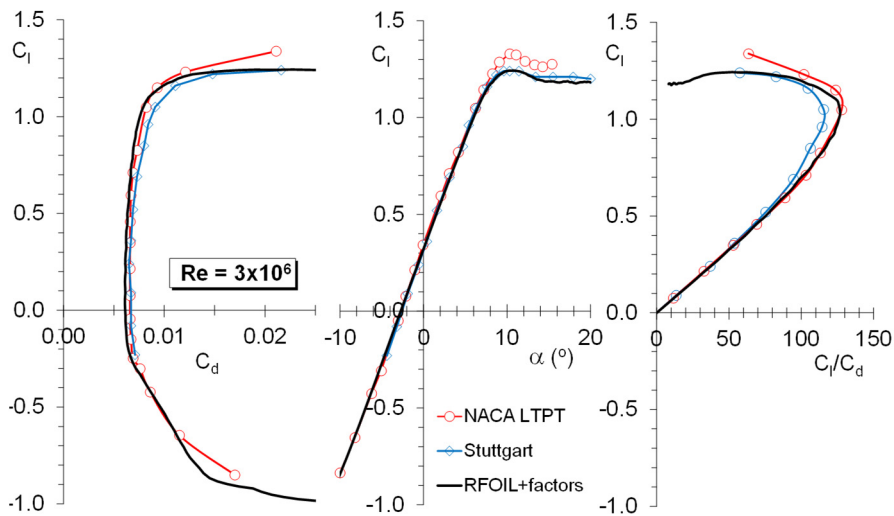


Figure 5.4: The aerodynamic characteristics of airfoil NACA 63-421 at  $Re=3 \times 10^6$ , measured in two different wind tunnels compared to RFOIL predictions using multiplication factors.

against 115) in favour of the NACA measurements. The modified RFOIL results confirm the maximum lift level measured in Stuttgart while the minimum drag coefficient is projected slightly lower, despite the applied factor on drag. The maximum RFOIL lift-drag ratio (126) compares well with the NACA data.

### 5.1.2 Test setup

The lift in the present test was also measured with the pressure reaction on the walls, using 4 pressure rows, two on each side of the model, containing 22 pressure orifices per row. An average pressure distribution for each side was established, from which the net reaction was determined, as described for the LTT by Tavernier (2021). In this way the average lift on the model is determined. The drag was measured with a wake rake. For every angle within the drag bucket a drag average over at least 10 cm of span was measured, taking into account the chord variation along the span.

#### 5.1.2.1 Data correction

The measured characteristics were corrected for wind tunnel wall interference according to the equations for streamlined flow listed in Appendix A. The correction for the angle of attack contains the uncorrected moment coefficient, which cannot be measured with the current setup. Instead, the NACA 63<sub>4</sub>-421 moment coefficients were calculated with RFOIL, both for free and fixed transition under the conditions for the measurements:  $Re=3 \times 10^6$  and  $M=0.15$ . The calculated  $\alpha$ - $C_m$  relation, multiplied with the factor 0.94 shown in fig. 5.3, was used to estimate the experimental corrected  $C_m$  for varying angle of attack. From this corrected  $C_m$  an in-tunnel (uncorrected) value was calculated using the reverse wind tunnel wall interference correction scheme, which finally was used for the angle of

attack correction. Although the angle correction is not very sensitive to moment coefficient changes, it may impact the lift gradient to some extent. At  $6^\circ$ , the difference in angle correction for  $C_m=0$  and a realistic value of  $-0.01$  amounts to  $0.2^\circ$ . For post stall angles of attack the wake is increasingly three-dimensional, which renders the wake rake method invalid. As the drag coefficient is used to calculate the wake blockage, which impacts the lift coefficient, when necessary an extrapolation was performed using the last 4 to 5 measured drag coefficients.

## 5.2 RESULTS

The model was tested in a number of configurations reflecting various stages of blade preparation.

### 5.2.1. Paint

The blade is generally covered with a polyurethane low-gloss paint to protect the epoxy resin from UV-radiation. It is applied with a roller. The first test concerns a model painted in this way without additional quality control measures. As figure 5.5 shows, particles in the paint cause premature transition near the leading edge. Part of the model span now shows transition at about 25%, while other, unaffected parts, have it at about 40%, which results in a whimsical drag pattern.

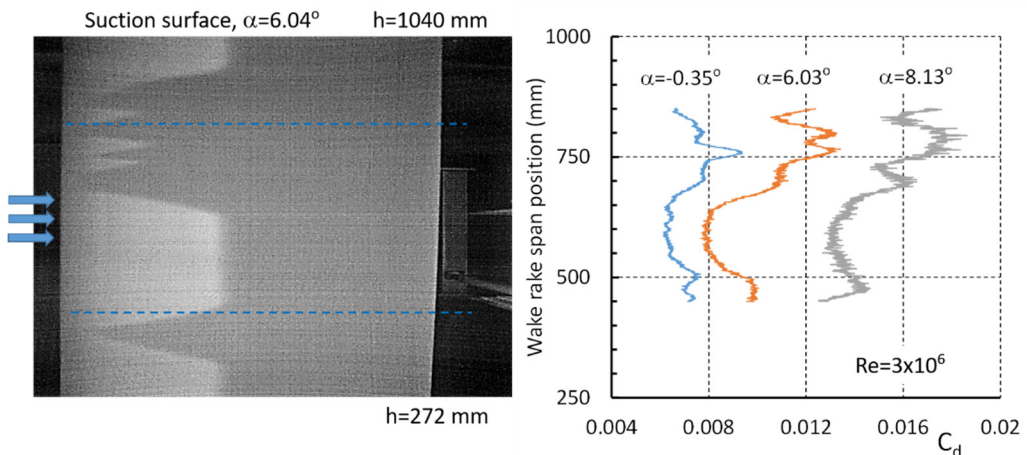


Figure 5.5: IR-picture (left) of the flow on the suction surface at  $6.04^\circ$ , showing turbulent wedges right from the LE. At the right the resulting drag distribution in span wise direction for 3 angles of attack. Flow coming in from the left as indicated

After lightly sanding the model with no. 600 sandpaper, the model showed an almost two-dimensional flow, with natural transition over the span (fig. 5.6).

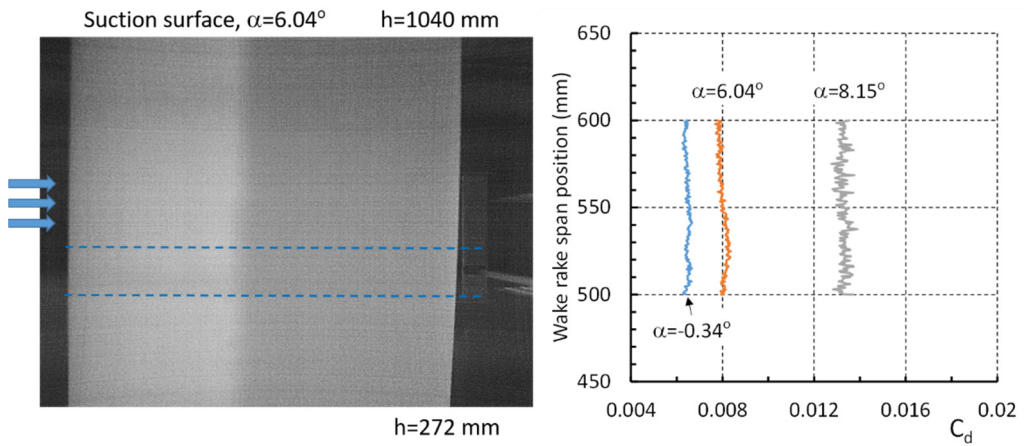


Figure 5.6: IR-picture (left) of the flow along the suction surface of the sanded model at  $6.04^\circ$ , showing natural transition over the entire span. At the right the resulting drag distribution between the dashed lines for 3 angles of attack. Flow coming in from the left as indicated.

The characteristics of both configurations are presented in fig. 5.7. While the lift is relatively unaffected, with the maximum lift coefficient a little lower, there is a significant difference between the drag and the lift-drag ratios in favour of the sanded model.

For positive lift coefficients, the sanded model appears to have a performance very close to the predictions with RFOIL using a factor of 1.10 on  $C_d$  and 0.955 on  $C_l$ . Even the predicted maximum lift-drag ratio (126) matches the experimental value (125). At the upper boundary of the drag bucket the drag increase starts at a lower lift coefficient, presumably due to the fact that the model is not two-dimensional, which may also be the

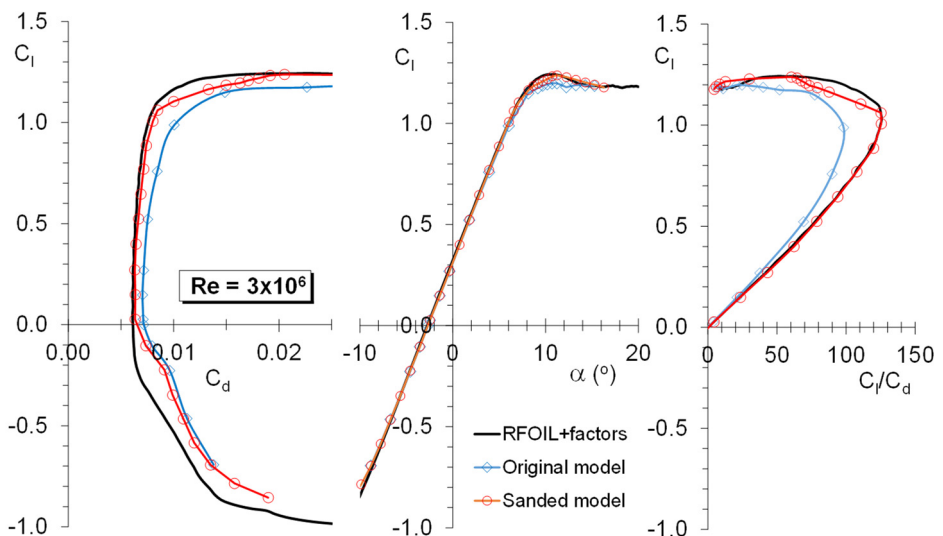


Figure 5.7: The characteristics of the original and the sanded model compared to RFOIL calculated results with multiplication factors on  $C_l$  and  $C_d$  derived from DU93 tests.

cause for the rather large deviation at negative angles of attack. While the differences in lift between the models before and after sanding only seem to occur around the maximum lift, the drag is much higher before sanding, reflected by a maximum lift-drag ratio of only 98.

### 5.2.2 Leading edge protection (LEP)

The standard leading edge protection on the blade consists of a polyurethane layer applied with a roller. After sanding, the second test model was treated accordingly with the layer running from  $x/c=4\%$  at the suction surface to  $x/c=4.5\%$  at the pressure surface. The model received no additional treatment. It appeared that the step at the edges of the layer, between 0.5 mm and 1.5 mm thick, significantly affected the location of transition. At the design angle of app.  $6.5^\circ$ , upper surface transition followed right behind the LEP edge, causing early separation. To mitigate the negative effect of flow distortion on the leading edge, semi triangular vortex generators (VG's) are generally a standard solution. Several locations and VG heights were investigated, however EWT's original VG height of 3 mm at 50% chord appeared to be the best combination. Fig. 5.8 depicts the impact of the LEP on the aerodynamic performance of the model and the restauration of lift provided by the VG's.

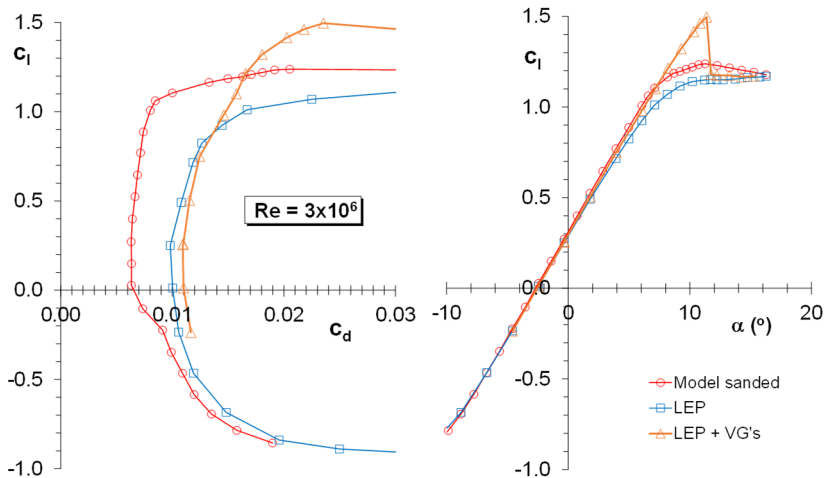


Figure 5.8: The impact of leading edge protection in combination with 3 mm high vortex generators at  $x/c=50\%$  at  $Re=3 \times 10^6$ .

It is clear that the vg's cannot make up for the increase in drag caused by the early transition induced by the leading edge protection layer. The vg's mixing process even produces additional drag. However, the loss in lift due to the thickening turbulent boundary layer and the consequential early separation at angles beyond  $5^\circ$  can be mitigated by the energizing effect of the vg's, until separation takes place upstream of the 50% chord location making the vg's ineffective.

### 5.2.3 Comparison with fixed transition.

The model was also tested with 0.3mm thick zigzag tape at  $x/c=0.06$  on the suction surface and  $x/c=0.065$  on the pressure side, to mimic the LEP's triggering of transition downstream the edges at  $x/c=0.04$  and  $0.045$  respectively. In fig. 5.9 the LEP and zigzag

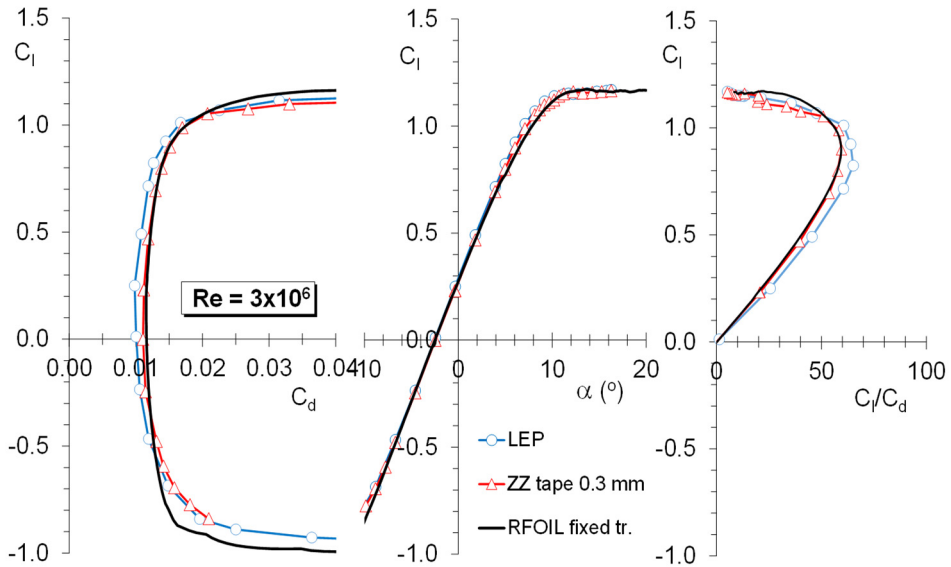


Figure 5.9: Comparison of the LEP performance with the performance having 0.3mm thick zigzag tape at  $x/c=6\%$  u.s. and  $6.5\%$  l.s. and RFOIL predictions with fixed transition at  $5\%$  u.s. and  $10\%$  l.s. using the factors 1.07 on drag and 0.94 on lift (see chapter 3).

tape configurations characteristics are compared to RFOIL calculations with fixed transition at  $x/c=5\%$  u.s. and  $10\%$  l.s. using the multiplication factors for tripped flow on DU93 mentioned in chapter 3 (1.07 on drag and 0.94 on lift). The RFOIL predictions come very close to the actual performance of the model with zigzag tape, matching both the maximum lift level and the maximum lift-drag ratio. In terms of lift, the LEP and zigzag tape measurements compare quite well. The drag of the LEP measurements is a bit lower, which might be caused by the fact that the boundary layer is not tripped right downstream the lower surface LEP edge over the entire span.

## 5.3 BLADE SECTION EFFICIENCY IN TURBULENT CONDITIONS

Turbulent inflow causes the angle of attack to vary with time, which may drastically affect the rotor performance if sections of the outboard part of the blade are driven into stall. Not only the time-averaged lift-drag ratio decreases dramatically, but the fluctuating forces contribute to blade fatigue and shorten rotor lifetime.

As an example, the angle of attack perturbations for this turbine induced by IEA standard NTM-3A turbulence were calculated using OpenFAST, which for the blade span location of the model is illustrated in fig. 5.10. At rated wind speed the mean angle of attack is about  $6.5^\circ$  and in 95.4 % of the time the angle of attack lies between  $1.7^\circ$  and  $11.3^\circ$  ( $\Delta\alpha=\pm 2\sigma$ ). Fig. 5.10 shows that the application of vg's in the LEP-configuration takes the

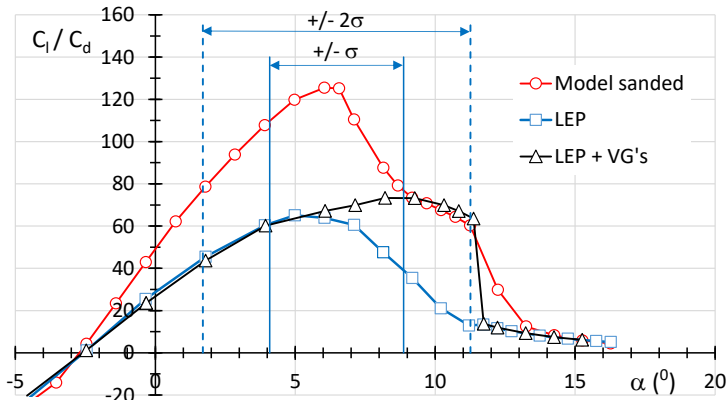


Figure 5.10: Operational range of angles of attack for the blade segment at rated wind speed.

level of the maximum lift-drag ratio (65) just to the boundary of the mean angle plus  $2\sigma$ , preventing a dramatic decrease to a value of 13. Coming from a maximum value of 125.5, the L/D of the clean model in the same  $\alpha$ -range is more than halved to a value of about 60.

The impact of leading edge transition (over the outer 45% of the blade span) on the power curve of this 1MW wind turbine under turbulent inflow is presented in fig. 5.11. Curves

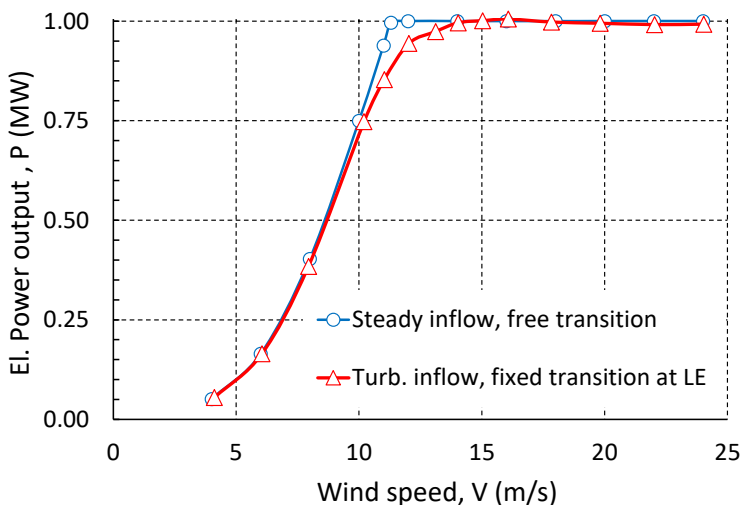


Figure 5.11: Calculated electric power curve for two blade configurations and inflow conditions.

Table 5.1: The calculated losses due to leading edge transition on the outer 45% of the blade span and turbulent inflow.

Configuration	AEP (GWh)	Loss (%)
Steady inflow, clean blade	3.505	
Steady inflow, fixed transition	3.431	2.1
Turbulent inflow, clean blade	3.427	2.2
Turbulent inflow, fixed transition	3.375	3.7

do not include peak shaving. Power data have been obtained from De Tavernier (2025). Table 5.1 presents the calculated losses in annual energy production resulting from two blade configurations and inflow conditions. AEP computed with a Rayleigh wind distribution at 7.5 m/s average wind speed at hub height.

### 5.4 MODIFIED LEADING EDGE PROTECTION

A new leading edge protection layer (LEP2) was applied to the first model, now running from  $x/c=0.13$  on the suction side to  $x/c=.135$  on the pressure surface. In contrast to the first LEP layer here the edges were carefully treated to give a smooth transition to the model surface. Still, some disturbances were found, as is depicted in the infrared pictures in figure 5.12 for  $6^\circ$  incidence. Most disturbances were removed, but, as is visible for the suction surface, the LEP-layer induces an irregular span wise transition pattern, which could only slightly be improved.

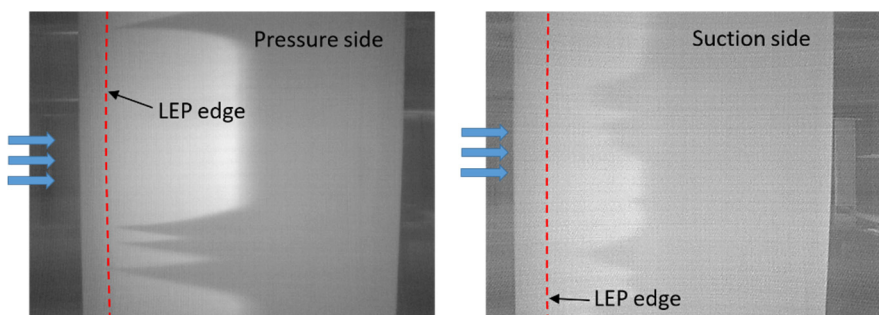


Figure 5.12: The impact of the second LEP layer on the location of transition for the lower (left) and upper (right) sides of the model at  $\alpha=6^\circ$ .

Nevertheless, as is shown in fig. 5.13, compared to the first LEP layer the performance was dramatically improved, with a good replication of the smooth model drag below  $4^\circ$  incidence. Above  $4^\circ$  the drag increases, most likely due to a more forward located transition as a result of disturbances induced by the LEP-edges, maybe slightly amplified by the varying angle of attack over the span. In general the lift curve was only slightly

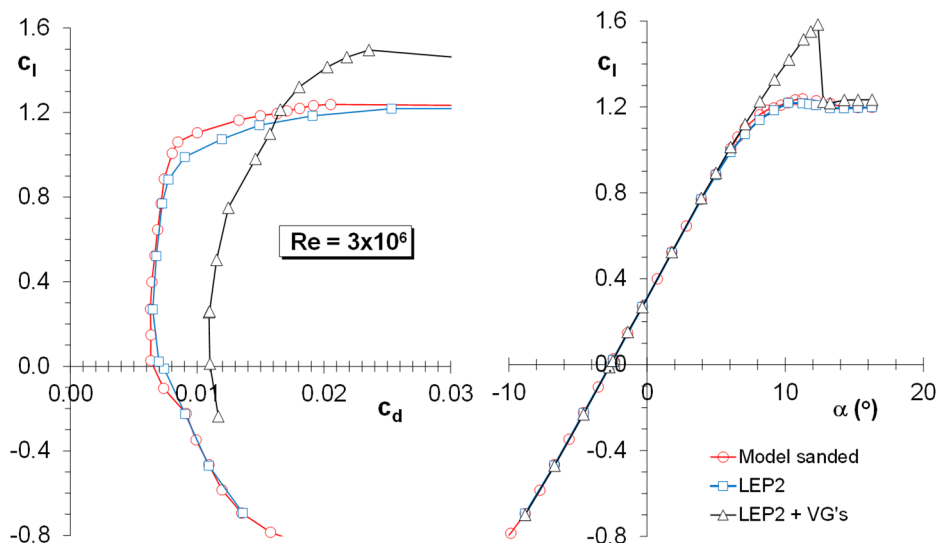


Figure 5.13: The impact of 3mm high vg's at  $x/c=50\%$  on the performance of the model equipped with the second layer of leading edge protection (LEP2).

affected near the upper boundary of the drag bucket. The application of the 3mm high vg's at 50% chord postponed separation and increased the maximum lift coefficient to 1.58. Without transition near the leading edge, the boundary layer is now much thinner at the 50% chord location, which makes the vg's more effective.

This can also be deduced from fig. 5.14, where the lift-drag ratio is presented for the smooth model and the model with LEP2 and LEP2 with vg's. Due to the higher drag at the upper boundary of the drag curve, the lift-drag ratio of the model with LEP2 is consistently about 20 points lower compared to the smooth model for angles higher than  $7^\circ$ , but

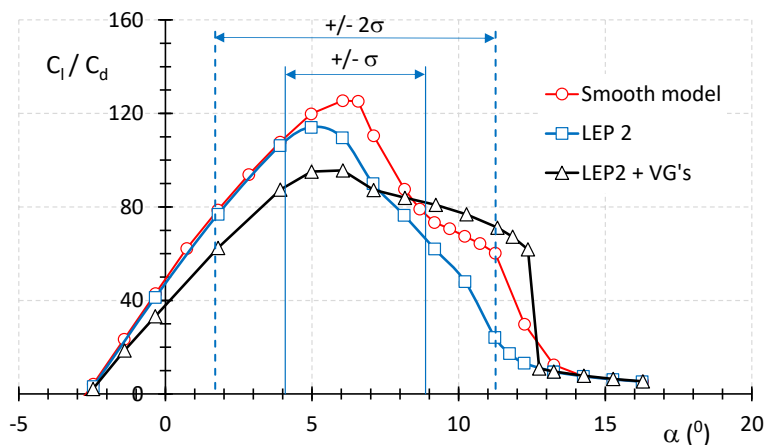


Figure 5.14: The impact of the second LEP layer and the configuration with vg's on the model efficiency in terms of the lift-drag ratio. Lines give calculated  $\alpha$ -variations due to turbulence at rated wind speed.

considerably higher than the first LEP configuration given in fig. 5.8. Due to the higher lift, at angles above  $8.5^\circ$ , the vg's even raise the lift-drag ratio above the level of the smooth model, until separation starts to develop upstream of the vg's at  $12.8^\circ$ , well outside the operational  $\alpha$ -range at rated wind speed.

Table 5.2 presents the expected lift-drag ratio under turbulent conditions according to equation 4.14. It shows the significant possible reduction of blade segment efficiency when erosion measures adversely impact drag. This can only partly be ameliorated by the application of vortex generators. When the leading edge protection does not harm the flow over the airfoil, in case of LEP2, vortex generators, although suppressing separation to some extent, contribute to losses due to their additional drag prior to stall.

*Table 5.2: The expected lift-drag ratio weighted over 90% occurrence of angle of attack perturbations*

	Clean	LEP	LEP+VG's	LEP2	LEP2+VG's
Average L/D	99.3	55.4	67.3	92.9	88
$\Delta$ (%)		-44.2	-32.2	-6.4	-11.4

## 5.5 TRAILING EDGE SERRATIONS

Aiming at attenuating the aerodynamic noise, predominantly coming from the outer 40% of the blade, thin sheet metal serrations are attached to the trailing edge. The depth of the serrations is scaled with the chord. Dimensions typical for the mid-span of the model are given in Fig. 5.15.

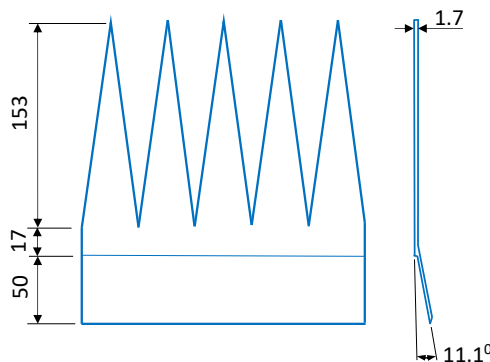


*Figure 5.15: Dimensions of the serrations.*

The serrations, which work as a flap, change the aerodynamic characteristics in two ways:

1) The added flap enlarges the “wing” surface and consequently also increases the model friction drag.

2) The flap angle changes the airfoil overall camber and affects the lift potential of the airfoil and consequently the zero-lift angle.

Especially the second consequence of adding a flap is very important, as it may significantly increase the loads on a blade segment and change the maximum lift coefficient, which may contribute to fatigue as well. Furthermore the efficiency of the blade segment in terms of the lift-drag ratio may be affected. The serrations work best in an attached flow. If the flow starts to separate in an early stage, e.g. due to increased camber, the serrations even may contribute to the noise.

### 5.5.1 The EWT-serrations

In the EWT-case the serrations are attached to the upper surface trailing edge where the relatively flat surface provides ease of installation. The angle  $\beta$  in the attachment plate matches the trailing edge angle, which brings the serrations in line with the chord. The added surface effectively increases the chord of 0.86m at the mid-span position to 0.9535m (ratio 1.1087), and changes the model maximum relative thickness to 18.9%, which parameters also have been used in the wall correction scheme.

Unfortunately, no test have been conducted in the operational configuration. Alternatively, the serrations were attached to the lower side trailing edge, putting the serrations in line with the upper surface trailing edge angle, resulting in a positive flap deflection of about  $11^\circ$ . The serrations cause a sinewave-like pattern in the drag recorded by the wake rake. The final average drag was calculated from a traverse containing 6 periods.

Serrations were attached to the model with the original LEP and to the model with the second, modified version (LEP2). To understand the differences with the configuration having the serrations in line with the chord, RFOIL calculations were performed on the NACA 63-421 airfoil with a TE-extension consisting of a 0.2% thick plate with a flap length

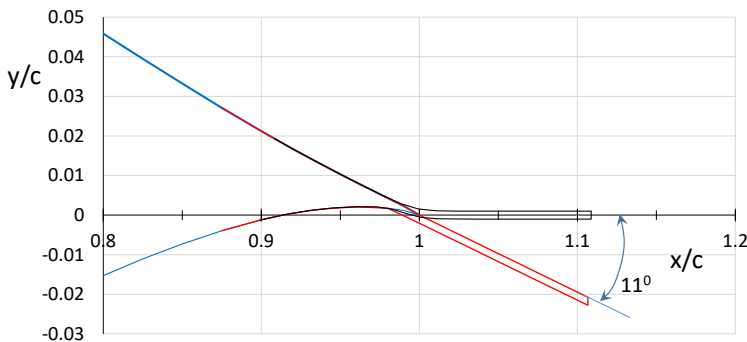


Figure 5.16: NACA 63<sub>4</sub>-421 airfoil section with metal sheet flap deflections  $\beta$  of  $0^\circ$  and  $11^\circ$  at the trailing edge.

of 10.87% of the chord. The resulting shapes are depicted in fig 5.16. All characteristics are shown with reference to the original model chord.

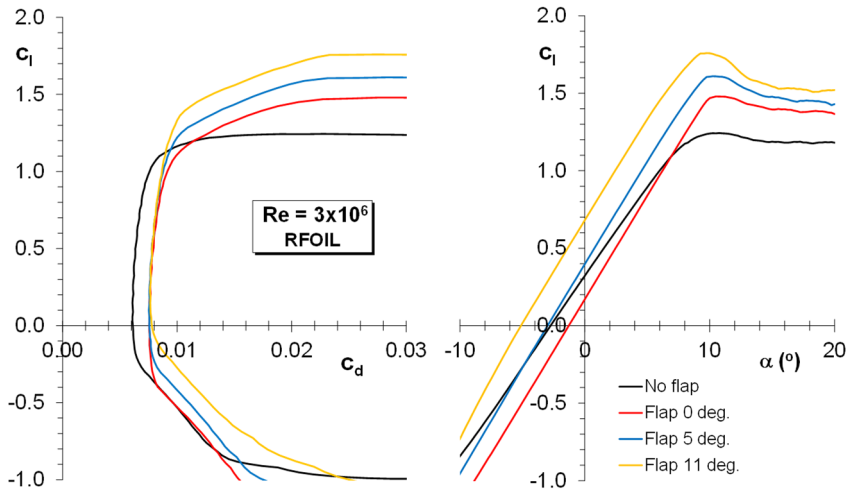


Figure 5.17: The RFOIL calculated impact of a flap addition and its deflection on the performance of airfoil NACA 63<sub>3</sub>-421.

Fig. 5.17 presents the impact of a flap addition and its deflection  $\beta$  on the performance, determined with RFOIL. The addition of the flap increases the drag in the low drag region with app. 0.0015. With varying flap angle this remains relatively constant and the performance shows the expected variation in the lift and drag associated with a change in airfoil camber. The  $\beta=0$  configuration de-cambers the airfoil and up to about  $8^\circ$  angle of attack the lift stays below the no-flap lift curve.

The flap carries a diminishing negative lift up to this angle. As the pressure distributions in fig. 5.18 show, at  $\alpha=8^\circ$  and  $\beta=0^\circ$ , the flap does not contribute to the lift. Beyond  $8^\circ$  the impact of separation is mitigated by the flap and the circulation is increased with respect to the no-flap configuration and the flap starts to carry positive lift.

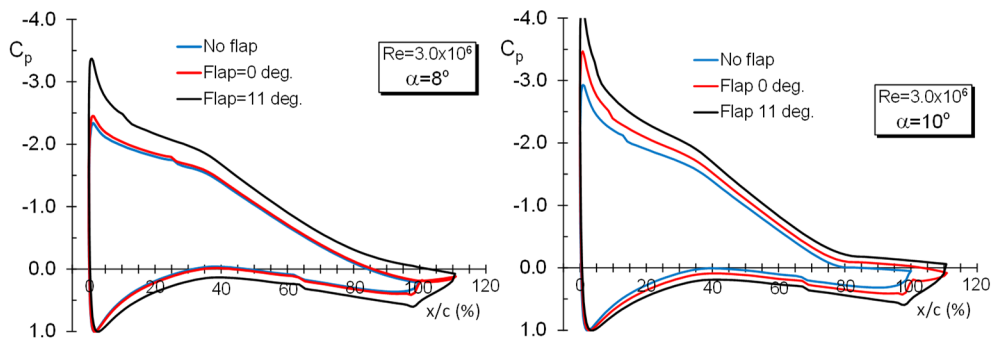


Figure 5.18: The impact of a flap and flap deflection variation on the pressure distributions of airfoil NACA 63<sub>3</sub>-421. RFOIL calculations, including weight factors.

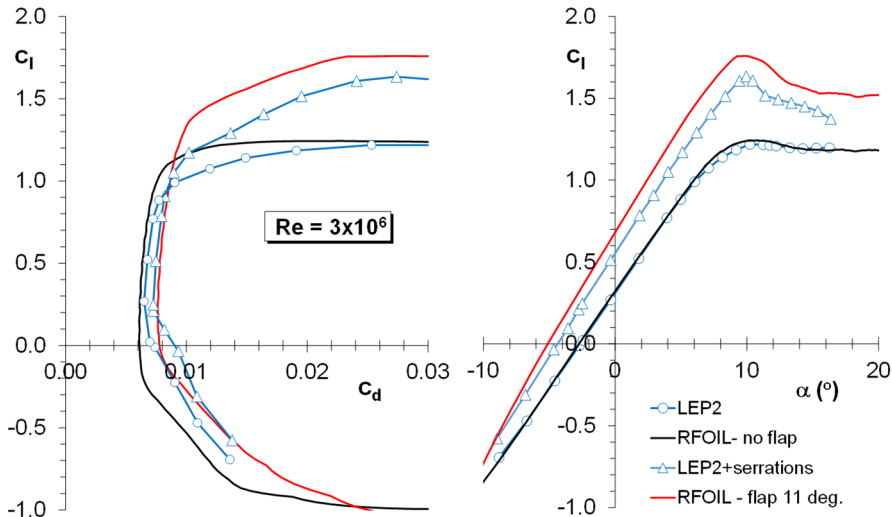


Figure 5.19: The impact of serrations on the performance of the model with the modified LEP (LEP2).

Comparison with the measurements, presented in fig. 5.19, shows that the drag increment due to the serrations in the test is smaller, in the order of 0.0007 to 0.00075 (which is about 50% of the difference between the RFOIL calculations). The RFOIL maximum lift and lift gradient are much higher than tested. The RFOIL predictions confirm the trend of the serrations under  $11^\circ$  deflection to increase the lift considerably. The maximum lift coefficient is raised from 1.219 to 1.633.

### 5.5.2 Approximation of the $\beta=0$ characteristics

Due to the serrations, the flap in the experiment will be less efficient in generating loads than an actual straight edged flap. With a serrations flap efficiency of 70% the RFOIL and experimental lift curves match relatively well, both for the LEP (computations with fixed transition) and LEP2 tests, as is depicted in fig. 5.20. Using the same flap efficiency, the lift curve for the configuration with the serrations pointing in chord wise direction can be determined from the RFOIL computations with  $\beta=0^\circ$ .

While the RFOIL computations in fig. 5.16 show no significant drag variation in the low-drag region due to a flap deflection, a study conducted by Llorente and Ragni (2020), including a 30% thick airfoil (ADO30) and an 18% thick airfoil (NACA 64<sub>3</sub>-418), reports various drag increments resulting from serrations deflection angles in the range of  $\beta=0^\circ$  to  $10^\circ$ .

In the low-drag region, the thicker airfoil showed a continuous increase in drag with increasing  $\beta$ , although the step from  $0^\circ$  to  $5^\circ$  was smaller than from  $5^\circ$  to  $10^\circ$ . In the low-drag region, the NACA airfoil only had a drag increase going from flap angle  $5^\circ$  to  $10^\circ$ . Using data from the NACA low-turbulence pressure tunnel (Abbott et al., 1945), Timmer (2009) showed, that considerable airfoil camber changes, e.g from NACA 64<sub>3</sub>-018 to 64<sub>3</sub>-

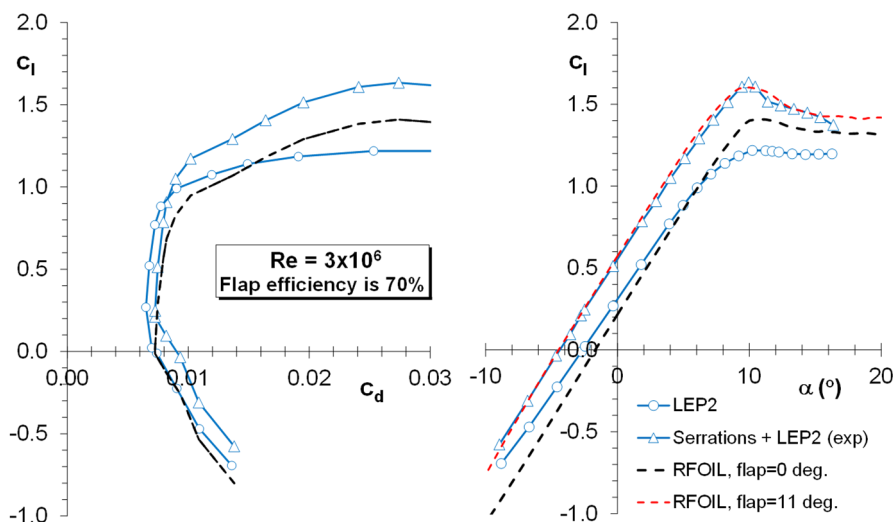


Figure 5.20: The impact of serrations with  $\beta=0^0$  and  $11^0$  on the characteristics of the model with LEP2, using 70% flap efficiency in the RFOIL lift calculations.

618, did not result in a notable increase in drag at incidences in the low-drag region. Taking this into account, the  $C_d$ - $C_l$  curve for  $\beta=0^0$  has been approximated by lowering the drag values of the  $\beta=11^0$  configuration with 0.00036 (half of the difference between the  $\beta=11^0$  and the LEP2 no-serrations configurations), and reducing the associated lift with the lift increment resulting from the camber change, as calculated by RFOIL and shown in fig 5.17. Finally, fig. 5.20 presents the resulting characteristics for the LEP2 configuration at  $\beta=0^0$ .

### 5.5.3 Blade segment efficiency

In terms of efficiency, fig. 5.21 shows the variation of the lift-drag ratio with angle of attack for the various configurations. Despite the fact that the drag increment due to the leading edge protection was minimized as much as possible, compared to the smooth model, the efficiency of the model with both LEP2 and serrations with  $\beta=0^0$  has decreased considerably in the operational range of incidences. Taking the level of occurrence in a normal distribution into consideration (68.2% of the time the angle is within  $4.1^0$  and  $8.9^0$  and 13.6% in the range  $1.7^0$  to  $4.1^0$  and  $8.9^0$  to  $11.3^0$ ), the efficiency at rated wind speed has decreased with almost 30%, of which 14% is due to the serrations.

As a result of the early transition triggered by the first LEP layer, the lift-drag ratios of the LEP configurations all are significantly below those of the smooth model (fig. 5.22). The  $\beta=0^0$  configuration here was obtained by taking the RFOIL fixed transition computation ( $x/c=5\%$  u.s. and  $10\%$  l.s.) for this angle and applying a 70% flap efficiency. As the experiment showed little drag difference between the LEP curve and the  $\beta=11^0$  configuration, the drag remained unchanged.

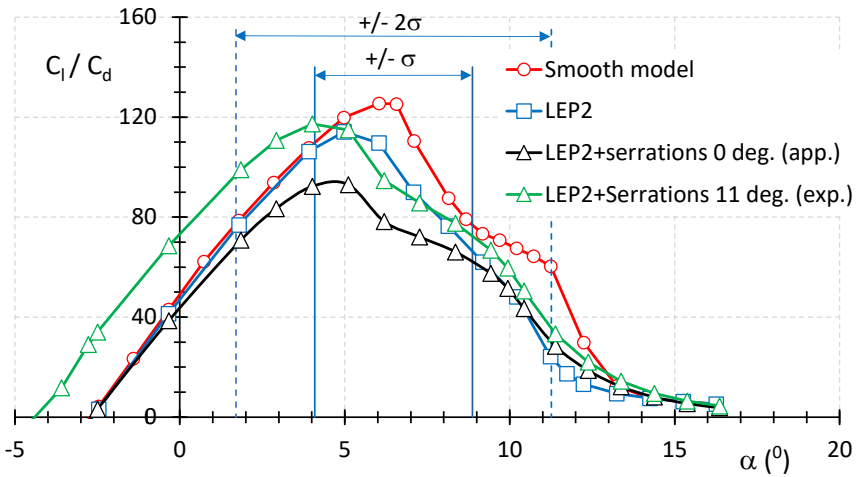


Figure 5.21: The impact of serrations angle  $\beta$  on the lift-drag ratio in the LEP2 configuration.  $0^\circ$  serrations data from previous graph.

While the serrations curves in fig. 5.22 are relatively flat in the operational range of incidences, the maximum lift-drag ratio's for increasing serrations angle of the LEP2-model tend to shift to lower incidences. When serrations are considered as an add-on in the design process, reducing the design angle (and staying closer to the initial design lift coefficient) lets the blade profit more from the top of the lift-drag curves at the rated wind speed.

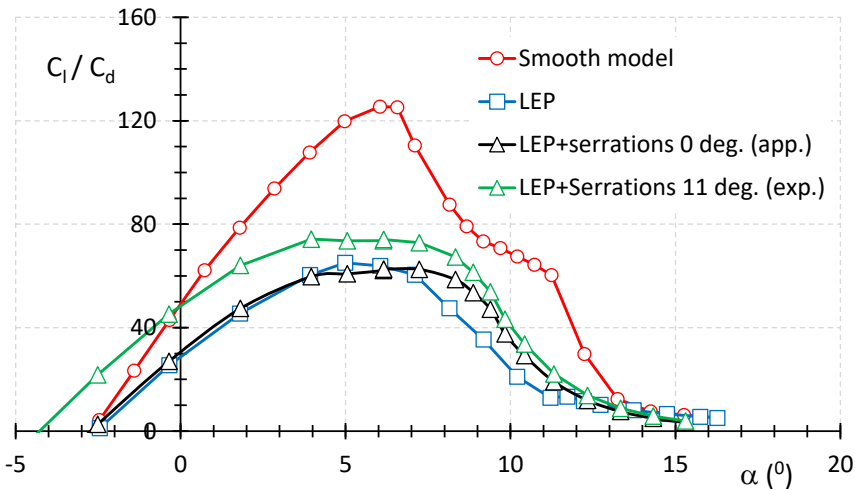


Figure 5.22: The impact of serrations angle  $\beta$  on the lift-drag ratio in the standard LEP configuration.

#### 5.5.4 Higher loads

It is clear from fig. 5.20 that, despite the de-cambering of the model due to the serrations at  $\beta=0^\circ$ , the maximum lift has increased, from 1.22 to 1.41, which means an increase in

maximum load of more than 15%. As fig. 5.17 indicates, any serrations angle will give a higher maximum lift. Combination of the  $\beta=0^\circ$  serrations with the VG's discussed in the previous paragraph (fig. 5.13 and 5.14) will increase the drag further and postpone separation to a higher angle. This will make the performance at angles of  $8^\circ$  and beyond more robust, but will most likely also increase the maximum lift coefficient, and consequently the loads, even more. The earlier mentioned study by Llorente and Ragni (2020) showed an improvement of the electric power due to serration extensions up to about 1.6% at a wind speed of 9 m/s for a 3MW turbine during field tests. Computations for this turbine also showed higher ultimate and fatigue loads.

### 5.5.5 Estimation of the lift increase due to serrations.

The lift curve for serrations with  $\beta=0^\circ$  was acquired by using a combination of RFOIL computations and experiment. Llorente and Ragni (2020) presented an equation to estimate the lift curve of a configuration with a specific serrations depth ( $l_{ser}$ ) and angle ( $\beta$ ):

$$C_{l_{ser}} = (C_{l_0} + 2\pi\beta \frac{l_{ser}}{c}) + 2\pi(1 + \frac{l_{ser}}{c})\alpha \quad (5.1)$$

in which  $C_{l_0}$  is the  $C_l$  of the base airfoil at  $\alpha=0^\circ$  and  $\alpha$  and  $\beta$  are in radians. The first part inside the parentheses at the right hand side of the equation is the new lift coefficient at  $\alpha=0^\circ$ , the following part is the new lift gradient. Figure 5.23 presents the 4 curves

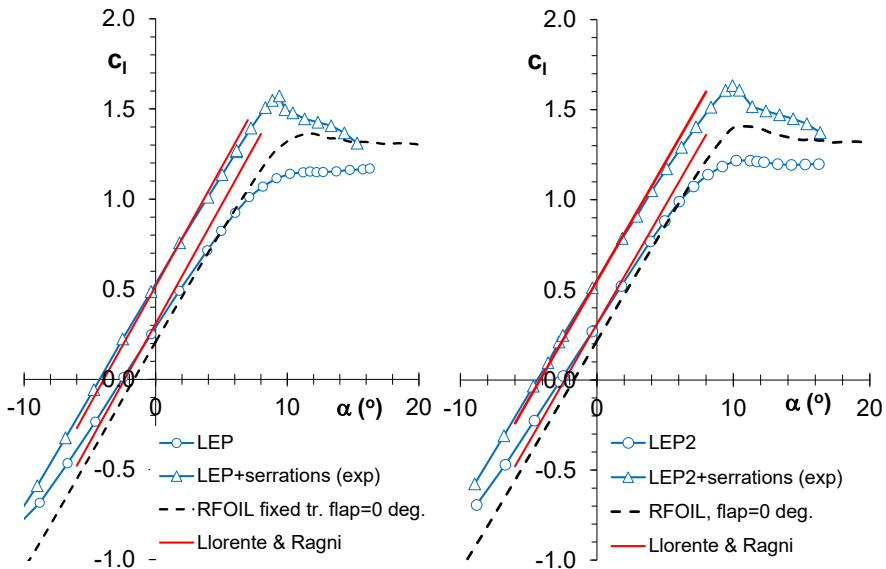


Figure 5.23: The lift curves for  $0^\circ$  and  $11^\circ$  serrations angle as predicted by Llorente and Ragni (eq. 3.20). The original leading edge protection layer is shown on the left and the modified version on the right.

predicted using equation 5.1. It is immediately clear that for  $\beta=0^\circ$  the predicted lift coefficient at  $\alpha=0^\circ$  using eq. 5.1 equals the value of the base airfoil, which is in contrast to what is shown in fig. 5.20. Intuitively, at  $\alpha=0^\circ$  and  $\beta=0^\circ$ , one would indeed expect a lift coefficient lower than the base airfoil, since the flow direction at the trailing edge is significantly bent upwards, bringing less curvature into the flow. For  $\beta=11^\circ$  the lift coefficient at zero incidence is well captured both with LEP and LEP2. The lift gradients, however, seem a bit too high.

Equation 5.1 does not seem to account for a less efficient flap resulting from the serrations. Furthermore, for  $l_{ser}=0$  (no serrations) the lift curve for the base airfoil should be replicated. While being reasonably accurate for thin airfoils, the  $2\pi$  theoretical lift gradient is too low for thicker airfoils having a smooth surface. In case of the LEP in figure 5.8 the base airfoil lift gradient is 0.1094 per degree ( $-2^\circ < \alpha < 6^\circ$ ), for which  $2\pi$  ( $0.1097/^\circ$ ) is perfect. The LEP2 configuration, however, gives  $0.1148/^\circ$ , a 4.4% higher lift gradient. To account for the serrations flap efficiency, the lower lift coefficient at  $\alpha=0^\circ$  when  $\beta=0^\circ$  and the deviant lift gradient for thicker airfoils with near natural transition, the following modification of eq. 5.1 is proposed:

$$C_{l_{ser}} = (C_{l_0} + \frac{2\pi}{57.3} (2\beta - 6)\eta \frac{l_{ser}}{c}) + \left( \frac{dC_l}{d\alpha} \right)_0 (1 + \eta \frac{l_{ser}}{c})\alpha \quad (5.2)$$

Here,  $\eta$  is a flap efficiency factor. The index 0 refers to the base airfoil. Angles are in degrees. Using  $\eta=0.7$  the current curves for  $\beta=0^\circ$  and  $11^\circ$  could be well reproduced, as is depicted in fig. 5.24. While equation 5.2 is giving very good results for the present

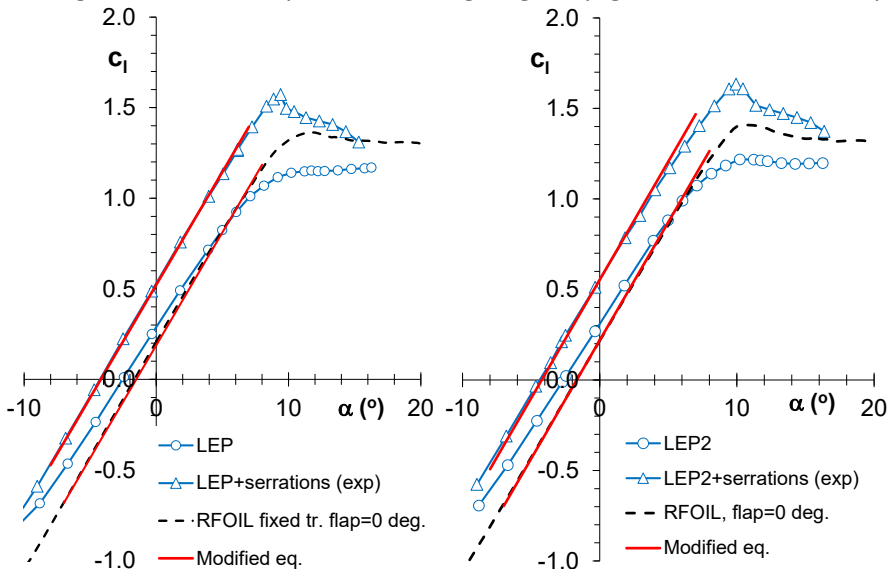


Figure 5.24: comparison of the lift curves generated with RFOIL for  $\beta=0^\circ$  and experiments for  $\beta=11^\circ$  with the prediction using eq. 5.2

configurations, it does not pretend to be generally applicable. Especially the term  $(2\beta-6)$  in combination with the efficiency factor  $\eta$  might be different for other type of serrations. The latter may be different, as in the EWT case the serrations do not start right at the trailing edge, as is show in fig. 5.15

## 5.6 CONCLUSIONS

### The impact of paint and LEP layers

The model, drawn from an actual wind turbine blade mould, resembles the NACA 63<sub>4</sub>-421 airfoil.

Using RFOIL with multiplication factors based on DU93 LTT-measurements, a good approximation of the NACA 63<sub>4</sub>-421 airfoil characteristics at  $Re=3 \times 10^6$  as would be measured in the LTT could be established.

Without additional quality checks, particles in the blade polyurethane paint already caused premature transition at many model span locations, leading to an approximate 22% reduction in efficiency of the affected area.

The application of a manufacturer standard LEP layer stretching from  $x/c=4\%$  at the upper side to 4.5% on the lower side resulted in a 48% reduction in maximum lift-drag ratio due to immediate transition at the LEP edges. This loss could be reduced with 6.5% using 3mm high vortex generators at  $x/c=50\%$ .

A second LEP-layer (LEP2) stretching from  $x/c=13\%$  on the upper side to 13.5% at the lower side with smoothed edges dramatically improved LEP-performance. At angles beyond  $4^\circ$  incidence the drag was higher, resulting in an efficiency reduction of 9%. Due to the additional pre-stall drag, the maximum lift-drag ratio could not be raised by a row of vortex generators.

The average lift-drag ratio of the section with these surface modifications under turbulence was calculated using eq. 4.14. The early transition induced by the standard LEP caused the average model L/D to drop from 99.3 to 55.4, which could be raised by vortex generators to 67.4, a loss of 32%. The second, modified, LEP showed an average L/D of 92.9. a loss of 6.4%. The example shows that it is of paramount importance to avoid early separation produced by the edges of LEP layers. A longer layer ending at a more aft located chord station with carefully smoothed edges is required to approach the intended clean average lift-drag ratio.

Taking into account the various sources potentially triggering early transition, it is hard to imagine that a blade section in normal operation will have a substantial laminar part. Atmospheric testing on rotating blades (Aagaard Madsen et al. 2019, Reichstein et al. 2019) reveals transition occurring close to the leading edge in a large portion of the test due to surface irregularities or blade contamination. This may potentially have implications for airfoil design, as optimization can be done for a fully turbulent flow.

### **The impact of serrations**

As the intended angle ( $\beta=0^\circ$ ) for installed standard serrations was not tested, the characteristics for this configuration were estimated using measurements with a serrations angle of  $\beta=11^\circ$  and RFOIL calculations on the airfoil with an additional 0.1087 chord thin plate flap, using a 70% efficiency to account for the flap having serrations, instead of a straight edge.

The lift-drag ratio for the standard LEP was improved slightly for incidences above the design angle. Due to the decambering effect of the serrations with  $\beta=0^\circ$ , the lift-drag ratio in the LEP2 configuration was always below the non-serrated case in the range of operational angles of attack.

## **5.7 REFERENCES**

Aagaard Madsen, H., Özçakmak, Ö.S., Bak, C., Troldborg, N., & Sørensen, N.N. (2019). *Transition characteristics measured on a 2MW 80m diameter wind turbine rotor in comparison with transition data from wind tunnel measurements.* In

De Tavernier, D.A.M. (2021) *Aerodynamic advances in vertical-axis wind turbines.* Doctoral thesis (2021), Delft University of Technology.

De Tavernier, D.A.M. (2025) *Personal correspondence.* December 2024 and January 2025.

Llorente, E. and Ragni, D. (2020) *Trailing-edge serrations effect on the performance of a wind turbine.* *Renewable Energy* 147 (2020) 437-446  
<https://doi.org/10.1016/j.renene.2019.08.128>

Proceedings of the AIAA Scitech 2019 Forum [0801] Aerospace Research Central (ARC).  
<https://doi.org/10.2514/6.2019-0801>

Reichstein, T., Schaffarczyk, A.P., Dollinger, C., Balaesque, N., Schüle, E., Jauch, C. and Fischer, A. (2019) *Investigation of Laminar–Turbulent Transition on a Rotating Wind-Turbine Blade of Multi-megawatt Class with Thermography and Microphone Array.* *Energies*, June 2019

Timmer, W.A. (2009) *An overview of NACA 6-digit airfoil series characteristics with reference to airfoils for large wind turbine blades*. AIAA 2009-268



# PART II

**Dynamic effects  
and performance  
in separated flow**



## BACKGROUND

As a result of the inherently unsteady environment, wind turbine blades always are subjected to dynamic effects. Turbulence, yaw misalignment and wind shear cause inflow variations. Blade flapping motions at angles close to maximum lift may result in a large overshoot of blade normal forces (dynamic stall). In case of variable-rpm, pitch machines, however, angle of attack excursions on the outer 50% of modern wind turbine blades, where most of the power is generated, are mostly restricted to  $4^\circ$  to  $5^\circ$  beyond the static stall angle. In case of stall control, when blade angles increase with higher wind speeds, excursions in angle of attack, as a result of dynamic inflow or blade motions, may cause

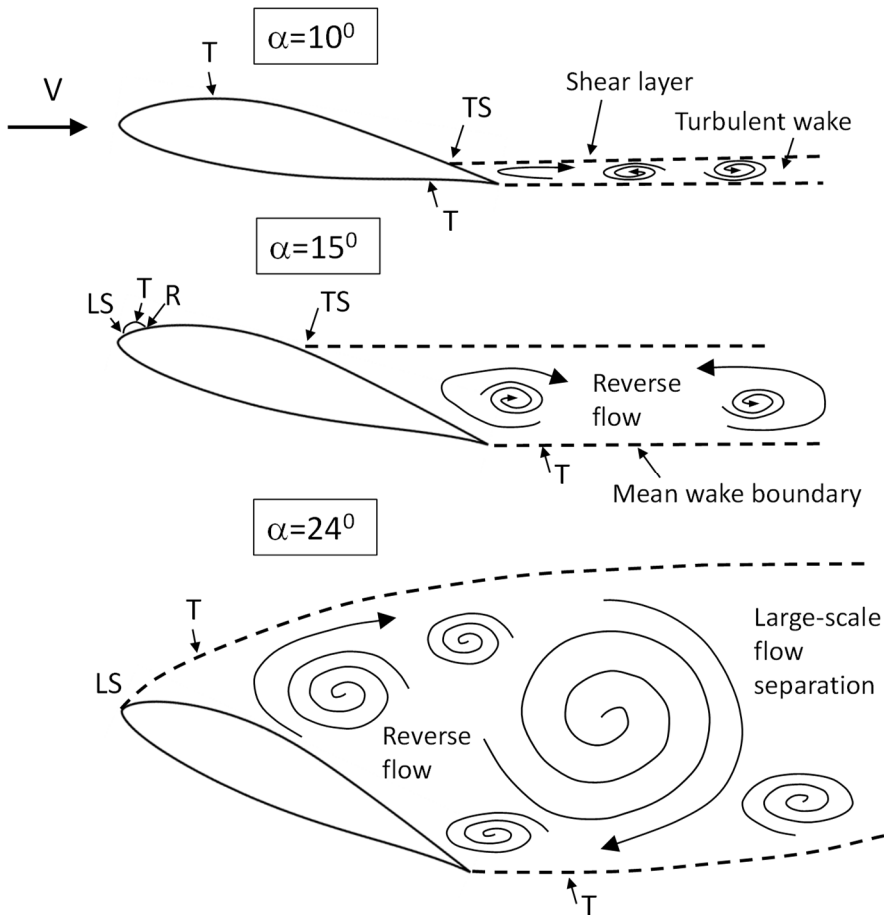


Figure PII-1: Sketch of the flow field around airfoil DU96-W-180 with increasing angle of attack. T is transition, TS is turbulent separation, LS is laminar separation, R is reattachment,  $Re=1 \times 10^6$ . Scale and direction of vortex structures merely shown to underline flow complexity.

leading edge separation, leading to drastic changes in loading. Fig. PII-1 shows dramatically simplified sketches of the flow field around DU96-W-180 with increasing angle of attack for  $Re=1.0 \times 10^6$ . At  $\alpha=10^\circ$  the airfoil is around the maximum lift coefficient

(1.27) with upper surface transition at  $x/c=25\%$  and turbulent separation at about  $x/c=90\%$ . The drag coefficient is 0.0139. At  $15^\circ$  a laminar separation bubble is present on the leading edge and turbulent separation takes place at about mid-chord ( $C_d=.085$  and  $C_l=1.08$ ). At an angle of  $24^\circ$  the shear layer has detached from the leading edge, resulting in massive separation over the airfoil. Transition takes place off surface most likely due to Kelvin-Helmholtz instabilities of the free shear layer. The lift coefficient has decreased to 0.85 and the drag coefficient has increased to 0.425.



*Figure PII-2: Flow visualization of an airfoil at about  $20^\circ$  incidence showing leading edge separation. Photo DLR-CC BY 3.0 (Wikimedia Commons)*

A classic picture of the flow field in this condition is depicted in figure PII-2. It shows what resembles a NACA 4415 or a Gö 387 airfoil at about  $20^\circ$  angle of attack featuring a detached shear layer at the leading edge. The flow was visualized with aluminum particles in water. Clearly larger and smaller counter-rotating vortices can be detected in the flow above the airfoil and in the wake. The leading edge vortices are convected downstream, where they interact with the shed vorticity of the trailing edge, forming a von Kármán vortex street. The unsteady flow just above the airfoil and in the wake, of which fig. PII-2 only shows a mean flow state, is very complex, as is depicted in fig PII-3.

It shows the vorticity magnitude from simulations with TCAE software (DES, with the  $k-\omega$  turbulence model) of the flow over a NACA 0012 airfoil at 6 consecutive time steps a) to f).  $Re=7 \times 10^4$  and  $\alpha=25^\circ$  (CFDSupport, 2023).

Conditions associated with leading edge separation are generally referred to as deep-stall, as also will be done in the remainder of this dissertation. Low angles of attack refer to angles between the primary minimum and maximum lift coefficients. In this document medium high incidences refer to angles between  $C_{l,max}$  and the deep-stall angle. High angles of attack are those beyond the deep-stall angle.

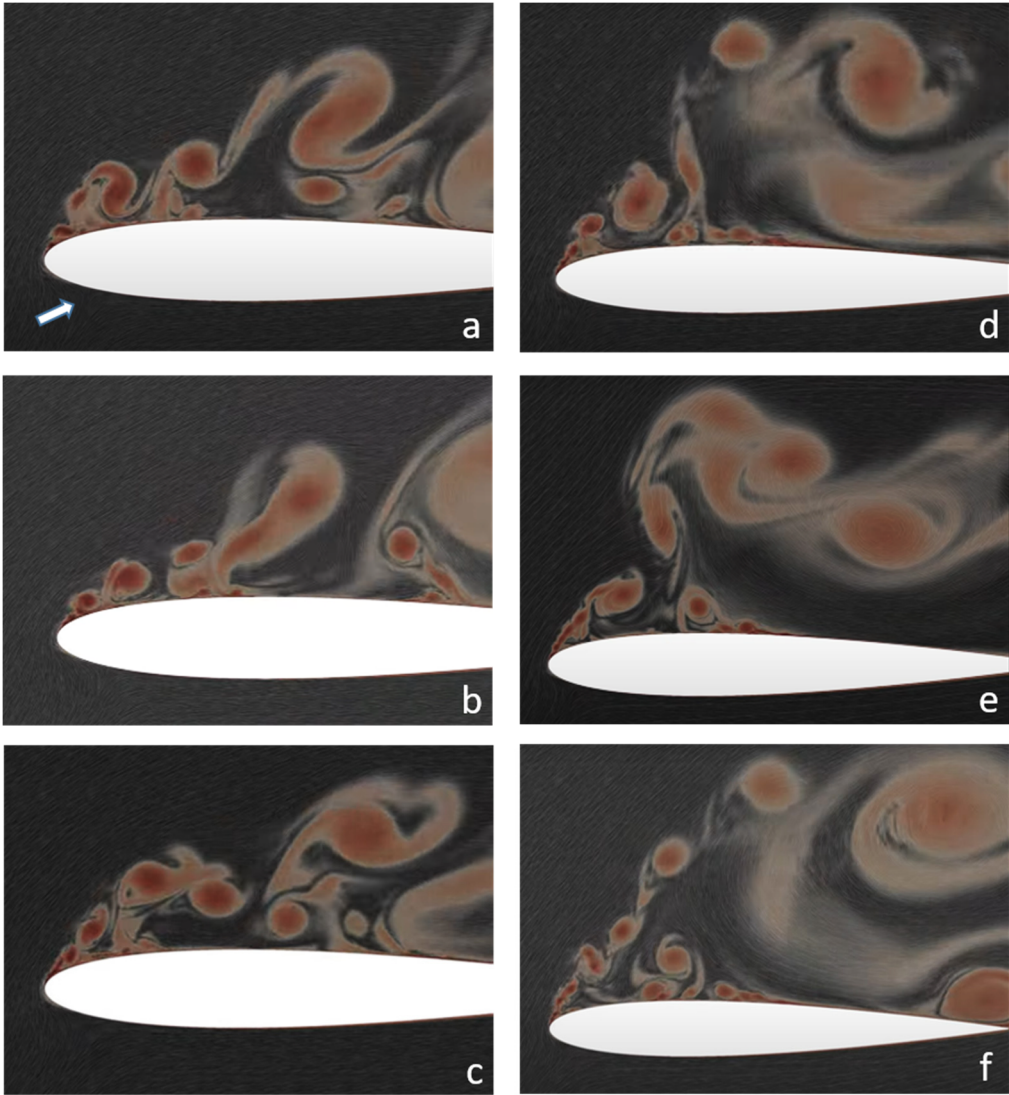


Figure PII-3: The vorticity magnitude during 6 consecutive time steps of the simulated flow over NACA 0012 at  $25^\circ$  incidence. Stills from a CFD-movie by CFDsupport (2023)

### AIRFOIL CHARACTERISTICS IN DEEP-STALL

During the introduction of stall rotors, in fact little was known about the detailed behaviour of airfoils in the deep-stall region. The few existing measurements, other than those on flat plates, were mainly performed for the purpose of helicopter blade analysis, such as on airfoil NACA 0012 (e.g. Critzos et al., 1955). Owing to compressibility effects these airfoils are relatively thin and the few measurements that existed showed performance in deep-stall conditions close to that of flat plates. Flat plate deep-stall data were consequently used as input to stall rotor BEM calculations and 3D-correction

methods (e.g. Viterna and Janetzke, 1982). It was not until the late nineteen seventies that a number of wind tunnel tests were devoted to measure the deep-stall characteristics of other airfoil shapes than those of the NACA family of airfoils (e.g. Satran and Snyder, 1977). Most of the existing data on high angle of attack characteristics date from the 1980's and 90's.

As the variable speed pitch machines made their entrance, the need to investigate the deep-stall characteristics in more detail vanished, leaving only the attention for symmetric airfoils with relatively moderate thickness in view of VAWT-application. However, during hoisting, starts and stops, idling and standstill also blades of modern horizontal axis wind turbines encounter conditions at which high angles of attack occur.

A computational study on rotor standstill vibrations has been performed e.g. by Skrzypinski (2014), using airfoil DU96-W-180. Mac Gaunaa et al. (2016) presented an engineering model approach to account for the forces on a blade in these situations, also based on CFD. Most of the studies, however, focus on a specific application or turbine. Despite the impressive increase of computational power and the versatility of CFD in recent years, still a thorough computation of a complete  $360^\circ$  polar with a high fidelity code for just one airfoil is a time consuming and expensive exercise (Sørensen and Timmer, 2017). Sørensen performed simulations on DU97-W-300 in the angle of attack range from  $0^\circ$  to  $360^\circ$  and found that 2D computations with RANS-methods for separated flow conditions either gave a severe undershoot of the drag coefficient in steady computations, or a severe overshoot of  $C_d$  for unsteady simulations. In both cases prediction of the trend in lift coefficient with angle of attack failed. The study revealed that a span of at least 4 times the chord was needed to resolve the 3D structures in the flow. Only 3D Delayed Detached Eddy Simulation (DDES) on a grid of 56 million cells gave results that compared favourably with experiments.

No doubt, looking at the rapid development of computational capabilities, maybe even within the coming decade, CPU time becomes cheap enough to generate computations within acceptable limits in terms of time and costs. Until then, and to validate computations at angles of attack giving leading edge separation, data from aerodynamic experiments on a variety of airfoils at such angles are indispensable. Also, many engineering models need airfoil data at large angles as input. This not only necessitates experiments on airfoils in deep-stall, but also justifies the effort to investigate any coherence between the performance of different airfoils in relation to their shape in the range of angles of attack showing flow separation over the entire chord.

It will be clear that these experiments have their own challenges, as an airfoil model at high incidence may cause severe blockage of the test section, in turn yielding inaccurate estimates of the aerodynamic forces. Blockage correction schemes devised in the past decades for "streamlined" objects featuring attached flow, may prove inadequate to

correct for the flow conditions developing over a blunt object, such as an airfoil at very high incidence. For high quality results, the validity, accuracy and boundaries of these corrections methods for high blockage will consequently be part of the investigation. Appendix A summarises the blockage corrections for attached flow conditions and provides a discussion on Maskell's method, which was followed in this dissertation. The method corrects for blockage at very high angles, featuring detached flow at the leading edge. Although comparisons of measurements in this dissertation and uncertainties in the theory (see Appendix A) seem to indicate that Maskell's semi-empirical blockage constant might need adjustment to a higher value (in the range 1 to 1.03), for the sake of aligning with existing literature here the classical value of 0.96 has been used.

## **CHAPTERS IN PART II**

The heavily separated flow region above an airfoil and in its wake discussed here, starts with the angle for which leading edge separation (LES) occurs, i.e. the boundary layer separates directly at the leading edge and enters the deep-stall region.

In Part II, first this angle for deep-stall will be further investigated as it differs significantly for thin and thick airfoils (Chapter 6). The impact of airfoil shape, blockage, Reynolds number and leading edge roughness will be discussed. In Chapter 7, the angle of attack will be extended up to and beyond  $90^\circ$  both for positive and negative values, with a discussion on the impact of Reynolds number, blockage ratio and model aspect ratio. Chapter 8 reports the vortex shedding frequency at these large angles for low and high Reynolds numbers. Next, chapter 9 presents a prediction method for airfoil maximum drag coefficients for low and high Reynolds numbers, in which the leading edge shape and the trailing edge angle play a prominent role. Chapter 10 concludes Part II. It treats the lift-drag ratio of airfoils in deep-stall, for two-dimensional cases as well as for situations where the airfoil is incorporated in a blade, both non-rotating and rotating.

Use has been made of a number of conference or journal contributions in which these subjects were first introduced: Timmer and van Rooij (2003), Timmer (2010) and Timmer (2020). The present document reports the most salient results from the above studies, with due modifications and additions resulting from advancing insight, made to fit them in the context of the present dissertation.

## **REFERENCES**

CFD Support website [www.cfdsupport.com/airfoil-aerodynamics-tutorial-naca-0012.html](http://www.cfdsupport.com/airfoil-aerodynamics-tutorial-naca-0012.html). Visited November 2023

Gaunaa, M., Larsen, T.J. (2002) *Stilstandslaster*; chapter in *Forskning i Aeroelasticitet*; ed. Bak, C.; Risø-R-1434(DA) in Danish, Risø DTU National Laboratory for Sustainable Energy;

Roskilde; 2002

Critzos, C.C., Heyson, H.H. and Boswinkle Jr., R.W. (1955) *Aerodynamic characteristics of NACA 0012 airfoil at angles of attack from 0 to 180 degrees*. NACA TN 3361, 1955

Skrzypinski, W. R., Zahle, F., & Bak, C. (2014) *Parametric approximation of airfoil aerodynamic coefficients at high angles of attack*. In Proceedings of EWEA 2014 European Wind Energy Association (EWEA).

Sørensen, N.N. and Timmer, W.A. (2017) *CFD prediction of airfoil deep stall performance using Improved Delayed Detached Eddy Simulations*. DTU Wind Energy, Department of Wind Energy, Lyngby, Denmark, June 2017.

Timmer, W.A. (2020) *A simple method to estimate the airfoil maximum drag coefficient*. *J. Phys.: Conf. Ser.* 1618 052068, (2020)

Timmer, W.A. (2010) *Aerodynamic characteristics of wind turbine blade airfoils at high angles-of-attack*. Proceeding of the 3rd EWEA Conference –Torque 2010: The Science of making torque from wind. Heraklion, Crete, Greece.

Timmer, W.A. and van Rooij, R.P.J.O.M. (2003) *Summary of the Delft University Wind Turbine Dedicated Airfoils*. *Journal of Solar Energy Engineering* 125(4) DOI:10.1115/1.1626129 (2003)

Viterna, A.L. and Janetzke, D.C. (1982) *Theoretical and experimental power from large horizontal-axis wind turbines*, 1982 DOE/NASA/20320-41 NASA TM-82944

Wikimedia Commons <https://commons.wikimedia.org/w/index.php?curid=61072555>. Accessed October 2023

# 6

## LEADING EDGE SEPARATION

### 6.1 INTRODUCTION

As CFD-codes still struggle with computing separated flows, a first step to understand leading edge separation phenomena is to study airfoils in a two-dimensional experimental environment. In this chapter this will be done using detailed wind tunnel measurements on a variety of models, mostly, but not exclusively, of DU airfoils. This enables us to study the impact on the deep-stall angle of airfoil shape, Reynolds number, leading edge roughness and test section blockage. Unless stated otherwise, the pressure distributions and the lift and drag curves presented in the following chapters have been corrected for wall interference.

### 6.2 RESEARCH QUESTION

Figure 6.1 presents the lift curves for two DU airfoils with a distinct difference in airfoil shape. The deep-stall angles clearly significantly differ, from  $23.5^\circ$  for the 18% thick airfoil

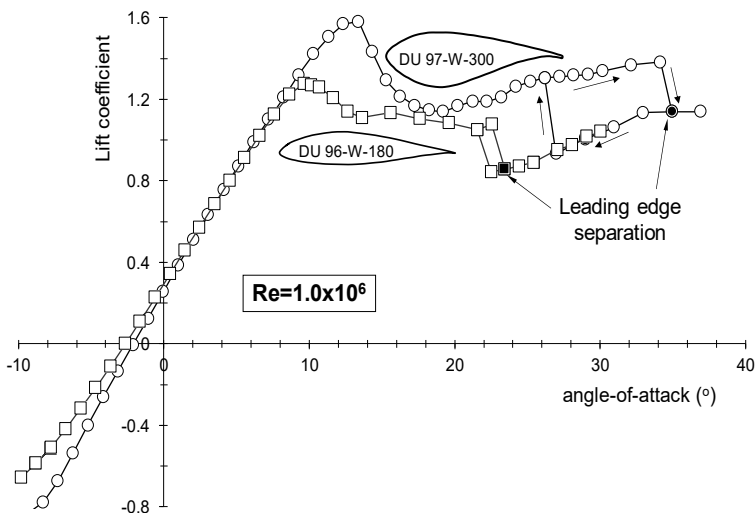


Figure 6.1: The lift curves of two DU airfoils showing leading edge separation.  
Experiments in TUD LTT

to  $35.3^\circ$  for the 30% thick DU 97-W-300. Both airfoils show a trailing edge separation type of stall. After passing the stall angle, the leading edge pressure peak grows with increasing incidence and BL-separation moves forward. Just before going into deep-stall, generally the flow already separates from the upper surface 20% to 25% chord station. With so much of the airfoil downwind side hidden in the wake, the development of the leading edge pressure peak mostly depends on the first 5% to 10% of the airfoil shape. Since this part of the airfoil obviously plays an important role, it was investigated if a first order prediction could be given for the link between the airfoil leading edge shape and the static deep stall angle on the basis of existing measurements. This was first briefly discussed in Timmer and van Rooij (2003). It brings us to the following research question:

*Research question RQ 6: Is there a connection between an airfoil deep-stall angle and its shape?*

Sub questions arise immediately:

*RQ 6.1: What is the impact of the leading edge shape?*

*RQ 6.2: What is the impact of the trailing edge shape?*

*RQ 6.3: What is the impact of the Reynolds number?*

*RQ 6.4: What is the impact of leading edge roughness?*

And, since this study focusses on wind tunnel measurements,

*RQ.6.5: Is there an impact of the testing environment?*

Each of these questions will be treated in the next chapters, using measurements of various airfoils, tested in the low-turbulence tunnel TUD LTT, if not indicated otherwise.

### 6.3 THE IMPACT OF THE LEADING EDGE SHAPE

Figure 6.2 (left) presents the lift curve of airfoil DU93-W-210 at a Reynolds number of  $1 \times 10^6$ . The sudden drop in lift at  $28.44^\circ$  for positive angles of attack, and at  $-25.09^\circ$  for negative angles, is associated with the collapse of the pressure peak at the leading edge

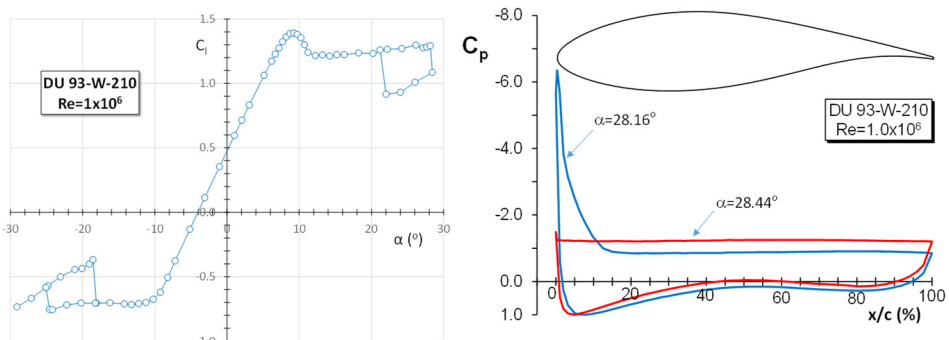


*Figure 6.2: The performance of airfoil DU93-W-210 (left) and the associated pressure distributions around the positive deep-stall angle (right) at a Reynolds number of  $1 \times 10^6$ .*

of the airfoil as a result of the bursting of a short laminar separation bubble on the upper and lower surface leading edges respectively.

For positive angles this bursting leads to the pressure distributions depicted on the right hand side in figure 6.2: the flow separates from the leading edge, causing a (time-averaged) constant pressure level over the entire airfoil upper surface.

### 6.3.1 The leading edge laminar separation bubble.

Figure 6.3 presents a schematic drawing of a short laminar separation bubble on the leading edge of an airfoil. Separation of the laminar BL takes place under the influence of an adverse pressure gradient. As a result of this separation, the wall shear stress locally vanishes. The separated shear layer becomes unstable at some distance from the separation point, developing either Kelvin-Helmholtz like instabilities (Alam and Sandham

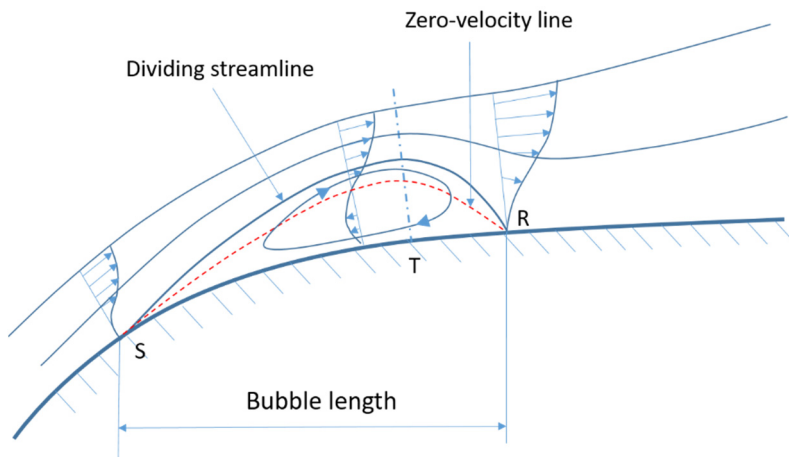


*Figure 6.3: A schematic of a laminar separation bubble on an airfoil leading edge. S is separation, T is transition and R is reattachment. Bubble size exaggerated*

2000, Wissink et al. 2004, Simoni et al. 2014, Rodriguez et al. 2021) or directly bursting into three dimensional fluctuations and eventually turbulence. Depending on certain flow conditions, of which the magnitude of the pressure rise over the bubble is the most important, the turbulent BL may fail to re-attach to the surface, a case referred to as bubble bursting. The separated area below the shear layer just after separation shows little velocity and on average behaves as a dead-air region. Circulation is stronger at the area of maximum displacement of the bubble.

The separated laminar shear layer initially shows the same instability as the upstream attached boundary layer under adverse pressure gradient (Diwan and Ramesh, 2009), which makes it highly sensitive to disturbances such as free-stream turbulence and changes in Reynolds number. Turbulent mixing homogenises the momentum distribution and as such it reduces the deficit close to the wall, eventually allowing the BL to re-attach

(Jahanmiri, 2011).

Laminar boundary layer separation, reattachment and bubble bursting has received ample attention in low-Reynolds number research, starting with the work of Thwaites (1949), followed e.g. by Gault (1955), Stratford (1957), Crabtree (1959), Tani (1964), Gaster (1967), and Horton (1968) in the fifties and sixties of the last century. The criteria developed over the years for laminar separation and bubble bursting, range from simple ones, depending on a single parameter (e.g. Stratford's criterion, treated in section 6.1.2), to those requiring the calculation of flow parameters such as the Reynolds number based on the momentum loss thickness at separation  $\theta_s$  and parameters containing both  $\theta$  at bursting and the pressure jump over the bubble. Bubble formation, size and final reattachment were found to be impacted by surface curvature, free-stream turbulence, Reynolds number and surface roughness.

Theories, like Stratford's laminar separation criterion and Crabtree's simple bubble bursting equation, were basically developed for the predominantly attached flow regime and for moderately thin airfoil sections approaching the primary stall angle, hence for angles of attack significantly lower than those discussed here, which occur in a flow regime of inherently unsteady nature. However, as the following will show, their theory appears to hold even for this type of unsteady flows and much thicker airfoils when applied to time-averaged characteristics.

As an example, separation and bubble bursting is studied using measurements on a DU97-W-300 airfoil at a Reynolds number of  $0.7 \times 10^6$ , of which the lift curve is shown in figure 6.4. Approaching the expected deep-stall angle, the angle of attack was increased with very small steps (which for clarity have not all been shown in the figure), until deep-stall was reached. Immediately prior to the deep-stall angle the pressure distribution was measured. The angle of attack reached  $33.14^\circ$  without the occurrence of leading-edge

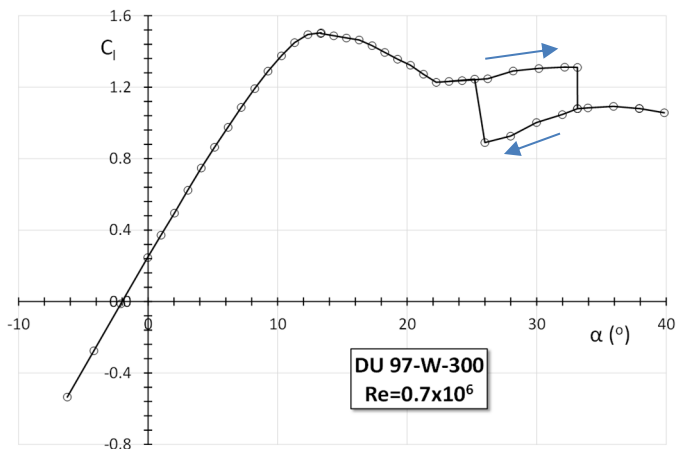


Figure 6.4: The measured lift curve of airfoil DU97-W-300 at  $Re=0.7 \times 10^6$ . Arrows denote angle of attack increase or decrease.

separation. The flow immediately separated once the angle of attack mechanism was activated to go to a higher incidence, giving a deep-stall angle of  $33.15^\circ$ . This makes this situation particularly suited to study both laminar separation and bubble bursting.

### 6.3.2 Stratford's separation criterion

A laminar separation bubble may form as a result of airfoil local adverse pressure gradients. A straightforward criterion for laminar separation, without solving the laminar BL, initially formulated by Stratford (1957) and modified by Curle and Skan (1957), reads as

$$\bar{C}_p \left( \bar{x} \frac{d\bar{C}_p}{d\bar{x}} \right)^2 = 0.0104 \quad (6.1)$$

where  $\bar{x}$  is based on an effective origin of the BL and the so-called canonical pressure recovery coefficient  $\bar{C}_p$  is defined as

$$\bar{C}_p = \frac{p - p_m}{\frac{1}{2} \rho u_m^2} = 1 - \left( \frac{u_e}{u_m} \right)^2 \quad (6.2)$$

with  $u_e$  the velocity at the edge of the BL at any  $x/c$  station and  $u_m$  the edge velocity at the point of minimum pressure.

Stratford's method was based on a trajectory of constant velocity equal to  $u_m$  originating from  $x=0$ , upstream of an area with decreasing velocity resulting from an adverse pressure gradient. Generally, though, the flow over the airfoil suction side starts at the stagnation point and experiences a favourable pressure gradient up to the location of the highest velocity, followed by an adverse pressure gradient, as is shown in figure 6.5.

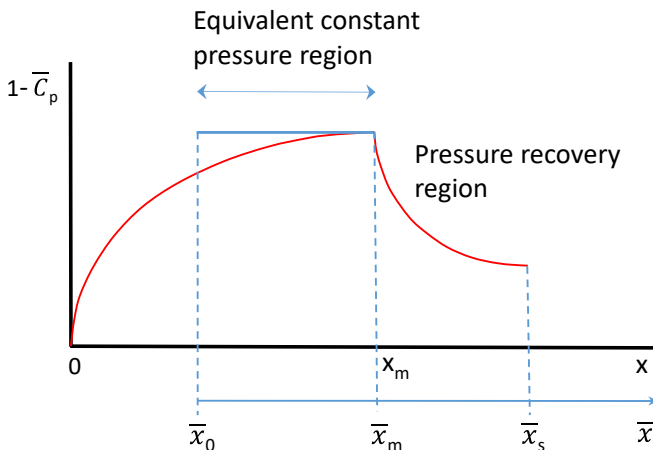


Figure 6.5: The equivalent constant pressure region in Stratford's laminar separation method. Red curve is actual distribution. Indices  $m$  and  $s$  denote maximum velocity and separation respectively.

To be able to use Stratford's method, an equivalent trajectory with constant velocity (constant pressure) needs to be found, starting at  $\bar{x}_o$ , with as equivalence criterion the momentum loss thickness at the location of the peak velocity of the actual flow (at  $x=x_m$ ). For a given velocity distribution this can be accomplished using Thwaites's method (1949):

$$\bar{x}_o = \int_0^{x_m} \left( \frac{u_e}{u_m} \right)^5 dx \quad (6.3)$$

where  $x=0$  is the start of the BL (the stagnation point) and  $\bar{x} = x - (x_m - \bar{x}_o)$ .

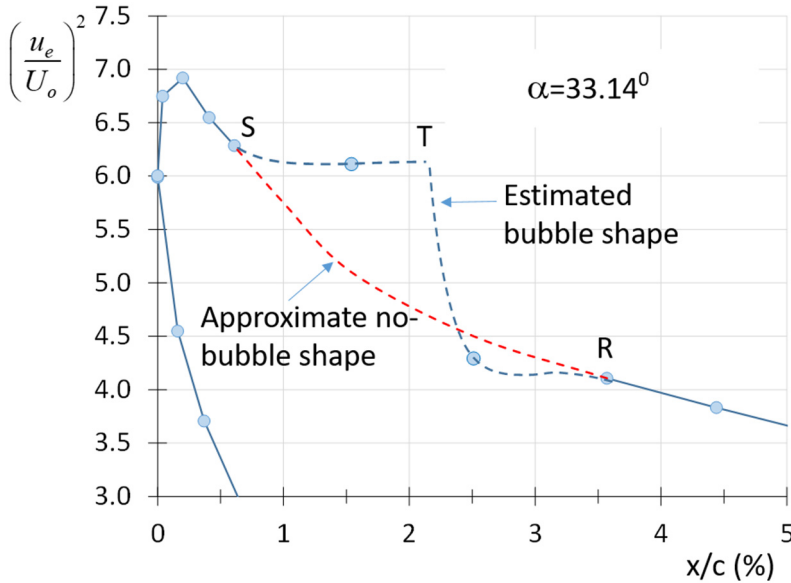
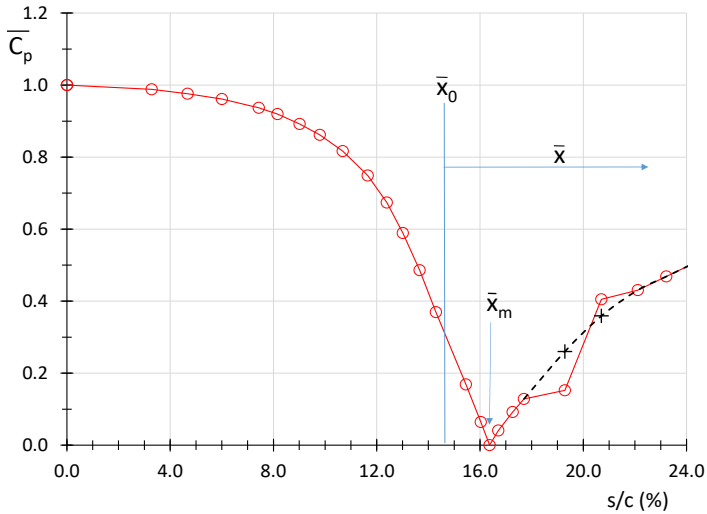
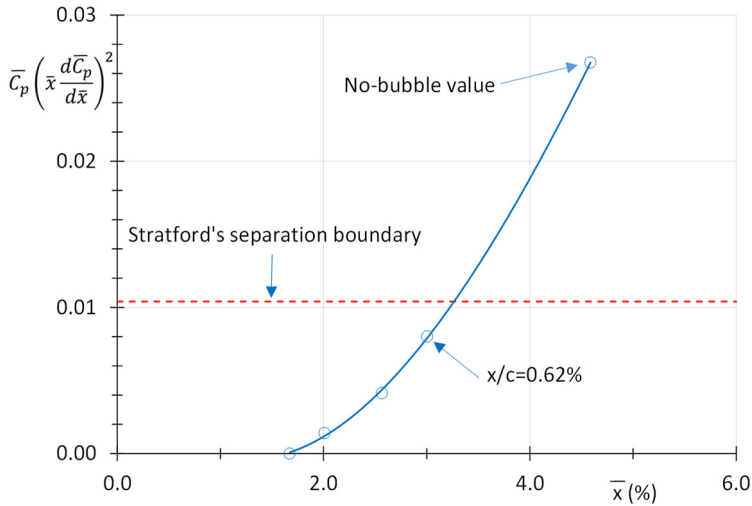


Figure 6.6: Bubble shape and velocity distribution for DU 97-W-300 at  $Re=0.7 \times 10^6$ ,  $\alpha=free-stream$ ,  $S=separation$ ,  $T=transition$  and  $R=reattachment$

Figure 6.6 presents the velocity distribution on the leading edge of the airfoil at  $\alpha=33.14^\circ$ . Sketched are the assumed bubble shape and the approximate velocity distribution without a bubble present (the presence of the bubble has a slight effect on the lift coefficient and hence on the pressure distribution, which effect is ignored here). To complete the calculation of the separation point according to Stratford's analysis, the  $x$ -coordinate has been replaced with  $s$ , the distance along the surface from the stagnation point, which in this case was found at  $x/c=10.16\%$  on the lower surface. The peak velocity was determined by intersecting the linear extrapolation of the pressures at  $x/c=0\%$  and  $0.04\%$  with the one using  $0.2\%$  and  $0.41\%$ . With equation 6.3 it was found that the equivalent distance between the origin of  $\bar{x}$  and the peak velocity coordinate was  $1.67\%$ , which is equivalent with  $s/c=14.70\%$ . Figure 6.7a shows the pressure recovery coefficient  $\bar{C}_p$  as a function of  $s/c$ . Departing from the peak velocity, Stratford's separation parameter develops as presented in fig. 6.7b. According to the figure, the flow



(a)



(b)

Figure 6.7: The pressure recovery factor according to equation 6.2 as a function of the  $s$ -coordinate along the wall (a) and Stratford's separation criterion (eq. 6.1) in relation to the equivalent  $x$ -coordinate. Black pluses in (a) denote approximate no-bubble values.

separates just downstream from the pressure orifice at  $x/c=0.62\%$  ( $s/c=17.70\%$ ), which is corroborated by figure 6.6.

### 6.3.3 Crabtree's bubble bursting criterion

Crabtree (1959) formulated a criterion to predict bubble bursting. He argued that if the jump in pressure between laminar separation and reattachment of the turbulent boundary layer is too large, the flow will separate. The condition for bubble bursting is:

$$\sigma = \frac{P_R - P_S}{\frac{1}{2} \rho u_s^2} = 1 - \left( \frac{u_r}{u_s} \right)^2 > 0.35 \quad (6.4)$$

where  $\sigma$  is the pressure recovery factor and the subscripts S and R indicate separation and re-attachment respectively. In terms of velocity ratios deduced from the pressure distribution this leads to the following equation for laminar bubble bursting:

$$\frac{\left( \frac{u_R}{U_o} \right)^2}{\left( \frac{u_S}{U_o} \right)^2} \leq 0.65 \quad (6.5)$$

For  $\alpha=33.14^\circ$  these velocity ratios can be determined from figure 6.6. Although the resolution of pressure orifices here is quite low and was not intended to be used like this, we can determine the bubble sitting between  $x/c=0.62\%$  and  $3.57\%$ . The associated squared velocity fractions are 6.29 and 4.11. For the bursting criterion we find  $4.11/6.29=0.653$ , which, according to Crabtree, is on the edge of bursting. And indeed, beyond  $33.14^\circ$ , the BL separates, as was found during the measurements.

### 6.3.4 Extrapolation of measurements to find bubble bursting

The measured deep-stall angle for the negative part of the lift curve of DU 93-W-210, shown in figure 6.1, is  $-25.09^\circ$ . Extrapolation of Crabtree's factor based on velocities using the preceding angles gives a value of  $-25.30^\circ$  (figure 6.8), which is relatively close to the measured value of  $-25.09^\circ$ , considering the fact that only 2 to 3 pressure orifices could be used to determine boundary layer separation and reattachment. Once in deep stall,

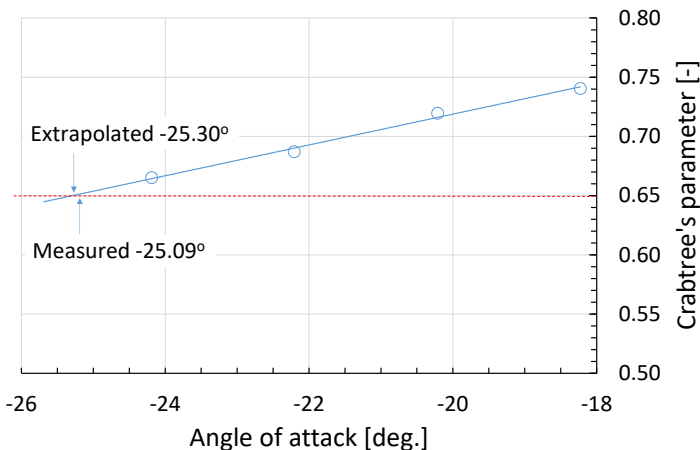


Figure 6.8: Comparison of measured and extrapolated deep stall angle for airfoil DU93-W-210 using Crabtree's parameter from equation 6.5.

further angle of attack increase (or decrease at negative angles) leads to the decrease of the entire upper surface pressure level, which results in an associated initial linear increase in the normal force coefficient.

### 6.3.5 Inviscid calculations

In many cases the leading edge, or “nose” radius is taken as a measure of the leading edge shape. However, the nose radius has only one value and for cambered airfoils the deep stall angle for positive and negative angles is not equal. So next to the nose radius another variable is required to predict both the negative and the positive deep stall. This cannot be the maximum camber of the airfoil, since, near deep-stall, most of the downwind airfoil curvature disappears in the separated region and does not significantly impact the flow. To study the primary stall of airfoils, Gault (1957) used the  $y/c$ -coordinate at  $x/c=0.0125$  as a representative for the airfoil leading edge shape to typify the nature of airfoil stall. He looked at other  $x$ -ordinates as well, but  $y/c$  at  $x/c=0.0125$  gave the most distinct differences. Bak et al. (1998) studied double stall phenomena on stall controlled rotors. They confirmed the existence of a leading edge separation bubble on a rotating blade for a Reynolds number of  $2.7 \times 10^6$ . Using Gault’s method, an inconsistency occurred for a Risø-1 airfoil, which was expected to have a combined leading edge and trailing edge stall, but, according to measurements, only had trailing edge stall. The search for an alternative for Gault’s parameter, which would include the Risø airfoil, resulted in the tangent ( $dy/dx$ ) at  $x/c=0.02$ .

The pressure peak for angles near deep stall, however, occurs much closer to the leading edge (see figure 6.6) than the  $x/c=2\%$  station suited for primary stall. In this light it was expected that the original parameter from Gault’s study would be more suited.

As will be clear from the above, the adverse pressure gradient downstream of the low-pressure peak on the leading edge plays a prominent role in laminar separation at these

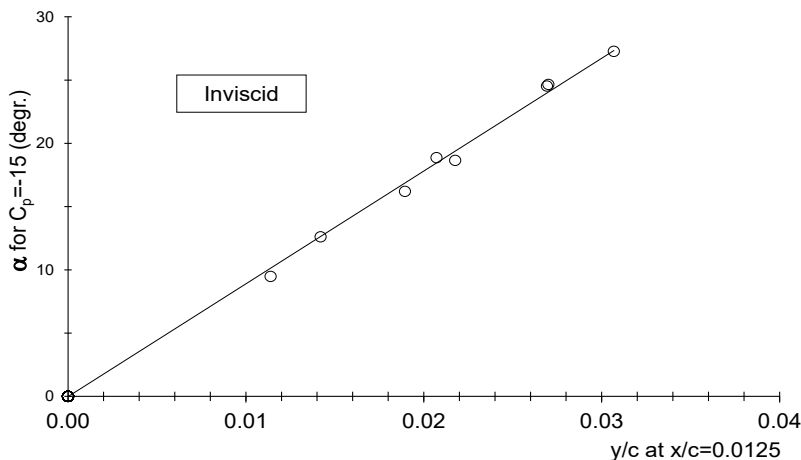


Figure 6.9: The angle of attack giving  $C_p=-15$  for the airfoils tabulated in table 6.1

Table 6.1: The incidence of several airfoils giving an inviscid  $C_p$  of -15

Airfoil	y/c	angle ( $^{\circ}$ )	$\alpha$ ( $C_L=0$ )	angle ( $^{\circ}$ )
Positive angles				
NACA 0009	0.01420	12.61	0.00	12.61
NACA 0012	0.01894	16.20	0.00	16.20
DU 96-W-180	0.02071	15.92	-2.91	18.83
NACA 64-018	0.02177	18.65	0.00	18.65
DU93-W-210	0.02693	19.92	-4.55	24.47
DU 91-W2-250	0.02700	20.61	-3.89	24.50
DU 97-W-300	0.03069	24.00	-3.27	27.27
Negative angles				
S805	0.01139	-11.89	2.41	9.48

large angles. The steeper the peak, the closer the BL will be to separation. The value of the minimum pressure coefficient largely depends on the shape of the nose region of the airfoil.

Since the pressure peak on the leading edge for a certain angle of attack and the nose shape of the airfoil are interrelated, inviscid pressure distributions were calculated with RFOIL for several airfoils and interpolated to find the angle for which a rather arbitrary chosen pressure peak of  $C_p=-15$  is reached. As the camber at the trailing edge of the airfoil affects circulation, the aerodynamic rather than the geometrical angles have been established, which means that the zero-lift angle was subtracted from the calculated values.

The results are tabulated in table 6.1 and graphically presented in figure 6.9. Though slightly scattered, the points seem to fall on a linear trend line. Since the relation should also apply to an infinitely thin flat plate, the curve essentially intersects the origin.

Airfoils we consider here are of the wind energy type that develop a growing low-pressure peak on the leading edge and have progressing TE-separation with increasing angle of attack.

## 6.4 MEASURED DEEP-STALL ANGLES

Tables 6.2 and 6.3 give the y/c-ordinate of a number of airfoils and the associated measured deep stall angle. The values are graphically presented in figure 6.10. Negative values in x/c denote lower surface ordinates. To exclude any impact turbulence intensity or testing environment may have, only measurements in the Delft-LTT are listed. The curve was forced to intersect the origin. All models were made of polyester or aluminum and manufactured by renowned companies active in this field, resulting in models with good to high accuracy. Table 6.2 contains airfoil models having a chord of 0.60m, leading

to comparable blockage effects (for which the data were corrected). All airfoils have laminar separation from the leading edge following advancing turbulent separation initially starting at the trailing edge. Models with a different chord or those reaching deep-stall or recovery from it through a long bubble are brought together in table 6.3.

For the deep-stall angle,  $\alpha_{DS}$ , at  $Re=1 \times 10^6$  (table 6.2) we find:

$$\alpha_{DS} = 1124.2 \cdot (y/c)_{x/c=0.0125} \quad (6.6)$$

The reason for excluding measurements from models with a chord other than 0.6m in this relation will be explained in chapter 6.7. To show the resolution of the measured deep-stall angles the tables also contain the previous angle, which is the last measured angle before deep-stall set in, still giving a pressure peak on the leading edge. It must be noted that the angles have been corrected for wall effects with the method for streamlined flow

Table 6.2: The deep-stall and recovery angles of 0.6m chord airfoil models measured in the TU Delft-LTT at  $Re=1.0 \times 10^6$ .

Airfoil	y/c@ x/c=.0125	$\alpha$ -deep stall (degr.)	previous angle	$\alpha$ - recovery (degr.)	previous angle	Remarks
Positive angles						
S809 <sup>1</sup>	0.01770	21.20		18.19		Somers (1997)
CENER L5T14	0.01987	23.07				
DU95-W-180	0.02055	23.55	23.14	21.81	22.19	Test 1995
DU95-W-180	0.02055	23.58	23.52	21.97	22.28	Test 2016
DU 95-W-180f2 (DU96)	0.02072	23.44	22.55	22.15	22.52	Test 1995
DU 95-W-180f2	0.02072	23.48	23.46	22.18	22.28	Test 2016
DU 08-W-180Mod	0.02257	27.06	26.16	23.17	24.05	
FFA W3-211	0.02608	29.4		24		
DU 93-W-210	0.02693	29.03	28.14	21.21	22.04	Test 1993/'94
DU 93-W-210	0.02693	28.44	28.16	21.21	22.03	Test 2016
DU 91-W2-250	0.02698	30.71				Test 1992
DU 91-W2-250	0.02698	30.51	30.42	23.17	23.22	Test 2019
DU 00-W-300	0.02967	33.65	33.59	26.55	26.60	
Airfoil <sup>2</sup>	0.03494	39.95	39.59			
Negative angles						
DU 91-W2-250	-0.03103	-34.48	-34.47	-26.48	-26.57	Test 2019
DU 00-W-300	-0.03042	-34.96	-34.91	-27.65	-27.71	
DU 93-W-210	-0.02229	-25.09	-24.59	-18.11	-18.57	Test 2016
FFA W3-211	-0.02075	-22.7		-17.6		
DU95-W-180	-0.01544	-15.51	-15.07	-13.70	-14.11	Test 1995
DU95-W-180	-0.01544	-15.76	-15.65	-14.16	-14.30	Test 2016
DU 95-W-180f2	-0.01533	-15.67	-15.55	-14.26	-14.40	Test 2016

<sup>1</sup> Data not recorded, but uncorrected angles visually established during test and correction added by the present author.

<sup>2</sup> Due to confidentiality no name presented

Table 6.3: The deep-stall angles of airfoil models measured in the Delft-LTT with a different chord or flow-mechanism,  $Re=1.0 \times 10^6$ .

Airfoil	y/c@ x/c=.0125	$\alpha$ -deep stall (degr.)	previous angle	$\alpha$ - recovery (degr.)	previous angle	Remarks
Positive angles						
S805	0.01807	20.06	19.13	17.13	18.13	Somers (1997), C=0.5 m
DU 10-W-240	0.02810	31.00	30.76	23.84	24.05	C=0.75
DU 97-W-300	0.03069	34.93	34.13	26.19	26.98	Test 1997, C=0.65 m
DU 97-W-300	0.03069	35.14	35.11	26.2	27.06	Test 2016
DU 97-W-300	0.03069	35.32	35.30	27.08	27.10	Test 2017
Negative angles						
DU 97-W-300	-0.03327	-41.52	-41.31	-33.11	-32.78	Test 2016
S809	-0.01504			-12.17		Via long bubble
S805	-0.01139	-13.04				Long bubble, Cp flat

explained in Appendix A. Differences with Maskell's method are still very small at these angles.

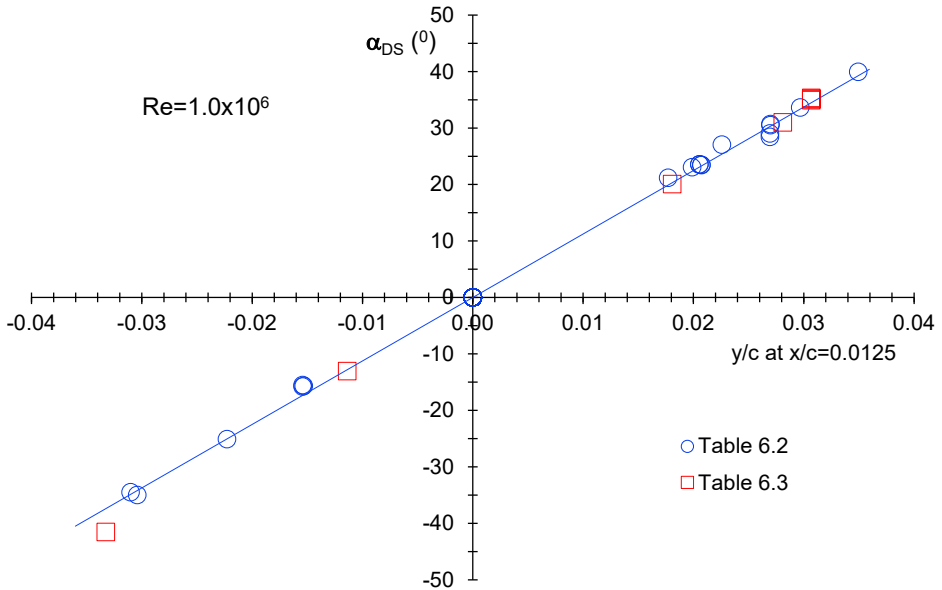


Figure 6.10: The deep-stall angle for 0.6m chord models (table 6.2) and other chord models (table 6.3) measured in the Delft LTT at  $Re=1 \times 10^6$ .

## 6.5 THE IMPACT OF THE REYNOLDS NUMBER ON THE DEEP-STALL ANGLE

An increase in Reynolds number (velocity) destabilizes the laminar boundary layer, including the separated layer, and consequently leads to earlier transition, which decreases the length of the laminar separation bubble and the pressure jump over the

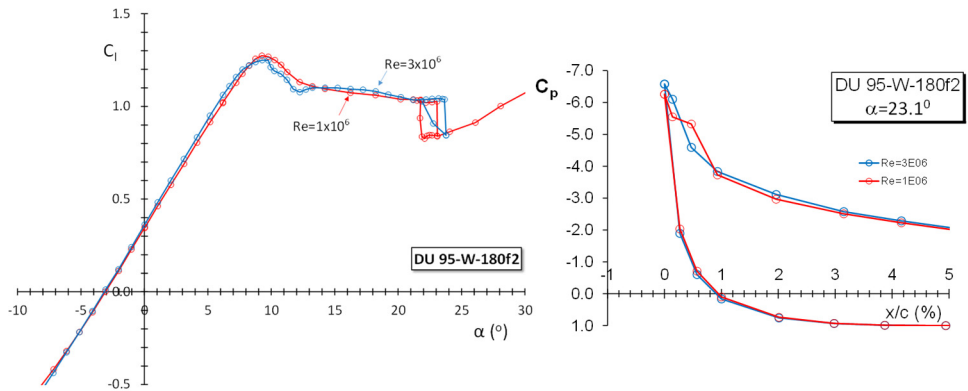


Figure 6.11: The varying deep stall angle with Reynolds number for airfoil DU 95-W-180f2 with the  $C_p$ -distribution at an angle of  $23.06^\circ$ . Original angle settings (without  $0.4^\circ$  correction for flap deflection)

bubble. This results in a higher angle for bubble-bursting, as is shown in figure 6.11. It presents the lift curves of airfoil DU95-W-180f2 for a Reynolds number of  $1 \times 10^6$  and  $3 \times 10^6$ , together with the pressure distribution for both Re-numbers at an angle of attack of  $23.06^\circ$ . This is the angle just prior to bubble bursting for the lower Re-number ( $23.08^\circ$ ). Although just a few pressure orifices indicate the bubble, it seems clear that the bubble for the higher Re-number at the same angle is smaller, giving some additional margin to bubble bursting ( $23.78^\circ$ ). The presented angles have not been corrected for the change in longest-chord orientation due to the  $2^\circ$  flap deflection ( $0.4^\circ$ ).

At this point it must be noted, that the Mach number changed from 0.07 to 0.23. If the local Mach number exceeds the critical Mach number, shocks will form, potentially also causing flow separation. The minimum  $C_p$ -value during the test at  $Re=3 \times 10^6$  (fig. 6.11) is -6.5, sufficiently far from the critical value causing shocks of  $C_p=-12.2$  associated with  $M=0.23$ .

Figure 6.10 is only valid for a Reynolds number of  $1 \times 10^6$  and a comparable testing environment: a smooth surface, low turbulence intensity and comparable blockage. In principle for every Reynolds number such a graph can be made. Figure 6.12 shows the relation for the deep-stall angle at a Reynolds number of  $0.7 \times 10^6$ . Although at first sight there is not much difference in the value of the angle of attack for deep-stall at the two Reynolds numbers the trend line is not as steep as the one for  $Re=1 \times 10^6$  in figure 6.10 (a gradient of 1075.4 against 1124.2 for  $Re=1 \times 10^6$ ).

## 6.6 THE EFFECT OF THE TE-FLOW ANGLE ON THE ONSET OF DEEP-STALL.

In contrast to the inviscid case, in the presentation of figures 6.10 and 6.12 the measured

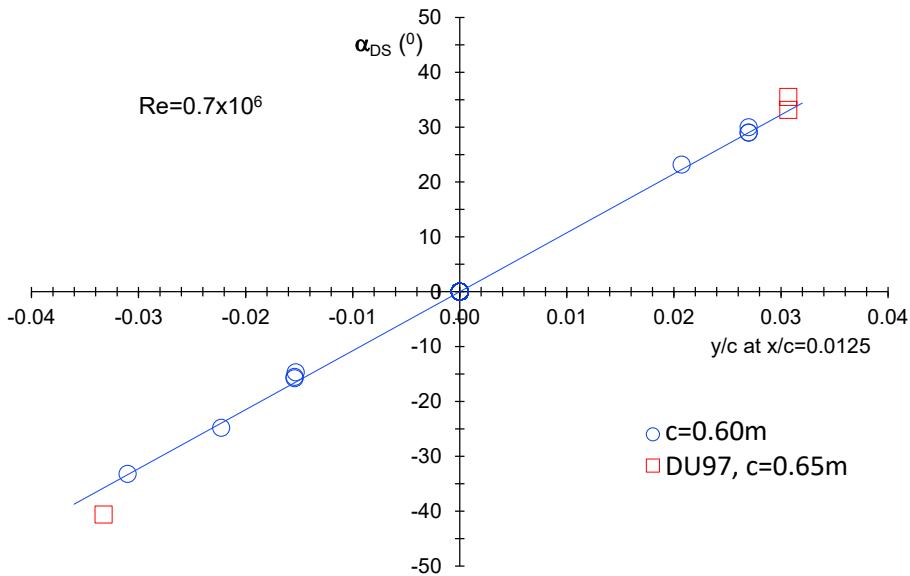


Figure 6.12: The deep stall angles for airfoils measured in the LTT for a Reynolds number of  $0.7 \times 10^6$ .

geometrical deep-stall angles are shown without subtracting the zero-lift angle. The reason is that due to the separation right from the leading edge most of the surface curvature below the separated BL has disappeared in the wake and does not affect the circulation around the airfoil.

It may be argued that the trailing edge curvature of the pressure side, at which the flow is attached, may still have an effect on the flow, although in most cases the trailing edge pressure is fully dominated by the suction of the separated region. This is corroborated by the fact that, for positive angles, there seems to be no significant deviation from the trend line either for an airfoil having an almost zero lower surface trailing edge angle (DU 95-W-180f2) nor for one with a TE-angle of  $15.2^{\circ}$  (DU 97-W-300).

As the DU95-W180 airfoil has a 20% chord trailing edge flap the impact of pressure surface curvature can be studied in more detail. Measurements have been performed at  $Re=1 \times 10^6$  and various flap deflections, resulting in the deep-stall and recovery angles tabulated in table 6.4, both for positive and negative angles of attack. The angles shown in the table include the effective angle-of-attack-change of the longest chord with flap deflection,  $\Delta\alpha$ , which was added to the measured angles to get the proper geometrical orientation of the airfoil.

To be able to compare the results with the data in figures 6.10 and 6.11, the airfoil needs to be defined at the longest chord at every flap deflection, effectively resulting in different

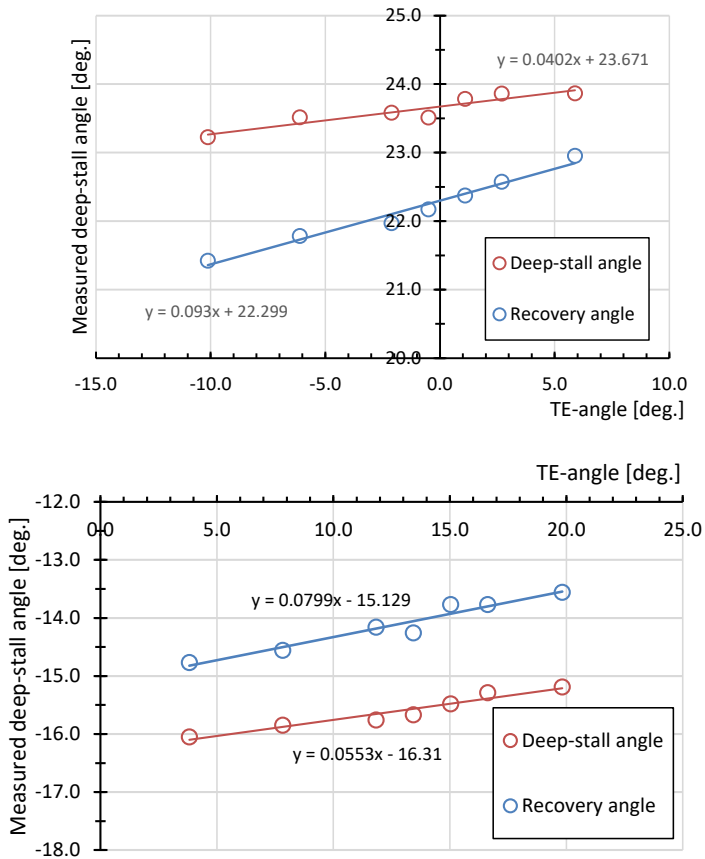


Figure 6.13: The deep-stall angles of airfoil DU95-W-180 for various flap deflections both for positive (top) as well as negative (bottom) angles of attack at  $Re=1 \times 10^6$ .

airfoil shapes, and consequently different  $y/c$  coordinates at  $x/c=.0125$ , giving the leading edge thickness coordinates and trailing edge angles  $\zeta$  presented in table 6.4. The data are graphically presented in figure 6.13.

The figure shows a relatively small effect of the TE-flow angle on the deep-stall angle, both

Table 6.4: the deep-stall (DS) and recovery (Rec) angles of DU95-W-180 for various flap deflections.

Positive angles						Negative angles			
Flap angle	$y/c$ u.s	$\zeta$ l.s.	$\Delta\alpha$	$\alpha$ -DS	$\alpha$ -Rec	$y/c$ l.s	$\zeta$ u.s.	$\alpha$ -DS	$\alpha$ -Rec
deg.		deg.	deg.	deg.	deg.		deg.	deg.	deg.
-10	0.01980	-10.12	-1.99	23.22	21.42	-0.01595	3.82	-16.05	-14.77
-5	0.02016	-6.11	-1.00	23.51	21.78	-0.01569	7.83	-15.85	-14.56
0	0.02055	-2.11	0.00	23.58	21.97	-0.01544	11.83	-15.76	-14.16
2	0.02071	-0.51	0.40	23.51	22.17	-0.01534	13.43	-15.67	-14.26
4	0.02087	1.09	0.80	23.77	22.37	-0.01525	15.03	-15.48	-13.77
6	0.02104	2.69	1.20	23.86	22.57	-0.01516	16.63	-15.29	-13.77
10	0.02139	5.89	2.00	23.86	22.95	-0.01499	19.83	-15.19	-13.56

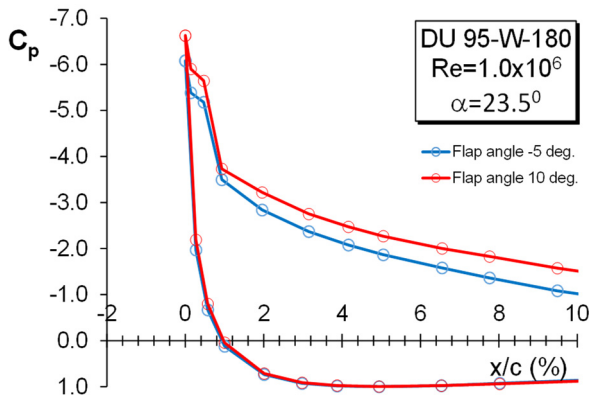


Figure 6.14: The  $C_p$ -distribution at the leading edge close to the deep-stall angle for two flap deflections, giving a trailing edge angle of + or  $-6^\circ$ .

for positive ( $0.04^\circ/\text{deg.}$  change of the TE-angle) as well as for negative angles ( $0.055^\circ/\text{deg.}$ ). Figure 6.14 depicts the pressure distributions on the leading edge at an angle near leading edge separation for positive angles of attack of the model with a negative and a positive TE-angle of about  $6^\circ$  (flap angles of  $-5^\circ$  and  $10^\circ$  respectively). The figure clearly shows lower  $C_p$  values (higher velocity) at the leading edge for the configuration with a flap deflection of  $10^\circ$ . This may expedite transition and consequently slightly reduce the size of the laminar separation bubble, which increases the margin with respect to bursting, leading to a higher angle for deep-stall.

The resolution of the pressure orifices, unfortunately, is too low to show any change in bubble size, which would give the measured difference in deep-stall angle of  $0.35^\circ$ . It must be noted that the differences in values are fairly small and despite the relatively long averaging times may be affected by the high unsteadiness in the flow.

By interpolation of the data in figure 6.13 for positive angles and extrapolation of the data for negative angles we can determine the  $y/c$  coordinate (or equivalent flap deflection) and deep-stall angle for which the TE-angle is zero. This gives  $y/c = 0.02076$  and  $23.67^\circ$  for positive angles and  $y/c = -0.01621$  and  $-16.31^\circ$  for negative angles, while the relation depicted in fig. 6.10 gives  $23.34^\circ$  and  $-18.23^\circ$  respectively.

Especially the latter gives a notable difference (app.  $1.9^\circ$ ) to what has been found from the DU95 measurements. Looking at the values for the deep-stall angle and the respective  $y/c$  values as a result of the flap deflections it appears that they are more or less situated on a straight line, however do not fit in the relation given by eq. 6.6.

The insensitivity of bubble bursting to any part of the airfoil located in the separated region may best be illustrated by figure 6.15, where the lift curves are presented of the

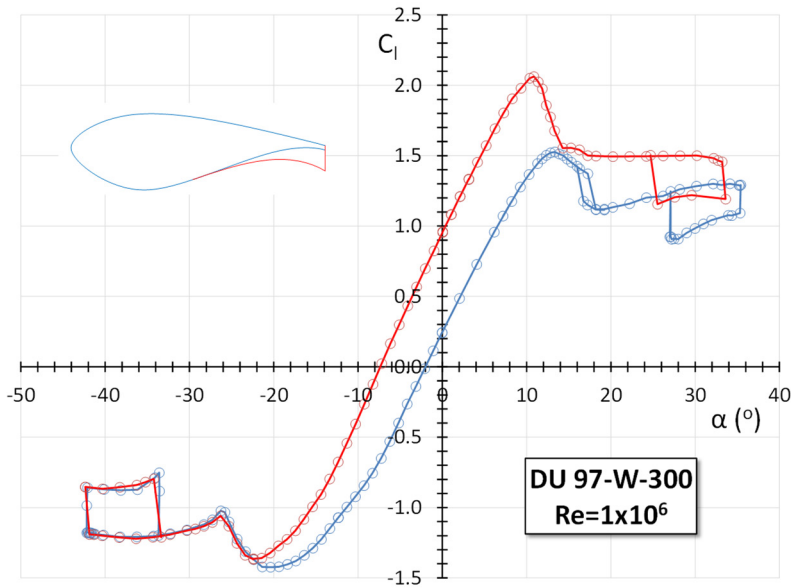


Figure 6.15: The measured deep-stall angles for airfoil DU97-W-300 with and without additional thickness at the lower side trailing edge.

DU97-W-300 airfoil with and without a thick trailing edge (flatback). The 10% thickness of the TE was achieved by adding material to the airfoil lower side (Ceyhan and Timmer, 2018). As is clear from the graph, despite the significant change in lower surface shape, the hysteresis loop for negative angles of attack, when the flat back entirely disappears in the separated region, shows no sign of deviation from the curve of the original airfoil.

The flatback measurements depicted in fig 6.15 refer to the chord orientation of the original model. Depending on the definition of the chord of the flatback airfoil the impact on bubble bursting at positive angles of the  $31.36^\circ$  TE-angle can be determined. For a chord line between (0,0) and the middle of the 10% thick TE with coordinate (1, -0.0413) the difference in chord angle compared to the original airfoil orientation is  $2.36^\circ$ . The longest chord, between coordinates (0,0) and (1, -0.0913), gives a difference of  $5.22^\circ$ . This brings the measured deep-stall angle from  $33.28^\circ$  to either  $35.64^\circ$  or  $38.50^\circ$ . The deep-stall angle of the original airfoil is between  $34.93^\circ$  (test 1997) and  $35.32^\circ$  (test 2017), with an average of  $35.13^\circ$ , giving differences with the flat back airfoil of  $0.52^\circ$  or  $3.37^\circ$ , depending on the chord definition.

In terms of sensitivity to changes in TE-angle this comes down to a maximum of 0.11 per degree TE-angle, about twice the value found for DU 95-W-180. It must be noted that, if we follow the longest chord approach, the chord orientation of the original DU97-W-300 airfoil, due to its thick TE of 1.74%, is  $0.5^\circ$ , bringing the difference with the flat back airfoil down to about  $3^\circ$  and a sensitivity to TE-angle changes to  $0.09^\circ$  per degree.

## 6.7 THE RECOVERY ANGLE; HYSTERESIS IN RELATION TO THE LEADING EDGE THICKNESS

Once in deep-stall at positive angles, decreasing the angle of attack shows for airfoils like DU91-W2-250 a fully separated flow with increasing base pressure, until an angle is reached for which the flow reattaches to part of the leading edge of the airfoil, giving a pressure peak at the leading edge. For a clean airfoil this angle is smaller than the deep-

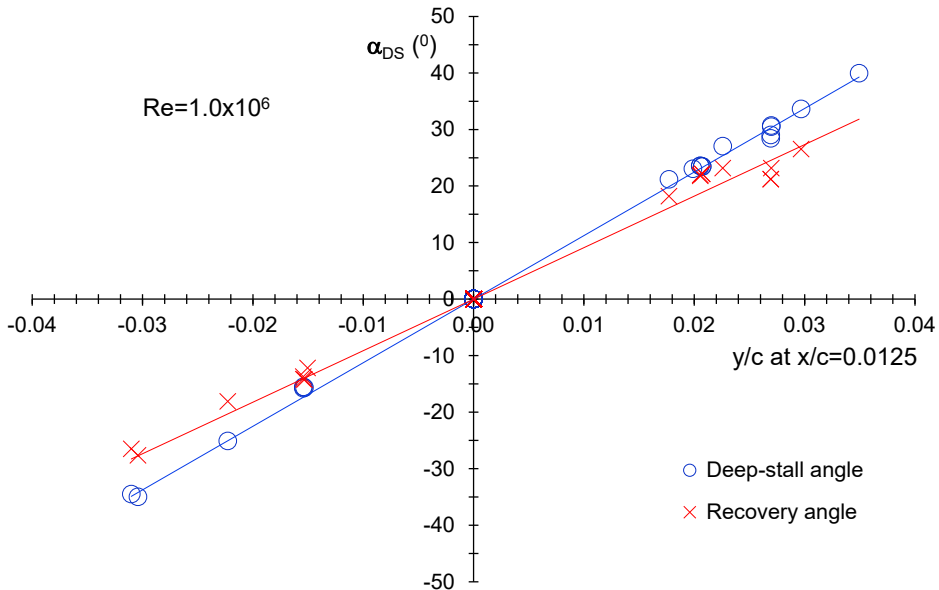


Figure 6.16: The recovery angle and the deep-stall angle for measurements in the Delft LTT

stall angle, thus showing a hysteresis loop in the airfoil performance, in the lift curve as well as in the drag and moment curves.

*Research question RQ 6.5: What flow or airfoil parameters determine the length of the hysteresis loop?*

During most of the measurements mentioned above also the recovery angle has been measured (table 6.2). Figure 6.16 presents both the leading edge separation angle and the recovery angle for models measured in the Delft LTT.

One would expect that, if the deep-stall angle depends on the shape of the leading edge, which determines the base pressure at the deep-stall angle, the recovery angle will also follow that same trend. It appears that the linear behaviour of the recovery line in figure 6.16 is less convincing than the one for the deep-stall angle, especially in the region of  $y/c < 0.022$ . This may partly be due to the unsteady nature of the flow in the fully separated

configuration, although other circumstances may play a role as well; the conditions under which the flow recovers from the leading edge separation are not entirely clear. However, measurements show that recovery requires the magnitude of the base pressure (or the

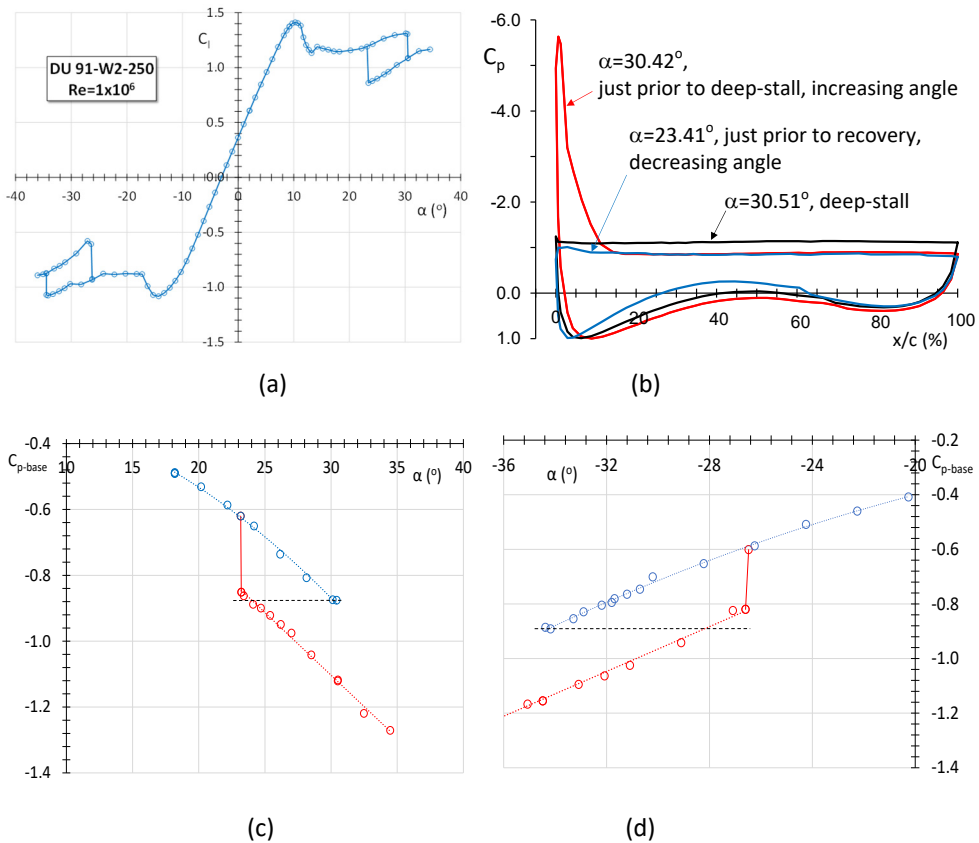


Figure 6.17: The hysteresis loop and associated pressure distributions and base pressures of airfoil DU91-W2-250 at a Reynolds number of  $1 \times 10^6$ .

trailing edge pressure) being at least equal to the one just prior to deep-stall. Figure 6.17a presents the hysteresis loop of airfoil DU91-W2-250. Both for the positive and negative angles the base pressure coefficient more or less linearly grows with decreasing angle (or increasing, for negative angles) in deep-stall until the magnitude of the base pressure that existed immediately prior to deep stall has been reached (fig. 6.17b). For positive angles, the flow then re-attaches at the leading edge shortly after (fig. 6.17c). For negative angles it still takes an angle of attack increase of  $1.76^\circ$  after passing the required base pressure for the flow to recover. For most airfoils from table 6.2, this angle can be determined from the deep-stall data as sketched above with an accuracy well within 1 degree if measurements around the deep-stall angle have sufficient incidence resolution. The procedure using the base pressure coefficient does not work for DU95, shown in figure 6.18.

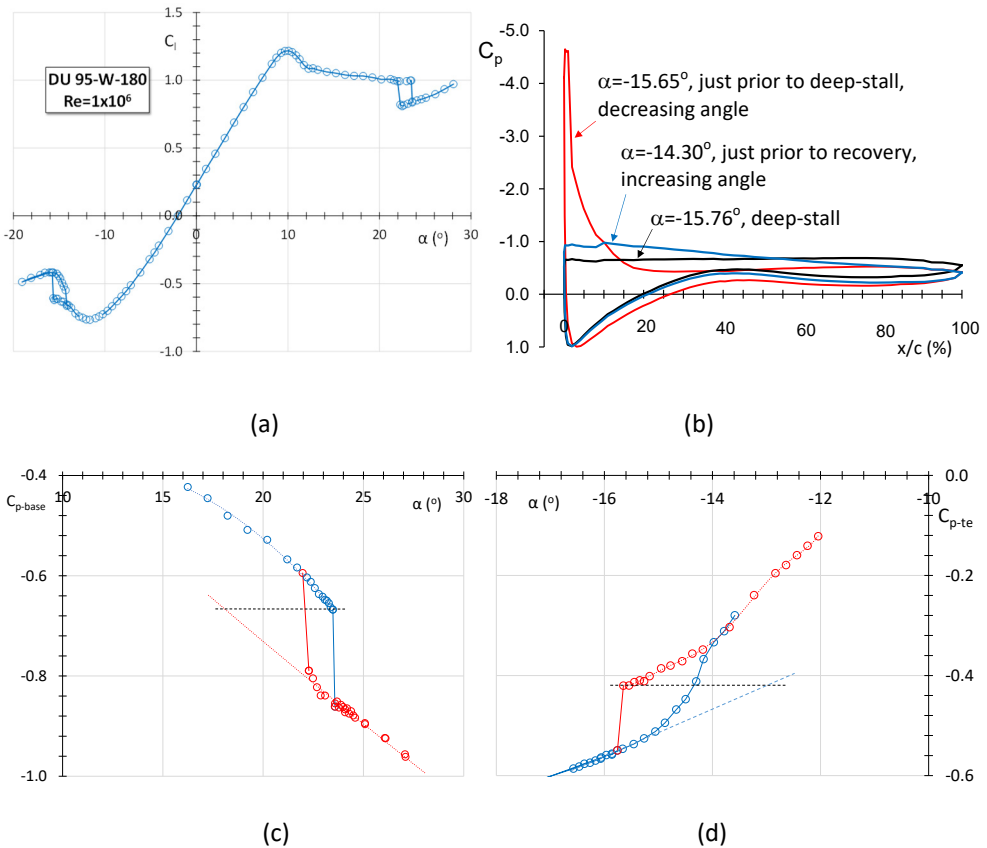


Figure 6.18: The hysteresis loop and associated pressure distributions and base pressures of airfoil DU95-W-180 at a Reynolds number of  $1 \times 10^6$ . Note d) has the trailing edge pressure.

For the negative angles no base pressure could be established as the pressure distribution on the suction side was not constant. Instead, in figure 6.18d the trailing edge pressure is given.

The intersections of the extrapolated deep-stall data and the lines for constant pressure just prior to leading edge separation give recovery angles of about  $19.5^\circ$  and  $-12.7^\circ$  for the positive and negative angles respectively, while the measured angles are in the order of  $22^\circ$  and  $-14^\circ$ . Between the deep-stall angle of  $-15.76^\circ$  and the recovery angle of  $-14.16^\circ$  the pressure distribution on the airfoil lower surface is tilted (fig. 6.18b), giving more negative pressures near the leading edge and an increase in pressure at the trailing edge, which apparently give an acceleration of the recovery process. Still, the value of the trailing edge pressure just prior to deep-stall has to be reached before recovery takes place.

Restoration for the relatively thin airfoils S805 ( $\gamma/c = -0.01139$ ) and S809 ( $\gamma/c = -0.01504$ ) at negative angles of attack (see Somers, 1997) takes place through a long bubble due to the

relatively sharp lower surface leading edges. The DU95 lower surface ( $y/c=-0.01544$ ) pressure distribution here does not show the typical long bubble shape covering 30% or 40% of the front part of the airfoil.

The restoration of the peak on the leading edge of DU95 with decreasing angle at positive incidences takes place at a  $2.5^\circ$  higher angle compared to the extrapolation (fig. 6.18c). The difference for the negative angles is  $-1.5^\circ$ .

The reason for the fast recovery of the pressure peak at the leading edge of DU95 both for the positive and negative angles may be traced back to the relatively small pressure step required for full recovery. Figure 6.19 presents the corrected base pressure coefficients for the airfoils of table 6.2 both just prior and at deep-stall. As was stated above, the base pressure of the airfoil for recovery from deep-stall should be higher, but at least equal, to the base pressure (or trailing edge pressure) on the airfoil just before

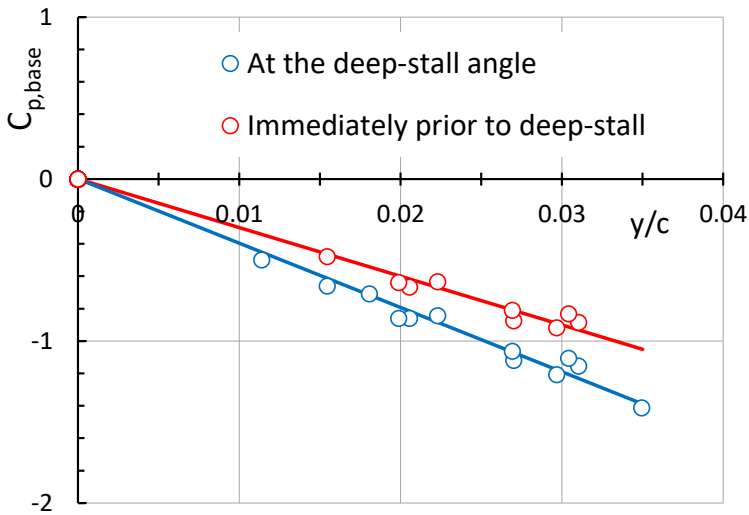


Figure 6.19: The base pressure coefficients at, and just prior to, deep-stall as a function of the leading edge thickness of the airfoils in table 6.2

going into deep-stall. Due to the inherently unsteady nature of the separated flow a lock-in effect might take place, giving a much faster recovery than for higher leading edge thicknesses, possibly partly induced by the vortex interference in the wake, in which the leading edge and trailing edge vortices come closer together with retreating angle.

A second explanation is based on the typical shape of the lower surface pressure distributions with retreating angle (fig. 6.18b). The first 10% of the airfoil lower side seems to show a separated region followed by a sudden speed-up, which might be caused by the presence of a secondary vortex close to the surface. The gradual decrease of the velocity visible towards the trailing edge instead of a constant pressure typical for a fully separated region might indicate that the leading edge vortices stay close to the aft part of the airfoil

while moving downstream. This creates lower velocities near the trailing edge due to the clockwise rotation of these vortices and more curvature in the flow, resulting in an increase of the negative lift.

The procedure of extrapolating the base pressure also does not give a satisfying result for the negative recovery angle of DU97 (extrapolated recovery angle higher with  $5.56^\circ$ ). This may be attributed to the large blockage present for this configuration, which will be the subject of the next chapter.

## **6.8 THE IMPACT OF BLOCKAGE ON THE DEEP-STALL AND RECOVERY ANGLES.**

The data given in table 6.2 result from measurements on airfoil models with a chord of 0.60 m. For representation of the characteristics of low-to-moderate angles of attack in the LTT such a chord length gives very good results using proper tunnel blockage correction (see Appendix A). However, at higher angles of attack blockage of the test section becomes a dominant factor.

The additional speed in the leading edge region as a result of severe blockage promotes transition. For moderate angles of attack, say up to  $20^\circ$  this is hardly noticeable in the characteristics since transition is in the leading edge region anyway. However, in the case of a short laminar separation bubble, like discussed above, this overspeed leads to a shorter bubble and in fact stabilizes the flow around the nose of the airfoil as it decreases the pressure difference across the bubble between separation and reattachment.

While, using the right correction scheme, the overall pressure distributions of two airfoil models with different size can be matched (e.g. the base pressure), blockage has a first order impact on the size -and as such also on the bursting- of a leading edge laminar separation bubble, which cannot be corrected. This makes the deep-stall angle directly proportional to the model-chord to test-section-height ratio (blockage factor)  $c/h$ . If, for a smaller model, at a certain angle the bubble would be on the verge of bursting, a bigger model in the same test section at the same incidence would allow for a higher angle, which gives a higher blockage with the associated over speed, allowing for an even higher angle of attack before bursting. This can give measured deep-stall angle differences for the same airfoil at the same Reynolds number but with different model size of several degrees. It may also explain the rather large negative value of the deep-stall angles of airfoil DU97 depicted in the lower left part of fig. 6.10 and 6.12, since the model had a chord length of 0.65 m ( $c/h=0.392$ ) instead of the regular 0.60 m of the other airfoil models ( $c/h=0.362$ ). As a result of the large  $y/c$  value at the leading edge, the airfoil already has a fairly high negative deep-stall angle, but it also has the highest blockage of all the airfoils listed.

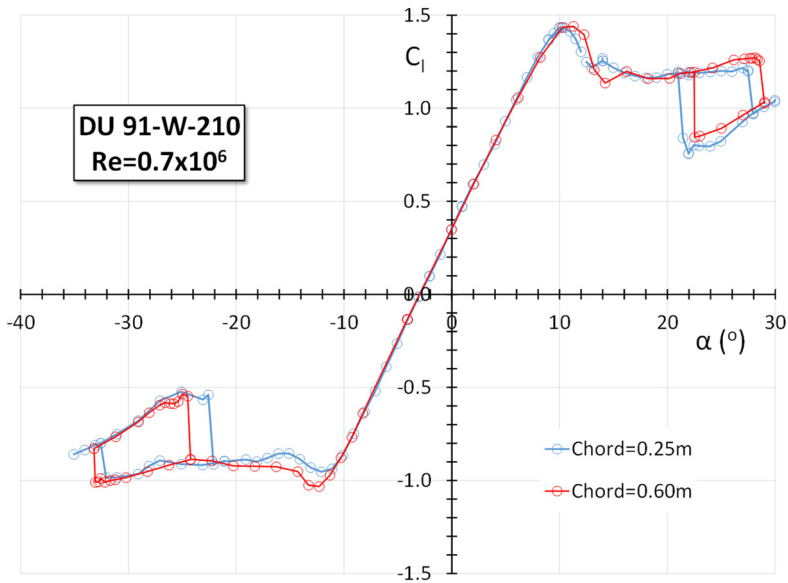


Figure 6.20: The lift performance of DU91 measured in the LTT for differently sized models giving  $c/h$  values of 0.151 and 0.362 respectively.

To underline the above, fig. 6.20 presents the lift curves of DU91 for a 0.25 m and a 0.60m model, both tested in the LTT at  $Re=1 \times 10^6$ . The respective  $c/h$  values are 0.151 and 0.362. The figure shows a small but distinct difference in the location of the hysteresis loop, both for positive and negative values, illustrating that the deep-stall angle, and implicitly the gradient of the line in figures 6.10, 6.12 and 6.16, is not only depending on the Reynolds number, but also on the blockage factor  $c/h$ . The length of the hysteresis loop seems not to be affected.

Table 6.5: The deep stall angle from measurements in other wind tunnel facilities than LTT,  $Re=1 \times 10^6$

Airfoil	$y/c$ @ $x/c=.0125$	$\alpha$ -DS (deg.)	$c/h$	Wind tunnel and reference
S809 (t/c=21%)	.01770	20	0.327	Ohio State University, Ramsey et.al., 1995-rev. 12/99
LS(1)-421Mod	.03665	39.8	0.327	Ohio State University, Ramsey et.al., (1995)
S814 (t/c=24%)	.02400	26	0.327	Ohio State University, NREL/TP-442-8161
S901 (t/c=18%)	-.01421	-17.07	0.309	Penn. State University, Somers, NREL/SR-500-36336
S903 (t/c=12%)	.01631	18.07	0.309	Penn. State University, Somers, NREL/SR-500-36336
S805 t/c=13.5%)	.01807	20.06	0.302	TU Delft LTT, $c=0.5m$ , Somers (1997)

Table 6.6: The deep stall angle from other facilities, various Reynolds numbers

Airfoil	$y/c$ @ $x/c=.0125$	$\alpha$ -DS (deg.)	$c/h$	Reference
NACA 64-012	.0149	16.4	0.267	Re=1.5x10 <sup>6</sup> , NACA LTT, Loftin & Smith (1949)
NLF(1)-0416	-0.01516	-16.08	0.267	Re=4x10 <sup>6</sup> , NASA LTPT, Somers (1981)

Data from other facilities, with a lower value of  $c/h$  compared to the ones in table 6.2 are brought together in tables 6.5 and 6.6 and graphically presented in fig. 6.21. The trend line shown is for  $c/h=0.327$

The NLF model, table 6.6, has a lower blockage, which would give a smaller deep-stall angle, however it has a higher Reynolds number, which would stabilize the flow and postpone bubble bursting. The net result is a value for the deep-stall angle fitting relatively well to the trend line for  $c/h=0.327$ .

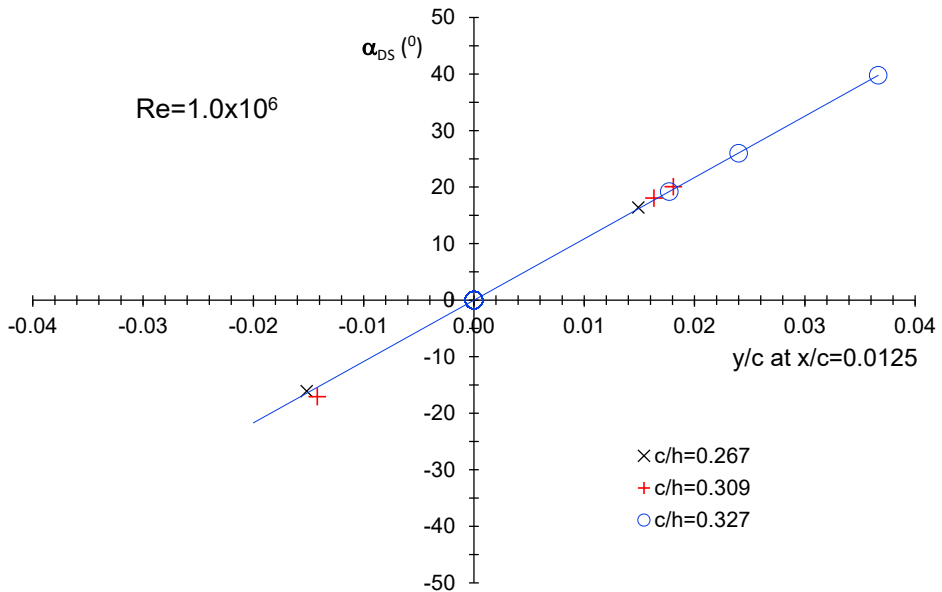


Figure 6.21: The deep-stall angle for various blockage factors, tables 6.5 and 6.6

## 6.9 BLOCKAGE-FREE DEEP-STALL AND RECOVERY ANGLES FOR DU91-W2-250.

As stated above, the impact of the blockage on the deep-stall and recovery angles cannot be corrected by tunnel correction schemes. The deep-stall performance of airfoil DU91 was also measured on a 15cm chord model in the range  $0.2 \times 10^6 < Re < 0.7 \times 10^6$  (Landstra

2011, van Roosbroeck 2013). As measurements were performed on three differently sized models at  $Re=0.7 \times 10^6$  ( $M < 0.22$ ), extrapolation of the results could give an estimate of the blockage-free values of the deep-stall and recovery angle for this specific Reynolds number. The gradients, like shown e.g. in fig. 6.10, have been listed in table 6.7. The extrapolation to blockage-free values is shown in fig. 6.22. With a gradient of 954.56 at  $c/h=0$  the deep-stall angles for positive incidences ( $\gamma/c=0.02698$ ) is  $25.75^\circ$  and for negative

Table 6.7: The deep-stall and recovery angles and associated gradients of airfoil DU91-W2-250 measured with models of different chord size.  $Re=0.7 \times 10^6$

Chord size	c/h	$\alpha$ -DS ( $^\circ$ )	$\alpha$ -Rec. ( $^\circ$ )	$\alpha$ -DS ( $^\circ$ )	$\alpha$ -Rec ( $^\circ$ )	Grad. DS	Grad. Rec.
0.15m	0.091	26.96	26.51	-30.07	-21.06	982.03	704.89
0.25m <sup>1)</sup>	0.151	27.95	20.98	-29.07	-22.59		
0.25m <sup>2)</sup>		27.94	20.97	-32.07	-22.10	1007.0	737.08
0.60m <sup>3)</sup>	0.362	29.0	22.17				
0.60m <sup>4)</sup>		29.0	22.48	-33.19	-24.24	1072.8	809.02
<sup>1)</sup> test 2003 <sup>2)</sup> test 2004 <sup>3)</sup> test 2010 <sup>4)</sup> test 2019							

angles ( $\gamma/c=-0.03103$ )  $-29.62^\circ$ . Recovery angles are  $18.22^\circ$  and  $-20.96^\circ$  respectively. Differences with the measurements on the 60cm chord model amount to about  $3^\circ$  to  $4^\circ$ , which is considerable. The lines in fig. 6.22 are quite parallel, which means that, as already noted earlier, the size of the hysteresis loop is hardly impacted by blockage. For  $c/h=0.4$  the difference with blockage-free values of the hysteresis loop length is in the order of  $0.5^\circ$ .

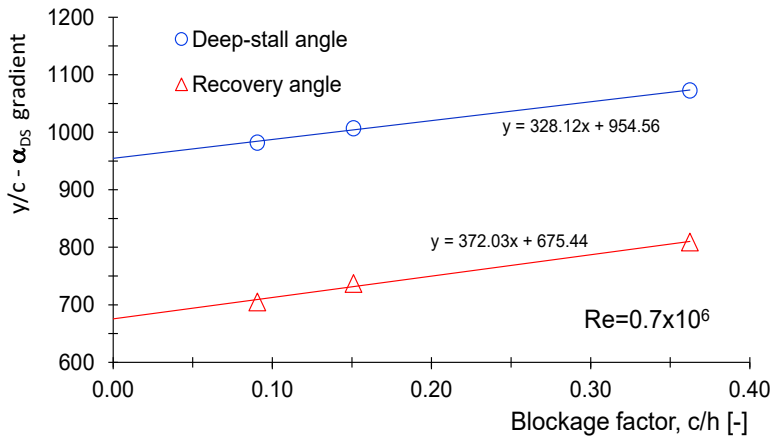


Figure 6.22: The impact of blockage on the deep-stall and recovery angles of airfoil DU91-W2-250 at  $Re=0.7 \times 10^6$ .

## 6.10 THE IMPACT OF LEADING EDGE ROUGHNESS ON THE HYSTERESIS LOOP.

The occurrence of a hysteresis loop resulting from a leading edge separation bubble leads to a situation in which we could encounter several different pressure distributions for an airfoil at one specific incidence, with associated values for the force and moment coefficients, as is illustrated in fig. 6.23 for an angle of approximately  $24^\circ$ .

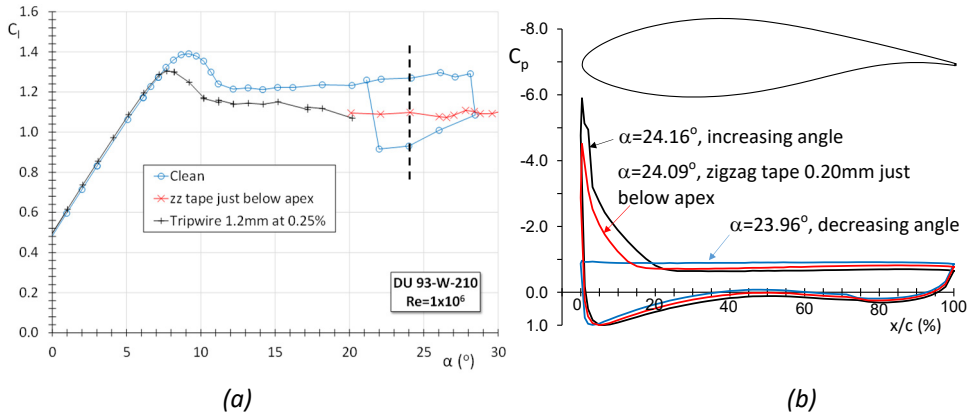


Figure 6.23: The impact of removing the leading edge separation bubble for airfoil DU93-W-210 at  $Re=1 \times 10^6$ .

Fig. 6.23b shows the pressure distributions of airfoil DU93-W-210 in the clean case with the typical  $C_p$ -shapes in the upper and lower hysteresis loop, with leading edge separation at  $\alpha=28.2^\circ$  and recovery at  $21.2^\circ$ . Triggering transition already in an early stage by zigzag tape just below the apex, comparable with the effect of the tripwire at the leading edge, removes the separation bubble and results in a pressure distribution of a turbulent boundary layer without hysteresis.

## 6.11 CONCLUSIONS

From the study on the deep-stall angle the following conclusions can be drawn: Despite the unsteady nature of the flow, in the post-stall region of angles of attack with separation already at stations near 20% chord, Stratford's laminar separation criterion and Crabtree's bursting parameter are applicable to time averaged performance characteristics and pressure distributions.

**Research question RQ 6: What is the connection between an airfoil's deep-stall angle and its shape?**

**RQ 6.1: How big is the impact of the leading edge shape?**

In this study the leading edge shape is represented by the  $y/c$  ordinate at  $x/c=0.0125$ . A

linear relation exists between the deep-stall angle and the  $y/c$  ordinate for airfoils measured in the TUDelft LTT at  $Re=1 \times 10^6$ . For positive angles the upper surface  $y/c$  ordinate is the key parameter, for negative angles the  $y/c$  at the lower surface

### **RQ 6.2 How big is the impact of the trailing edge (TE) shape?**

The impact of the TE shape, here translated into TE-angle is relatively small. A sensitivity of the deep stall angle to TE-angle changes between  $0.04^\circ/\text{deg}$  for DU95 to  $0.09^\circ/\text{deg}$ . for DU97 with a thick TE could be established.

### **RQ 6.3: What is the impact of the Reynolds number?**

An increasing Reynolds number stabilizes the flow in the leading edge region by decreasing the LE-separation bubble size. Consequently, the magnitude of deep-stall angles will increase. The linear relation for  $Re=1.0 \times 10^6$  (fig. 6.10) will be steeper than the one at  $Re=0.7 \times 10^6$  (fig. 6.12)

### **RQ.6.4: Is there an impact of the testing environment?**

Similar to an increase in Reynolds number, a higher blockage increases the velocity in the leading edge region and stabilizes the local flow. The gradient of the linear relation between the deep-stall angle and the leading edge thickness parameter increases with increasing blockage. This cannot be corrected by wall correction schemes.

### **Research question RQ 6.5: What flow or airfoil parameters determine the length of the hysteresis loop?**

A linear relation of the recovery angle with the  $y/c$  ordinate is less obvious as for the deep stall angle. This goes especially for thinner airfoils. The base pressure on an airfoil, while reducing the angle of attack in deep stall, increases. Recovery only takes place when the base pressure (or trailing edge pressure) is at least equal to the value just prior to bubble bursting.

Any flow state decreasing the size of the leading edge laminar separation bubble, such as increased turbulence in the inflow, will increase the deep-stall angle, unless the bubble is completely eliminated. In this case, comparable with the impact of leading edge roughness, laminar separation to deep-stall conditions, and consequently hysteresis, is suppressed.

## **6.12 REFERENCES**

Alam, M. and Sandham, N.D. (2000) *Direct numerical simulation of 'short' laminar separation bubbles with turbulent reattachment*. J. Fluid Mech., 410, 1–28, 2000.

Ceyhan Yilmaz, Ö and Timmer, W.A. (2018) *Experimental evaluation of a non-conventional flat back thick airfoil concept for large offshore wind turbines*. AIAA-2018-3287, USA, 2018

Crabtree, J.F. The formation of regions of separated flow on wing surfaces. R&M 3122, 1959.

Curle, N. and Skan, S.W. (1957) Approximate methods for predicting separation properties of laminar boundary layers, *Aeronautical Quarterly*, Vol. VIII (Aug 1957).

Diwan, S. S., and Ramesh, O. N. (2009) On the origin of the inflectional instability of a laminar separation bubble, *J. Fluid Mech.* (2009), Vol. 629, pp. 263–298.

Gaster, M. (1967) The structure and behaviour of separation bubbles. ARC R&M 3595. (1967)

Gault, D.E. (1955) An experimental investigation of regions of separated laminar flow. NACA Technical note 3505, USA, September 1955.

Gault, D.E. (1957) A correlation of low-speed, airfoil-section stalling characteristics with Reynolds number and airfoil geometry. NACA Technical note 3963, USA, March 1957.

Horton, H. P. (1968) Laminar separation bubbles in two and three dimensional incompressible flow. PhD thesis, Queen Mary College, University of London. (1968)

Jahanmiri, M. (2011) Laminar Separation Bubble: Its structure, dynamics and control. Research report 2011:06, ISSN 1652-8549, Division of Fluid Dynamics, Department of Applied Mechanics, Chalmers University of Technology, Göteborg Sweden. 2011

Landstra, F. (2011) *An Improved Wind Tunnel Blockage Correction method for Two-Dimensional Profile Testing in Deep Stall*. Master thesis Delft University of Technology, March 2011

Loftin, L.K. and Smith, H.A. (1945) *Aerodynamic characteristics of 15 NACA airfoil sections at seven Reynolds numbers from  $0.7 \times 10^6$  to  $9.0 \times 10^6$* . NACA Technical note 1945.

Ramsey, R.R., Hoffman, M.J. and Gregorek, G.M. (1995) *Effects of grit roughness and pitch oscillations on the LS(1)-0421MOD airfoil*. NREL/TP-422-6473. December 1995

Ramsey, R.R., Hoffman, M.J. and Gregorek, G.M. (1995) *Effects of grit roughness and pitch oscillations on the S809 airfoil*. NREL/TP-442-7817. December 1995, revised 12/99

Rodríguez, D., Gennaro, E., & Souza, L (2021) *Self-excited primary and secondary instability of laminar separation bubbles*. Journal of Fluid Mechanics, 906, A13. doi:10.1017/jfm.2020.767, 2021

Roosbroeck, M. van (2014) *The Effect of Leading Edge Thickness on the Maximum Drag Coefficient of Airfoils 90° to the Wind*. Master thesis Delft University of Technology, September 2014

Simoni, D., Ubaldi, M. and Zunino, P. (2014) *Experimental investigation of flow instabilities in a laminar separation bubble*. J. Therm. Sci. 23, 203–214 (2014). <https://doi.org/10.1007/s11630-014-0697-3>

Somers, D.M. (1981) *Design and experimental results for a natural laminar flow airfoil for general aviation applications*. NASA Technical paper 1861, USA, June 1981.

Somers, D.M. (1997) *Design and experimental results for the S805 airfoil*. NREL/SR-440-6917, USA, January 1997

Somers, D.M. (1997) *Design and experimental results for the S809 airfoil*. NREL/SR-440-6918, USA, January 1997

Stratford, B.S. (1957) *Flow in the Laminar Boundary Layer Near Separation*, Aeronautical Research Council, Technical Report R&M No. 3002 (1957).

Tani, I. (1964) *Low speed flows involving bubble separations*. Prog. Aerosp. Sci., 5, pp. 70–103. (1964)

Thwaites, B. (1949) *Approximate calculation of the laminar boundary layer*. Aero. Quart., 1, p. p. 245-280 (1949).

Timmer, W.A. and van Rooij, R.P.J.O.M. (2003) *Summary of the Delft University Wind Turbine Dedicated Airfoils*. Journal of Solar Energy Engineering 125(4) DOI:10.1115/1.1626129 (2003).

Wissink, J., Rodi, W. (2004) *DNS of a laminar separation bubble affected by free-stream disturbances*. In: Friedrich, R., Geurts, B.J., Métais, O. (eds) Direct and Large-Eddy

Simulation V. ERCOFTAC Series, vol 9. Springer, Dordrecht. [https://doi.org/10.1007/978-1-4020-2313-2\\_23](https://doi.org/10.1007/978-1-4020-2313-2_23), 2004.

# 7

## PERFORMANCE CHARACTERISTICS AT HIGH INCIDENCES.

### 7.1 INTRODUCTION

During standstill, starts, stops and hoisting, the blades of both horizontal and vertical axis wind turbines are subjected to large angles-of-attack. In these nominally non-rotating situations the blade acts as a medium-to-high aspect ratio wing. To calculate the mean blade loads, the characteristics of blade segments are in general related to the two-dimensional aerodynamic characteristics of the airfoils. There still is quite some uncertainty in how to translate the 2D-characteristics to the non-rotating blade loads, but even large discrepancies exist in the results of two-dimensional wind tunnel tests on airfoils at high angles of attack. In literature, a number of experiments can be found dealing with the mean aerodynamic performance of airfoils over the entire 360° range of angles of attack; Pope (1947), Critzos et al. (1955), Satran and Snyder (1977), Sheldahl and Klimas (1981), Michos et al. (1983), Templin and Wickens (1984) and, more recent, Rainbird (2015), Lind and Jones (2016), and Madsen and Hansen (2017). Although the list is growing, still there's no abundant amount of data available. As test setup, measurement equipment, model accuracy, data acquisition and reduction and applied wind tunnel blockage correction schemes all differ to some degree in the various publications, or have not been sufficiently described, it can be difficult to extract the most essential information in a direct fashion. Moreover, the heavily fluctuating forces in the deep stall region give rise to large data scatter, which increases uncertainties and makes the mean performance characteristics heavily depending on averaging times. Measured aerodynamic characteristics for the same airfoil in many cases do not match well, an example of which is shown in the next section.

On the whole, airfoil deep-stall performance still is quite uncharted territory, leading to assumptions of time averaged loads, which may very well be too optimistic or too pessimistic

To be able to address these uncertainties and to further map the DU airfoils performance, a number of Delft University wind turbine airfoils have been tested at high angles of attack

and results of tests found in literature have been studied. An additional goal was to investigate if some general description of airfoil key parameters at high angles of attack would be possible on the basis of the existing data, in order to better predict general airfoil two-dimensional performance characteristics in the entire  $360^\circ$  range of incidences. Next to the mean aerodynamic characteristics, this chapter will focus on the impact of airfoil shape, Reynolds number, model blockage ratio and aspect ratio on the deep-stall characteristics.

## 7.2 THE IMPORTANCE OF ESTABLISHING THE RIGHT TEST SECTION DYNAMIC PRESSURE

One of the most tested airfoils at high angles of attack is NACA 0012, mostly due to its application in helicopter blades in the past, but also with a view to use it in blades of (small) vertical axis turbines. Fig 7.1 presents the results in terms of the drag coefficient of a number of studies into the characteristics of this airfoil from  $0^\circ$ - $180^\circ$  angle of attack in the Reynolds number range of  $0.5 \times 10^6$  to  $1.8 \times 10^6$ . Significant differences in the maximum drag coefficient (in the order of 15%) are shown, even for comparable Reynolds numbers.

The same mismatch can be found in the lift and moment data. It shows that testing the same airfoil at high angles of attack does not guarantee results are replicated. The heavily unsteady nature of the flow certainly may have played a role in the variations present,

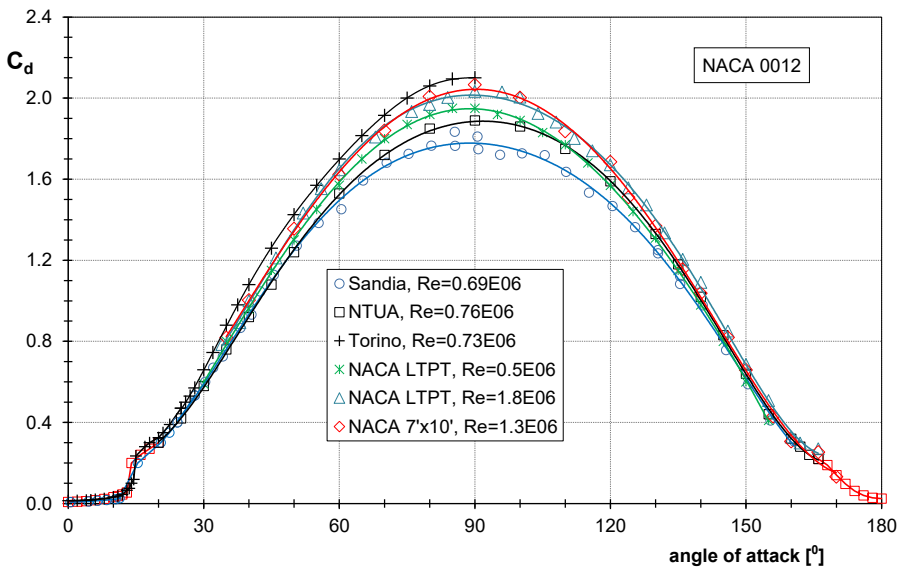


Figure 7.1: Measured two-dimensional aerodynamic characteristics of airfoil NACA 0012 from various sources

but unfortunately not much is known about the data acquisition.

With the exception of the NTUA (Michos et al., 1983) and Torino (Massini et al., 1988) data, all measured characteristics of Sandia (Sheldahl and Klimas, 1981) and from the NACA tunnels (Critzos et al., 1955) were reported to be corrected for wall interference with methods for streamlined flow, e.g. those presented by Allen and Vincenti (1944). The blockage factors  $c/h$  (the chord-to-tunnel height ratio) during the measurements ranged from .067 to 0.257, which may be a source of differences as well. In most of the studies the dynamic pressure was measured in the test section upstream of the model and may have been affected by its static pressure field. The non-dimensional coefficients are normalized with the test section dynamic pressure and the corrections for wind tunnel wall interference are added as increments based on the uncorrected coefficients, so that they refer to the true dynamic pressure. Hence, the dynamic pressure plays a prominent role in the variation encountered. To eliminate this aspect, the ratio of the drag coefficient over the drag coefficient at  $70^\circ$  angle of attack was calculated for the data of fig. 7.1. To avoid introducing differences due to the higher data scatter as a result of the large flow unsteadiness with the section normal to the flow, the value at  $70^\circ$  instead of  $90^\circ$  has been chosen. It appears that, once the dynamic pressure effect is eliminated, the different curves from fig. 7.1 collapse to a reasonable extent, see fig. 7.2. It shows that it is of the

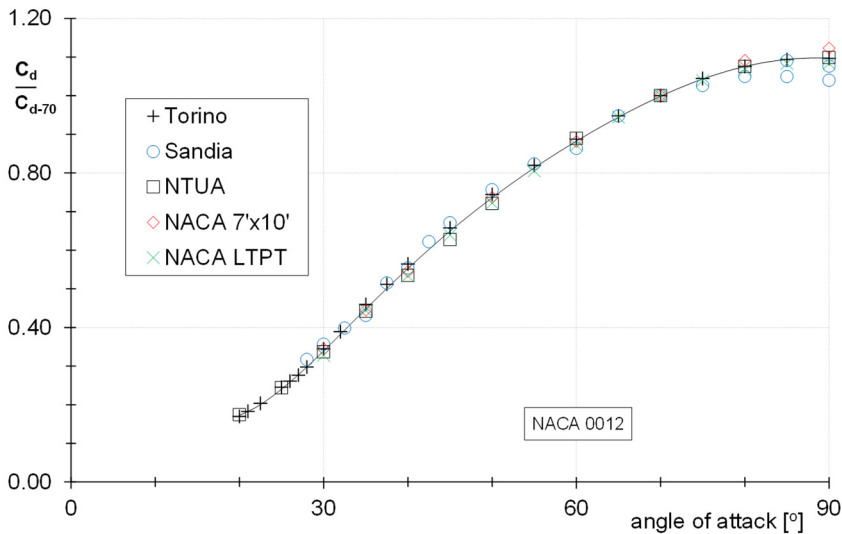


Figure 7.2: The ratio of drag coefficients shown in fig.7.1 with the  $C_d$  at  $\alpha=70^\circ$

utmost importance to establish the right uncorrected dynamic pressure in the test section and to apply the appropriate blockage corrections. Appendix A describes methods to correct wind tunnel measurements at incidences beyond the deep-stall angle. Based on this discussion the method of Maskell was adopted to correct the coefficients and pressure distributions for wind tunnel wall interference (Appendix A, chapter A3.1).

It is interesting to note that, although Maskell's original method published in 1963 was found to overcorrect measurements in a number of cases, the latest additions by Hackett and Cooper in 2001 named Maskell III, which elaborate on a modification by Hackett in 1996, point in the direction again of the original method of correcting the drag, lift and moment coefficients, by multiplying the measured force coefficients with Maskell's initial dynamic pressure ratio (although not explicitly mentioned, see Appendix A):

$$\frac{q'}{q} = \frac{1}{1 + \theta \frac{S}{C} C_d'} \quad (7.1)$$

The primes denote uncorrected values. In a two-dimensional configuration  $\theta=0.96$  and the blockage parameter  $S/C$  (wing area to test section area ratio) is equal to  $c/h$ , the airfoil chord to section height ratio.

### 7.3 FLAT PLATE DEEP-STALL CHARACTERISTICS

Despite the fact that a flat plate at high incidence can be considered as the simplest form of a bluff body, having almost zero thickness and fixed separation points at the plate edges, the number of experimental studies reporting two-dimensional inclined thin flat plate performance characteristics up to  $\alpha=90^\circ$  is very limited. Most studies focussed on aspect ratio's in the range of 1 to 10. For decades the tests of Fage and Johansen (1927) remained the major source for drag and lift coefficients of a two-dimensional inclined flat plate in the range of  $10^\circ < \alpha < 90^\circ$ . In these tests, pressure distributions were measured at  $Re=1.5 \times 10^5$  and integrated to normal force coefficients, from which the lift and drag coefficients were derived, assuming a zero tangential force:  $C_d=C_n \sin \alpha$  and  $C_l=C_n \cos \alpha$ . The study also focussed on the edge velocity and the vortex shedding frequency of flat plates in terms of the non-dimensional Strouhal number, which will be further discussed in

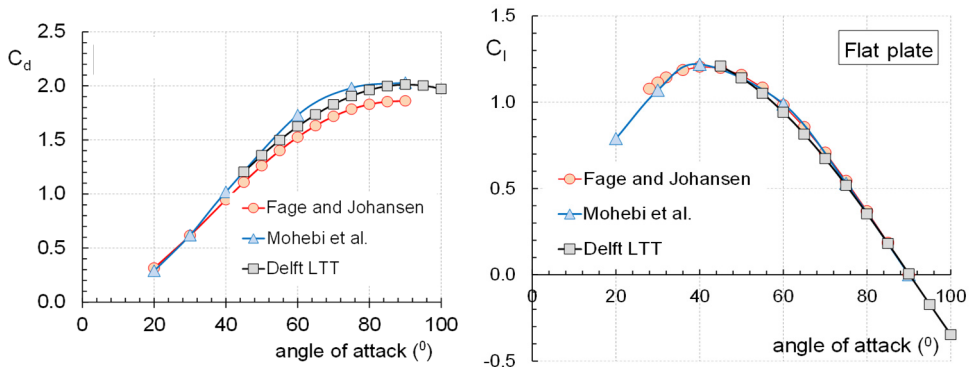


Figure 7.3: Flat plate experimental drag and lift coefficient variation with angle of attack from three sources.

Chapter 8. One of their test results was used by Maskell (1963) for his calculation of the blockage parameter  $\theta=0.96$  (Appendix A).

For the present comparison, the uncorrected data from the report by Fage and Johansen were corrected with Maskell's method, using  $c/h=0.071$ . In fig. 7.3 the resulting corrected lift and drag coefficients are compared to more recent data from Mohebi et al. (2017) from measurements in a 0.5m diameter open jet at a plate Reynolds number of  $0.66 \times 10^4$ . With a span of 560 mm, the plate extended out of the flow. No end plates nor wall corrections were applied. A chord of only 12.8 mm gives a flow aspect ratio of 39 and a very small blockage ratio of .0225. The maximum drag coefficient was found to be 2.03. It must be noted that, in contrast to closed test section measurements, wall corrections of open jet measurements result in higher drag values. Also presented in the graph, data from balance measurements in the Delft LTT at  $Re=4.6 \times 10^5$ , performed in the framework of the study on airfoil maximum drag coefficients, which will be discussed in chapter 9.

While the differences in lift coefficient are relatively small, particularly the drag coefficients of Fage and Johansen are rather low, with a maximum corrected drag coefficient of 1.86. The literature reviews in the studies of Lisoski (1993) and Mohebi et al. (2017) suggest a value in the order of 2 for the mean maximum drag coefficient of a flat plate normal to the flow in the Reynolds number range of  $5.3 \times 10^3$  to  $1.5 \times 10^5$ , which corresponds to test results in the Delft LTT. The Reynolds number range can be extended to  $5.3 \times 10^5$  on the basis of the LTT measurements, as is shown in figure 7.4.

The maximum value of around 2 for  $C_d$  was already found by Wieselsberger in 1923 (2.01) and Flachsbart in 1932 (1.96). Hoerner (1965) suggested 1.98. Aiming at a maximum drag coefficient of 2, the corrected drag coefficients of Fage and Johansen in the range

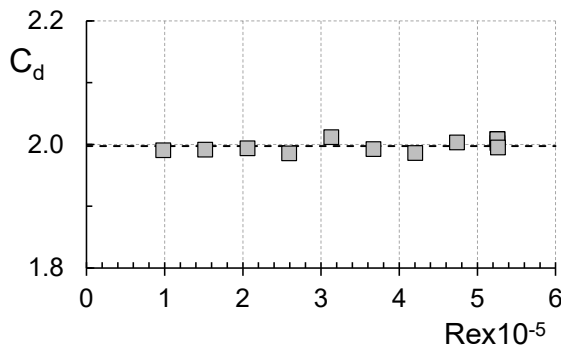


Figure 7.4: The experimental maximum drag coefficient of a flat plate normal to the flow in relation to the Reynolds number. Measurements Delft LTT

$45^\circ < \alpha < 90^\circ$  are consistently about 7.5% lower compared to the Delft tests. From their description of the test setup it remains unclear what the reason for this discrepancy might be. It cannot be the neglect of the tangential force coefficient, as for a flat plate it is generally less than 0.5% of the normal force coefficient in the range  $20^\circ < \alpha < 90^\circ$ . There's

no clear indication what caused the deviant values of Fage and Johansen.

Based on thin airfoil theory, Hoerner (1985, chapter 4.6) comes to an approximation of the lift and drag characteristics of a flat plate given by:

$$C_l = 1.98 \sin \alpha \cos \alpha \quad (7.2)$$

$$C_d = 1.98 \sin^2 \alpha \quad (7.3)$$

These equations originate from the theoretical lift function  $C_l = 2\pi \sin \alpha$ . To account for the loss of suction around the leading edge, the equation is multiplied by  $\cos \alpha$ . The constant term  $2\pi$  needs to be reduced to account for the loss of circulation due to separation.

Figure 7.5 shows these values of lift and drag compared to the experiment in the LTT. The LTT model had a chord of 200mm and a thickness of 4mm. The measurements were restricted to a  $\pm 45^\circ$  rotation relative to the position normal to the flow to prevent a hat stiffener at the mid-chord downwind side to impact the flow around the model. The

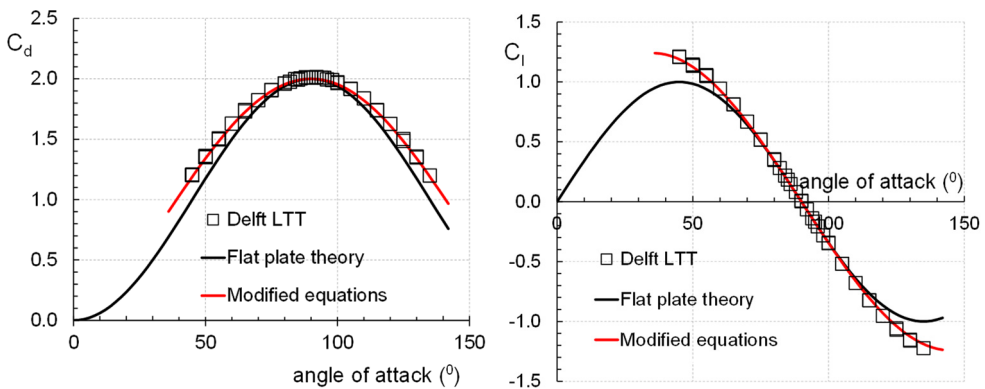


Figure 7.5: Theoretical and experimental flat plate lift and drag coefficients

blockage factor  $c/h$  is 0.121.

Starting at  $90^\circ$ , the lift and drag values increasingly differ for higher and lower angles. In the range  $45^\circ < \alpha < 135^\circ$  the LTT data can be approximated by the equations:

$$C_l = 2.01 \cos \alpha \sqrt{\sin \alpha} \quad (7.3)$$

$$C_d = 2.01 \sin \alpha \sqrt{\sin \alpha} \quad (7.4)$$

Hoerner (1985, chapter 11) redefined the normal force coefficient on a flat plate. Based on the Rayleigh-Kirchoff theory, (von Kármán and Burgers, 1935), the normal force coefficient on an inclined flat plate is defined as

$$C_n = \frac{2\pi \sin \alpha}{4 + \pi \sin \alpha} \quad (7.5)$$

The theory, however, uses  $C_p=1$  for the base pressure, and eq. 7.5 consequently only gives the theoretical force coefficient based on the dynamic pressure on the front of the plate, which results in  $C_n=0.88$  for a plate normal to the flow. With a base pressure  $C_p$  value of -1.1 (Hoerner, 1965)  $C_n$  at  $90^\circ$  is equal to 1.98. Based on experiments it is suggested that the base pressure varies in the same manner as the pressure on the front of the plate. Multiplication of the right hand side of eq. 7.5 with  $1.98/0.88$  leads to Hoerner's equation of the normal force coefficient of an inclined flat plate:

$$C_n = \frac{1}{0.222 + 0.283/\sin \alpha} \quad (7.6)$$

Lift and drag coefficients follow from  $C_d=C_n \sin \alpha$  and  $C_l= C_n \cos \alpha$ .

At this point it must be noted that Fage and Johansen found a base pressure of -1.38. Corrected with Maskell's method this gives -1.08, which is close to the value reported by Hoerner. With an upwind surface contribution of 0.88 following from eq. 7.5, the drag value of the plate normal to the flow measured by Fage and Johansen would give 1.96 instead of the corrected value of 1.86.

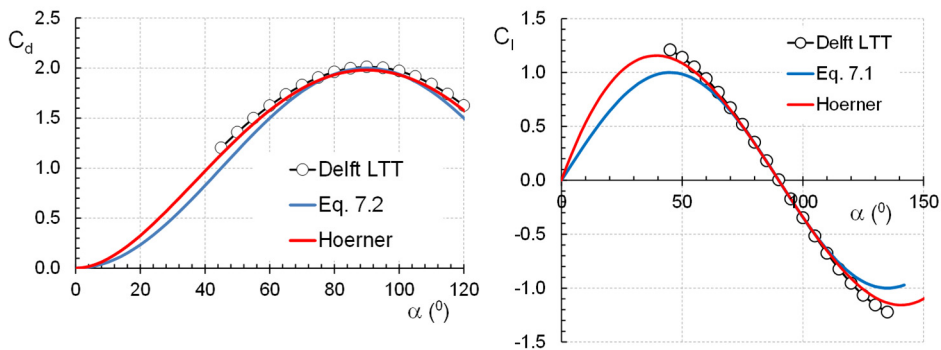


Figure 7.6: Variation of the lift and drag force coefficients with angle of attack according to theory and measurements.

The theoretical and experimental lift and drag coefficients are presented in fig. 7.6. The experimental results are much closer to the values given by equation 7.6, both for the lift and the drag, although the drag differences at  $45^\circ$  are still approximately 6%. The lift-drag ratios in the range of angles of attack shown in fig 7.6 all collapse on the same curve. For clarity of the figures, the Delft data in fig. 7.5 and 7.6 are those from a 6<sup>th</sup> degree polynomial regression.

## 7.4 DEEP-STALL PERFORMANCE OF 3 DU-AIRFOILS.

The deep-stall performance of three 0.25m chord DU-airfoil models was measured using the dedicated 6-component mechanical balance of the LTT. Various configurations were setup to establish test conditions giving two-dimensional values of the force coefficients.

### 7.4.1 Measurements on DU96-W-180 and DU97-W-300

Airfoil DU96-W-180 was tested using the setup shown in figure 7.7. (Timmer and van Rooij, 2001) The -what is called - reflection plate (or plane) spans the entire width of the

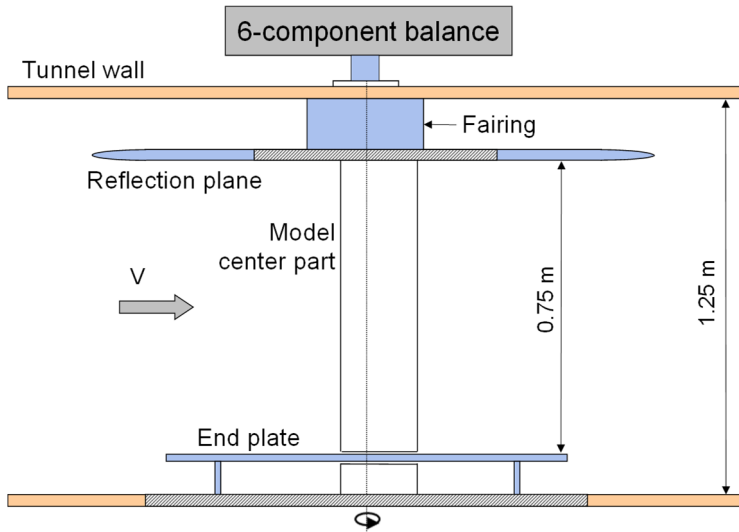


Figure 7.7: Test setup for the measurements on DU96-W-180 with a model chord of 0.25m.

test section. The table diameter, opposite the model lower end, is 1m. The gap between the model and the table was generally kept below 0.6 mm. It proved to be difficult to arrange equal blockage throughout the entire test section area, since the upper streamline strut (fairing) between the reflection plane and the tunnel wall, housing the coupling to the balance, is a fixed arrangement and does not change with angle of attack. Maintaining a uniform blockage in the test section is of key importance for the right forces on the model, as will be further explained in chapter 8. A small plate with the model chord was placed in front of the strut and it was manually rotated every  $5^\circ$  angle of attack, following the mechanical incidence settings. Although in itself a workable setup, it proved to be also quite time consuming, since the plate could only be accessed through a small hatch in the test section upper wall. The test setup for DU97 was therefore changed into the one depicted in figure 7.8. Also here the gaps were kept as small as possible, never exceeding 2 mm. At high angles of attack the entire test section now shows the same blockage.

This setup, however, suffered from the fact that the model, being cantilevered from the

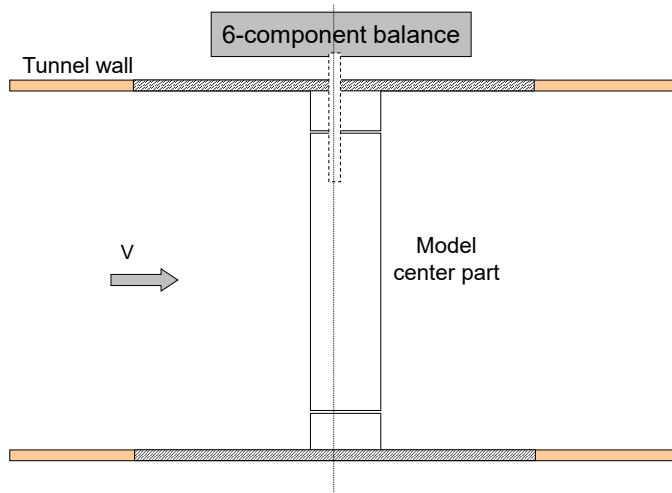


Figure 7.8: Early test setup to test DU97-W-300

balance system, tilted slightly under high loading, giving deflections at the very end of the model, resulting in misalignment of the model and the lower part. The majority of the DU 97 measurements were therefore performed with the setup presented in figure 7.9.

The span of the model is 0.9m. Co-rotating metric model parts between the walls and the tables provide uniform blockage. The wake rake, visible in the back, was used to determine the drag coefficient at the angles between the positive and negative maximum lift coefficients.

The balance system co-rotates with the angle of attack and consequently measures the normal and tangential forces on the model. The mechanical system, though very accurate,

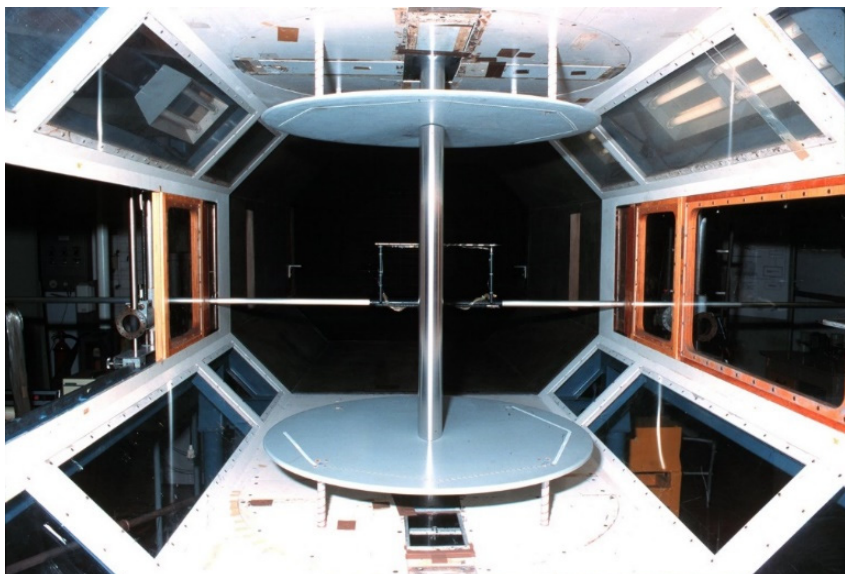


Figure 7.9: Final test setup to test DU97-W-300

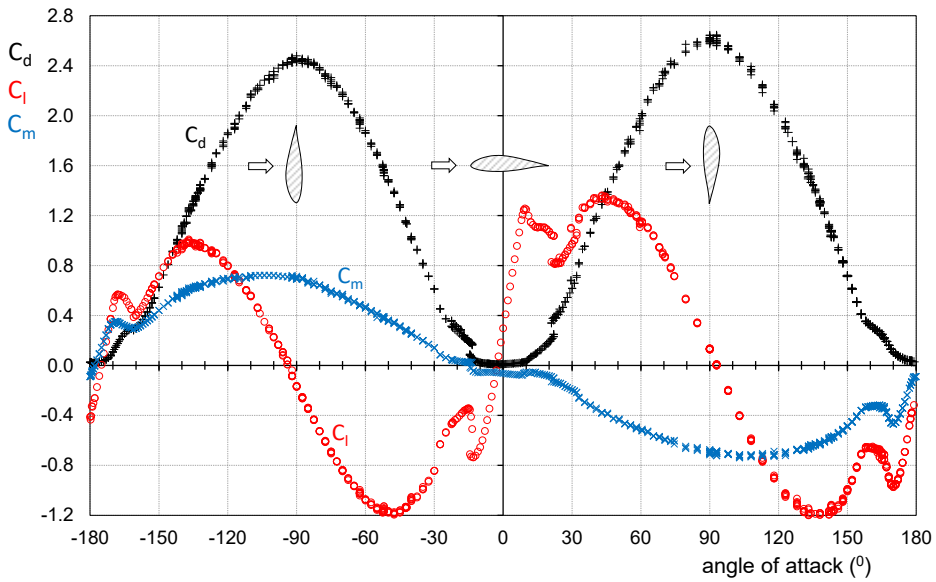


Figure 7.10: The uncorrected DU96-W-180 airfoil characteristics in the range  $-180 \leq \alpha \leq 180$  at  $Re=0.7 \times 10^6$ . Forces by balance measurements.

is relatively slow in its reaction to fast variations in loading and data points are taken with a sampling rate of 5 Hz. This has an averaging effect. Per angle of attack some 25 points were taken. As a result the variations in lift and drag are relatively small. Due to the fact that the angle of attack mechanism was limited to  $\pm 45^\circ$ , the entire  $360^\circ$  range was covered in 5 steps, leaving enough overlap to secure good alignment with the other

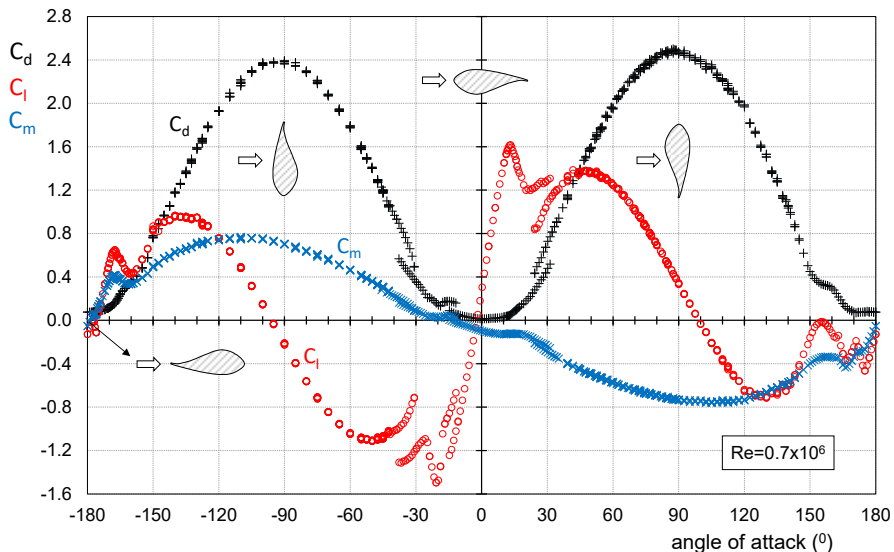


Figure 7.11: The uncorrected DU97-W-300 airfoil characteristics in the range  $-180 \leq \alpha \leq 180$  at  $Re=0.7 \times 10^6$ . Forces by balance measurements.

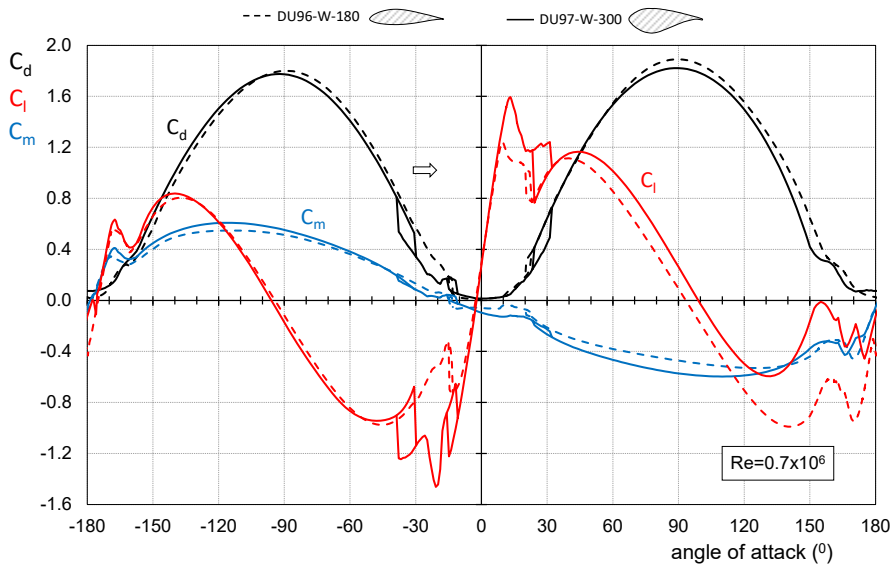


Figure 7.12: The corrected lift, drag and moment coefficients of DU96-W-180 and DU97-W-300 at  $Re=0.7 \times 10^6$

segments. The uncorrected coefficients calculated from the recorded forces are presented in figures 7.10 and 7.11. In the separated regions, e.g. between  $30^\circ$  and  $150^\circ$ , the curves were approximated with a 6<sup>th</sup> order polynomial and corrected with Maskell's method discussed in Appendix A.

The maximum drag coefficient of DU96 at  $90^\circ$  angle of attack is corrected from about 2.60 to 1.891 and at  $-90^\circ$  from 2.435 to 1.800. The corrected values for the DU97 airfoil are 1.831 and 1.781 respectively. Figure 7.12 presents the corrected curves for the two airfoils.

The differences in the maximum drag coefficients for the airfoils will be discussed in chapter 8. Between  $120^\circ$  and  $180^\circ$  the 30% thick airfoil has massive separation due to its thick curved lower side with a cusp, bringing the lift almost to zero.

Since the airfoil upper and lower side maximum thickness do not differ much, in this flow condition the separation almost turns the airfoil into a symmetric shape for the outer flow. Due to the low Reynolds number we can see a number of hysteresis loops around the deep stall angles, both for the positive and the negative incidences.

## 7.4.2 Measurements on DU91-W2-250

### 7.4.2.1 Model chord of 0.25m

Experiments were conducted on a 25cm chord DU91-W2-250 model using the overhead LTT balance system (Boorsma, 2003).

The model was also equipped with pressure orifices and two 32 port pressure sensors inside the model, with a range of 1 and 2.5 psi respectively, to acquire more information



*Figure 7.13 One of the sensors inside the 0.25 m chord DU91-model (with the lower side removed, leading edge at the left) and the test setup of the complete model in the test section, Boorsma (2003)*

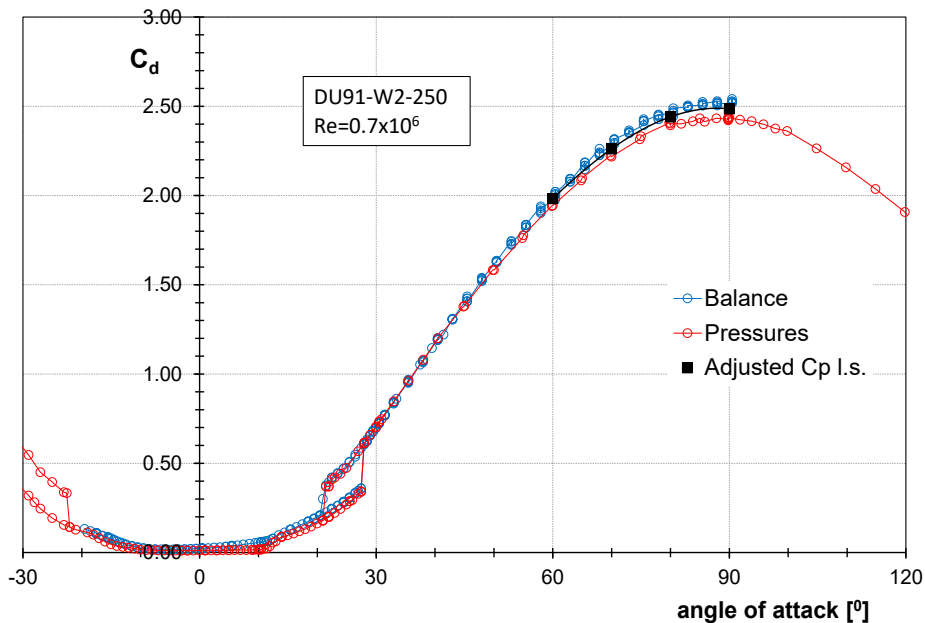
on the surface pressures at high incidences and record any differences between the two measurement systems.

Pictures of one of the sensors inside the model and the model setup in the test section are shown in figure 7.13. A wake rake is situated downstream to determine the drag at the lower angles of attack.

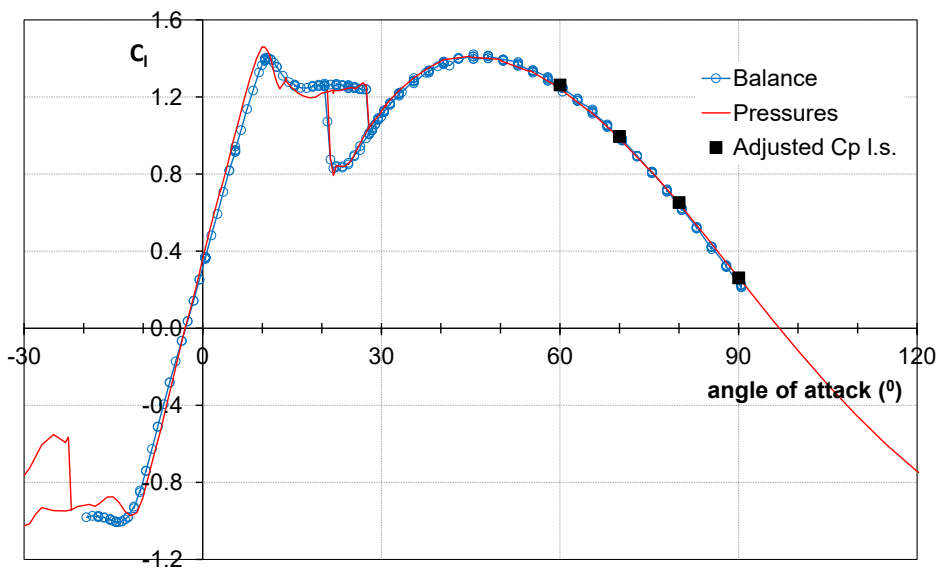
The model spanned the entire test section height, apart from small gaps at each end of the model and the wall (<1.5 mm). The results are depicted in fig. 7.14.

At angles between the negative and positive  $C_{l,max}$  the small gaps turn the model into a high aspect ratio wing. The balance lift gradient, therefore, is somewhat smaller compared to the one derived from the pressure measurements (Timmer, 2018) and the drag is higher. Once in the fully stalled condition, from the deep-stall angle up to  $45^\circ$ , the drag and lift measured by both systems coincide.

Beyond  $45^\circ$  the balance test appears to give a higher drag than the one derived from the



(a)



(b)

Figure 7.14: The uncorrected high angle of attack characteristics of DU91 from balance and pressure measurements.

pressure distributions. This is, however, not caused by difference in the measurement system, but by the limited number of pressure orifices near the trailing edge. The  $C_p$ -distribution at  $90^\circ$  is shown in fig. 7.15. Integration of the pressure distribution with the existing pressure orifices misses the contribution of the normal and tangential force

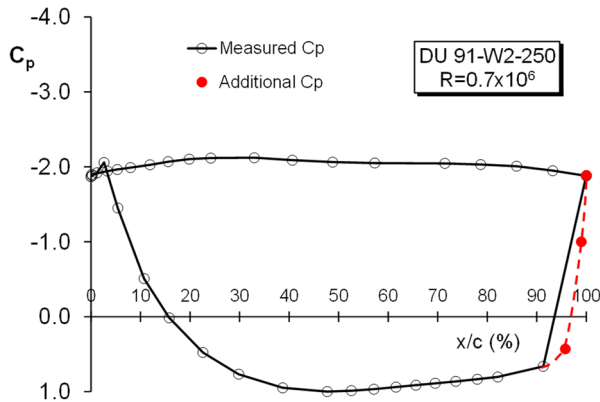


Figure 7.15: The additional pressure coefficient values added to the measured DU91 pressure distribution at  $90^\circ$  angle of attack.

coefficients at the trailing edge. The estimated lower surface pressure distribution near the trailing edge has been sketched in fig. 7.15 as well. For 4 angles, two pressure coefficients have been added to the distribution.

The re-calculated drag and lift forces come very close to those from the balance measurements. The conclusion is that the integrated forces over the span of the model correspond with those on section level and that any end-effects, which may be present in the balance measurements, are of minor impact on the overall force coefficients. For this setup, the characteristics are indifferent from the measurement method, provided that the pressure orifice distribution in the upper and lower surfaces has sufficient resolution, especially near the trailing edge. It also appears that the interference effects with the tunnel boundary layers at the model ends have no significant impact on the balance readings at high incidences. This also gives confidence in the validity of the DU96 and DU97 datasets acquired with the same balance system.

#### 7.4.2.2 Model chord of 0.15 m

The deep-stall characteristics of DU91 were also measured with a pressure tapped 15cm chord model, at positive angles by Landstra (2011 and Van Roosbroeck (2014), at negative incidences by Timmer (2021). Fig. 7.16 indicates that Maskell's correction scheme with theta is 0.96 gives good results in the deep-stall region. (see also Appendix A). It shows the corrected characteristics of the 25cm and 15cm chord models of DU91 at a Reynolds number of  $0.7 \times 10^6$ . The agreement is very good. The difference in maximum drag at positive as well as negative angles is in the order of 0.5%.

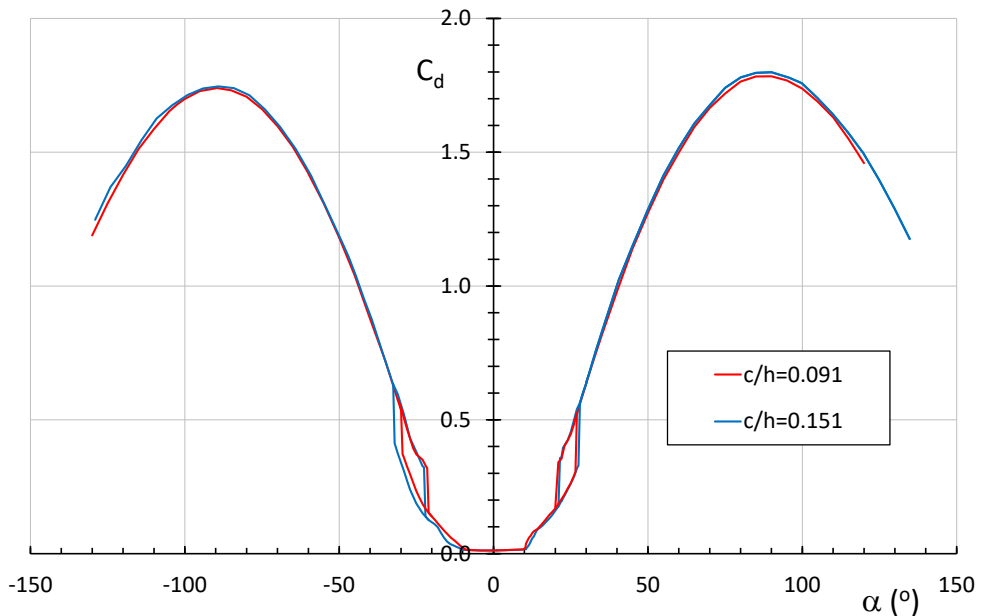


Figure 7.16: The corrected drag characteristics of airfoil DU91-W2-250 at  $Re=0.7 \times 10^6$  for two models with chords of 15cm and 25cm respectively, measured in the LTT.

## 7.5 THE IMPACT OF THE REYNOLDS NUMBER

In view of the increase in blade Reynolds numbers associated with ongoing wind turbine upscaling, particularly high Reynolds number data are of interest. To determine the impact of the Reynolds number on airfoil deep-stall characteristics, three data sets were examined next to the ones reported above, all including DU airfoils, giving the lift, drag and moment performance in the range of Reynolds numbers up to  $Re=8 \times 10^6$ . The latter experiments were conducted in the high pressure wind tunnel (HDG) in Göttingen, Germany. The tunnel was operated by DNW until 2020.

### 7.5.1 DU00-W-212

#### 7.5.1.1 Reynolds numbers between $0.5 \times 10^6$ and $1.7 \times 10^6$

Deep-stall measurements on a 0.3m chord DU00-W-212 model were performed in the low-speed wind tunnel of LM Wind Power in Denmark in the framework of the European AVATAR research project (Madsen and Hansen, 2017). Fig. 7.17 presents the aerodynamic characteristics for  $Re=0.5 \times 10^6$  and  $Re=1.5 \times 10^6$ . The uncorrected data at deep-stall angles were corrected using Maskell's method described in Appendix A. Due to blockage effects ( $c/h=0.11$ ) the Reynolds numbers vary between  $0.5 \times 10^6$  and  $0.56 \times 10^6$  for the lower Reynolds number and between  $1.5 \times 10^6$  and  $1.68 \times 10^6$ , the higher Re-value being reached at  $\alpha=90^\circ$ .

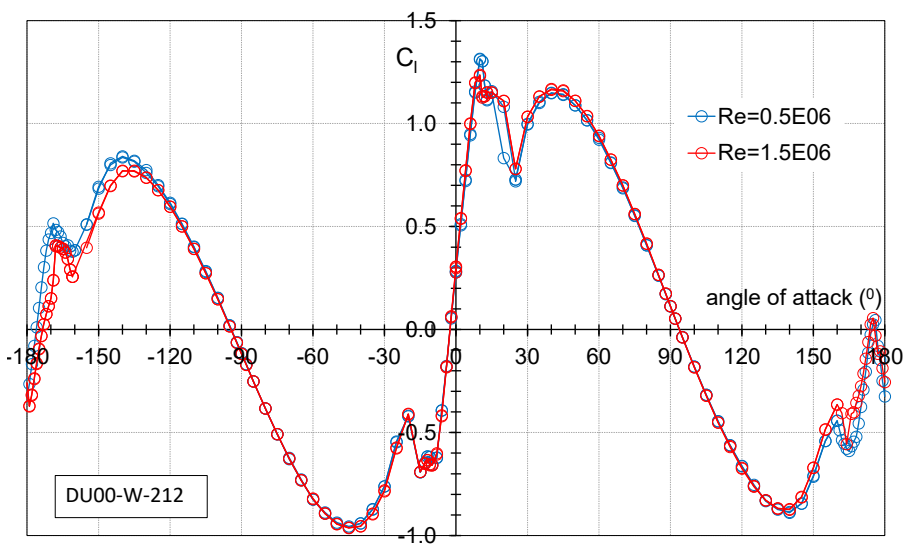
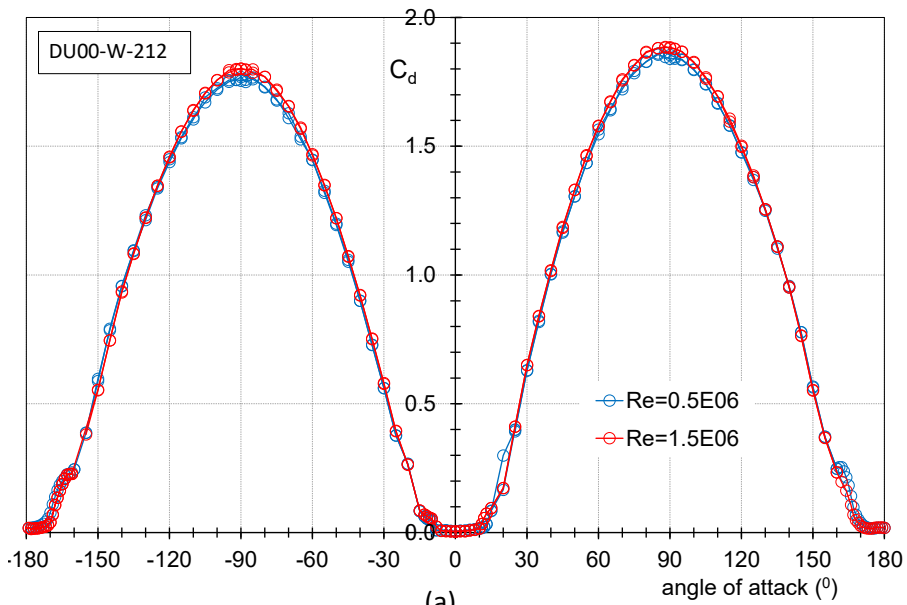


Figure 7.17: The measured high angle of attack characteristics of airfoil DU00-W-212 for two Reynolds numbers, corrected for blockage. Uncorrected data from Madsen and Hansen (2017).

The turbulence intensity of the LM tunnel is in the order of 0.1%.

For the drag coefficient (a) the most distinctive differences due to variation of the Reynolds number lie around the maximum drag. At first sight, an increase of the Reynolds number from  $0.5 \times 10^6$  to  $1.5 \times 10^6$  seems to lead to a higher drag coefficient in the deep-stall region of angles of attack. This is, however, only a Mach number effect, which increases at  $\alpha=90^\circ$  from  $M=0.078$  to  $M=0.246$ .

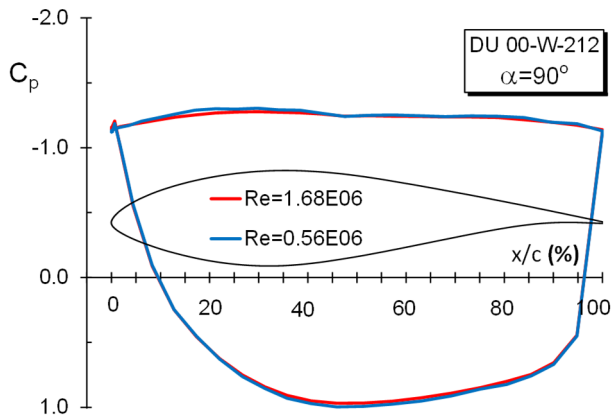


Figure 7.18: The pressure distributions of airfoil DU00-W-212 at  $\alpha=90^\circ$  for two different Reynolds numbers, corrected for blockage and Mach number. Uncorrected data from Madsen and Hansen (2017)

The pressure distributions at  $\alpha=90^\circ$ , presented in fig. 7.18, show very little variation when corrected for the difference in Mach number using the Prandtl-Glauert rule:  $C_{p0} = C_p \sqrt{1 - M^2}$ , in which  $C_{p0}$  is the incompressible pressure coefficient. At  $Re=1.7 \times 10^6$ , the Mach-correction reduces the maximum drag coefficient at positive angles from 1.885 to 1.827, while at the lowest Reynolds number the drag coefficient decreases from 1.850 to 1.846, giving a variation in the order of 1% in drag coefficient between the two Reynolds numbers.

The lift coefficient (fig. 7.17b) shows the biggest variation in a  $\pm 45^\circ$  angle of attack range

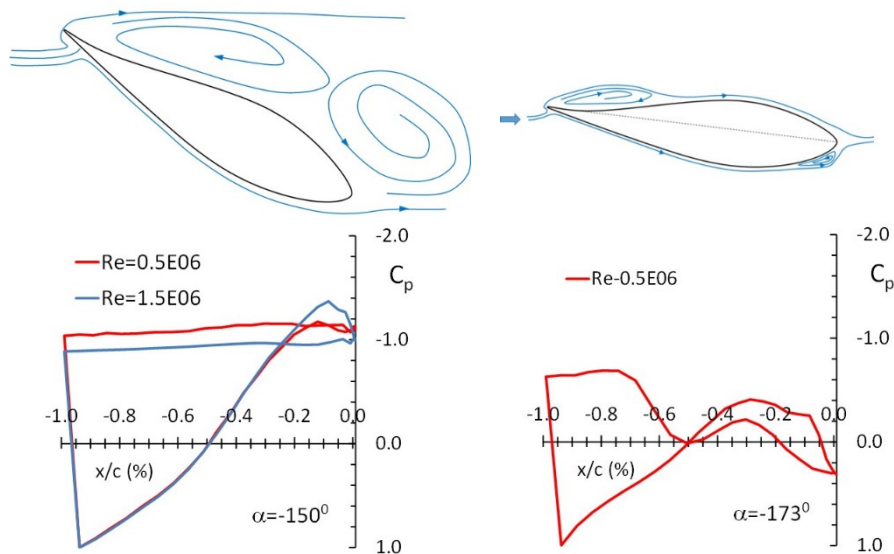
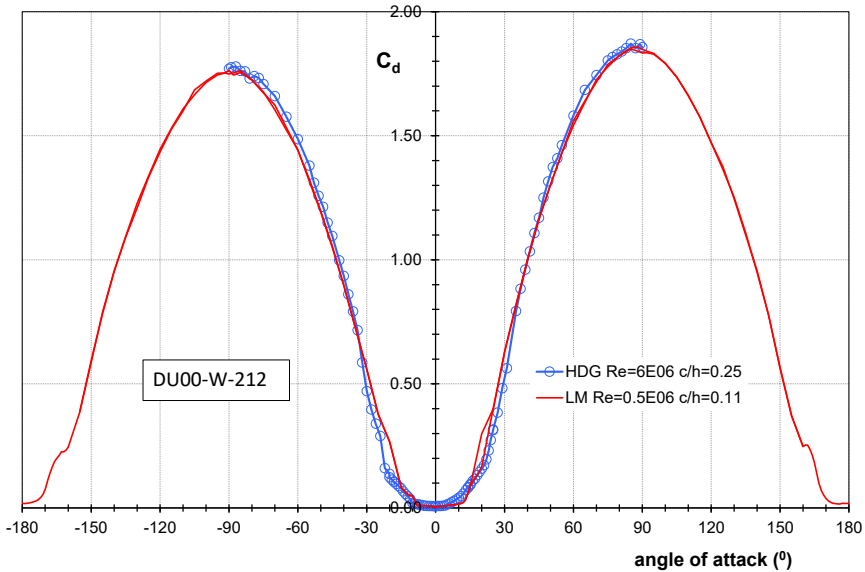
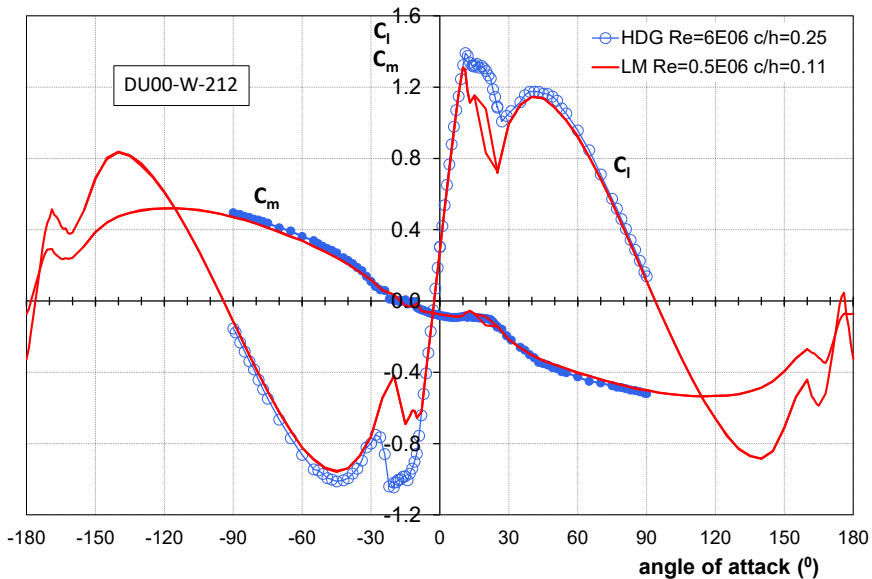


Figure 7.19 The pressure distribution and estimated flow topology at  $-150^\circ$  and  $-173^\circ$  angle of attack. Data corrected for Mach number.  $x/c$  values negative to follow flow direction on airfoil.

around the  $-180^\circ$  position. At e.g.  $-150^\circ$  the orientation of the airfoil is with the trailing edge first and with the lower side up, as is shown in the left picture of fig. 7.19. The stagnation point is close to the upwind trailing edge. Due to the sharp trailing edge the entire downwind side has separated, giving a suction force in upward (positive) direction. Separation at the upwind side takes place close to the leading edge, now located



(a)



(b)

Figure 7.20: The measured high angle of attack characteristics of airfoil DU00-W-212 for Reynolds numbers of  $0.5 \times 10^6$  and  $6 \times 10^6$  to  $8.1 \times 10^6$ , corrected for blockage.

downstream. With increasing Reynolds number the separation location moves closer to the leading edge, creating more suction on the airfoil upper side, while at the same time the base pressure increases, which both contribute to a lower lift coefficient.

Starting at  $\alpha=-150^\circ$ , with decreasing angle the airfoil lower side remains entirely separated until  $\alpha=-165^\circ$ , then the flow over the top side gradually starts to attach to the rear of the airfoil. After  $-169^\circ$  the flow over the upwind side starts forming a laminar separation bubble, as is shown in the right picture of fig. 7.19.

#### 7.5.1.2 Reynolds numbers between $6 \times 10^6$ and $8.1 \times 10^6$

Within the EU-AVATAR project, the DU00-W-212 airfoil was also tested in the high pressure tunnel (HDG) of the DNW in Göttingen, Germany, for angles in the range  $-90^\circ \leq \alpha \leq 90^\circ$  (Jacobs 2015). These measurements were performed with constant velocity and tunnel pressure in the entire range of angles of attack. With a chord of 0.15m and a test section height of 0.60m this results in high blockage effects at angles around  $90^\circ$  and  $-90^\circ$ . Consequently, the Reynolds number ranges from about  $6 \times 10^6$  at  $\alpha=20^\circ$  to  $8.1 \times 10^6$  at  $\alpha=90^\circ$ .

The blockage factor  $c/h$  during these tests was 0.25. Although measurements on airfoil NPU-WA-210 shown in Appendix A suggest that up to  $90^\circ$  incidence results from such measurement deviate little from those at lower blockage, some caution should be exercised in the interpretation of the data here, as it is not completely clear how the high blockage has affected the performance.

The results of the balance measurements are depicted in fig. 7.20, together with the curve at  $Re=0.5 \times 10^6$  from fig. 7.17, to show the Reynolds number impact without an associated Mach number effect (the corrected Mach number in the HDG at  $90^\circ$  is .04). Data points results from 30 seconds averages. Figure 7.20 shows close agreement in the deep-stall region between the data sets, when corrected with Maskell's method. The overall differences in drag coefficient in the higher angle of attack range are small, despite the much higher Reynolds number in the HDG. There's only a small difference in the  $C_{d,max}$  (HDG 1.862 for the balance measurements and 1.853 for the pressure data, against LM 1.846). The LM drag values at the lower Reynolds number come from pressure distributions, which at  $\alpha=\pm 90^\circ$  have an estimated loss in drag coefficient of about .010 to .012 due to the limited resolution of pressure information close to the trailing edge. This brings the maximum drag coefficients of the HDG balance measurements and the LM pressure data with supplemented pressure distribution at a comparable level.

Although the separation locations and the drag are nearly the same (about 1% difference in maximum pressure drag), the pressure distributions at  $\alpha=90^\circ$  presented in fig. 7.21 indicate that the separation mechanisms differ. The combination of the higher HDG-

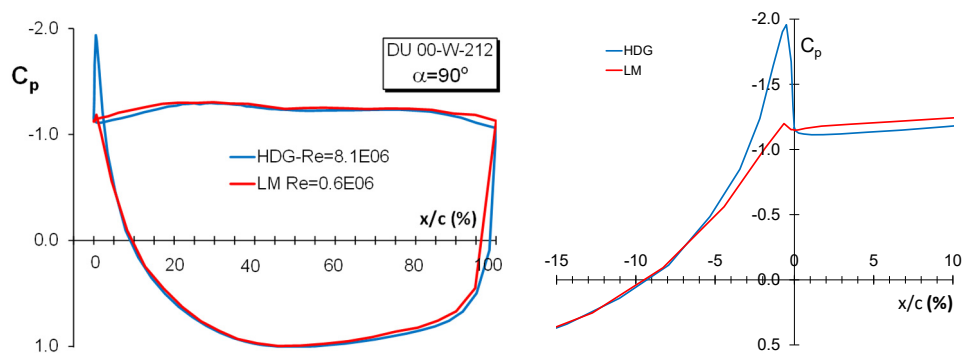


Figure 7.21: The measured pressure distributions for the configurations of fig 7.18 at  $90^\circ$  angle of attack. At the right a detail at the leading edge, with the lower side x-ordinates presented negative.

tunnel turbulence intensity (between 0.2% and 0.5%, against 0.1% for the LM-tunnel) and the much higher Reynolds number leads to attached flow up to the very leading edge. A pressure peak is generated, of which the strong adverse pressure gradient downstream induces transition just before the apex, followed by turbulent separation right at the apex. Due to the presence of the pressure peak one would expect a slightly lower drag for the HDG measurement. The lower Reynolds number flow has laminar separation and off-surface transition.

The pressure distributions around the leading edge at the righthand side of fig. 7.21 show the pressure deviation at the upwind side between the two Reynolds numbers in more detail. Starting at the upwind side 6% chord station the pressure difference suggests a rapidly growing boundary layer thickness at the lower Reynolds number, followed by flow detachment after the lower side 0.66% chord station, which is also close to the apex. After an initial small disparity at the downwind side leading edge the base pressures do not show much difference.

### 7.5.2 DU91-W2-250

An interesting case of high Reynolds number characteristics for a thicker airfoil is depicted in fig. 7.22. It shows the performance of a 10cm chord DU91-W2-250 model in the Reynolds number range of  $6.0 \times 10^6$  (at  $\alpha=20^\circ$ ) to  $7.1 \times 10^6$  (at  $\alpha=90^\circ$ ). (Jacobs and Benkel, 2014).

Distinct differences exist, both in lift and drag coefficient. Throughout the deep-stall region the drag is lower and the lift higher at the higher Reynolds number.

At  $90^\circ$  the behaviour is comparable to the DU00-W-212 airfoil. Taking the  $C_p$ -resolution of the models near the trailing edge into account, the maximum pressure drag coefficient is reduced with 3% .

The biggest drag differences, though, can be seen just after the deep-stall hysteresis loop of the LTT model. Here, at  $\alpha=30^\circ$ , the HDG model shows a drag reduction of more than 50%. Looking at the pressure distributions at this angle, presented in fig. 7.23, it is clear that the drag reduction is caused by a substantial difference in separation location. The model at  $Re=0.5 \times 10^6$  has laminar separation from the leading edge with off-surface transition, while the model at the higher Reynolds number shows

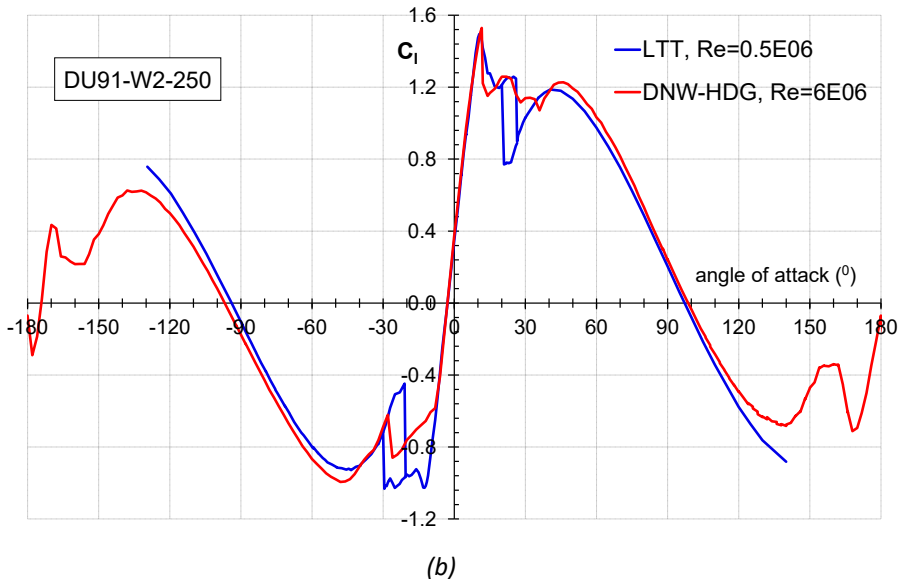
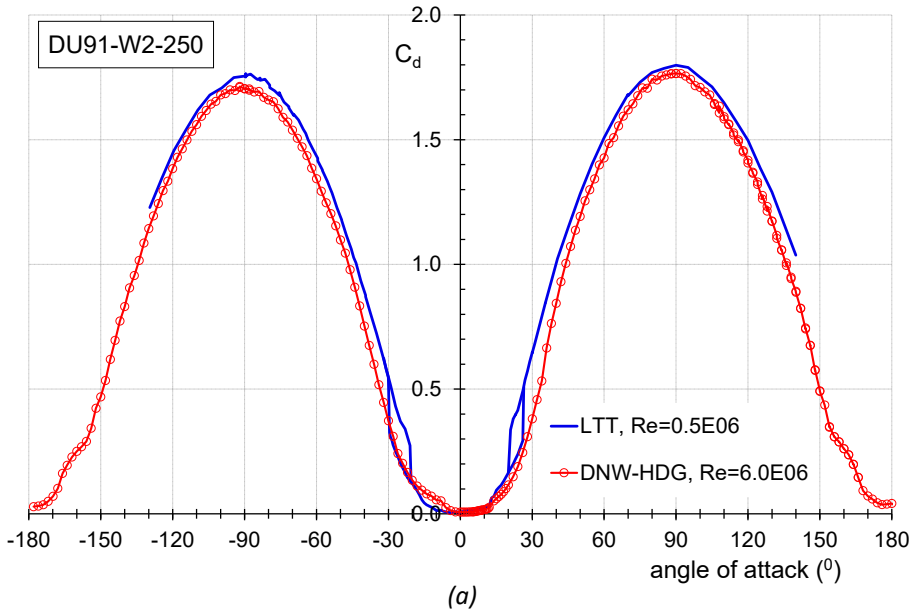


Figure 7.22: Comparison of the aerodynamic deep-stall drag (a) and lift (b) characteristics of DU91-W2-250 at  $Re=0.5 \times 10^6$  and  $Re=6 \times 10^6$ . Uncorrected HDG data courtesy DNW.

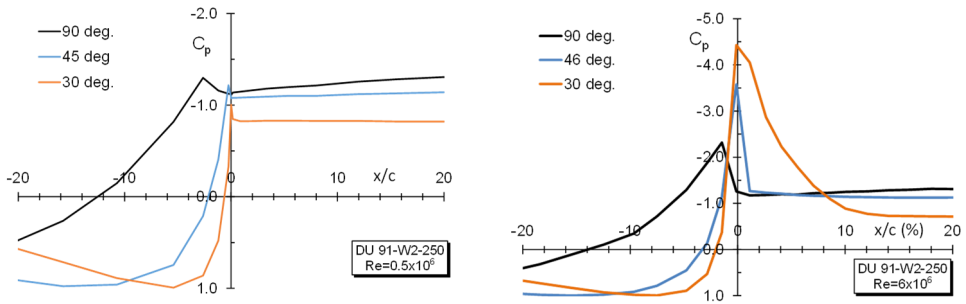


Figure 7.23: The pressure distributions of the LTT (left) and HDG measurements (right) between  $30^\circ$  and  $90^\circ$  incidence, showing the impact of the Reynolds number on the location of flow separation.

turbulent separation from the upper surface 14% chord station after a pressure peak of about -5, leading to a significantly higher base pressure over more than 90% of the chord ( $C_p = -0.837$  against  $-0.706$ ). This situation shows similarity with cylinder flow. In subcritical conditions ( $Re \leq 2 \times 10^5$ ) the flow separates at the upwind side, with off-surface transition and a drag coefficient of 1.2. At Reynolds numbers beyond  $4 \times 10^5$  turbulent separation follows shortly after a laminar separation bubble located at the cylinder downwind side, resulting in a significant drag reduction to about 0.3.

Starting at  $30^\circ$  incidence, with increasing angle of attack, the DU91 separation locations for the higher Reynolds number shown in fig. 7.23 gradually move upstream to the leading edge at  $90^\circ$ , while separation at  $Re = 0.5 \times 10^6$  moves from the leading edge to stations located at the upwind side of the airfoil.

## 7.6 THE IMPACT OF SHAPE, REYNOLDS NUMBER AND INCIDENCE ON THE BASE PRESSURE

Figure 7.23 shows varying separation locations with increasing angle of attack. To investigate how this impact the base pressure, fig. 7.24 presents the pressure distributions of airfoils DU91 and DU00 normal to the incoming flow at Reynolds numbers of  $0.5 \times 10^6$  (left) and  $Re = 7.1 \times 10^6$  (right). Both figures indicate that the differences in drag coefficient come from variations in the upwind side pressure distribution. The set-up of these measurements included  $c/h$  values between 0.111 and 0.167, according to Appendix A giving good results when corrected for blockage with Maskell's method.

As the base pressures for DU91 and DU00 at  $90^\circ$  as well as  $-90^\circ$  (for DU91 not shown) are similar, it is suggested that, for measurements at comparable blockage, the base pressure only depends on the airfoil orientation towards the incoming flow, irrespective of airfoil shape and Reynolds number.

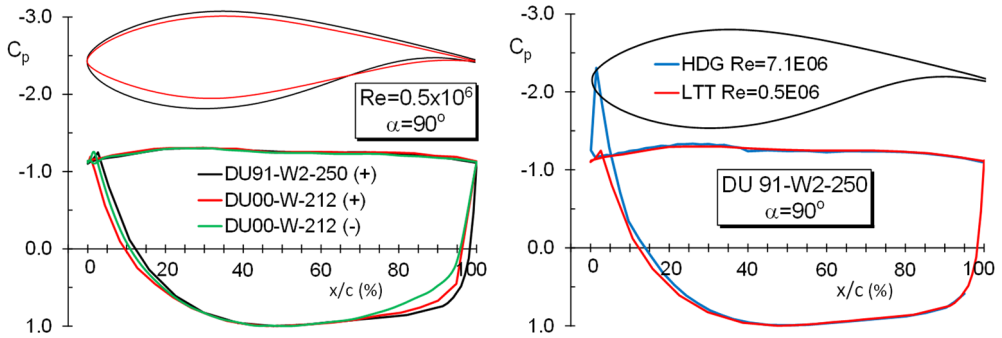


Figure 7.24: The pressure distributions of airfoils DU91 and DU00 placed normal to the flow at significantly different Reynolds numbers. (+) and (-) denote a positive and a negative angle respectively.

To investigate this, average base pressures were determined for DU00 and DU91 at  $Re=0.5 \times 10^6$  for positive as well as negative angles in the deep-stall region (fig. 7.25). The DU00 base pressure values all appear to greatly coincide in the range of  $\alpha=60^\circ$  to  $120^\circ$ . However, for airfoil DU91 there is a slight offset of  $-0.018$  at negative incidences. When this offset is removed (the black dashed line in the graph) also here the base pressures coincide in the same range of angles of attack.

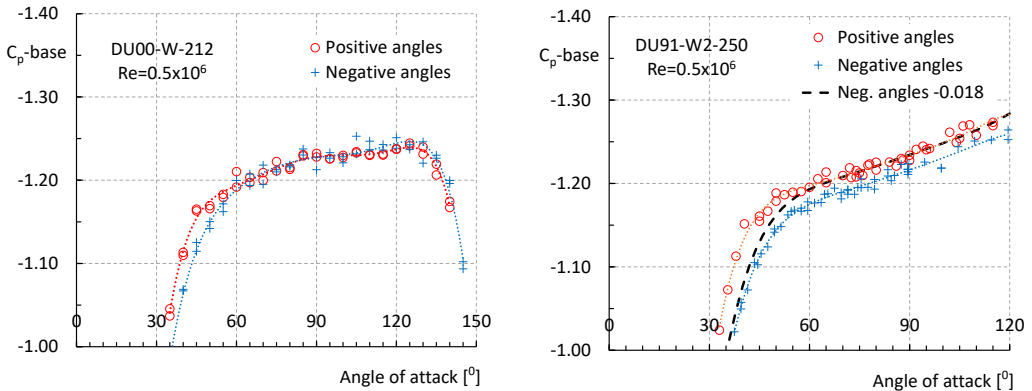


Figure 7.25: Average base pressures at  $Re=0.5 \times 10^6$  for airfoils DU00-W-212 (left) and DU91-W2-250 (right). The black dashed line in the DU91 graph is a 6-degree polynomial for the base pressures at negative angles reduced with  $0.018$ .

The cause for this slight offset can be found in the rear part of the downwind pressure distribution, as is shown in fig. 7.26 (left), presenting the  $C_p$ -distributions at  $80^\circ$  incidence. Apparently, unlike generally adopted, the airfoil downwind shape, and more in particular the rear part, does impact the flow in deep-stall. Although separation occurs right at the sharp trailing edge for positive as well as negative angles, the very different downwind tail shape may affect the path of the trailing edge vortices.

The deceleration of the shear layer at the aft part of the airfoil at negative angles can be traced back to the concave shape in the DU91 airfoil lower side, which differs significantly

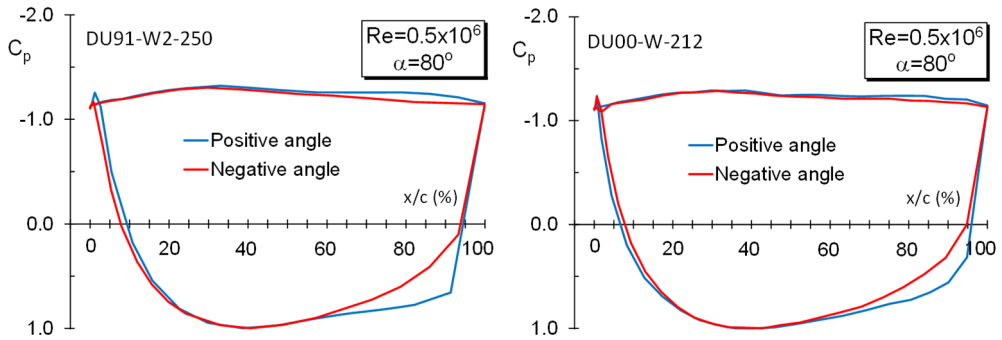


Figure 7.26: The DU91(left) and DU00 (right) pressure distributions at  $\alpha=-80^\circ$  and  $80^\circ$ .

from the relatively straight upper side tail (trailing edge angles of  $-10.2^\circ$  and  $16^\circ$ , see also chapter 8).

The DU00 shape difference between the upper and lower side rear parts is much less pronounced, (trailing edge angles of approximately  $0^\circ$  and  $14^\circ$ ) which reflects the nearly coinciding base pressures at positive and negative angles in fig. 7.25 (right). The divergence in leading edge shape of the two airfoils does not seem to impact the first 60% chord base pressure. These differences in base pressure may be aggravated with increasing blockage. A confidential study on airfoil performance at relatively high blockage and small model aspect ratio, reveals that this difference in base pressure at the aft part of the section between a positive and a negative incidence appears to be typical for every airfoil with a distinct difference in upwind and downwind side tail shape, like is

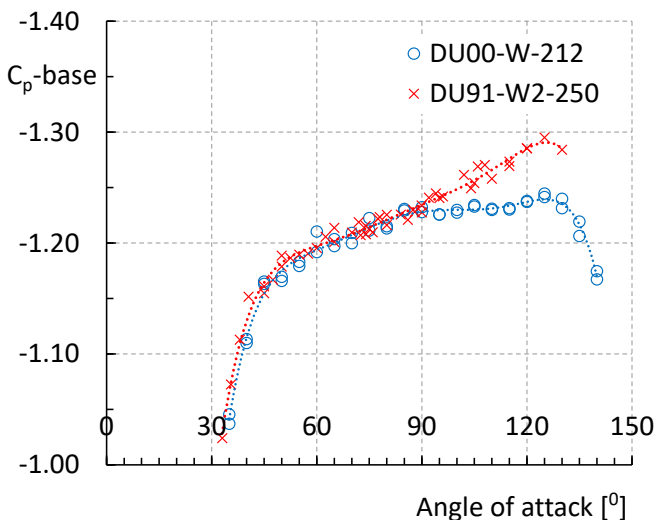


Figure 7.27: The DU91 and DU00 base pressure coefficients at positive angles of attack.  $Re=0.5 \times 10^6$ .

present in airfoils with high camber or an aft-loading lower side cusp.

Comparison of the DU91 and DU00 base pressure coefficients at positive angles presented in fig 7.27, shows an approximate linear relation with incidence in the range of angles between  $60^\circ$  and  $90^\circ$  with values of -1.20 at  $60^\circ$  to -1.23 at  $90^\circ$  ( $\pm 0.004$ ). At these angles of attack separation occurs at (TE) or close to (LE) the airfoil edges. Outside this range the characteristics are sensitive to airfoil shape and the Reynolds number.

## **7.7 THE IMPACT OF MODEL ASPECT RATIO ON THE DEEP-STALL CHARACTERISTICS.**

What remained underexposed up to this point is the impact of the aspect ratio of the model. A numerical study performed by Sørensen (Sørensen and Timmer, 2017) on the prediction of the deep-stall characteristics of DU97-W-300 revealed an exponential decay of the drag coefficient at  $\alpha=90^\circ$  with increasing aspect ratio. It was shown that only unsteady computations on a configuration with a span in the order of 4 times the chord came close to the experimental results presented in fig. 7.12, where the model had an aspect ratio of 3.6. Apparently, some span is needed to resolve existing 3D structures in the flow. This suggests, that also in experiments the results may not only be impacted by the blockage ratio  $c/h$ , but also by the model aspect ratio  $AR=b/c$ , where  $b$  is the span of the model.

Varying the blockage ratio by using increasingly larger model chords, unfortunately also leads to reductions in aspect ratio, as generally the model span is fixed, which makes it difficult to identify the specific contributions to the final result.

An example is the study of Wang et al. (2015), shown in Appendix A. Testing chords of 0.5 m, 0.65m and 0.8m in the  $1.6 \times 3.0 \text{m}^2$  rectangular test section gave blockage ratios of 0.167, 0.217 and 0.267 and aspect ratios of 3.2, 2.5 and 2, respectively.

The corrected lift and drag characteristics for  $c/h=0.17$  and  $0.22$  are presented in fig. 7.28, which contains data from fig. A10b, but now for clarity only showing the 6<sup>th</sup> degree polynomials through the points. Differences at negative angles are small, confined to incidences around the maximum drag coefficient, in the order of the measurement error. Angles beyond  $90^\circ$  show more systematic deviations, with higher drag resulting from increasing blockage and decreasing aspect ratio, along with only small differences in lift.

A result with similar blockage can be obtained from fig. B.4b in Appendix B where two experimental data sets for airfoil DU96-W-180 are compared. The 6<sup>th</sup> degree polynomial regressions are depicted in fig. 7.29. Despite the DWG higher blockage ratio and lower aspect ratio, differences in drag are small. The higher drag at  $c/h=0.22$  beyond  $\alpha=90^\circ$ , seen in fig. 7.28, is not present here. In this case the differences in lift are more

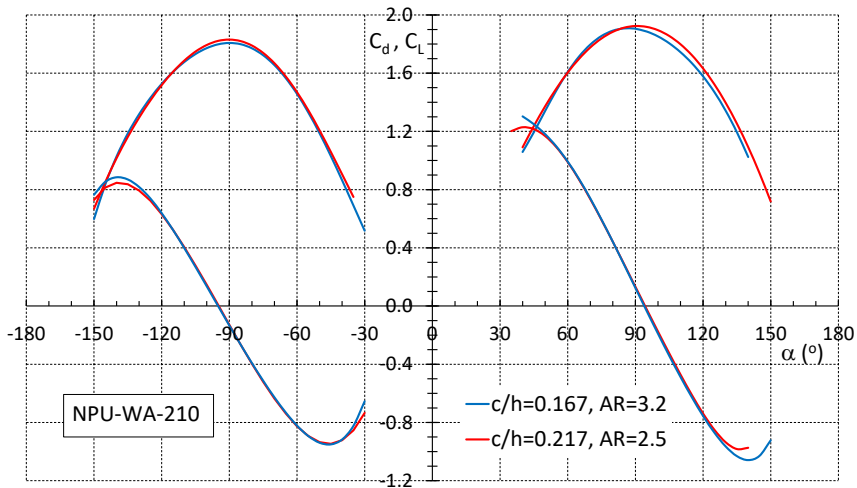


Figure 7.28: The corrected lift and drag characteristics for airfoil NPU-WA-210 (Wang et al., 2015) for various blockage and associated aspect ratios

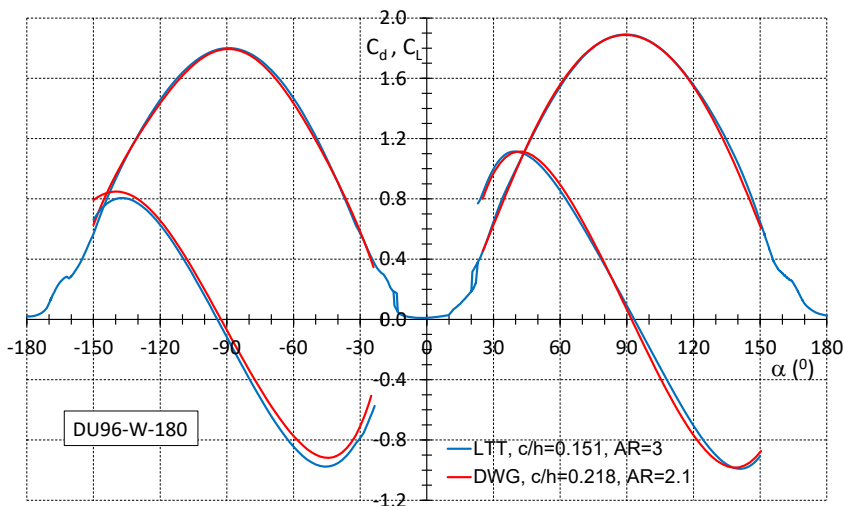


Figure 7.29: The corrected lift and drag characteristics for airfoil DU96-W-180 (Appendix B and fig. 7.12) for various blockage and associated aspect ratios.

pronounced.

Both model aspect ratio's in fig 7.29 seem rather low, in the light of the computational results mentioned earlier. A second DU96 model for the LTT was constructed, with the same chord of 25 cm, now spanning the 1.8 m width of the test section, giving a blockage ratio of 0.217 (effective height 1.15m) and an aspect ratio of 7.2. During the first tests, however, the model attachment to the angle of attack mechanism at both sides of the model started to slip due to the high aerodynamic moments occurring deep into stall both for negative as well as positive angles. The tests were discontinued and unfortunately

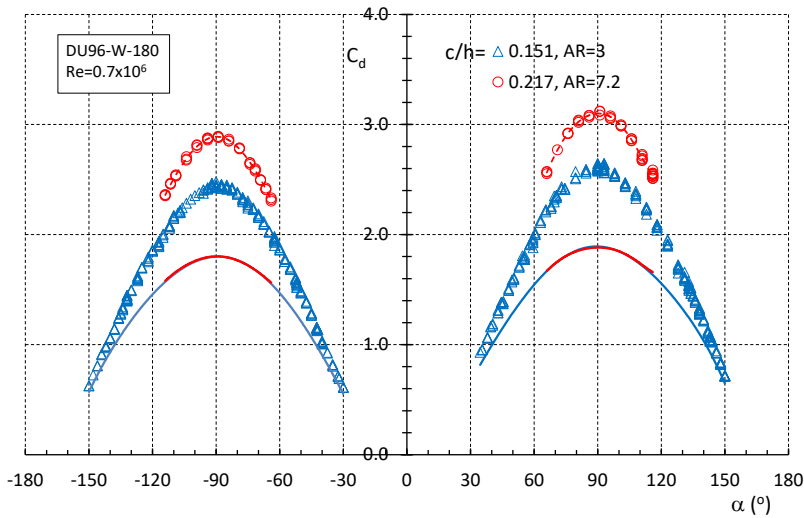


Figure 7.30: The uncorrected (symbols) and corrected (solid line) drag characteristics of airfoil DU96-W-180 from two different setups in the Delft LTT.

never finalized, leaving only results in a small range of angles of attack around the normal position at  $Re=0.5 \times 10^6$ . This test result does show, however, a good match between the drag coefficients in a range of  $\pm 20^\circ$  around the airfoil position normal to the flow (fig. 7.30). The high Re-number drag of DU00 in fig. 7.21 is higher than the lower Re-number drag, while the opposite is expected, which may be attributed to the high blockage of 0.25. The moderate aspect ratio of the model ( $AR=4$ ) may be the reason that the differences are relatively small.

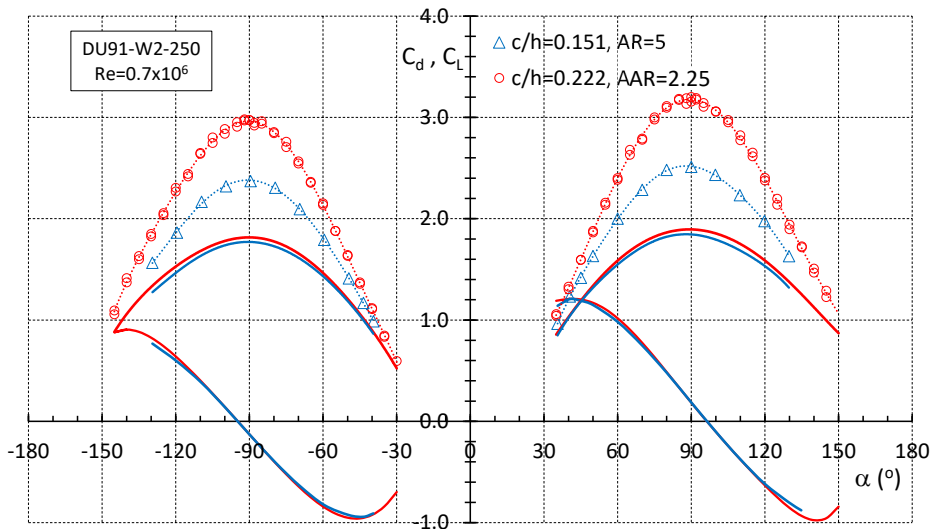


Figure 7.31: The DU91 lift and drag characteristics for two different combinations of blockage and aspect ratio. ( $c/h=0.22$  uncorrected data from Madsen and Hansen, 2017). Corrected curves given as solid lines.

Figures 7.29 and 7.30 show that, for the 18% thick DU96, tests with  $c/h$  values of 0.15 and 0.22 give comparable corrected drag results and that aspect ratio plays a minor role. However, fig. 7.28 suggests otherwise, where a 21% thick model featuring  $c/h=0.22$  and an aspect ratio of 2.5 does give distinct differences in drag, while the reverse is true for the lift.

Measurements on airfoil DU91-W2-250, presented in fig 7.31, unfortunately also do not give a decisive answer. Here a blockage ratio of 0.22 and an aspect ratio of 2.25 give differences in drag above  $60^\circ$  incidence in the order of 2% to 5%, while the corrected lift curves do not show significant differences in a range of  $\pm 30^\circ$  around the model normal position.

The pressure distributions in fig. 7.32 depict how the velocities around the models are corrected for wall interference. The lower blockage values originate from the measurements on the 0.15m and 0.25m models in the LTT. It is shown that, while the

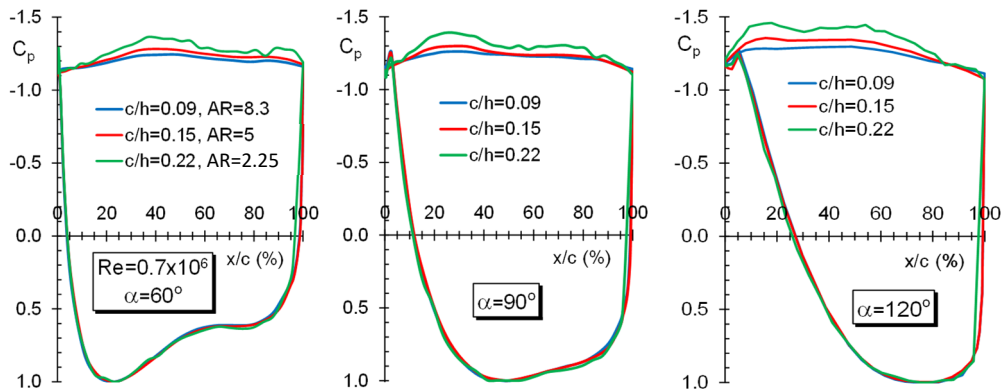


Figure 7.32: The impact of combined blockage and aspect ratio on the  $C_p$ -distribution of airfoil DU91-W2-250.

upwind side pressure distributions largely coincide (with a slight tendency of over correction for the larger  $c/h$  value), wall interference leads to larger distortion of the downwind side pressure distribution with blockage, which is not adjusted by a single correction of the dynamic pressure. It appears that, even with the relatively high aspect ratio and fairly moderate blockage of the 0.25m model, this distortion is noticeable.

Figures 7.28 and 7.31 indicate that for  $c/h \approx 0.22$  and  $AR \leq 2.5$  the drag coefficients, especially for  $\alpha > 90$  and  $\alpha < -90$  have a tendency to be higher due to noticeable flow distortion. The reason this is not the case for the DWG measurements on DU96 depicted in fig. 7.29 might be the fact that these data come from measurements with a balance, which integrates the forces over the span. Apparently, as is suggested by the CFD computations mentioned before, In situations with high blockage and a relatively low

aspect ratio, the fact that the forces in deep-stall conditions are measured with a row of pressure orifices locally on the model makes a difference. Of course, care must be taken here, since fig. 7.29 is only one example. However, aspect ratio plays a pivoting role here, as the test on DU96 shown in fig. 7.30 also has  $c/h=0.22$ , but with an aspect ratio larger than 7 (and using a balance).

A comparison of the extremities in the available data is presented fig. 7.33. It shows the impact on the drag characteristics of the highest blockage ratio combined with the lowest aspect ratio ( $c/h=0.33$ , uncorrected data acquired from Madsen and Hansen, 2017) for airfoil DU9-W2-250. The pressure distribution depicts the amount of overcorrection on the upwind side pressures at  $120^\circ$  incidence, due to the complete distortion of the flow

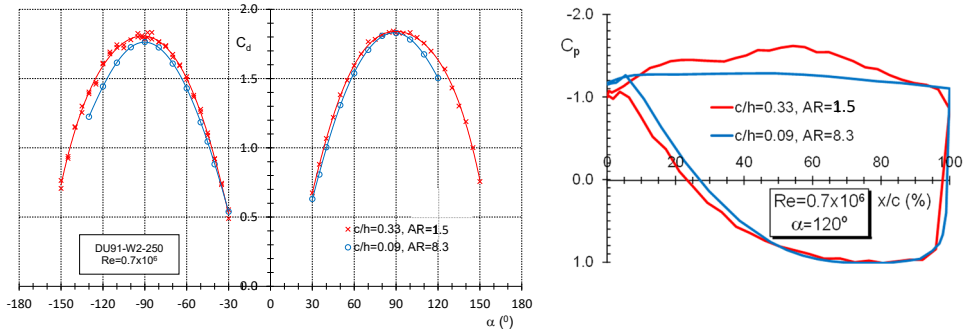


Figure 7.33: The impact of high blockage combined with low aspect ratio on the DU91 drag characteristics and pressure distribution at  $120^\circ$ .

over the model, leading to a difference in drag coefficient at this angle of  $9.3\%$ . Based on the drag due to distortion, the upwind pressures would best be corrected with  $\theta=0.7$  instead of  $0.96$ . The good match of maximum drag at  $90^\circ$  may give a false impression, since the pressure distributions at this angle are not at all comparable. Here, the overcorrection on the upwind side is compensated by the lower pressure at the downwind side.

The comparison of the base pressure coefficients in figure 7.27 has been made based on experiments with comparable blockage ratio's ( $0.15$  and  $0.11$ ) with aspect ratios of  $5$  and  $3$  respectively.

## 7.8 THE IMPACT OF ROUGHNESS

Due to an increased Reynolds number, fig. 7.23 shows a postponed separation on the upwind side leading edge, leading to a higher pressure peak and a lower drag. This suggests that tripping the boundary layer might have a comparable effect. Critzos et al. (1955) present measurements on airfoil NACA 0012 at  $Re=1.8 \times 10^6$ , both with the airfoil

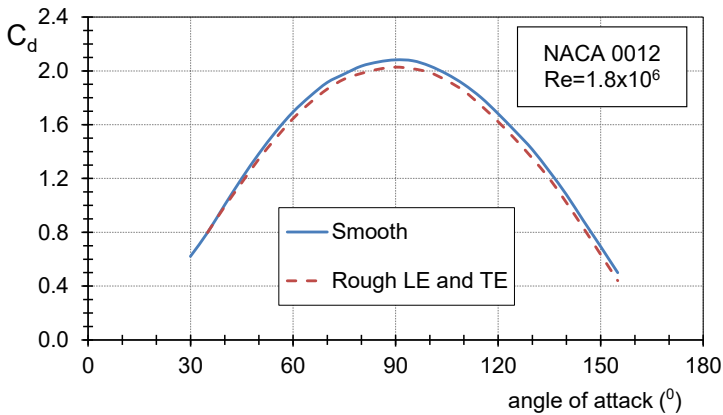


Figure 7.34: The impact of a rough LE and TE on the drag performance of airfoil NACA 0012 (Critzos et al. 1955). Unknown correction on measured data. No roughness details given.

smooth and with a rough leading edge and trailing edge. The impact on the drag coefficient is shown in fig. 7.34. It must be noted that the maximum drag coefficient is larger than 2. The data directly come from the report and are given with unknown wake blockage corrections, coming from wall pressure measurements directly above and below the model. Starting at  $35^\circ$ , the application of roughness reduced the drag coefficient, with a maximum of about 0.06 at  $90^\circ$ , going from 2.08 to 2.02 (-2.9%).

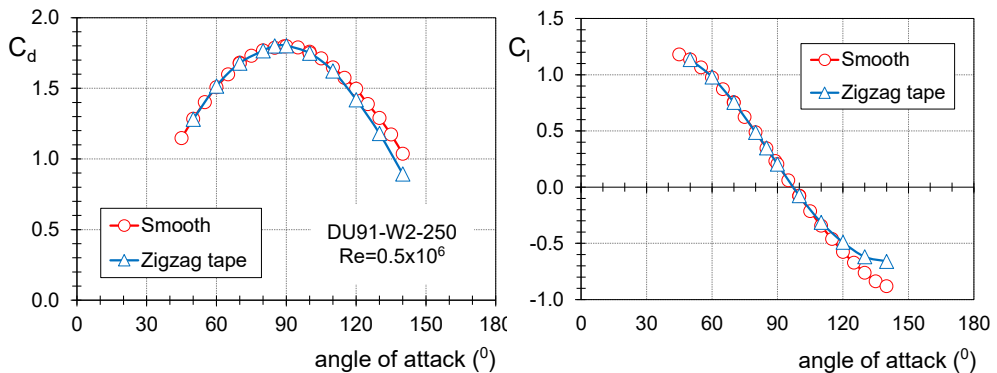


Figure 7.35: The impact of zigzag tape at the lower surface 20% chord station on the lift and drag coefficients. Tape thickness is 0.9mm

Fig. 7.35 presents the impact on the lift and drag coefficients of 0.9mm thick zigzag tape at the lower surface 20% chord station of the DU91-W2-250 25cm chord model measured in the Delft LTT. The effect is only visible at angles beyond  $90^\circ$ . For lower angles the tape is not effective, despite the rather high 0.9 mm thickness of the tape, which might be caused by the continuous flow acceleration on the lower surface from the stagnation point (at half-chord at  $90^\circ$ ) towards the leading edge; a negative pressure gradient makes

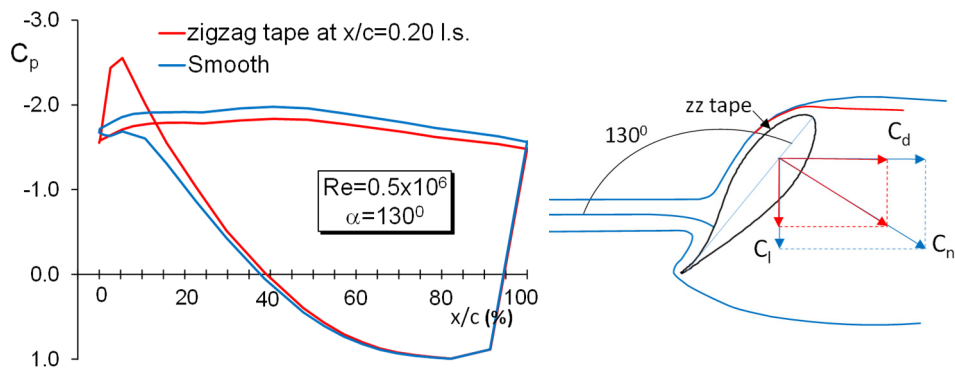


Figure 7.36: The pressure distributions at  $\alpha=130^\circ$ , showing the impact of zigzag tape at the lower surface 20% chord station (left) and the orientation of the normal force and its decomposition in lift and drag direction (right).

it more difficult to destabilize the boundary layer in such a way that separation is postponed.

The pressure distribution presented in fig. 7.36, at an angle of  $130^\circ$  where the tape does work, shows a pressure peak at the lower side leading edge. As a result, the flow seems to separate just at the apex, forming a smaller wake, while the flow at the smooth lower surface appears to separate at approximately 8% chord. The normal force coefficient is reduced, partly due to the better pressure recovery, which leads to a higher base pressure. As the tangential force in this range of angles of attack is relatively small, in the order of -0.25, a significant reduction of the normal force coefficient is translated into a reduced drag coefficient and an increase in the lift coefficient, as is shown in the right figure, where, for the sake of simplicity, the tangential force components of the lift and drag are omitted.

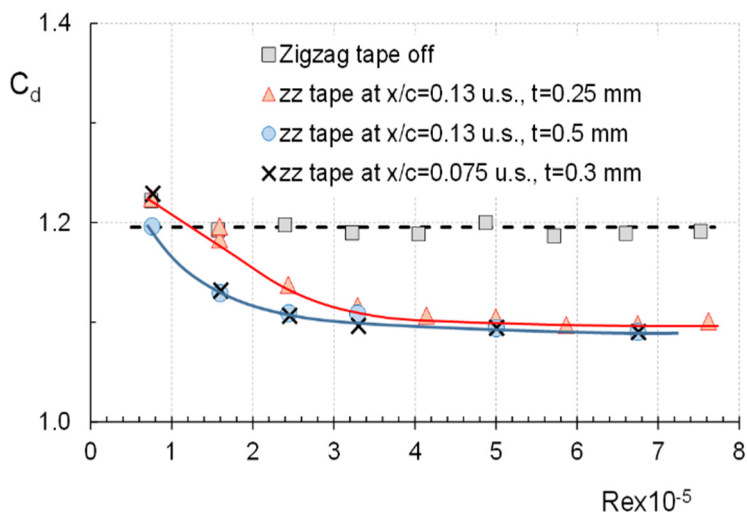


Figure 7.37: The impact on the drag coefficient of zigzag tape at different chord locations and different thicknesses. Airfoil DU91-W2-250, 0.15 cm chord model,  $\alpha=-130^\circ$ .

Difference in zigzag tape location and thickness may cause some variation in the lift and drag coefficients, but only for relatively low Reynolds numbers, as is shown in fig. 7.37, presenting measurements on the 15cm model of DU91-W2-250 at  $-130^\circ$  incidence. In this case only zigzag tape on the upper surface at angles lower than  $-90^\circ$  causes the flow to stay attached until the apex. The graph shows the impact at  $\alpha=-130^\circ$  of two different thicknesses ( $t$ ) at the same location and two different locations with about the same tape thickness.

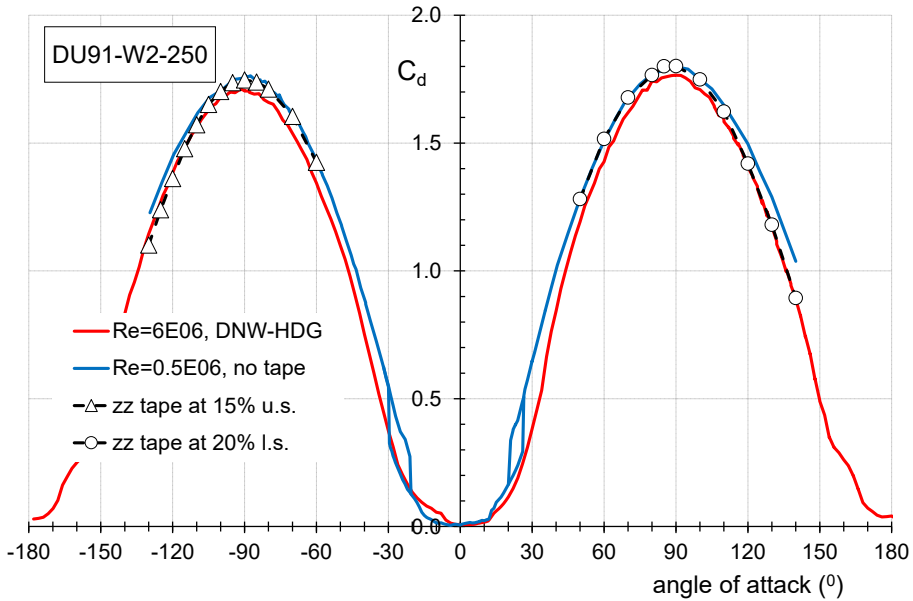


Figure 7.38: The impact of Reynolds number and roughness on the  $\pm 180^\circ$  drag characteristics of airfoil DU91-W2-250

A combined effect of chord location and tape thickness is visible. For Reynolds numbers below  $3 \times 10^5$  a tape chord location of 13% with a thickness of 0.5 mm has a similar effect as tape at  $x/c=7.5\%$  with a thickness of 0.3 mm. Apparently the flow is still attached at the latter position, otherwise the tape would be ineffective. Once the boundary layer is turbulent, at Re-numbers higher than  $3.5 \times 10^5$ , little variation in  $C_d$  occurs.

When the flow approaching the leading edge is made completely turbulent, the characteristics at lower Reynolds numbers take the shape of those at higher Reynolds numbers, as is depicted in fig. 7.38. It presents the drag performance of fig. 7.22 complemented with the lower Re-performance under tripped conditions at positive and negative angles. It clearly shows that when the tape is effective at the lower Reynolds number, both for angles smaller than  $-110^\circ$  and higher than  $110^\circ$ , the performance at the much higher Reynolds number is matched. The same is found for the lift characteristics.

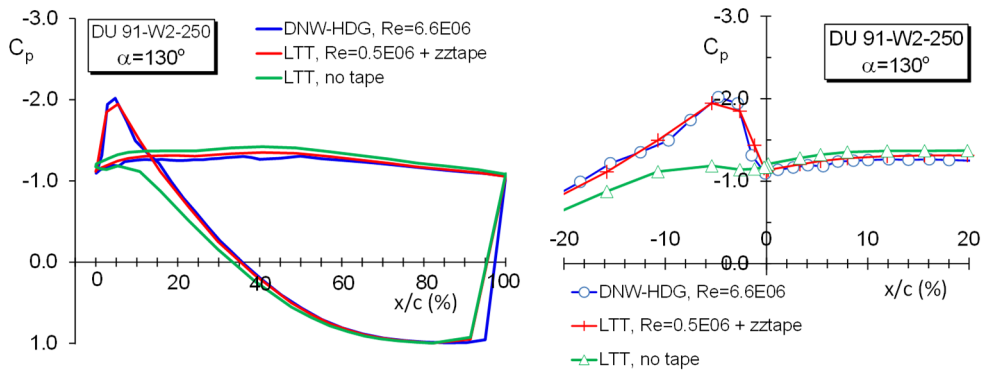


Figure 7.39: The pressure distributions at  $\alpha=130^\circ$ , showing the good match between the curves for  $Re=0.5 \times 10^6$  with zigzag tape at 20% chord on the lower surface and  $Re=6.6 \times 10^6$ . The graph at the right hand side shows a detail with negative lower surface orifice  $x/c$  values.

Comparison of the pressure distributions at  $130^\circ$  in fig. 7.39 shows good agreement between the LTT measurements with zigzag tape and the HDG model at a Reynolds number of about  $6.6 \times 10^6$ . The turbulent flow separates from the apex, while separation for the model without tape is located between the lower surface 6% and 10% chord stations.

## 7.9 CONCLUSIONS

Measurements were performed on a number of DU airfoils for angles of attack in the range  $-180^\circ$  to  $180^\circ$ . The main difference between the 18% thick DU96-W-180 and the 30% thick DU97-W300 is found in the range of incidences after  $90^\circ$ , where, due to the thick lower side with a cusp the magnitude of the lift decreases. Laminar separation from the point with lower side maximum thickness combined with laminar separation on the other side virtually turns the airfoil into a symmetric section at  $\alpha=155^\circ$ , bringing the lift almost to 0.

The drag calculated from the pressure distribution at deep-stall angles of attack increasingly differs from balance measurements with reducing pressure tap resolution at the upwind trailing edge.

The deep-stall lift, drag and moment characteristics of airfoil DU00-W-212 measured at  $Re=0.6 \times 10^6$  with  $c/h=0.11$  only slightly differ from the performance measured at  $Re=8.1 \times 10^6$  with a blockage ratio of 0.25. The main difference can be found at the upwind leading edge, where due to the formation of a negative pressure peak turbulent separation occurs at the higher Reynolds number.

Due to the pressure peak at the leading edge, DU91-W2-250 deep-stall drag values at  $Re=6 \times 10^6$  ( $c/h=0.167$ ) are consistently lower than drag characterises at  $Re=0.5 \times 10^6$

( $c/h=0.151$ ). Lift values are consistently higher.

The reason why the drag values at the higher Re-number of the DU00 airfoil are just slightly higher compared to the low Re-number instead of lower, despite the peak at the leading edge (comparable with DU91), presumably can be found in the high blockage ratio.

With increasing blockage, pronounced curvature in the downwind airfoil contour impacts the flow and becomes visible in the downwind side pressure distribution

Airfoils with little curvature (e.g. without a pronounced aft-loading cusp) in the downwind contour have similar base pressures in the range of incidences between  $60^\circ$  and  $90^\circ$ , irrespective of Reynolds number. The differences in drag come from the upwind side pressure distribution, resulting from differences in upwind leading edge thickness and trailing edge angle.

To generate reliable high angle of attack data, an upper boundary of the blockage ratio would be in the range of 0.15 to 0.2, combined with an aspect ratio of at least 4.

At blockage ratios beyond 0.22, aspect ratios smaller than approximately 3 result in increasingly heavy distortion of the flow over the section downwind side, giving strong three-dimensionality of the flow. This renders span dependency of time-averaged pressure measurements. Hence, it is not a good idea to combine high blockage with low aspect ratio.

At low Re-numbers roughness only impacts the section characteristics beyond  $90^\circ$  or  $-90^\circ$ . Roughness placed at the upwind side suppresses laminar separation and creates a negative pressure peak at the leading edge, similar to the high Re-number case, giving comparable lift and drag characteristics.

## 7.10 REFERENCES

Allen H.J. and Vincenti W.G. (1947) *Wall interference in a two-dimensional wind tunnel, with consideration of the effect of compressibility*. NACA Report no. 782

Bearman, P.W. (1967) *On vortex street wakes*. J. Fluid Mech.28: 625-641, 1967.

Bloy, A.W. and Roberts, D.G. *Aerodynamic characteristics of the NACA 63<sub>2</sub>-215 aerofoil for*

use in wind turbines, *Wind Engineering* Vol. 17, No.2, 1993, pp.67-75

Boorsma, K. (2003) *Comparison of Experimental and Computational Aerodynamic Section Characteristics of DU91-W2-250 Profile*. Master thesis, Delft University of Technology, 2003.

Chen, J.M. and Fang, Y. *Strouhal numbers of inclined flat plates*. *Journal of Wind Engineering and Industrial Aerodynamics*, **61**, pp. 99-112, July 1996

Critzos, C.C., Heyson, H.H. and Boswinkle Jr R.W. *Aerodynamic characteristics of NACA 0012 airfoil at angles of attack from 0 to 180 degrees*. NACA TN 3361, 1955

Fage, A. and Johansen, F.C. *On the flow of air behind an inclined flat plate of infinite span*. British ARC R&M, No. 1104. (1927)

Flachsbart, O. *Messungen an Eben und Gewölbten Platten*. Ergebnisse der Aerodynamischen Versuchsantalt zu Göttingen, IV. Lieferung, edited by L. Prandtl and A. Betz, Verlag von R. Oldenbourg, Munich, 1932, pp. 96-100.

Hoerner S.F. (1965) Fluid dynamic drag, published by the author, 1965

Hoerner S.F. (1985) Fluid dynamic lift, published by Mrs. Liselotte A. Hoerner, 1985

Jacobs, M. and Benkel, A. *Measurements on airfoil DU91-W2-250 from the DNW-HDG High Pressure Tunnel in Göttingen, Germany*. E-mail correspondence with M. Jacobs, February 2014 and A. Benkel, September 2023

Jacobs, M. *High Reynolds Number Airfoil Test in DNW-HDG*. Report DNW-GUK-2014 C-04. Göttingen, July 2015

Kármán, Th. von and Burgers, J.M. *General aerodynamic theory - Perfect fluids*. *Aerodynamic Theory* Vol. II, W.F. Durand ed., Springer Berlin, 1935

Landstra, F. *An Improved Wind Tunnel Blockage Correction method for Two-Dimensional Profile Testing in Deep Stall*. MSc thesis TUDelft, March 2011

Lisoski, D.L.A. *Nominally 2-dimensional flow about a normal flat plate*. Thesis for the degree of Doctor of Philosophy. California Institute of Technology, 1993

Madsen, J. and Hansen, R. *Uncorrected data from the LM Windpower low-speed wind tunnel*. Lunderskov, Denmark, February 2017. Personal correspondence.

Madsen, J. *LM Wind Power wind tunnel measurements. Task 2.3 of the European AVATAR project. Progress meeting April 2017*.

Massini, G., Rossi, E. and D'Angelo, S. *Wind tunnel measurements of aerodynamic coefficients of asymmetrical airfoil sections for wind turbine blades extended to high angles of attack*. EC DG-XII Contract number: EN3W - 0018 - I, Conclusive Report. ENEA, Roma, 1988

Michos, A., Bergeles, G. and N. Anthanassiadis, (National Technical University of Athens) *Aerodynamic characteristics of NACA 0012 airfoil in relation to wind generators*. Wind Engineering Vol. 7, No. 4 pp. 247-261, 1983

Mohebi, M., Wood, D. H. & Martinuzzi, R. J. 2017 The turbulence structure of the wake of a thin flat plate at post-stall angles of attack. *Experiments in Fluids* (2017) 58: 67. DOI 10.1007/s00348-017-2352-8

Ostowari, C. and Naik, *Post stall studies of untwisted varying aspect ratio blades with NACA44XX series airfoil sections – Part II*, Wind Engineering, Vol. 9, No. 3, 1985

Pope, A., 1947. *The Forces and Pressures over an NACA 0015 Airfoil Through 180 Degrees Angle of Attack*. Georgia Institute of Technology.

Rainbird, J.M., Peiro, J., Graham, J.M.R. (2015) *Blockage-tolerant wind tunnel measurements for a NACA0012 at high angles of attack*. *J.WindEng.Ind. Aerodyn.*145,209–218.

Roosbroeck, M. van. (2014) *The Effect of Leading Edge Thickness on the Maximum Drag Coefficient of Airfoils 90° to the Wind*. Master Thesis, Faculty of Aerospace Engineering, TUDelft, September 2014

Roshko, A. *Perspectives on bluff body aerodynamics*. *Journal of Wind Engineering and Industrial Aerodynamics* 49(1–3), 79–100, 1993

Satran, D. and Snyder, M.H. *Two-dimensional tests of GA(W)-1 and GA(W)-2 airfoils at angles-of-attack from 0 to 360 degrees*. Wind Energy report no. 1, Wind Energy Laboratory, Wichita State University, Kansas, USA, January 1977

Sheldahl, R.E., and Klimas, P.C. *Aerodynamic characteristics of seven Symmetrical airfoil sections through 180-degree angle of attack for use in aerodynamic analysis of vertical axis wind turbines*. Report SAND80-2114, Sandia Laboratories, Albuquerque, March 1981.

Sørensen, N.N. and Timmer, W.A. *CFD prediction of airfoil deep stall performance using Improved Delayed Detached Eddy Simulations*. DTU Wind Energy, Department of Wind Energy, Lyngby, Denmark, June 2017.

Swalwell, K.E. *The effect of turbulence on stall of horizontal axis wind turbines*. MSc thesis, Department of Mechanical Engineering, Monash University, Melbourne, Australia, 2005.

Tangler, J. and Kocurek, J. D. *Wind turbine post-stall performance characteristics guidelines for blade-element momentum methods*. AIAA conference paper NREL/CP-500-36900 October 2004.

Templin, R.J. and Wickens, R.H. *Aerodynamic characteristics of the NACA 0018 airfoil at high Reynolds numbers and at angles of attack from 0° to 360°*. TM-WE-020, National Research Council Canada, July 1984.

Timmer, W.A. and Rooij, R.P.J.O.M. van, (2001) *Some aspects of high angle-of-attack flow on airfoils for wind turbine application*. Proceedings of the European Wind Energy Conference, Copenhagen, Denmark 2001.

Timmer, W.A. *Unpublished results from measurements on a 25cm chord model of airfoil DU91-W2-250*, Delft University of Technology, May 2018.

Timmer, W.A. *Unpublished results from measurements on a 15cm chord model of airfoil DU91-W2-250*, Delft University of Technology, May 2021.

Wieselsberger, C. *Der Widerstand verschiedener Körper*. Ergebnisse der Aerodynamische Versuchsanstalt zu Göttingen, II. Lieferung, pp 33-35, 1923, in: Göttingen Klassiker der Strömungsmechanik, Bd. 5, Universitätsverlag Göttingen 2009.

Xu, H., Qiao, C., Yang, H., Ye, Z. *Delayed detached eddy simulation of the wind turbine airfoil S809 for angles of attack up to 90 degrees*. Energy, Vol. 118, pages 1090-1109, January 2017, <https://doi.org/10.1016/j.energy.2016.10.131>



# 8

## UNSTEADY FORCES AND VORTEX SHEDDING FREQUENCY IN DEEP-STALL

The unsteadiness of bluff body flows has received ample attention since the work of von Kármán (1911), e.g. Howarth (1935), Zdravkovich (1981), Schewe (2001), Bearman (2011) and Derakhshandeh and Alam (2019). Most of the studies aimed at investigating the cyclic loads on structures resulting from periodic vortex shedding and the associated vibrations. Particularly the vortex shedding from circular cylinders, due to their simple geometric shape but relatively complex flow, has been extensively investigated. Rosko (1993) and Buresti (1998) give a review on bluff body flow and Lekkala et al. (2022) present a comprehensive overview of experimental and numerical studies involving circular cylinders.

Fage and Johansen (1927) were the first to report measurements with a hot-wire in the unsteady wake behind inclined flat plates to study the vortex shedding frequency, which results later have been experimentally verified by Chen and Fang (1996).

Apart from the DU-experiments reported below, studies covering periodic loads on *airfoils* due to vortex shedding at large angles of attack are relatively rare and even more scarce are experiments on the subject at Reynolds numbers pertinent to wind turbines. Pelligrino and Meskell (2013) performed CFD computations on the behaviour of airfoil S809 at high angles of attack for  $Re=10^6$ . Swalwell (2005) tested the same airfoil and also conducted measurements on two other 21% thick airfoils: NACA 0021 and NACA 4421 at a nominal Reynolds number of about  $2.7 \times 10^5$ . Lind and Jones (2016) measured unsteady airloads on NACA 0012, NACA 0024 and two elliptical sections at  $Re 6.6 \times 10^5$  and Fallahpour et al. (2023) performed unsteady flow experiments on NACA 4412 at  $1.5 \times 10^5$ .

### 8.1 THE STROUHAL NUMBER

The shedding frequency of the vortices generally is expressed in the non-dimensional Strouhal number, defined as

$$St = \frac{f_{char}}{V_o} \quad (8.1)$$

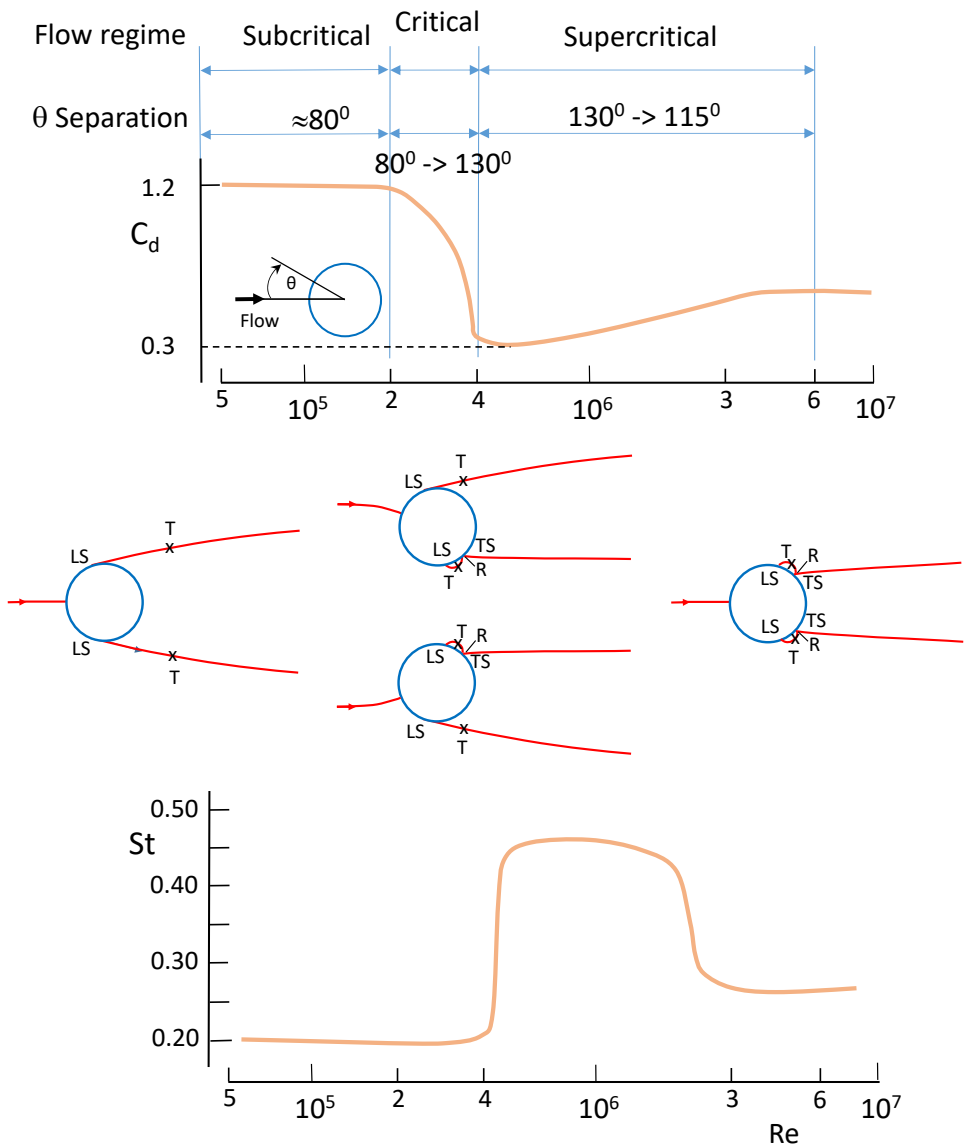


Figure 8.1: Variation of cylinder drag coefficient, flow topology and Strouhal number with Reynolds number. T=transition, TS= turbulent separation, LS = laminar separation, R=reattachment. (Polhamus 1984, Schewe 2001)

in which  $f$  is the shedding frequency,  $l_{char}$  is a characteristic length, which in this case is the airfoil chord, and  $V_0$  is the free-stream velocity.

Fig. 8.1 schematically presents the variation of the drag coefficient, the flow topology and the vortex shedding Strouhal frequency of a circular cylinder with Reynolds number (Polhamus 1984, Schewe 2001). In the subcritical Re-number range laminar separation takes place at an azimuth angle  $\theta$  in the order of  $80^\circ$ . Transition follows off-surface in the detached shear layer. Vortex shedding has a clear dominant periodicity. In this condition

the Strouhal number is  $0.20 \pm 0.014$  (Mondal and Alam, 2023), and the drag coefficient is approximately 1.2. When the Re-number increases, laminar separation moves downstream and transition moves upstream, closer to the cylinder, until a laminar separation bubble occurs and turbulent transition takes place shortly after reattachment of the turbulent boundary layer. At these Re-numbers, between  $2 \times 10^5$  and  $4 \times 10^5$ , the cylinder flow shows what is also known as “the drag crises”; a significant reduction of the drag due to increasingly attached flow and a smaller wake, with free-shear layer transition or transition through a laminar separation bubble, alternating between the upper and lower sides. The latter leads to significant measured lift coefficients, predominantly in the range of  $3 \times 10^5$  to  $4 \times 10^5$ . At the start of the supercritical regime, turbulent separation, at small distance of an upstream laminar separation bubble, has reached a separation angle of  $130^\circ$ . With increasing Re-numbers the transition location moves upstream until the bubble has disappeared. The wake has become significantly smaller and the Strouhal numbers much higher, approximately 0.5 (Schewe, 2001) compared to the subcritical regime.

Rosko (1954) coupled the shedding frequency to the width of the wake, which is directly linked to the distance of the vortex sheets, and consequently to the drag of an object; bluff bodies have lower Strouhal numbers. For moderate, subcritical, Re-numbers the circular cylinder seems to be an upper boundary, as it has two rounded edges and a much wider wake than its diameter due to laminar separation at the upwind side. The other side of the spectrum is the flat plate normal to the flow, with two sharp edges. Chen and Fang (1996) performed measurements on a number of bevelled sharp edged plates of various chord lengths in the range  $3.5 \times 10^3 < Re < 3.2 \times 10^4$ . The correction to a zero-blockage value of the Strouhal number at  $\alpha=90^\circ$  is shown in fig. 8.2. Experimental values of Fage and Johansen (1927) and Novak (1973) seem to correlate fairly well with the curve. The

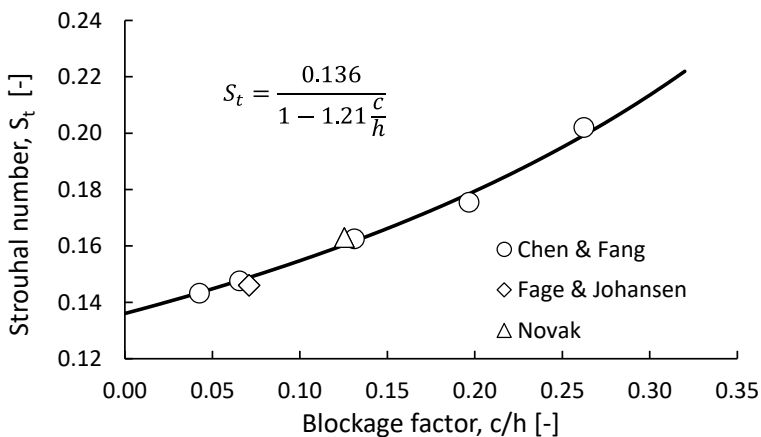


Figure 8.2: Wall correction of the measured flat plate Strouhal numbers by Chen and Fang (1996). Plate normal to the flow

blockage-free value of  $St$  is 0.136, which matches the value calculated from the data of Fage and Johansen (0.146 at  $c/h=0.071$ ) using Maskell's correction method for bluff body flows. The correction equation given in fig. 8.2, which basically is for the greater part a correction on velocity, is only suited for the test conditions of Chen and Fang and does not reflect a general correction for the velocity in a test section due to blockage. Correction of a data set with  $c/h=0.22$  using this equation compared to Maskell's correction, which, according to Appendix A, still holds for this value of the blockage parameter, resulted in a severe over correction of the drag coefficient.

Airfoils generally have one rounded and one sharp edge, with a drag coefficient at an angle normal to the wind much higher than the cylinder value of approximately 1.2 and closer to, but lower than, the flat plate value of about 2 (see also chapter 9). Consequently, airfoil Strouhal numbers at angles normal to the wind are expected to lie between 0.136 and 0.2 (and closer to the lower value), under conditions where laminar separation plays a prominent role. The Strouhal number grows as the angle of attack decreases (due to smaller wake widths and lower drag).

## 8.2 UNSTEADY FLOW FIELD OF DU91-W2-250

### 8.2.1 Measurements on a 25cm chord model

The setup of DU91, described in section 7.3, was used to capture the shedding frequency with increasing angle of attack for  $Re=0.7 \times 10^6$ . Measurements were performed at maximum acquisition rate of the sensors and the entire pressure distribution could be measured with a frequency of 250 Hz. To ensure an equal time response of the local pressure signals the length of the 1.6 mm diameter tubes between the orifices and the sensor was between 150 to 160mm. The response of the system was found to be approximately 50 Hz. Further details of the setup can be found in Boorsma (2003). The unsteady pressure distributions were measured for 6 angles of attack in the range of  $25^\circ$

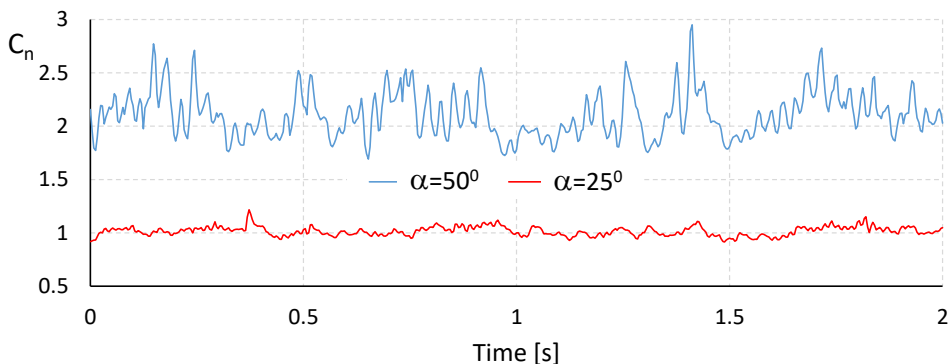


Figure 8.3: The unsteady normal force coefficient during a time series of 2 sec. for two angles of attack at  $Re=0.7 \times 10^6$ .

to  $60^\circ$  during 32 seconds. A time series of the normal force over 2 seconds is shown in fig. 8.3 for two angles of attack.

Figure 8.4 shows the result of a fast Fourier transformation (FFT) on the normal force coefficient of the model for the two angles. Since the model was cantilevered from the

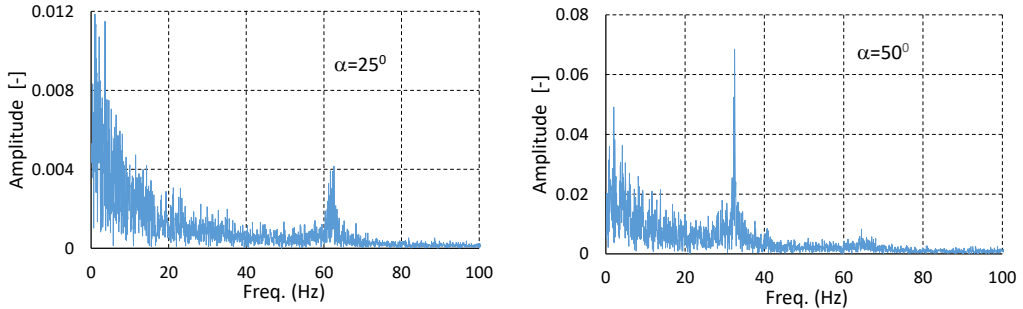


Figure 8.4: FFT of the normal force coefficient at  $Re=0.7 \times 10^6$  for two angles of attack

balance system some vibrations in the lower frequency range may be found. The results are shown in table 8.1 The table contains the measured frequency and the for blockage corrected test section velocity and the corrected Strouhal number. For correction the balance drag was used. The measurement at  $25.45^\circ$  was made while decreasing the angle coming from a deep-stall situation, which means that it is situated in the high drag region of a hysteresis loop, with the flow also separating from the leading edge.

Table 8.1: The Strouhal number calculated from the measured shedding frequency, corrected for blockage for a 25 cm chord model of DU91 at  $Re=0.7 \times 10^6$  and a 15 cm chord model at  $Re=0.5 \times 10^6$  (right).

$\alpha$ ( $^\circ$ )	f (Hz)	V (m/s)	St	St.sin $\alpha$
25.45	62.57	42.36	0.369	0.159
30.45	52.93	42.83	0.309	0.157
35.45	47.86	44.99	0.266	0.154
40.45	39.64	41.95	0.236	0.153
45.45	37.73	44.28	0.213	0.152
50.45	32.48	41.35	0.196	0.151
60.45	28.45	40.97	0.174	0.151

$\alpha$ ( $^\circ$ )	f (Hz)	V (m/s)	St	St.sin $\alpha$
30	107.33	51.50	0.313	0.156
50	71.03	53.59	0.199	0.153
70	58.38	54.76	0.160	0.151
90	55.49	55.15	0.151	0.151
110	59.29	55.10	0.161	0.152

### 8.2.2 Measurements on a 15cm chord model

The study of Van Roosbroeck (2014) on the DU91 15cm chord model also contained measurements of the vortex shedding at high incidences, at  $Re=0.2 \times 10^6$  and  $0.5 \times 10^6$ . In this case the acquisition system allowed for collecting  $C_p$ -distribution data with a speed of 650 Hz. The length of the tubes, unfortunately, was about 1.5m, which will have reduced the response of the system considerably. However, despite phase lag and damping due to the long tubes between the model surface and the sensors, it was believed that the

dominant frequencies of the vortex street could be determined from the data.

The results in terms of vortex shedding frequency and corrected Strouhal numbers are summarized in table 8.1 as well. Here, the blockage correction was performed using the drag from the pressure distribution with additional pressure information at the lower side trailing edge, as depicted in fig. 7.15. The results seem to corroborate the outcome of the tests with the 25cm model. The Strouhal number based on airfoil chord reduces with increasing angle of attack, from a value of 0.376 at 25° to a minimum value at 90° of 0.151. Using the same DU91 15cm chord model, Xu et al. (2025) conducted unsteady surface pressure and PIV measurements. There is a perfect match of the drag curves at  $Re=5 \times 10^5$  in both studies for positive incidences. For negative angles the drag of Xu et al. was about 6.6% lower compared to the study of Timmer, which, looking at their pressure distributions, could be traced back to a deviant base pressure measurement. The uncorrected Strouhal numbers were obtained from the first author and corrected with the full pressure distributions as derived for the Van Roosbroeck and Timmer studies in chapter 7. The resulting Strouhal numbers are presented in table 8.2.

*Table 8.2: The Strouhal numbers of the study by Xu et al. (2025) corrected for blockage with the drag coefficients from van Roosbroeck and Timmer computed from complemented pressure distributions.*

$\alpha$ (°)	f (Hz)	V (m/s)	St	St.sin $\alpha$	$\alpha$ (°)	f (Hz)	V (m/s)	St	St.sin $\alpha$
30.0	109.67	52.85	0.311	0.156	-50.1	87.59	57.35	0.229	0.176
32.0	104.09	53.13	0.294	0.156	-55.0	78.98	58.23	0.203	0.167
34.0	96.96	52.88	0.275	0.154	-60.0	75.06	59.17	0.190	0.165
36.0	92.74	53.19	0.262	0.154	-65.0	72.07	60.22	0.179	0.163
38.0	88.09	53.22	0.248	0.153	-70.0	67.83	60.34	0.169	0.158
40.0	84.44	53.46	0.237	0.152	-75.0	66.90	60.85	0.165	0.159
50.0	71.63	54.05	0.199	0.152	-80.0	64.98	61.36	0.159	0.156
60.0	63.41	54.37	0.175	0.152	-85.0	65.00	61.70	0.158	0.157
70.0	58.56	54.77	0.160	0.151	-90.0	65.50	61.82	0.159	0.159
80.0	55.82	54.78	0.153	0.151	-95.0	66.32	61.97	0.161	0.160
90.0	55.61	55.11	0.151	0.151	-100.0	66.76	62.10	0.161	0.159
100.0	56.94	55.25	0.155	0.152	-105.0	68.65	62.18	0.166	0.160
110.0	60.86	55.42	0.165	0.155	-110.0	69.36	61.83	0.168	0.158
					-115.0	71.79	61.98	0.174	0.157
					-120.0	74.34	61.42	0.182	0.157
					-125.0	77.29	61.39	0.189	0.155
					-130.0	80.18	60.06	0.200	0.153

The results at positive angles are in very good agreement with the earlier findings presented in table 8.1, and slightly higher, as expected, compared to the results of Fage and Johansen (1927). Based on the measured normal force coefficients their flat plate data were corrected for blockage to the values shown in figure 8.5 together with the data from tables 8.1 and 8.2

For a sharp flat plate the two separation points are fixed and the distance  $d$  between the origins of the vortex sheets is given by the projection of the chord perpendicular to the

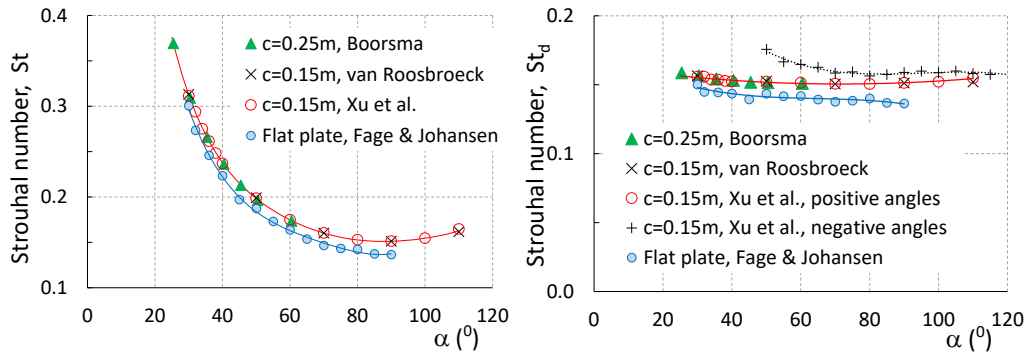


Figure 8.5: The Strouhal numbers of the 25cm and 15cm chord models for positive angles presented in tables 8.1 and 8.2. Strouhal numbers based on the projection of the chord normal to the flow,  $St_d$  (right). Comparison with flat plate data of Fage and Johansen (1927).

flow,  $d=c\sin\alpha$ . If the shedding frequency is normalised with this new characteristic length ( $l_{\text{char}}=d$  in eq. 8.1) instead of the original chord, the Strouhal number is nearly constant in the range of angles between  $40^\circ$  and  $110^\circ$  with a value of  $0.152 \pm 0.001$ . The corrected data of Fage and Johansen fall into the range  $St_d=0.140 \pm 0.004$ . The same value ( $St_d=0.14$ ) was found by Lam and Leung (2005) for an inclined plate at  $30^\circ$  incidence in an open jet test section in the range  $5 \times 10^3 < Re < 2.5 \times 10^4$

### 8.3 THE STROUHAL NUMBER OF OTHER AIRFOILS

Pellegrino and Meskell calculate Strouhal numbers for S809 non-dimensionalised with the projected length of 0.12 to 0.16 in the range of angles between  $-40^\circ$  and  $-150^\circ$  and from 0.11 to 0.15 for angles between  $40^\circ$  and  $140^\circ$ . Their calculations, however, were conducted with a URANS solver (Unsteady Reynolds-Averaged Navier-Stokes computations), which is known to significantly overpredict drag coefficients in the deep-stall region (e.g. Xu et al., 2017, studying the same airfoil with both URANS and Detached Eddy Simulation, DES, methods). The maximum drag coefficients in the computations reached values over 3. The actual Strouhal numbers will therefore presumably be much higher than computed.

The study by Swalwell (2005) covered inflow conditions varying in turbulence intensity and scale by utilizing different grids installed upstream. The three airfoils tested (S809, NACA 0021 and NACA 4421) form an interesting combination as they all are 21% thick, but quite different in shape. The Strouhal numbers were based on a test section reference velocity of 34 m/s. Unfortunately, these tests suffered from uncertainties in inflow velocity (limited power to maintain a constant flow-speed at high drag) and air density in the test section (unknown temperature and atmospheric pressure variation), leading to

variation in test section dynamic pressure and Reynolds number. Furthermore no blockage correction was applied. With  $c/h=0.0625$  the blockage is relatively low, but still may account for a 5% to 6% higher test section speed at full blockage at  $90^\circ$ . An accurate correction, however, is not possible, as the drag followed from integration of the pressure distributions, which unfortunately had a very poor resolution of the orifices near the trailing edge. The pressure in the last 10% to 13% of the chord could not be measured. Especially at angles higher than  $60^\circ$  this significantly impacts the drag coefficients.

Rough estimates of the S809 projected Strouhal numbers found during their tests with a smooth airfoil and no turbulence grid are approximately 0.180 at  $30^\circ$ , decreasing to 0.155 at  $90^\circ$ , significantly higher than the simulations of Pellegrino and Meskell. Due to the large uncertainties no further actions were undertaken to establish more accurate and corrected values for the three airfoils. Owing to incomplete pressure distributions also the studies of Fallahpour et al. and Lind & Jones were disregarded to extract accurate Strouhal data from, as the drag curves could not well be established to correct the velocity for blockage. In addition, the experiment of Lind and Jones was performed using splitter plates, resulting in unevenly distributed blockage over the test section (see also chapter 9).

### 8.4 THE STROUHAL NUMBER AT A HIGH REYNOLDS NUMBER

The DU00-model measured in the HDG tunnel in the framework of the AVATAR-project was equipped with 5 miniature single pressure transducers /microphones in the model upper and lower surfaces to record unsteady pressures with a rate of 31kHz. The data were used for a frequency analysis in the deep-stall region at the conditions depicted in figure 7.20: an angle of attack range of  $-90^\circ$  to  $90^\circ$  in a Reynolds number range of  $6 \times 10^6$  to

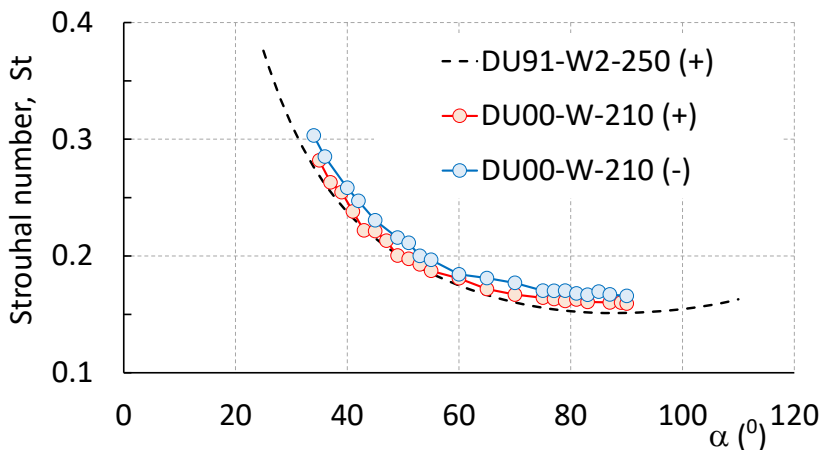


Figure 8.6: The variation with angle of attack of the corrected DU00 Strouhal number compared to the values of DU91 at positive angles (table 8.1). (+) and (-) denote positive and negative angles respectively.

$8 \times 10^6$ . Strouhal numbers associated with deep-stall vortex shedding were calculated using the dominant frequencies and the test section velocity corrected for blockage. Figure 8.6 shows the resulting St-values compared to DU91 values presented in tables 8.1 and 8.2. The DU00 St-values at positive angles are overall a little higher than the DU91 values but consistently lower than those at negative angles.

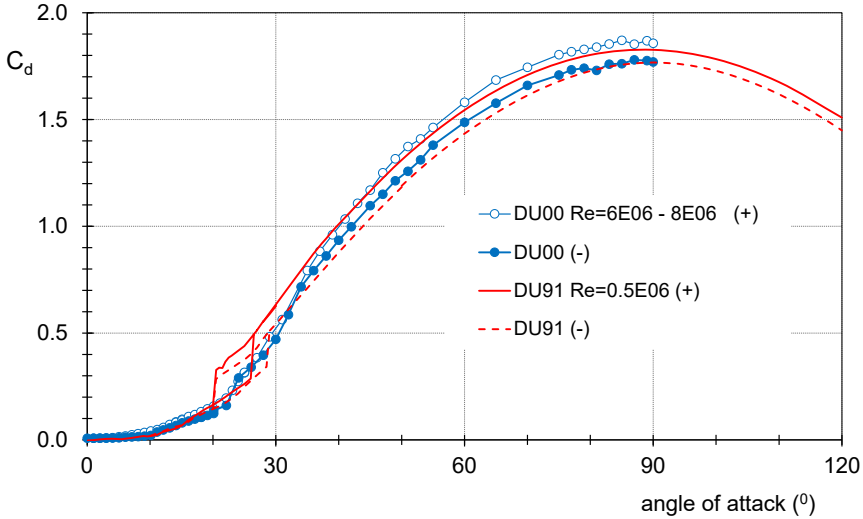


Figure 8.7: The drag curves for DU91-W2-250 at  $Re=0.5 \times 10^6$  and DU00-W-210 at Reynolds numbers between  $6 \times 10^6$  (at low angles) and  $8.1 \times 10^6$  (at  $90^\circ$ ). (+) and (-) denote positive and negative angles.

As Roshko (1954) linked the Strouhal number to the drag of an object, the pressure distributions may give some information on what aspect of the drag is causing the differences in shedding frequency. The drag curves for both airfoils are presented in fig. 8.7, where the negative angles are mirrored around the y-axis. The DU00 drag at negative angles is smaller than at positive angles, which is reflected in the higher Strouhal numbers. The DU00  $C_p$ -distributions at  $\alpha=70^\circ$  and  $-70^\circ$  are depicted in fig. 8.8a.

The base pressures are overall quite similar, hence differences in St must originate from

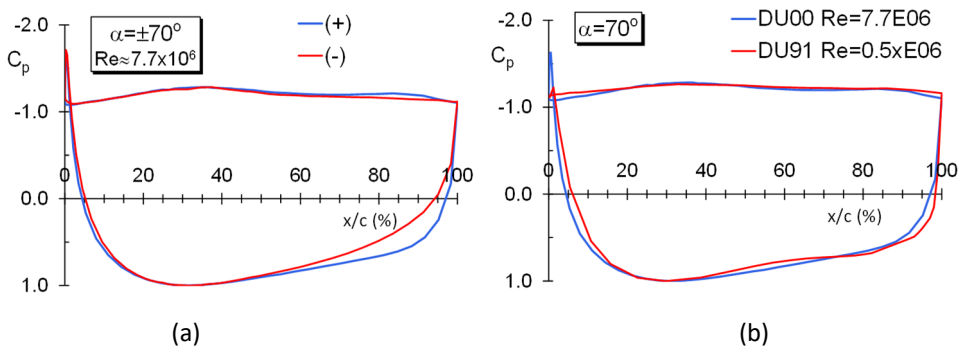


Figure 8.8: The pressure distributions of DU00 at  $70^\circ$  and  $-70^\circ$  incidence (a) and of DU91 and DU00 at  $\alpha=70^\circ$  (b)

the upwind side. With comparable leading edge pressures, the higher velocity over the aft part of the upper side at a negative angle is the only significant difference between the two pressure distributions. Although the velocities near the trailing edge in the flow outside the boundary layer are the same for both angles, the boundary layer over the upper side facing upwind can constantly speed up into the wake right from the stagnation point at  $x/c=0.3$ . Here, the source for the higher Strouhal number must be found in the vortex shedding from the trailing edge. At the same time, the higher velocity over the upwind side gives a lower pressure and combined with a similar base pressure this results in a smaller normal force and consequently at high angles in a smaller drag. The presumed higher velocity in the boundary layer destabilizes the free shear layer more and promotes earlier roll-up to a vortex. Higher velocity over the upwind side and higher Strouhal numbers can thus be associated with lower drag.

At  $\alpha=70^\circ$  (fig. 8.8b), both DU91 and DU00 show comparable velocities near the upwind side trailing edge, where both shapes have a concave part, the DU91 more pronounced than the DU00. In this case the largest difference is the velocity right at the leading edge, which is much higher for the DU00 airfoil, which would explain the higher Strouhal number. The DU91 exhibits laminar separation upstream of the leading edge followed by off-surface transition in the free shear layer, comparable with the cylinder at sub-critical conditions. Due to the higher Reynolds number of the DU00 airfoil, its upwind side boundary layer stays attached and speeds up towards the leading edge, where it separates. This is in contrast to the cylinder, for which at super-critical Re-numbers the wake reduces dramatically due to separation at the downwind side of the cylinder, resulting in much higher St-values.

If we adopt the theorem that a lower drag gives a higher Strouhal number, figures 8.6 and 8.7 contradict each other. For  $\alpha>45^\circ$  the DU00 drag is higher, yet the Strouhal number is also higher compared to the DU91 airfoil.

Owing to the relatively high blockage of the DU00 test, also caution should be exercised here. While the Strouhal number is sensitive to the pressure peak at the leading edge resulting from the high Re-number, the high blockage causes higher drag instead of lower, which may be the reason for the mismatch.

## **8.5 THE VARIATION OF THE STROUHAL NUMBER WITH THE DRAG COEFFICIENT**

Since the drag coefficient and the Strouhal frequency are strongly interrelated, comparison of the measured data in a  $C_d$ -St graph may give some additional insight in the predictability of the Strouhal number for various airfoils.

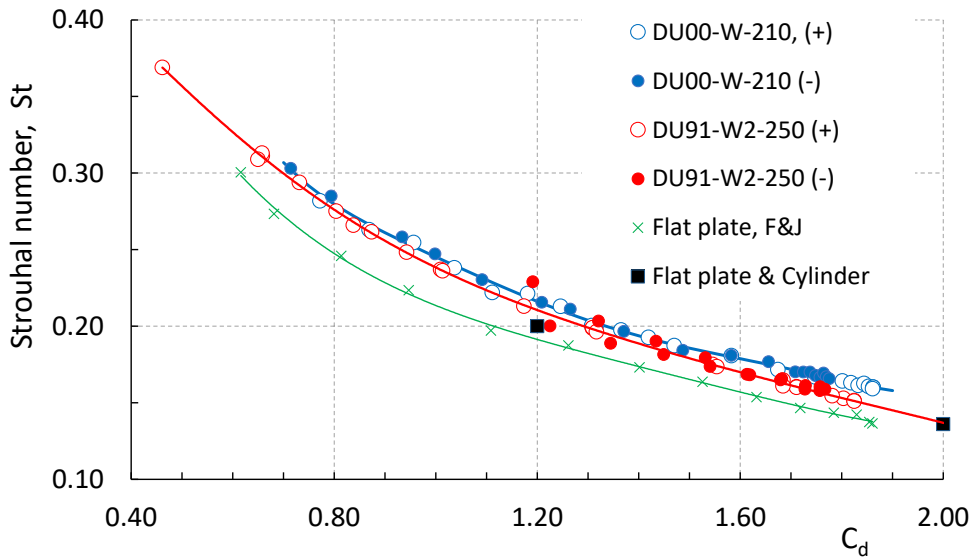


Figure 8.9: The variation of the Strouhal number with drag coefficient for various objects.

Figure 8.9 presents the variation of  $St$  with  $C_d$  of DU91, DU00, the flat plate values of Fage and Johansen and adapted values for the cylinder ( $St=0.20$  at  $C_d=1.2$ ) and the flat plate normal to the flow. The latter contains the  $St$ -value found by Chen and Fang corrected for blockage ( $St=0.136$ ), combined with a  $C_d$ -value of 2.

Due to the large uncertainty in the Swalwell data, unfortunately no curves from that study can be presented.

The following conclusions can be drawn from the comparisons in figure 8.9.

- The DU91 data for positive and negative angles generally fall on the same curve, and so do the DU00 data
- The  $St$  variation with  $C_d$  of DU91 and DU00 actually occurs in a small band, despite the large distinction in Reynolds number. Differences in  $St$  of DU00 with DU91 amount to 0% at  $C_d=0.6$  to a maximum of 7% at  $C_d=1.85$ .
- The two points for the cylinder and the flat plate normal to the flow (indicated as extremities in  $St$  value at  $\alpha=90^\circ$ ) have a good to fair fit with the (extended) curve for the DU91 airfoil.
- In the range  $C_d=0.7$  to 2.0 the flat plate data according to Fage and Johansen have a constant offset of  $\Delta C_d=0.14$  to the DU91 curve.

The data in fig. 8.9 suggest that, certainly for Reynolds numbers where laminar separation at the LE occurs, objects have Strouhal numbers that come close or fall on the DU91-curve. Knowing that due to high blockage the DU00-curve might have slightly too high drag values, becoming more pronounced at angles around  $90^\circ$ , it is tempting to assume that even the high Re-number case eventually falls on top of the DU91 curve. Although maybe

not generally valid for all airfoils and Reynolds numbers, figure 8.9 may give a good indication of the expected Strouhal number when only the drag coefficient of a clean airfoil is measured, once properly corrected for blockage.

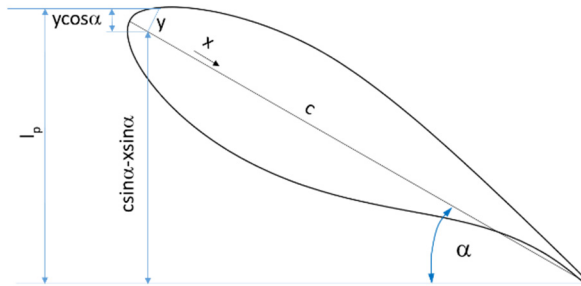


Figure 8.10: The projected length of an airfoil perpendicular to the flow

## 8.6 THE PROJECTION OF THE AIRFOIL PERPENDICULAR TO THE FLOW.

Rosko (1954) took the width of the wake as a measure of the drag of a bluff body and linked the flat plate  $St$  values to the projection of the plate normal to the flow,  $c \sin \alpha$ . Bluffer bodies have higher drag and lower Strouhal numbers. Airfoils, however, have a finite thickness at the leading edge and from a pure mathematical viewpoint will have a longer projected length than  $c \sin \alpha$ , as is shown in fig. 8.10.

The non-dimensional projection  $l_p / c$  depends on the shape of the leading edge and the thickness of the trailing edge and for positive angles is given by:

$$\frac{l_p}{c} = \left(1 - \frac{x}{c}\right) \sin \alpha + \left(\frac{y}{c} \cos \alpha\right)_{\max} - \left(\frac{y}{c}\right)_{TE} \cos \alpha \quad (8.2)$$

When separation takes place before reaching the most upper point of the leading edge, the wake directly behind the airfoil cannot be smaller than the projection  $l_p$ .

Hence, the projection length for airfoils varies with leading edge shape and trailing edge thickness and consequently with positive and negative angles.

The length of  $l_p$  relative to  $c \sin \alpha$  is given in fig. 8.11. It shows that due to the NACA 4421 airfoil thick upper surface, it's  $l_p$  at positive angles is longer compared to DU97, despite the smaller maximum thickness. Relating  $St$  of airfoils at the lower angles of attack to  $c \sin \alpha$  as the wake width in fact underestimates the wake width and hence overestimates  $St_d$ , which divergence grows with increasing thickness of the airfoil leading edge. By dividing the  $St_d$  values by the ratio given in figure 8.11, this is resolved.

Application of the ratio depicted in fig 8.11 for DU91 would decrease the Strouhal numbers in the lower positive angles of attack range, now giving  $St_d = 0.150 \pm 0.002$  for  $30^\circ \leq \alpha \leq 100^\circ$  instead of  $St_d = 0.153 \pm 0.003$ .

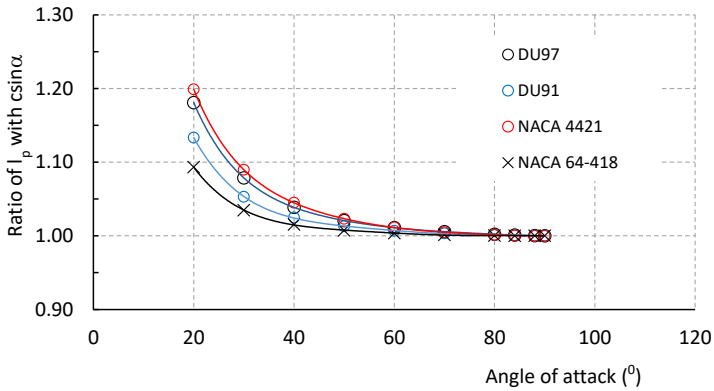


Figure 8.11: The ratio of  $l_p$  with  $c \sin \alpha$  for a number of airfoils with various leading edge shape and thickness.

### 8.7 STANDARD DEVIATION OF FLUCTUATIONS OF $C_L$ AND $C_D$

Fig. 8.12 depicts the 95% confidence interval of the fluctuations in the corrected lift and drag coefficients. The variation in the lift around the mean at  $60^\circ$  is about  $\pm 20\%$ , which is considerable.

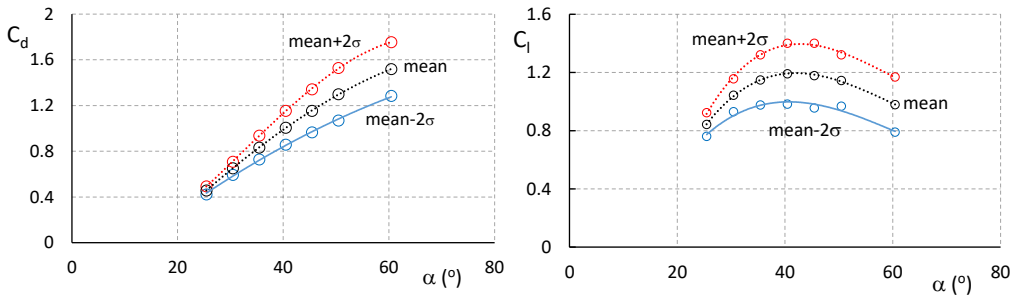


Figure 8.12: The variation of the corrected lift and drag coefficient of the 25 cm chord model in terms of twice the standard deviation, at  $Re=0.7 \times 10^6$ .

### 8.8 CONCLUSIONS

Strouhal numbers were established at deep-stall incidences for DU91 at  $Re$ -numbers below  $Re=0.7 \times 10^6$  and for DU00 at  $6 \times 10^6 \leq Re \leq 8.1 \times 10^6$ . Higher drag gives lower  $St$ -numbers and vice-versa, due to the fact that both are connected to the velocity near the upwind side leading and trailing edges. If the velocity at the leading edge is high at separation, this destabilizes the free shear layer and stimulates roll-up to a vortex, which is then shed into the wake with a higher frequency. At the same time higher velocity between the stagnation point and the upwind trailing edge gives a lower drag. A similar reasoning is true for velocity differences at the trailing edge. Both situations are depicted

in fig. 8.8.

In a  $C_d$ -St curve, values found for positive and negative angles fall on the same curve.

The Strouhal number data found, suggest that the  $C_d$ -St curve established for DU91 might be generally valid for most airfoils.

## 8.9 REFERENCES

- Bearman, P.W. *Circular cylinder wakes and vortex-induced vibrations*. J. Fluid Struct., 27 (5–6) (2011), pp. 648-658, 10.1016/j.jfluidstructs.2011.03.021
- Boorsma, K. *Comparison of Experimental and Computational Aerodynamic Section Characteristics of DU91-W2-250 Profile*. Master thesis, Delft University of Technology, 2003.
- Buresti, G. *Vortex shedding from bluff bodies*. In: Wind Effects on Buildings and Structures, (Riera J.D., Davenport A.G., Eds.), Balkema, Rotterdam, 1998, pp. 61-95.
- Chen, J.M. and Fang, Y. *Strouhal numbers of inclined flat plates*. Journal of Wind Engineering and Industrial Aerodynamics, **61**, pp. 99-112, July 1996
- Derakhshandeh, J.F., Alam, M.M. *A review of bluff body wakes*. Ocean Eng., 182 (2019), pp. 475-488, 10.1016/j.oceaneng.2019.04.093
- Fage, A. and Johansen, F.C. *On the flow of air behind an inclined flat plate of infinite span*. British ARC R&M, No. 1104. (1927)
- Fallahpour, N., Mani, M. and Lorestani, M. (2023) *Experimental investigation of vortex shedding of an airfoil at post-stall incidences*. Proc IMechE Part G: J Aerospace Engineering 2023, Vol. 237(4) 883–898 DOI: 10.1177/09544100221112718
- Howarth, L. *Note on the flow past a circular cylinder*. Mathematical Proceedings of the Cambridge Philosophical Society, vol. 31, Cambridge University Press (1935), pp. 585-588, 10.1017/S0305004 10001358X
- Kármán, T. Von, *Über den Mechanismus des Widerstandes, den ein bewegter Körper in einer Flüssigkeit erfährt*. Nachr. kgl. Ges. Wiss. Göttingen, mat.-phys. Kl, 509 (1911),

<http://eudml.org/doc/58812>

Lam, K.H. and Leung, M.Y.H. (2005) *Asymmetric vortex shedding flow past an inclined flat plate at high incidence*. European Journal of Mechanics B/Fluids 24 (2005) 33–48, (2005)

Lekkala, M.R. , Latheef, M., Jung, J.H., Coraddu, A. , Zhu, H., Srinil, N., Lee, B., Kim, D.K. *Recent advances in understanding the flow over bluff bodies with different geometries at moderate Reynolds numbers*. Journal of Ocean Engineering 261 (2022), <https://doi.org/10.1016/j.oceaneng.2022.111611>

Lind, A.H. and Jones, A.R. (2016). *Unsteady airloads on static airfoils through high angles of attack and in reverse flow*. Journal of Fluids and Structures, Open Access Volume 63, Pages 259 - 279, May 01, 2016

Mondal, R., Alam, M.M. *Blockage effect on wakes of various bluff bodies: A review of confined flow* Journal of Ocean Engineering 286 (2023) 115592

Novak, J. *Strouhal number and flat plate oscillation in an air stream*. Acta Tech. Cossav, 4 (1973), pp. 372-386.

Pellegrino, A. and Meskell, C. *Vortex shedding from a wind turbine blade section at high angles of attack* . J.WindEng.Ind.Aerodyn.121(2013)131–137

Polhamus, E.C. *A review of some Reynolds number effects related to bodies at high angle of attack*. NASA Contractor Report 3809, 1984

Roosbroeck, M. van. *The Effect of Leading Edge Thickness on the Maximum Drag Coefficient of Airfoils 90° to the Wind*. Master Thesis, Faculty of Aerospace Engineering, TUDelft, September 2014

Roshko, A. *A new hodograph for free-streamline theory*. NACA TN 3168, 1954

Schewe, G. *Reynolds-number effects in flow around more-or-less bluff bodies*. J. Wind Eng. Ind. Aerod., 89 (14–15) (2001), pp. 1267-1289, 10.1016/S0167-6105(01) 00158-1

Swalwell, K.E. *The effect of turbulence on stall of horizontal axis wind turbines*. MSc thesis, Department of Mechanical Engineering, Monash University, Melbourne, Australia, 2005.

Xu, G., Yu, W., Sciacchitano, A., & Simao Ferreira, C. (2025). An Experimental Study of the

Unsteady Aerodynamics of a Static DU91-W2-250 Airfoil at Large Angles of Attack. *Wind Energy*, 28(3), Article e2974. <https://doi.org/10.1002/we.2974>

Zdravkovich, M.M. *Review and classification of various aerodynamic and hydrodynamic means for suppressing vortex shedding*. *J. Wind Eng. Ind. Aerod.*, 7 (2) (1981), pp. 145-189, 10.1016/0167-6105(81)90036-2

# 9

## THE AIRFOIL MAXIMUM DRAG COEFFICIENT

### 9.1 INTRODUCTION

As was shown in chapter 8, the dynamics of the flow play an important role in the instantaneous forces. However, it appears also possible to extract a meaningful “two-dimensional” characteristic for a particular airfoil with large scale separation using sufficient averaging time at a low blockage ratio. Because the entire airfoil downwind side features flow separation at deep-stall angles of attack, variation of the downwind shape of the airfoil does not play a significant role in the aerodynamics, provided that the blockage is low and this shape does not protrude deep into the wake where the motion of the vortex street behind the airfoil will be affected. At  $\alpha=90^\circ$ , the downwind cusp of DU91 has only a minor effect (1%) on the drag.

Since all airfoils generally have one relatively sharp (trailing) edge, from which the flow will detach immediately when placed normal to the flow, differences in maximum drag

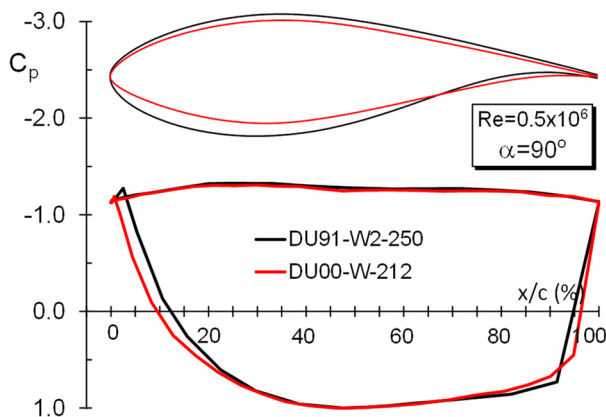


Figure 9.1: The measured and corrected pressure distribution at  $90^\circ$  incidence for two DU airfoils with different thickness and shape.

are predominantly related to the contour of the airfoil upwind side, as is shown in fig. 9.1. As was discussed in chapter 7, it appears that the difference in airfoil drag coefficient is strongly affected by the pressure distribution downstream of the stagnation point at the

upwind 50% chord station. Apparently, as long as there is laminar separation from the upwind side near the leading edge, the base pressure of different airfoils shows no variation at comparable Reynolds numbers, trailing edge angle and blockage.

Timmer (2010) showed that the maximum drag coefficient of airfoils decreases with increasing leading edge thickness. Lindenburg (2003) correlates the maximum value of  $C_d$  to the leading edge radius and the flow direction at the trailing edge, also based on several other shapes found in literature such as wedges and (half-)cylinders. However, the leading edge cannot be represented by the nose radius alone, as there is only one, while for negative and positive angles the maximum drag coefficient for non-symmetrical airfoils with comparable upper and lower surface trailing edge angles differs, which would necessitate a second parameter near the leading edge to account for the differences. Similar to the study on the deep-stall angle, the  $y/c$  ordinate at  $x/c=0.0125$ , was adopted here to represent the leading edge thickness. In this case, however, the upwind  $y/c$  value is the important parameter.

Apart from the thickness at the leading edge, the angle at which the flow leaves the trailing edge ( $\zeta$ ) when the chord is normal to the flow can be identified as a key parameter. The study presented in this chapter aims at quantifying the contribution of the leading edge thickness and the trailing edge angle to the maximum drag coefficient.

As became clear in chapter 7, the Reynolds number affects the nature of the flow around the leading edge as well. While the base pressure does not significantly change with Reynolds number when the airfoil is normal to the incoming flow, as is e.g. shown in fig. 7.21 and 7.24, the formation of a pressure peak on the upwind leading edge reduces the drag coefficient. The impact of the Reynolds number particularly on the maximum drag coefficient will also be further addressed.

## **9.2 THE IMPACT OF THE LEADING EDGE THICKNESS**

To distinguish the contributions to the total maximum drag of the leading edge and the trailing edge, a set of airfoil models with systematically varying leading edge thickness and zero trailing edge angle ( $\zeta=0$ ) was designed and measured in the LTT (van Roosbroeck, 2014). The airfoil shapes of the 0.2 m chord numerically milled aluminium models are depicted in figure 9.2. They have different elliptical leading edges for the upper and lower sides up to 34% of the chord, such that the 3 models cover the range of  $y/c$  values at  $x/c=0.0125$  between .010 and .035. The last 20% of the airfoils are straight and the 4 mm thick trailing edges are sharp.

Van Roosbroeck also performed simulations with the CFD code Numeca. While the 2d-computations may not give the right level of (base) pressure, the pressure distributions of the airfoils with  $y/c=0.010$  and 0.035 presented in fig. 9.2 do corroborate what was found in chapter 7:

With the airfoil normal to the flow, the base pressure is largely invariant across section shape and Reynolds number.

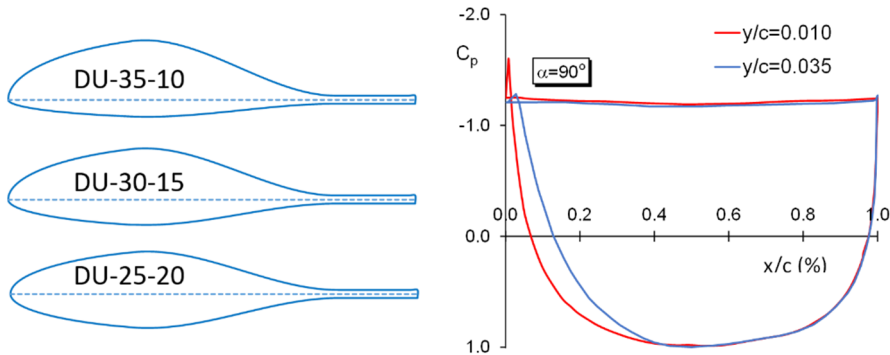


Figure 9.2: DU airfoils with prescribed upwind thickness at  $x/c=0.0125$  (left) and the  $C_p$ -distribution of the two extremes, computed by NUMECA (van Roosbroeck, 2014)

This is also the reason why a single parameter near the leading edge can represent the drag coefficient. The difference in drag is almost exclusively caused by the velocity over the upwind part of the airfoil, between the stagnation point at 50% chord and the leading edge. The thicker the shape, the higher the velocity and the smaller the contribution of this part of the pressure distribution to the overall normal force (=drag) coefficient. The  $y/c$  at  $x/c=0.0125$  is just one parameter indicative for the local thickness of the section. It could also be the  $y/c$  at any other  $x/c$  coordinate in the vicinity of the leading edge. As the airfoils have been systematically shaped, a gradual change of the drag coefficient can be expected.

### 9.2.1 Test setup and data handling.

The models were tested using the LTT 6-component external mechanical balance system. They were cantilevered from the overhead balance and were mounted normal to the flow. The angle of attack range departing from this position was  $\pm 45^\circ$ , the maximum range of the balance system without re-orienting the model. The three models were tested first with the thicker upper surface pointing upwind (addressing angles of attack between  $-45^\circ$  and  $-135^\circ$ ), then rotated  $180^\circ$  to test the model with the lower surface facing the incoming flow (incidences between  $45^\circ$  and  $135^\circ$ ). The 19% thick models (with comparable stiffness characteristics) completely spanned the 1.25m height of the tunnel, but with a gap of approximately 2.0mm with the tunnel walls.

The models were attached only at one end to the balance. To avoid heavy vibrations the Reynolds number in the study by van Roosbroeck in 2013 was limited to  $1.5 \times 10^5$ . In a later stage the attachment of the models to the support was improved, enabling higher

Reynolds numbers up to  $0.45 \times 10^6$ , which are reported here.

The measured forces were recorded with 5 Hz and averaged over 40 seconds. In view of the strong dynamics in the flow the sampling time of 5Hz might seem very low, however due to the inertia of the balances (rotating spindles with running weights) strong fluctuations will not be followed, which already averages out large and fast variations effectively.

### 9.2.2 Blockage corrections

To correct for the large overspeeds due to test section blockage the method of Maskell (Appendix A) was applied. As is concluded in Appendix A for  $c/h$  values up to 0.15 the method can be used without significant danger of over correction. The drag measurements presented here have a  $c/h$  value of 0.121 (a chord of 0.2m and an effective test section width of 1.656 m).

### 9.2.3 Results

Figures 9.3a to 9.3c present the corrected drag measurements for all 6 configurations. The maximum drag coefficients shown in figure 9.3d and tabulated in table 9.1 were extracted from 6<sup>th</sup> degree polynomials through the measured points of the various models. The relation between the  $y/c$  at  $x/c=0.0125$  and the maximum drag coefficient is

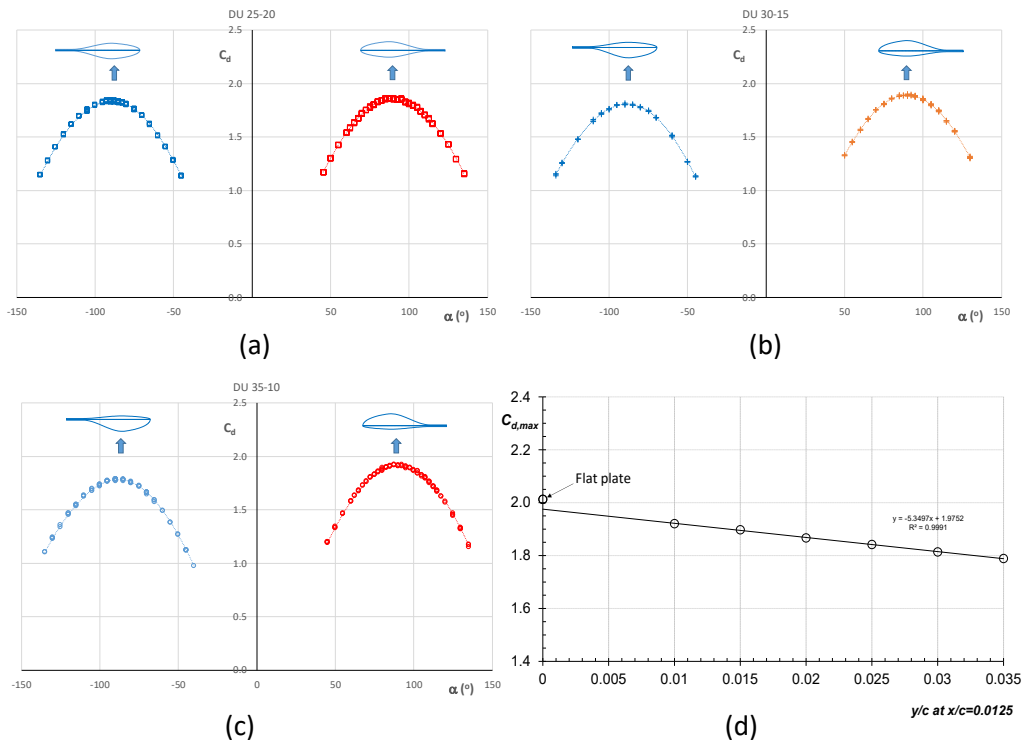


Figure 9.3: The measured and corrected drag coefficients for the 3 models depicted in figure 9.2.

Table 9.1: Maximum drag coefficients deduced from a 6<sup>th</sup> degree polynomial

Airfoil	positive angles		negative angles	
	y/c	Cd -max	y/c	Cd -max
Flat plate	0	2.012		
DU-25-20	0.020	1.867	0.025	1.842
DU-30-15	0.015	1.898	0.03	1.814
DU-35-10	0.010	1.921	0.035	1.789

found to be :

$$C_{d,max} = 1.976 - 5.366 * (y / c)_{x/c=0.0125} \quad (9.1)$$

To show that the test yields near-two-dimensional drag coefficients also a flat plate was measured, giving a maximum drag coefficient of 2.012. Note that eq. 9.1 returns Hoerner's maximum drag coefficient of 1.98 for a flat plate (y/c=0).

With a 0° trailing edge angle and the base pressure being invariant across section shape, the linear  $C_{d,max}$  relation in fig. 9.3d can also be found by using the upwind section area along the x-axis.

### 9.3 THE IMPACT OF THE TRAILING EDGE ANGLE

The flat plate and the model of DU35-10 were also used to determine the impact of the trailing edge angle on the drag coefficient. To this end a number of 1 mm thick sheet metal flaps were manufactured with nominal angles of 0°, 10°, 15° and 20°. The flaps were attached to the model as shown in figure 9.4.

The drag curves for the airfoil with flap were determined with 60 second averages of the force readings at a Reynolds number of  $4 * 10^5$ . Due to the elongation of the model the c/h value now has increased to 0.15. To determine the maximum drag coefficient the same procedure was followed as described above for the base airfoils.

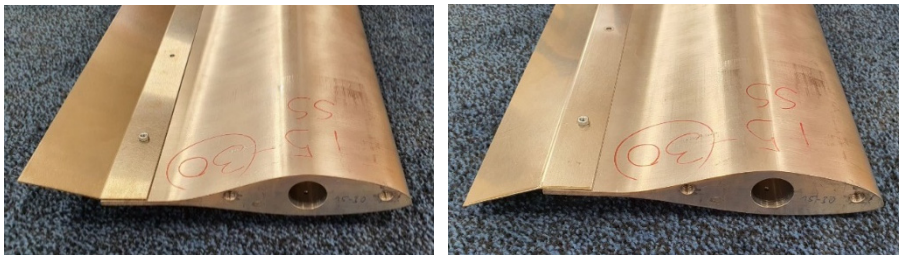


Figure 9.4: One of the DU-XX models showing a 20° negative (left) and positive (right) trailing edge (flap) angle.

Due to tunnel time constraint not all y/c and flap configurations were tested, however all the extreme values were covered. Figure 9.5 presents the measured values of the maximum drag coefficient in relation to the true trailing edge flow angle when the longest

chord of the airfoil (the line between the trailing edge and the leading edge) is normal to the flow. The TE-angle is positive counter-clockwise.

Probably due to more vibrations the flat plate measurements show more variation around the trend line, despite the “hat”-stiffener that was attached to the back of the plate. The other models are much stiffer. The 1 mm step between the flap and the airfoil surface was smoothed out with thin aluminium tape. Account was made for the change in angle of attack of the model with flap deflection, as the trailing edge moves away from its original chord position, which also causes small changes in the length of the longest chord of the airfoil. As can be deduced from figure 9.5, the effect of a TE-angle on the maximum

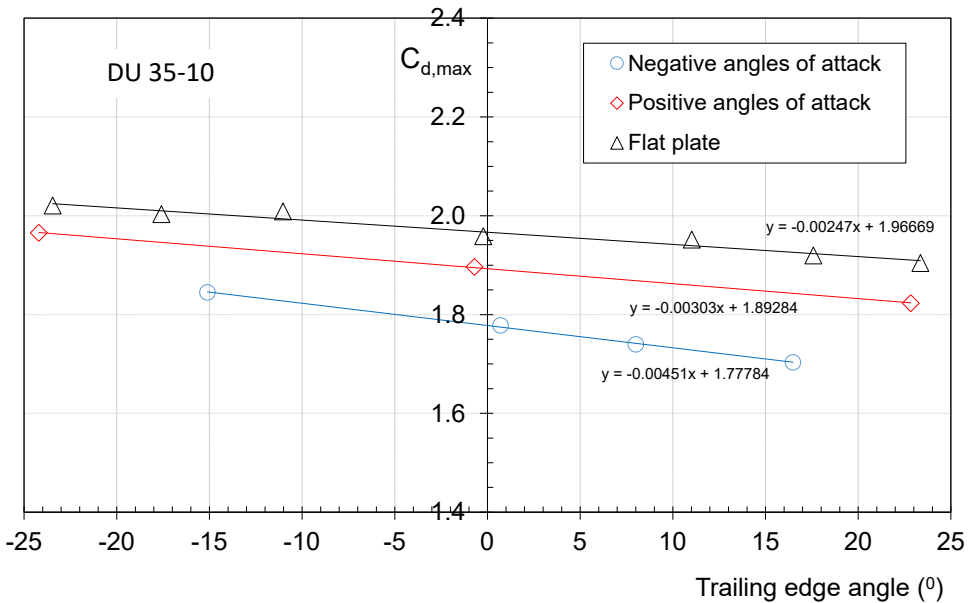


Figure 9.5: The maximum drag coefficients of the flat plate and of airfoil DU35-10 for various trailing edge flow angles. The flow angle is positive moving ant-clockwise.

drag coefficient is not constant for all leading edge thicknesses. It appears that the thicker the leading edge of the airfoil, the larger the impact of a trailing edge angle.

Figure 9.6 shows this “sensitivity” to changes in the TE-angle in relation to the leading edge  $y/c$ . The sensitivity factor is found to be :

$$F_{TE} = -0.00246 - 0.05815 * (y / c)_{x/c=0.0125} \quad (9.2)$$

This sensitivity increase with LE-thickness can be explained from the fact that the circulation due to a different TE-angle might be slightly affected, changing the velocities at the leading edge. On a thick leading edge the flow can stay attached longer and variation in the pressure gradients at the nose may cause small changes in the separation point, leading to small variations to the wake width and the drag coefficient accordingly.

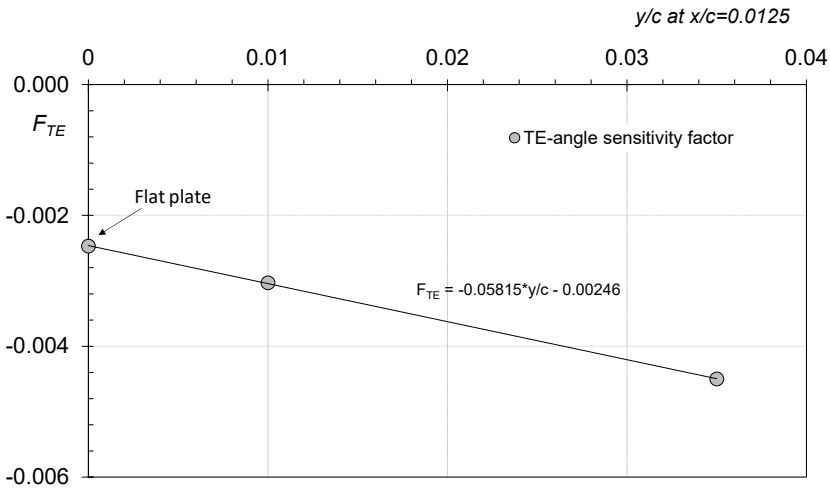


Figure 9.6: The variation of the sensitivity of the airfoil maximum drag to changes in the TE-flow angle with airfoil leading edge thickness

The leading edge of a flat plate does not allow for a change in separation location; it is so sharp that this leads to immediate flow detachment, no matter what change in circulation may exist. The contribution of the TE-angle to  $C_{d,max}$  of an airfoil with a specific  $y/c$  is:  $F_{TE} * \zeta$ . The final equation to estimate the maximum drag coefficient of the airfoils tested at Reynolds numbers around  $0.5 \times 10^6$  is:

$$C_{d,max} = 1.976 - 5.366 * (y/c)_{x/c=0.0125} + (-0.00246 - 0.05815 * (y/c)_{x/c=0.0125}) \zeta \quad (9.3)$$

## 9.4 THE IMPACT OF THE REYNOLDS NUMBER.

Following the discussion in chapter 7, there may be a small impact of the Reynolds number in the present measurements, not coming from changes in base-pressure, but from small variation of the upwind velocity near the leading edge.

Figure 9.7 presents the maximum drag coefficient of the flat plate and of DU-10-35 at  $90^\circ$  and  $-90^\circ$  for  $10^5 \leq Re < 5 \times 10^5$ . As expected, the flat plate is not sensitive to Reynolds number changes. It appears there is a very light tendency of the  $C_{d,max}$  to grow with increasing Reynolds number, both for the thick as well as the thin upwind leading edge (app. 1% between the lowest and the highest Reynolds number). If any, one would expect a small decrease of the drag with Re-number. As the drag was measured with a balance it could also very well be the changing interference with the test section boundary layer, of which the thickness decreases with increasing test section velocity. The Mach number at  $0.45 \times 10^6$  is approximately 0.1.

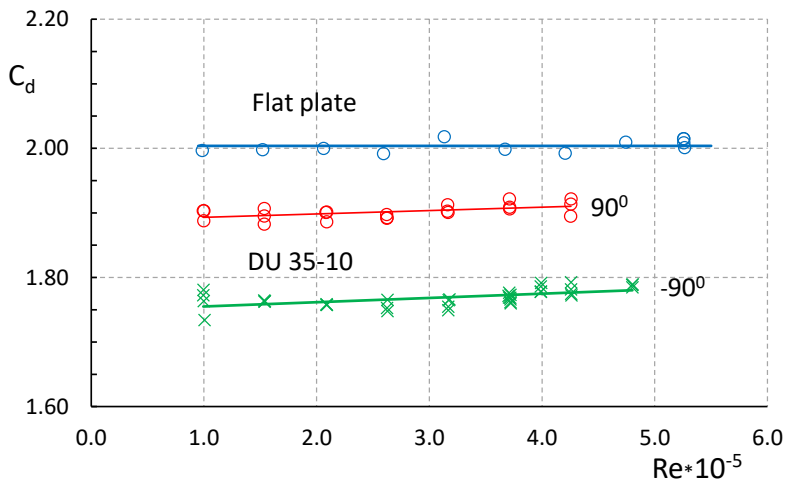


Figure 9.7: The variation of the maximum drag coefficient with Reynolds number for DU-10-35 and the flat plate.

## 9.5 NEAR-SURFACE FLOW TOPOLOGY

Fluorescent oil flow pictures were taken to show the averaged flow structure at the leading edge and in the wake of DU-35-10. Figure 9.8 presents the model with the thick side facing upwind (model at  $-90^\circ$  angle of attack). Clearly visible are the relatively sharp lines where the flow separates from the upper and lower surfaces. The picture shows there's no time-average 3-dimensional pattern of the separation, like generally is the case just after the primary stall of airfoils (the mushroom pattern of stall cells). The flow also doesn't seem to be influenced by the horseshoe vortex at the wall in front of the model. Figure 9.9 shows the leading edge in more detail. On the left, the upper (upwind) side leading edge and on the right the lower side. The right picture shows the two yellow separation bands on upwind and downwind side, where the oil gathers from left and right and drips down due to gravity.

They demarcate an area consisting of two parts divided by a third thin line on the apex. On the left and right of the apex there's no clear indication of direction of the flow, which means that the shear stress is close to zero: the leading edge has two separation bubbles with weak counter-rotating vortices.

The separation mechanism on the upwind and downwind sides differ. On the upwind side the BL separates due to the steep gradient of the airfoil contour, to some extent comparable with a backward facing step. There is no sign of a substantial velocity deficit near the surface. This is in contrast to the downwind side, where the oil drips down under influence of gravity due to a gradually diminishing surface shear stress. The separated upper and lower surface boundary layers merge and roll up in a vortex, which is convected downstream.

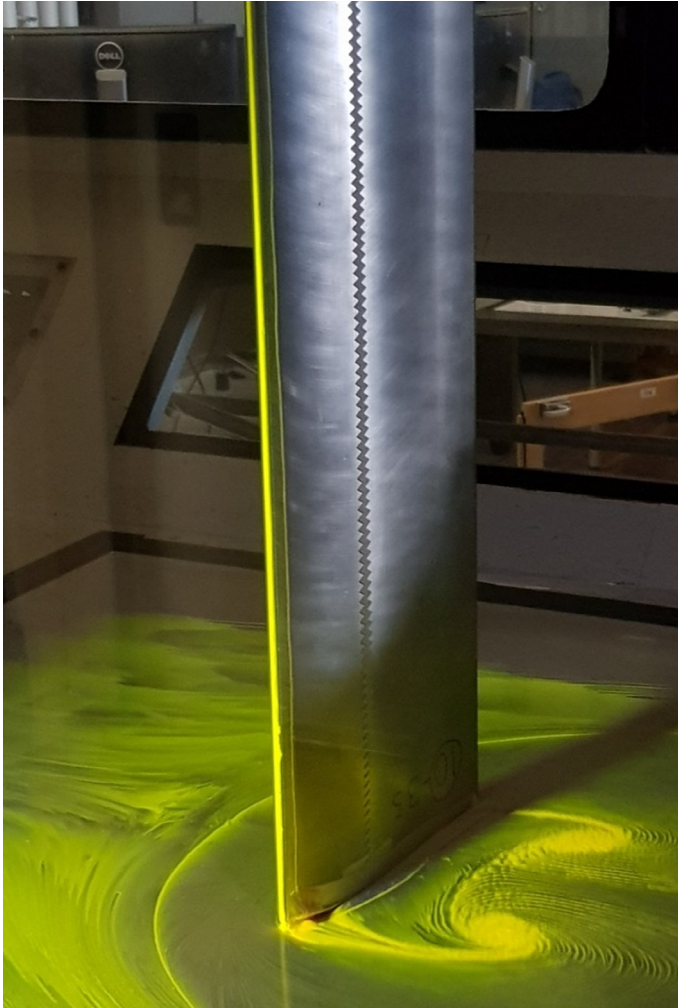


*Figure 9.8: The time average flow field on model DU-35-10 at  $-90^\circ$ , showing separation lines on upper and lower surface at the leading edge.  $Re=0.40 \times 10^6$ . The zigzag tape does not induce boundary layer transition in this case (separated flow).*

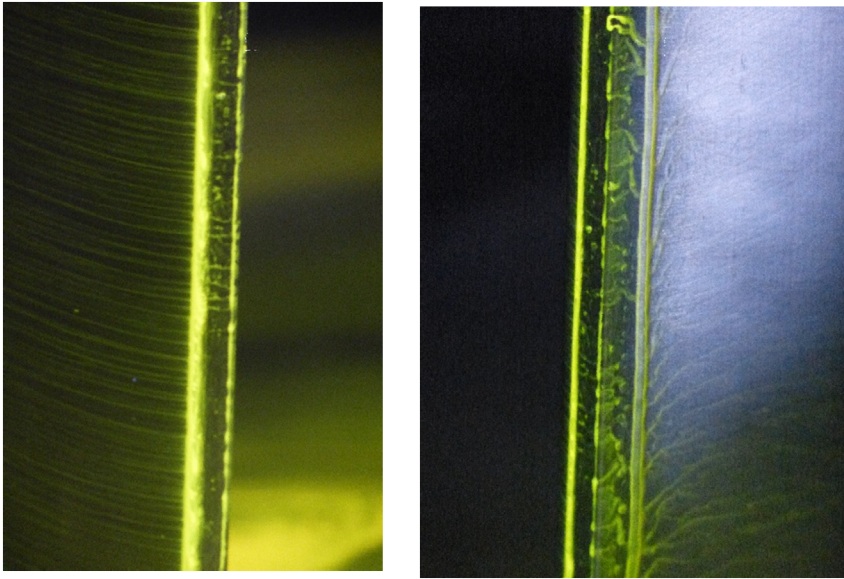


*Figure 9.9 The separated area at the leading edge of DU-35-10 at  $-90^\circ$ . Left : upwind side, right: downwind side.*

In fig. 9.10 the wake is captured until about 3.5 chords downstream. The dotted line defines the boundary of the recirculation area with the outer flow. The bubble due to the vortex structures is about 3 chords long. It seems to end in a viscous wake with a width of about half the chord length. The approximate 3 chords bubble length agrees well with

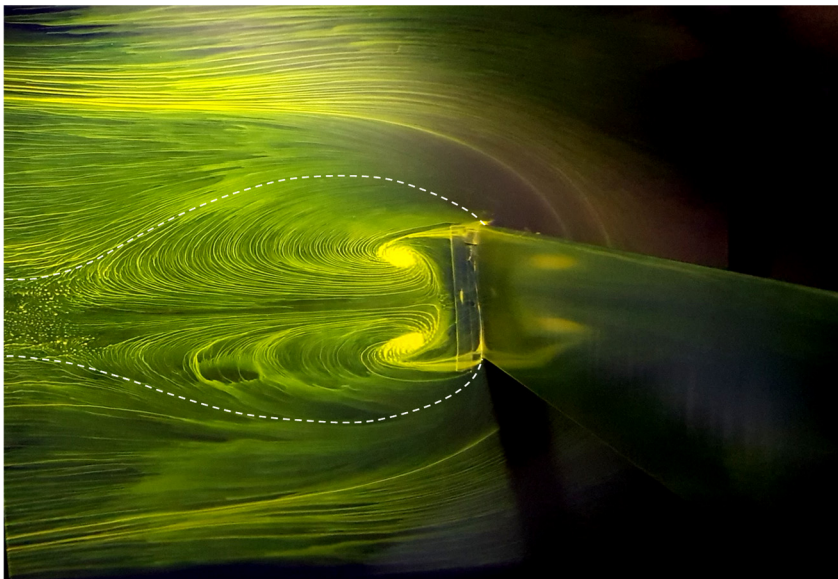


*Figure 9.10: The time average vortex wake behind the model. The dotted line is the boundary between the recirculation zone and the outer flow.*

PIV-measurements on the DU91-W2-250 15cm chord model at  $\alpha=90^\circ$  performed by XU et al. (2025) in the LTT (just over 2.95) and fairly well with the value for a two-dimensional flat plate (2.82) found by Fail et al. (1959).

In summary the following conclusions can be drawn from the pictures:

- The separation on the upwind surface forms a straight line, there's no variation along the span.
- On the leading edge two area's with very low velocity exist, separated by a zero-shear stress line at the apex.
- The time average vortex wake bubble is about 3 chords long.

## **9.6 PREDICTION OF AIRFOIL MAXIMUM DRAG COEFFICIENT**

The relations discussed above enable us to predict the maximum drag coefficient of the airfoils tested, simply on the basis of their geometrical appearance, for Reynolds numbers around  $0.5 \times 10^6$ . If the formulation is also suited to predict the  $C_{d,max}$  of other airfoils, will be discussed below.

### **9.6.1 Results from literature.**

As already mentioned in the introduction, many variables impact the results of measurement campaigns at high angles of attack found in literature. Apart from the wind tunnel wall correction scheme, of which insight in the suitability progressed with time, two equally important aspects play a paramount role.

The first one is the test setup. To utilize the height of large test sections often inserts are used. In combination with a relatively small chord of a model spanning the inserts a fairly small blockage parameter  $c/h$  can be reached. In addition, there is no need to manufacture a model with a large span, which saves costs and mitigates problems of model stiffness. However, complications arise when the model is set to deep-stall angles of attack, thus significantly blocking only the middle part of the large test section. The flow will partly avoid this blockage, which increases the velocity in the other parts of the passage. Consequently, the flow speed between the inserts will increase due to the blockage, but not to the degree found in a test section with uniform blockage.

The second aspect is the method of determining the free-stream dynamic pressure, which was also briefly discussed in chapter 7. When measured with a pitot-static tube, the probe location plays a dominant role. If it is somewhere far upstream of the test section formed by the inserts, (or when a calibration using pressure orifices in the contraction upstream in a wider area of the tunnel channel is used), generally the lift and drag coefficients after correction are too low, resulting from an assumed –but not realized- velocity increase over the model based on uniform blockage. In this situation the characteristics of the

model can be recalculated, taking into account the appropriate amount of blockage at the model location, as will be shown in paragraph 9.6.2. If, instead, the tube is located between the inserts upstream of the model it may pick up part of the actual velocity increase of the flow approaching the model due to blockage, but it may also be too close to the model, as its static pressure field, especially at very large angles, will affect the static pressure reading of the pitot-static tube. This combination can lead to either overestimation or underestimation of the coefficients. In general it is unknown what impact both aspects have on the measured dynamic pressure. As a result, it is difficult to find an appropriate method to recalculate the characteristics for these measurements. Unfortunately, quite a number of tests found in the public domain contain measurements at high angles of attack in test sections with inserts without uniform blockage measures. Table 9.2 gives an overview of the most relevant ones.

Due to the uncertainties associated with the use of test section inserts, unfortunately none of the data sets from measurement campaigns mentioned in table 9.2 can be directly used with sufficient confidence in the reported drag values. For example, the uncorrected data of Massini et al. (1993) for NACA 0012 when corrected with Maskell's method return a near flat plate  $C_{d,max}$  value of 1.995. Other studies also often referred to are shown in table 9.3. The first two references mentioned in table 9.3 do not give specific correction schemes, although Ostowari and Naik (1985) and also Sheldahl and Klimas (1981) and Snyder et al. (1984) refer to Pope and Harper (1966), which classic book does not contain explicit high angle of attack correction methods. The maximum drag coefficients of Ostawari and Naik are higher than 2, which points in the direction of a free-stream dynamic pressure offset. The measurements of Critzos et al. (1955) were performed using a gimball arrangement at one end of the model, while the other end was attached to a balance. With such a setup *approximately* half the load is measured, which may have affected the accuracy of the force measurement.

### 9.6.2 Re-calculating available data

As the report of Satran and Snyder (1977) explicitly gives the applied correction formulae, which unfortunately do not apply to deep-stall measurements, it is possible to use Maskell's method after re-calculating the available data to uncorrected values. The following drag correction equation was applied to un-correct the drag data:

$$C_{d_u} = C_d / (1 - 2\Lambda\sigma - 2\tau C_{d_u}) \quad (9.4)$$

$$\Lambda = 1.75 * \left(\frac{t}{c}\right) + 1.875 * \left(\frac{t}{c}\right)^2, \quad \sigma = \frac{\pi^2}{48} \left(\frac{c}{h}\right)^2 \quad \text{and} \quad \tau = \frac{1}{4} \left(\frac{c}{h}\right) \quad (9.5)$$

where  $t/c$  is the relative thickness of the airfoil and the index  $u$  denotes uncorrected

Table 9.2: Reports containing data of attack using test section inserts

Authors	Airfoil	c/h	Correction scheme	Remarks
Michos et al., 1983	NACA 0012	0.257	Maskell, $\theta=0.96$	Rather large c/h for the present study. Dynamic pressure at entrance of t.s, but corrected (2%)
Bloy and Roberts, 1993	NACA 63-215	0.138	Maskell, $\theta=0.96$	Small model aspect ratio (2.5). Distance to pitot tube is 2.5 chords
Satran and Snyder, 1977	LS(1)-0413, LS(1)-0417	0.166	for low angles	Virginia Tech University (VTU) 2.13 m x 3.05 m wind tunnel,
Sheldahl and Klimas, 1981	NACA 0009, 0012, 0015	0.071	not given	VTU 2.13 m x 3.05 m wind tunnel, pitot in test section
Snyder et al., 1984	NACA 23018, 24 and 30 NACA 64-618	0.107	not given	VTU 2.13 m x 3.05 m wind tunnel
Massini et al., 1993	Various, e.g. NACA 0012	0.135	Maskell	Correction using base pressure. Circular test section, pitot at 6.6 chords upstream from model Uncorrected data

Table 9.3: Reports containing data of test campaigns at high angles of attack using the entire test section

Authors	Airfoil	c/h	Correction scheme	Remarks
Ostowari and Naik, 1985	NACA 4409, 12, 15 and 18	0.100	not given	Texas A&M 2.13 m x 3.05 m test section. Wooden models
Critzos et al., 1955	NACA 0012	0.067		Langley LPT 0.914 m x 2.134 m test section. Gimball arrangement. Uncorrected data
Critzos et al., 1955	NACA 0012	0.100		Langley 2.13 m x 3.05 m test section. Uncorrected data
Matsumiya and Tsutsui, 1995	FX 84-W-140	0.214		MEL wind tunnel, 1.4 x 1.4m test section. Uncorrected data

values. After a few iterations the uncorrected drag coefficient can be determined. The dynamic pressure ratio was then calculated using Maskell’s correction, assuming the passage between the inserts is the test section. However, as the velocity increase is spread over the entire test section with area 5.678 m<sup>2</sup> (assuming the inserts are 15 cm thick), and not only occurs in the middle passage (A=1.951 m<sup>2</sup>), about one third of the velocity increase (0.3436) is realized at the model location. The new dynamic pressure ratio for correction is given by equation 9.6:

$$\frac{q_{cor}}{q_u} = \left[ 1 + \left( \sqrt{\frac{q_M}{q_u}} - 1 \right) * 0.3436 \right]^2 \quad (9.6)$$

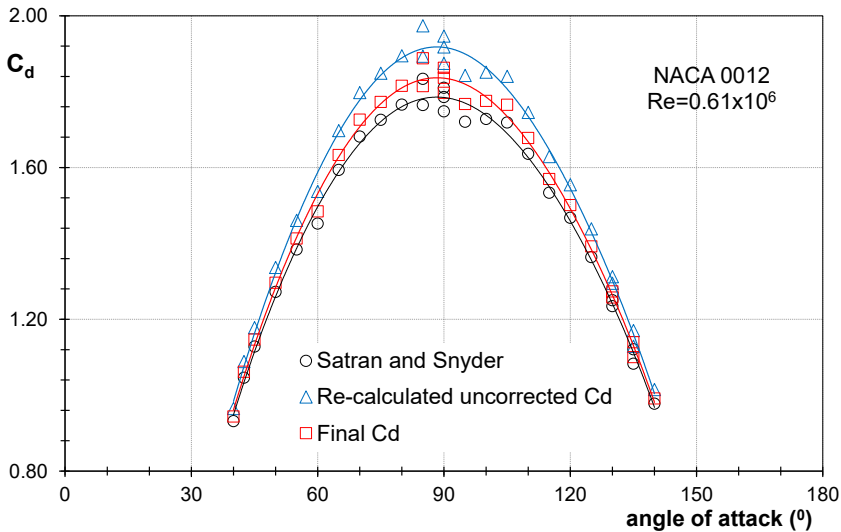


Figure 9.11: The re-calculated drag coefficients to account for the actual blockage between test section inserts in the study by Satran and Snyder (1977).

where the index M refers to Maskell’s method for the test section formed by the inserts. Blockage corrections of the measurements by Sheldahl and Klimas (airfoils NACA 0009, 0012 and 0015) and Satran and Snyder (LS(1)-0413 and LS(1)-0417) at a Reynolds number of approximately 0.6x10<sup>6</sup> were re-calculated accordingly.

Figure 9.11 presents the differences in drag values between the data from the report and the ones corrected with the method discussed above. The data from Snyder et al. (1984) were not processed as it is unclear what correction equations were used.

## 9.7 COMPARISON OF PREDICTIONS WITH MEASUREMENTS.

All the maximum drag coefficients presented here have been determined with a 6<sup>th</sup> degree polynomial through the drag coefficients in a range of approximately ±45<sup>o</sup> around the -90<sup>o</sup> or 90<sup>o</sup> angle of attack. The Reynolds number ranges from 0.5x10<sup>6</sup> to about

Table 9.4: Measured and predicted  $C_{d,max}$  for airfoils tested in the Delft LTT

Airfoil	y/c	$\zeta$	$C_{d,max}$		
			deg.	measured	predicted
Positive angles					
Flat plate	0	0	2.013	1.976	-1.8
DU 96-W-180	0.01533	-0.51	1.891	1.894	0.1
DU 91-W2-250	0.03103	-10.23	1.859	1.853	-0.3
DU 97-W-300	0.03327	-15.16	1.831	1.864	1.8
NACA 0018 *	0.02841	11.85	1.800	1.774	-1.4
Negative angles					
DU 96-W-180	0.02072	13.43	1.800	1.814	0.8
DU 97-W-300	0.03069	15.16	1.781	1.747	-1.9
DU 91-W2-250	0.02698	16.04		1.766	

\*c/h=0.217, AR=7.2

0.75x10<sup>6</sup>.

Table 9.4 shows the predicted and measured maximum drag coefficients for a number of airfoils tested in the Delft LTT. The NACA 0018 results, from tests with a c/h value of 0.217 and an aspect ratio of about 7, are yet unpublished data. DU 96 and DU 97 results were previously reported in Timmer (2010). The trailing edge angle was determined using the upper or lower surface dy/dx gradient at the trailing edge calculated from a 4<sup>th</sup> degree polynomial through coordinates of approximately the last 4% of the airfoil contour described by 200 coordinates. All the tests in table 9.4 were performed using the same force balance system. The comparison of measured and predicted values shows

Table 9.5: Measured and predicted  $C_{d,max}$  for various other airfoils found in literature

Airfoil	y/c	$\zeta$	$C_{d,max}$		$\Delta$ (%)
			deg.	measured	
Positive angles					
LS(1)-0413	0.01531	-10.58	1.940	1.929	-0.6
FX-84-W-140 <sup>1</sup>	0.01536	-4.95	1.944	1.910	-1.7
DU 00-W-212	0.01756	-1.26	1.861	1.886	1.3
NACA 63-215	0.01793	3.47	1.960	1.867	-4.7
LS(1)-0417	0.02129	-9.92	1.912	1.898	-0.7
NACA 0009	0.01894	6.00	1.860	1.880	1.1
NACA 0012 <sup>2</sup>	0.02072	7.99	1.921	1.846	-3.9
NACA 0012 <sup>3</sup>	0.02072	7.99	1.902	1.846	-2.9
NACA 0012 <sup>4</sup>	0.02072	7.99	1.835	1.846	0.6
NACA 0015 <sup>4</sup>	0.02841	9.94	1.821	1.811	-0.6
Negative angles					
FX 84-W-140	0.02120	7.58	1.838	1.834	-0.2
DU 00-W-212	0.02142	13.39	1.771	1.811	2.3
LS(1)-0417	0.03011	14.92	1.770	1.751	-1.1
LS(1)-0413	0.03069	14.38	1.829	1.790	-2.1

<sup>1</sup> Matsumiya and Tsutsui, 1995, Re=0.55E+06

<sup>2</sup> Critzos et al. 1955, NACA LTPT, Re=1.8E+06

<sup>3</sup> Critzos et al. 1955, Langley 7'x10' wind tunnel, Re=1.3E+06

<sup>4</sup> Sheldahl and Klimas 1981, after re-correction. Re=0.62E+06

differences of roughly  $\pm 1.9\%$  with an average of  $-0.2\%$ .

Table 9.5 presents the prediction of the maximum drag coefficient for various other airfoils. The NACA 63-215  $C_{d,max}$  value originates from a test using inserts with a pitot-static tube about 2.5 chords upstream of the model. The NACA 0012 value from Critzos et al. (1955) was determined using Maskell's correction on uncorrected data from the NASA Langley 2.13 x 3.05 m wind tunnel. The overall differences amount to about  $\pm 2.3\%$  with an average of  $-0.1\%$ .

Tables 9.4 and 9.5 are graphically presented in figure 9.12. The two points with zero trailing edge angle from the flapped DU95 study at  $Re=0.7 \times 10^6$ , reported in Appendix B, fit the curve with  $\zeta=0^\circ$  very well.

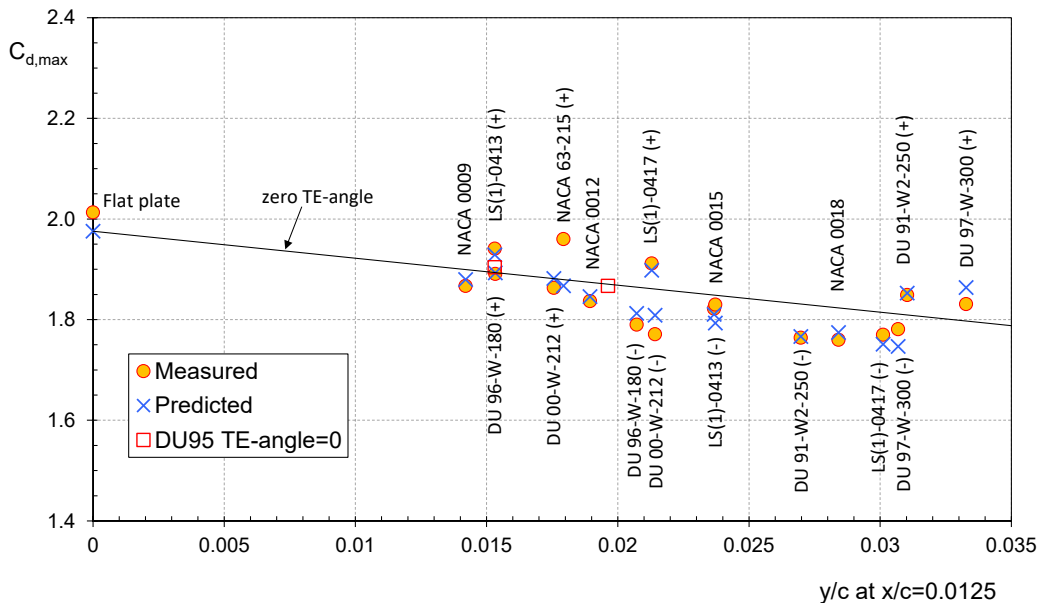


Figure 9.12: The measured and predicted maximum drag coefficients from tables 9.4 and 9.5. Plususes and minuses denote positive and negative angles of attack. The squares are from the DU95 measurements by DWG, interpolated to  $\zeta=0$  (Appendix B).

## 9.8 PREDICTION OF THE MAXIMUM DRAG COEFFICIENT AT HIGHER REYNOLDS NUMBERS

The predictions described above are based on measurements at relatively low Reynolds numbers of approximately  $0.5 \times 10^6$ , and Mach numbers of about 0.1. But, as was shown in fig 9.6, the variation in  $C_{d,max}$  with increasing Reynolds number is very small, for airfoil DU-35-10 of approximately 1%.

### 9.8.1 Reynolds number traverse measurements for DU91-W2-250

Fig. 9.13 presents the variation of the DU91-W2-250 maximum drag coefficient with

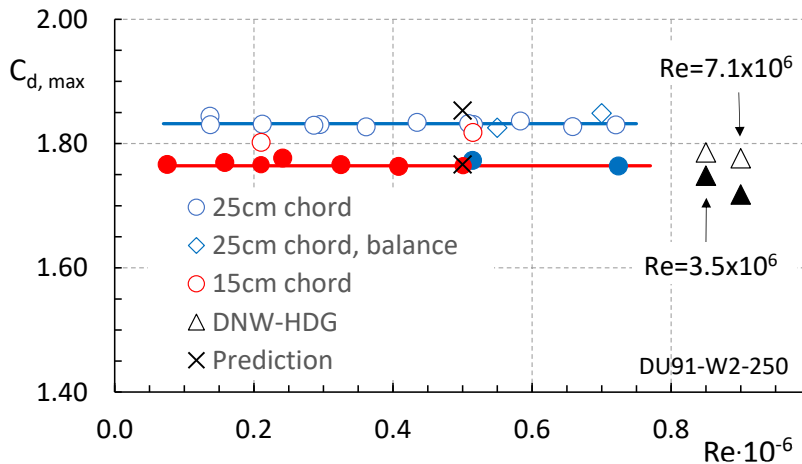


Figure 9.13: The variation of the maximum drag coefficient with Reynolds number for airfoil DU91-W2-250. Solid symbols denote negative angles. Maximum corrected Mach number at model approximately 0.15.

Reynolds number corrected for blockage. The values come from pressure distributions, while the predictions are based on balance measurements. The LTT and HDG models had different pressure orifice resolution at the trailing edge. To bring the integrated drag values close to the level of the balance measurements the  $C_p$ -distributions from both models in that region were treated as sketched in fig 7.15. Note that the graph x-axis stops at  $Re=0.8 \times 10^6$ .

For ease of comparison the high Reynolds number values of the HDG measurements are given next to the low-Reynolds number traverse. Figure 9.13 shows constant average drag coefficients in the range  $10^5 \leq Re < 8 \times 10^5$ , for positive angles (+) at a value of 1.832, with virtually no variation of the associated base pressure. Negative angles (-) give  $C_{d,max}=1.768$ . At the much higher Reynolds numbers of  $7.1 \times 10^6$ , the drag coefficients reduce to 1.776 (+) and 1.719 (-).

The reason for this reduction in maximum drag coefficient is depicted in figure 9.14. It shows the variation in pressure distributions of DU91 at  $Re=0.5 \times 10^6$  and  $7.1 \times 10^6$  both at a Mach number of about 0.09.

It is clear from the graph, that the reduction in drag coefficient at  $Re=7.1 \times 10^6$  does not come from substantial variation in the base pressure, but is predominantly due to the existence of a pressure peak at the leading edge, resulting from thinner boundary layers. While at  $Re=0.5 \times 10^6$  laminar separation seems to occur at the lower side 2.6% chord station, the occurrence of the peak at the higher Reynolds number induces turbulent separation right at the leading edge. This situation is in fact similar to the one depicted in fig. 7.21 for airfoil DU00-W-212. Differences with  $Re=3.5 \times 10^6$  are mainly due to the height of the pressure peak and the thickness of the boundary layer downstream from the stagnation point. While the prediction for the lower Reynolds numbers is considerably

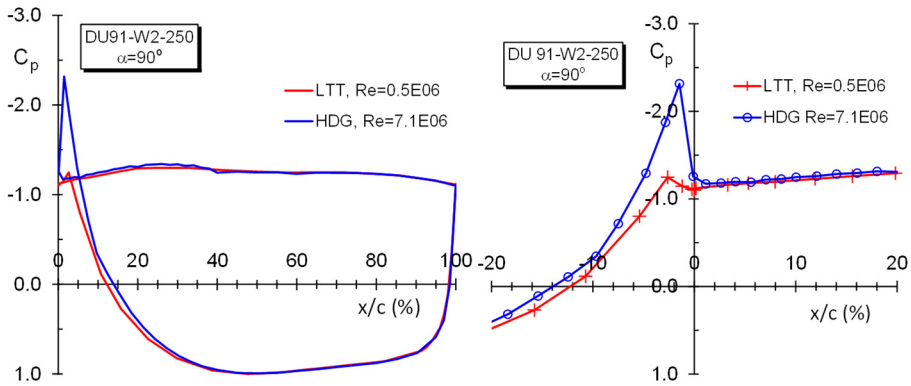


Figure 9.14: The pressure distribution of DU91 at  $\alpha=90^\circ$  for significantly different Reynolds numbers. Mach number for both measurements approximately 0.09. Right figure gives negative  $x/c$  values for lower side.

accurate with a maximum drag disparity of 0.2%, differences with the values at  $Re=7.1 \times 10^6$  amount to 4.3% (+) and 2.7% (-).

The prediction divergence for airfoil DU00-W-212, going from  $Re=0.6 \times 10^6$  to  $8.1 \times 10^6$ , is smaller, approximately 1.3% (+) and 2.7% (-).

### 9.8.2 A new formulation for $C_{d,max}$ at high Reynolds numbers

The differences found above suggest that the deviation from the low-Reynolds number prediction becomes more substantial when the airfoil leading edge is thicker, which agrees with the assumption that the shape of the leading edge near the apex determines the pressure peak at high Reynolds numbers.

This is corroborated by fig. 9.15, which presents the pressure peak with the airfoil normal to the flow. It shows good correlation of the minimum pressure coefficient with the  $y/c$

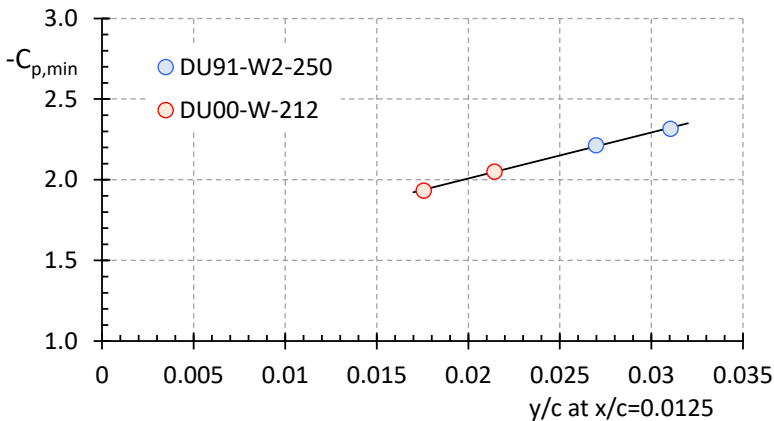


Figure 9.15: The pressure peak at the leading edge of two airfoils normal to the wind for Reynolds numbers of  $7 \times 10^6$  and  $8 \times 10^6$ .

parameter. Based on the high Reynolds number  $C_{d,max}$  data, the associated zero trailing edge drag values can be derived by subtracting the contribution of the trailing edge angle using the prediction method described before.

This leads to fig. 9.16, showing the resulting  $\zeta=0$  values for Reynolds numbers around  $7 \times 10^6$  to  $8 \times 10^6$ . The values are tabulated in table 9.6.

With the assumption that the measured flat plate value given in table 9.5 is also valid at high Reynolds numbers, the trend line gives

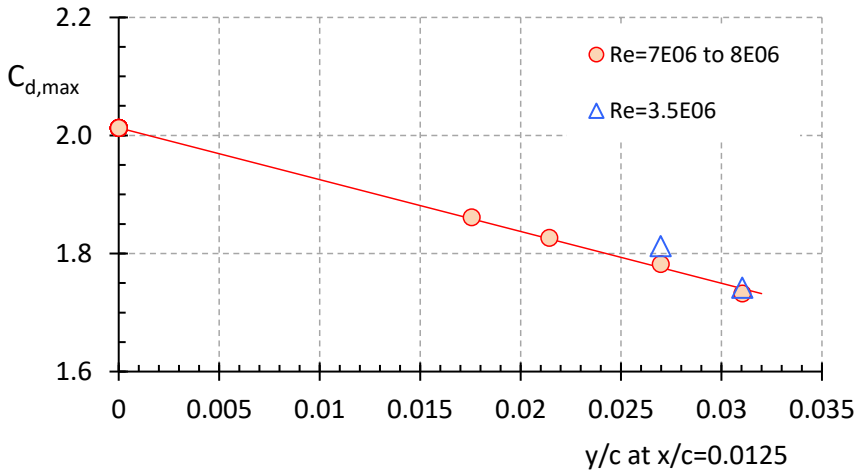


Figure 9.16: Variation of the high Reynolds number zero trailing edge angle maximum drag values with leading edge thickness. Airfoils DU91-W2-250 and DU00-W-212 and a flat plate.

$$C_{d_{max,0}} = 2.013 - 8.7665 * (y / c)_{x/c=0.0125} \quad (9.7)$$

It must be noted that the values shown in fig. 9.16 were calculated with TE-angle contributions derived from low Reynolds number measurements. Higher Reynolds numbers give smaller boundary layer displacement thicknesses, which brings the effective trailing edge angle closer to the geometric one. This effect now resides in the zero-trailing edge drag coefficients. However, it is expected that this will not substantially impact the final maximum drag values. Using equation 9.7 and the existing formulation for the contribution of the trailing edge, prediction errors reduce to values smaller than 0.5%.

Table 9.6: The high Reynolds number zero trailing edge angle maximum drag values for airfoils DU91-W2-250 and DU00-W-212.

Airfoil	y/c	$\zeta$	$C_{d,max}$	$\Delta C_d$	$C_{d,0}$
Positive angles		deg.	measured	due to $\zeta$	
Flat plate	0	0	2.013	0.00	2.013
DU 91-W2-250	0.03103	-10.23	1.776	0.044	1.732
DU 00-W-212	0.01756	-0.11	1.862	0.000	1.862
Negative angles					
DU 91-W2-250	0.02698	16.04	1.718	-0.065	1.783
DU 00-W-212	0.02142	14.01	1.775	-0.052	1.827

### 9.8.2.1 Application of the high $Re$ -number equation in conditions with roughness.

Chapter 7.6 shows that, once laminar leading edge separation was suppressed by promoting transition with roughness, the resulting leading edge pressure peak renders similar performance as under high Reynolds number conditions. Consequently, the formulation for the maximum drag at high Reynolds numbers possibly may be used to estimate the effect of leading edge roughness at the lower Reynolds numbers. This was done for NACA 0012, for which the applied roughness gave a reduction in maximum drag of 2.9% (fig. 7.34). The predicted maximum drag of 1.846 given in table 9.5 changes to 1.803 using eq. 9.7 instead of eq. 9.2, a reduction of 2.3%. This compares fairly well with the found value of 2.9%, especially when the uncertainty in the actual measured drag value is taken into account.

## 9.9. CONCLUSIONS

A method is presented to predict the maximum drag coefficient of airfoils at Reynolds numbers below approximately  $1.7 \times 10^6$  (tables 9.4 and 9.5) based on measurements in the TUDelft low-speed low-turbulence wind tunnel. The method calculates a contribution due to the airfoil leading edge thickness in terms of the upwind  $y/c$ -coordinate at  $x/c=0.0125$  using airfoil models with varying leading edge thickness and zero trailing edge angle. The contribution of the trailing edge combines the flow angle at the trailing edge with a sensitivity factor related to the afore mentioned  $y/c$  coordinate. Comparison with measured airfoil maximum drag coefficients in the same Reynolds number range found in the public domain gives differences up to 2.1% with an average of -0.2%

For Reynolds numbers in the range of  $3.5 \times 10^6$  to  $8 \times 10^6$  the contribution of the leading edge thickness was redefined based on measurements in the HDG wind tunnel. Using the existing formulation for the contribution of the trailing edge angle to the maximum drag coefficient, prediction errors for airfoils DU91-W2-250 and DU00-W-212 amount to values less than 0.5%.

## 9.10 REFERENCES

Bloy, A.W. and Roberts, D.G. *Aerodynamic characteristics of the NACA 63<sub>2</sub>-215 aerofoil for use in wind turbines*, Wind Engineering Vol. 17, No.2, 1993, pp.67-75

Critzos, C.C., Heyson, H.H. and Boswinkle Jr R.W. *Aerodynamic characteristics of NACA 0012 airfoil at angles of attack from 0 to 180 degrees*. NACA TN 3361, 1955

Ewald, B.F.R. (ed). *Wind tunnel wall corrections*. AGARDograph 336. North Atlantic Treaty Organization, October 1998

Fail, R., Lawford, J.A. and Eyre, C.W. Low-speed experiments on the wake characteristics of flat plates normal to an airstream. ARC technical Report , R&M. No. 3120.

Lindenburg, C., *Investigation into Rotor Blade Aerodynamics*. Report ECN-C-03-025, Energy Research Centre of the Netherlands. The Netherlands, July 2003

Massini, G., Rossi, E. and D'Angelo, S. Wind tunnel measurements of aerodynamic coefficients of asymmetrical airfoil sections for wind turbine blades extended to high angles of attack. EC DG-XII Contract number: EN3W - 0018 - I, Conclusive Report. ENEA, Rome, 1993.

Matsumiya, H. and Tsitsui, Y. *Wind tunnel test data of FX84-W-140*. Mechanical Engineering Laboratory, MITI, Tsukuba, Japan, Through personal correspondence with H. Matsumiya, July 1995.

Michos, A., Bergeles, G. and N. Anthanassiadis, (National Technical University of Athens) *Aerodynamic characteristics of NACA 0012 airfoil in relation to wind generators*. Wind Engineering Vol. 7, No. 4 pp. 247-261, 1983

Ostowari, C. and Naik, *Post Stall Studies of Untwisted Varying Aspect Ratio Blades with NACA44XX series Airfoil Sections – Part II*, Wind Engineering, Vol. 9, No. 3, 1985

Pope, A and Harper, J.J. *Low-speed wind tunnel testing*. John Wiley and Sons, New York 1966

Roosbroeck, M. van, The Effect of Leading Edge Thickness on the Maximum Drag Coefficient of Airfoils 90° to the Wind. TUDelft Master thesis, September10, 2014

Satran, D. and Snyder, M.H. *Two-dimensional tests of GA(W)-1 and GA(W)-2 airfoils at angles-of-attack from 0 to 360 degrees*. Wind Energy report no. 1, Wind Energy Laboratory, Wichita State University, Kansas, USA, January 1977

Sheldahl, R.E., and Klimas, P.C. *Aerodynamic Characteristics of Seven Symmetrical Airfoil Sections Through 180-Degree Angle of Attack for Use in Aerodynamic Analysis of Vertical Axis Wind Turbines*. Report SAND80-2114, Sandia Laboratories, Albuquerque, March 1981.

Snyder, M.H., Wentz, W.H. and Ahmed, A. *Two-dimensional tests of four airfoils at angles of attack from 0 to 360 degrees*. Wind Energy Reports no 16. Wichita State University,

1984.

Timmer, W.A. *Aerodynamic characteristics of wind turbine blade airfoils at high angles-of-attack*. Proceeding of the 3<sup>rd</sup> EWEA Conference –Torque 2010: The Science of making torque from wind. Heraklion, Crete, Greece (2010).

Timmer, W.A. *A simple method to estimate the airfoil maximum drag coefficient*. Journal of Physics: Conference Series, 1618(5), [052068]. <https://doi.org/10.1088/1742-6596/1618/5/052068>, 2020

# 10

## THE LIFT-DRAG RATIO OF AIRFOILS IN DEEP-STALL

### 10.1 INTRODUCTION

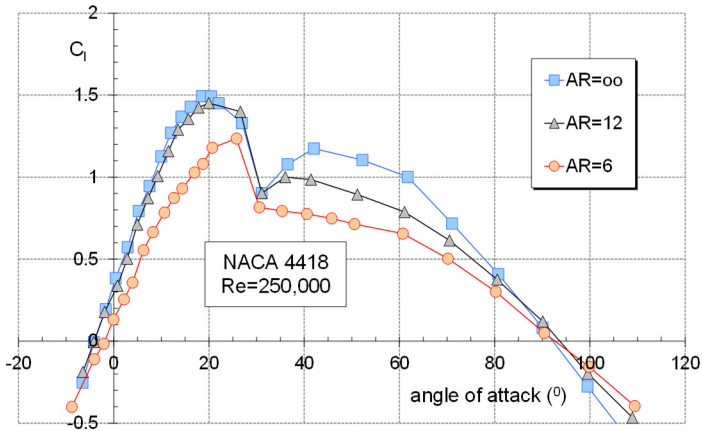
The origin of both the lift and the drag forces acting on an airfoil is the surface pressure distribution, which, in deep-stall conditions, is severely dominated by the separated region over the downwind side. While the separate experimental drag and lift coefficients at very high incidences (either determined by a balance or derived from the pressure distribution) may be influenced by the followed test procedure or the applied correction scheme, the lift-drag ratio generally may not, as the most frequent parameter causing deviations, the test section dynamic pressure and its correction for blockage, cancels out. As such, the lift-drag ratio is a relevant parameter, since it gives the bare potential of the airfoil under the given conditions.

### 10.2 THE IMPACT OF ASPECT RATIO

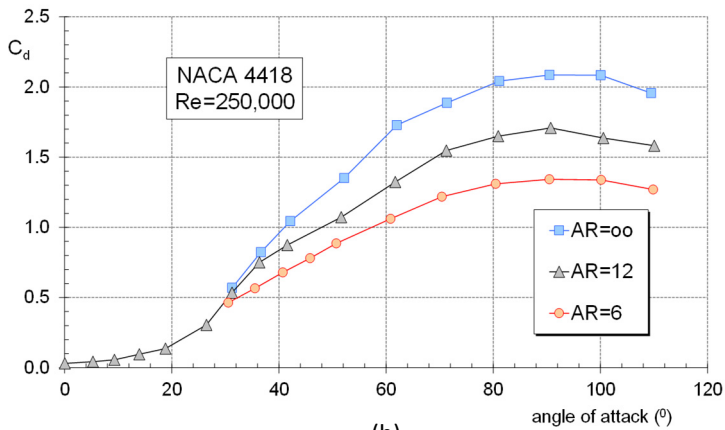
#### 10.2.1 Airfoils NACA 4415 and NACA 4418

Ostowari and Naik (1984 and 1985) studied experimentally the aerodynamic performance of airfoils from the NACA 44 series with thicknesses between 9% and 18% for various Reynolds numbers ranging from  $0.25 \times 10^6$  to  $1 \times 10^6$  and aspect ratios, in the  $\alpha$ -range  $-10^\circ$  to  $110^\circ$ . Their drag curves mostly show maxima above 2 for infinite aspect ratios, presumably resulting from a dynamic pressure error, which for the greater part may be due to the applied wall correction scheme. However, for the reason discussed above, the lift-drag ratios can be used to study the impact of aspect ratio.

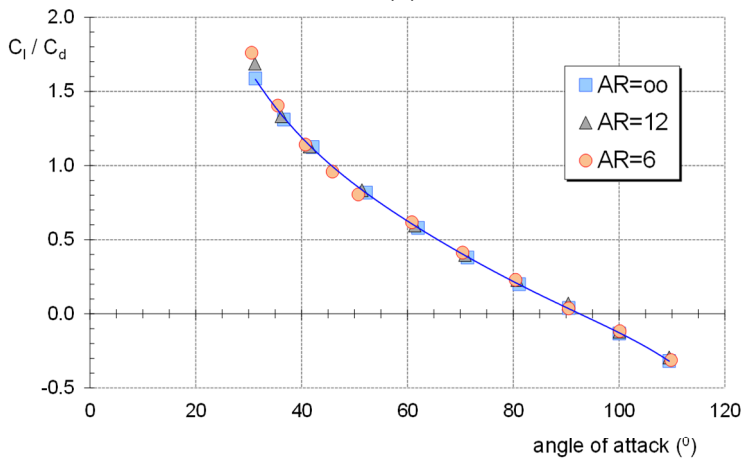
In part I (1984), which deals with the characteristics of NACA 4415, Ostowari and Naik concluded that the lift-drag ratio is independent of aspect ratio. This is not only true for NACA 4415, but also for NACA 4418, as is shown in fig. 10.1. It presents the lift and drag curves measured for airfoil NACA 4418 at  $Re=0.25 \times 10^6$  for various aspect ratios (part II, 1985). Figures 10.1a and b show that in deep stall both the maximum drag value and the



(a)



(b)



(c)

Figure 10.1: The lift (a) and drag (b) data of airfoil NACA 4418 and the associated lift-drag ratio (c) for various aspect ratios. Ostowari & Naik (1985)

lift decrease with decreasing aspect ratio. At an aspect ratio of 6, the secondary stall lift peak has completely disappeared. Figure 10.1c illustrates that, although the lift and drag

curves differ significantly, the lift-drag ratio for aspect ratios 12 and 6 coincides with the curve for two-dimensional flow.

### 10.2.2 The flat plate

The insensitivity of  $C_l/C_d$  to aspect ratio variation was already shown by Flachsbart (Flachsbart, 1932) for a flat plate. His measurements, presented in fig. 10.2, show that the lift-drag ratios of flat plates with aspect ratios of 1 and 5 all coincide with the two-dimensional flat plate curve for angles higher than  $25^\circ$ .

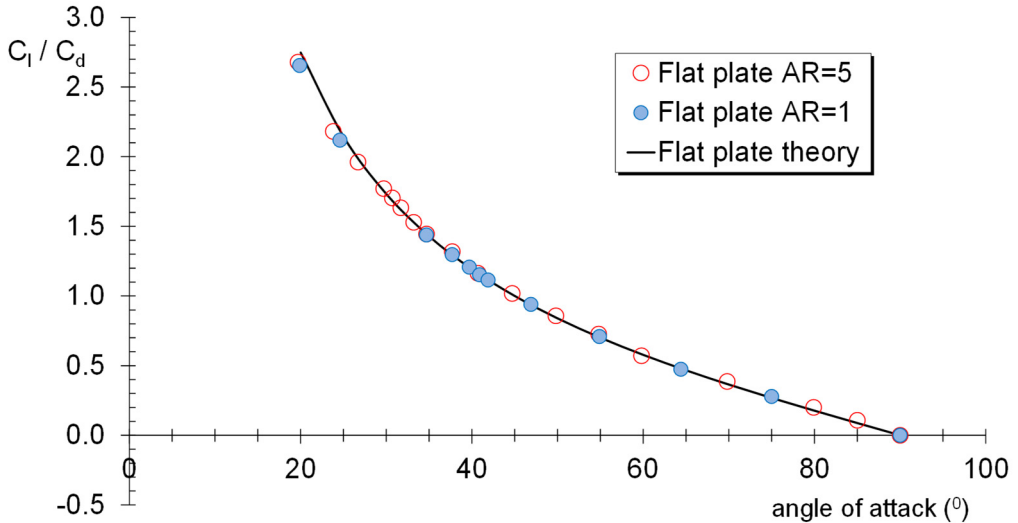


Figure 10.2: lift-drag values from measurements by Flachsbart (1932) for two aspect ratio's compared to flat plate theory.

### 10.2.3 The variation of pressure distribution with aspect ratio

The insensitivity of the lift-drag ratio to aspect ratio in conditions with laminar leading edge separation is due to the fact that it is predominantly the magnitude of the average base pressure that changes with aspect ratio. With the absence of detailed information in the public domain on the variation of the pressure distribution over an airfoil with aspect ratio, an assumed change in the  $C_p$ -distribution is sketched in fig. 10.3 for airfoil DU91-W2-250 at an incidence of  $50^\circ$  and  $Re=0.7 \times 10^6$ . It shows a variation in the base pressure between -0.8 and the measured and corrected two-dimensional value of -1.165. As the variation in lift coefficient is mostly due to the varying base pressure and not the result of

Table 10.1: Force coefficients due to the pressure distributions of fig. 10.3

$C_{p_b}$	$C_n$	$C_t$	$C_l$	$C_d$	$C_l/C_d$	$C_t/C_n$
-1.165	1.716	-0.044	1.136	1.286	0.884	-0.026
-1	1.569	-0.040	1.039	1.176	0.884	-0.026
-0.8	1.412	-0.036	0.935	1.058	0.884	-0.026

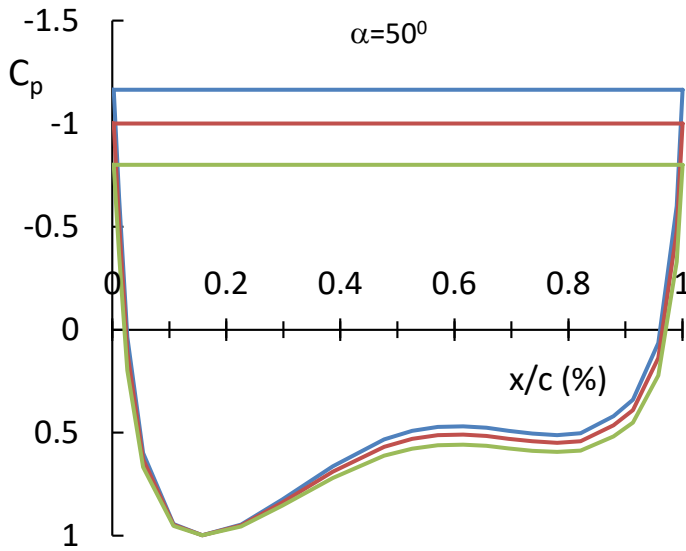


Figure 10.3: Assumed pressure distributions on airfoil DU91-W2-250 at 50° angle of attack as a result of aspect ratio variation. The lowest base pressure is the two-dimensional value.

variation in flow-curvature, the stagnation location hardly changes. It is assumed that the velocities along the lower surface vary in the same way as those on the upper side.

Table 10.1 presents the force coefficients for the three values of the base pressure. The very small dependency of the lift-drag ratio to aspect ratio variation in cases of leading edge separation can also be shown when  $C_l/C_d$  is written in terms of the normal and tangential force coefficients (eq. 10.1).

$$\frac{C_l}{C_d} = \frac{C_n \cos \alpha - C_t \sin \alpha}{C_t \cos \alpha + C_n \sin \alpha} = \frac{1 - \frac{C_t}{C_n} \tan \alpha}{\frac{C_t}{C_n} + \tan \alpha} \quad (10.1)$$

In situations similar to fig. 10.3, the tangential force coefficient is very small and the ratio  $C_t/C_n$  even smaller, as is also shown in table 10.1. With  $C_t/C_n \ll 0$  we can write

$$\frac{C_l}{C_d} \approx \frac{1}{\tan \alpha} \quad (10.2)$$

This is equal to the relation for a flat plate using eq. 7.1 and 7.2 or 7.3 and 7.4

As long as the magnitude of  $C_t/C_n$  is very small, the lift-drag ratio of an airfoil is predominantly depending on the angle of attack and is very close, but not necessarily equal, to the flat plate value. As  $\tan(45^\circ)=1$ , the lift-drag ratio at 45° for most airfoils will be (very) close to 1.

### 10.3 THE RATIO OF FORCES ON A WIND TURBINE BLADE.

Since figures 10.1c and 10.2 confirm that the lift-drag ratio curves of the two-dimensional configuration and the various aspect ratios coincide for high angles of attack, and with the

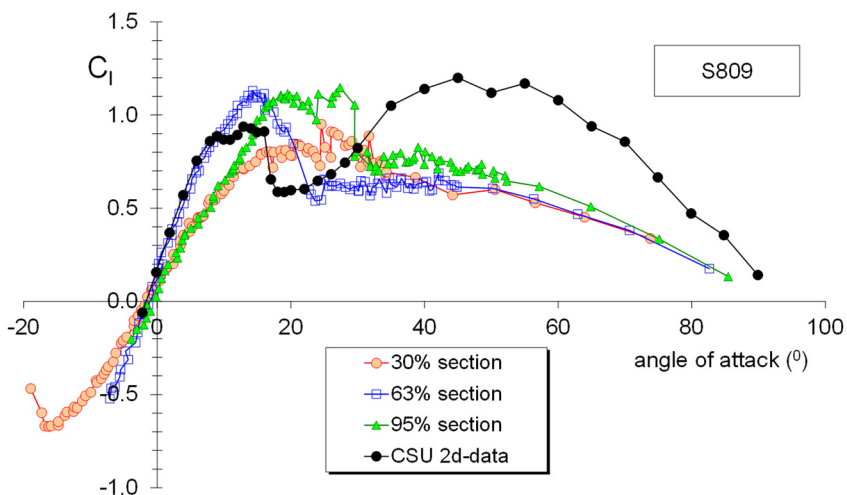
help of eq. 10.1, with a fair amount of confidence the assumption can be made that the same relation holds for an airfoil in a non-rotating wind turbine blade.

### 10.3.1 The non-rotating blade

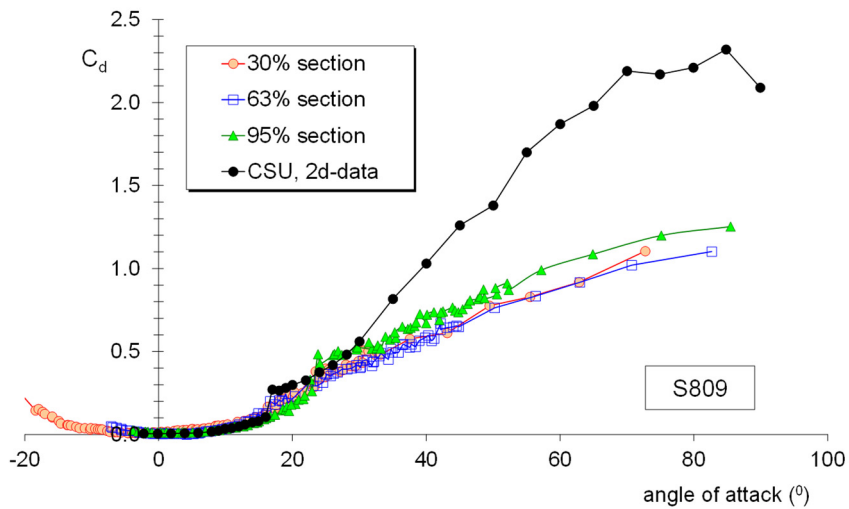
Figure 10.4a and b show the lift and drag coefficients at three blade stations of the NREL UAE (unsteady Aerodynamics Experiment) phase VI twisted and tapered blade measured in the NASA Ames wind tunnel in Mountain View, CA, USA. Airfoil S809 was exclusively applied over 3.772 m of the 5.029m blade radius.

The curves were taken from the work of van Rooij & Meng (2006), where the measured pressure distributions were coupled to the right angle of attack using corrections on the local inflow angle measured with a 5-hole probe. These corrections include angle of attack changes due to the upflow in front of the airfoil, calculated by the Biot and Savart law, and smaller corrections due to a  $0.9^\circ$  blade pitch misalignment, a 5-hole probe orientation misalignment and the difference in twist between the location of the probe and the nearest blade station at which the pressure distributions were measured.

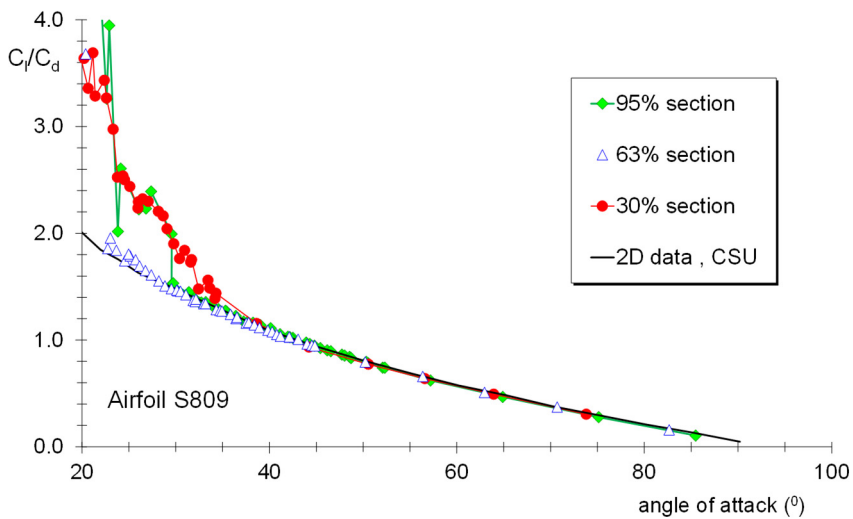
By iteration, the lift and drag coefficients were calculated from the estimated angle of attack and the airfoil normal and tangential force coefficients from the pressure distributions. Not all data points for the non-rotating blade are shown here. For the higher angles averaged data points were presented by van Rooij & Meng and they were also used in the graphs of figure 10.4. Also given in the figure the two-dimensional characteristics as measured in the wind tunnel of the Colorado State University (CSU, Butterfield et al. 1992). The CSU wind tunnel data show a corrected two-dimensional  $C_d$  at  $90^\circ$  well over 2. As has been discussed previously, this may point in the direction of a dynamic pressure



(a)



(b)



(c)

Figure 10.4: The lift (a) and drag (b) curves and the lift-drag ratio (c) for the non-rotating NREL Phase VI blade and the two-dimensional characteristics at a Reynolds number of 500,000 from the CSU wind tunnel.

error, which cancels out by taking the lift-drag ratio.

Since the blade in the non-rotating configuration is a wing of finite span, the resulting lift and drag force coefficients show much lower values in the deep-stall region compared to the two-dimensional case. Based on the aerodynamic part of the blade, the aspect ratio is about 7. End effects seem to be more visible in the 30% section data than at the 95% station. The maximum lift at the 63% and 95% sections is much higher than in the two-dimensional case. This is believed to be caused primarily by the difference in Reynolds

number. The non-rotating blade measurements were made at an average wind velocity of 30.2 m/s. This results in a varying Reynolds number between  $1.4 \times 10^6$  at the root to  $0.75 \times 10^6$  at the tip, compared to the  $0.5 \times 10^6$  of the CSU test. Measurements from the Delft University wind tunnel at a Reynolds number of  $1 \times 10^6$  gave a maximum lift coefficient of 1.061 (Somers, 1997), quite close to the value at the 63% section (1.100)

As was the case with the different aspect ratios in figures 10.1 and 10.2, the characteristics of the various blade sections in terms of lift and drag differ significantly compared to the two-dimensional case, especially in the deep stall region where leading edge separation is present for angles beyond about  $18^\circ$ . Figure 10.4c demonstrates a good agreement between the lift-drag ratios of the two-dimensional curve and of the various blade stations in the incidence range from  $35^\circ$  to  $85^\circ$ . The same holds for the 47% and 80% span sections, which for clarity reasons have not been plotted in the graph. End effects are noticeable in the onset of leading edge separation for the 30% and 95% blade stations, since their deep-stall angle lies between  $30^\circ$  and  $35^\circ$  compared to the two-dimensional value of about  $18^\circ$ .

Differences with flat plate data, though percentage-wise quite substantial, are relatively small in absolute sense for angles beyond about  $40^\circ$  ( $\pm 0.07$ ). Starting at  $40^\circ$  incidence, decreasing the angle leads to increasingly higher deviation from the flat plate curve, both for the two-dimensional case and the 30% section (lower values) as well as for the 63% and 95% sections (higher values).

The compilation of the three-dimensional Mexico rotor section characteristics at standstill made by Khan (2018), confirms the above for the inner two blade sections (25% and 30% span), formed by the DU91-W2-250 airfoil. The aspect ratio of the Mexico blade is 14.

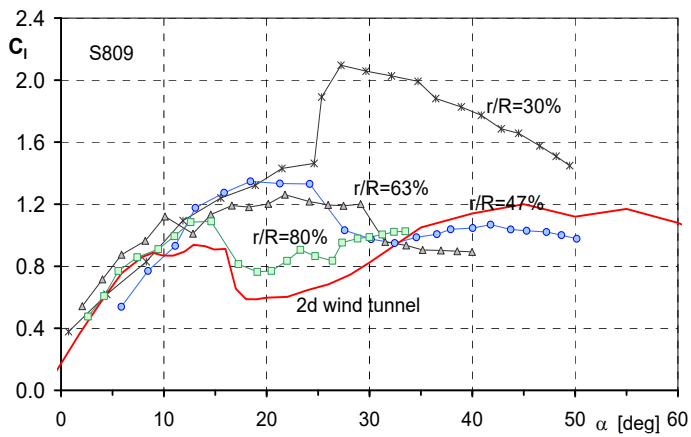
### 10.3.2 The rotating blade.

Tangler and Kocurek (2004) state that the lift-drag ratios of the five sections of the blade described above in the *rotating* situation (Fingersh et al., 2001) closely follow flat plate values in the range of angles between  $20^\circ$  and  $90^\circ$ , based on

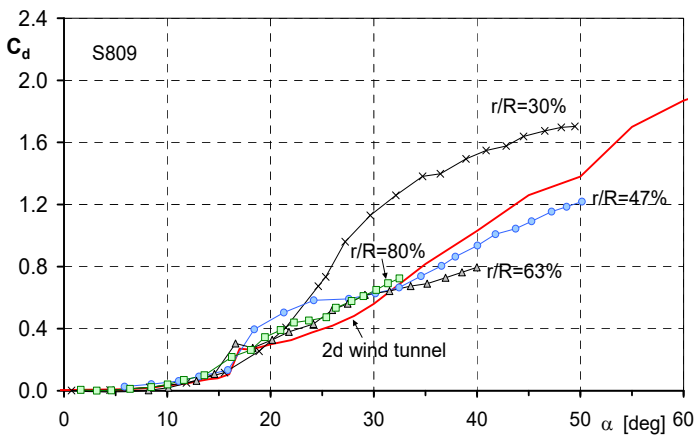
$$C_l = 2 \sin \alpha \cos \alpha \quad (9.1)$$

$$C_d = 2 \sin^2 \alpha \quad (9.2)$$

According to fig 10.4c, this implies that rotation does not impact the lift-drag ratio of an airfoil in a rotor blade at high incidences. Unfortunately, figure 8 of the paper by Tangler and Kocurek, showing the lift-drag ratio of the 5 sections of the rotating UAE blade against angle of attack, does not show results beyond  $30^\circ$  and has a rather high maximum value



(a)



(b)

Figure 10.5: The lift and drag curves for a number of sections of the UAE-rotating blade.

of 25 along the  $C_l/C_d$  axis. The latter masks the potential differences between the various sections, since beyond about  $20^\circ$  the lift-drag ratio has already decreased to values below 5.

Although these high angles seldom are encountered in normal operation of modern turbines, for the sake of completeness it was decided to look at the results for various sections up to  $90^\circ$  incidence in more detail.

Figure 10.5 gives the lift curves for 4 of the 5 sections of the UAE experiment (sequence H), for which the lift and drag have been derived from the measured pressure distributions with the method described above for the non-rotating blade.

Augmented lift is clearly present in the figure compared to the two-dimensional curve from the CSU wind tunnel. However, the associated drag, e.g. for the 30% section, is also significantly higher relative to the two-dimensional case.

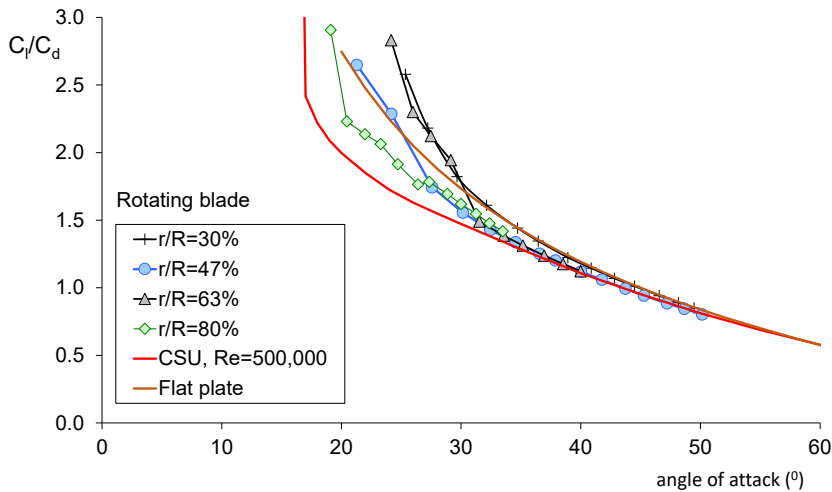


Figure 10.6: The lift-drag ratios of 4 sections of the UAE rotating blade compared to those of a flat plate and the 2d wind tunnel curve measured at CSU.

Figure 10.6 presents the lift-drag ratios for the sections of figure 10.5. The graph demonstrates that the lift-drag ratio of the rotating sections eventually all coincide with the two-dimensional curve. The 30% section is projected to touch the 2d curve at about 55° degrees, while the other three sections all fall on this curve at 35° to 40°. Only the 30% section follows the flat plate curve, starting at about 30°. They all converge to the flat plate values around 55°.

It must be noted that the blade sections only contained 22 pressure orifices. Especially at high angles of attack, with leading edge separation present, this may give substantial differences in the normal force coefficient. Since the angle of attack through the Biot and Savart law is determined using the normal force and lift force coefficients, this may be a source of deviations, which may even bring the 30% section results closer to the others. Even considering the various corrections in angle of attack due to misalignments and off sets it seems clear that overall the lift-drag ratio of the rotating blade sections follow the two-dimensional curve quite close for angle of attack between 35° and 90°.

As the same was concluded for the non-rotating blade, it can be stated that, for angles between 35° and 90°, the ratio of the airfoil lift and drag forces will be the same irrespective of rotation, since they originate from the pressure distribution dominated by the upper side suction pressure induced by the separated flow at the leading edge. Since the curve for the S809 two-dimensional values does not deviate much from the flat plate curve in the mentioned range of incidences, lift-drag ratios from the various blade sections in the non-rotating and rotating configuration follow the flat plate curve to a fair degree.

## 10.4 THE VARIATION OF THE LIFT-DRAG RATIO WITH AIRFOIL SHAPE.

In chapters 6 and 9 it was shown that both the deep-stall angle and the drag coefficient of an airfoil normal to the flow substantially vary with airfoil leading edge shape. The measurements presented in chapter 9 enable us to get insight in the impact of the leading edge thickness and the trailing edge angle separately.

### 10.4.1 Variation with airfoil leading edge thickness

Fig. 10.7 illustrates the effect on the lift-drag ratio of the upwind leading edge  $y/c$  coordinate at  $x/c=0.0125$  with zero trailing edge angle.

It shows an increasing  $C_l/C_d$  at  $90^\circ$  incidence (as a result of increased suction at the LE)

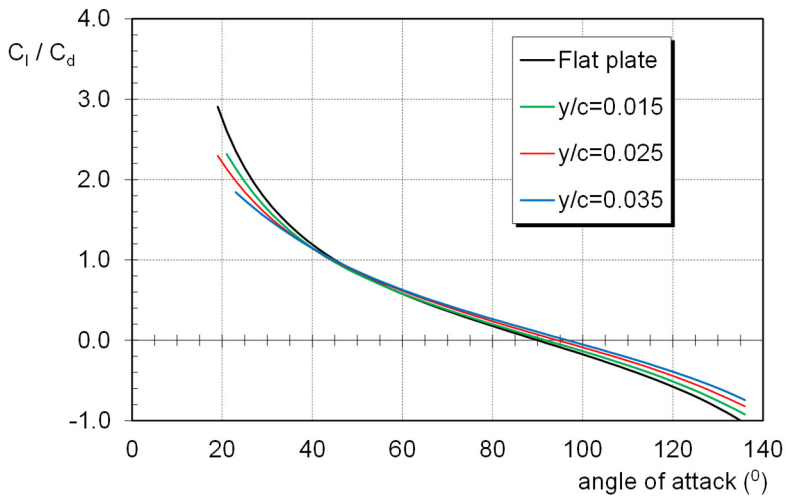


Figure 10.7: The lift-drag ratio of airfoils with varying upwind leading edge ordinate at  $x/c=0.0125$  at a Reynolds number of approximately  $0.5 \times 10^6$ .

and zero-lift angle ( $C_l/C_d=0$ ) with an increase in the upwind leading edge thickness parameter. At  $45^\circ$  the lift-drag ratio is around 1 for all configurations.

### 10.4.2 Variation with airfoil trailing edge angle

Similar to the maximum drag coefficient, the lift-drag ratio in deep-stall might be sensitive to the trailing edge angle, as this impacts the width of the wake and consequently the airfoil drag.

It is shown in fig. 10.8 that the lift-drag ratio increases with increasing trailing edge angle  $\zeta$ , both for the flat plate and the thick leading edge airfoil DU35-10. Note that  $\zeta$  is positive when the angle varies counter-clockwise, in contrast to the flap deflection definition.

Figure 10.9 shows the zero-lift angle ( $C_l/C_d=0$ ) and the lift-drag ratio at  $\alpha=90^\circ$  in relation to the trailing edge angle for the two configurations presented in fig. 10.8. The values were calculated using linear regression in a  $20^\circ$  range of angles of attack around the zero-

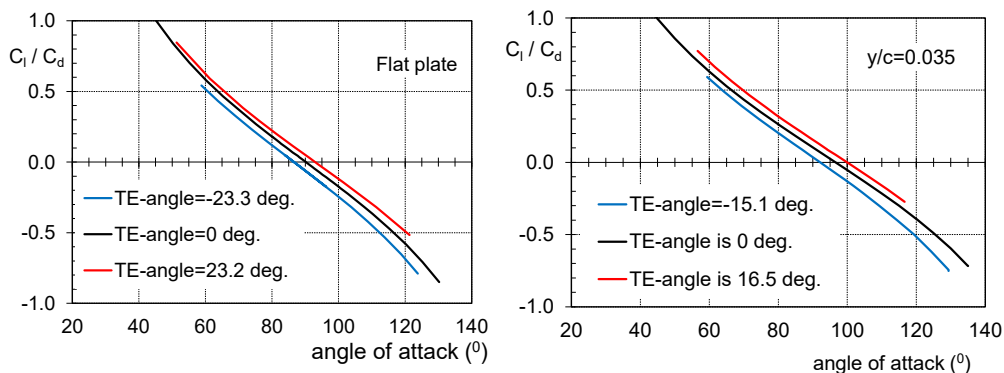


Figure 10.8: The impact of the trailing edge angle on the lift-drag ratio in deep-stall for two configurations.

lift angle or around  $\alpha=90^\circ$ . The values have been tabulated in table 10.1. The gradient of the linear relation is the sensitivity to trailing edge angle variation, which significantly differs for the flat plate and the airfoil with  $y/c=0.035$ . It appears that, similar to the maximum drag coefficient, also variation in the zero-lift angle, or implicitly in the lift-drag ratio with the airfoil normal to the flow, with trailing edge angle is sensitive to the upwind leading edge thickness parameter: the higher the upwind  $y/c$ , the greater the variation in zero-lift angle or lift-drag ratio at  $\alpha=90^\circ$  with one degree of trailing edge change.

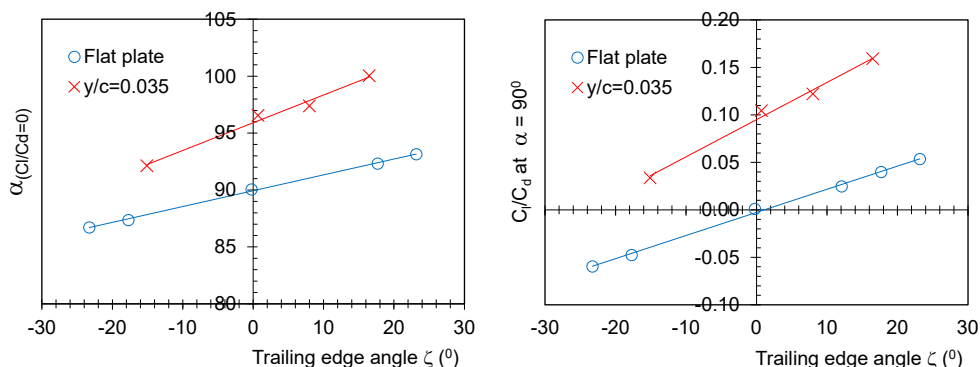


Figure 10.9: The variation of the zero-lift angle and the lift-drag ratio at  $\alpha=90^\circ$  with the trailing edge angle for the flat plate and DU 35-10,  $Re=4.5 \times 10^5$ .

### 10.4.3 Sensitivity to variation in Reynolds number

The Reynolds number during the measurements was  $0.45 \times 10^6$ . However, as is depicted in fig. 10.10 for two airfoils, the magnitude of  $C_l/C_d$  is unaffected by the Reynolds number as long as separation in the vicinity of the upwind side leading edge is present. As is explained in chapter 6, the deep-stall angle is Reynolds number sensitive, which marks the point at which the curve touches the deep-stall  $C_l/C_d$  relation for the first time.

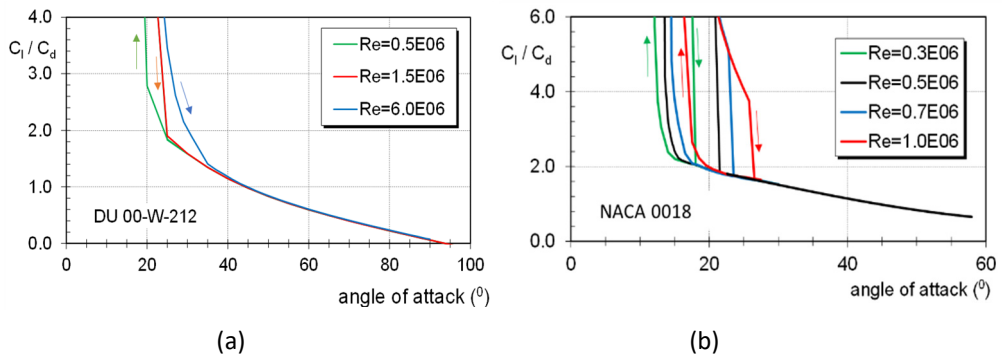


Figure 10.10: Re-number sensitivity of the lift-drag ratio in the deep-stall region for two airfoils. Data from Madsen and Hansen (2017), Jacobs (2015) and Timmer (2008).

Table 10.1: The variation with trailing edge angle of the zero-lift angle and the lift-drag ratio at  $90^\circ$  incidence for two airfoil configurations

	Flat plate			$y/c=0.035$		
Flap defl.	$\zeta$ ( $^\circ$ )	$\alpha_{C_l=0}$ ( $^\circ$ )	$(C_l/C_d)_{90}$	$\zeta$ ( $^\circ$ )	$\alpha_{C_l=0}$ ( $^\circ$ )	$(C_l/C_d)_{90}$
19.66	23.17	93.15	0.0535	16.48	100.04	0.159
14.8	17.68	92.33	0.0400			
9.36	12.08		0.0248	8.00	97.39	0.122
0	-0.23	90.06	0.001	0.70	96.55	0.105
-9.36	-12.1					
-14.8	-17.73	87.36	-0.0475			
-19.66	-23.27	86.71	-0.0595	-15.11	92.14	0.034

## 10.5 CONCLUSIONS

A number of experimental airfoil characteristics at angles of attack in the deep-stall range have been studied, with a focus on the lift-drag ratio. The impact on the lift-drag ratio of airfoil shape, aspect ratio and of rotation has been presented. The study leads to the following conclusions:

In deep-stall, with leading edge separation present,

- the lift-drag ratio of an airfoil is largely independent of aspect ratio.
- the lift-drag ratio of an airfoil is independent of Reynolds number.
- the lift-drag ratios of the various sections of a wind turbine blade coincide with the two-dimensional curve, irrespective of rotation.
- the lift-drag ratio varies with leading edge upwind thickness parameter. The higher the upwind  $y/c$  at  $x/c=0.0125$ , the higher the zero-lift angle and lift-drag ratio at  $\alpha=90^\circ$ .

- the lift-drag ratio varies with trailing edge angle. The higher the trailing edge angle (measured positive counter-clockwise), the higher the zero-lift angle and the lift-drag ratio at  $90^\circ$  incidence.

## 10.6 REFERENCES

Butterfield, C.P., Musial, W.P. and Simms, D.A. (1992) *Combined Experiment Phase I, Final Report*. NREL/TP-257-4655, October 1992.

Fingersh, L.J., Simms, D., Hand, M., Jager, D., Contrell, J., Robinson, M., Schreck, S., and Larwood, S. (2001) *Wind Tunnel Testing of NREL's Unsteady Aerodynamics Experiment*. AIAA-2001-0035, 2001 ASME Wind Energy Symposium, Reno, NV, Jan. 2001.

Madsen, J. and Hansen, R. (2017) *Uncorrected data from the LM Windpower low-speed wind tunnel*. Lunderskov, Denmark, February 2017.

Jacobs, M. (2015) *High Reynolds Number Airfoil Test in DNW-HDG*. Report DNW-GUK-2014 C-04. Göttingen, July 2015.

Khan, M.A. (2018) *Dynamic Stall Modeling for Wind Turbines*. Master thesis, Delft University of Technology, July 2018.

Ostowari, C. and Naik, D. (1984) *Post Stall Studies of Untwisted Varying Aspect Ratio Blades with NACA44XX series Airfoil Sections – Part I*, Wind Engineering, Vol. 8, No. 3, pp.176–194, 1984.

Ostowari, C. and Naik, D. (1985) *Post Stall Studies of Untwisted Varying Aspect Ratio Blades with NACA44XX series Airfoil Sections – Part II*, Wind Engineering, Vol. 9, No. 3, pp. 109-164, 1985.

Somers, D.M. *Design and experimental results for the S809 airfoil*. NREL/SR-440-6918, National Renewable Energy Laboratory, USA, January 1997.

Tangler, J., Kocurek, J. D., *Wind turbine post-stall performance characteristics guidelines for blade-element momentum methods*. AIAA conference paper NREL/CP-500-36900 October 2004.

Timmer, W.A. and van Rooij, R.P.J.O.M., *Some aspects of high angle-of-attack flow on airfoils for wind turbine application*. Proceedings of the European Wind Energy Conference, pp 355-358, Copenhagen, Denmark 2-6 July 2001.

Timmer, W.A. Two-dimensional low-Reynolds number wind tunnel results for airfoil NACA 0018. *Wind Engineering*, Volume 32, No. 6, 2008, pp 525–537.

van Rooij, R.P.J.O.M. and Meng, F.Z. (2006) *The steady state parked configuration*, Proceedings of the 2006 Joint meeting of IEA R&D Wind Annex XI: Joint action on the aerodynamics of wind turbines and IEA R&D Wind annex XX: HAWT aerodynamics and models from wind tunnel measurements, National Renewable Energy Laboratory, Golden, Colorado, USA, 2006.





# APPENDICES



# APPENDIX A

## Wind tunnel wall corrections for two-dimensional testing

This Appendix contains part of a comprehensive description of the various correction methods provided in Timmer (2021). For the sake of brevity, only a summary of the correction method for two-dimensional attached flow and an expose of Maskell's method for separated flow are reported here. The chapter on Maskell's method additionally contains a review on the value of the blockage factor  $\theta=0.96$ .

### A1 BLOCKAGE IN ATTACHED FLOW

The classical correction equations most commonly used in two-dimensional sub-sonic wind tunnel testing find their origin in the assumption of linearized potential flow between the model and the walls. With a (limited) number of singularities, such as vortices to represent the lift, sources for the wake and source-sink doublets to represent the model volume, a theoretical model of the object and its wake is made. The method of images is then used to calculate the interference effects at the model location. The corrections refer to a situation in which the thickness and camber of the airfoil are small, the chord is small with respect to the tunnel height and the induced velocities everywhere in the test section are small compared to the undisturbed flow velocity. This justifies the neglect of higher powers and products of the interference factors and enables the superposition of interference effects and consequently makes it possible to consider the influence of camber and thickness and of model and wake blockage separately.

#### A1.1 General form

In a closed test section the presence of the model and its wake gives rise to an increase at the model location of the undisturbed (apparent) velocity  $U'$ :

$$U = (1 + \epsilon_b)U' \tag{A.1}$$

where  $\epsilon_b$  is the total blockage factor. The prime denotes the uncorrected value. The dynamic pressure correction then follows from

$$q = q'(1 + \varepsilon_b)^2 \quad (\text{A.2})$$

For small blockage factors, and including the Mach number, to the first order of  $\varepsilon_b$  we arrive at

$$\frac{q}{q'} = \left(1 + (2 - M^2)\varepsilon_b\right) \quad (\text{A.3})$$

### A1.2 Solid and wake blockage

Assuming the model is small compared to the tunnel test section and the lift is not too large, the blockage due to the model (solid blockage) and to the wake (wake blockage) can be treated separately:

$$\varepsilon_b = \varepsilon_s + \varepsilon_w \quad (\text{A.4})$$

For the solid blockage, Allen and Vincente (1944) found:

$$\varepsilon_s = \frac{\Lambda \sigma}{\beta^3} \quad (\text{A.5})$$

with the tunnel blockage factor

$$\sigma = \frac{\pi^2}{48} \left(\frac{c}{h}\right)^2 \quad (\text{A.6})$$

The body-shape factor  $\Lambda$  is defined as

$$\Lambda = \frac{16}{\pi} \int_0^1 \frac{y}{c} \sqrt{\left(1 - C_p\right) \left(1 + \left(\frac{dy}{dx}\right)^2\right)} dx \frac{x}{c} \quad (\text{A.7})$$

in which  $C_p$  is the inviscid zero-incidence pressure coefficient at the chord-wise station  $x$  and  $y$  is the ordinate of the symmetric (base) profile. Allen and Vincenti give values for a number of base profiles.

The solid blockage equations were essentially derived with the assumption that the blockage is independent of lift. Based on the work of Batchelor, (Garner et al., 1966) it is suggested that the simple theory expressed in equation (A.5) can be adapted to deal with the solid blockage of an airfoil at an angle of attack  $\alpha$  by writing:

$$\varepsilon_s(\alpha) = \varepsilon_s \left[ 1 + \beta \frac{1.1}{(t/c)} \alpha^2 \right] \quad (\text{A.8})$$

with  $\alpha$  expressed in radians.

### A1.2.2 Wake blockage

The wake effect is simulated by a system of source images. Source strength is related to the measured drag coefficient using conservation laws with the boundary condition that the flow field far upstream remains unchanged. Under these assumptions the wake blockage at the tunnel centre can be determined (Garner et al, 1966) from:

$$\varepsilon_w = \frac{1}{4} \left( \frac{c}{h} \right) \frac{1 + 0.4M'^2}{\beta^2} C'_d \quad (\text{A.9})$$

### A1.2.3 The total blockage factor

The total blockage factor can now be composed from the contributions of the solid and the wake blockages. Using the notation of Allen and Vincenti this gives:

$$\varepsilon_b = \frac{\Lambda \sigma}{\beta^3} \left[ 1 + 1.1\beta \frac{\alpha^2}{(t/c)} \right] + \frac{1}{4} \left( \frac{c}{h} \right) \frac{1 + 0.4M'^2}{\beta^2} C'_d \quad (\text{A.10})$$

The two-dimensional approach of the derivations essentially implies a rectangular test section. However, many wind tunnels have working sections with corner fillets, which raises the question what value of the tunnel height  $h$  should be used. From considerations of continuity an effective height  $h_e$  can be derived from the test section area divided by the span of the model.

Insertion of eq. (A.10) into eq. (A.2) or (A.3) yields the change of the dynamic pressure due to the blockage inside the test section. For small values of the blockage factor we may use

$$\frac{q'}{q} = \frac{1}{(1 + (2 - M'^2)\varepsilon_b)} \approx (1 - (2 - M'^2)\varepsilon_b) \quad (\text{A.11})$$

To correct forces and moments for blockage using eq. A.31 we may write

$$C_a = C'_a \frac{q'}{q} = C'_a (1 - (2 - M'^2)\varepsilon_b) \quad (\text{A.12})$$

### A1.3 Wake buoyancy

Apart from a blockage effect, the developing wake induces a velocity increase in flow direction and consequently, applying Bernoulli's equation, also gives rise to a pressure

gradient along the model which would not exist in free air. This pressure gradient is felt by the model as buoyancy and the associated increase in drag follows from a derivation by Allen and Vincenti based on the work of Glauert:

$$C_d = C_d' \left[ 1 - \frac{1 + 0.4M'^2}{\beta^3} \Lambda \sigma \right] \frac{q'}{q} \quad (\text{A.13})$$

Combined with eq. (A.12) and written to the first order the corrected drag coefficient is given by

$$C_d = C_d' \left[ 1 - \frac{1 + 0.4M'^2}{\beta^3} \Lambda \sigma - (2 - M'^2) \varepsilon_b \right] \quad (\text{A.14})$$

with  $\varepsilon_b$  given by eq. (A.10).

Debate exists on the applicability of the buoyancy correction if the drag is derived from the pressures in the wake, reduced in the usual way. Allen and Vincenti state that the correction equations are primarily derived for drag measured with a balance, but that for normal chord-to-height ratio's values differ by less than 0.5%. Rogers (Garner et al., 1966) argues that in particular the wake buoyancy equation should not be applied when the drag is measured with a wake rake. It is indeed questionable whether the impact of the drag increase due to the wake-wall interference is captured by the wake rake data reduction, since the speed-up due to the expanding wake for reasons of continuity mainly takes place outside the wake, which is discarded if the wake survey method is used in the conventional way. It can be argued that the wake buoyancy correction should only be applied if the drag is derived from balance measurements or from the model pressure distribution.

#### **A1.4 Lift interference**

A straight walled closed test section prevents the normal curvature of the flow around an airfoil producing lift since the streamlines along the walls are straight. As a result the model appears to have more camber showing increased lift and moment coefficients and an induced upwash, changing the angle of attack.

This problem of lift interference (streamline curvature) is evaluated for a thin airfoil with its chord on the tunnel centre line. The load on the airfoil is approximated by distributed vorticity along the chord. Vortex theory is used on a system of images with alternating signs to mimic the tunnel walls.

With the requirement that the distribution of lift along the chord and especially the magnitude of the lift component near the leading edge of the airfoil shall be the same both in free air as in the tunnel, this evaluation leads to a set of relations in the form of

$$\alpha = \alpha' + \Delta\alpha$$

$$c_l = (c_l' + \Delta c_l) \frac{q'}{q} \quad (\text{A.15})$$

$$c_m = (c_m' + \Delta c_m) \frac{q'}{q}$$

The angle of attack is in radians. Based on work of Havelock (Garner et al., 1966) the additional components are expanded to the order  $(c/h)^4$

$$\Delta\alpha = \frac{\sigma}{2\pi\beta} (C_l' + 4C_m') - 0.525 \frac{\sigma^2}{\pi\beta^3} C_l' \quad (\text{A.16})$$

$$\Delta C_l = C_l' \left( -\frac{\sigma}{\beta^2} + 5.25 \frac{\sigma^2}{\beta^4} \right) \quad (\text{A.17})$$

$$\Delta C_m = C_l' \left( \frac{\sigma}{4\beta^2} - 1.05 \frac{\sigma^2}{\beta^4} \right) \quad (\text{A.18})$$

### A1.5 Overview of corrections on coefficients for streamlined flow

A combination of the correction relations in the foregoing paragraphs for lift interference, blockage and wake buoyancy leads to the following set of correction equations

$$\alpha = \alpha' + \frac{\sigma}{2\pi\beta} (C_l' + 4C_m') \quad (\text{A.19})$$

$$C_l = C_l' \left[ 1 - \frac{\sigma}{\beta^2} + 5.25 \frac{\sigma^2}{\beta^4} - \frac{(2-M'^2)}{\beta^3} \Lambda \sigma \left( 1 + \frac{1.1\beta}{(t/c)} \alpha'^2 \right) \right] +$$

$$-C_l' \left[ \frac{(2-M'^2)(1+0.4M'^2)}{4\beta^2} \left( \frac{c}{h} \right) C_d' \right] \quad (\text{A.20})$$

$$C_d = C_d' \left[ 1 - \Delta C_d^* - \frac{(2-M'^2)}{\beta^3} \Lambda \sigma \left( 1 + \frac{1.1\beta}{(t/c)} \alpha'^2 \right) \right] +$$

$$-C_d' \left[ -\frac{(2-M'^2)(1+0.4M'^2)}{4\beta^2} \left( \frac{c}{h} \right) C_d' \right] \quad (\text{A.21})$$

The wake buoyancy correction  $\Delta C_d^* = 0$  for wake rake measurements and  $\Delta C_d^* = \Lambda \sigma \frac{1+0.4M^2}{\beta^2}$  for drag measured with a balance or calculated from the pressure distribution.

$$C_m = C_m' \left[ 1 - \frac{(2-M^2)}{\beta^3} \Lambda \sigma \left( 1 + \frac{1.1\beta}{(t/c)} \alpha'^2 \right) - \frac{(2-M^2)(1+0.4M^2)}{4\beta^2} \left( \frac{c}{h} \right) C_d' \right] + C_l' \left( \frac{\sigma}{4\beta^2} - 1.05 \frac{\sigma^2}{\beta^4} \right) \quad (\text{A.22})$$

$$q = q' \left[ 1 + \frac{(2-M^2)}{\beta^3} \Lambda \sigma \left( 1 + \frac{1.1\beta}{(t/c)} \alpha'^2 \right) + \frac{(2-M^2)(1+0.4M^2)}{4\beta^2} \left( \frac{c}{h} \right) C_d' \right] \quad (\text{A.23})$$

$$\text{Re} = \text{Re}' \left[ 1 + \frac{(1-0.7M^2)}{\beta^3} \Lambda \sigma \left( 1 + \frac{1.1\beta}{(t/c)} \alpha'^2 \right) + \frac{(1-0.7M^2)(1+0.4M^2)}{4\beta^2} \left( \frac{c}{h} \right) C_d' \right] \quad (\text{A.24})$$

The angle of attack in the equations is expressed in radians. In equation (A.19) the term dealing with  $(c/h)^4$  is omitted because it is negligibly small. For the angle of attack expressed in degrees we write:

$$\alpha = \alpha' + \frac{57.3\sigma}{2\pi\beta} (C_l' + 4C_m') \quad (\text{A.25})$$

### A1.6 Correction of the pressure distribution

The solid and wake blockage and the lift interference correction should obviously also appear in the correction of the pressure distribution.

The correction for lift interference  $\Delta C_p$  follows from

$$\Delta C_p = \frac{4}{\pi} \left( \frac{\sigma}{\beta^2} - \frac{5.25}{\beta^4} \sigma^2 \right) C_l' \sqrt{\frac{x}{c} \left( 1 - \frac{x}{c} \right)} \quad (\text{A.26})$$

given to the 4<sup>th</sup> power of  $c/h$ . Hence,

$$C_{p_u} = 1 - (1 - (C'_{p_u} + \Delta C_p)) \frac{q'}{q} \quad (\text{A.27})$$

$$C_{p_l} = 1 - (1 - (C'_{p_l} - \Delta C_p)) \frac{q'}{q} \quad (\text{A.28})$$

Allen and Vincenti argue that the two contributions should be treated separately; a correction for the blockage due to the base profile and a correction for streamline curvature applied to the lift per unit chord. To this end the pressure distribution of an airfoil is expressed as

$$C_{p_u} = 1 - \frac{\left[ \left( 1 - C_{p_{sym}} \right) + \frac{1}{4} (C_{p_l} - C_{p_u}) \right]^2}{\left( 1 - C_{p_{sym}} \right)} \quad (\text{A.29})$$

$$C_{p_l} = 1 - \frac{\left[ \left( 1 - C_{p_{sym}} \right) - \frac{1}{4} (C_{p_l} - C_{p_u}) \right]^2}{\left( 1 - C_{p_{sym}} \right)} \quad (\text{A.30})$$

where  $C_{p,sym}$  is the pressure coefficient of the base (symmetrical) profile.

For the blockage correction as a result of the presence of the base profile the lift is removed by taking the average of the kinetic pressures on the upper and lower surface at the same chord location. If the pressure orifices on upper and lower surface do not have the same chord location (x-ordinate) an interpolation between two pressure orifices is performed. If the pressure coefficients on upper and lower surface are related to the true instead of the apparent dynamic pressure we can write:

$$C_{p_u} = 1 - \frac{\left[ \left( \frac{\sqrt{q_u^*} + \sqrt{q_l^*}}{2} \right)^2 + \left( \frac{q_u^* + q_l^*}{4} - \left( \frac{\sigma}{\pi\beta^2} - 5.25 \frac{\sigma^2}{\pi\beta^4} \right) C'_l \sqrt{1 - \left( 1 - \frac{2x}{c} \right)^2} \right)^2 \right]}{\left( \frac{\sqrt{q_u^*} + \sqrt{q_l^*}}{2} \right)^2} \quad (\text{A.31})$$

$$C_{p_l} = 1 - \frac{\left[ \left( \frac{\sqrt{q_u^*} + \sqrt{q_l^*}}{2} \right)^2 - \left( \frac{q_u^* + q_l^*}{4} - \left( \frac{\sigma}{\pi\beta^2} - 5.25 \frac{\sigma^2}{\pi\beta^4} \right) C'_l \sqrt{1 - \left( 1 - \frac{2x}{c} \right)^2} \right)^2 \right]}{\left( \frac{\sqrt{q_u^*} + \sqrt{q_l^*}}{2} \right)^2} \quad (\text{A.32})$$

Where  $q_u^*$  and  $q_l^*$  are given by:

$$q_u^* = (1 - C_{p_u}') \frac{q}{2} \quad (\text{A.33})$$

respectively

$$q_l^* = (1 - C_{p_l}') \frac{q}{2} \quad (\text{A.34})$$

The ratio of the corrected and uncorrected dynamic pressures in the latter equations can be calculated from (A.23).

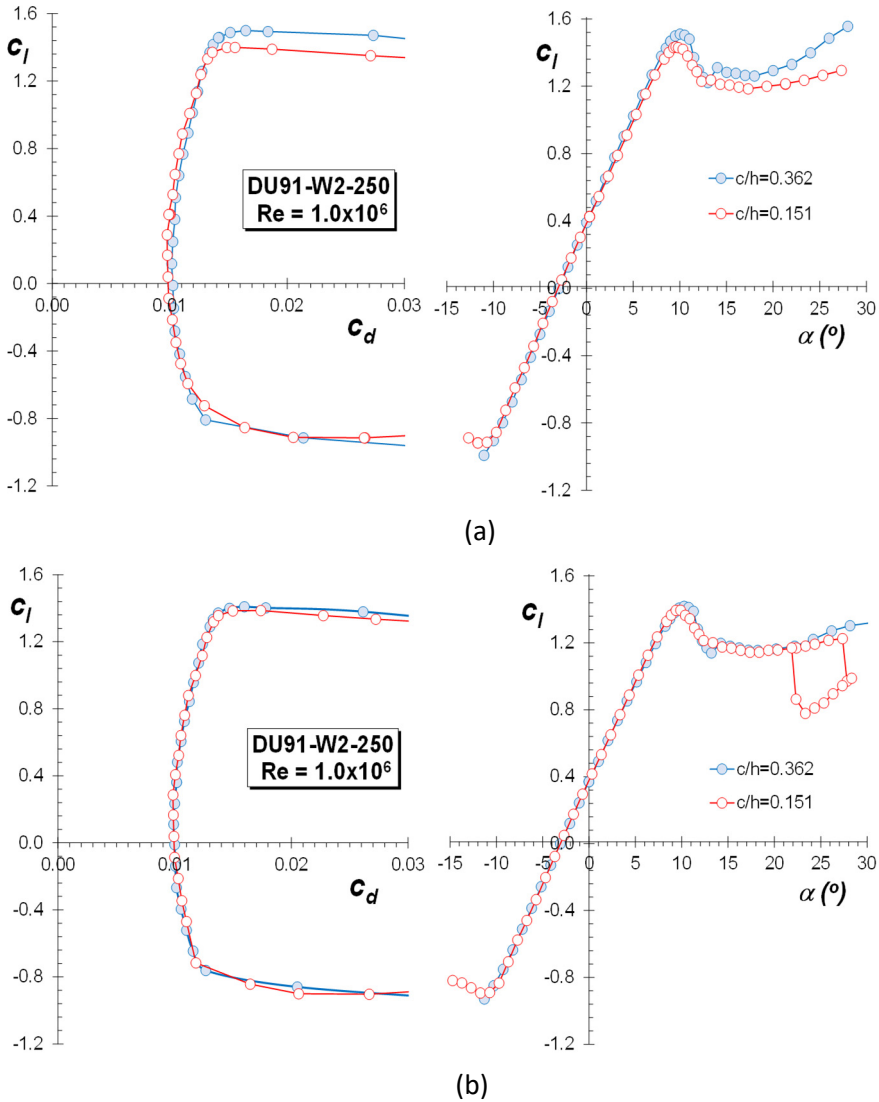


Figure A.2: The uncorrected (a) and corrected (b) characteristics of airfoil DU91-W2-250 for two different chord-to-height ratios. Data corrected for Mach number.

The pressure distribution corrected in this way corresponds to the corrected angle of attack and lift- and moment coefficients.

The correction method appears to work very well, even at relatively high blockage ratios, an example of which is given in fig. A.2.

Figure A.2a presents the measured uncorrected two-dimensional characteristics of the 25% thick airfoil DU91-W2-250 for two different models with chords of 0.25m and 0.60m. The tests were performed in the 1.25x1.80m<sup>2</sup> Delft University (TUDelft) Low-speed Low-turbulence wind tunnel (LTT).

The test section has 0.42m corner fillets and the models were setup vertically, which leads to an effective height of 1.656m, giving  $c/h$  values for the two different models of 0.151 and 0.362.

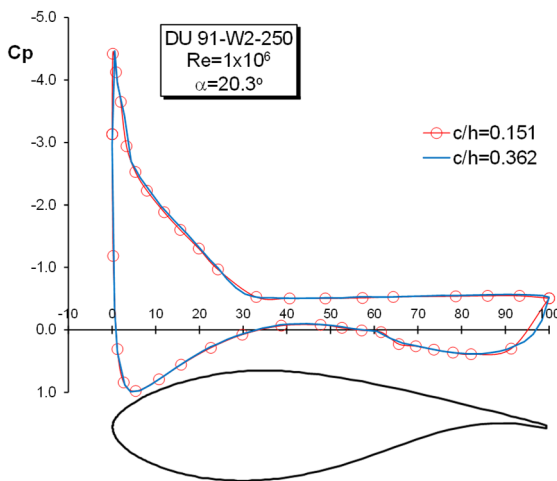


Figure A.3: The corrected pressure distributions for two values of the chord-height ratio at an angle of attack of 20.3°.

Figure A.2b shows a very good agreement between the corrected characteristics, both for the lift and the drag curves. Noteworthy is the fact that even up to an angle of attack of 20° the correction scheme is capable of matching the lift curves. Figure A.3 shows the pressure distributions for both models at  $\alpha=20.3^\circ$ . Even with flow separation at about 30% of the chord, overall there's a perfect agreement, especially between the corrected base pressures.

## A2 CORRECTION OF MEASUREMENTS IN THE DEEP-STALL REGION.

With increasing separation on the wind tunnel model the blockage due to the wake becomes increasingly important and eventually will become a dominant factor of the total blockage inside the test section. In these cases the classical treatment of small perturbations due to blockage is no longer valid. In the deep-stall region of angles of

attack, where the flow separates from the leading edge, the two-dimensional airfoil model starts to behave like a bluff body.

Correction methods accounting for the wall interference of bluff bodies in closed test sections can be divided into methods using the measured drag of the model and those relying on the measured static pressure distribution on the walls: the wall-signature method. Maskell's method, a simple, yet fairly effective correction scheme belongs to the first category and is discussed in the following.

### A2.1 Maskell's method

Maskell (1963) developed a method to correct for wall interference effects when dealing with separated flow over bluff bodies. In its simplest form the method only uses the measured drag due to separation and some geometric parameters in combination with a semi-empirical constant to establish a dynamic pressure correction. His method was primarily developed for the flow over bluff bodies, but can also be used for stalled wings since the flow in the heavily separated region of the model shows resemblance with bluff body wakes.

#### A2.1.1 Corrections on drag

Maskell considers the flow depicted in figure A4. The wake of the bluff body is represented by a stream surface originating from the edge of the body, extending downstream. In plane 2 the cross section of the wake reaches its maximum. Plane 1 is far ahead of plane 2 and contains the undisturbed velocity  $U$ . A constant pressure  $p_b$  is

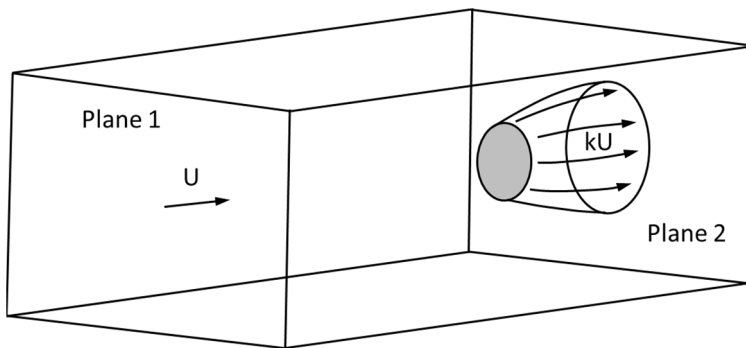


Figure A.4: The bluff body flow model considered by Maskell (1963).

present on the surface of this wake bubble with associated velocity  $kU$ , where  $k$  is the ratio of wake edge velocity over undisturbed velocity. This pressure is equal to the base pressure acting at the back of the bluff body. Maskell argues that the pressure distribution on the model in the test section is invariant under the constraint imposed by the walls. This means that the flow field simply scales with the amount of blockage, which leads to

the expression:

$$\frac{C_D'}{k'^2} = \frac{C_D'}{(1 - C'_{pb})} = \text{const.} \quad (\text{A.34})$$

Where  $C_D'$  is the measured drag coefficient, defined as  $D'/q'S$ .  $S$  is a representative area of the body,  $q'$  is the dynamic pressure and  $C'_{pb}$  is the base pressure coefficient. Maskell confirmed experimentally the invariance principle using drag and base pressure measurements on a set of square flat plates positioned normal to the flow in two different wind tunnels, thus varying the amount of blockage. The  $S/C$  values, where  $C$  is the cross sectional area of the tunnel and  $S$  the frontal area of the plates, ranged from 0.0019 to .0451 and base pressure coefficients from -0.386 to -0.589.

Also for two-dimensional flow this invariance can be shown, as is presented in figure A.5, with measurements on two DU91-W2-250 airfoil models in the TUDelft

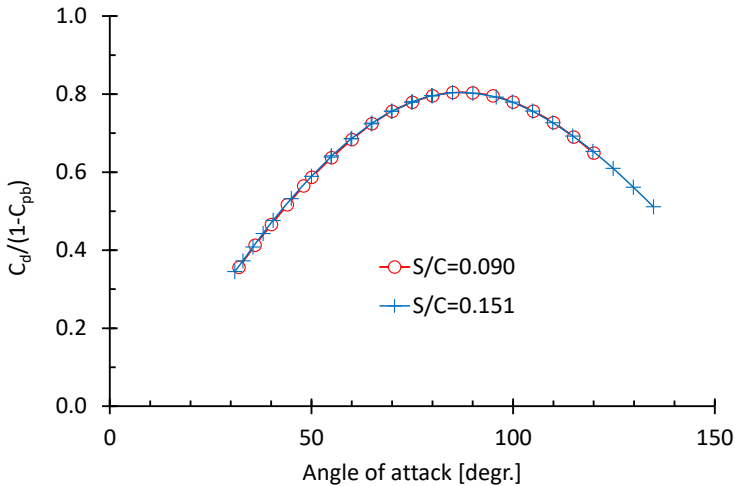


Figure A.6: The invariance of  $C_D/k^2$  (eq. A.59) for two different blockage factors of airfoil DU91-W2-250,  $Re=0.7 \times 10^6$

LTT, giving relatively small values of  $S/C$ , but well outside the range tested by Maskell (0.091 and 0.151 respectively).

Considerations of conservation of momentum in the fluid passing the control surface shown in figure A.4 lead to the expression

$$C_D' = m \left( k'^2 - 1 - m \frac{S}{C} \right) \quad (\text{A.35})$$

where  $m=B/S$  and  $B$  is the maximum cross section of the wake (in plane 2). Equation (A.35) was derived with the assumption that the contribution to the momentum balance of the in-plane orthogonal components of the velocity in cross-section 1, far ahead of the object,

and in cross-section 2, outside the wake, are negligibly small. This is true for two-dimensional flow, however with the argument that there is a tendency of the wakes of three-dimensional bodies to become axial-symmetric far downstream this also holds for other objects.

If the increase of the velocity in the closed test section would only come from blockage due to the presence of the wake, Maskell arrives at

$$\frac{k'^2}{k^2} = \frac{C'_D}{C_{D_M}} = 1 + \frac{C_{D_M}}{k^2 - 1} \frac{S}{C} \quad (\text{A.36})$$

where  $C_{D_M}$  is the corrected drag coefficient. However, wall constraint impacts the free expansion of the wake. The effect of this wake distortion on the value of B (through m) in eq. (A.35) was determined by the assumption that this distortion is proportional to the contraction of the stream outside the wake  $(C-B)/C$ . Neglecting higher order terms of  $S/C$ , Maskell found that the net result of incorporating wake distortion in the derivation is to replace the corrected drag coefficient in eq. (A.36) by the measured drag coefficient:

$$\frac{C'_D}{C_{D_M}} = 1 + \frac{C'_D}{k^2 - 1} \frac{S}{C} \quad (\text{A.37})$$

Hence

$$C_{D_M} = \frac{C'_D}{1 + \theta \frac{S}{C} C'_D} \quad (\text{A.38})$$

where  $\theta$  is the blockage factor for bluff-body flow:

$$\theta = \frac{1}{k^2 - 1} \quad (\text{A.39})$$

The parameter  $k^2$  can be derived from eq. A.36 through iteration using the measured mean base pressure as a starting value,  $(k^2)_0 = k'^2$ :

$$(k^2)_n = k'^2 \left[ 1 + \frac{1}{(k^2)_{n-1} - 1} C'_D \frac{S}{C} \right]^{-1} \quad (\text{A.40})$$

### A2.1.2 Two-dimensional models

To calculate the blockage factor for a two-dimensional flat plate normal to the flow, Maskell used experimental results from Fage and Johansen (1927), who presented measurements on a number of two-dimensional flat plates with different chords in the

NPL 7' octagonal test section (UK). Only for one of the plates enough parameters were measured to calculate  $\theta$ . Next to the base pressure with  $C_p=-1.38$ , they found a constant pressure along the edge of the wake, which Maskell determined to give  $C_p=-1.30$ . As indicated, it appeared that these two pressures are not equal, hence an average  $C_p$  was calculated over the measured maximum width of the wake (which was 1.85 times the chord), giving  $C_p=-1.34$ . With  $C_D'=2.13$  and  $S/C=0.0715$ , eq. (A.39) and (A.40) give  $\theta=0.960$ . The corrected drag coefficient then becomes 1.858.

The average corrected drag coefficient at  $90^\circ$  incidence of the 4 thin two-dimensional plates tested by Fage and Johansen was 1.86, which deviates appreciably from the commonly adopted value of around 2.0. This might find its origin in the setup of these tests. The drag was determined from the pressure distribution around the mid-span of the plate with pressure orifices in only one side of the plate. To complete the pressure distribution around the plate, it had to be rotated  $180^\circ$ . For stiffness purposes one side of the plate was not completely flat, but formed a wedge with a 3% thickness at mid-chord. Figure A.7 shows the difference in the two-dimensional drag curves corrected with the

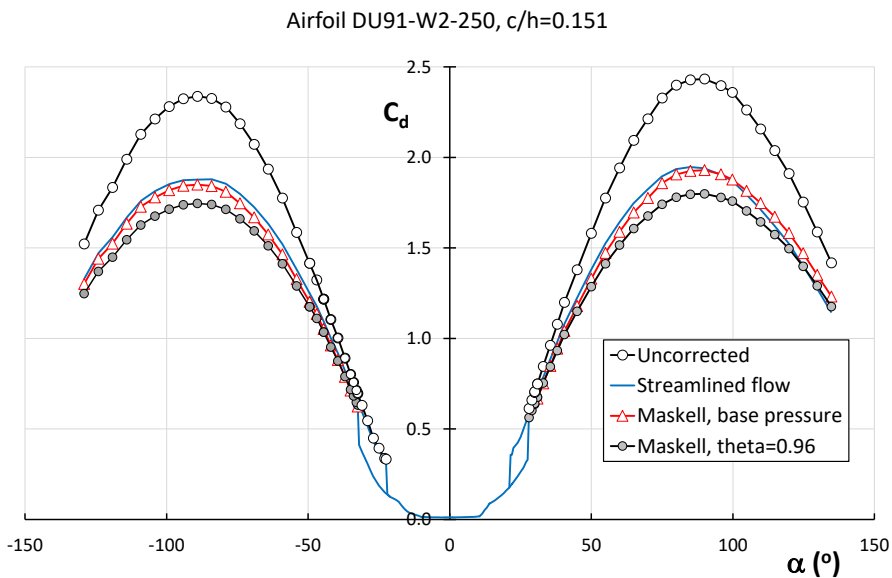


Figure A.7: Comparison of corrected drag curves using various correction schemes.  $Re=0.7 \times 10^6$

various methods. Data come from measurements on a 0.25m chord model in the Delft University LTT, with a  $S/C (=c/h, \text{ with } h \text{ the effective test section height})$  value of 0.151. It appears that the method using the base pressures gives results close to those resulting from the correction scheme for streamlined flow. The difference with the curve using Maskell's value of 0.96 for the blockage factor  $\theta$  is substantial.

The comparison with a 40% smaller model in the same tunnel, depicted in figure A.8, shows that only the method using  $\theta=0.96$  brings the two drag curves close together, with

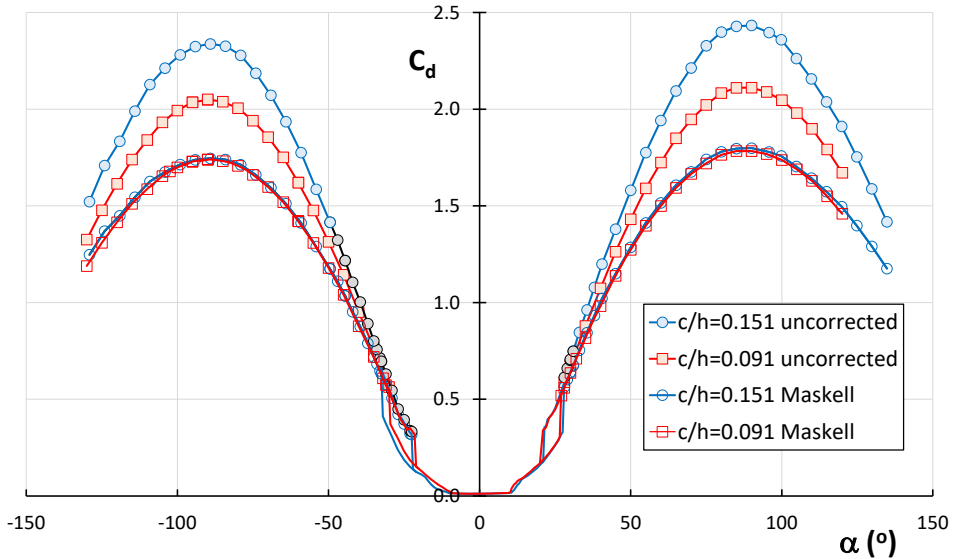


Figure A.8: The corrected drag curves for measurements on two models with  $c/h$  values of 0.091 and 0.151 using Maskell's method with  $\theta=0.96$ .  $Re=0.7 \times 10^6$

a difference in the maximum drag coefficient of only 1%.

It is clear that the method solely based on the model rear pressure does not work for two-dimensional flow with  $S/C$  values appreciably larger than those in Maskell's measurements (see chapter A2.1.7). Despite the fact that the value of 0.96 apparently was derived from one measurement on a two-dimensional flat plate it holds also quite well for measurements in the deep-stall region on an airfoil with a significant thickness of 25%.

Based on the measurements presented in figure A.8 a value slightly larger than 0.96 for the blockage factor, in the range of 1 to 1.03, is necessary to match both drag curves.

It must be noted that the drag curves shown in figures A.7 and A.8 come from pressure measurements. Depending on the number and distribution of the pressure orifices, especially in the lower surface trailing edge region, the calculated drag coefficient may differ slightly from the one resulting from balance measurements. Hence, when comparing drag curves with different  $c/h$ , some of the variations may be attributed to differences in measurement technique.

Strictly, the uncorrected drag coefficient in the blockage parameter  $S/C C_D'$  in equation A.38 is the one due to separation. For angles in the deep-stall region the full uncorrected value can be used, as the difference is negligibly small.

### A2.1.3 Correction on the angle of attack

When the airfoil is producing lift, the corrections on angle of attack for streamlined flow

are based on the fact that the curvature of the streamlines is altered by the presence of the walls. For two-dimensional models in deep stall the streamlines at the model location are on average straight and the increase in lift predominantly comes from the fact that the entire upper surface has a time-averaged constant pressure, which decreases with angle of attack. Hence it can be argued that there is no need for an angle of attack correction in deep stall.

#### A2.1.4 Corrections on lift and moment coefficients

Hackett (1996) recognized that the wake distortion correction in Maskell's method comes as part of a dynamic pressure correction, while it in fact is a drag increment, which should be removed from the dynamic pressure correction before correcting the lift and moment coefficients.

In a two-step approach Hackett writes:

$$\Delta C_D = C_{D_M} - C_{D_{d_e}} \quad (\text{A.41})$$

Where  $C_{D_M}$  again is the corrected drag coefficient using Maskell's method and  $C_{D_{d_e}}$  is the corrected drag coefficient without distortion. Eq. (A.36) and (A.39) then give

$$C_{D_{d_e}} = C_{D_M} - \Delta C_D = \frac{C_{D_M}}{1 + \theta \frac{S}{C} (C_{D_M} - \Delta C_D)} \quad (\text{A.42})$$

Combining equations (A.38) and (A.42) and solving the quadratic equation in  $\Delta C_D$  yields:

$$\Delta C_D = C_{D_M} - \frac{-1 + \sqrt{1 + 4\theta \frac{S}{C} C'_D}}{2\theta \frac{S}{C}} \quad (\text{A.43})$$

The lift, moment and pressure coefficients can now be corrected for wake blockage using

$$\left(\frac{q'}{q}\right)_H = \frac{C_{D_{d_e}}}{C'_D} = \frac{1}{1 + \theta \frac{S}{C} (C_{D_M} - \Delta C_D)} \quad (\text{A.44})$$

Where the index H denotes Hackett's correction. Note that equation (A.43) needs to return a negative value of  $\Delta C_d$  as  $C_{d_e}$  is larger than  $C_{D_M}$ .

Hackett and Cooper (2001) proposed additional corrections on  $C_l$  and  $C_m$ , based on the consideration that the tunnel-induced drag increment  $\Delta C_D$  results from a changed base pressure. For an arbitrary angle of attack in the deep-stall region, they suggest

$\Delta C_n = \Delta C_D / \sin \alpha$  and, assuming  $\Delta C_l = \Delta C_n \cos \alpha$ ,  $\Delta C_t = \Delta C_D / \tan \alpha$ . The change in moment coefficient around the quarter-chord point follows from  $\Delta C_m = -\Delta C_n / 4$ . The total correction of the lift and moment coefficients now is given by:

$$C_l = C'_l \left( \frac{q'}{q} \right)_H + \Delta C_D / \tan \alpha \quad (\text{A.45})$$

$$C_m = C'_m \left( \frac{q'}{q} \right)_H - \frac{\Delta C_D}{4 \sin \alpha} \quad (\text{A.46})$$

where the ratio of dynamic pressures is given in eq. A.44.

#### A2.1.5 Correction of the pressure distribution

The resulting correction on the pressure distribution is not given by Hackett and Cooper, but is not difficult to derive. The additional correction on  $C_n$  results in a dynamic pressure correction increment on top of the one given in eq. (A.44). The complete dynamic pressure correction to correct the pressure distribution now is presented by:

$$\left( \frac{q'}{q} \right)_{HC} = \left( \frac{q'}{q} \right)_H + \frac{\Delta C_n}{C'_n} \quad (\text{A.47})$$

with the index HC denoting Hackett and Cooper's solution.

At  $\alpha=90^\circ$ ,  $C_n'=C_d'$  and, consequently,  $\Delta C_n = \Delta C_D$ . Combining eq. (A.44) and (A.47) gives

$$\left( \frac{q'}{q} \right)_{HC} = \left( \frac{C_{d_\infty}}{C'_d} \right)_H + \frac{\Delta C_d}{C'_d} = \frac{C_{d_\infty} + \Delta C_d}{C'_d} = \frac{C_{d_M}}{C'_d} = \left( \frac{q'}{q} \right)_M \quad (\text{A.48})$$

Where the index M denotes Maskell's initial dynamic pressure correction. It appears that, at least at  $\alpha=90^\circ$  and  $270^\circ$ , the measured drag and lift coefficients should be corrected with Maskell's initial dynamic pressure correction. The difference between Maskell's dynamic pressure correction and the one formulated by Hackett and Cooper in eq. (A.47) for the measurements depicted in fig. A.7 is below -0.5%, with the biggest differences around the angles for which the magnitude of the  $C_t$ -component of the forces is the largest (between  $80^\circ$  and  $130^\circ$ , for both positive and negative angles). This may find its origin in the fact that in the formulation of Hackett and Cooper the incremental contribution of the tangential force coefficient  $\Delta C_t$  is neglected. Theoretically, the basis for  $\Delta C_D$  and  $\Delta C_l$  is given by:

$$\Delta C_d = \Delta C_n \sin \alpha + \Delta C_t \cos \alpha \quad (\text{A.49})$$

$$\Delta C_l = \Delta C_n \cos \alpha - \Delta C_t \sin \alpha \quad (\text{A.50})$$

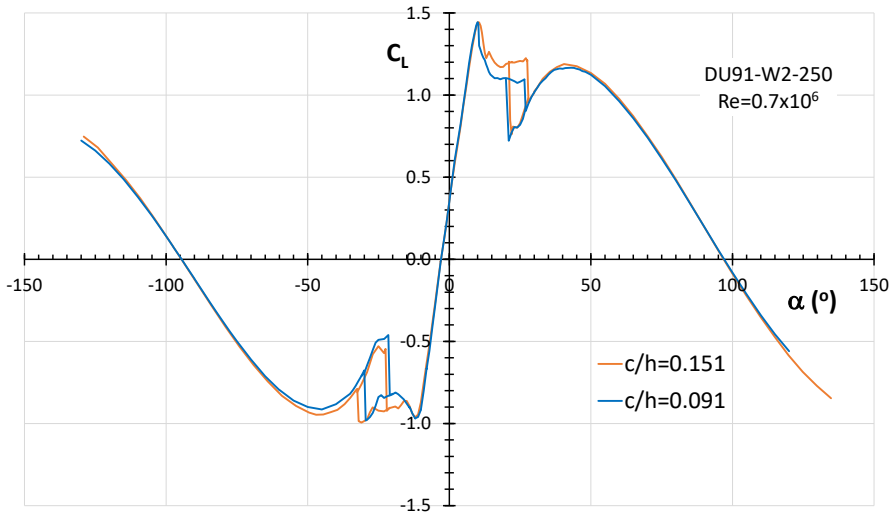


Figure A.9: The aerodynamic characteristics of DU91-W2-250 for two models with  $c/h=0.091$  and  $0.151$  respectively, corrected with the dynamic pressure correction of Maskell's original analysis.

It seems justified to assume that the incremental component  $\Delta C_t$  is very small, but not negligible, and that consequently over the entire angle of attack range in deep-stall the uncorrected force and moment coefficients can be corrected with Maskell's dynamic pressure correction:

$$C_l = C'_l \left( \frac{q'}{q} \right)_M = C'_l \left( \frac{C_{D_M}}{C'_D} \right) \quad (\text{A.51})$$

$$C_m = C'_m \left( \frac{q'}{q} \right)_M = C'_m \left( \frac{C_{D_M}}{C'_D} \right) \quad (\text{A.52})$$

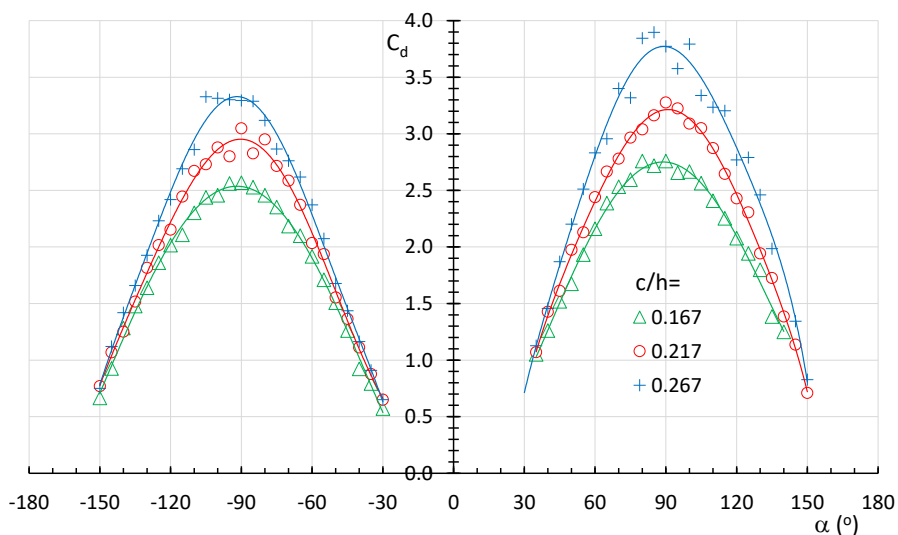
$$C_p = 1 - (1 - C'_p) \left( \frac{q'}{q} \right)_M \quad (\text{A.53})$$

A comparison of the lift coefficients from the models of fig. A.8 corrected according to eq. A.51 is presented in fig. A.9.

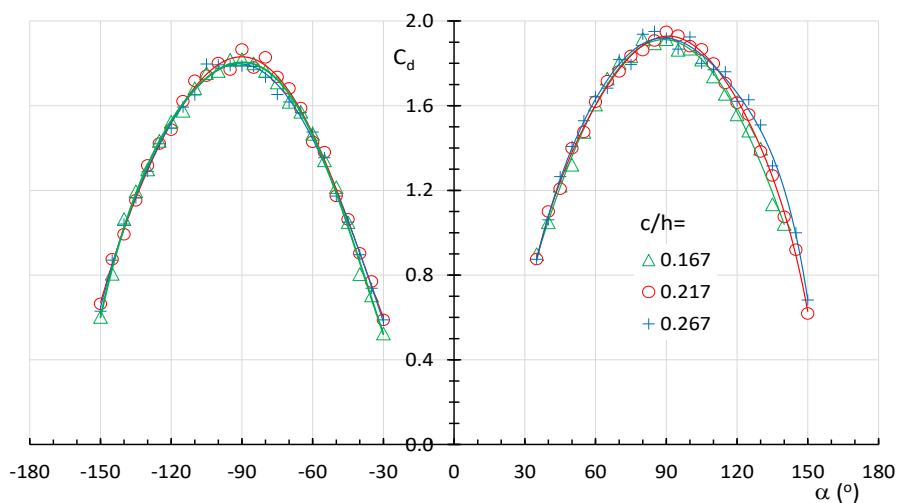
In the deep-stall region of angles of attack the agreement is very good. The differences in lift coefficients between the two models in the range of angles between maximum lift and deep stall come from a small irregularity near the upper surface leading edge of the smaller model in the vicinity of the pressure orifices

#### A2.1.6 Higher values of $c/h$

The systematic neglect of higher order terms of  $S/C$  in Maskell's derivation may limit the applicability of the method for tests with increasingly higher  $c/h$  values. According to Cooper in Agardograph 336 (Ewald 1998), Maskell's method has



(a)



(b)

Figure A.10: The uncorrected (a) and Maskell-corrected (b) drag curves for airfoil WA-210 with varying chord to tunnel height ratio's,  $Re=0.75 \times 10^6$ . Uncorrected data from Wang et al. (2015).

been found to over-correct at high area ratio's. Figure A.10 may shed some light on the differences that exist when using Maskell's method with  $\theta=0.96$  to correct measurements with  $c/h$  values higher than 0.15.

The measurements shown in figure A.10 and A.11 were performed by Wang et al (2015) in the NF-3 wind tunnel of Northwestern Polytechnical University in Xi'an, China. Three models of airfoil WA-210 with chord lengths of 0.5, 0.65 and 0.8 meter were tested in the  $1.6 \times 3.0 \text{m}^2$  test section, giving chord-to-height ratios of 0.167, 0.217 and 0.267 respectively. The uncorrected data were taken from the paper and corrected with

Maskell's method using  $\theta=0.96$ .

The Reynolds number was  $0.75 \times 10^6$  and for clarity of the graph only the high angle of attack region is shown.

It appears that the corrected drag curve between the deep-stall angle and  $90^\circ$  incidence, does not deviate much for increasing  $c/h$ , both for positive and negative angles.

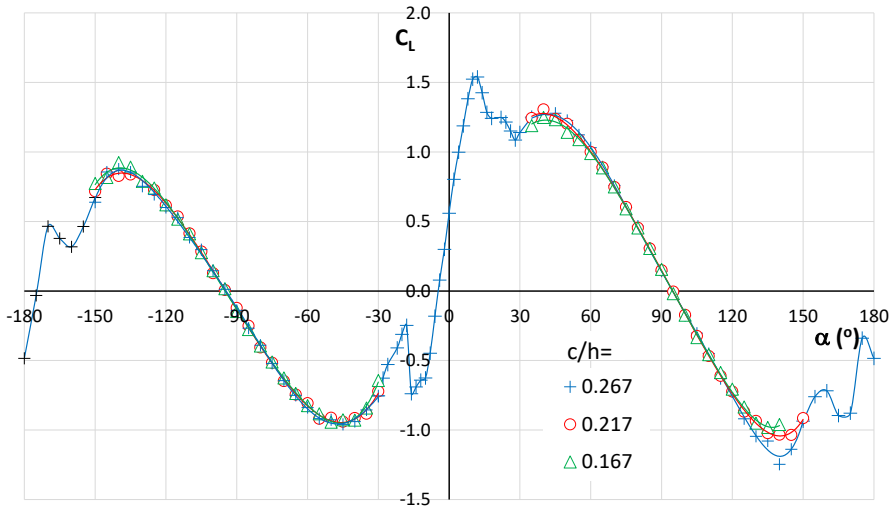


Figure A.11: The Maskell corrected lift curves for airfoil WA-210 with varying chord to tunnel height ratio's.

Differences in the maximum corrected drag coefficient for the lowest and the highest  $c/h$  are smaller than 1% and fall well within the experimental error. At these  $c/h$  values there seems to be no over correction using Maskell's method to correct the drag. Beyond  $90^\circ$ , the  $C_d$  increases with increasing blockage, which may be traced back to the increasing blockage in combination with the decreasing aspect-ratio of the model. Without available pressure distributions this is difficult to establish. The corresponding corrected lift curves in figure A.11 generally show very good agreement up to  $120^\circ$ .

#### A2.1.7 Maskell's blockage constant

Maskell's blockage constant  $\theta=0.96$  for leading edge separated flow in two-dimensional testing is surrounded by quite some uncertainty. The parameters leading to the value of 0.96 were taken from the work of Fage and Johansen (1927), as described in paragraph A2.1.2. Each of the parameters will be discussed in the following.

##### a) The base pressure assumption.

Maskell's analysis is based on the assumption that the pressure on the surface of the separation body (the wake), shown in fig. A4, is equal to the base pressure of the model. Fage & Johansen measured the average velocity with a hot wire at the edge of the wake

just behind the flat plate ( $V_{\text{edge}}/V_0=1.49$ ). Within the experimental accuracy they also established that the static pressure along the wake edge is more or less constant. Assuming that also the total pressure along the wake edge is constant, this gives  $C_p'=-1.22$  along the surface of the body. It is obvious that this differs from the plate base pressure (which comes from the pressure measurements on the plate,  $C_p'=-1.38$ , assuming that the static pressure through the wake is constant). Maskell takes the average, on which also the maximum wake width  $B$  of  $1.85*c$  is based (m in eq. A.35). For comparison: the wake width estimated from the flow picture in fig. 9.10 is in the order of  $1.87c$ . From this point on, however, it is unclear how the resulting average base pressure  $C_p'=-1.34$  over area  $B$  in plane 2, which is to be used in eq. A.39 and A.40, is determined. Assuming  $B$  has an area of  $1xc$  with the original base pressure  $C_p'=-1.38$  and that on both sides of  $B$  the pressure linearly reduces from  $-1.30$  at the wake edge to  $-1.38$  inwards, the average pressure over  $B$  would be  $-1.36$ . Only if we take  $C_p'=-1.22$  at the wake edge we find  $-1.34$  as an averaged base pressure. This is however in contradiction to the assumption of  $C_p'=-1.30$  at the wake edge. The value  $C_p'=-1.36$  would give a blockage constant  $\theta=0.939$ . As an alternative, Maskell may have again taken the average of  $C_p'=-1.30$  and  $-1.38$ . In that case, however, it would not have been necessary to mention the maximum width of the wake.

For 2d-flows Maskell's base pressure assumption does not hold. As fig. A7 shows, simply using the measured base pressure leads to under correction. That 3D configurations are generally well corrected may have to do with the fact that the model base pressure and the wake edge pressures in such flow fields do not differ much.

#### b) The area ratio $S/C$

The experiment of Fage and Johansen was performed in the  $7 \times 7 \text{ft}^2$  wind tunnel of the Royal Aircraft Establishment (RAE) National Physics Laboratory (NPL) at Farnborough (UK). The test section layout was not given, but it is assumed to be the same as later described by Gould (1970). This test section indeed has a width and height of 7ft, but it also has 2ft corner fillets, which brings the test section area at the location of the balance attachments down to  $4.18 \text{m}^2$ , giving an  $S/C$  value of 0.0771, instead of  $S/C=0.0715$  used by Maskell. With Maskell's value for the average base pressure  $C_p'=-1.34$ , this would give  $\theta=0.986$ .

#### c) The uncorrected drag coefficient $C_d=2.13$ .

With  $C_d'=2.13$ , the corrected drag coefficient using  $\theta=0.96$  is 1.86, which is relatively low compared to the now common value of around 2. The value of 2.13 must be seen in connection with the measured plate base pressure of  $-1.38$ . As, according to theory,  $C_d'/(1-C_{pb}')$  is constant under the amount of blockage, potential differences with a situation giving a corrected drag coefficient of 2 may not affect the calculation of  $\theta$  drastically. Fig. A.12, demonstrates the sensitivity of Maskell's blockage constant

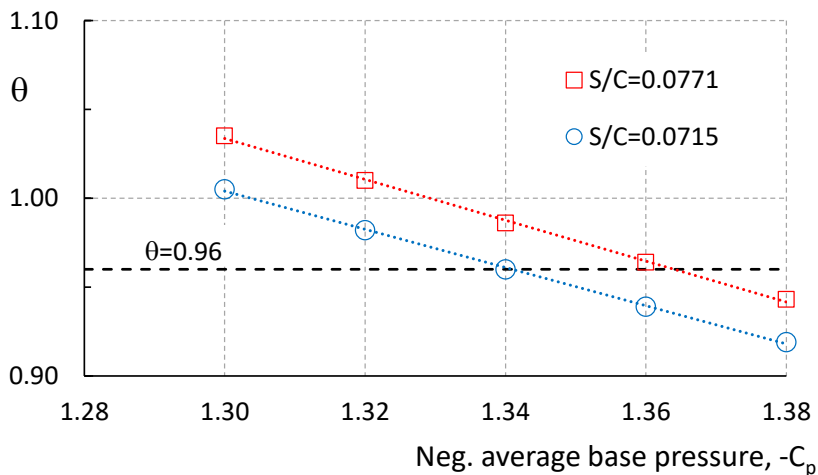


Figure A.12: The variation of Maskell's blockage constant with assumed base pressure for two area ratio's, using  $C_d'=2.13$

calculations to assumed base pressure coefficient and area ratio.

**The following conclusion can be drawn from the investigation:**

Maskell's assumption of equal pressure along the wake edge and on the base of the model does not hold for two-dimensional flows. It is unclear how Maskell came to the value of -1.34 for the base pressure coefficient to be used in his calculations. Furthermore, the measured uncorrected drag is lower than can be expected. In combination with a possible difference in S/C value, the determined blockage constant of 0.96 may be higher, in the order of 1, or slightly above. This is in accordance with the findings in chapter A2.1.2 (different c/h values) and of Timmer (2021) in which the Maskell corrected drag curve is compared with the corrected curve using a wall pressure method. Both hint at a value of  $\theta$  in the order of 1 to 1.03 for an optimal match.

**A3 REFERENCES**

Allen, H.J. and Vincenti, W.G. (1944) *Wall interference in a two-dimensional wind tunnel, with consideration of the effect of compressibility*. NACA Report no. 782, 1944.

Ewald, B.F.R. (Ed) (1998) *Wind tunnel wall corrections*. AGARDograph 336.

Fage, A. and Johansen, F.C. (1927) *On the flow of air behind an inclined flat plate of infinite span*. British ARC R&M, No. 1104.

Garner, H.C., Rogers, E.W.E., Acum, W.E.A. and Maskell, E.C. (1966) *Subsonic wind tunnel wall corrections*. AGARDograph 109.

Gould, R.W.F. (1970) *Wake Blockage Corrections in a Closed Wind Tunnel for One or Two Wall-Mounted Models Subject to Separated Flow*. British ARC R&M No. 3649.

Hackett, J.E. *Tunnel-induced gradients and their effect on drag*. AIAA 34th Aerospace Sciences Meeting, Reno NV, Jan. 1996, paper 96-0562. AIAA Transactions, Vol. 34, No. 12. (1996)

Hackett, J.E. and Cooper, K.R. *Extensions to Maskell's theory for blockage effects on bluff bodies in a closed wind tunnel*. The Aeronautical Journal, August 2001, pp. 409-416 (2001)

Maskell, E.C. (1963) *A theory of the blockage effects on bluff bodies and stalled wings in a closed wind tunnel*. British ARC R&M, No. 3400.

Timmer W.A. *Wind Tunnel Wall Corrections for Two-Dimensional Testing up to Large Angles of Attack*. (2021) In: Stoevesandt B., Schepers G., Fuglsang P., Yeping S. (eds) *Handbook of Wind Energy Aerodynamics*. Springer, Cham. [https://doi.org/10.1007/978-3-030-05455-7\\_27-1](https://doi.org/10.1007/978-3-030-05455-7_27-1)

Wang, L., Jiao, Y. and Gao, Y. (2015) *Airfoil wind tunnel correction for angles of attack from -180° to 180°*, *Wind Energy*, vol.18, pp.1487–1500.

## APPENDIX B

# The impact of a flap deflection on the maximum drag coefficient of airfoil DU95-W-180

### B1 INTRODUCTION

The wind tunnel of the Deutsche Wind Guard Engineering (DWG) in Bremerhaven, Germany, features a test section of  $1.25 \times 2.75 \text{ m}^2$ , which enables the exchange of models between DWG and the TUDelft Low Speed Laboratory, since models tested in the TU Delft LTT have the same span of 1.25m. Wind turbine blade manufacturers also profit from this possibility as it gives an alternative since wind tunnel slots are scarce. Fig. B1 gives an impression of the inside of the test section (with a flat plate attached to the balance system) and a side view on a 0.2 m chord model.

The tunnel was used for a number of studies, predominantly in view of the difference in blockage. A 0.6m chord model has a  $c/h$  value in the LTT of 0.362, while in the DWG tunnel this becomes 0.218.

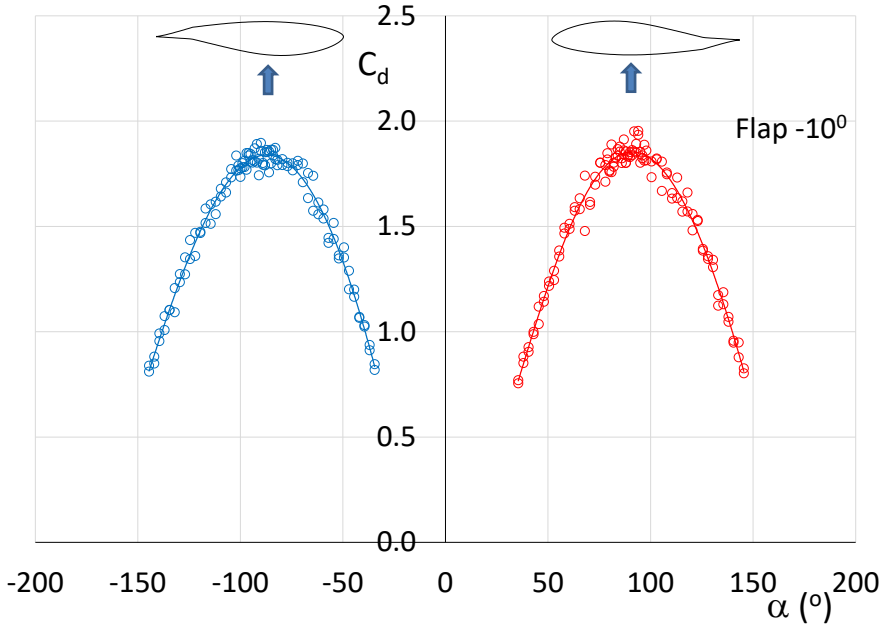


*Fig. B1: The  $1.25 \times 2.75 \text{ m}^2$  test section of the DWG, showing a flat plate attached to the balance system under  $90^\circ$  incidence (left) and a 0.2m model (right). Courtesy DWG*

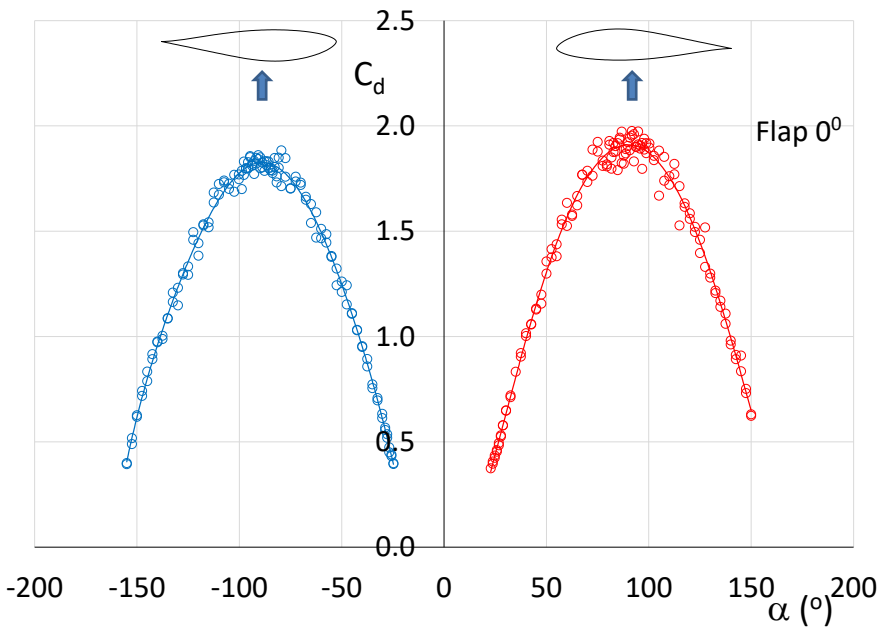
### B2 THE IMPACT OF A FLAP ANGLE ON THE DRAG CHARACTERISTICS

In view of mutual interest, DWG performed a study using the flapped 0.60 m chord model of DU95-W-180 to measure the low-speed characteristics in the  $-180^\circ$  to  $180^\circ$  angle of

attack range for 6 flap angles between  $-10^\circ$  and  $10^\circ$  at a Reynolds number of  $0.83 \times 10^6 \pm .07 \times 10^6$ . The model was attached to a balance and the angle of attack was slowly adjusted through a  $-180^\circ$  to  $180^\circ$  rotation and back. The data were binned in  $1^\circ$  intervals both for  $\pm 10^\circ$  around the maximum drag and in  $2.5^\circ$  intervals in the



(a)



(b)

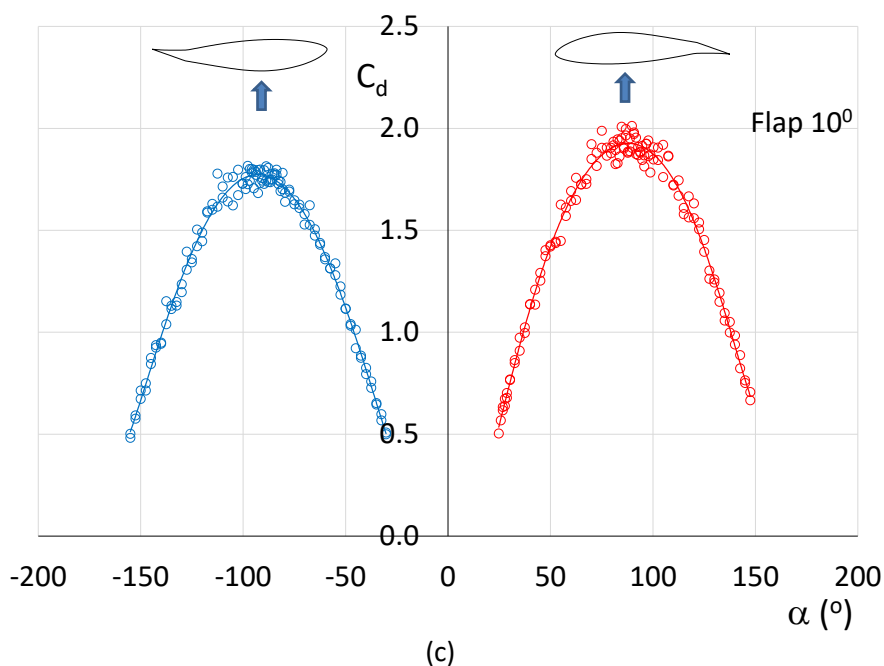


Figure B2: The corrected drag coefficients in the interval  $-180^{\circ}$  to  $180^{\circ}$  for flap angles of  $-10^{\circ}$  (a),  $0^{\circ}$  (b) and  $10^{\circ}$  (c) measured in the  $1.25 \times 2.75 \text{m}^2$  wind tunnel of DWG

rest of the rotation. Figures B2 (a) to (c) give the corrected drag data for flap angles of  $-10^{\circ}$ ,  $0^{\circ}$  and  $10^{\circ}$ . The maximum drag coefficients were determined from 6<sup>th</sup> degree polynomials and were corrected for the small chord reduction due to the flap deflection. For every flap angle the  $y/c$  coordinates at the  $x/c=0.0125$  station were determined, with the airfoil at the longest chord. In addition, the trailing edge angle was calculated at the lower surface trailing edge for positive angles of attack and vice versa. The data are presented in table B1.

Table B1: The measured maximum drag coefficients for 6 flap settings of airfoil DU95-W-180 with the associated TE-angle.

$\alpha < 0$ (y/c and TE-angle u.s.)				$\alpha > 0$ (y/c and TE-angle l.s.)		
Flap angle	y/c u.s.	$\zeta$ l.s.	$C_{d,max}$	y/c l.s.	$\zeta$ u.s.	$C_{d,max}$
deg.		deg.			deg.	
-14.78	0.01963	0.0				
-10	0.01980	3.82	1.845	0.01595	10.12	1.859
-5	0.02016	7.83	1.825	0.01569	6.11	1.886
0	0.02055	11.83	1.823	0.01544	2.11	1.912
2	0.02071	13.43	1.785	0.01534	0.51	1.900
2.64				0.01531	0.0	
6	0.02104	16.63	1.763	0.01516	-2.69	1.887
10	0.02139	19.83	1.769	0.01499	-5.89	1.942

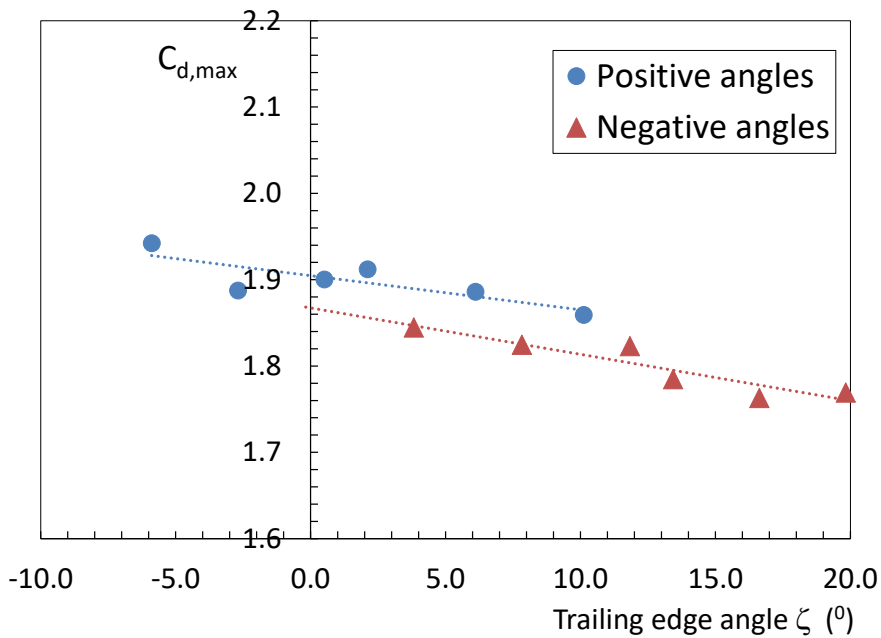
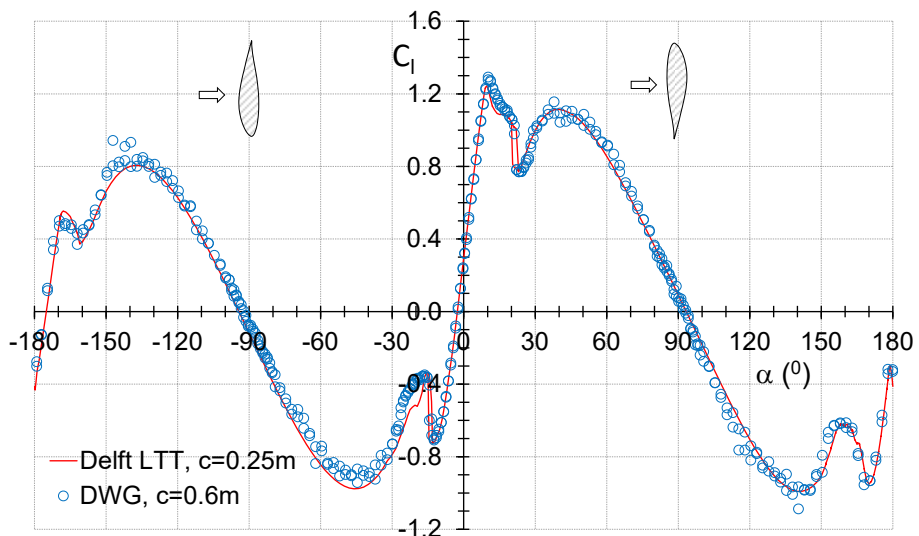


Figure B3: The measured drag coefficients from DWG measurements on DU95-W-180 for several flap deflections.

The table also shows the  $y/c$  coordinates for a zero TE-angle. Values for  $\zeta$  are positive when the TE moves counter-clockwise. Fig. B3 is a graphical representation of the table. Interpolation for positive angles and extrapolation for the negative angles to  $\zeta=0$  gives  $C_{d,max}$  values of 1.867 and 1.905 for  $y/c = 0.01963$  and  $0.01531$  respectively. In fig. B4 the measurements at a flap angle of  $2^\circ$  are compared with the results of the DU96 tests with the 0.25m chord model ( $c/h=0.151$ ) The DWG angle was corrected with



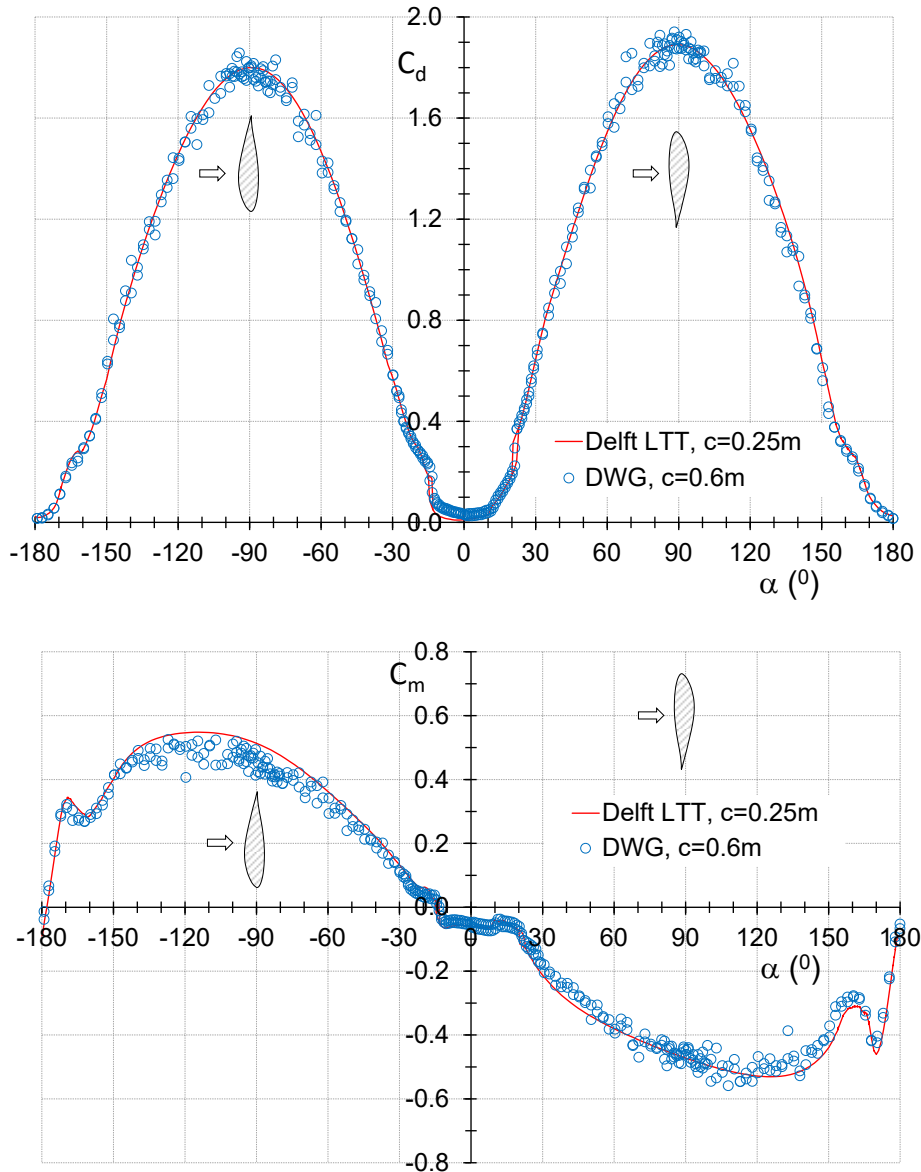


Figure B4: Comparison of the lift, drag and moment coefficients of the DU96 0.25m chord model tested in the LTT ( $Re=0.7 \times 10^6$ ) and the 0.6m chord DU95 with a flap deflection of 2 degrees measured at DWG. DWG angles adjusted with  $0.4^\circ$ ,  $Re \approx 0.8 \times 10^6$

$0.4^\circ$  to put the chord parallel to the flow at  $\alpha=0$  and match the DU 96 zero-lift angle. There is a generally good agreement between the datasets considering the differences in chord and test setup.



# LIST OF PUBLICATIONS

What follows is a list of international publications in books, scientific journals and proceedings of conferences, both as first author and as co-author.

## BOOK CHAPTERS

Timmer, W.A., Bak, C. (2023) *Aerodynamic characteristics of wind turbine blade airfoils*. (2023) *Advances in Wind Turbine Blade Design and Materials*, second edition, pp. 129-167. Elsevier Limited. DOI: 10.1016/B978-0-08-03007-3.00011-2

Timmer W.A. (2021) *Wind Tunnel Wall Corrections for Two-Dimensional Testing up to Large Angles of Attack*. In: Stoevesandt B., Schepers G., Fuglsang P., Yuping S. (eds) *Handbook of Wind Energy Aerodynamics*. pp. 601-629. Springer International Publishing, DOI: 10.1007/978-3-030-31307-4\_27

Timmer, W.A., Bak, C. (2013) *Aerodynamic characteristics of wind turbine blade airfoils*. *Advances in Wind Turbine Blade Design and Materials*, pp. 109-149. Woodhead Publishing Limited, UK. DOI: 10.1533/9780857097286.1.109

Timmer, W.A., van Bussel, G.J.W. (2007) *Wind turbine airfoil design and testing*. In JF. Brouckaert (Ed.), *Wind turbine aerodynamics: A state-of-the-art* (pp. -). von Karman Institute.

## JOURNALS AND CONFERENCE PROCEEDINGS

Mouton, S., Schaffarczyk, A.P. and Timmer, N. (2024) *Wind Tunnel Tests of a Thick Wind Turbine Airfoil*. *Wind Energy*, 27(10), 994-1010. <https://doi.org/10.1002/we.2938>

Timmer, N., Veldhuis, L. (2021) *The impact of skinsuit zigzag tape turbulators on speed skating performance*. *Journal of Applied Sciences*, 11 (3), art. no. 988, pp. 1-18. DOI: 10.3390/app11030988

Timmer, W.A. (2020) *A simple method to estimate the airfoil maximum drag coefficient*. *Journal of Physics Conference Series*, 1618 (5), art. no. 052068, DOI: 10.1088/1742-6596/1618/5/052068

Steiner, J., Viré, A., Benetti, F., Timmer, N., Dwight, R. (2020) *Parametric slat design study for thick-base airfoils at high Reynolds numbers*. *Wind Energy Science*, 5 (3), pp. 1075-1095. DOI: 10.5194/wes-5-1075-2020

Baldacchino, D., Ferreira, C., Tavernier, D.D., Timmer, W.A., van Bussel, G.J.W. (2018). *Experimental parameter study for passive vortex generators on a 30% thick airfoil*. Wind Energy, 21 (9), pp. 745-765. DOI: 10.1002/we.2191

De Oliveira, G., Pereira, R., Timmer, N., Van Rooij, R. (2018) *Improved airfoil polar predictions with data-driven boundary-layer closure relations*. Journal of Physics Conference Series, 1037 (2), DOI: 10.1088/1742-6596/1037/2/022009

Pereira, R., De Oliveira, G., Timmer, W.A., Quaeghebeur, E. (2018) *Probabilistic Design of Airfoils for Horizontal Axis Wind Turbines*. Journal of Physics Conference Series, 1037 (2), DOI: 10.1088/1742-6596/1037/2/022042

De Oliveira, G., Timmer, W.A. and van Oudheusden, B.W. (2018) *Integral Equations for Boundary Layers with Streamwise Vortices*. Proc. 52nd 3AF International Conference on Applied Aerodynamics: 27 – 29 March 2017, Lyon – France

Pires, O., Munduate, X., Boorsma, K., Ceyhan Yilmaz, O., Aa Madsen, H., Timmer, W.A. (2018). *Experimental investigation of Surface Roughness effects and Transition on Wind Turbine performance*. Journal of Physics Conference Series, 1037 (5), art. no. 052018, DOI: 10.1088/1742-6596/1037/5/052018

Yilmaz, O.C., Timmer, W.A. (2018) *Experimental evaluation of a non-conventional flat back thick airfoil concept for large offshore wind turbines*. Applied Aerodynamics Conference, AIAA 2018-3827, DOI: 10.2514/6.2018-3827

Pereira, R., Timmer, W.A., de Oliveira, G., van Bussel, G.J.W. (2017) *Design of HAWT airfoils tailored for active flow control*. Wind Energy, 20 (9), pp. 1569-1583. DOI: 10.1002/we.2109

Baldacchino, D., Manolesos, M., Ferreira, C., González Salcedo, Á., Aparicio, M., Chaviaropoulos, T., Diakakis, K., Florentie, L., García, N.R., Papadakis, G., Sørensen, N.N., Timmer, N., Troldborg, N., Voutsinas, S., Van Zuijlen, A. (2016) *Experimental benchmark and code validation for airfoils equipped with passive vortex generators*. Journal of Physics Conference Series, 753 (2), DOI: 10.1088/1742-6596/753/2/022002

Ubbens, H.H., Dwight, R.P., Sciacchitano, A., Timmer, N. (2016) *Some Results on Bobsleigh Aerodynamics*. Procedia Engineering, 147, pp. 92-97. DOI: 10.1016/j.proeng.2016.06.195

Llorente, E., Gorostidi, A., Jacobs, M., Timmer, W.A., Munduate, X., Pires, O. (2014). *Wind tunnel tests of wind turbine airfoils at high Reynolds numbers*. Journal of Physics Conference Series, 524 (1), art. no. 012012, DOI: 10.1088/1742-6596/524/1/012012

Pereira, R., Van Bussel, G.J.W., Timmer, W.A. (2014). *Active stall control for large offshore horizontal axis wind turbines; A conceptual study considering different actuation methods*. Journal of Physics Conference Series, 555 (1), art. no. 012082, DOI: 10.1088/1742-6596/555/1/012082

Pereira, R., Van Bussel, G.J.W., Timmer, W.A. (2014) *Global optimization of horizontal axis wind turbine rotors including active stall control*. EWEA 2014, Barcelona, Spain.

Saunders-Smiths, G.N., Roling, P., Brügemann, V., Timmer, N., Melkert, J. (2012) *Using the engineering design cycle to develop integrated project based learning in aerospace engineering*. EE 2012 International Conference on Innovation Practice and Research in Engineering Education Conference Proceedings.

Timmer, W.A. (2010). *Aerodynamic characteristics of wind turbine blade airfoils at high angles-of-attack*. Conference proceedings TORQUE 2010: The Science of Making Torque from Wind, June 28-30 2010, Crete, Greece. DOI: 10.1533/9780857097286.1.109

Timmer, W.A. (2009) *An overview of NACA 6-digit airfoil series characteristics with reference to airfoils for large wind turbine blades*. 47th AIAA Aerospace Sciences Meeting Including the New Horizons Forum and Aerospace Exposition, art. no. 2009-0268,

Timmer, W.A. (2008) *Two-dimensional low-Reynolds number wind tunnel results for airfoil NACA 0018*. Wind Engineering, 32 (6), pp. 525-537. DOI: 10.1260/030952408787548848

Timmer, W.A., Schaffarczyk, A.P. (2004) *The effect of roughness at high Reynolds numbers on the performance of aerofoil DU 97-W-300Mod*. Wind Energy, 7 (4), pp. 295-307. DOI: 10.1002/we.136.

Timmer, W.A., Van Rooij, R.P.J.O.M. (2003) *Summary of the Delft University wind turbine dedicated airfoils*. ASME 2003 Wind Energy Symposium Wind2003, pp. 11-21. DOI: 10.1115/wind2003-352

Timmer, W.A., Van Rooij, R.P.J.O.M. (2003) *Summary of the Delft University wind turbine dedicated airfoils*. (2003) Journal of Solar Energy Engineering Transactions of the ASME, 125 (4), pp. 488-496.

DOI: 10.1115/1.1626129

Timmer, W.A. (2003) *Airfoil performance at high angles-of-attack*. EWEC conference, Madrid, 16-19 June 2003.

Van Rooij, R.P.J.O.M., Timmer, W.A. (2003) *Roughness sensitivity considerations for thick rotor blade airfoils*. ASME 2003 Wind Energy Symposium Wind2003, pp. 22-31. DOI: 10.1115/wind2003-350

Van Rooij, R.P.J.O.M., Timmer, W.A. (2003) *Roughness sensitivity considerations for thick rotor blade airfoils*. Journal of Solar Energy Engineering Transactions of the ASME, 125 (4), pp. 468-478.

DOI: 10.1115/1.1624614

Timmer, W.A., van Rooy, R.P.J.O.M. (2001) *Some aspects of high angle-of-attack flow on airfoils for wind turbine application*. In: Proceedings of the European Wind Energy Conference 2001, July 2-6, Copenhagen, Denmark.

Vermeer, N.J., Timmer, W.A. (1999) *Identification of Operational Aerofoil State by means of Velocity Measurements*. Proceedings European Wind Energy Conference, Nice, France March 1999.

Timmer, W.A. and van Rooij, R.P.J.O.M. (1993) *Wind tunnel results for a 25% thick airfoil*. Proc. European Community Wind Energy Conference, March 8-12 1993, Lübeck-Travemünde, Germany.

Timmer, W.A., van Rooy, R.P.J.O.M. (1992). *Thick airfoils for HAWTs*. Journal of Wind Engineering and Industrial Aerodynamics, 39 (1-3), pp. 151-160. DOI: 10.1016/0167-6105(92)90541-H

Bruining, A., Timmer, W.A. (1992) *Airfoil characteristics of rotating wind turbine blades*. Journal of Wind Engineering and Industrial Aerodynamics, 39 (1-3), pp. 35-39. DOI: 10.1016/0167-6105(92)90530-N

Timmer, W.A., van Rooij, R.P.J.O.M. (1991). *Thick airfoils for HAWT's*. Proc. European Wind Energy Conference, October 14-18 1991, Amsterdam, The Netherlands.

Timmer, W.A., (1990) *WECS-blade airfoils; the NACA 63-4xx airfoil family*, European Community Wind Energy Conference, September 1990 Madrid, Spain.

Boermans, L.M.M., Donker Duyvis, F.J.D., van Ingen, J.L., Timmer, W.A. (1989) *Experimental aerodynamics characteristics of the airfoils LA 5055 and DU 86-084/18 at low Reynolds numbers*. Proc. Low Reynolds Number Aerodynamics Conf., Notre Dame USA, June 5-7 1989, T. J. Mueller (ed.)



# CURRICULUM VITAE

Wijnand Alex (Nando) Timmer was born on March 15<sup>th</sup> 1956 in Hierden, The Netherlands. After attending the VWO at the Christelijk College Nassau Veluwe in Harderwijk from 1968 to 1974, he studied Aerospace Engineering at Delft University of Technology, from which he graduated in 1984 with a thesis on the experimental performance of sailplane airfoil HQ17/14.38. Next, he started to work as an aerodynamicist for the TU Delft Wind Energy Institute, which later on was embedded in the Faculty of Civil Engineering, until it became a regular section of the Aerospace Faculty Department of Aerodynamics, Wind Energy and Flight Performance & Propulsion (at present Department of Flow Physics and Technology). Throughout his career at TU Delft he has been involved in both wind energy and aerospace education and in (experimental) research on airfoils and wind turbine blades.

With a background in aerodynamics and wind tunnel testing he was also engaged in low-drag race suit design for (Olympic) athletes, particularly in speed-skating and time trial cycling and of performance enhancement in bob-sleighting.

He was responsible for the design of the Delft University Aerospace Faculty 7.48m<sup>2</sup> Open Jet Wind Tunnel Facility (OJF) for rotor testing, the design of the 0.6x0.9m<sup>2</sup> low-speed wind tunnel (SLT) and the aerodynamic re-design of the 0.6m diameter aero-acoustic wind tunnel (A-tunnel).

In 2014 he was appointed Scientific Director of the Aerospace Faculty wind tunnel laboratories, which task he performed for 9 years. He retired in October 2023. He's the father of Eefje, Jonas and Marieke and currently lives in The Hague with his partner Gera.





